

Springer Geology

Tatiana Chaplina *Editor*

Processes in GeoMedia—Volume II

 Springer

Springer Geology

Series Editors

Yuri Litvin, Institute of Experimental Mineralogy, Moscow, Russia

Abigail Jiménez-Franco, Del. Magdalena Contreras, Mexico City, Estado de México, Mexico

Soumyajit Mukherjee, Earth Sciences, IIT Bombay, Mumbai, Maharashtra, India

Tatiana Chaplina, Institute of Problems in Mechanics, Russian Academy of Sciences, Moscow, Russia

The book series Springer Geology comprises a broad portfolio of scientific books, aiming at researchers, students, and everyone interested in geology. The series includes peer-reviewed monographs, edited volumes, textbooks, and conference proceedings. It covers the entire research area of geology including, but not limited to, economic geology, mineral resources, historical geology, quantitative geology, structural geology, geomorphology, paleontology, and sedimentology.

More information about this series at <http://www.springer.com/series/10172>

Tatiana Chaplina
Editor

Processes in GeoMedia— Volume II

 Springer

Editor
Tatiana Chaplina
Institute of Problems in Mechanics
Russian Academy of Sciences
Moscow, Russia

ISSN 2197-9545

Springer Geology

ISBN 978-3-030-53520-9

<https://doi.org/10.1007/978-3-030-53521-6>

ISSN 2197-9553 (electronic)

ISBN 978-3-030-53521-6 (eBook)

© The Editor(s) (if applicable) and The Author(s), under exclusive license to Springer Nature Switzerland AG 2021

This work is subject to copyright. All rights are solely and exclusively licensed by the Publisher, whether the whole or part of the material is concerned, specifically the rights of translation, reprinting, reuse of illustrations, recitation, broadcasting, reproduction on microfilms or in any other physical way, and transmission or information storage and retrieval, electronic adaptation, computer software, or by similar or dissimilar methodology now known or hereafter developed.

The use of general descriptive names, registered names, trademarks, service marks, etc. in this publication does not imply, even in the absence of a specific statement, that such names are exempt from the relevant protective laws and regulations and therefore free for general use.

The publisher, the authors and the editors are safe to assume that the advice and information in this book are believed to be true and accurate at the date of publication. Neither the publisher nor the authors or the editors give a warranty, expressed or implied, with respect to the material contained herein or for any errors or omissions that may have been made. The publisher remains neutral with regard to jurisdictional claims in published maps and institutional affiliations.

This Springer imprint is published by the registered company Springer Nature Switzerland AG
The registered company address is: Gewerbestrasse 11, 6330 Cham, Switzerland

Contents

Determination of the Condition of Road Coverings by Acoustic Noise Data	1
K. V. Fedin, Yu. I. Kolesnikov, and L. Ngomayezwe	
Diagnosis of the Technical Condition of Standing Wave Support for Pipeline	5
K. V. Fedin, Yu. I. Kolesnikov, and L. Ngomayezwe	
Determination of Ice Thickness Using Standing Waves	9
K. V. Fedin, Yu. I. Kolesnikov, and L. Ngomayezwe	
Development of Methods for Wind Speed and Wave Parameters Forecasting in Inland Waters	15
Fedor Loktev, Alexandra Kuznetsova, Georgy Baydakov, and Yulia Troitskaya	
The Geoecological Assessment of the Internal and External Biogenous Load of the Waters of the Gulf of Taganrog of the Sea of Azov	21
A. Yu. Zhidkova, T. A. Bednaya, and V. V. Podberesnij	
Manifestation of Downward Solar Radiation Flux in the Variability of Sea Ice Concentration and Krill Fishery in the Antarctic	31
A. A. Bukatov and M. V. Babiy	
Estimation of Waters Vertical Structure in the Barents and Kara Seas	41
A. A. Bukatov, E. A. Pavlenko, and N. M. Solovei	
Variational Identification of the Underwater Pollution Source Power	55
Sergey Vladimirovich Kochergin and Vladimir Vladimirovich Fomin	

Analytical Solution of the Test Three-Dimensional Problem of Wind Flows	65
Vladimir Sergeevich Kochergin, Sergey Vladimirovich Kochergin, and Sergey Nikolaevich Sklyar	
Seasonal Variations of the Significant Altitude of the Waves in the Black Sea	73
N. N. Voronina	
Calculation of the Turbulent Exchange Intensity in the Sea Upper Homogeneous Layer	81
A. M. Chukharev and A. S. Samodurov	
Modelling of Fracture Acidizing	89
Regina Kanevskaya and Aleksei Novikov	
Underground Density-Driven Convection of Saline Fluids with Constant and Variable Viscosity	107
E. B. Soboleva	
Phase Spectra of a Multicomponent Wave Field	115
A. S. Zapevalov	
Modeling the Dispersion Distribution of Sea Surface Slopes Over the Ranges of Waves Creating Them	123
A. S. Knyazkov and A. S. Zapevalov	
Determination of Permeability–Porosity–Stresses Dependence for Loose Media Based on Inverse Problem Solution by Lab Test Data	133
Leonid Nazarov, Larisa Nazarova, Dominique Bruel, and Nikita Golikov	
Incompressible Viscous Steady Fluid Flows in a Plane Diffuser	143
S. A. Kumakshev	
On Relationship Between Variations in Total Atmospheric Methane Levels and Climate Warming in the Russian Far East in Summer Months	153
A. V. Kholoptsev and S. A. Podporin	
Geology and Gold Mineralization of Lower Carboniferous Deposits of the Kommercheskoye Deposit (Kumak Ore Field)	163
A. V. Kolomoets, V. S. Pantelev, N. R. Kutuyeva, A. B. Mumenov, and D. F. Yakshigulov	
Direct Numerical Simulation of Droplet Deformation in External Flow at Various Reynolds and Weber Numbers	169
Anna Zotova, Yulia Troitskaya, Daniil Sergeev, and Alexander Kandaurov	

North Atlantic Oscillation and Arctic Air Outbreaks	175
A. V. Kholoptsev, S. A. Podporin, and T. Ya. Shulga	
Information Resources of Marine Hydrophysical Institute, RAS: Current State and Development Prospects	187
T. M. Bayankina, E. A. Godin, E. V. Zhuk, A. V. Ingerov, E. A. Isaeva, and M. P. Vetsalo	
Sea Bottom Sediments Pollution of the Crimean Coast (The Black and Azov Seas)	199
E. A. Tikhonova, E. A. Kotelyanets, and O. V. Soloveva	
Uppermost Sediments Diapirism in the Western Mediterranean	213
A. A. Schreider and A. E. Sazhneva	
Method for Detection of the Vessel Trace Anomalies in the Sea Surface Images Based on Analysis of Color Gradient Correlations	219
M. K. Klementiev, V. N. Nosov, V. I. Timonin, and L. M. Budovskaya	
Current Water and Salt Regime of the Sivash Bay	225
E. E. Sovga, E. S. Eremina, L. V. Kharitonova, and T. V. Khmara	
Continuum Model of Layered Medium for Reservoir of Bazhenov Formation	235
V. I. Golubev, A. V. Ekimenko, I. S. Nikitin, and Yu. A. Golubeva	
Intensifying Mixing During Vortex Motion in a T-Shaped Micromixer	247
A. Yu. Kravtsova, Yu. E. Meshalkin, M. V. Kashkarova, A. V. Bilsky, and I. V. Naumov	
Manifestation of the Quintet of the Fundamental Spheroidal Mode ${}_0S_2$ of Earth's Free Oscillations in Electromagnetic Variations at the Mikhnevo Observatory	257
S. A. Riabova, A. A. Spivak, and V. A. Kharlamov	
Structure Factors of Gold Mineralization Formation on the Example of Kumak Gold Deposit (Eastern-Urals Uplift)	265
A. V. Kolomoets, P. V. Pankratev, M. Yu. Nesterenko, R. S. Kisil, and V. S. Panteleev	
About the Modern System of Three Energy-Carrying Intensive Vortices in the Earth's Mantle	273
S. Y. Kasyanov and V. A. Samsonov	
Multidecadal Variability of the Hydrothermodynamic Characteristics of the North Atlantic Subpolar Gyre	293
N. A. Diansky and P. A. Sukhonos	

On the Factors Affecting Mixed Layer Depth in the Inland Water Objects	301
D. Gladskikh, V. Stepanenko, and E. Mortikov	
The Forecasting and Searching Gemstone Deposits. Criteria for Forecasting	311
V. G. Gadiyatov, V. V. Bagdasarova, P. I. Kalugin, O. V. Sibirskikh, and A. I. Demidenko	
Weddell-Scotia Continental Bridge Destruction	329
A. A. Schreider and A. E. Sazhneva	
Influence of Large-Scale Atmospheric Circulation Modes on the Danube Runoff Anomalies During the Flood Period	335
V. L. Pososhkov	
Experimental Study of the Effect of Filtration for Low-Mineralized Water with High Temperature on Changes in Elastic and Strength Properties of Reservoir Rocks	343
S. N. Popov and A. S. Kusaiko	
Study of the Sea Foam Impact on the Wind-Wave Interaction Within the Laboratory Modeling	351
G. A. Baydakov, M. I. Vdovin, A. A. Kandaurov, D. A. Sergeev, and Yu. I. Troitskaya	
On the Influence of Stratification and Shear on the Turbulent Mixing in Inland Waters	357
D. Gladskikh, I. Soustova, Yu. Troitskaya, and E. Mortikov	
Experimental Studies of the Earth Rotation Impact on Tides in the Curvilinear Bays	365
V. N. Zyryanov and M. K. Chebanova	
Mathematical Modeling of the Dynamics of a Rotating Layer of an Electrically Conducting Fluid with Magnetic Field Diffusion Effects	377
S. I. Peregudin, E. S. Peregudina, and S. E. Kholodova	
Geomagnetic Diurnal Variation at Mikhnevo Geophysical Observatory	389
Riabova Svetlana	
Modeling of the Extreme Wind Waves in the Gorky Reservoir	399
E. V. Stolyarova, S. A. Myslenkov, G. A. Baydakov, and A. M. Kuznetsova	

Determination of the Condition of Road Coverings by Acoustic Noise Data



K. V. Fedin, Yu. I. Kolesnikov, and L. Ngomayezwe

Abstract To ensure the safe operation of roads, periodic monitoring of the condition of the road surface is necessary. Recently, such studies are widely used methods of shallow geophysics. The article presents the results of full-scale experiments, demonstrating the possibility of detecting cavities under a hard road surface by bending standing waves. To isolate standing waves from the acoustic noise recorded on the surface of the coating, we used the accumulation of amplitude spectra of a large number of noise records. The fact that under the influence of acoustic noise bending standing waves are formed in the coating, which are absent in other places, indicates the absence of hard contact at its lower boundary. Thus, by the size of the area on which bending standing waves are formed, it is possible to estimate the horizontal dimensions of the cavity. In addition, the article shows that the analysis of standing waves of vertical compression-tension arising in the coating under the influence of noise makes it possible to control the thickness of the coating.

Keywords Standing waves · Roads · Microseisms

To ensure the safe operation of roads, it is necessary to periodically monitor the condition of the road surface. Such monitoring may be carried out by various methods with the help of visual inspection, drilling with sampling and subsequent core analysis, deflection measurement with deflectometers, etc.

K. V. Fedin (✉) · Yu. I. Kolesnikov
Trofimuk Institute of Petroleum Geology and Geophysics SB RAS, Akademika Koptyuga Pr. 3,
630090 Novosibirsk, Russia
e-mail: fedinkv@ipgg.sbras.ru

K. V. Fedin · Yu. I. Kolesnikov · L. Ngomayezwe
Novosibirsk State University, Pirogova Street 2, 630090 Novosibirsk, Russia

K. V. Fedin
Novosibirsk State Technical University, Karl Marx Avenue 20, 630073 Novosibirsk, Russia

Lately, to study the quality and condition of pavements, near-surface geophysical methods are increasingly being applied. Most often, geo-radar technologies are used to solve such problems (Kulizhnikov 2001), but there are also other examples of geophysical methods which are used for studying the condition of roads, for example, electric tomography (Olenchenko and Kondratiev 2017) and others. This paper presents study results showing the possibility of using elastic standing waves to detect and delineate cavities under a rigid pavement.

In previously published works (Kolesnikov and Fedin 2015; Kolesnikov and Fedin 2018), we proposed a passive seismic method to detect underground voids, based on the separation of standing waves from a noise field generated by microseisms in the space between the earth surface and the sharp edge closest to it - the upper surface of the cavity or the base of the near-surface low velocity layer (LVL). As shown by the results of physical modeling and field experiments, the accumulation of a large number of amplitude spectra of relatively short fragments of the records of the vertical component of microseisms leads to the appearance of regular peaks on the averaged spectrum corresponding to standing compression-extension waves. The method for detecting voids is based on the fact that the frequencies of standing waves above the voids and the sole of the VMS differ sharply.

In the case of a hard pavement lying on a softer foundation, the frequencies of the standing compression-extension waves over the undisturbed foundation and over the cavity under the coating practically do not change, which makes the application of this method ineffective. We hypothesized that in this case, analysis of bending standing waves generated in the road surface directly above the cavity may turn out to be more effective.

To assess the possibility of diagnosing rigid pavements with elastic standing waves, we carried out experimental work on the registration of noise records on the sidewalk of Pirogova street in the Novosibirsk Akademgorodok (Fig. 1a). The sidewalk has a rigid pavement, the upper part of which is an asphalt layer with a thickness of 4–4.5 cm, according to visual assessments. On the sidewalk detailed areal observations over the gully formed under the asphalt surface at its edge were made (Fig. 1b).

The dimensions of the cavity were approximately 105 cm along the sidewalk edge and 65–70 cm at the widest point in the transverse direction. In this section, the measurements were performed at the nodes of the square grid on the areal observation system with dimensions of 120 cm in the direction along the sidewalk and 70 cm across with a step of 2 cm between adjacent observation points. Due to the uneven edge of the pavement near its edge (in a strip of about 7–10 cm), no observations were made. Two perpendicular profiles shown in Fig. 1b with red lines give an idea of the relative dimensions of the observing system and the gaps under the asphalt pavement. The data for these profiles were analyzed in more detail than for the remaining points of the areal observation system.

To register noise signals, we used equipment already used in laboratory experiments on physical modeling (Kolesnikov and Fedin 2018) that records signals in a different frequency range.

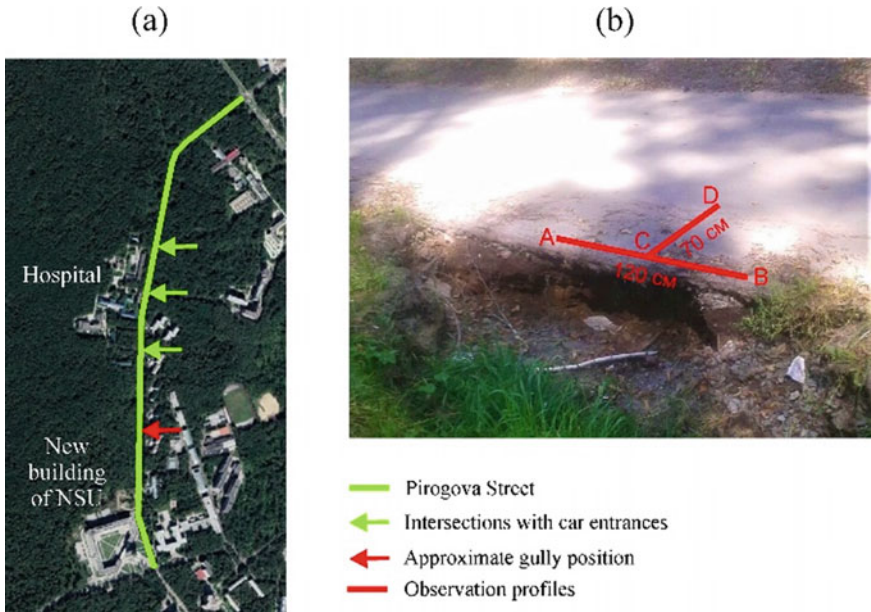


Fig. 1 a Scheme of the work site, b the position of two perpendicular profiles of the areal observational system over the gully formed under the asphalt pavement

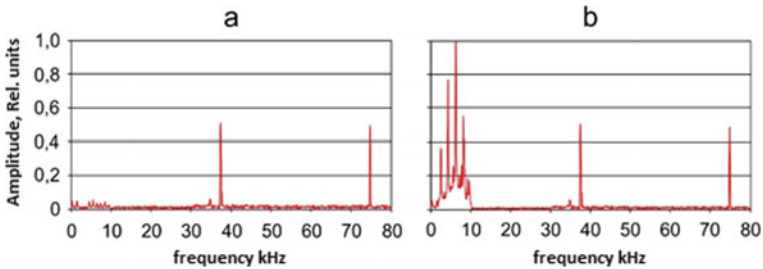


Fig. 2 Examples of averaged amplitude spectra of noise records obtained a away from the gully and b above it

During processing, the noise records were divided into fragments of approximately 33 ms, after which the amplitude spectra of these fragments were accumulated. Examples of averaged amplitude spectra for observation points away from and above the cavity are shown in Fig. 2. It can be seen that outside the cavity (Fig. 2a), two sharp peaks with frequencies of 37.4 kHz and 74.8 kHz are observed in the spectrum, which is consistent with Equation.

These peaks correspond to standing waves of vertical compression-tension.

Above the cavity (Fig. 2b), the averaged spectrum has significant differences from that shown in Fig. 2a, the peaks correspond to bending standing waves. Figure 3 shows

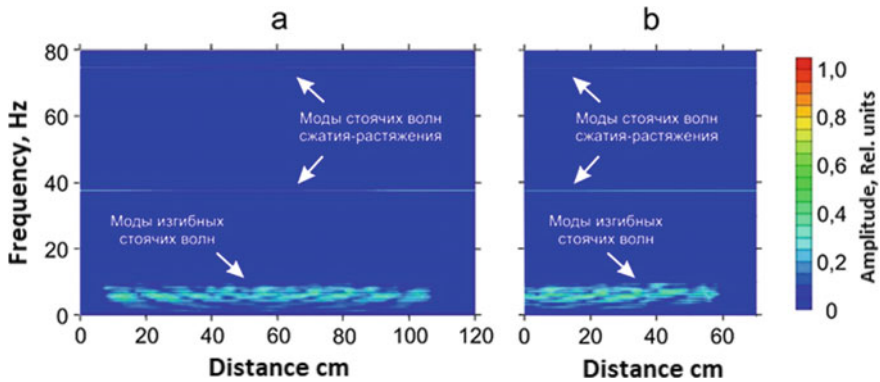


Fig. 3 Distribution of averaged amplitude spectra of noise recordings along profiles **a** AB and **b** CD

the averaged amplitude spectra of noise records recorded at all points of two profiles, which are shown in Fig. 1 red lines.

The obtained experimental results showed that the standing wave method can be successfully used to detect voids under a hard road surface, as well as to control its thickness and estimate the ratio of acoustic stiffness of the coating and the underlying layer. Standing waves can be extracted from the noise field by accumulating a large number of amplitude spectra of noise signals recorded on the surface of the road surface.

Although the proposed method in this modification is not very technologically advanced, it can be successfully used for a detailed study of pavement areas on which gullies or cavities of a different nature periodically appear, as well as to refine the results of more productive but less accurate methods. Moreover, the manufacturability of the method can be increased, for example, by using more powerful artificial sources of both noise and non-noise types, for example, vibrators in the mode of emission of sweep signals with a sufficiently wide frequency range.

References

- Kolesnikov YuI, Fedin KV (2015) Detection of underground voids by microseisms: physical modeling. *Seismic Explor Technol* (4):89–96. (in Russian)
- Kolesnikov YuI, Fedin KV (2018) Detecting underground cavities using microtremor data: physical modelling and field experiment. *Geophys Prospect* 66(2):342–353
- Kulizhnikov AM (2001) Application of georadar technologies in the road service. *Prospect and protection of mineral resources*, 3:32–34. (in Russian)
- Olenchenko VV, Kondratiev VG (2017) Geophysical investigations within the defonnation section of a motorway constructed on a frozen base. *Bull North-Eastern State Univ* (27):116–119. (in Russian)

Diagnosis of the Technical Condition of Standing Wave Support for Pipeline



K. V. Fedin, Yu. I. Kolesnikov, and L. Ngomayezwe

Abstract Field experiments were conducted to record acoustic noise on the surface of an above-ground pipeline (existing heating main). Research was carried out on sections of the pipeline with various types of fastening—rigid (pipes welded to the support) and non-rigid (heat-insulating tube freely lies on the support rack). Experiments have shown that noise waves can create certain frequencies and shapes of bending waves that occur in spans of a pipeline. Depending on how rigid and reliable the fasteners are, they can be used to diagnose sections of the pipeline by acoustic noise. In computer simulation by the finite element method, the frequencies of bending waves were obtained, which are close to some experimental ones. The interaction between the nodes and beams of bending waves passing along the spans of pipes with different types of fastening to quality is consistent with laboratory experiments conducted earlier.

Keywords Standing waves · Buckling · Microseisms

Periodically occurring accidents on pipelines cause damage to the environment, increase land pollution and sometimes human losses.

A significant decrease in the rigidity of the pipe fastening to the support leads to an actual increase in the length of the span of the pipeline, which can lead to damage or even destruction of this pipeline section. On the other hand, such an increase in the span length should lower its natural frequencies, which can serve as an indicator of a decrease in the stability of a pipeline section at an early stage of this process, when its consequences are not yet visible by naked eye.

K. V. Fedin (✉) · Yu. I. Kolesnikov
Trofimuk Institute of Petroleum Geology and Geophysics SB RAS, Akademika Koptyuga Pr. 3,
630090 Novosibirsk, Russia
e-mail: fedinkv@ipgg.sbras.ru

K. V. Fedin · Yu. I. Kolesnikov · L. Ngomayezwe
Novosibirsk State University, Pirogova Street 2, 630090 Novosibirsk, Russia

K. V. Fedin
Novosibirsk State Technical University, Karl Marx Avenue 20, 630073 Novosibirsk, Russia



Fig. 1 **a** Pipeline section with rigid pipe fastening to the support **b** pipes laid on the rack without rigid fastening recorder and **c** geophone mounted on the pipe

In this paper (Kolesnikov et al. 2012), the results of physical modeling showed that the acoustic noise data recorded on the surface of both empty and fluid-filled pipes can determine the frequencies and modes of oscillations of bending standing waves generated between their supports. To do this, it is sufficient to accumulate a large number of amplitude spectra of acoustic noise records. This information makes it possible to unambiguously diagnose a violation of a rigid pipe fastening to a support, since in places of rigid fastenings there should be no oscillations of standing waves (these are their nodal points), and if there is a violation of hard contact, vibrations in such places can be observed at least at some natural frequencies of the pipe.

To determine the natural frequencies of the pipeline elements, various techniques are used. For example, this can be done by exciting vibrations using artificial sources such as shock (Al-Sahib et al. 2010) or mechanical vibrations (Li and Guo 1990; Al-Sahib et al. 2010). This paper presents the results of a full-scale experiment demonstrating the possibility of diagnosing the technical condition of pipeline supports by standing waves generated in pipes by acoustic noise.

Two spans of the existing above-ground pipeline (heat pipeline) were selected for experimental work. The pipeline consists of two parallel steel pipes with a diameter of 46 cm, partially covered with thermal insulation materials. Every 10 m pipes are rigidly welded to massive steel supports (Fig. 1a), between which they are raised by an average of 25–30 cm above the surface of the earth, except for the intersection of sharp local landslides. with the exception of places where sharp local relief depressions intersect. In such places, pipes are laid without hard mount on higher steel stands (Fig. 1b).

A pipe filled with hot water flowing under pressure was selected for measurements. In one span, the pipe was rigidly fastened to the supports on both sides, as shown in Fig. 1a. In the second span, on one side there was a rigid fastening and on the other, the pipe was loosely laid on the stand shown in Fig. 1b. Measurements were

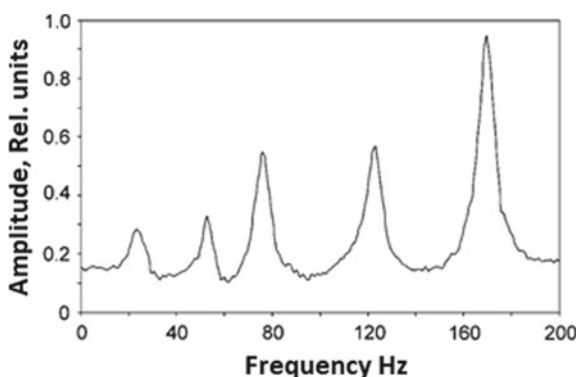


Fig. 2 Generalized amplitude spectrum of noise recordings recorded on the pipe surface between two rigid supports

carried out using vertical geophones GS-20DX and single-channel digital recorders RefTek-125A (Fig. 1c) with a sampling rate of 1 kHz. Geophones were attached to the pipe using magnetic disks. On each span, continuous noise recording was carried out for 10 min at points along the upper part of the pipe with a step of 20 cm along the entire span length.

During processing, the noise recordings recorded at each observation point were broken down into fragments with a duration of approximately 8.2 s (8192 counts), the amplitude spectra of these fragments were calculated and averaged. As a result, sharp quasi-regular peaks appear on the averaged amplitude spectra, which, as it will be shown below, correspond to the bending standing waves. For more accurate determination of the frequencies of these peaks, generalized spectra averaged over all points of the profile were also constructed. A generalized spectrum for the passage of a pipe between two rigid supports is shown in Fig. 2.

The joint visualization of the averaged spectra obtained for all observation points in each pipe span (Fig. 3) allows us to verify that the peaks observed in the amplitude spectra correspond to standing waves. It can be seen that at the frequencies of the spectral peaks (natural frequencies of the pipes), alternation of the maxima and minima of the spectral amplitudes is observed along the spans.

Since, in the general case, standing waves of different types can form in the pipes, we compared the experimental results for a span with a pipe rigidly fixed on both sides (Figs. 2 and 3a) with the results of numerical simulation in the MSC Nastran finite element system. The comparison showed that the experimentally observed alternations of the maxima and minima of the spectral amplitudes correspond to the nodes and antinodes of the five modes of bending standing waves. The differences in the frequencies of standing waves obtained in the field experiment and as a result of numerical simulation do not exceed 5.5%.

Returning to the experimental results, we note that the nature of the distribution of nodes and antinodes along the span for the two cases under consideration is significantly different. The sharp quasiregular peaks in the spectrum for a pipe with

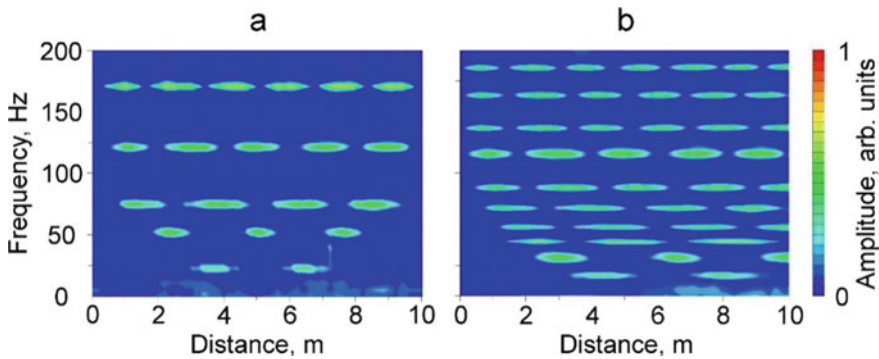


Fig. 3 (a) Distribution of averaged amplitude spectra of noise recordings on rigidly fixed supports on both sides of the pipe section and (b) on the pipe section rigidly fixed on one side and freely lying on the rack on the other side

two rigid fixtures (Fig. 3a) are located on the frequency axis approximately two times less often than for a pipe rigidly fixed on one side only (Fig. 3b).

This pattern means that in the second case, noise generated by bending standing waves are formed in a double span. This is also confirmed by the distribution features of the antinodes and nodes of standing waves along the spans. Thus, from Fig. 3a it follows that at the extreme points of the observation profile corresponding to the places of rigid fastening of the pipe to the supports, there are practically no vibrations, that is, these are the nodal points of all the bending standing waves formed in the span.

Figure 3b differs significantly from Fig. 3a. In addition to doubling the number of natural frequencies, the distribution of amplitude maxima and minima at these frequencies indicates the absence of hard contact at a point at 10 m, corresponding to the place where the pipe rests without rigid fastening on the rack shown in Fig. 1b. This is evidenced by the presence of antinodes in this place for every second mode of standing waves, which could not have been in the case of a rigid fastening in this place.

The results showed that acoustic noise recordings can be successfully used to diagnose the stability loss of sections of above-ground pipelines caused by a decrease in the rigidity of fixing pipe spans.

References

- Al-Sahib ANK, Jameel AN, Abdulateef OF (2010) Investigation into the vibration characteristics and stability of a welded pipe conveying fluid. *Jordan J Mech Ind Eng* 4(3):378–387
- Kolesnikov I, Fedin V, Kargapolov AA, Emanov AF (2012) On diagnosing the loss of stability of pipe supports by acoustic noise. *Fiz-Tech Prob Bit Useful Fossil* 48(4):59–67
- Li T-X, Guo B-L (1990) Natural frequencies of U-shaped bellows. *Int J Pressure Vessels Pip* 42(1):61–74

Determination of Ice Thickness Using Standing Waves



K. V. Fedin, Yu. I. Kolesnikov, and L. Ngomayezwe

Abstract The article presents the results of field experiments demonstrating the possibility of determining the thickness of the ice cover by acoustic noise. The accumulation of amplitude spectra of a large number of noise records was used. The obtained results clearly demonstrate the possibility of using the resonance method for fast and fairly accurate determination of the ice thickness. In addition, we can confidently talk about where the contact of ice with the ground ends (the nature of the frequency distribution changes). In addition, the article shows that the analysis of standing waves of vertical compression-tension arising in the coating under the influence of noise makes it possible to control the thickness of the coating and to evaluate the ratio of acoustic stiffnesses of the coating and the underlying layer at a qualitative level.

Keywords Ice thickness · Acoustic noise · Standing waves

The need to measure the thickness of the ice cover formed over the water surface at low temperatures may arise as a solution to many practical problems, such as: to ensure the safe movement of people on frozen water bodies and vehicles on ice crossings and winter roads, flood forecasting, assessment of the quality of ice maps created on the basis of satellite methods for remote monitoring of the ice situation, etc.

Among the methods for determining the thickness of the ice cover, the most accurate, but also the most time-consuming, is the direct method, which involves drilling holes and measuring the thickness of ice with an ice gauge.

K. V. Fedin (✉) · Yu. I. Kolesnikov
Trofimuk Institute of Petroleum Geology and Geophysics SB RAS, Akademika Koptyuga Pr. 3,
630090 Novosibirsk, Russia
e-mail: fedinkv@ipgg.sbras.ru

K. V. Fedin · Yu. I. Kolesnikov · L. Ngomayezwe
Novosibirsk State University, Pirogova Street 2, 630090 Novosibirsk, Russia

K. V. Fedin
Novosibirsk State Technical University, Karl Marx Avenue 20, 630073 Novosibirsk, Russia

The most common method for determining the thickness of ice is based on electromagnetic sounding of the ice cover by geo-radar (Kulizhnikov 2016; Singh et al. 2012; Fu et al. 2018). This method is characterized by high productivity and fairly good accuracy, but with large variability of the electrical parameters of ice (for example, in salt-water), it may require periodic calibration of the equipment.

Acoustic methods are also used to determine the thickness of ice. As a rule, these are active methods, for example, echolocation from the ice surface (Kirby and Hansman Jr 1986). The results of applying a passive acoustic method to determine the thickness of ice are presented below. The method is based on the extraction of standing waves from acoustic noise recorded on the ice surface.

This method has been repeatedly used before, for example, in physical modeling and field experiments to determine voids in ground sediments (Kolesnikov et al. 2018). The method is reduced to the registration of acoustic noise on the surface of the investigated limited object and the accumulation of amplitude spectra of a large number of noise records. This makes it possible to distinguish standing waves from the noise formed under its influence in the object.

In our case, such a limited object is an ice layer lying on the surface of water or frozen soil. Depending on the conditions of reflection, either an integer number of half-lengths or an odd number of quarters of the lengths of standing waves (like standing waves in rods that are not fixed or fixed at one end) should be placed in such a layer during the formation of standing waves between its lower and upper boundaries (Khaikin 1971).

The frequencies of standing waves of vertical compression-tension in the layer (natural frequencies of the layer) in these two cases are determined, respectively, by the equations:

$$f_n = \frac{nV_p}{2h}, \quad (1)$$

for ice under which there is water or air, or

$$f_n = \frac{nV_p}{2h}, \quad (2)$$

for ice lying on top of frozen ground. Where n is the mode number of standing waves, V_p is the velocity of longitudinal waves, h is the distance between the boundaries of the layer.

To assess the possibility of using a passive acoustic method to determine the ice thickness, based on the extraction of standing waves from acoustic noise, in late January—early February 2019, full-scale experiments were conducted on two reservoirs in the area of Novosibirsk Akademgorodok—on the Zyryanka river and on the beach “Zvezda” on the Ob reservoir. Registration of noise records was carried out on linear profiles with a step of 1 m. On the river, the profile 20 m long was oriented along the banks and was approximately in its middle part, and obviously above the water, since its murmur was clearly heard from under the ice. On Zvezda

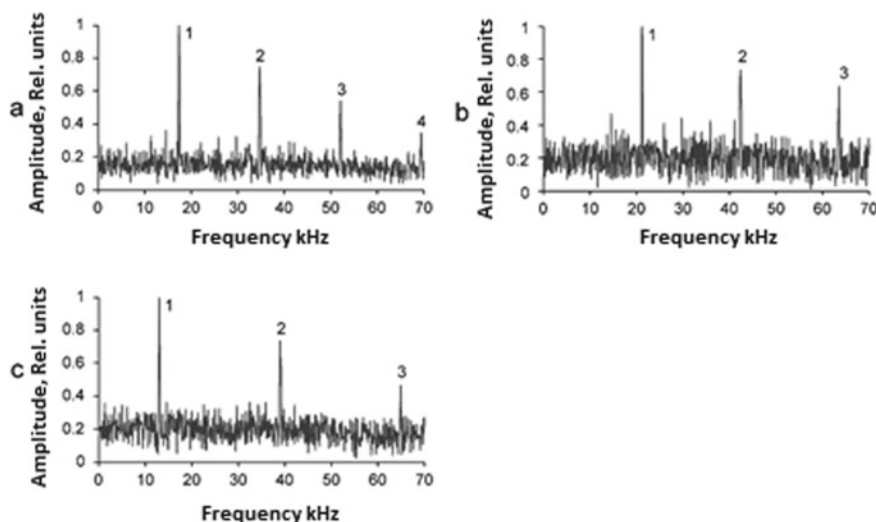


Fig. 1 Examples of normalized averaged amplitude spectra of noise records recorded on the ice sheet of the **a** river Zyryanka, **b** near the shoreline of the Ob reservoir on ice above water and **c** above frozen sand

beach, the observation profile was approximately perpendicular to the coastline and was located partly above the water, partly above the frozen sand.

Acoustic noise was recorded using a digital oscilloscope B-423 with a sampling frequency of 100 kHz. A wide-band piezoceramic piston-type sensor with a vertically directed axis of maximum sensitivity was used as a receiver, which was installed directly on the cleaned ice surface during measurements. The total duration of the noise recordings at each point was 30 s.

During processing, the records were divided into fragments with a duration of 8192 samples, after which the amplitude spectra of these fragments were accumulated. The frequencies of the resonance peaks emitted from the averaged amplitude spectra were used to determine the thickness of the ice cover at the observation points using Eq. (1). It was assumed that the longitudinal wave velocity V_p for ice is known and varies insignificantly at different observation points. Therefore, in the calculations, the value $V_p = 4090$ m/s, determined by the pulsed method on an ice core obtained by drilling a control hole near the Zvezda beach, was used.

Figure 1 shows examples of averaged spectra of noise recordings recorded at two observation sites. It can be seen, even with a relatively short duration of registration of noise in their spectra, several regular resonant peaks can be confidently distinguished. The regularity of the peaks in the amplitude spectra and the agreement with Eqs. (1) and (2) allow us to identify these peaks as resonances at the frequencies of standing waves.

Indeed, if ice covers water at a lower speed relative to it, then these peaks are located on the frequency axis with high accuracy in accordance with Eq. (1). For example, in Fig. 1a, the frequencies of the first four modes of standing waves are

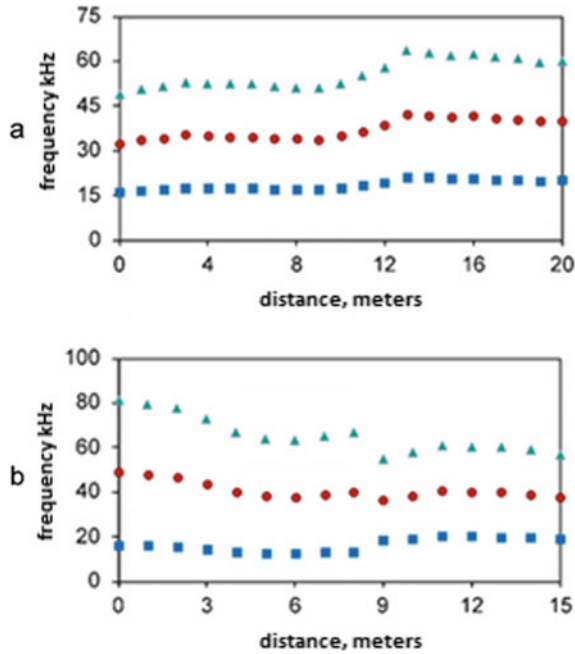


Fig. 2 The frequencies of the first (square markers), second (round markers) and third (triangular markers) modes of standing compression-extension waves for observation profiles on **a** the river. Zyryanka and **b** on Zvezda beach

17.4 kHz, 34.8 kHz, 52.1 kHz, and 69.5 kHz. At the same time, over the frozen sand (Fig. 1c), the distribution of peaks is consistent with Eq. (2), which indicates its greater acoustic rigidity compared to ice (mainly, apparently, due to the higher density of mineral grains).

The correspondence of the distinguished regular peaks to the standing waves of vertical compression-tension of the ice layer, and not to the standing waves of other types, is due to the use of a sensor that measures mainly the vertical component of acoustic noise during measurements. The thickness of the ice measured above the water by the rail was approximately 10.2 cm. The lowest mode frequency determined from the noise recorded near the hole is $f_1 = 19.92$ kHz, which, at the measured velocity $V_p = 4090$ m/s, in accordance with Eq. (1), gives almost the same thickness 10.27 cm. This example, in addition, confirms the correctness of the application of the method in question to determine the thickness of the ice cover of water bodies.

The frequencies of the three lowest modes for all observation points of two experiments are shown in Fig. 2. In this figure, it is clearly seen that for observations on the Zyryanka river, the frequencies of the second and third modes exceed the frequency of the first mode by 2 and 3 times, respectively, which is consistent with formula (1). The same pattern is observed for measurements performed on Zvezda beach, but only for a section of a profile of 9–15 m. For a part of a profile from 0 to 8 m,

the frequency interval between adjacent modes is equal to twice the frequency of the lowest mode, which is consistent with formula (2). It follows that from 0 to 8 m the profile passes over frozen sand, from 9 to 15 m above water, and between the marks of 8 and 9 m there is a border of these zones.

In summary, it can be noted that the experiments have shown the effectiveness of the use of acoustic noise to determine the thickness of the ice cover of water bodies, as well as to assess the type of underlying medium (water or frozen ground) on which the ice layer lies.

References

- Fu H, Liu Z, Guo X, Cu H (2018) Double-frequency ground penetrating radar for measurement of ice thickness and water depth in rivers and canals: development, verification and application. *Cold Regions Sci Technol* 154:85–94
- Khaikin SE (1971) Physical foundations of mechanics. Science 752 p
- Kirby MS, Hansman Jr RJ (1986) Method and apparatus for measurement of ice thickness employing ultrasonic pulse echo technique. United States Patent, Number: 4,628,736, Date of Patent 16 Dec 1986
- Kolesnikov YuI, Fedin KV (2018) Detecting underground cavities using microtremor data: physical modelling and field experiment. *Geophys Prospect* 66(2):342–353
- Kulizhnikov AM (2016) Georadar surveys of ice crossings. *Eng Surv* (8): 22–29
- Singh SK, Rathore BP, Bahuguna IM, Ramnathan AL (2012) Estimation of glacier ice thickness using ground penetrating radar in the Himalayan region. *Curr Sci.* 103(1):68–73

Development of Methods for Wind Speed and Wave Parameters Forecasting in Inland Waters



Fedor Loktev, Alexandra Kuznetsova, Georgy Baydakov,
and Yulia Troitskaya

Abstract The methods of wave forecasting at short fetches and wind forecasting in close proximity to the water/surface border are developed. The preliminary results of atmospheric model WRF and wave model WAVEWATCH III coupling are presented. Coupling of WW3 and WRF models is implemented using the modified code of OASIS software package to perform the exchange of time-varying Charnock parameter between the models. WRF LES simulations coupled to the wave model WW3 show a noticeable improvement in the quality of calculation of the wind speed.

Keywords Coupling · Atmosphere · Wave · WRF · WAVEWATCH III · Short fetch

1 Introduction

Determining the parameters of wind and surface waves in large and middle-sized inland water bodies is an important practical task. In particular, waves and wind conditions are the most important factors determining the erosion of the coast, their consideration is necessary to ensure the safety of navigation, especially small vessels. A regular publicly available wind and wave forecast is organized on NOAA's Great lakes website (<https://www.weather.gov/greatlakes/>). Parameters of wind waves to a large extent determine the surface condition of the reservoir and have an impact on the thermo-hydrodynamic regime of the reservoir and turbulent flows in the surface layer of the atmosphere, contributing to the features of the microclimate of adjacent areas.

However, when modeling wind and waves in inland waters of small and medium size with typical linear dimensions of not more than 100 km, a number of problems remain. The spatial resolution of the calculated surface wave characteristics and atmospheric parameters used for global projections varies between 0.205° and 2.5° , which is rough enough for inland waters. Attempts of regular usage of global models

F. Loktev · A. Kuznetsova (✉) · G. Baydakov · Y. Troitskaya
Institute of Applied Physics, Russian Academy of Sciences, 46 Ul'yanov Street, 603950 Nizhny,
Novgorod, Russia
e-mail: alexandra@ipfran.ru

for local forecasting on a smaller grid without special adaptation usually lead to results that are very different from the measurement data, since the conditions of the reservoir have a number of features, primarily small wind fetches.

2 Method

In the previous works (Kuznetsova et al. 2016) the features of the development of surface waves on short fetches typical for the conditions of inland waters were studied on the basis of adaptation of existing global wave models to the conditions of inland waters. For example, WAVEWATCH III (WW3) ((WW3DG) 2016), which was focused primarily on ocean conditions.

The accuracy of the wave model results is highly dependent on the wind model used for forcing. The requirements for meteorological models are increasing for enclosed coastal waters or enclosed basins, where wind fields are highly dependent on local conditions that are not described by global meteorological models. Their reanalysis data have spatial variability, which allows more accurate modeling of the waves. But in inland water bodies this approach is not applicable due to the too low spatial resolution. To account for the complex orography of coastal waters and enclosed basins, numerical weather prediction models are created that use mathematical models of the atmosphere and ocean to predict weather based on current weather conditions.

Thus, a method of taking into account the spatial variability using wind forcing from the WRF model is proposed. Setting the wind field from WRF with high spatial resolution provides the possibility of predicting waves with high resolution, which is a popular solution for both inland water bodies and coastal zones (Rusu et al. 2014).

This method of specifying wind pumping from the atmospheric WRF model was carried out, for example, in (Alves et al. 2014). In addition, a regional adaptation of the WRF atmospheric model is presented in (Kuznetsova et al. 2019). Briefly, model settings can be described in a Table 1.

The development of methods for forecasting of microclimate and weather conditions is possible with the use of adapted and linked models and is presented in this paper. This is a new direction of research, “coupled models”, implemented, for example, in (Chen et al. 2013). The idea is that wind waves affect the atmospheric properties of surface wind and heat flows through surface roughness, and surface roughness, in turn, affect the parameters of the atmosphere. Models with two-way coupling (“2-way coupling”) allow taking into account the two-way interaction in the atmosphere-water system.

The two-way feedback method between WW3 and WRF models is being developed and implemented. The area containing the Gorky reservoir is chosen to test the method.

Table 1 WRF model settings used for the simulations

Model characteristic	Setting
Number of domains	4
Resolution of the smallest domain	1 km
Land model	MODIS LAKES (30 s)
Initial and boundary conditions	NCEP climate forecast system version 2 (CFSv2) 6-hourly products
Micro physics option	WRF single-moment 3-class scheme
Planetary boundary layer (PBL) physics options	Large eddy simulation (LES)
Cumulus parameterization option	Kain-Fritsch Scheme
Shortwave and longwave option	Dudhia shortwave scheme, RRTM longwave scheme
Land surface option	5-layer thermal diffusion scheme
Surface layer options	Revised MM5 scheme

Coupling of WW3 and WRF models is implemented using the OASIS software package (Anthony et al. 2017), which is modified to allow the exchange of Charnock parameter between models. Charnock parameter is responsible for water surface roughness and can be used for more accurate prediction not as a constant but as a time-varying parameter. Modification of the source code of the models is performed to add the possibility of exchanging Charnock parameter between the models, as well as the possibility of exchanging wind velocity at a standard meteorological altitude of 10 m between the models. The data about these parameters obtained in one of the models is taken by the other at each time step and used instead of the initial data, thus creating feedback between the models.

Thus, in this paper, the preliminary results of calculating the wind velocity using the atmospheric model coupled with the wave model are presented. The 10 m wind speed distribution is compared at the same moment for the WRF LES simulation and WRF LES coupled with WW3 (Fig. 1). Option LES, i.e. Large-Eddy Simulation enabled the calculation of the first three domains under the Yonsei University (YSU) scheme for surface boundary layer and as surface layer modeling is based on similarity theory of Monin-Obukhov, taking into account the viscous sublayer in the Carlson-Boland form. Simulation of wind speed in the fourth domain is made in the planetary boundary layer as well, and for the near-surface layer, Monin-Obukhov parameterization is used.

WRF LES coupled with WW3 means that the wind speed calculated by the large-eddy simulation method in the WRF model was used as the “forcing” for the WW3 wave model. The Charnock parameter values obtained by the wave model were taken in the next calculation by the WRF model at each time step. This is so-called feedback. The wind wave interaction implies, first of all, the momentum exchange in the water-atmosphere system. The value of the wave momentum flux is determined by the roughness of the wavy surface. Setting the exact roughness of the excited

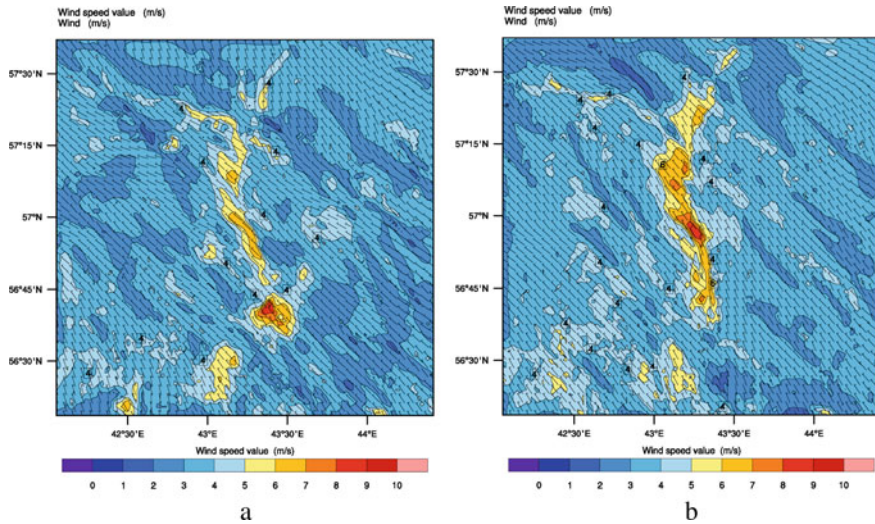


Fig. 1 Wind speed distribution (a) WRF LES, (b) WRF LES coupled with WW3 in the test day 08.08.2017

surface to the atmospheric model will allow us to refine the calculated atmospheric parameters.

3 Results and Discussion

The results of simulations obtained in the coupled models allowed to achieve better spatial variability compared to the WRF LES simulation results.

Then, the wind velocity and direction obtained at the point of measurement were compared from four sources. First, the reference data were in situ measurements made by our group on the test day. Second, CFSv2 reanalysis data of the highest accuracy of 0.205° available to date were used. Third, calculations were made by the WRF with large-eddy simulation used (WRF LES). Fourth, WRF LES coupled with WW3.

A comparison of the behavior of 10 m wind speed and direction, calculated by using different options is shown in Fig. 2. Here, the time starts in advance and corresponds to the beginning of the simulation. The zero point corresponds to the Moscow time 11:00 on the test day 08/08/2017 and is close to the time of the beginning of the in situ measurements. The results of the WRF run are given for the test day 08.08.17. The comparison shows that the use of the considered WRF calculations is better consistent with the experiment than the direct use of reanalysis. The calculations of WRF LES showed good time variability corresponding to in situ observations as for the velocity module (see Fig. 2a), and for its direction (see Fig. 2b). Although

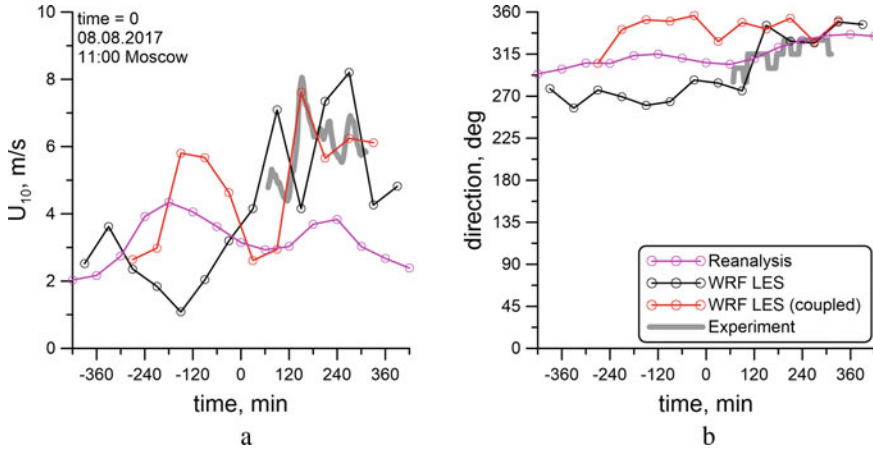


Fig. 2 The results of the WRF model of wind speed (a) wind direction (b) using different parameterizations of the surface boundary layer and the surface layer of the atmosphere: WRF LES, WRF LES (coupled with wave model), reanalysis data in comparison with measured data in situ in a test day 08.08.2017

the experimental data and WRF LES are much better in magnitude, there is some inconsistency in them. In particular, a maximum of 150 min in the experimental data corresponds to a minimum in the model data. The reason for this inconsistency is that in reality the role of feedback in the wave-wind system is great, the effect of waves on the wind is taken into account in coupling models (WRF-LES (coupled)).

WRF LES calculations, passed through the coupling with the wave model WW3 (“coupled”), show a noticeable improvement in the quality of calculation of the wind speed. In this case, the value of wind speed directions has a deviation from the measurement data. More calculations will be performed for a set of statistics. However, preliminary data suggests that the exchange of parameters at each step of the calculations of both models leads to increase of the accuracy of calculations and reduce the dependence of the simulation results on the input data from reanalysis.

4 Conclusions

The WRF model was applied to a region containing a medium-sized inland body of water, and the region containing the Gorky Reservoir was selected as a test area. WRF modeling was carried out for 4 nested domains with a minimum cell size of 1 km. The input parameter was a reanalysis of CFSv2. Large Eddy Simulation (LES) approach was used. The results were compared with in situ measurements. The coupling of the WRF atmospheric model and WAVEWATCH III wave model

is performed. WRF LES calculations, passed through the coupling with WAVEWATCH III, show a noticeable improvement in the quality of calculation of the wind speed.

Acknowledgements A. Kuznetsova acknowledges Russian Science Foundation grant 19-17-00209 for the support of the development of the forecasting methods at short fetches. Yu. Troitskaya acknowledges RFBR grant 17-05-41117 for the support of the development of the coupling method.

References

- Alves J-HG, Chawla A, Tolman HL, Schwab D, Lang G, Mann G (2014) The operational implementation of a Great Lakes wave forecasting system at NOAA/NCEP. *Weather Forecast* 29(6):1473–1497
- Anthony C, Valcke S, Coquart L (2017) Development and performance of a new version of the OASIS coupler, OASIS3-MCT_3.0. *Geosci Model Dev* 10(9):3297–3308
- Chen SS, Zhao W, Donelan MA, Tolman HL (2013) Directional wind–wave coupling in fully coupled atmosphere–wave–ocean models: results from CBLAST-Hurricane. *J Atmos Sci* 70(10):3198–3215
- Kuznetsova AM, Baydakov GA, Papko VV, Kandaurov AA, Vdovin MI, Sergeev DA, Troitskaya YuI (2016) Adjusting of wind input source term in WAVEWATCH III model for the middle-sized water body on the basis of the field experiment. *Adv Meteorol* 1:1–13. article ID 574602
- Kuznetsova A, Baydakov G, Sergeev D, Troitskaya Yu (2019) High-resolution waves and weather forecasts using adapted WAVEWATCH III and WRF models. *J Phys Conf Ser* 1163:012031
- Rusu L, Bernardino M, Guedes Soares C (2014) Wind and wave modelling in the Black Sea. *J Oper Oceanography* 7(1):5–20
- The WAVEWATCH III Development Group (WW3DG) (2016) User manual and system documentation of WAVEWATCH III (R) version 5.16. Technical Note 329, NOAA/NWS/NCEP/MMAB, College Park, MD, USA, 2016. 326 pp. Appendices
<https://www.weather.gov/greatlakes/>

The Geoecological Assessment of the Internal and External Biogenous Load of the Waters of the Gulf of Taganrog of the Sea of Azov



A. Yu. Zhidkova, T. A. Bednaya, and V. V. Podberesnij

Abstract Eutrophication of natural water bodies is understood as the process of growth of the overall productivity of the ecosystem of a water body, including water masses, bot-tom sediments, organisms inhabiting them and relations between them. The process of eutrophication leads to the increase of the organic matter in the water. Geoecological studies on modeling and assessment of the external and internal biogenous loads (namely, loads from nitrogen and phosphorus) on waters of the Gulf of Taganrog of the Sea of Azov are conducted. The study is important because the degree of the eutrophication of the water body depends on the size of its external and internal biogenous loads. Calculation of the overall biogenous load of the ecosystem is carried out, its analysis and an assessment is made. Two methodological techniques are proposed for calculating nitrogen fluxes from the bottom sediments into the water of the Gulf of Taganrog of the Sea of Azov. Conclusions are drawn on the size of the overall internal and external loads of the waters.

Keyword General biogenous load · The external load · The internal load · Nitrogen · Phosphorus · The Gulf of Taganrog of the Sea of Azov

1 Introduction

Eutrophication of natural water bodies is understood as the process of growth of the overall productivity of the ecosystem of a water body, including water masses, bottom sediments, organisms inhabiting them and relations between them. The process of eutrophication leads to the increase of the organic matter in the water of the reservoir.

A. Yu. Zhidkova (✉) · V. V. Podberesnij

Rostov State University of Economics, Bolshaya Sadovaya st., 69, Rostov-on-Don 344002, Russia
e-mail: soleils@bk.ru

T. A. Bednaya

Don State Technical University, 1 Gagarin square, Rostov-on-Don 344000, Russia

The degree of eutrophication of a reservoir depends on the size of its external and internal biogenous loads (phosphorus and nitrogen) and can be slowed down by reducing them. Ways to decrease the external biogenous load of the Gulf of Taganrog of the Sea of Azov were discussed earlier (Zhidkova et al. 2014, 2018; Zhidkova 2017; Zhidkova and Gusakova 2014a, b). In this work we consider internal biogenous load of this water object and we define it as a flux of biogenes from the Gulf bottom with the subsequent inclusion in biotic circulation; the internal load is determined by the amount of phosphorus and nitrogen accumulated by the bottom sediments, and the rate of their desorption from the bottom sediments into the water.

The characteristic feature of the Sea of Azov, caused by climatic factors, is the high variability of elements of the water balance and the components of the chemical runoff that predetermines the variability of the biogenous elements balance and forces to look for new methodical approaches to its assessment, analysis and forms of representation (Sukhinov 2006). Many researchers (Zhidkova and Gusakova 2014; Sukhinov et al. 2016; Sukhinov 2006) specify that the concentration of the biogenous elements in the waters of the Sea of Azov substantially depends on the short-period weather phenomena when the structure of the internal chemical and biological processes in the reservoir is broken. These phenomena mention all thickness of waters, the sea “lives” from a storm to storm.

A number of modern works questions deal with issues of anthropogenic eutrophication, including the Sea of Azov. For example, Sukhinov et al. (2016) developed the mathematical model of the solution of the eutrophication of waters of a shallow reservoir considering the movement of a water stream, microturbulent diffusion, gravitational subsidence, spatial and uneven distribution of temperature and salinity, and also the polluting biogenous substances, oxygen phyto- and a zooplankton, etc. Such number of the input data in the model differs in complexity, the need of use of a huge data file and the supercomputing system that does it very expensive and imposes certain restrictions on use of the method in environmental practice when monitoring a water body.

In reservoirs it is almost impossible to define the origin of phosphorus or nitrogen in connection with the different sources of their receipt. On the one hand, this is the input of biogens from outside the catchment areas (precipitation, groundwater, etc.). And on the other hand, due to the internal capabilities of the reservoir: phyto- and zooplankton organisms that decompose in the water column, products excretion of planktonic organisms, bottom sediments from which the biogens enter the photic zone, release the dissolved organic compounds by algae and bacteria, which break down to form dissolved biogens. Besides, there is an allocation of biogenes with excrement planktonic, bentosny, invertebrate and fishes. All these factors make internal load of a reservoir. The internal biogenic load indicates the intensity of the nutrient cycle, because the balance of substances reflects the redistribution of individual chemical elements in the process of geochemical and biogeochemical migration. Management of these processes will allow operating ecosystems of reservoirs.

Thus, the aim of this study is to assess the value of internal biogenic loads on the ecosystem of the Gulf of Taganrog of the Sea of Azov from the standpoint of eutrophication, namely, phosphorus and nitrogen loads.

2 Materials and Methods

Mineral phosphorus is present at water mainly in the form of phosphate and hydrophosphate. It is a part of any organic substance, but in water its contents very small and in pure reservoirs is estimated in thousand shares of a milligram per liter.

During seasonal changes phosphate, as well as nitrate, almost disappear in the near-surface zone of the water area in summer. When organisms die, part of the phosphate enters the water, and also settles in the upper layer of the bottom sediments. Favorable conditions for the accumulation of phosphate arise in the anaerobic conditions inherent to the bottom layers of the shallow, well heated area in the absence of wind hashing. In water from the bottom sediments phosphorus comes back together with iron and again comes to biotic circulation. The increased number of compounds of phosphorus serves in water and rainfall as the evidence of accumulation of organic substance. Therefore, it is considered to be The low indicator of phosphorus in a reservoir is considered to be the indicator of pure water.

The increase in the flow of phosphorus from the bottom of the reservoir (an increase in ecosystem productivity) indicates the increase of the eutrophication of the ecosystem. According to Martynova (2008), at production of the phytoplankton of 200 g/cm² per year, the internal phosphorus load (a phosphorus stream from the bottom of the water body) sharply increases and becomes comparable with external phosphorus load of the water area. As a result, the eutrophication of the reservoir is accelerated. The most moveable form of phosphorus in the solid phase of the bottom sediments is considered its sorbate. The main reason of the increase of the internal phosphorus load in the eutrophic water object is the increase in the area of the bottom sediments with anaerobic conditions. The formed zones with the deficiency of oxygen in the benthonic layer accelerate the release of the phosphate sorbed in the aerobic conditions by the iron compounds. Alexandrova, Matishov and coauthors (Alexandrova et al. 2013; Matishov et al. 2015), describes such zones in the Sea of Azov. For example, in 2013, the distribution over the water area, as well as in the water column, was studied for the content of dissolved oxygen, pH, nutrients (nitrogen, phosphorus, silicic acid). The development of thr powerful clogging phenomena in the sea was noted because of the density stratification of the water column, the formation of a restoration situation in the surface layer of bottom sediments, which contributed to the enrichment of the water column by the biogenic elements.

Phosphates are well sorbed by the hydroxides of aluminum, manganese and clay materials, but iron is the main sorbent of phosphates. Even in those bottom sediments where the part of phosphate is connected with the aluminum hydroxide, other part them is connected with the iron hydroxide, so, there is a dependence of size of a stream of phosphate on redox-conditions.

The destruction of the organic matter also plays a significant role in formation of the stream of phosphorus from the bottom. The higher eutrophic index of the water body, the more powerful the flow of phosphorus if other is equal. The bond between the internal load of phosphorus and the organic matter in the bottom sediments is linear and depends on the eutrophication of the water body (the eutrophic index) (Martynova 2008).

The compounds of nitrogen and phosphorus coming to the reservoir in a solid phase are partially buried in the bottom sediments and partially returned to water.

The difference in the storage capacity of the bottom in relation to nitrogen and phosphorus is defined by the size of the particles. Therefore, the considerable part of the phosphorus entering the bottom is connected with the mineral particles, which reach the bottom almost without destruction. Nitrogen is precipitated almost exclusively only with the organic matter, most of which is mineralized in water. Therefore, nitrogen is removed from the bottom sediments more actively: 45–70% from accumulated at the bottom whereas phosphorus: 5–25%.

By the size of the particles of the bottom of the Sea of Azov, the following types of the bottom sediments are distinguished: pelitic (clay) and fine aleuritic silts; large silts; fine sand; seashell. Pelitic silts prevail in the Gulf of Taganrog, occupying the entire eastern and central parts of the Gulf in the interval of depths of 4.5–6.5 m. The underwater slope of the Gulf in the range of depths of 2.5–4.5 m is made up of large siltstone and fine aleurite silt. Fine-grained sands are deposited along the perimeter of the Gulf from the edge to depths of 1.5–2.5 m.

The increase of the eutrophication of the water body leads to the increase in the flow of the organic matter to the bottom. As a result, the processes of biochemical oxidation in the bottom sediments are intensified, redox conditions change, and the content of mobile forms of nitrogen and phosphorus increases; namely, their flow from the bottom to the water intensifies. In the eutrophic water bodies, this flow can become a source of the secondary nutrient intake. Thus, the eutrophic level of the reservoir is one of the main factors that determines the internal load of reservoirs.

3 Results

Let us carry out an assessment of the size of the flux of biogenous matter from the bottom of the Gulf of Taganrog of the Sea of Azov in water, based on the ideas of its mechanisms as concentration diffusion and convective transport.

Two methodological techniques are proposed for calculating nitrogen fluxes from the bottom sediments into the water of the Gulf of Taganrog of the Sea of Azov. The first of them involves the use of the Fick equation, the second is developed by Neverova-Dziopak (2003), who constructed a mathematical dependence of the nitrogen flux from the bottom sediments into water on the weight ratio of the concentration of organic carbon to the concentration of total nitrogen (C/N). The lower the ratio, the greater the percentage in the decomposition products of organic substances is ammonia nitrogen (NH_4^+) (Kuznetsov 1970). The nitrogen flux from the bottom

sediments into water increases with decreasing C/N ratio. The experimental data were approximated by Neverova-Dziopak E. as the linear equation:

$$J_N = 122.5 - 7.82 \cdot x \quad (1)$$

where

J_N the nitrogen flux from the bottom sediments, mg N/m² day;

x the C/N relation.

The diffusive movement of the dissolved matter in the bottom sediments obeys the first law of Fick:

$$J = \chi C \cdot D \quad (2)$$

where

J the size of the diffusive flux, mg/m² day;

χC gradient of the matter concentration in the pore solution of the bottom sediments and the bottom water;

D coefficient of diffusion, m²/day.

Concentration of nitrogen and phosphorus in the pore solution of the bottom sediments are defined by the mineralization speed of the organic substances in the bottom sediments. When concentration of matter in natural waters is 1–2 and more orders lower, than in steam solution, the concentration gradient χC can be accepted equal in size of concentration of substance in the pore solution.

The coefficient of diffusion depends on the diameter and length of the pores, temperature, charge and the mass of the ion, etc. For the diffusion of ammonium ion and phosphate the following data on its value are presented:

$$2.4 \times 10^{-6} \text{cm}^2/\text{s} \text{ and } 0.93 \times 10^{-6} \text{cm}^2/\text{s} (T = 24 \text{ }^\circ\text{C}) \text{ (Kuznetsov 1970)}.$$

In view of mean annual values of the content of carbon, nitrogen and phosphorus in the bottom sediments of the Gulf of Taganrog of the Sea of Azov, calculate the biogenous internal load of the studied water area.

The mean annual concentration of carbon and nitrogen in the water of the Gulf of Taganrog:

- $C = 0.348 \text{ mg/l}$;
- $N = 0.062 \text{ mg/l}$.

The water area square is:

$$S = 5300 \text{ km}^2.$$

Then the internal load of nitrogen of the studied water area is:

$$J_N = 75.58 \text{ mg N/m}^2 \text{ day}.$$

The average volume weight of the bottom sediments is about 1.5 t/m^3 . Then the mass of the active layer of the bottom sediments (M_a) in the studied water area is:

$$M_a = 159 \times 10^6 \text{ t.}$$

At average humidity of the bottom sediments of 38%, the mass of the air solid (the mass of the active layer of the bottom sediments of the Gulf of Taganrog) in the bottom sediments is:

$$M_s = 98.6 \times 10^6 \text{ t.}$$

At concentration of nitrogen in the top layer of the studied bottom sediments of 0.062 g/g , the mass of the general nitrogen in the active layer of the bottom sediments of the Gulf of Taganrog of the Sea of Azov is:

$$M_N = 6.11 \times 10^6 \text{ t.}$$

At calculation of the intake of nitrogen for the Fick equation, accept that the mass of nitrogen in the 2 cm layer of the bottom sediments is $6.11 \times 10^6 \text{ t}$.

The process of ammonification is described by exponential dependence with the constant 0.03 days^{-1} . Then the receipt of ammonium ion is:

$$M_{NH_4^+} = 183 \times 10^3 \text{ t/day.}$$

The concentration of nitrogen in the pore solution is 1700 mg/l .

The coefficient of diffusion is 2.4×10^{-6} .

The flux quantity of the bottom sediments in the water is:

$$J_N = 35 \text{ mg N/m}^2 \text{ day.}$$

Thus, at average size $1700 \text{ mg N/m}^2 \text{ day}$ the internal load of nitrogen for the Gulf of Taganrog is $67.7 \times 10^3 \text{ t/year}$.

As for the influence of the secondary intake of nitrogen on the processes of the eutrophication in the Gulf of Taganrog of the Sea of Azov, the daily gain of the concentration of nitrogen in the water is:

$$\Delta N = 0.7 \text{ mg/l,}$$

where the capacity of the water area is $25 \times 10^9 \text{ l}$.

Phosphorus of the bottom sediments. The accumulation of phosphorus in the bottom sediments happens both in the organic, and in the mineral forms, and from 40 to 80% of the organic phosphorus getting to the reservoir is mineralized.

The dissolved mineral phosphorus is present as the orthophosphate, which concentration is limited by the solubility and depends on the redox conditions, pH and water salinity. The dissolved phosphates form compounds with iron, aluminum and calcium. In aerobic conditions, the speed of the removal of phosphate from silts to water is 5–10 times lower, than in the anaerobic.

In the water area of the Sea of Azov, the huge zone of the anaerobic contamination of the ground (about 1000 km) is fixed from year to year. It is characterized by almost the total absence of the oxygen in the benthonic layer at calms or close to them wind

situations. Several such zones were also found in the waters of the Gulf of Taganrog (Sukhinov et al. 2016); however, their lifetime is calculated in days due to the shallow water and the agitated waters.

Sizes of sorption and desorption of phosphorus in the aerobic and anaerobic zones of the Gulf of Taganrog of the Sea of Azov have to differ considerably owing to the distinctions of the redox potential in the benthonic sheets of water, pH and salinity.

In the aerobic zones, the phosphorus flux from the bottom sediments in the water is be defined, mainly, by the ratio of speed of the mineralization of the organic phosphorus and the speed of the chemisorption of the mineral phosphorus. Thus the speed of the chemisorption is commensurable or even higher the speed of the mineralization.

In the anaerobic zones the phosphorus flux, is be defined generally both the desorption speed of the mineral phosphorus and the speed of the mineralization of the organic phosphorus. Whereupon $V_{\text{desorb}} \geq V_{\text{sorb}}$.

For the fresh-water silts the following values of the coefficient of diffusion of hydro phosphate is given in literature: 0.31×10^{-6} – 0.93×10^{-6} cm²/s (Kuznetsov 1970).

Let us calculate a phosphorus flux from the bottom sediments of the waters of the Gulf of Taganrog when the value of the coefficient of diffusion is maximum.

The top 5 mm of the silt bottom sediments are oxidized when the concentration of the dissolved oxygen is more than 8 mg/l in natural waters. Iron and manganese are present mainly in the form of the hydroxides. The mineral phosphorus is occluded on hydroxides or forms insoluble compounds. Therefore, the intake of phosphate from the bottom sediments to water strongly decreases in the aerobic conditions.

The bottom sediments become “a trap” for phosphorus. At the aerobic exchange the bulk of the phosphate, deleted from the bottom sediments, is the flux, formed owing to the mineralization of the organic substance.

The calculation of the phosphorus flux from the bottom sediments of the waters of the Gulf of Taganrog is made based on the following assumptions:

- the processes of the chemisorption of the mineralized phosphorus are not considered;
- the source of phosphate is the organic phosphorus;
- the process of the phosphatification is described by the exponential dependence;
- the constant of speed of the phosphatification is 0.018 days^{-1} (Neverova-Dziopak 2003);
- the volume of pore solution is equated to the volume of the active layer of the bottom sediments (2 cm thickness)— $10.6 \times 10^6 \text{ m}^3$;
- the gradient of the concentration of phosphate is equal to the concentration in the pore solution;
- the coefficient of diffusion is $0.93 \times 10^{-6} \text{ cm}^2/\text{s}$.

Then the mass of the organic phosphorus in the bottom sediments of the Gulf of Taganrog is:

$$M_p = 344.5 \times 10^3 \text{ tons,}$$

where the average annual concentration of phosphorus in the bottom sediments is 0.065×10^{-5} t/t.

The maximum size of the intake of the mineralized phosphorus from the bottom sediments to the water is 337.6 tons in the first 24 h.

The concentration of phosphorus in the pore solution is calculated by analogy with the concentration of nitrogen (3180 mg/l).

At the accepted coefficient of diffusion (0.93×10^{-6} cm²/s), the size of the diffusion flux of phosphorus in the waters of the Gulf of Taganrog is:

$$J_{P.M} = 25.5 \text{ mg P/m}^2 \text{ day.}$$

Thus, the internal load of phosphorus for the waters of the Gulf of Taganrog is:

$$J_p = 4.93 \text{ t/year.}$$

The maximum daily gain of the mineral phosphorus in the water is 0.54×10^{-3} mg/l.

4 Discussion

Calculation of the intake of nitrogen and phosphorus made oversized. In fact, the phosphorus flux from the bottom sediments to the waters of the the Gulf of Taganrog is less.

We do not give the similar calculation for the anaerobic zones in the water area because of the small amount of the time of the existence of such zones in the Gulf of Taganrog. Nevertheless, the general approaches to the calculations are as follows.

It is known that when the value of the redox potential of the bottom water decreases to 0.24 V, the active diffusion of iron, manganese and phosphorus begins from the bottom sediments due to the reduction of hydroxides and the destruction of the complex compounds. Under these conditions, the bottom sediments can be a significant source of the secondary intake of phosphate.

Besides, solubility of phosphate increases when the salinity does. With a high content of organic elements in the silts, a significant fraction may also be the flux of phosphorus formed during the mineralization of the organic compounds.

Therefore, in calculating the flux of phosphorus from the bottom sediments in the anaerobic zones, where there is a deficit of oxygen in the bottom layers, both the organic and mineral phosphorus should be taken into account.

With the 5300 km² area of water body, average annual concentrations of phosphorus (0.348 mg/l) and nitrogen (0.062 mg/l):

the flux quantity of the bottom sediments in the water is 35 mg N/m² day;

the internal load of nitrogen for the Gulf of Taganrog is 67.7×10^3 t/year;

the size of the diffusion flux of phosphorus in the waters of the Gulf of Taganrog is 25.5 mg P/m² day;

the internal load of phosphorus for the waters of the Gulf of Taganrog is 4.93 t/year;
the external load of the Gulf of Taganrog is defined by the Don River runoff and the sewage;
the external load of phosphorus is 4580 tons per year,
the external load of nitrogen is 25,559 tons per year;
the size of the internal nitrogen load is 67,700 tons per year,
the size of the internal phosphorus load is 4930 tons per year;
the overall nitrogen load is 93,259 tons per year;
the overall phosphorus load is 9510 tons per year.

Thus, in spite of the fact that the calculation of the intake of nitrogen and phosphorus to the water area of the Gulf of Taganrog is made with a reserve, the size of the internal nitrogen and phosphorus loads of the water is represented rather high and has to be considered at calculations of the eutrophication processes.

The factors of the overall biogenous load that can change the current state of the waters of the Gulf of Taganrog are absent at present. No measures to reduce phosphorus and nitrogen loads are carried out.

References

- Alexandrova ZV, Baskakova TE, Kartamysheva TB, Shevtsova EA, Syundyukov ShZ (2013) Characterization of hydro chemical indicators of the southeastern part of the Sea of Azov. *Environ Protect Oil Gas Sector* 12:19–25
- Ecosystem studies of the Sea of Azov and the coast. Collective authors (2002) Publ. Kola Science Center RAS, p 447
- Kuznetsov SI (1970) Micro flora of lakes and its geochemical activity. *Science* 318
- Martynova MV (2008) The influence of the chemical composition of bottom sediments on the internal phosphorus load. *Water Resour* 35(3):358–363
- Matishov GG, Stepanyan OV, Grigorenko KS, Kharkovsky VM, Povazhniy VV, Sawyer VG (2015) Features of the hydrological and hydro chemical regime of the Azov and Black Seas in 2013. *Bull South Sci Center* 11(2):36–44
- Neverova-Dziopak EV (2003) Theoretical, methodological and engineering support for the protection of surface waters from anthropogenic eutrophication: Dis. Doctors Tech. Science, p 345
- Sukhinov AI (2006) Precision models of hydrodynamics and the experience of their application in predicting and reconstructing emergency situations in the Sea of Azov. *News SFU Tech Sci* 3(58):228–235
- Sukhinov AI, Nikitina AV, Chistyakov AE, Semenov IS, Semenyakina AA, Khachunts DS (2016) Mathematical modeling of eutrophication processes in shallow water bodies on a multiprocessor computing system. In: *Parallel computing technologies (PaVT 2016) proceedings of an international scientific conference*, pp 320–333
- Sukhinov AI, Nikitina AV, Khachunts DS, Chistyakov AE (2016) Mathematical modeling of spatially heterogeneous hydrobiological processes in the Sea of Azov. *Monograph*, p 172
- Zhidkova AYU (2017) Eutrophic status of the Gulf of Taganrog northeastern part. *Monitor Sci Technol* 4(33):13–21
- Zhidkova (Guseva), Yu A, Gusakova NV (2014a) Determination of the external load of biogenous matter on the Gulf of Taganrog of the Sea of Azov. *Life safety* 1:36–41

- Zhidkova AYu, Gusakova NV (2014b) Development of the model for determining of the trophic status of shallow-water reservoir. *Adv Mater Res* 838–841:2578–2581
- Zhidkova (Guseva) AYu, Gusakova NV, Petrov VV (2014) Pilot studies of the reservoir eutrophication in system of ecological safety of the region. In: *Proceedings of the Southern Federal University. Technical science Technological int of SFU*, vol 9, pp 254–259
- Zhidkova AYu, Petrov VV, Gusakova NV (2018) The research of Waters eutrophication of the Gulf of Taganrog of the Sea of Azov for ecological monitoring Purposes. *Exploration and Monitoring of the Shelf Underwater Environment* edited by Iftikhar B Abbasov Wiley-Scrivener 318. ISBN: 978-1-119-48828-6

Manifestation of Downward Solar Radiation Flux in the Variability of Sea Ice Concentration and Krill Fishery in the Antarctic



A. A. Bukatov  and M. V. Babiy 

Abstract The investigation of the correlation between the sea ice concentration and the downward solar radiation flux was made on the base of NCEP data from 1982 to 2016. The regional distribution of the correlation coefficients is analyzed and areas with high correlation are identified. The calculation and analysis of the temporal trends of downward solar radiation flux and sea ice concentration has been carried out. The relationship between annual total values of downward solar radiation flux and the annual catch capacity of Antarctic krill in subareas 48.1–48.3 of the Convention of the Conservation of Antarctic Marine Living resources was estimated for period from 1993 till 2016.

Keywords The Antarctic · Sea ice · Sea ice concentration · Downward solar radiation flux · Antarctic krill

1 Introduction

Climate changes in recent decades are among the most important problems of our time. The processes occurring in the Polar Regions have an impact on the regional climate and the planet as a whole (Baidin and Meleshko 2014; Frolov et al. 2010; Lagun et al. 2010; Ionov and Lukin 2017; Turner et al. 2016). The presence in these regions of such an important indicator that responds to climate fluctuations, such as sea ice, makes it possible to assess the manifestation of these changes due to various feedbacks (Bukatov et al. 2016). Its dynamics leads to a change in the sea surface properties, which affects on the interaction between Ocean and Atmosphere (Bukatov et al. 2016; Ereneyev et al. 2013; Gudkovich and YeG 2002; Shuleikin 1968).

The intensity of the energy processes in the Southern Polar Region is largely determined by the heat flux from the Sun and the conditions of the underlying surface, which is especially evident in the conditions of the Polar day and night (Frolov et al.

A. A. Bukatov (✉) · M. V. Babiy
Marine Hydrophysical Institute RAS, Sevastopol, Russia
e-mail: newisland@list.ru

2010; Borisenkov 1970). As a result, this leads to variability in the formation and growth of ice, its spatial distribution, as well as in the appearance of zones with weak ice concentration and open water. This in turn affects on the time and fishing of the bioresources in the Antarctic, one of the richest regions of the World Ocean (Petrov 2016).

In this paper, a study was made of the correlation between the downward solar radiation flux and the sea ice concentration on a climatic scale, and their trends were estimated. The results of the analysis of the relationship between the fluctuations of the annual total values of the downward solar radiation flux and the annual catch of Antarctic krill in Subareas 48.1–48.3 of the Convention of the Conservation of Antarctic Marine Living Resources (CAMLR Convention) are presented.

2 Method and Data

Research is executed on the basis of NCEP data from 1982 to 2016 by sea ice concentration at 1° grids in the Antarctic (<http://nomad1.ncep.noaa.gov>) and downward solar radiation flux (W/m^2) at the surface level of the Earth (<https://www.esrl.noaa.gov>) reduced to 1° grids using spline interpolation. Also it's used data of catch of Antarctic krill in tons per year from 1993 to 2016 for Subareas 48.1, 48.2, 48.3 (<https://www.camlr.org/en/fisheries/krill>).

To assess the relationship between sea ice concentration and downward solar radiation flux a correlation analysis of detrended data series is performed and correlation coefficients being significant at the level of 95% are determined for each one-degree grid node for the considered time period. Their significance was determined by the magnitude P of the probability of correlation absence within the confidence interval (Bendat and Piersol 1974). For the correlation coefficients values given in the text $P \leq 0.05$. The investigation area is bounded from the south by Antarctica and from the north by 50°S . The calculation and analysis of linear trends of downward solar radiation flux and sea ice concentration in the Antarctic for the period from 1982 to 2016 has been performed.

For Subareas 48.1, 48.2, 48.3 of the CAMLR Convention a cross-correlation analysis was made between the detrended series of annual total values of downward solar radiation flux and the annual capacity of caught Antarctic krill for the period 1993–2016. Previously in each 1° grid the total value of the downward solar radiation flux was found for each year from the period under consideration.

3 Analysis of Results

It is known that the best coordination of the intra-annual cycle of sea ice concentration is manifested with the determination of the natural seasons duration in the Antarctica as follows: winter from April to September, spring from October to November,

summer from December to January, autumn from February till March (Bukatov et al. 2016). This is connected, among other things, with the phenomenon of the Polar night and the Polar day, when the Sun mainly does not rise above the horizon or it is not hidden behind it. The Polar day in the Antarctic lasts from the end of September to March, and the Polar night from April to September.

In Fig. 1 shows the intra-annual climatic spatial distribution of the correlation coefficients (R) between the sea ice concentration and the downward solar radiation flux. The color scale characterizes the value of R and the numbers indicate the months. It is seen that in February, a month with a minimum area of floating ice, a direct correlation with $R > 0.6$ appears in the western Antarctic mainly. Maximum $R \sim 0.81$ are in the Weddell Sea. In March, with the beginning of the ice accumulation process,

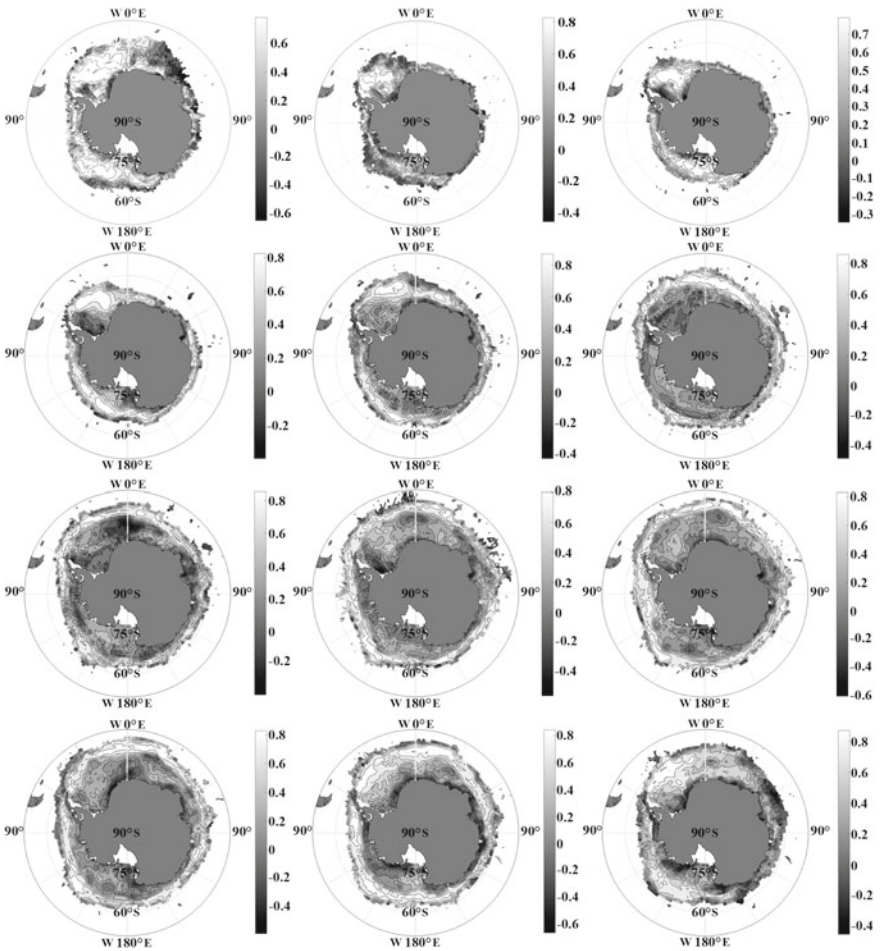


Fig. 1 Distribution of correlation coefficients R between sea ice concentration and downward solar radiation flux

the areas of interaction with large positive R significant on the 95% confidence interval remain the same, but their area begins to expand. The intra-annual climatic distribution of $P \leq 0.05$ values in the region, characterizing the significance of R , is presented in Fig. 2.

The influence of the Polar night on the Southern Ocean begins to appear in April and gradually increases by June (Fig. 3). Consequently, areas with sea ice, where

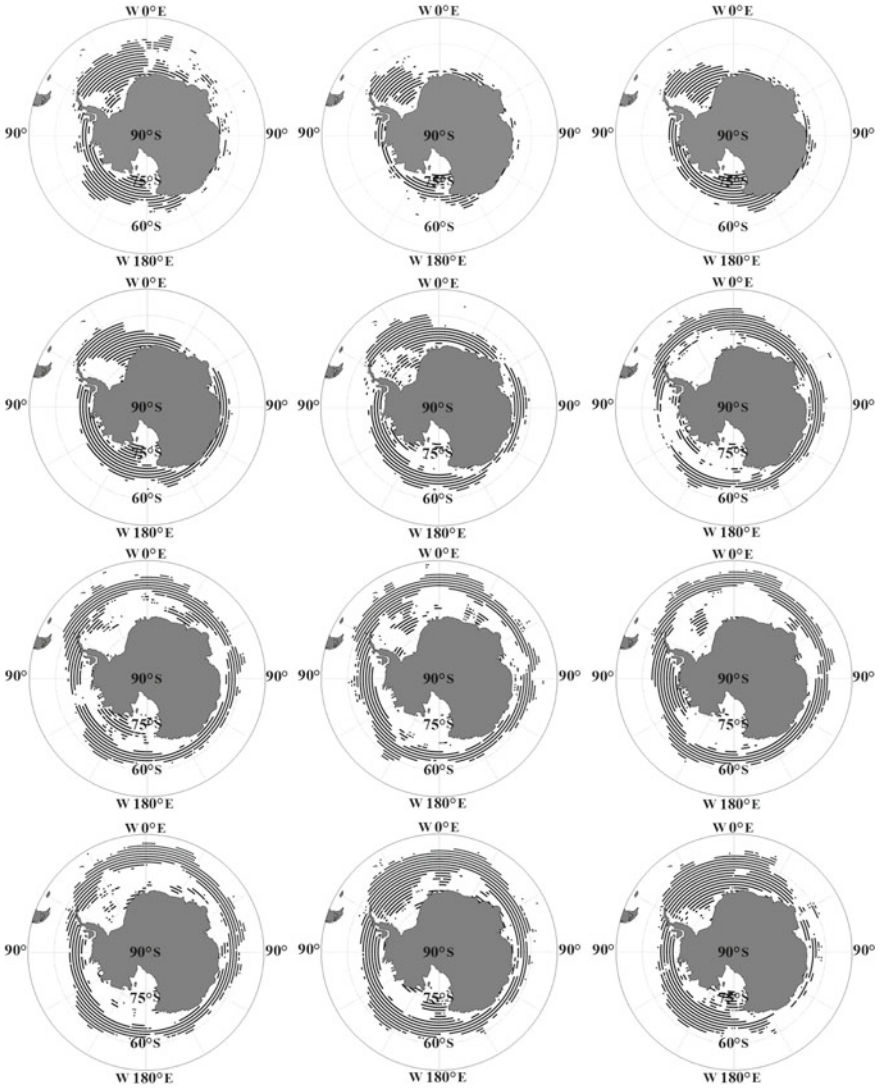


Fig. 2 Distribution of probability values of correlation absence P between ice concentration and downward radiation for $P \leq 0.05$

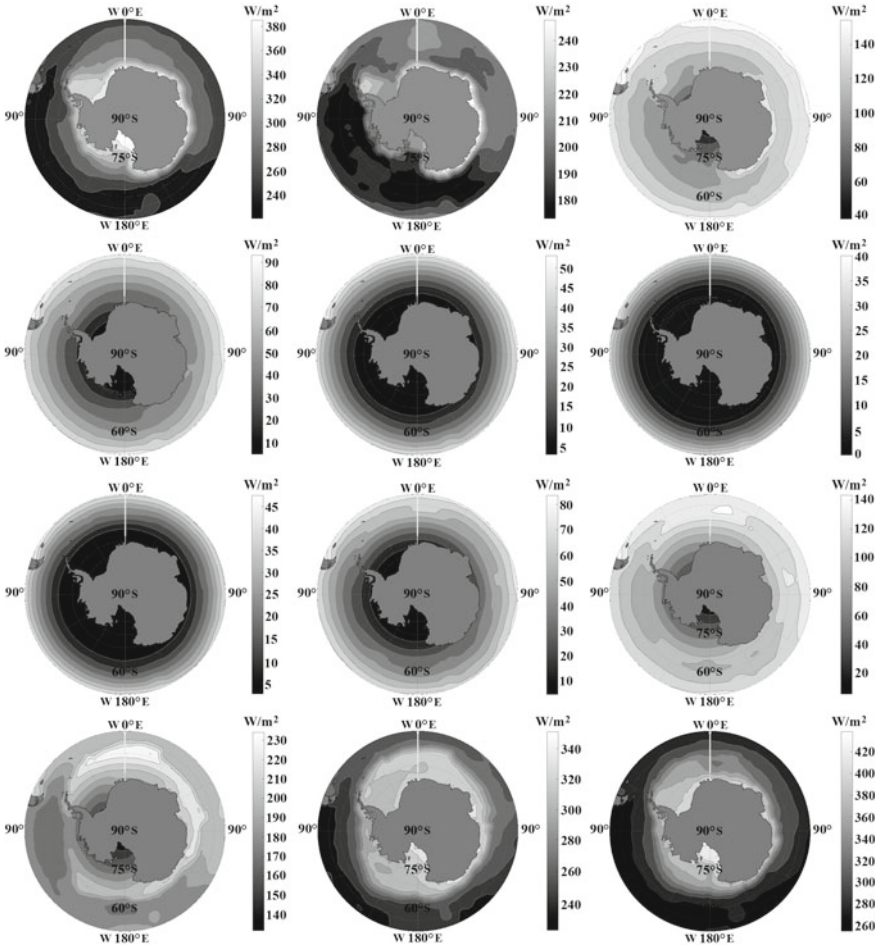


Fig. 3 Intra-annual climatic distribution of downward solar radiation flux. The color scale characterizes the value of downward solar radiation flux. The numbers indicate the months

solar radiation on the surface is not equal to zero, are removed from the coast from month to month. For example, the value of downward solar radiation flux at the latitude of the Polar circle in these months varies from $35 W/m^2$ to 0. During this period, intensive formation of sea ice (see Fig. 1 in (Eremeyev et al. 2013)) is caused by cooling conditions, mainly due to the lack of illumination of high latitudes of the Southern Hemisphere. Step-by-step from the coastal waters of Antarctica, areas with significant correlation coefficients shift to the north. This is especially visible in the Weddell, Lazarev, Bellingshausen, Amundsen and Ross Seas. Maximum $R \sim 0.83$ are located in a wide band along the ice sheet edge. Despite the fact that the unlighted region of the Southern Ocean almost completely disappears by September, in July, August and September the $R \approx 0.8$ values are located closer to the outer edge of

the ice sheet surrounding Antarctica. In this band ice is located with a concentration of 80% or less. The downward solar radiation flux in September at the latitude of Antarctic Circle is $\approx 90 \text{ W/m}^2$.

In October, when the Polar day has already come, the ice begins to decrease with concentration close to 100%. At the latitude of the Polar circle, the value of downward solar radiation reaches 225 W/m^2 . The outer ice boundary is slightly deformed and retreats towards the coast. However, better consistency between concentration and solar radiation ($R > 0.7$) remains on the periphery of the ice sheet in areas of weak concentration and influence of the Antarctic circumpolar current (Sokolov and Rintoul 2009). The heat of solar radiation is spent on the melting of sea ice, which leads to a decrease in the concentration.

In November, with beginning of intensive ice melting, the sea ice area increases with a concentration from 60 to 80%. The areas of significant correlation coefficients with large values located along the perimeter of the ice massif expand in the direction of the Antarctica coast. The total space of areas with high correlation in this month is maximal.

In December and January, the months of intense sea ice destruction, the best connection between ice concentration and downward solar radiation is observed on a large part of the Weddell Sea and in certain areas of the Amundsen Sea, and in January in the D'Urville Sea too. Here there is a direct relationship with $R \sim 0.83$ in December and with $R \sim 0.7$ in January. The maximum values of downward radiation at the Polar circle latitude are 380 and 340 W/m^2 for December and January respectively.

The linear trends calculation of downward solar radiation flux showed that not all areas with high correlation coefficients between ice concentration and of downward solar radiation flux coincide with areas of large trends. In the intra-annual climatic distribution of the Polar region under consideration, a geographically stable region with a significant positive trend has been present in the Somov Sea for five months (from December to April). In Fig. 4 shows the increment of downward solar radiation flux in the region over 10 years during 1982–2016. The color scale characterizes the value of the increment of downward solar radiation. The numbers indicate the ordinal number of the month. It seen that the maximum increment is observed in December in the Somov Sea and the eastern part of the Ross Sea. Large values of sea ice concentration trends also coincide with the Somov Sea. In addition to this area, they are found from June to November at the outer edge of the ice mass, and in February and March in the Weddell Sea. In these regions determinates the largest R between ice concentration and solar radiation. In addition to the positive trends of the sea ice concentration, there are areas with a negative trend. They are located in the western Antarctic in the Bellingshausen and Amundsen Seas from January to May essentially.

The forecast and assessment of the ice situation in the Southern Ocean is important for the active development of biological resources in the Antarctic Seas. In connection with the above-shown spatiotemporal relationship between downward solar radiation flux and sea ice concentration, a correlation analysis was made between downward solar radiation flux and the catch capacity of Antarctic krill, which is a promising commercial target. The traditional areas of the krill fishery are located near the South

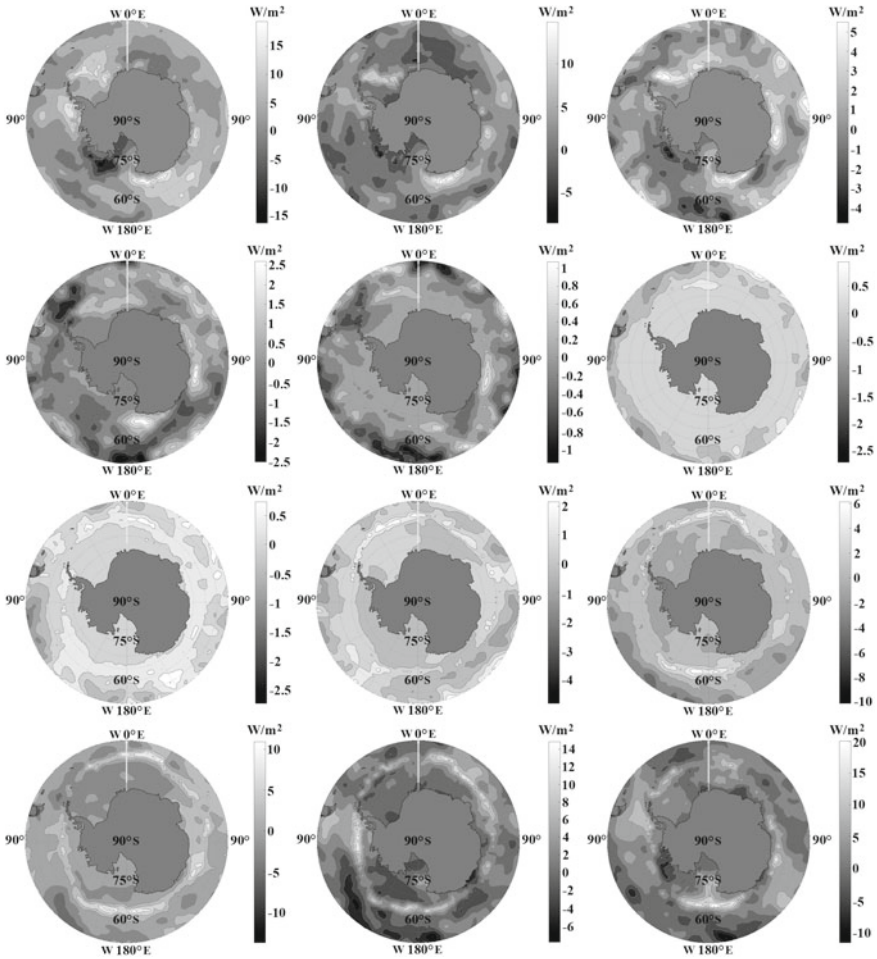


Fig. 4 The increment of downward solar radiation flux over 10 years in a period 1982–2016

Shetland Islands on the Antarctic Peninsula (Subarea 48.1), the South Orkney Islands (Subarea 48.2) and Fr. South Georgia (Subarea 48.3) in the Atlantic sector of the Antarctic (Petrov 2016; Sologub and Bizikov 2017).

From the obtained correlation dependences it follows that for the three considered Subareas (48.1, 48.2, 48.3), between the annual total values of the downward solar radiation and the annual capacities of krill catch, there is a direct correlation with $R \sim 0.77, 0.79, 0.86$ respectively. When calculating the cross-correlation functions of detrended series it was established that in Subarea 48.1 there is direct correlation between the catch capacity of krill and the changing in total downward radiation with maximum $R \sim 0.68$ with shift one year. In Subarea 48.2, inverse correlation is determined with maximum $R \sim -0.67$ with time shift one year too. In Subarea

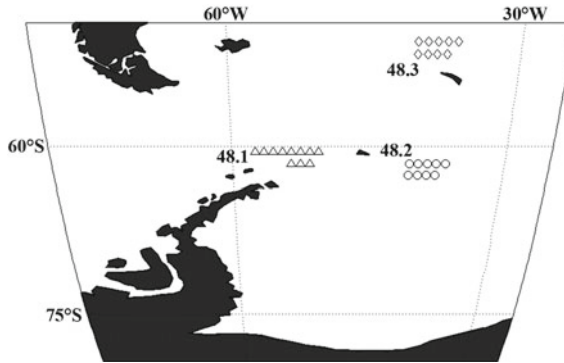


Fig. 5 Location of the areas of maximum correlation coefficients R between an annual total value of downward solar radiation flux and the annual catch of Antarctic krill. Numbers denote Subareas in accordance with CAMLR Convention

48.3, inverse correlation was observed with a response to changes in total downward radiation in the krill catch capacity after 5 years with $R \sim -0.57$. All correlation coefficients are significant at the 95% confidence interval. Note that on the calculated cross-correlation functions can be traced 11 year solar cycle (Schwabe Cycle) and a cycle of about 3 years. The geographical location of the regions with a high cross-correlation in the Subareas under consideration is presented in Fig. 5.

4 Conclusion

The analysis of the relationship between sea ice concentration and downward solar radiation flux for the period 1982–2016 has been performed. An intra-annual climatic regional distribution of the correlation coefficients between ice concentration and downward solar radiation flux significant at the 95% confidence interval is obtained. It is shown that in the Weddell Sea, the regions with the maximum significant correlation coefficients $\sim 0.83, 0.68, 0.81, 0.75$ are determined in December, January, February and March respectively. During the period of intensive sea ice formation (Polar night) regions with $R \approx 0.8$ are shifted northward and located closer to the outer edge of the ice sheet surrounding Antarctica. From April to September, this dynamic is clearly visible in the Weddell, Lazarev, Bellingshausen, Amundsen and Ross Seas.

An analysis of calculated trends of downward solar radiation flux and sea ice concentration showed that a geographically stable region with a significant positive trend from December to April is present in the Somov Sea.

Investigation of the relationship between the annual total values of downward solar radiation flux and the annual catch capacities of Antarctic krill in the considered Subareas showed a high correlation. Significant $R \sim 0.68, -0.67, -0.57$ were

obtained on the 95% confidence interval for the Subareas 48.1, 48.2, 48.3 respectively. The response of the amount of krill caught during the year to changes of the value of the annual total downward radiation is manifested across one year (Subareas 48.1, 48.2) and after 5 years (Subarea 48.3).

Acknowledgements The present study is carried out within the framework of the State Order No. 0555-2019-0003

References

- Baidin AV, Meleshko VP (2014) Response of the atmosphere at high and middle latitudes to the reduction of sea ice area and the rise of sea surface temperature. *Russ Meteorol Hydrol* 39(6):361–370
- Bendat JS, Piersol AG (1974) *Random data: analysis and measurement procedures*. Mir, Moscow. (Transl. from English)
- Borisenkov EP (1970) Numerical methods for analysis and prediction of hydrometeorological fields in the polar regions. *Problemy Arktiki i Antarktiki* 36–37:67–85 (in Russian)
- Bukatov AE, Bukatov AA, Babiy MV (2016) Solar activity manifestation in the variability of sea ice regional distribution in the Antarctic. *Process GeoMedia* 2(16):104–111 (in Russian)
- Bukatov AE, Bukatov AA, Babiy MV (2016b) Regional variability of Antarctic sea ice extent. *Russ Meteorol Hydrol* 41(6):404–409
- Eremeyev VN, Bukatov AE, Babiy MV, Bukatov AA (2013) Spatial-temporary variability of the Antarctic sea ice distribution. *Geoinformatika* 1:63–71 (in Russian)
- Frolov IE, Gudkovich ZM, Karklin VP, Smolyanitsky VM (2010) Climate change in the Arctic and Antarctic – result of natural causes. *Problemy Arktiki i Antarktiki*. *Arctic Antarct Res* 85(2):52–61 (in Russian)
- Gudkovich ZM, Kovalev YeG (2002) On some mechanisms of cyclic climate changes in the Arctic and Antarctic. *Oceanology* 42(6):815–821. (in Russian)
- Ionov VV, Lukin VV (2017) The 10 years long monitoring of climatically significant thermic characteristics of the surface of Southern ocean by means of in situ measurements and satellite remote sensing. *Problemy Arktiki i Antarktiki* 3(113):5–15 (in Russian)
- Lagun VYe, Klepikov AV, Danilov AI, Korotkov AI (2010) On the warming over the Antarctic peninsula. *Problemy Arktiki i Antarktiki*. *Arctic Antarct Res* 85(2):90–101 (in Russian)
- Petrov AF (2016) On state of understanding for bioresources of Antarctic, their status and commercial using. *Izv TINRO* 184:41–53 (in Russian)
- Shuleikin VV (1968) *Physics of the sea*. Nauka, Moscow (in Russian)
- Sokolov S, Rintoul SR (2009) Circumpolar structure and distribution of the Antarctic circumpolar current fronts: 1. Mean circumpolar paths. *J Geophys Res* 114:C11018
- Sologub DO, Bizikov VA (2017) Seasonal dynamics of Antarctic krill (*Euphausia superba*) abundance in the Atlantic Antarctic sector. *Trudy VNIRO* 166:3–21 (in Russian)
- Turner J, Lu H, White I et al (2016) Absence of 21st century warming on Antarctic Peninsula consistent with natural variability. *Nature* 535:411–415
- <http://nomad1.ncep.noaa.gov>
- <https://www.esrl.noaa.gov>
- <https://www.ccamlr.org/en/fisheries/krill>

Estimation of Waters Vertical Structure in the Barents and Kara Seas



A. A. Bukatov , E. A. Pavlenko , and N. M. Solovei 

Abstract Investigation of the features of spatial-temporary distribution of the Brunt-Väisälä frequency maximum and its occurrence depth in the Barents and Kara Seas is considered on the basis of the World Ocean Atlas 2013 reanalysis for the period 1955–2012 with $0.25^\circ \times 0.25^\circ$ grid. The regional features of the vertical structure of the buoyancy frequency are revealed. Correlations between intra-annual variability of the Brunt-Väisälä maximum frequency and climatic indexes are investigated.

Keywords Arctic · Barents Sea · Kara Sea · Brunt-Väisälä frequency · Vertical water structure · Water stability

1 Introduction

Climate change occurring in the modern epoch is especially noticeable in the Polar Regions, the most sensitive to changes in hydrometeorological conditions and in turn having a serious impact on regional and global climate processes (Frolov et al. 2010; Matishov 2008). In recent decades, in the Arctic region there are significant fluctuations in the area of sea ice and an increase in surface air temperature, also changes in the vertical structure of the upper Ocean layer are observed (Frolov et al. 2010; Bukatov et al. 2017; The second estimating report on climate changes and their consequences in the territory of the Russian Federation 2014; Tsaturov and Klepikov 2012). The Barents and Kara Seas are the two most western seas of the Russian Arctic. They are separated by the Novaya Zemlya archipelago, which serves as a barrier on the way from the Atlantic of warm air masses and warm and saline Ocean waters. Owing to the North Cape Current a significant part of the Barents Sea area from the coast to 75° N does not freeze. The Kara Sea is climatically more severe than the Barents Sea: it is covered with ice completely or over a large area (Bukatov et al. 2017; Dobrovolsky and Zalogin 1982; Karklin et al. 2017).

A. A. Bukatov (✉) · E. A. Pavlenko · N. M. Solovei
Marine Hydrophysical Institute RAS, Sevastopol, Russia
e-mail: newisland@list.ru

A major role in the hydrological regime formation of the Arctic seas is played by the flow of fresh continental waters. The river flow of the Barents Sea is small relative to the area of the sea, its maximum is observed at the end of spring. The Kara Sea has about 55% of the total fresh water which flow into all seas of the Siberian Arctic. It is considerably higher than the volume of river water entering in the Barents Sea. The maximum of river water in the Kara Sea is noted at the end of summer—beginning of autumn. Almost half of the sea area is under the influence of continental waters (Dobrovolsky and Zalogin 1982).

The most important characteristic of the hydrological regime is vertical stratification. A comprehensive study of the vertical structure of the Barents and Kara Seas waters is relevant for understanding of the functioning of their ecosystems, as well as ensuring the sustainable economic development of the Russian Arctic. Climatic conditions, the presence of currents, continental runoff and composite bottom relief contribute to the appearance of features of the water vertical structure. The indicator characterizing the stratification of the water column is the buoyancy frequency (the Brunt-Väisälä frequency), which is also called the frequency of stratification. It expresses the magnitude of stability and it is a fundamental variable in the dynamics of a stratified fluid. The shape of the vertical profile of the buoyancy frequency is an indicator of the presence of certain water masses and the intensity of various hydrodynamic processes (Sherstyankin and Kuimova 2009).

The purpose of this work is to study the spatial-temporary variability of the vertical structure of the Brunt-Väisälä frequency in the Barents and Kara Seas.

2 Method and Data

The study was carried out on the base of World Ocean Atlas 2013. The calculations used the values of temperature and salinity obtained for the time period 1955–2012 in the $0.25^\circ \times 0.25^\circ$ grid with a step of 5 m in depth to the horizon of 100 and 25 m—to the horizon 150 m (Locarnini et al. 2013; Zweng et al. 2013). Field of study is from 16° to 105° E and from 66° to 82° N.

According to monthly average data on temperature and salinity the density was calculated. The obtained density arrays were checked for the presence of inversions. If necessary they were corrected by replacing the inversion values with values interpolated over neighboring horizons (Artamonov et al. 2004). Based on the formed density arrays the buoyancy frequency (N) was calculated. The maximum Brunt-Väisälä frequency by depth ($N_{max}(z)$) was determined and its occurrence depth ($HN_{max}(z)$) too. To identify consistency between the maximum of Brunt-Väisälä frequency and climatic indices NAO (North Atlantic Oscillation), SOI (Southern Oscillation), AO (Arctic Oscillation), TDO (Pacific Decade Oscillation) (https://www.cpc.ncep.noaa.gov/products/site_index.shtml), GSNW (Gulfstream Current Index) (<https://web.pml.ac.uk/gulfstream/data.htm>) the calculations of the correlation coefficients $R_{N_{max}\sim NAO}$, $R_{N_{max}\sim SOI}$, $R_{N_{max}\sim AO}$, $R_{N_{max}\sim TDO}$, $R_{N_{max}\sim GSNW}$ were made.

3 Analysis of Results

To characterize the horizontal distribution of the waters stability of the Barents and Kara Seas the maps of the geographical distribution of the monthly mean climatic values of the maximum of the Brunt-Väisälä frequency and its occurrence depth were obtained. Analysis of the maps for the cold months shows that in these months the waters stability of the Barents Sea is small or close to an unstable state. The values of the maximum of buoyancy frequency of in the Kara Sea are times higher than $N_{max}(z)$ in the Barents Sea. As an illustration, the map of the spatial distribution of $N_{max}(z)$ in the Barents and Kara Seas in the coldest month (February) of the year in this region is presented (Fig. 1).

The geographical distribution of the Brunt-Väisälä frequency maximum in the Barents and Kara Seas in June is presented in Fig. 2. It is seen, that in June waters with maximum stability are located in the coastal areas: along the northeast coast of the Kola Peninsula and the western coast of the Yamal Peninsula, in the mouth areas of the Ob and Yenisei. The central part of the Barents Sea is occupied by waters with small values of $N_{max}(z)$ (less than 5 cycles/hour). To the north of 75° parallel, the maximum of buoyancy frequency rises to 10 cycle/hour. The central part of the Kara Sea is also occupied by waters with relatively low values of $N_{max}(z)$. From 75° to 80° N the values of the Brunt-Väisälä frequency maximum are about 15 cycles/hour. The increased stability in June in the southern part of the Barents and Kara Seas is due to the influx of fresh continental waters creating a salinity gradient in the coastal zone. Surface heating also creates a temperature gradient at this time of the year, but it does not have such a large effect on stability which has a salinity gradient (Timofeev 1946). The high stability of the waters in the Barents Sea in June to the north of the 75th parallel is caused exceptionally by the salinity gradient which is result of the ice melting. The low stability in the central part of the Barents Sea (contour of $N_{max}(z) = 5$ cycle/hour) is explained by the fact that the Atlantic waters of the North Cape

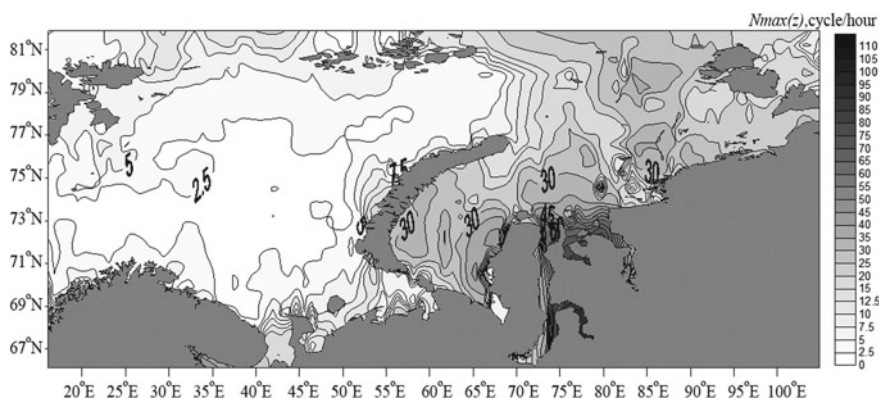


Fig. 1 The distribution of the maximum of the Brunt-Väisälä frequency (cycle/hour) in the Barents and Kara Seas in February

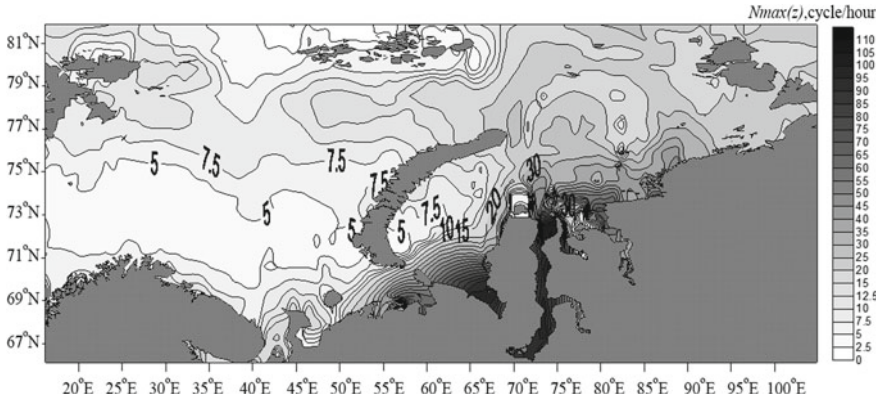


Fig. 2 The distribution of the maximum of the Brunt-Väisälä frequency (cycle/hour) in the Barents and Kara Seas in June

Current, which have high salinity and temperature, pass through here. While these waters moving eastward they are cooled which leads to an increase in density and to a smoothing of the difference in density between the layers (Timofeev 1946).

The relatively low values of the buoyancy frequency maximum in the central part of the Kara Sea in June are due to the fact that the coastal waters desalinated by river flow have not yet spread far to the north.

Stability in July increases over the entire area of the Seas (Fig. 3). Especially large increase is observed in the southeastern part of the Barents Sea (in the southern tip of Novaya Zemlya) and the southwestern part of the Kara Sea (the western coast of the Yamal Peninsula), the deltas of the Ob and Yenisei Rivers, and the Pyasinsky Bay. The rise in water stratification in these zones is explained by the increase in the flow of Siberian Rivers. The increase in stability from June to July in the central part of the

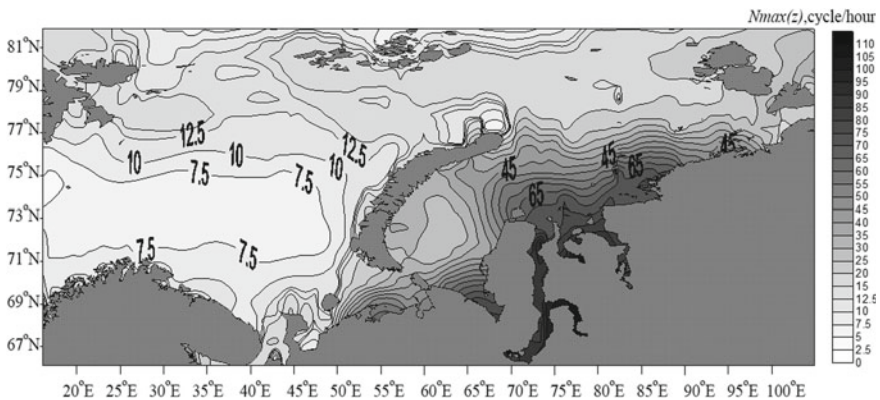


Fig. 3 The distribution of the maximum of the Brunt-Väisälä frequency (cycle/hour) in the Barents and Kara Seas in July

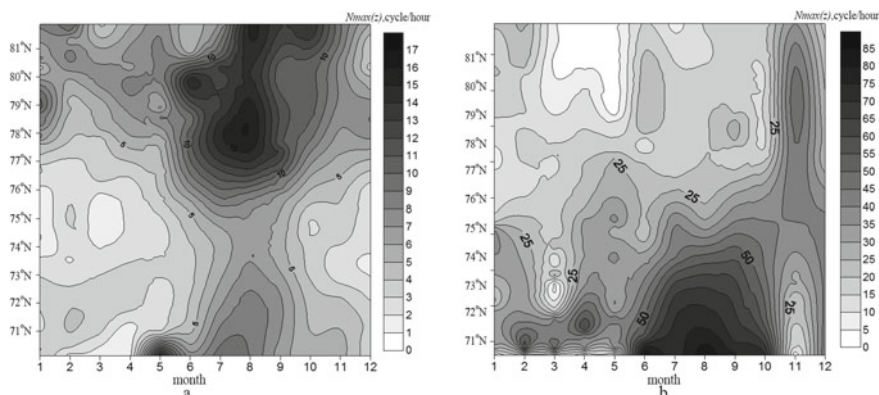


Fig. 4 Annual variation of the Brunt-Väisälä frequency maximum in **a** Kola (32° E), **b** Yamal (73° E) meridians

Barents Sea is primarily due to the more intensive influx of freshened waters from the north to this region, as well as by the weaker surface cooling of warm Atlantic waters coming from the west.

The distribution of the buoyancy frequency maximum in August–September over the Barents and Kara Seas remains the same as in July, although the values of $N_{max}(z)$ changes.

In order to assess and compare the annual behavior of sustainability in the Barents and Kara Seas, graphs of the climatic intra-annual variability of the Brunt-Väisälä frequency maximum at the Kola (32° E) and Yamal (73° E) meridians were created (Fig. 4a, b). From the presented Figures it can be seen that the highest values of water stability on the Kola meridian occur in May–September and can reach 15 cycle/hour in the region of 70° N and 17 cycle/hour in the region of 78° N. The maximum stability at 70 parallels is due to the May river flow, at 78° N—intense ice melting in August. The maximum values of $N_{max}(z)$ on the Yamal meridian are observed from June to October and can be 85 cycle/hour in the region of 73° N (influence of the river Ob flow). Such a significant excess of $N_{max}(z)$ in the Kara Sea over $N_{max}(z)$ in the Barents Sea is due to the difference in the flow of fresh continental waters. River flow in the Barents Sea is about 163 km³ per year; in the Kara Sea is about 1300 km³ per year (Dobrovolsky and Zalogin 1982).

For a quantitative characteristic of the waters stability fluctuations of the Barents and Kara Seas, the average value of the Brunt-Väisälä frequency ($\overline{N_{max}(z)}$) and the average occurrence depth of the maximum on the meridional sections ($\overline{HN_{max}(z)}$) were calculated (Figs. 5 and 6). The values $\overline{N_{max}(z)}$ and $\overline{HN_{max}(z)}$ are obtained as arithmetic averages on sections.

It seen that the maximum stability in the Barents Sea comes in July–August, and in the Kara Sea in August–September. In the zone of influence of the Ob and Yenisei Rivers, the values of $\overline{N_{max}(z)}$ reach 40–45 cycle/hour, and in the Barents Sea $\overline{N_{max}(z)}$ does not exceed 10–12 cycles/hour. In addition, there is one more of

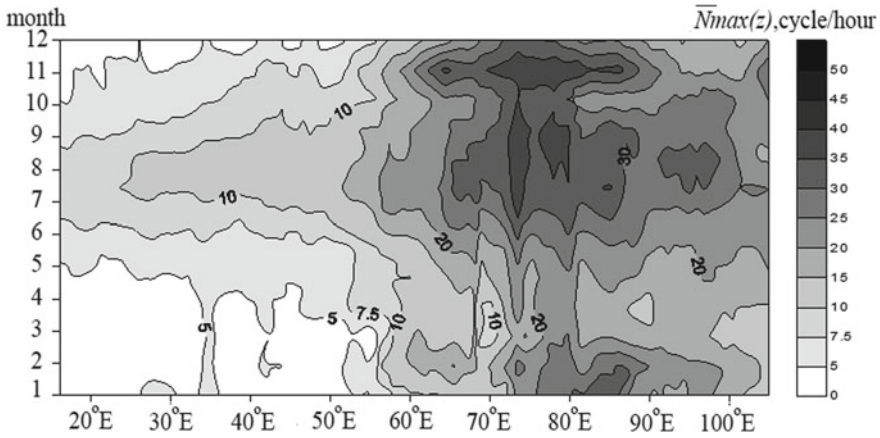


Fig. 5 The average along the meridian buoyancy frequency maximum

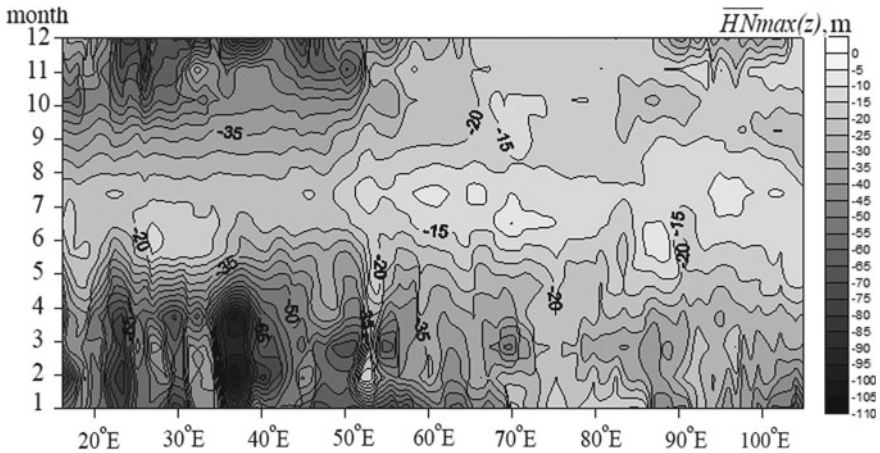


Fig. 6 The average along the meridian occurrence depth of the buoyancy frequency maximum

stability maximum in November in the meridional sector 70–80° E. In October, in the Kara Sea with the beginning of the process of ice formation, stability decreases everywhere. In November, with the formation of an ice cover, the river waters begin to spread in the under-ice horizons. It is leads to an increase in stability in the mouths of the Ob and Yenisei. From Fig. 6 it can be seen that in summer the layer of density jump rises to the surface, and in winter it deepens. In summer, the average depth of the pycnocline is 20–25 m in the Barents Sea and 10–15 m in the Kara Sea. In winter, the average depth of the density jump layer reaches 100 min the Barents Sea and 40 min the Kara Sea. The calculated correlation coefficient between the average for the meridian of the buoyancy frequency maximum and the average for the meridian of occurrence depth of the density jump layer is equal to -0.7 . This indicates that there

is an inverse relationship between $\overline{Nmax}(z)$ and $\overline{HNmax}(z)$: the large (summer) values of the density gradient are observed at shallow depths (10–25 m), and vice versa, the small values (winter) at relatively large depths (40–100 m).

The intra-annual variability of the average value of the buoyancy frequency maximum and the depth of its occurrence by sectors are shown on Fig. 7. Sector 1—20°–50° E (Barents Sea), sector 2—50°–70° E (Novozemelsky district), sector 3—70°–100° E (Kara Sea). It is seen from the figures that in the Barents Sea, the maximum of the waters stability is reached in August, in the Novaya Zemlya sector—in July and November, in the Kara Sea—in September and November. At the same time, the differences in the annual behavior of sustainability associated with the regional features of the hydrological waters structure are clearly visible. Average values of the buoyancy frequency maximum in the Barents Sea are relatively small (4–12 cycles/hour), in the Novaya Zemlya region they are already 8–22 cycles/hour, and in the Kara Sea—16–34 cycles/hour. The minimum occurrence depth of $\overline{Nmax}(z)$ is observed in July: in the Barents Sea it is 19 m, near Novaya Zemlya—10 m, in the Kara Sea—12 m.

For a more detailed analysis of the vertical structure of the Barents and Kara Seas density field, horizontally averaged Brunt-Väisälä frequency profiles were created in the physiographic regions proposed in Gorbatsky (1970). In the Barents Sea 5 areas are allocated: (1) Southwest or Medvezhinsky; (2) Northwest or Spitsbergen; (3) North; (4) Northeast; (5) Southeast or Kolguevo-Vaigachsky (Fig. 8).

The basis for allocate of the Southwest region is the influence of the North Cape Current, which is decisive in climate forming and the hydrological regime of this part of the Barents Sea. Northwest and North regions are considered as regions of the Arctic Zone. The Northeast region is influenced by the Atlantic waters. It is characterized by a maritime climate with anomalously mild for high latitudes winter.

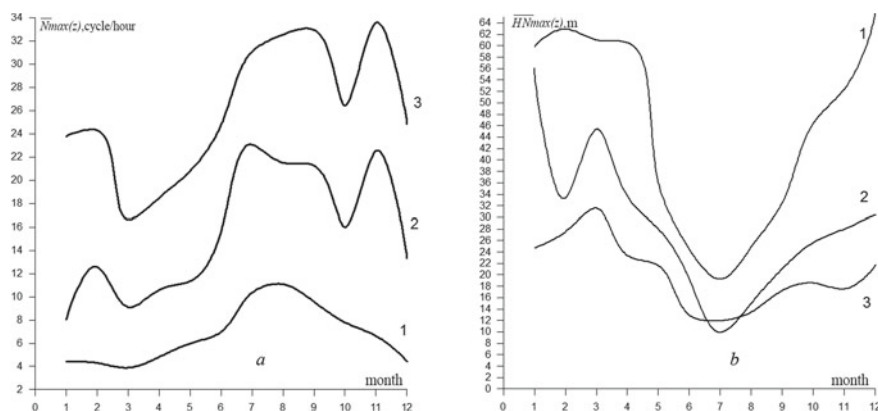


Fig. 7 Intra-annual variability of the average value of the buoyancy frequency maximum (a) and its occurrence depth (b) by sectors: curve 1—sector 20°–50° E, curve 2—sector 50°–70° E, curve 3—sector 70°–100° E

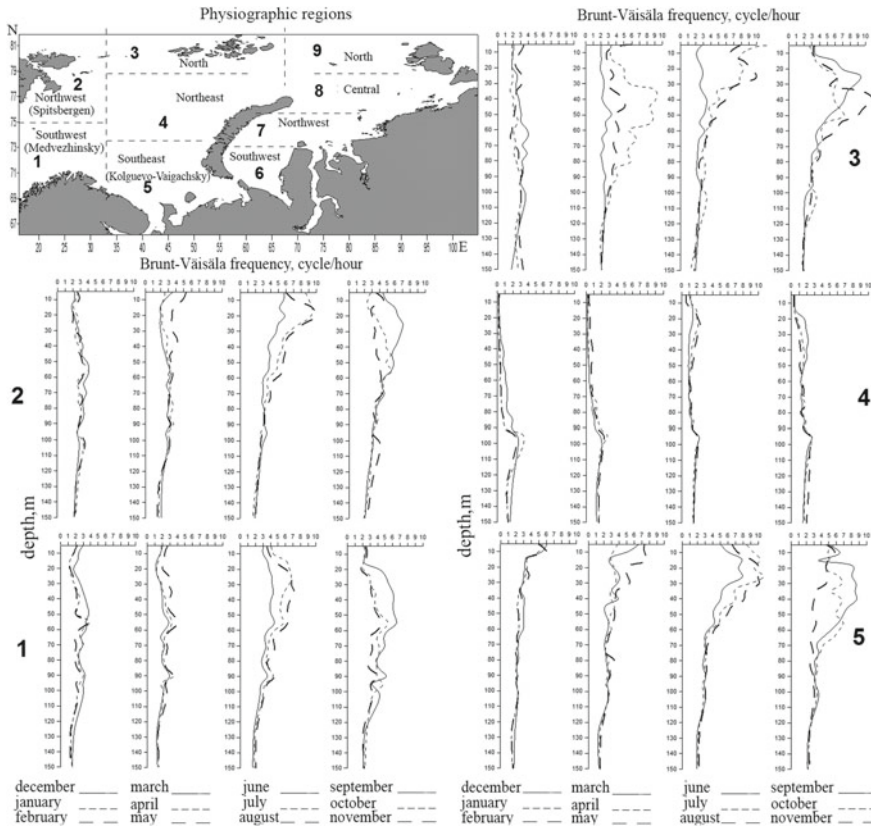


Fig. 8 Averaged profiles of Brunt-Väisälä frequency in the regions of the Barents Sea: 1—Southwest, 2—Northwest, 3—North, 4—Northeast, 5—Southeast

In a relatively shallow Southeast region there is a vast waters zone with low salinity, formed under the influence of the Pechora River flow (Gorbatsky 1970).

In the Kara Sea 4 regions are allocated: (6) Southwest, (7) Northwest, (8) Central, (9) North (Fig. 9). The boundaries of the regions are given approximately. In the southwestern part the Kara Sea is affected by warmer and saltier Barents Sea waters through the straits of the Yugorsky Shar, the Karsky Gates, what is the basis for allocate the Southwestern region.

The hydrological regime of the Northwest region of the Kara Sea is formed under the influence of the Barents Sea waters (Matochkin Strait) and waters of the Ob and Yenisei. Desalination of the surface layer by river water affects on hundreds of kilometers north of river mouths. The hydrological regime of the Central region of the Kara Sea is affected by the runoff of the Siberian Rivers (Ob, Yenisei, Pyasina). More salty and warmer Atlantic waters penetrate into the North region of the Kara Sea through the troughs of St. Anne and Voronin between the Franz Josef Land and Novaya Zemlya (Petrov 2008).

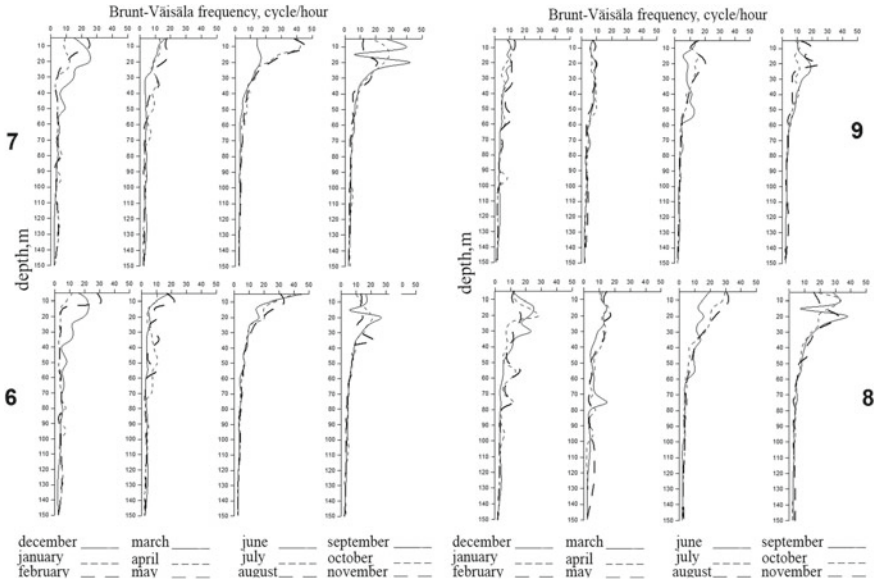


Fig. 9 Averaged profiles of the Brunt-Väisälä frequency in the Kara Sea regions: 6–Southwest, 7–Northwest, 8–Central, 9–North

The vertical structure of the buoyancy frequency space-averaged in the Barents Sea is shown in Fig. 8. It can be seen that in each of the selected areas the vertical structure of the buoyancy frequency has regional features. Thus, the structure of the Southwest (1) and Northwest (2) regions is of the same type (zone of Atlantic waters): the density jump layer is expressed from July to October, the occurrence depth of $\bar{N}_{max}(z)$ is 20–30 m in summer and 40–50 m—in the autumn. In the North region (3) the seasonal density jump layer is practically not observed in the winter months. In spring, summer and autumn, seasonal pycnocline is distinctly, $\bar{N}_{max}(z)$ values can exceed 10 cycle/hour, $\overline{HN}_{max}(z)$ is 30–60 m. A constant pycnocline is traced at a depth of 90–110 m, values $\bar{N}_{max}(z)$ here are 3–5 cycle/hour. In the Northeast region of the Barents Sea (4) the stability in winter and spring is close to indifferent, from July to September a mild pycnocline is traced: the $\bar{N}_{max}(z)$ values at a depth of about 30 m do not exceed 3 cycles/hour. At the same time throughout all the year at the depth of about 100 m there is a slight constant density jump, which is most distinctly in winter. In the Southeast (5) district, seasonal pycnocline is traced from May to October.

On Fig. 9 the profiles of averaged values of the Brunt-Väisälä frequency in the Kara Sea is shown. It is seen that in the Southwest (6) and Northwest (7) regions, the density jump layer persists throughout the year. In May–June a seasonal pycnocline begins to form. From June to December the layer of density jump is distinctly.

The average values of the Brunt-Väisälä frequency reach 30 cycles/hour. The occurrence depth of the averaged $N_{max}(z)$ is 15–20 m. The Brunt-Väisälä frequency profile in regions 6, 7, 8 has a special view in September. At a depth of about 15 m there is a decrease of \bar{N} and then at 20–25 m, the buoyancy frequency reaches its maximum. Perhaps this is due to the beginning of the processes of convective mixing and ice formation in the zone of water low salinity.

To assess the consistency of the maximum of the Brunt-Väisälä frequency with climate indices the correlation coefficients between $N_{max}(z)$ and NAO, SOI, AO, TDO, GSNW ($R_{N_{max}\sim NAO}$, $R_{N_{max}\sim SOI}$, $R_{N_{max}\sim AO}$, $R_{N_{max}\sim TDO}$, $R_{N_{max}\sim GSNW}$) were obtained (Fig. 10). At a 90% confidence interval significant values $R > 0.497$ (Brooks and Karuzers 1963). It is obtained, that between the maximum of the Brunt-Väisälä frequency and the North-Atlantic Oscillation index a positive correlation is observed on the large part of the Barents Sea (Northeast physiographic region) with a maximum correlation coefficient of 0.9. In the Kara Sea near the northern tip of Novaya Zemlya and at the mouth of the Ob $R_{N_{max}\sim NAO}$ reach ~ 0.8 . There is a positive correlation between $N_{max}(z)$ and AO in the North physiographic region of the Barents Sea with $R_{N_{max}\sim AO} \sim 0.8$ and negative correlation in the North and Central regions of the Kara Sea with $R_{N_{max}\sim AO} \sim -0.7$. In the North region of the Barents Sea and in the North and Central regions of the Kara Sea, there is a negative correlation between $N_{max}(z)$ and SOI, $N_{max}(z)$ and TDO. The values of $R_{N_{max}\sim SOI}$, $R_{N_{max}\sim TDO}$ reach ~ -0.9 . A positive correlation is observed between $N_{max}(z)$ and GSNW in the North and Central regions of the Kara Sea with maximum values of $R_{N_{max}\sim GSNW} \sim 0.9$.

4 Conclusions

Based on thermohaline data for the period 1955–2012 with a resolution of $0.25^\circ \times 0.25^\circ$, the features of the spatial-temporary distribution of the buoyancy frequency maximum and its occurrence depth in the Barents and Kara Seas were studied. Regional peculiarities of the vertical structure of Brunt-Väisälä frequency are revealed. The correlation relationships of the intra-annual variability of the buoyancy frequency maximum with climatic indices: NAO, SOI, AO, TDO and GSNW were studied.

It is shown, that the values of the buoyancy frequency maximum in the Kara Sea are several times higher than $N_{max}(z)$ in the Barents Sea, due to the difference in the volume of freshwater flow of continental waters.

It was revealed that the maximum waters stability in the Barents Sea comes in July–August, in the Kara Sea—in September, November. These months the averaged over the meridian values of the buoyancy frequency maximum in the Barents Sea is 10–12 cycles/hour, in the Kara Sea—35–40 cycles/hour.

It is established, that between the maximum of the Brunt-Väisälä frequency and the occurrence depth of the density jump layer there is distinctly relationship with $R \sim -0.7$. The large (summer) values of $N_{max}(z)$ are observed at relatively shallow depths (10–25 m), and vice versa, the small (winter) values—at large depths (40–100 m).

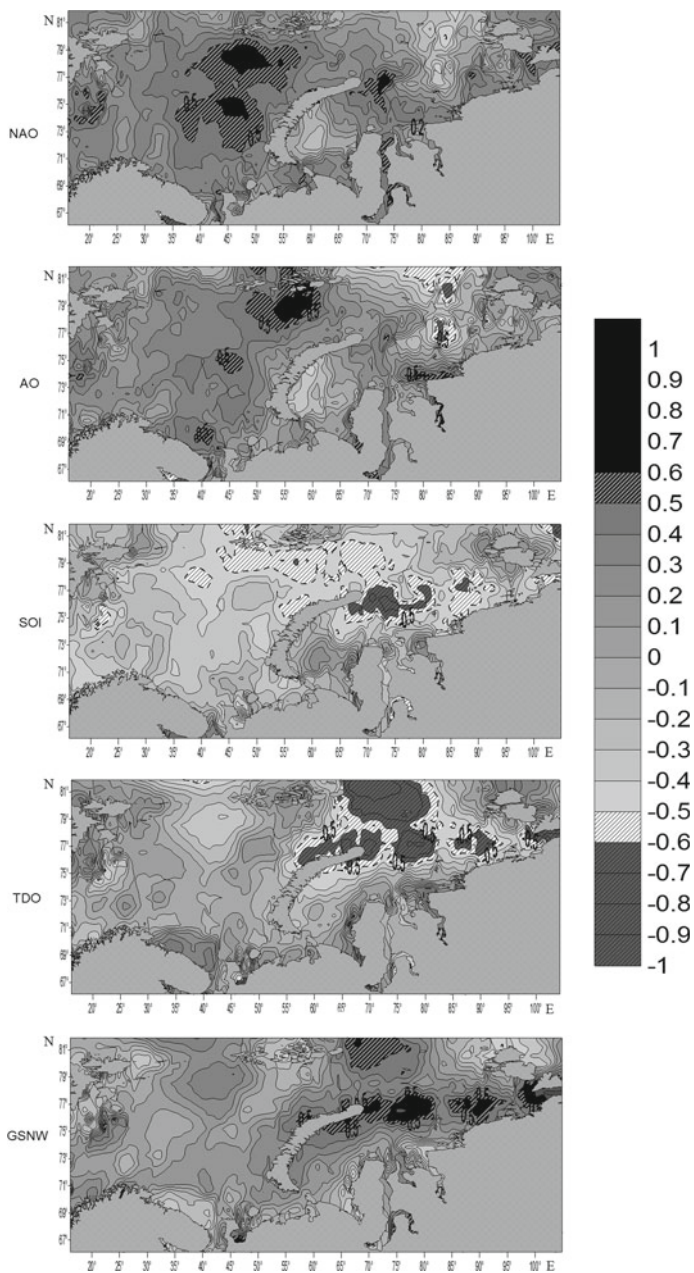


Fig. 10 Regional distribution of correlation coefficients $N_{max}(z)$ with climatic indices: NAO, SOI, AO, TDO and GSNW

It is shown, that between $Nmax(z)$ and NAO, $Nmax(z)$ and AO there is a significant positive correlation in the North and Northeast regions of the Barents Sea. The correlation coefficients reach ~ 0.8 . There is a positive correlation with a maximum coefficient ~ 0.9 between $Nmax(z)$ and GSNW in the North and Central regions of the Kara Sea. In the North region of the Barents Sea, in the North and Central regions of the Kara Sea there is a negative correlation relationship between $Nmax(z)$ and SOI, $Nmax(z)$ and TDO with $R \sim -0.9$.

Acknowledgements The present study is carried out within the framework of the State Order No. 0827-2019-0003.

References

- Artamonov YV, Bukatov AE, Solovei NM (2004) Seasonal variability of a depth of a maximum of frequency of Vyasyalya-Brent in the Atlantic Ocean. Environmental monitoring systems. MHI NASU, Sevastopol, pp 217–219 (in Russian)
- Brooks K, Karuzers N (1963) Application of statistical methods in meteorology. L.: Gidrometeoizdat (in Russian)
- Bukatov AE, Bukatov AA, Babiy MV (2017) Spatial and temporal variability of the Arctic sea ice distribution. Earth's Cryosphere XXI(1):78–85
- Dobrovolsky AD, Zalogin BS (1982) Seas of the USSR. MSU, Moscow, 192 p (in Russian)
- Frolov IE, Gudkovich ZM, Karklin VP, Smolyanitsky VM (2010) Climate change in the Arctic and Antarctic—result of natural causes. Probl Arctic Antartct 2(85):52–61 (in Russian)
- Gorbatsky GV (1970) Physico-geographical zoning of the Arctic. Part 2. L.: ed. Leningrad State University (in Russian)
- https://www.cpc.ncep.noaa.gov/products/site_index.shtml
- <https://web.pml.ac.uk/gulfstream/data.htm>
- Karklin VP, Yulin AV, Sharatunova MV, Mochnova LP (2017) Climate variability of the Kara sea ice massifs. Probl Arctic Antartct 4(14):37–46 (in Russian)
- Locarnini RA, Mishonov AV, Antonov JI, Boyer TP, Garcia HE, Baranova OK, Zweng MM, Paver CR, Reagan JR, Johnson DR, Hamilton M, Seidov D (2013) World Ocean Atlas 2013. Temperature, vol 1. In: Levitus S (ed), Mishonov A (Technical ed) NOAA Atlas NESDIS 73, 40 p
- Matishov GG (2008) Influence of variability of the climatic and ice regimes on navigation. Bull RAS 78(10):896–902 (in Russian)
- Petrov KM (2008) Principles of physical-geographical differentiation of the Arctic Seas: Kara Sea. Izv Akad Nauk Ser Geogr 6:19–30
- Sherstyankin PP, Kuimova LN (2009) Vertical stability and the Brunt-Väisälä frequency of deep natural waters by the example of Lake Baikal, Lake Tanganyika, and the World Ocean. Dokl Earth Sci 429(2):1553–1558
- The second estimating report on climate changes and their consequences in the territory of the Russian Federation. M.: Federal Hydrometeorology and Environmental Monitoring Service, 1009 p (2014) (in Russian)

- Timofeev VT (1946) Stability of waters of the Barents Sea. *Probl Arctic* 3:5–37 (in Russian)
- Tsaturov YS, Klepikov AV (2012) The modern climate change of the Arctic: results of the new estimating report of the Arctic Council. *Arctic Ecol Econ* 4:76–81 (in Russian)
- Zweng MM, Reagan JR, Antonov JI, Locarnini RA, Mishonov AV, Boyer TP, Garcia HE, Baranova OK, Johnson DR, Seidov D, Biddle MM (2013) World Ocean Atlas 2013. Salinity, vol 2. In: Levitus S (ed), Mishonov A (Technical ed) NOAA Atlas NESDIS 74, 39 p

Variational Identification of the Underwater Pollution Source Power



Sergey Vladimirovich Kochergin  and Vladimir Vladimirovich Fomin 

Abstract This article is devoted to the development of a variational procedure for identifying the rate of water discharge at the outlet of an underwater source, as well as the analysis of the sensitivity of the algorithm to the level of random noise in the measurement data. The estimation of the input parameters of the problem was carried out on the basis of the iterative procedure of minimization of the quadratic functional. As a result of numerical experiments, the efficiency of the linearization algorithm is shown.

Keywords Functional minimization · Parameter identification · Linearization method · Numerical simulation · Problem in variations · Measurement data assimilation

1 Introduction

The ecology situation in marine coastal zones is highly dependent on the damping of pollutants from underwater sources. Data about the state in the water area of source can be obtained on the basis of mathematical modeling and assimilation of contact and remote measurement data (Bondur and Grebenyuk 2001; Bondur 2005, 2011).

Due to implementing numerical models, the problem of identifying model parameters from measurement data naturally arises. Known methods of searching for optimal parameters consist of minimization of cost functions, which determine the residuals between values of concentration and measurement data. One of the effective procedures for finding optimal parameters is the estimation algorithm based on the linearization method (Alifanov et al. 1988; Gorsky 1984).

S. V. Kochergin (✉) · V. V. Fomin
Marine Hydrophysical Institute RAS, Sevastopol 299029, Russian Federation
e-mail: vskocher@gmail.com

The purpose of this work is to build and test the variational procedure for finding the input parameters of the transfer model. The paper uses a dynamic model (Ivanov and Fomin 2016), in which the parameter to be identified is the flow rate (w_p) at the vent of the underwater source. In work (Kochergin and Fomin 2019) identification of pollution concentration (C_p) for the investigated model is made.

2 Dynamic Model

With the help of baroclinic nonlinear model (Ivanov and Fomin 2008, 2016; Bondur et al. 2018) fields of velocity, impurity concentration, temperature and salinity was calculated. The three-dimensional equations of ocean dynamics in σ -coordinate with the Boussinesque approximation and hydrostatics approximations have following form (summation is assumed by repeated indices α and β from 1 to 2):

$$\frac{\partial}{\partial t}(Du_\alpha) + \Lambda u_\alpha + \varepsilon_{\alpha\beta} f Du_\beta + gD \frac{\partial \eta}{\partial x_\alpha} + DB_\alpha = \frac{\partial}{\partial x_\beta}(D\tau_{\alpha\beta}) + \frac{\partial}{\partial \sigma} \left(\frac{K_M}{D} \frac{\partial u_\alpha}{\partial \sigma} \right), \quad (1)$$

$$\frac{\partial \eta}{\partial t} + \frac{\partial}{\partial x_\alpha}(Du_\alpha) + \frac{\partial w_*}{\partial \sigma} = 0, \quad (2)$$

$$\frac{\partial}{\partial t}(DT) + \Lambda T = \frac{\partial}{\partial x_\beta} \left(A_T \frac{\partial T}{\partial x_\beta} \right) + \frac{\partial}{\partial \sigma} \left(\frac{K_T}{D} \frac{\partial T}{\partial \sigma} \right), \quad (3)$$

$$\frac{\partial}{\partial t}(DS) + \Lambda S = \frac{\partial}{\partial x_\beta} \left(A_S \frac{\partial S}{\partial x_\beta} \right) + \frac{\partial}{\partial \sigma} \left(\frac{K_S}{D} \frac{\partial S}{\partial \sigma} \right), \quad (4)$$

$$\frac{\partial}{\partial t}(DC) + \Lambda C = \frac{\partial}{\partial x_\beta} \left(A_C \frac{\partial C}{\partial x_\beta} \right) + \frac{\partial}{\partial \sigma} \left(\frac{K_C}{D} \frac{\partial C}{\partial \sigma} \right), \quad (5)$$

$$\rho = \rho(T, S), \quad (6)$$

$$\Lambda \varphi = \frac{\partial}{\partial x_\beta}(Du_\beta \varphi) + \frac{\partial}{\partial \sigma}(w_* \varphi), \quad B_\alpha = \frac{g}{\rho_0} \left(\frac{\partial}{\partial x_\alpha} D \int_\sigma^0 \rho d\sigma' + \sigma \frac{\partial D}{\partial x_\alpha} \rho \right), \quad (7)$$

$$\tau_{\alpha\alpha} = 2A_M \frac{\partial u_\alpha}{\partial x_\alpha}, \quad \tau_{\alpha\beta} = \tau_{\beta\alpha} = A_M \left(\frac{\partial u_\beta}{\partial x_\alpha} + \frac{\partial u_\alpha}{\partial x_\beta} \right), \quad (8)$$

where $(x_1, x_2) = (x, y)$; σ —vertical coordinate, varying from -1 to 0 ; $D = h_0 + \eta$ —dynamic depth; $A_M, K_M, A_T, K_T, A_S, K_S, A_C, K_C$ —coefficients of turbulent viscosity and diffusion; $\tau_{\alpha\beta}$ —components of the turbulent stress tensor; f —Coriolis

parameter; g —acceleration of free fall; ρ_0 —average water density; $\varepsilon_{\alpha\beta} = 0$ at $\alpha = \beta$; $\varepsilon_{12} = -1$; $\varepsilon_{21} = 1$.

The required variables of the system (1)–(8) are: $(u_1, u_2) = (u, v)$ —horizontal velocity components, w_* —normal to the surface $\sigma = \text{const}$ of the flow velocity component, fields T, S, C and the field of seawater density ρ .

On a free surface $\sigma = 0$, the boundary conditions have the form:

$$w_* = 0, \frac{K_M}{D} \frac{\partial u_\alpha}{\partial \sigma} = 0, \frac{K_T}{D} \frac{\partial T}{\partial \sigma} = 0, \frac{K_S}{D} \frac{\partial S}{\partial \sigma} = 0, \frac{K_C}{D} \frac{\partial C}{\partial \sigma} = 0. \quad (9)$$

Boundary conditions at the bottom outside the source ($\sigma = -1, x \neq x_p, y \neq y_p$) are written as follows:

$$w_* = 0, \frac{K_M}{D} \frac{\partial u_\alpha}{\partial \sigma} = \mu |u| u_\alpha, \frac{K_T}{D} \frac{\partial T}{\partial \sigma} = 0, \frac{K_S}{D} \frac{\partial S}{\partial \sigma} = 0, \frac{K_C}{D} \frac{\partial C}{\partial \sigma} = 0, \quad (10)$$

where $|u| = \sqrt{u_1^2 + u_2^2}$, μ —the bottom friction coefficient.

At the bottom in the outlet area ($\sigma = -1, x = x_p, y = y_p$) boundary conditions can be written as (Bondur et al. 2018):

$$w_* = w_p, \frac{K_M}{D} \frac{\partial u_\alpha}{\partial \sigma} = \mu |u| u_\alpha, \quad (11)$$

$$w_p T - \frac{K_T}{D} \frac{\partial u_\alpha}{\partial \sigma} = w_p T_p, w_p S - \frac{K_S}{D} \frac{\partial S}{\partial \sigma} = w_p S_p, w_p C - \frac{K_C}{D} \frac{\partial C}{\partial \sigma} = w_p C_p. \quad (12)$$

Initial conditions have the following form:

$$u = U_0, v = w = 0, \eta = 0, T = T_0(\sigma), S = S_0(\sigma), C = 0. \quad (13)$$

Here u, v, w —components of the velocities along x, y, σ respectively; U_0 is a constant depth rate of background currents; T, S —the temperature and salinity of water; $T_0(\sigma)$ —background temperature distribution; $S_0(\sigma)$ —background distribution of salinity; C —concentration of contaminants Q_p —water consumption; d —the horizontal size of the source; $w_p = Q_p/d^2$ —the rate of outflow of water; T_p, S_p —the temperature and salinity of the inflowing water; C_p —impurity concentration at the exit of the source.

The numerical procedure for solving the system of equations is described in detail in Ivanov and Fomin (2008). The Smagorinsky formula is used to calculate the coefficients of horizontal turbulent diffusion (Smagorinsky 1963). Mellor-Yamada model (Mellor and Yamada 1982) is used for determined the coefficients of vertical turbulent viscosity and diffusion. Advective terms approximation in the model is done on the basis of TVD schemes (Harten 1984; Fomin 2006).

The model is implemented on a time period $[0, t_0]$ for a rectangular area $\Omega = \{0 \leq x \leq L, 0 \leq y \leq L, 0 \leq \sigma \leq L\}$; with a free surface and open lateral border. By $t > 0$ at the bottom of the pool ($\sigma = -1$) in area Ω_p begins to operate the source of contamination with the following parameters: w_p —the rate of outflow of water from the source; T_p, S_p —the temperature and salinity of the flowing water; C_p —concentration of impurity at the exit of the source.

3 Algorithm for Identifying the Rate of Flow from the Outlet

Let we need to identify w_p —the velocity of source flow. Method of linearization (Alifanov et al. 1988) can be used for solving of this task. Following (Kochergin and Kochergin 2017), we have identified in accordance with the model (1)–(13) the problem in variations with constant A_M, K_T, K_S, K_C :

$$\begin{aligned}
 & \frac{\partial}{\partial t}(D\delta u_\alpha) + \Lambda\delta u_\alpha + \delta\Lambda(u_\alpha) + \varepsilon_{\alpha\beta}fD\delta u_\beta + gD\frac{\partial\delta\eta}{\partial x_\alpha} + D\delta B_\alpha \\
 & = \frac{\partial}{\partial x_\beta}(D\delta\tau_{\alpha\beta}) + \frac{\partial}{\partial\sigma}\left(\frac{K_M}{D}\frac{\partial\delta u_\alpha}{\partial\sigma}\right), \\
 & \frac{\partial\delta\eta}{\partial t} + \frac{\partial}{\partial x_\alpha}(D\delta u_\alpha) + \frac{\partial\delta w_*}{\partial\sigma} = 0, \\
 & \frac{\partial}{\partial t}(D\delta T) + \Lambda(\delta T) + \delta\Lambda(T) - \frac{\partial}{\partial x_\beta}\left(A_T\frac{\partial\delta T}{\partial x_\beta}\right) - \frac{\partial}{\partial\sigma}\left(\frac{K_T}{D}\frac{\partial\delta T}{\partial\sigma}\right) = 0, \\
 & \frac{\partial}{\partial t}(D\delta S) + \Lambda(\delta S) + \delta\Lambda(S) - \frac{\partial}{\partial x_\beta}\left(A_S\frac{\partial\delta S}{\partial x_\beta}\right) - \frac{\partial}{\partial\sigma}\left(\frac{K_S}{D}\frac{\partial\delta S}{\partial\sigma}\right) = 0, \\
 & \frac{\partial}{\partial t}(D\delta C) + \Lambda(\delta C) + \delta\Lambda(C) - \frac{\partial}{\partial x_\beta}\left(A_C\frac{\partial\delta C}{\partial x_\beta}\right) - \frac{\partial}{\partial\sigma}\left(\frac{K_C}{D}\frac{\partial\delta C}{\partial\sigma}\right) = 0. \quad (14)
 \end{aligned}$$

in (14) the following designations are used:

$$\begin{aligned}
 & \delta\rho = \delta\rho(T, S), \text{ depends on the type of function } \rho = \rho(T, S) \\
 & \delta\Lambda\varphi = \frac{\partial}{\partial x_\beta}(D\delta u_\beta\varphi) + \frac{\partial}{\partial\sigma}(\delta w_*\varphi), \\
 & \delta\Lambda\varphi = \frac{\partial}{\partial x_\beta}(Du_\beta\varphi) + \frac{\partial}{\partial\sigma}(\delta w_*\varphi), \\
 & \delta B_\alpha = \frac{g}{\rho_0}\left(\frac{\partial}{\partial x_\alpha}D\int_\sigma^0\delta\rho d\sigma' + \sigma\frac{\partial D\delta\rho}{\partial x_\alpha}\right), \\
 & \delta\tau_{\alpha\alpha} = 2A_M\frac{\partial\delta u_\alpha}{\partial x_\alpha}, \delta\tau_{\alpha\beta} = \delta\tau_{\beta\alpha} = A_M\left(\frac{\partial\delta u_\beta}{\partial x_\alpha} + \frac{\partial\delta u_\alpha}{\partial x_\beta}\right). \quad (15)
 \end{aligned}$$

The model uses the boundary conditions, on a free surface:

$$\delta w_* = 0, \frac{K_M}{D} \frac{\partial \delta u_\alpha}{\partial \sigma} = 0, \frac{K_T}{D} \frac{\partial \delta T}{\partial \sigma} = 0, \frac{K_S}{D} \frac{\partial \delta S}{\partial \sigma} = 0, \frac{K_C}{D} \frac{\partial \delta C}{\partial \sigma} = 0, \quad (16)$$

outside the source at the bottom ($\sigma = -1, x \neq x_p, y \neq y_p$):

$$\begin{aligned} \delta w_* &= 0, \frac{K_M}{D} \frac{\partial \delta u_\alpha}{\partial \sigma} = \mu |u| \delta u_\alpha + \mu \delta(|u|) u_\alpha, \\ \frac{K_T}{D} \frac{\partial \delta T}{\partial \sigma} &= 0, \frac{K_S}{D} \frac{\partial \delta S}{\partial \sigma} = 0, \frac{K_C}{D} \frac{\partial \delta C}{\partial \sigma} = 0 \\ \delta |u| &= \frac{1}{2} (u_1^2 + u_2^2)^{-1/2} \cdot (2u_1 \delta u_1 + 2u_2 \delta u_2), \end{aligned}$$

at the bottom in the source area ($\sigma = -1, x = x_p, y = y_p$):

$$\begin{aligned} \delta w_* &= 1, \frac{K_M}{D} \frac{\partial \delta u_\alpha}{\partial \sigma} = \mu |u| \delta u_\alpha + \mu \delta(|u|) u_\alpha, \\ w_p \delta T + T - \frac{K_T}{D} \frac{\partial \delta u_\alpha}{\partial \sigma} &= w_p \delta T_p + T_p, \\ w_p \delta S + \delta S - \frac{K_S}{D} \frac{\partial \delta S}{\partial \sigma} &= w_p \delta S_p + S_p, \\ w_p \delta C - \frac{K_C}{D} \frac{\partial \delta C}{\partial \sigma} &= w_p \delta C_p + C_p. \end{aligned} \quad (17)$$

Let the model (14)–(17) decided for period $[0, t_0]$ inside domain Ω . To find the optimal parameters of model we can find the minimum of cost function:

$$J = \frac{1}{2} \langle P(RC - C_{obs}), P(C - C_{obs}) \rangle, \quad (18)$$

where $\langle a, b \rangle = \int_0^{t_0} \iint_{\Omega} ab d\Omega dt$ —the scalar product; C_{obs} —the measured values of C at the given points of the domain Ω at time moment t_0 ; R —a projection operator to the points of observations; P —the fill operator the residuals field with zeros in the case of lack data measurements.

Let's write the variable as follows:

$$C = \bar{C} + \delta C_{w_p} (w_p - w_p^*), \quad (19)$$

where \bar{C} —some value of the concentration, and w_p^* —its value, to be determined. From (19) in (18) we obtain:

$$J = \frac{1}{2} \langle P(R(\bar{C} + V(w_p - w_p^*)) - C_{obs}), P(R(\bar{C} + V(w_p - w_p^*)) - C_{obs}) \rangle. \quad (20)$$

And due to condition $\frac{\partial J}{\partial C_p} = 0$, we have:

$$w_p^* = w_p + \frac{\langle P(RC - C_{obs}), PRV \rangle}{\langle PRV, PRV \rangle} \tag{21}$$

If data is received from sea surface, formula (21) is also correct. In this case you must select necessary operators P and R .

The problem of numerical realization of the problem in variations even in the approximation of constant coefficients A_M, K_T, K_S, K_C is quite difficult to solve. Therefore, a simplified identification algorithm for w_p based on the direct modeling method is implemented. Variation δC_p is determined by solving a series of basic problems at different values w_p near the true value $w_p = w_p^*$ by averaging over the ensemble of realizations. After solving the main problem, the required value w_p is specified iteratively.

4 Numerical Experiments and Results

Numerical experiments were carried out for the coastal zone of the Sevastopol city in the area of the Blue Bay, where urban sewage is mainly located. The computational domain had a horizontal size $L = 2$ km, depth $h_0 = 30$ m Fig. 1. Horizontally, uniform rectangular grid was used with a step $d = 20$ m and vertically step equal 1 m was selected. The time step time was 5 s. On the western boundary of the

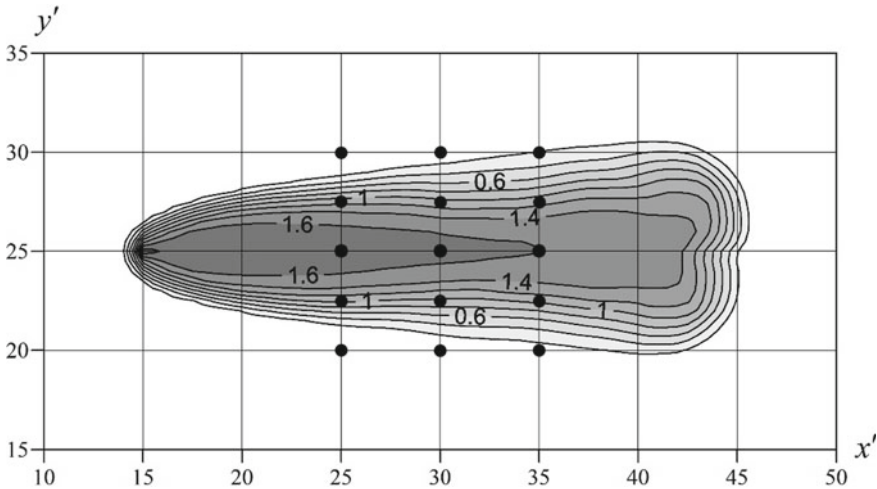


Fig. 1 Relative concentration of the mixture C (%) in the area of the underwater source at $\sigma = -0.3166$ ($z = -9.5$ m)

estimated domain ($x = 0$) was used conditions of the form 13. In the remaining fluid boundaries conditions were used to smooth continue.

The center of the outlet was located at the point with coordinates: $x_p = 600$ m; $y_p = 1000$ m. Horizontal size of the source in x, y axes was equal to the step of the calculated grid d . It was meant that the water flowing from the source is zero salinity ($S_p = 0$), and its temperature is equal to the ambient temperature, i.e. $T_p = T_0(-1)$. The results of sounding in the area of underwater release were used as T_0 and S_0 . Due to Morozov et al. (2016), the value of U_0 was taken to be 0.05 m/s.

Initially, a model calculation of the characteristics of the model with a given value C_p^* is 0.05 kg/m³ was done. The spatial distribution of the polluted water field on a fixed horizon is shown in Fig. 1. Here are the contours of the relative concentration $c = 100\% \cdot C/C_p^*$ for a finite moment in time. Dimensionless horizontal coordinates have the form $x' = x/2d, y' = y/2d$. The horizon corresponds to the depth of the layer of the jump in which the impurity is mainly concentrated. A detailed description of the effect of sea water density stratification and background flow velocity on the impurity field is given in Fomin (2006), Kochergin and Kochergin (2017).

Some numerical experiments was implemented to test the parameter w_p identification algorithm. It was believed that the measurements of all fifteen vertical profiles C , at points arranged according to the scheme in Fig. 1, performed simultaneously at t is 4 h. the results of recovery w_p at different noise levels in the input data are shown in Table 1. As you can see, at a noise level of 1.25% and below, the value is restored almost exactly. The greatest decrease of the functional (18) occurs at the first iterations. In this numerical experiment, information was absorbed from all stations, including uninformative ones, located on the periphery of the pollution spot. At assimilation of data from the stations located in the area of maximum values of conditionality of the solved problem is improved that leads to improvement of the received results.

Table 1 Results of recovery of the rate of water outflow from an underwater source at different noise levels in the input data

$r, \text{kg/m}^3$	Noise level $100\% + r/C_p^*, \%$	Restored $w_p, \text{m/s}$	Error recovery $100 \cdot \left 1 - w_p/w_p^* \right , \%$
0.0000	0.0	$34,991,985 \times 10^{-3}$	0.0
0.00675	1.25	$35,180,813 \times 10^{-3}$	0.5
0.0125	2.5	$38,568,601 \times 10^{-3}$	10.2
0.0250	5.0	$46,490,142 \times 10^{-3}$	32.8

5 Conclusions

Numerical experiments have shown reliable operation of the linearization method when searching for the values of the identifiable parameters. In continuation of the work (Kochergin and Fomin 2019), in which the concentration of pollution in the source is determined, a variational algorithm for identifying the rate of entry of polluted water into the basin is constructed and tested. The problem in variations is constructed and the search for the solution of the problem in variations in the simplest case is implemented. The proposed algorithm has a good convergence rate and accuracy of recovery of the required parameter. The realized procedure can be used for solving different ecological.

The work was carried out within the framework of the state task on the topic 0827-2018-0004 “Complex interdisciplinary studies of Oceanological processes that determine the functioning and evolution of ecosystems of the coastal zones of the Black and Azov seas” (“Coastal studies”) and supported by grant RFFI 18-45-920035 p_a.

References

- Alifanov OM et al (1988) Extreme methods for solving ill-posed problems. Nauka, Moscow, 286 p
- Bondur V (2005) Complex satellite monitoring of coastal water areas. In: 31st International symposium on remote sensing of environment, 20–24 June, St. Petersburg, p 7
- Bondur VG (2011) Satellite monitoring and mathematical modelling of deep runoff turbulent jets in coastal water areas. In: Waste water, evaluation and management. <https://www.intechopen.com>
- Bondur VG, Grebenyuk YV (2001) Remote indication of anthropogenic influence on marine environment caused by depth waste water plum: modeling, experiment. *Issledovanie Zemli iz Kosmosa* 6:49–67
- Bondur VG, Ivanov VA, Fomin VV (2018) Features of propagation of contaminating water from an underwater out falling a stratified environment of coastal water. *Izvestiya RAN Fizika Atmosfery i Okeana* 54(4):453–461
- Fomin VV (2006) Application of TVD schemes to numerical modeling of frontal salinity zones in a shallow sea. *Meteorol Gidrol* 2:59–68
- Gorsky VG (1984) Planning of kinetic experiments. Nauka, Moscow, 240 p
- Harten A (1984) On a class of high resolution total-variation-stable finite-difference schemes. *J Numer Anal* 21(1):1–23
- Ivanov VA, Fomin VV (2008) Mathematical modelling of the dynamic processing in the sea-land zone. *ECOSI-Gidrophisika*, Sevastopol, 363 p
- Ivanov VA, Fomin VV (2016) Numerical modelling of propagation of underwater runoff in the coast of Heracleean Peninsula. *Phys Oceanogr* 6:82–95
- Kochergin SV, Fomin VV (2019) Determination of the concentration of contaminants at the outlet of the underwater source based on the variational algorithm. In: Physical and mathematical modeling of earth and environment processes. 4th International Scientific School for Young Scientists, Ishlinskii Institute for Problems in Mechanics of Russian Academy of Science, Springer International Publishing AG, part of Springer Nature, pp 41–50
- Kochergin VS, Kochergin SV (2017) Variational algorithm for identifying power pulsed source pollution. *Ecologicheskii vestnik nauchnyh centrov Chernomorskogo ehkonomicheskogo sotrudnichestva*, no 3, pp 62–72

- Mellor GL, Yamada T (1982) Development of a turbulence closure model for geo-physical fluid problems. *Rev Geophys Space Phys* 20(4):851–875
- Morozov AN, Ivanov VA, Shutov SA et al (2016) Spatial structure of currents near Heracleon Peninsula according ADCP-observations in 2015. In: *Ecologicheskaya bezopasnost' pribrezhnoj i shel'fovoj zon morya*, MGI, Sevastopol, issue 1, pp 73–79
- Smagorinsky J (1963) General circulation experiments with primitive equations. I. The basic experiment. *Mon Weather Rev* 91(3):99–164

Analytical Solution of the Test Three-Dimensional Problem of Wind Flows



Vladimir Sergeevich Kochergin , Sergey Vladimirovich Kochergin ,
and Sergey Nikolaevich Sklyar 

Abstract The paper considers an analytical solution for a three-dimensional model of wind flows. Formulas for the vertical velocity component are used in testing and analysis of various algorithms for its calculation.

Keywords Dimensionless problem · Wind currents · Test problem · Analytical solution · Vertical velocity

1 Introduction

Numerical modeling of ocean dynamics in solving environmental monitoring problems is of great importance. The development of computer technology has allowed to solve such problems with a large discretization in space and time for a more correct description of the dynamic processes taking place in the ocean. However, the development of the models and methods of their numerical implementation is far from exhausted. Due to choosing a particular model, the scheme of its numerical realization, it is desirable to have a test solution with which to compare. Most often there is a comparison of the results obtained by one model with others, but this comparison is often subjective. Therefore, the presence of an accurate (analytical) solution of a problem allows you to make the correct choice of the used schemes and algorithms for its numerical implementation. There are analytical solutions for the simplest productions, for example, the Stommel model (Stommel 1948, 1965a, b; Kochergin 1978). In Eremeev et al. (2008), Kochergin and Dunec (1999) such a problem is realized by the method of dynamic operator inversion (Kochergin 1978) for the study of applied computational schemes of a special kind for the calculation of velocity fields. In this paper, we consider a more complex problem (Kochergin et al. 2019) the solution of which allows us to obtain an analytical solution for the

V. S. Kochergin (✉) · S. V. Kochergin
Marine Hydrophysical Institute RAS, Sevastopol 299029, Russian Federation
e-mail: vskocher@gmail.com

S. N. Sklyar
American University of Central Asia, Bishkek, Kyrgyzstan

barotropic component of the velocity, its three-dimensional additional part and the vertical component.

2 The Problem in a Dimensionless Form

Let the surface of the water basin in the xOy plane have the shape of a rectangle:

$$\Omega_0 \times [0, r][0, q].$$

its depth $H > 0$. The axes of the Cartesian coordinate system are directed as follows: Ox —to the East, Oy —to the North, Oz —vertically down. In the three-dimensional domain $\Omega = \{(x, y, z) | (x, y) \in \Omega_0, 0 \leq z \leq H\}$, we consider a system of equations of motion in a dimensionless form:

$$\begin{cases} -lv = -\frac{\partial P^s}{\partial x} + \frac{\partial}{\partial z} \left(k \frac{\partial u}{\partial z} \right) \\ lu = -\frac{\partial P^s}{\partial y} + \frac{\partial}{\partial z} \left(k \frac{\partial v}{\partial z} \right), t > 0, (x, y, z) \in \Omega^0, \\ \frac{\partial u}{\partial x} + \frac{\partial v}{\partial y} + \frac{\partial w}{\partial z} = 0 \end{cases} \quad (1)$$

with boundary conditions:

$$\{t > 0, z = 0, (x, y) \in \Omega_0^0\} : k \frac{\partial u}{\partial z} = -\tau_x, k \frac{\partial v}{\partial z} = -\tau_y, w = 0, \quad (2)$$

$$\{t > 0, z = H, (x, y) \in \Omega_0^0\} : k \frac{\partial u}{\partial z} = -\tau_x^b, k \frac{\partial v}{\partial z} = -\tau_y^b, w = 0, \quad (3)$$

$$\{t > 0, 0 \leq z \leq H, (x, y) \in \partial\Omega_0\} : U \cdot n_x + V \cdot n_y = 0, \quad (4)$$

and initial data:

$$\{t = 0, (x, y, z) \in \Omega\} : u = u^0, v = v^0, w = w^0, \quad (5)$$

where Ω^0 and Ω_0^0 are interior points of Ω and Ω_0 .

In (4) the dimensionless integral velocity are defined as follows:

$$U(t, x, y) = \int_0^H u(t, x, y, z) dz, V(t, x, y) = \int_0^H v(t, x, y, z) dz,$$

and in (3) the following variant of parametrization of bottom friction is used:

$$\tau_x^b = \mu \cdot U, \tau_y^b = \mu \cdot V, \mu \equiv const > 0. \quad (6)$$

In accordance with the model Stommel, suppose:

$$l = l_0 + \beta \cdot y, k \equiv \text{const}; \quad (7)$$

$$\tau_x = \frac{F \cdot q}{\pi} \cos\left(\frac{\pi y}{q}\right), \tau_y = 0.$$

We will look for the horizontal components of the velocity vector in the form:

$$u = U \cdot H^{-1} + \hat{u}, v = V \cdot H^{-1} + \hat{v}, \quad (8)$$

where the first terms are called barotropic, and the second are called additional components of speed.

3 Analytical Solution

In work (Kochergin et al. 2019) analytical expressions for barotropic component of velocity, additional components and vertical component of velocity for the task are obtained. The obtained analytical solutions for velocities were used for calculations in various ways, including the formula obtained in Kochergin et al. (2019).

4 Numerical Example (Black Sea)

To illustrate, consider as a model object a rectangular body of water with a flat bottom with characteristic dimensions of the Black sea:

$$\begin{aligned} a &= 11 \times 10^7 \text{ (sm)} = 1100 \text{ (km)}, R = 0.02 \text{ (sm/s)}, \\ b &= 5 \times 10^7 \text{ (sm)} \approx 500 \text{ (km)}, D = 2 \times 10^5 \text{ (sm)} = 2000 \text{ (m)}, \\ G &= 1 \left(\frac{\text{dyn}}{\text{sm}^2} \right), E = 1 \text{ (sm}^2/\text{s}), \rho = 1 \text{ (g/sm}^3\text{)}, \\ f_0 &= 10^{-4} \left(\frac{1}{\text{s}} \right), f_1 = 2 \times 10^{-13} \left(\frac{1}{\text{sm s}} \right). \end{aligned}$$

We choose characteristic scales:

$$L = 10^7 \text{ (sm)}, h = 2 \times 10^5 \text{ (sm)}, u_0 = 10 \text{ (sm/s)}.$$

Then we have:

$$r = 11, q = 5, H = 1, k = 0.05, l_0 = 1, \beta = 0.002,$$

$$\beta = 0 \text{---without } \beta \text{-effect}, F = \frac{\pi}{2} \times 10^{-3}, \mu = 0.001, w_0 = 0.2.$$

Finding the solution of the problem (1)–(5), the solution of the dimensional problem is determined by the formulas:

$$\bar{u} = \bar{u}(Lx, Ly, hz) = u_0 \cdot u(x, y, z),$$

$$\bar{v} = \bar{v}(Lx, Ly, hz) = u_0 \cdot v(x, y, z),$$

$$\bar{w} = \bar{w}(Lx, Ly, hz) = w_0 \cdot w(x, y, z), w_0 = \frac{hu_0}{L},$$

where the line denotes the components of the velocity vector for the dimensional problem.

5 Algorithms for Calculating Vertical Velocity

Imagine horizontal speed by following formulas:

$$u = U + \hat{u}, v = V + \hat{v},$$

where U, V —barotropic components, \hat{u}, \hat{v} —variable over space, additional three-dimensional components of velocity.

We write the continuity equation in the form:

$$\frac{\partial w}{\partial z} + \frac{\partial u}{\partial x} + \frac{\partial v}{\partial y} = 0. \quad (9)$$

For barotropic components it's true that:

$$\frac{\partial U}{\partial x} + \frac{\partial V}{\partial y} = 0, \quad (10)$$

therefore, from (9) we have:

$$\frac{\partial w}{\partial z} + \frac{\partial \hat{u}}{\partial x} + \frac{\partial \hat{v}}{\partial y} = 0. \quad (11)$$

It should be noted that Eq. (11) can be used to reduce errors in the calculation w . Integrate (9) from 0 to z taking into account boundary conditions $w(0) = 0$, $w(H) = 0$, where H —the depth of the sea, 0—corresponds to its surface. Then have:

$$w(z) = - \int_0^z \left(\frac{\partial u}{\partial x} + \frac{\partial v}{\partial y} \right) dz. \quad (12)$$

Similarly, from (11) we obtain:

$$w(z) = - \int_0^z \left(\frac{\partial \hat{u}}{\partial x} + \frac{\partial \hat{v}}{\partial y} \right) dz. \quad (13)$$

Equation (9) following (Eremeev et al. 2008) can be written with the second order of approximation:

$$\frac{w_{k+1} + w_k}{\Delta z_{k+1/2}} = \frac{f_{k+1} + f_k}{2}, \Delta z_{k+1/2} = z_{k+1} - z_k, \quad (14)$$

or

$$\frac{w_k + w_{k-1}}{\Delta z_{k-1/2}} = \frac{f_k + f_{k-1}}{2}, \Delta z_{k-1/2} = z_k - z_{k-1}, \quad (15)$$

where

$$f = S_x D_x u + S_y D_y v, \quad (16)$$

or

$$f = S_y D_x u + S_x D_y v. \quad (17)$$

The following difference operators are used in (16) and (17):

$$D_x \Phi(x, y) = \frac{\Phi\left(x + \frac{\Delta x}{2}, y\right) - \Phi\left(x - \frac{\Delta x}{2}, y\right)}{\Delta}, \quad (18)$$

$$D_y \Phi(x, y) = \frac{\Phi\left(x, y + \frac{\Delta y}{2}\right) - \Phi\left(x, y - \frac{\Delta y}{2}\right)}{\Delta y}, \quad (19)$$

$$S_x \Phi(x, y) = \frac{\Phi\left(x + \frac{\Delta x}{2}, y\right) + \Phi\left(x - \frac{\Delta x}{2}, y\right)}{2}, \quad (20)$$

$$D_y \Phi(x, y) = \frac{\Phi\left(x, y + \frac{\Delta y}{2}\right) - \Phi\left(x, y - \frac{\Delta y}{2}\right)}{2}, \tag{21}$$

where $\Phi(x, y)$ is some function.

Subtract from (14) the expression (15), then we have:

$$\frac{1}{\Delta z_{k+1/2}} w_{k+1} - \left(\frac{1}{\Delta z_{k+1/2}} + \frac{1}{\Delta z_{k-1/2}} \right) w_k + \frac{1}{z_{k-1/2}} w_{k-1} = \frac{1}{2} (f_{k+1} - f_{k-1}) \tag{22}$$

Using (16), we obtain, for example, a Central difference discretization. Note that (22) is realized by the method of run (Godunov and Ryaben’kij 1977) taking into account both boundary conditions for w on the surface and at the bottom.

To control the quality of the calculation of the vertical velocity component, we will compare the obtained values w with the exact analytical solution \bar{w} . The comparison will be made in the following norms:

$$NC = \frac{\max_{\Omega} |w - \bar{w}| \times 100\%}{\max_{\Omega} |\bar{w}|}, \quad NL = \frac{\sum_{\Omega} |w - \bar{w}| \times 100\%}{\sum_{\Omega} |\bar{w}|}, \tag{23}$$

where \bar{w} —the calculated value according to the analytical formula and w —the estimate of the vertical velocity obtained in one way or another.

6 Results of Numerical Experiments

Numerical experiments have shown that the worst result in the sense of these norms is obtained by calculating the vertical velocity from the continuity Eq. (12) at full velocities, taking into account the barotropic and additional components of the velocity field. The calculation results are presented in Table 1. A significant improvement in the results is obtained by using the formula (13). The implementation of the formula run algorithm (22) in both cases (using the full speed and its additional component) gives comparable results.

Table 1 Values of NC and NL norms

	Formula (5)	Formula (6)	Run (14) for (5)	Run (14) for (6)
NC (%)	84.116	25.449	4.9329	4.9300
NL (%)	41.06	23.349	4.6529	4.6529

7 Conclusion

Based on the comparison of the calculated values of the vertical velocity component obtained by various methods, a comparison with the exact values is made. As a result of the comparative analysis, the advantage of using the run algorithm over the standard approach for calculation is shown. The results can be used in the construction of numerical models of the dynamics of the ocean and various reservoirs.

The work was carried out within the framework of the state task on the theme № 0827-2018-0004 “Complex interdisciplinary studies of Oceanological processes determining the functioning and evolution of ecosystems in the coastal zones of the Black and Azov seas”.

References

- Eremeev VN, Kochergin VP, Kochergin SV, Sklyar SN (2008) Mathematical modeling of hydrodynamics of deep-water basins. ECOSI-Gidrophisika, Sevastopol, 363 p
- Godunov SK, Ryaben'kij VS (1977) Raznostnye skhemy (Vvedenie v teoriyu). M: Nauka, 440 p
- Kochergin VP (1978) Theory and methods of ocean currents. Nauka, Moscow, 127 p
- Kochergin VP, Dunec TA (1999) Vychislitel'nyj algoritm dlya opredeleniya naklonov urovnya v zadachah dinamiki vodoemov. Morskoy Gidrofizicheskij zhurnal 3:20–28
- Kochergin VS, Kochergin SV, Sklyar SN (2019) Analiticheskaya testovaya zadacha vetrovyh techenij. Processy v geosredah 2(20):193–198
- Stommel H (1948) The westward intensification of wind-driven ocean currents. Trans Am Geophys Union 29:202–206
- Stommel H (1965a) The Gulf stream. A physical and dynamical description. University of California Press, Berkeley, 227 p
- Stommel H (1965b) Gulf stream. IL, Moscow, 227 p

Seasonal Variations of the Significant Altitude of the Waves in the Black Sea



N. N. Voronina 

Abstract Based on mathematical modeling, the variability of the intensity of waves in different regions of the Black Sea was studied. For analysis, we used the global MFWAM model of the International Marine Environmental Operative Monitoring Service, Copernicus. The seasonal variation of significant wave height on north-western shelf, in eastern, central and western parts of the Black Sea was analyzed. Dependencies are constructed that describe the annual course of a significant wave height. Also built are dependencies describing the deviations of the “instantaneous” values of the significant wave height from its average value over 30 days. Correlation coefficients for instantaneous values of significant wave height are close level of 0.5. It is shown that the correlation of the monthly average wave intensity in selected regions is close to the level of 0.9 and higher.

Keywords Black sea · Significant waves height · Seasonal variability

1 Introduction

Information on a significant waves height is necessary when solving a wide range of fundamental and applied problems. First of all, this information is necessary for tasks related to the impact of waves on ships and coastal structures (Taskar et al. 2016; Özbahçec 2004). It is also necessary in the analysis of remote sensing data from spacecraft (Pokazeev et al. 2013; Gómez-Enri et al. 2006), calculation of hydroacoustic radiation by the sea surface (Zapevalov and Pokazeev 2016), etc.

Data on significant waves height on a global scale are obtained with help of space-based radio altimeters (Hayne 1980). Significant limitations in the direct use of these data are associated with the binding to the time of flight of the satellite over the study area, as well as with the relatively narrow strip of the sea surface that forms the

N. N. Voronina (✉)

Marine Hydrophysical Institute RAS, Sevastopol, Russian Federation

e-mail: voronina.nataly@mail.ru

altimeter signal. The second approach to obtaining information on the variability of the field of surface waves is based on the construction of hydrodynamic wave models (Hasselmann et al. 1988). A limitation of this approach is the insufficient accuracy of the obtained characteristics.

In recent years, an intensive direction has been developing in oceanography, within the framework of which various approaches have been synthesized; mathematical modeling and taking measurements have been combined (Knysh et al. 2016). Mathematical wave models are constructed in which data of direct or distance measurements are assimilated. For assimilation, data from waveographic buoys or data on a significant waves height obtained using altimeters are used (Francis and Stratton 1990). The assimilation of data from three waveform buoys located in the Arabian Sea in the WAM model allowed for this region to increase accuracy by 30% (Sannasiraj and Goldstein 2009). The assimilation of altimetry measurement data is more effective than buoy data, since altimetry data is not tied to a single point. The accuracy of determining the significant waves height increases with increasing number of used spacecraft (Yu et al. 2018).

The aim of the present work is to analyze seasonal variability of the intensity of wind waves in the Black Sea. The analysis is based on the MFWAM model (Ardhuin et al. 2010; Janssen et al. 2014).

2 Wave Field Characteristics

The main contribution to the energy of the wave field, which is determined by the dispersion of the elevations of the surface, is made by waves with frequencies corresponding to the peak in the wave spectrum. There is a wide range of characteristics defining wave energy.

A significant waves height is chosen here as a parameter characterizing the intensity of the wave. It is defined as the average height of 1/3 of the highest waves. For a Gaussian distribution, the significant wave height is

$$H_s = 4\sqrt{\xi^2}, \quad (1)$$

where ξ is elevation of the surface. The distribution of elevations of sea surface waves is quasi-Gaussian (Zapevalov et al. 2011), but the deviations from it are not large. This gives reason to use Eq. (1) for sea waves. Equation (1) can also be represented in the form

$$H_s = 4\sqrt{\int \Psi(\omega) d\omega} \quad (2)$$

where $\Psi(\omega)$ is elevation spectrum of the sea surface; ω is frequency. Representation H_s in the form (2) is due to the fact that the spectral characteristics of the wave field are constructed in the MFWAM model, which is used here.

3 Model MFWAM

In this work, the analysis of significant wave heights is carried out based on the GLOBAL_ANALYSIS_FORECAST_WAV_001_027 data array (https://marine.copernicus.eu/services-portfolio/access-to-products/?option=com_csw&view=details&product_id=GLOBAL_ANALYSIS_FORECAST_WAV_001_027). This array is one of 228 products of the International Marine Environmental Operative Monitoring Service Copernicus (<https://marine.copernicus.eu/services-portfolio/access-to-products/>), covering almost all marine regions of the Earth and presenting data on 15 geophysical parameters in various time frames on a regular basis. The dataset used here was obtained using the MFWAM model (Ardhuin et al. 2010; Janssen et al. 2014), intended for analysis and forecasting of the field of sea surface waves.

The scattering conditions for the ECWAM-IFS-38R2 code were developed by Ardhuin et al. (2010). This code is used in the MFWAM model. Later, the improvements obtained as a result of the researches of the European project “My Wave” (Janssen et al. 2014) made it possible to modernize the MFWAM model. Using 2-min global topographic data ETOPO2/NOAA, it is possible to generate the average bathymetry of the model. Native model grid changes with decreasing distance in the latitude direction near the poles. Accordingly, the distance in the latitudinal direction at the equator is relatively fixed with the largest grid size of $1/10^\circ$. The 6-h analysis and 3-h forecast winds from the IFS-ECMWF atmospheric system form the basis for the MFWAM operating model. The wave spectrum is converted from continuous to discrete in 24 directions and 30 frequencies, from 0.035 to 0.58 Hz. Assimilation of altimeters is used in the MFWAM model with a 6-h time step. The global wave system provides analysis 4 times a day and a forecast for 5 days at 0:00 UTC. The separation used by the wave model MFWAM is necessary for stratification of the swell spectrum into primary and secondary swells.

Model calculations were carried out on a grid with mesh sizes of $1/12$ degrees (approximately 8 km) in steps of 3 h. The MFWAM model assimilates data on significant wave heights, which are determined using altimeters installed on spacecraft. The data obtained from the Jason 2 and 3, Saral, and CryoSat-2 spacecraft are used. Assimilation is carried out with a time step of 6 h (<https://marine.copernicus.eu/documents/PUM/CMEMS-GLO-PUM-001-027.pdf>).

In altimetric measurements, the calculation of the significant wave's height is carried out according to the shape of the reflected radio pulse (Hayne 1980). The greater the height, the greater the slope of the leading edge of the reflected radio pulse.

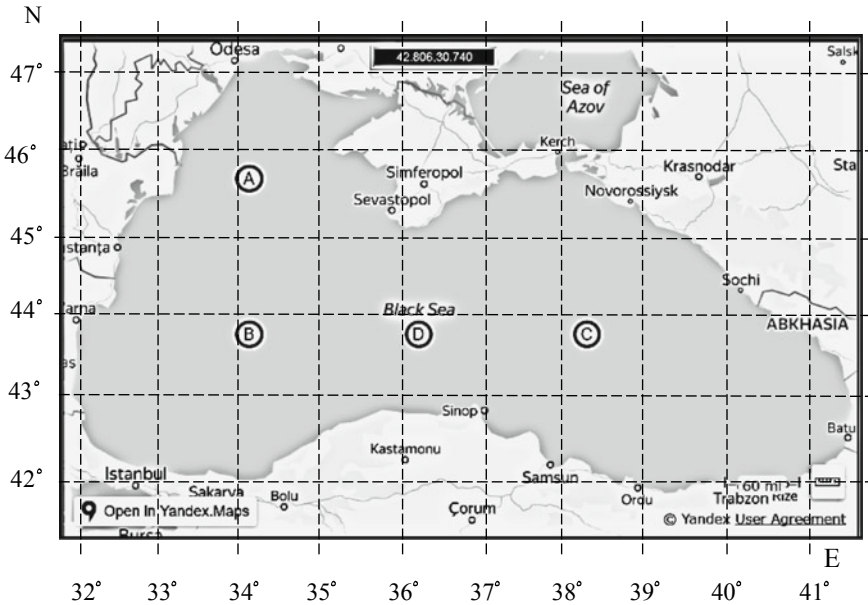


Fig. 1 Geographical points at which the seasonal variability of the intensity of wind waves was analyzed

4 Researched Water Areas

Four regions were chosen to analyze the seasonal variability of the wave characteristics of the Black Sea. Area A is located on the Northwest shelf. This is a shallow area, the hydrological characteristics of which differ markedly from the characteristics of the deep-sea of the Black Sea. Three other areas (B, C, D) are located in the deep-sea of the Black Sea, respectively, in its western, eastern and central parts. The distance from the coast to the studied areas in all cases exceeds 100 km.

The geographic areas selected for analysis are shown in Fig. 1.

5 Temporary Variability of Significant Waves Height in Region D

To analyze the temporal variability of a significant waves height, region D was chosen. The seasonal variation of the parameter for region D, the changes in time H_s recorded during the year are shown in Fig. 2. When plotting, a series with a resolution of 3 h was used. The time period from 08/11/2018 to 08/11/2019 is considered. Roman numerals in Fig. 2 shows the numbers of the months.

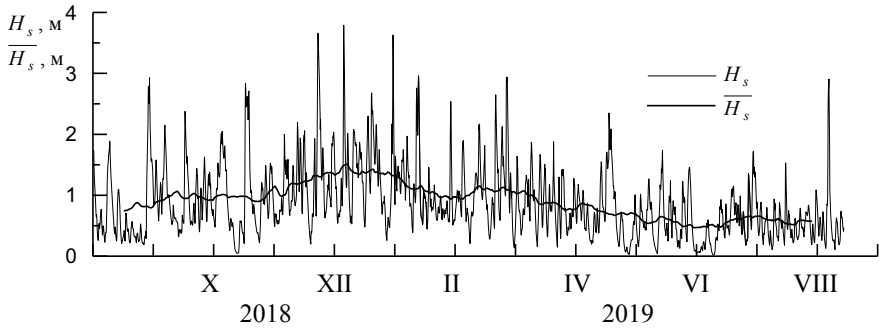


Fig. 2 The annual course of current values H_s and smoothed values \overline{H}_s significant waves height at point D

It can be seen that the parameter H_s has significant variability. It is advisable to consider how the average characteristics change. To do this, let us pass a series of values through a moving average filter, the length of which corresponds to 30 days. Presented in Fig. 2, the smoothed curve \overline{H}_s shows the well-defined annual variation of the parameter H_s . The maximum average values are observed in the winter period (January–February), the minimum—in the summer period (June).

A comparison of the parameters H_s and \overline{H}_s shows that the deviations of the “instantaneous” significant height from its monthly average value mainly occur towards large values. Hereinafter, instantaneous values mean values obtained with a three-hour time interval. This indicates a strong asymmetry of the parameter distribution H_s . The values of the skewness coefficient mainly lie in the range from 1 to 8. The highest skewness occurs in the summer, when \overline{H}_s is small, in the winter, when \overline{H}_s is large, the skewness decreases.

Next, we consider the behavior of another parameter σ , defined as the standard deviation H_s from the average \overline{H}_s over a period of 30 days. The annual variation of the parameters \overline{H}_s and σ determining the intensity of the waves is similar at the selected geographical points (see Fig. 3). There is a slight delay in the parameter \overline{H}_s , calculated for the easternmost geographical point (point C). In general, the annual course in all areas under consideration is similar. The strongest variability of the wave field, which is characterized by the parameter σ , takes place in the center of the Black Sea (point D) (Fig. 4).

The highest values of the parameters \overline{H}_s and σ observed the winter period, which indicates both the high intensity of the waves and its strong variability.

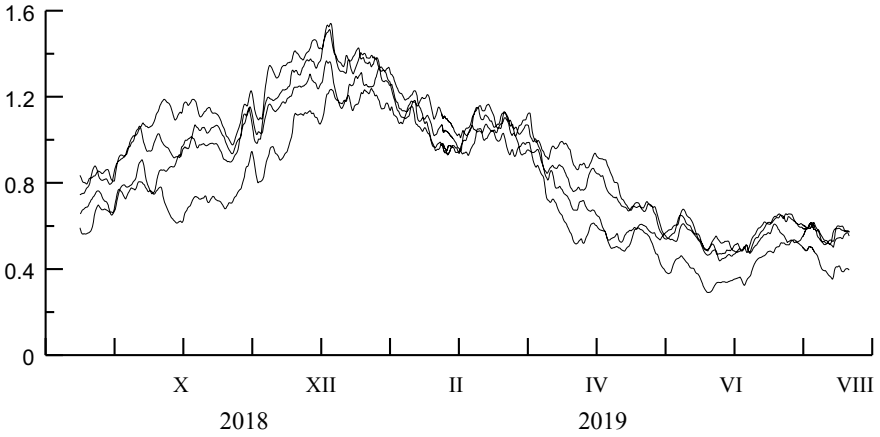


Fig. 3 The annual course of the parameter $\overline{H_s}$

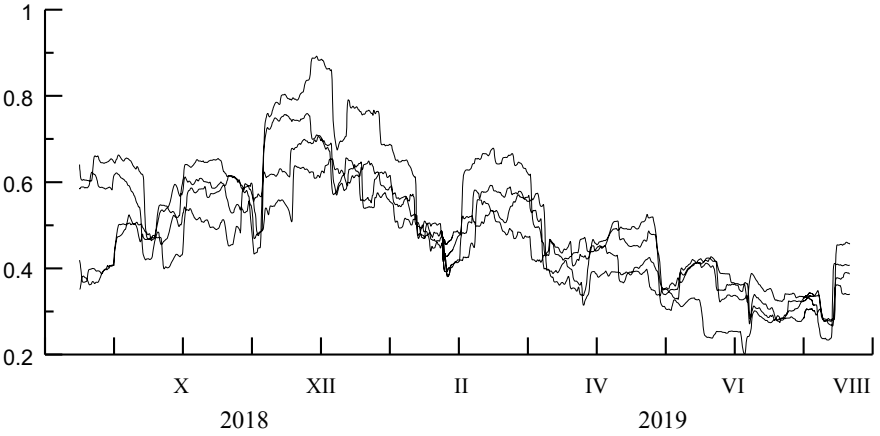


Fig. 4 The annual course of the parameter σ

6 Spatial Correlation of Wave Energy

Let us consider how the parameter values H_s , determined in the four selected areas are statistically interconnected. To do this, we calculate the correlation matrix. The calculation results are presented in Table 1.

From Table 1 it follows that the instantaneous values H_s are correlated with each other at the level of 0.4–0.5. The only exception is the correlation between the region on the northwest shelf and the region in the western part of the Black Sea. For these areas, correlation level is 0.75.

Table 1 Parameter correlation matrix H_s , calculated for four regions of the Black Sea

Region	D	C	B	A
D	1	0.40	0.48	0.49
C	0.40	1	0.53	0.46
B	0.48	0.53	1	0.75
A	0.49	0.46	0.75	1

Table 2 Parameter correlation matrix $\overline{H_s}$, calculated for four regions of the Black Sea

Region	D	C	B	A
D	1	0.93	0.98	0.94
C	0.93	1	0.88	0.89
B	0.98	0.88	1	0.94
A	0.94	0.89	0.94	1

The correlation of the mean values of the significant waves height $\overline{H_s}$ is high. Its values are presented in Table 2. The highest correlation is between the values $\overline{H_s}$, determined for the central and western regions of the Black Sea.

7 Conclusion

The analysis of the variability of the intensity of unrest in the Black Sea is carried out. For analysis, we used data obtained using the global MFWAM model of the International Service for the Operational Monitoring of the Marine Environment Copernicus.

A seasonal variation of the significant wave height on the northwestern shelf, in the eastern, central and western parts of the Black Sea, is constructed. Dependencies are obtained that describe the annual course of a significant wave height. Also built are dependencies describing the deviations of the “instantaneous” values of the significant wave height from its average value over 30 days.

It is shown that the instantaneous values of significant waves height in different regions are relatively weakly correlated with each other. The correlation coefficient lies in the range 0.4–0.5. At the same time, the correlation of the monthly average wave intensity in the selected regions exceeds the level of 0.9.

The work was carried out as part of a state assignment on the topic No. 0827-2018-0003 “Fundamental research of oceanological processes that determine the state and evolution of the marine environment under the influence of natural and anthropogenic factors, based on observation and modeling methods”.

References

- Ardhuin F, Magne R, Filipot J-F, Van der Westhuyzen A, Roland A, Quefeulou P, Lefevre JM, Aouf L, Babanin A, Collard F (2010) Semiempirical dissipation source functions for wind-wave models: Part I, definition, calibration and validation at global scales. *J Phys Oceanogr* 40:1917–1941. <https://doi.org/10.1175/2010jpo4324.1>
- Copernicus marine environment monitoring service. <https://marine.copernicus.eu/services-portfollio/access-to-products/>
- Francis P, Stratton RA (1990) Some experiments to investigate the assimilation of SEASAT altimeter wave height data into a global wave model. *Q J R Meteorol Soc* 116(495):1225–1251. <https://doi.org/10.1256/smsqj.49511>
- Global ocean waves analysis and forecast updated daily. https://marine.copernicus.eu/services-portfolio/access-to-products/?option=com_csw&view=details&product_id=GLOBAL_ANALYSIS_FORECAST_WAV_001_027
- Gómez-Enri J, Gommenginger CP, Challenor PG, Srokosz MA, Drinkwater MR (2006) ENVISAT radar altimeter tracker bias. *Mar Geodesy* 29:19–38. <https://doi.org/10.1080/01490410600582296>
- Hasselmann S, Hasselmann K, Bauer E, Janssen PAEM, Komen GL, Bertotti L, Lionello P, Guillaume A, Cardone VJ, Greenwood JA, Reistad M, Zambresky L, Ewing JA (1988) The WAM model—a third generation ocean prediction model. *J Phys Oceanogr* 18:1775–1810. [https://doi.org/10.1175/1520-0485\(1988\)018<1775:twmtgo>2.0.co;2](https://doi.org/10.1175/1520-0485(1988)018<1775:twmtgo>2.0.co;2)
- Hayne GS (1980) Radar altimeter mean return waveforms from near-normal-incidence ocean surface scattering. *IEEE Trans Antennas Propag* 28(5):687–692. <https://doi.org/10.1109/tap.1980.1142398>
- Janssen P, Aouf L, Behrens A, Korres G, Cavalieri L, Christiansen K, Breivik O (2014) Final report of work package I in my wave project
- Knysh VV, Korotaev GK, Lishaev PN (2016) Procedure of application of three-dimensional fields of the Black Sea temperature and salinity reconstructed based on altimetry and scanty measurements in the operational prognostic model. *Phys Oceanogr* 2:46–61
- Özbahçec BÖ (2004) Effect of wave grouping, spectral shape and extreme waves in a wave train on the stability of rubble mound breakwaters. A thesis submitted to the graduate school of natural and applied sciences of Middle East Technical University
- Pokazeev KV, Zapevalov AS, Pustovoytenko VV (2013) The simulation of a radar altimeter return waveform. *Mosc Univ Phys Bull* 68(5):420–425. <https://doi.org/10.3103/s0027134913050135>
- Product user manual for global ocean waves analysis and forecasting. <https://marine.copernicus.eu/documents/PUM/CMEMS-GLO-PUM-001-027.pdf>
- Sannasiraj SA, Goldstein MG (2009) Optimal interpolation of buoy data into a deterministic wind-wave model. *Nat Hazards* 49(2):261–274. <https://doi.org/10.1007/s11069-008-9291-x>
- Taskar B, Yum KK, Steen S, Pedersen E (2016) The effect of waves on engine-propeller dynamics and propulsion performance of ships. *Ocean Eng* 122:262–277. <https://doi.org/10.1016/j.oceaneng.2016.06.034>
- Yu H, Li J, Wu K, Wang Z, Yu H, Zhang S, Hou Y, Kelly RM (2018) A global high-resolution ocean wave model improved by assimilating the satellite altimeter significant wave height. *Int J Appl Earth Obs Geoinf* 70:43–50. <https://doi.org/10.1016/j.jag.2018.03.012>
- Zapevalov AS, Pokazeev KV (2016) Modeling the spectrum of infrasonic hydroacoustic radiation generated by the sea surface under storm conditions. *Acoust Phys* 62(5):554–558. <https://doi.org/10.1134/s1063771016050195>
- Zapevalov AS, Bol'shakov AN, Smolov VE (2011) Simulating of the probability density of sea surface elevations using the Gram–Charlier series. *Oceanology* 51(3):406–413. <https://doi.org/10.1134/s0001437011030222>

Calculation of the Turbulent Exchange Intensity in the Sea Upper Homogeneous Layer



A. M. Chukharev  and A. S. Samodurov 

Abstract The results of experimental studies of the intensity of turbulent exchange in the upper homogeneous layer of the sea and the comparison of field measurements with various models are discussed. Experimental data were collected on a stationary oceanographic platform in the coastal zone of the Black Sea under varied hydrometeorological conditions. A fairly complete set of equipment provided the measurement of basic hydrophysical characteristics (including pulsating values) and background meteorological and hydrological parameters. The turbulent energy dissipation rate was determined from the pulsation spectra of the vertical velocity component using the Kolmogorov hypothesis. Particular attention is paid to the analysis of the influence of the most important mechanisms of turbulence generation, with the completeness of accounting and adequate parameterization of which the objectivity of any model is associated. For verification, we used the well-known models of turbulent exchange for the surface layer of the sea, including the multiscale model of one of the authors of this work. It is noted that the multiscale model, which takes into account the three main mechanisms of turbulence generation, most accurately describes the depth distribution of the dissipation rate in a fairly wide range of hydrometeorological conditions. Its advantage over other models is most pronounced in strong winds, in stormy weather. It is shown that taking into account the actually measured characteristics of the waves and the shear of flow velocity improves the consistency of the multiscale model with experiment.

Keywords Marine boundary layer · Turbulent exchange · Turbulent energy dissipation · Field experiments · Model verification · Multiscale model

A. M. Chukharev (✉) · A. S. Samodurov
Marine Hydrophysical Institute of RAS, Sevastopol, Russia
e-mail: alexchukh@mail.ru

A. S. Samodurov
e-mail: anatol_samodurov@mail.ru

A. M. Chukharev
Sevastopol State University, Sevastopol, Russia

1 Introduction

The upper layer of the sea plays a crucial role in the formation of climate and weather on Earth due to the intense exchange with the atmosphere of heat, moisture and other substances. Dissolved chemicals, gases, biogenic elements are necessary for the life of organisms in the upper layer, and the processes of vertical metabolism have a significant impact on the bio-production cycles and the ecological state of water areas.

Vertical mixing in the upper quasi-homogeneous layer occurs due to various physical mechanisms, the most important of which is turbulent diffusion. Due to the active interaction with the atmosphere, various motions occur in this layer in a wide range of scales, which complicates the theoretical description of the exchange processes. Different approaches have been proposed to evaluate the intensity of turbulent exchange by various authors, in which, to simplify the problem, hypotheses have been put forward that some mechanism of turbulence generation dominates, which allows, neglecting other mechanisms, parameterization of turbulent momentum and heat fluxes.

Schematically, the main sources of energy input to marine turbulence in the near-surface layer are shown in Fig. 1.

One of the first attempts to calculate the intensity of turbulent exchange in this layer was the work of Dobroklonsky (1947) where surface waves were assumed to

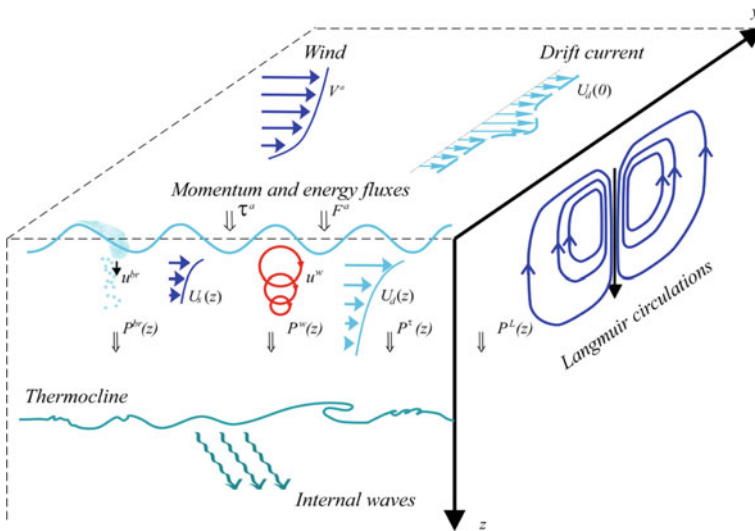


Fig. 1 The main sources of energy for marine turbulence in the near-surface layer. The following notation is introduced in the figure: V_a is the wind velocity, U_d is the drift current velocity, τ^a and F^a are the momentum and energy fluxes from the atmosphere, U_S is the Stokes drift velocity, u^w is the orbital wave velocity, $P^{(i)}$ is the energy influx to turbulence from various sources: shear velocity, nonlinearity of surface waves and breaking waves

be a single source of turbulence, and the coefficient of turbulent viscosity was calculated through the parameters of the waves. Later Benilov (1973) obtained another formula, which made it possible to determine the dissipation rate of turbulent energy also from the wave characteristics. In Csanady (1984) the drift flow velocity shear was considered the main mechanism of turbulence generation and the formula for calculating the dissipation rate was similar to the formula for a solid wall.

Later models (Craig and Banner 1994; Benilov and Ly 2002; Kudryavtsev et al. 2008) take into account primarily breaking waves as the main source of turbulence but also include a shear of drift current velocity the role of which becomes more important as you move away from the surface.

In the multiscale model for calculating the turbulence characteristics near the sea surface (Chukharev 2013) in addition to surface breaking waves and velocity shear, the nonlinearity of waves is also taken into account as another mechanism of turbulence generation. The importance of taking into account the latter is indicated by many experimental and theoretical works (Babanin et al. 2012; Kuznetsov et al. 2015).

However, despite significant progress in describing the turbulent structure of the near-surface layer, confirmed by experimental studies, in many cases, theoretical models do not give a sufficiently good agreement between calculations and measurements. One possible reason is the non-universality of the proposed parameterizations of the turbulence sources and the incomplete consideration of the generation mechanisms that affect the turbulent mode of the layer under study.

The aim of this work is to compare with various models of field data obtained in recent years by the staff of the Marine Hydrophysical Institute of RAS (MHI) and to determine the most objective methods for assessing the intensity of turbulent exchange in the upper mixed sea layer.

2 Experimental Data

Field measurements of turbulence characteristics in the near-surface layer of the sea were carried out from a stationary oceanographic tower of MHI. The platform is located at 450 m from the coast with a sea depth of about 30 m. With the direction of waves and currents that move from the open sea in the azimuthal range of 60–250°, the existing conditions up to a depth of ~20 m in the area of the platform can be considered good approximation to deep water and do not take into account the influence of the bottom and shore.

In studies, the positional version of the “Sigma-1” complex was used (Samodurov et al. 2005), a general view of which is shown in Fig. 2. Registration and writing of information are carried out in real time. An original system was developed for measurements at different depths (from 0 to 20 m) (Barabash et al. 2015). The measuring device is placed away from a stationary platform, this location eliminates the influence of the supports on the measurement area, and that is, data is obtained in the natural environment. The turbulent energy dissipation rate ε was calculated

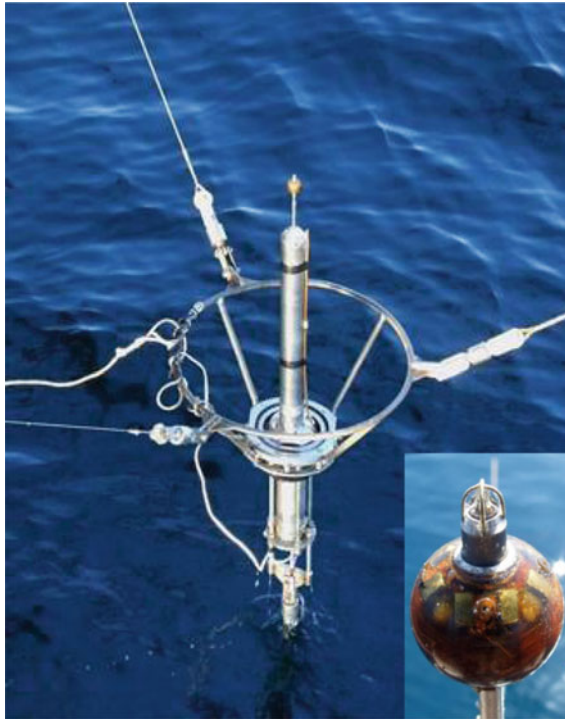


Fig. 2 Positional version of the “Sigma-1” measuring complex for studying turbulence in the near-surface layer. In the inset—an enlarged view of the sensors unit

according to the method proposed by Stewart and Grant (1962). In this case, the distortions carry in into the signal by the waves and vibrations of the device do not significantly affect the result. In more detail, the method of measuring and calculating the turbulence characteristics in our experiments is described in Chukharev (2013), Chukharev et al. (2007).

Figure 3 shows examples of recording the three components of the velocity pulsations and the calculated energy spectra at different depths.

The measurements were carried out under various hydrometeorological conditions, while the basic background parameters were recorded: wind and current velocity and direction, wave characteristics, water and air temperature, humidity, etc. The accumulated experimental material allows us to verify theoretical models for specific hydrometeorological situations and evaluate the intensity of turbulent exchange depending on the determining parameters.

In recent years, an acoustic flow meter has become an additional tool, with the help of which the velocity and direction of the current were recorded in the upper three-meter layer of the sea, the most inaccessible for measurements.

It should be noted that only part of the experiments are presented in the work, with the most characteristic conditions under moderate and strong winds. The results

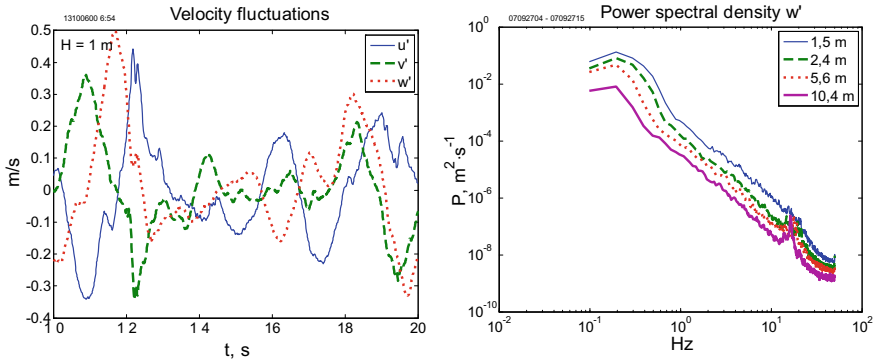


Fig. 3 On the left is a fragment of recording of three components of velocity pulsations at a depth of 1 m. On the right are the calculated spectra for the vertical velocity component at various depths

with a wide scatter of experimental points are not presented, as they are difficult to model and are apparently caused by the influence of local factors that are not taken into account in the models and the variability of conditions over time.

Comparison with field measurements carried out according to the programs SWADE (Drennan et al. 1996) and WAVES (Terry et al. 1996) showed good agreement between our data, namely, the calculated values of the dissipation rate when normalized to the energy flux to waves from the atmosphere.

3 Comparison of Experiments and Model Calculations

The values of the turbulent energy dissipation rate obtained in our experiments generally do not contradict the three-layer depth distribution ϵ (Terry et al. 1996), where the layer adjacent to the surface and directly affected by the waves has the highest level of turbulence, below is an intermediate layer, where the influence of diffusion of turbulence from the upper layer is noticeable, and even lower is a layer in which turbulence is determined by a shear of the flow velocity.

For comparison with experimental data, we took the well-known models (Craig and Banner 1994; Benilov and Ly 2002; Kudryavtsev et al. 2008), as well as the multiscale numerical model (Chukharev 2013). In model (Craig and Banner 1994) in figures denoted C&B, the roughness parameter z_0 was selected for each case according to the best fit between calculation and experiment, model (Kudryavtsev et al. 2008) (K&al.) was calculated with the coefficients recommended in their article (Kudryavtsev et al. 2008). In the model (Chukharev 2013) denoted in figures as *MultiScal* the coefficient mainly varied affecting the energy influx to turbulence from surface waves, and, instead of model dependences from wind speed for the wave spectrum and flow velocity profile real measured values were introduced for comparison.

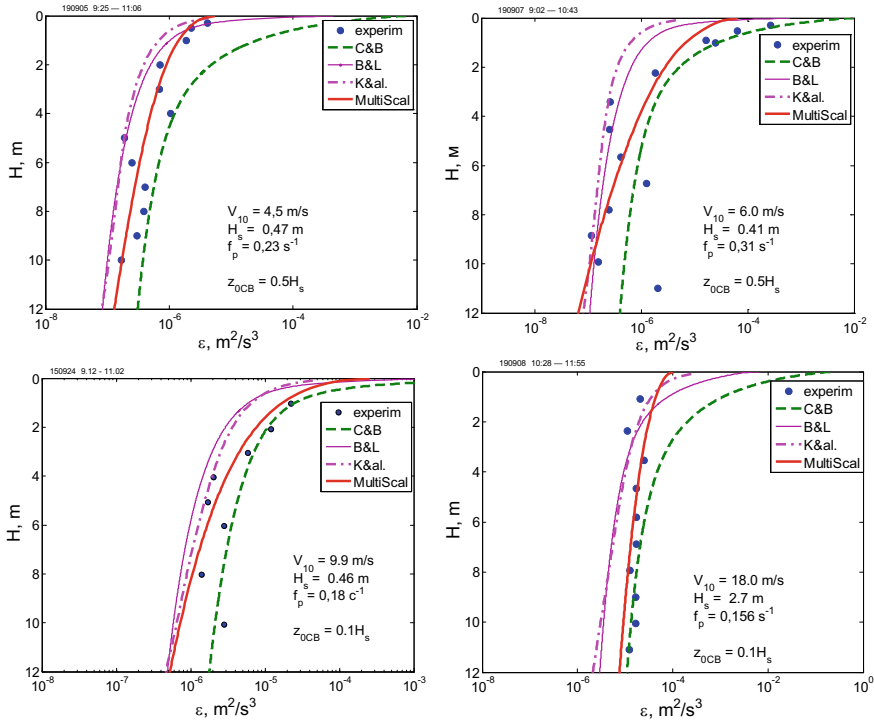


Fig. 4 Comparison of model calculations and experimental data. Designations in the figures: V_{10} is the wind speed at a height of 10 m, H_s is the height of significant waves, f_p is the frequency of the spectral peak of the waves, z_{0CB} is the roughness parameter for the model (Craig and Banner 1994)

Some typical results of calculations for various models and experimental data describing the dependence of the turbulent energy dissipation rate on depth are presented in Fig. 4. The main hydrometeorological characteristics are also shown in the figures.

At this stage of the research, a number of conclusions can be drawn from the analysis of the comparison of models and experiments.

1. With weak winds, none of the models gives a satisfactory agreement with the experiment, all calculations are significantly lower than the experimental values.
2. The model (Craig and Banner 1994) in many cases lays rather well on the experimental points, but at the same time, the roughness parameter z_0 has to be changed within very large limits. In a number of cases, in order to achieve agreement between calculations and experiment, the parameter z_0 must be many times higher than the wave height. It turns out, in a sense, a paradoxical situation when, at a higher wave height, the roughness parameter should be much smaller than in cases for a small wave amplitude.

3. The model (Benilov and Ly 2002), in addition to generating turbulence by a shift in the flow velocity, also takes into account the influx of energy from surface waves, but, apparently, the proposed method does not give the desired effect—the calculated curve was very slightly different from the logarithmic curve (model for a solid wall), and only in the uppermost layer with a thickness of 1–2 m. In most cases, this model did not correspond well to the measurements.
4. In the model (Kudryavtsev et al. 2008), in most cases, the calculation results were less than the measured values, which could be due to the use of only one set of coefficients, regardless of hydrometeorological conditions.
5. The multiscale model (Chukharev 2013), as a rule, was in good agreement with experiments, but in some cases a noticeable discrepancy was observed. The introduction of the measured values of the wave characteristics and the flow velocity profile (especially in the upper three-meter layer) instead of parametrizations into the model, clearly improves the agreement between calculations and experiments.
6. The verification results of various models indicate the need to include at least three basic mechanisms of turbulence generation in the turbulent exchange model for the near-surface layer: drift flow velocity shear, nonlinear effects of surface waves and their breaking. It is also important to note that the parameterization of both the profile of the flow velocity and the spectrum of surface waves require further improvement, possibly taking into account the regional characteristics of the basin.

Thus, from the considered models, the most preferable was the model (Chukharev 2013), which in most cases gives quite satisfactory agreement with the experiments, but the model dependences of the wave characteristics on the wind speed (Donelan model 1985) and the flow velocity profile used in it did not always correspond actual values that reflected on the results. With further refinement of the multiscale model, it is assumed that Langmuir circulations are taken into account as a mechanism for generating turbulence and the refinement of the parametrizations of the wave parameters and the drift flow velocity shift.

Acknowledgements The work was carried out in the framework of state tasks on the topics № 0827-2018-0003 and № AAAA-A18-118020790209-9.

References

- Babanin AV, Onorato M, Qiao F (2012) Surface waves and wave-coupled effects in lower atmosphere and upper ocean. *J Geophys Res* 117:C00J01. <https://doi.org/10.1029/2012JC007932>
- Barabash VA, Samodurov AS, Chukharev AMA (2015) Measuring system for studying small-scale turbulence in the surface layer of the sea. Patent of the Russian Federation No. 2549250
- Benilov AY (1973) On the generation of turbulence in the ocean by surface waves. *Izv Atmos Oceanic Phys* 9:293–303 (in Russian)
- Benilov AY, Ly LN (2002) Modeling of surface waves breaking effects in the ocean upper layer. *Math Comput Model* 35:191–213. [https://doi.org/10.1016/S0895-7177\(01\)00159-5](https://doi.org/10.1016/S0895-7177(01)00159-5)

- Chukharev AM (2013) Multitime scale model of turbulence in the sea surface layer. *Izv Atmos Oceanic Phys* 49:439–449. <https://doi.org/10.1134/S0001433813040026>
- Chukharev AM, Barabash VA, Zubov AG, Pavlenko OI (2007) Turbulent structure of the subsurface layer of the sea according to the data of the “Sigma-1” measuring complex. *Phys Oceanogr* 17:75–87
- Craig PD, Banner ML (1994) Modelling of wave-enhanced turbulence in the ocean surface layer. *J Phys Oceanogr* 24:2546–2559 (1994). [https://doi.org/10.1175/1520-0485\(1994\)024%3C2546:MWETIT%3E2.0.CO;2](https://doi.org/10.1175/1520-0485(1994)024%3C2546:MWETIT%3E2.0.CO;2)
- Csanady GT (1984) The free surface turbulent shear layer. *J Phys Oceanogr* 14:402–411. [https://doi.org/10.1175/1520-0485\(1984\)014%3c0402:TFSTSL%3e2.0.CO;2](https://doi.org/10.1175/1520-0485(1984)014%3c0402:TFSTSL%3e2.0.CO;2)
- Dobroklonsky SV (1947) Turbulent viscosity in the surface layer of the sea and waves. *Dokl USSR Acad Sci* 58:1345–1348 (in Russian)
- Donelan MA, Hamilton J, Hui WH (1985) Directional spectra of wind-generated waves. *Philos Trans R Soc Lond A* 315:509–562
- Drennan WM, Donelan MA, Terray EA, Katsaros KB (1996) Oceanic turbulence dissipation measurements in SWADE. *J Phys Oceanogr* 26:808–815. [https://doi.org/10.1175/1520-0485\(1996\)026%3c0808:OTDMIS%3e2.0.CO;2](https://doi.org/10.1175/1520-0485(1996)026%3c0808:OTDMIS%3e2.0.CO;2)
- Kudryavtsev V, Shrira V, Dulov V, Malinovsky V (2008) On the vertical structure of wind-driven sea currents. *J Phys Oceanogr* 38:2121–2144. <https://doi.org/10.1175/2008JPO3883.1>
- Kuznetsov SY, Saprykina YV, Dulov VA, Chukharev AM (2015) Turbulence induced by storm waves on deep water. *Phys Oceanogr* 5:22–31. <https://doi.org/10.22449/1573-160X-2015-5-22-31>
- Samodurov AS, Dykman VZ, Barabash VA, Efremov OI, Zubov AG, Pavlenko OI, Chukharev AM (2005) “Sigma-1” measuring complex for the investigation of small-scale characteristics of hydrophysical fields in the upper layer of the sea. *Phys Oceanogr* 15:311–322
- Stewart RW, Grant HL (1962) Determination of the rate of dissipation of turbulent energy near the sea surface in the presence of waves. *J Geophys Res* 67:3177–3180. <https://doi.org/10.1029/JZ067i008p03177>
- Terray EA, Donelan MA, Agrawal YC, Drennan WM, Kahma KK, Williams AJ III, Hwang PA, Kitaigorodskii SA (1996) Estimates of kinetic energy dissipation under breaking waves. *J Phys Oceanogr* 6:792–807. [https://doi.org/10.1175/1520-0485\(1996\)026%3c0792:EOKEDU%3e2.0.CO;2](https://doi.org/10.1175/1520-0485(1996)026%3c0792:EOKEDU%3e2.0.CO;2)

Modelling of Fracture Acidizing



Regina Kanevskaya and Aleksei Novikov

Abstract Acid impact is the highly efficient kind of carbonate reservoir stimulation. In contrast to hydraulic fracturing acid impact improves matrix permeability that remains high while production. In this case propagation of reactive flow into matrix brings stimulation that means that the flow factor is crucial for fracture acidizing. This paper is focused on the reactive flow modelling in the existing fracture and oil saturated matrix. Two phase multicomponent Darcy flow which takes into account dissolution kinetics is modelled in two domains (fracture, matrix). Using prescribed porosity permeability relationship the stimulated permeability field is calculated. Acid propagation into matrix is investigated for different injection control regimes. Stimulated productivity is assessed at the final stage of stimulation in the enlarged domain. Obtained results show that the injection time plays a key role for stimulated productivity. Sensitivity analysis to the other parameters is also given.

Keywords Reactive flow · Matrix dissolution · Acidizing

1 Introduction

Modern economical and social conditions require hydrocarbon field development to be safe, reliable and highly efficient. Among the methods which satisfy these requirements, acid impact is one of the most cost-efficient and simplest way of reservoir stimulation. It has become a common technique of production stimulation in carbonate formations. However, the accurate simulation of acid impact remains challenging.

Acid impact of any kind includes an injection stage when acid solution is pumped into formation. Once acid gets in contact with formation minerals, it dissolves them that ease its propagation further into formation. This process leads to a significant permeability increase in the affected area which determines enhanced well productivity.

R. Kanevskaya · A. Novikov (✉)
Gubkin University, 65, Leninsky av., Moscow, Russia
e-mail: cranon@yandex.ru

© The Author(s), under exclusive license to Springer Nature Switzerland AG 2021
T. Chaplina (ed.), *Processes in GeoMedia—Volume II*, Springer Geology,
https://doi.org/10.1007/978-3-030-53521-6_12

The mathematical formulation of this problem is multiphase multicomponent reactive flow in porous medium. Since dissolution affects flow characteristics the problem becomes strongly nonlinear. In a heterogeneous formation the dissolution front is unstable. Passing through formation, it creates wormholes, thin long channels, which are difficult to be taken into account in formation-scale simulation. The irreducible uncertainty in the properties of formation makes such consideration ambiguous.

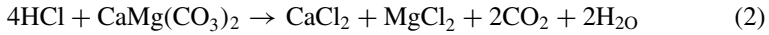
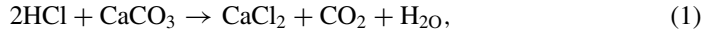
Recent advances in numerical modelling of matrix acidizing are related to Darcy-scale simulation using Darcy-Brinkman-Stokes (DBS) Equation (Golfier et al. 2002; Cohen et al. 2008; Soulaire and Tchelepi 2016; Schwalbert et al. 2017; Shaik et al. 2018) that is valid when porosity near unity and can take into account natural and induced fractures, wormholes and immersed boundary conditions. In (Golfier et al., 2002), authors used Darcy-Brinkman equation instead of Darcy equation derived from momentum balance law. Results of calculations were validated by acid-flood core experiments and discussed in terms of dissolution regimes that depends on dimensionless numbers (Damkohler number, Peclet number, kinetic number). This approach was developed in (Cohen et al., 2008), where geometry influence on dissolution regimes was considered. Distribution of petrophysical properties and its anisotropy influence on propagation of wormholes was investigated in (Schwalbert et al., 2017). A comparison of conventional Darcy modelling and DBS simulation related to matrix acidizing was presented in (Shaik et al., 2018). An intermediate upscaling was used to adopt existing Darcy-scale dissolution models at the field scale in (Golfier et al., 2004), (Golfier et al., 2006), where closure problems for proposed mapping variables were considered and corresponding transport and dissolution equations were derived. The authors used Darcy-like constitutive relation while averaging. Field-scale Darcy-like model of two-phase multicomponent reactive flow was applied to simulation of carbonate matrix acidizing in the cases of vertical, horizontal wells and fracture (Volnov and Kanevskaya 2009; Zhuchkov and Kanevskaya 2013). Carbon dioxide influence was considered in (Tukhvatullina and Posvyanskii, 2012).

In this paper, we couple field-scale Darcy-like model of two-phase multicomponent reactive flow in porous medium (Volnov and Kanevskaya 2009; Zhuchkov and Kanevskaya 2013) with convection-diffusion problem in fracture to simulate fracture acidizing. We use analytical expressions for velocity field in fracture (Berman 1953). Such a joint model takes into account kinetics of acid-mineral interaction while acid propagates through porous medium. It assumes existing rectangular hydraulic fracture of fixed width. Relative permeability modification with porosity changes is also employed. Fully implicit finite volume scheme is used for numerical solution of coupled system. This approach provides exact permeability distribution around fracture and allows calculating transmissibility along fracture caused by any particular acid stimulation on the basis of balance equations. Additional stage is performed to calculate productivity for this permeability field within enlarged domain. The objective of this work is to identify main hydrodynamical factors and conditions that affect the productivity of stimulated fracture.

2 Mathematical Formulation

2.1 Reaction Kinetics and Phase Content

The most common carbonate minerals are calcite CaCO_3 and dolomite $\text{CaMg}(\text{CO}_3)_2$. We consider hydrochloric acid interactions with these minerals according to the following reactions:



Hydrochloric acid is a strong acid, which dissociates in water to H^+ , Cl^- ions. Actually, dissolution reaction happens between H^+ cations and minerals. Besides, products and reverse reaction have negligible influence on the reaction kinetics in the case of hydrochloric acid. The kinetic model in this case can be represented in the form (Nierode and Williams, 1971):

$$-r_k = A_k (b_w (X_a - X_a^{eq}))^n \exp\left(-\frac{E_k}{RT}\right), \quad (3)$$

where A_k —reaction rate constant, n —order of the reaction, b_w —molar density of water phase, E_k —activation energy, X_a^{eq} —equilibrium molar acid concentration in water phase. X_a^{eq} differs from zero substantially in the case of organic or weak acids, whereas in the case of hydrochloric acid it is equal to zero $X_a^{eq} = 0$. Other constants used in model (3) are listed in Table 1.

The reaction rate of pure hydrochloric acid is very fast, so that it is well known that overall dissolution rate of limestone is limited by acid transport (Lund et al. 1973). The same is true for dolomites while temperature is 50°C and higher (Lund et al. 1975). Below this temperature the rate of reaction kinetics also become important.

We consider two phase five component fluid flow that consists of water and oil phases $\alpha = \{w, o\}$ and oil, water, acid, salt and carbon dioxide components $i = \{o, \text{H}_2\text{O}, a, s, \text{CO}_2\}$. Water phase represents acid solution injected into matrix (sk). We assume that all the products of the reactions (1), (2) are instantly dissolved in water phase whereas the oil phase consists of oil component only. The amount of carbon dioxide produced in the reaction is negligible and can not significantly change solution (Zhuchkov and Kanevskaya 2013; Tukhvatullina and Posvyanskii 2012).

Table 1 Reaction kinetics constants of HCl-mineral interactions (Lund et al. 1973, 1975)

Mineral	n	$A_k \left(\frac{\text{kg mol HCl}}{\text{m}^2} \right)$	$\frac{E_k}{R} (K)$
Calcite	0.63	7.291×10^7	7.55×10^3
Dolomite	0.3 – 0.6	$\frac{9.4 \times 10^{11}}{10^{3n}}$	11.32×10^3

For simplicity, we also neglect the influence of phase composition on phase densities, phase viscosities, phase mobilities (except phase saturations and porosity) and reaction rate (except acid concentration in (3)).

2.2 Governing Equations

Porous Medium. Mass balance equations for two phase multicomponent reactive flow in porous media are

$$\frac{\partial}{\partial t} (msb_w X_i) + \nabla \cdot (b_w X_i \mathbf{v}_w) = q_i, \quad (4)$$

$$\frac{\partial}{\partial t} (m(1-s)b_o) + \nabla \cdot (b_o \mathbf{v}_o) = 0, \quad (5)$$

$$\frac{\partial}{\partial t} ((1-m)b_{sk}) = q_{sk} \quad (6)$$

where m —porosity, b_α —molar density of α -th phase, X_i —molar concentration of i -th component, s —water saturation, q_i —molar sources.

Phase flow velocities \mathbf{v}_α are given by Darcy equation:

$$\mathbf{v}_\alpha = -\frac{K k_{r\alpha}}{\mu_\alpha} (\nabla p - \rho_\alpha \mathbf{g}), \quad (7)$$

where K is an absolute permeability tensor, $k_{r\alpha}$ —relative α -th phase permeability, ρ_α —density of α -phase, μ_α — α -th phase viscosity. We neglect capillary pressure between phases.

Molar sources q_i caused by chemical interactions has the following general form:

$$q_i = -\sum_k r_k (v''_{ik} - v'_{ik}) \Omega, \quad (8)$$

where v''_{ik} , v'_{ik} —stoichiometric indices of i -th component in k -th reaction, Ω —volumetric reaction surface, r_k —denotes of surface area specific molar reaction rate of in k -th reaction.

Volumetric reaction surface, Ω , highly affects overall reaction rate but in practice it is a rather uncertain parameter. Moreover, reaction surface changes while matrix dissolution. It relates to porosity and water saturation as $\Omega \sim s(1-m)$. However, strong dissolution leads to the change of pore structure making this relation nonlinear. We use the power relation

$$\frac{\Omega}{\Omega_0} = s \frac{1-m}{1-m_0}, \quad (9)$$

where Ω_0 —initial volumetric reaction surface, m_0 —initial porosity.

To complete the model the constitutive relation between porosity and permeability is needed. It may be determined from core test, well logs and well tests. Widely known Kozeny-Carman equation make rather fitting approximation of this relationship in the case of sandstones or other terrigenous matrixes. Permeability variations in carbonates are often approximated by the exponential relationship (Thayer 2020)

$$\frac{k}{k_0} = e^{A(m-m_0)}, \quad (10)$$

where A is an empirical constant. In calculations we use this kind of relationship, but the approach does not imply any restrictions on its form. In calculations we regard a diagonal permeability tensor $K = \text{diag}\{k_x, k_x, k_z\}$ where $k_y = k_x$ and k_x, k_z depend on porosity according to (10).

Acid impacts on porous medium by enlarging pores and channels. These changes lead to not only absolute permeability increase but also influence on relative phase mobilities. This fact is reflected by relative phase permeability modification according to the expression (Zhuchkov and Kanevskaya 2013):

$$k_{r\alpha}(m, s) = \frac{m - m_0}{m^* - m_0} k_{r\alpha}^* + \frac{m^* - m}{m^* - m_0} k_{r\alpha 0}, \quad (11)$$

$$k_{r\alpha}^* = \begin{cases} s, & \text{if } \alpha = w \\ 1 - s, & \text{if } \alpha = o \end{cases}$$

where $m_0, k_{r\alpha 0}$ —initial porosity and relative permeability of α -th phase, m^* —maximum porosity value. This is a linear interpolation between initial relative phase permeability and the highest possible one, when it depends linearly on saturation.

Fracture. We consider the fracture as a three-dimensional rectangular fixed region. The y axis is perpendicular to the fracture walls, x axis is extended along fracture length, z axis—along fracture height. Such an 3D approach does not imply knowledge of mass transfer coefficient and assumptions about acid concentration at fracture surfaces (Settari et al. 1998).

We assume hydrodynamic equilibrium in fracture, which means that pressure transient time is much shorter compared to the time of acid convection and diffusion in fracture. Thus, we consider incompressible stationary fluid flow whose velocity field is guessed from analytical solution for laminar flow between parallel permeable plates (Berman 1953). We also regard solute transport in fracture. As a result, we have mass balance equation for incompressible flow and convection-diffusion equation in such a form

$$\nabla \cdot \mathbf{v} = 0 \quad (12)$$

$$\frac{\partial X_a}{\partial t} + \mathbf{v} \cdot \nabla X_a = \frac{\partial}{\partial y} \left(D_{ef} \frac{\partial X_a}{\partial y} \right), \quad (13)$$

where X_a —molar concentration of acid in fracture, D_{ef} —effective molecular diffusion coefficient. In the case of newtonian fluid flow velocities are given by the following expressions:

$$v_x = -\frac{w^2}{8\mu} \frac{\partial p}{\partial x} \left(1 - \left(\frac{2y}{w} \right)^2 \right), \quad (14)$$

$$v_y = v_L \left(\frac{3}{2} \left(\frac{2y}{w} \right) - \frac{1}{2} \left(\frac{2y}{w} \right)^3 \right), \quad (15)$$

$$v_z = -\frac{w^2}{8\mu} \left(\frac{\partial p}{\partial z} - \rho g \right) \left(1 - \left(\frac{2y}{w} \right)^2 \right), \quad (16)$$

w is fracture width, v_L means leakoff fluid velocity through the fracture walls.

Initial and Boundary Conditions. Initially, matrix pressure, fracture saturation is assumed to be constant in corresponding domains. The two computational domains—matrix and fracture—must be coupled on the fracture wall.

$$\begin{aligned} p^{(m)}(\mathbf{r}, t = 0) &= p_0(\mathbf{r}), & s^{(m)}(\mathbf{r}, t = 0) &= s_0(\mathbf{r}) \\ p^{(f)}(\mathbf{r}, t = 0) &= p_0(\mathbf{r}), & X_a^{(f)}(\mathbf{r}, t = 0) &= 0, \end{aligned} \quad (17)$$

where superscripts m , f mean “matrix” and “fracture” correspondingly.

Models of reactive flow in matrix and flow in fracture mentioned above are coupled on the fracture walls. There are following boundary conditions:

$$\mathbf{v}_w|^{(m)} = \mathbf{v}_L|^{(f)}, \quad (18)$$

$$X_a \mathbf{v}_w|^{(m)} = (X_a \mathbf{v}_L + D_{ef} \nabla X_a)|^{(f)}, \quad (19)$$

where leakoff velocity \mathbf{v}_L calculation is based on (18). Consequently, expression (18) is satisfied by \mathbf{v}_L definition and we have to put additional condition in order to establish relationship between pressure in fracture and matrix. We require the same linear dependence of pressure between two fracture cells and one matrix cell closest to the bound. Conditions (18), (19) imply that the fracture can contain water phase only without both salt and carbon dioxide components

$$s^{(f)} = 1, \quad X_s^{(f)} = X_{co2}^{(f)} = 0. \quad (20)$$

The common acid fracturing schedule includes several stages. At the first stage injected viscous pad creates a fracture and prevent fluid losses of following acid which subsequently comes into contact with matrix. Acid dissolves carbonate minerals whereas the products of these interactions propagate deeper into matrix. In order to control acid losses this stage often consists of a few alternating pad and acid injections. At the second stage, well is shut off to allow injected acid to react

completely. Acid reaction rate with particular matrix determine parameters of this stage. Finally, overflush may be used in order to clean wellbore, fracture and affected matrix of the residual acid, pad and reaction products.

We consider two stages of the procedure—acid injection and well shut off. While injection pressure and acid concentration are specified on the inlet of the fracture (21). Shut off implies no-flow boundary condition on the fracture inlet (22)

$$p^{(f)} = p(t), \quad X_a^{(f)} = X_a(t), \quad \text{while injection} \quad (21)$$

$$\frac{\partial p^{(f)}}{\partial \mathbf{n}} = 0, \quad X_a^{(f)} = 0, \quad \text{while stop.} \quad (22)$$

We put constant aquifer condition on the contrary to fracture matrix bound. No-flow condition is put on the all other either matrix or fracture bounds except fracture inlet.

2.3 Numerical Solution Details

The problem of acid impact on the reservoir matrix has several spatial scales. Firstly, field scale can be characterized by the distance from well to aquifer. Secondly, pressure significantly changes inside a few meters area near wellbore or fracture. Fronts of water saturation and reaction products also propagate within this scale. Finally, permeability increases exponentially near fracture surfaces at less than one centimeter distance. Thus, we have to make grid denser towards wellbore or fracture. Here, we do not take into account wormholing that has to be considered at smaller scale.

For the simulation of acid propagation in matrix we use two-region rectangular logarithmic (along y axis) grid extended from the fracture grid to the aquifer (Fig. 1). The first one properly resolves the width of forming fracture w where permeability varies by several orders. The second one covers another part of matrix (up to r_e). Initial fracture is covered by three-dimensional rectangular uniform grid.

In order to assess stimulated productivity we simulate production in the permeability field in the stimulated area obtained from the modelling of previous stages (Fig. 2). Single phase well inflow is modelled within enlarged domain ($R_e > r_e$) up to the reaching a steady state solution.

Permeability field in the stimulated area was averaged across the fracture (y -axis). x -axis and y -axis permeabilities are arithmetic and harmonic averages over cells respectively.

Fully implicit finite volume scheme is employed for numerical solution. We adopt rectangular three-dimensional uniform grid in fracture and a rectangular grid in matrix that are logarithmically concentrated to the fracture surface. Schemes for i -th component in water phase H_{ij} , oil phase H_{oj} and matrix H_{skj} mass balance equations written for j -th grid cell are

Fig. 1 Grid covers several computational domains in the injection stage modelling. 1—initial fracture, 2—stimulated area, 3—reservoir

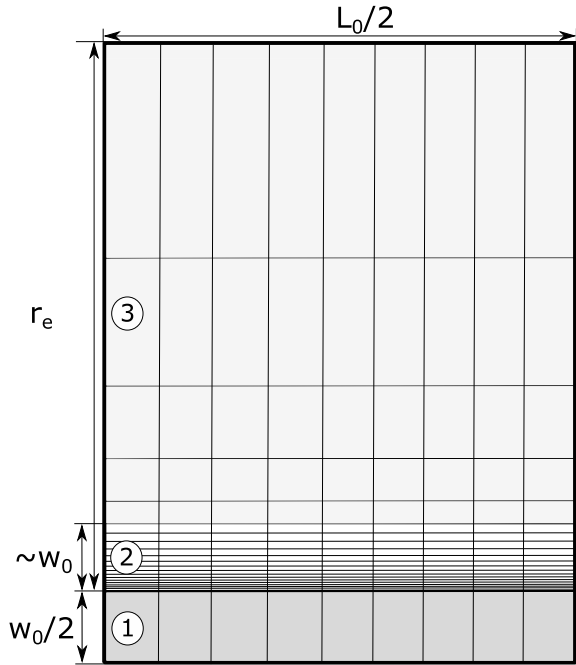
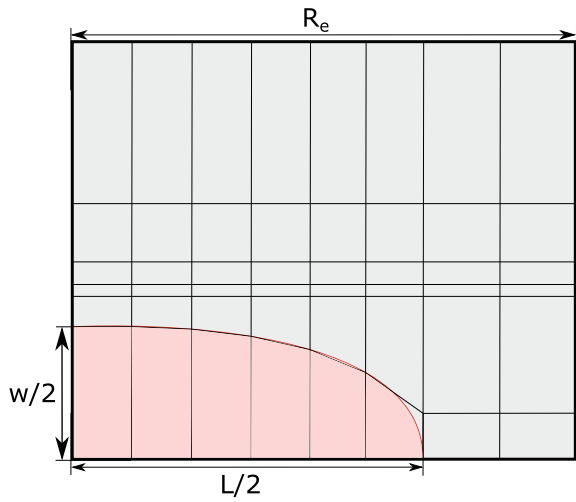


Fig. 2 Computational grid in the calculation of stimulated productivity. Red area denotes to the stimulated area



$$H_{ij}^{n+1} = msX_i b_w |_{j,n}^{j,n+1} - \tau_{n+1} q_{ij}^{n+1} + \frac{\tau_{n+1}}{V_j} \sum_{\beta} T_{j\beta}^{n+1} \left(X_i b_w \frac{k_{r\alpha}}{\mu_w} \right)_{j\beta}^{n+1} (p_j^{n+1} - p_{\beta}^{n+1}), \quad (23)$$

$$H_{oj}^{n+1} = m(1-s)b_o |_{j,n}^{j,n+1} + \frac{\tau_{n+1}}{V_j} \sum_{\beta} T_{j\beta}^{n+1} \left(b_o \frac{k_{ro}}{\mu_o} \right)_{j\beta}^{n+1} (p_j^{n+1} - p_{\beta}^{n+1}), \quad (24)$$

$$H_{skj}^{n+1} = (1-m)b_{sk} |_{j,n}^{j,n+1} - \tau_{n+1} q_{skj}^{n+1}, \quad (25)$$

where subscript “ β ” means neighbor of j -th cell, $T_{j\beta}$ —transmissibility between j and β cells which is weighted harmonic mean of cell permeabilities, V_j denotes to the volume of j -th cell, τ_{n+1} is a particular time step.

Equations in fracture are represented by the following schemes:

$$H_{f_1 j}^{n+1} = \frac{\tau_{n+1}}{V_j} \sum_{\beta} \mathbf{v}_{j\beta}^{n+1} \cdot \mathbf{n}_{j\beta}, \quad (26)$$

$$H_{f_2 j}^{n+1} = X_a |_{n+1}^{n+1} + \frac{\tau_{n+1}}{V_j} \sum_{\beta} (X_a \mathbf{v}^*)_{j\beta}^{n+1} \cdot \mathbf{n}_{j\beta}, \quad (27)$$

where $\mathbf{v}_{j\beta}$ flow velocity between j and β cells, $\mathbf{n}_{j\beta}$ —normal vector that has magnitude equal to surface area, $\mathbf{v}_{j\beta}^*$ —flow velocity between cells that takes into account diffusion fluxes in y-axis direction. All inter-cell $j - \beta$ approximations use linear interpolation by pressure and upwind scheme by saturation and concentration.

Nonlinearity of proposed equations is handled with Newton iterations. Derivation of analytical expressions of Jacobian matrix elements for the schemes (23)–(27) appears routine and unreliable in the context of code writing, especially in the case of multiphase multicomponent reactive flow. We exploit ADOL-C library (Walther and Griewank 2012) that provides with easy-to-use automatic differentiation facilities, including computations of sparse Jacobians and Hessians based on graph coloring methods.

In order to improve conditioning of resulting matrix, dimensionless parameters are chosen. Besides, multiplication of matrix equations based on grid geometry also decrease matrix condition number. ILU(0, 1), ILUT preconditioner accompanied by BiCGStab are employed to solve obtained linear systems.

3 Analysis of Results

Fracture that are not packed with propping agent will close and will not provide lasting productivity increase. In the case of acid fracturing stimulation is achieved by porosity and consequently permeability increase in matrix around fracture. Fracture

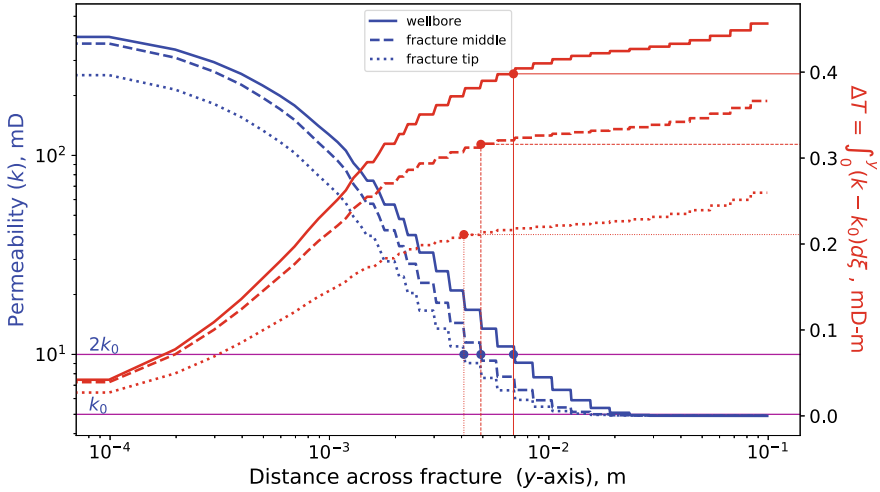


Fig. 3 Transmissibility estimation based on the integration of the permeability field. Profiles are presented in three fracture cross-sections—near wellbore, at fracture middle and at fracture tip

transmissibility is a common way to evaluate its ability to conduct flow (Zhuchkov and Kanevskaya 2013). It is

$$T(x, z) = \int_0^{y_s} k(x, y, z) dy \tag{28}$$

where y_s is the effective depth of acid penetration into matrix.

The sample of permeability profiles calculated by the end of injection are presented in Fig. 3. Based on the permeability field transmissibility was calculated as a function of upper integral limit, y_s . We define the half width of acid fracture as an area where permeability is two times higher than its initial value. This cut-off was determined empirically and corresponds to the start of transmissibility flattening region. Input parameters of this simulation are listed in Table 2.

Proposed approach allows transmissibility profiles along fracture to be calculated. In this particular case (Fig. 3) the whole length of the initial fracture was stimulated and permeability at the fracture tip was a bit lower compared to at wellbore. In general, permeability at the tip can be significantly lower, especially when acid has not attained it at all.

In scope of our approach we assume initial hydraulic fracture exists before acid injection (Fig. 1). It has fixed prescribed geometry and is out of consideration after injection stage. Here, we call “acid fracture” the stimulated matrix region near occurred hydraulic fracture. We also suppose that only acid fracture contributes to the resulting conductivity what is equivalent to say that there is no stimulation from hydraulic fracture which becomes completely closed after injection.

Table 2 Main input parameters

Parameter	Value
Solution volume (m ³)	50
Solution concentration	0.15
Initial fracture length (m)	120
Depression (bar)	80
Reservoir permeability (mD)	5
Reservoir height (m)	18.87
Initial reaction surface (m ⁻¹)	1E + 5
Maximum porosity	0.4
Reaction order	1
Reaction constant (m/s)	0.24

Stimulated productivity is numerically evaluated after all stimulation stages. Fracture is produced at constant drawdown and fluid rate behavior determines productivity. Estimation of steady-state productivity requires calculation of sufficiently longer period of time than it was calculated in stimulation stages. That’s why this calculation is performed in significantly larger region (Fig. 2).

3.1 Numerical Convergence

Several spatial scales of the problem puts additional requirements on the maximum cell size. The presented grid allow us to accurately resolve all features of the solution using minimal number of cells where the solution remains stable. In order to examine the convergence of used numerical scheme and the fact that grid properly resolve solution a number of simulations with different grid sizes were performed. Injection of the certain amount of acid solution was modelled with fixed wellbore pressure (Dirichlet boundary condition). Several runs were made for a range of cell sizes along fracture (*x*-axis) and across it (*y* – *axis*). Reaction surface (9) was set to constant $\Omega = \Omega_0$ in all runs. Input parameters are listed in Table 2.

Statistics of performed simulations is presented in Tables 3, 4. The most accurate simulation was set as reference for the calculation of relative error in each table.

Table 3 Statistics of calculations with different grid size along fracture

#	Num. of cells	Min. cell size (m)	Rel. error (%)
1	10	12	0.016
2	20	6	0.012
3	40	3	0.006
4	80	1.5	–

Table 4 Statistics of calculations with different grid size across fracture

#	Num. of cells	Min. cell size (m)	Rel. error (%)
5	50	2.4E-6	14.1
6	75	1.6E-6	9.1
7	100	1.2E-6	6.5
8	200	5.8E-7	-

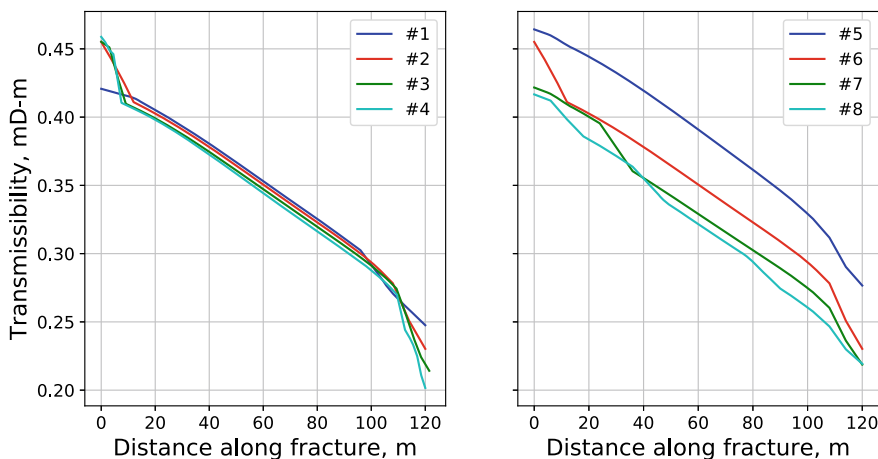


Fig. 4 Transmissibility profile along fracture calculated with different size of cells along fracture (left) and across it (right)

As you can see, the grid resolution in the direction perpendicular to the fracture is more affecting on the accuracy of calculations. Figure 4 illustrates the convergence of estimated transmissibility along fracture.

3.2 Acid Propagation

Acid stimulation is achieved by the dissolution of minerals that enlarge void spaces in matrix. On the one hand, propagating through matrix acid determines the area of stimulation. On the other hand, stimulation contributes to further propagation. This fact is expressed in nonlinear nature of the governing equations. In this case there are many affecting factors on the stimulation. Let us start from the observation of non-stationary acid propagation through matrix. We consider two possible ways to control the flow at the fracture inlet—fixed wellbore pressure or fixed rate. In other words, Dirichlet and Neumann types of boundary condition.

Injection with the fixed wellbore pressure starts from a fast fluid flow which then slows down. As a result, water phase together with all components propagates deeply

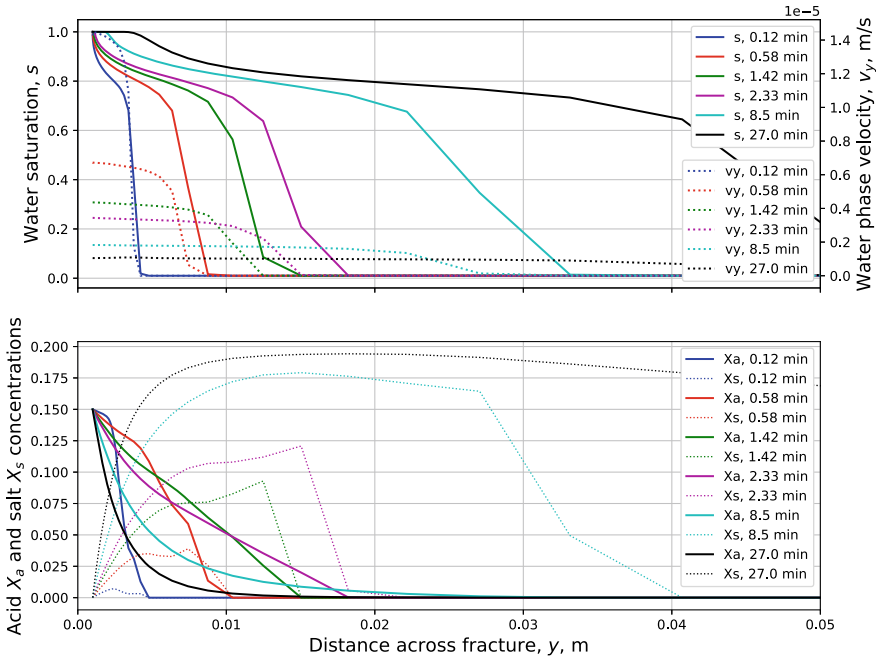


Fig. 5 Acid solution propagation into formation during injection with constant wellbore pressure (27 min). Acid concentration profile is smoothing and returns back after some period of time

at the early times (Fig. 5). However, after some period of time acid profile becomes smooth and comes back. Smoothing is a result of intensive reaction whereas the acid return is caused by a high initial fluid velocity. Other components keep going deeper into matrix.

In the case of fixed fluid rate (Fig. 6) its velocity remains constant over the distance of velocity front propagation. Acid concentration profile moves deeper into matrix over all period of injection. The shape of its profile depends on many factors like fluid injection rate, reservoir permeability, reaction kinetics and maximum porosity. In the case of high reaction speed which takes place in limestone acidizing by hydrochloric acid the acid profile stabilizes after some short period of time and then moves without any changes in the shape of profile.

15% HCl is often used for limestone acidizing. However, field engineers use other concentrations as well. Higher concentration provides faster reaction kinetics that might not have a positive effect. As it was mentioned before, the dissolution of limestones is limited by acid transport and the higher rate of reaction kinetics does not increase dissolution rate.

Injection of 10, 15, 20% acid solutions were simulated. Acid concentration and permeability profiles are presented in Fig. 7. Fixed volume of acid were injected in each case over the different period of time with fixed wellbore pressure. Although, the solution of higher concentration was reacted faster, it provides lower stimulation

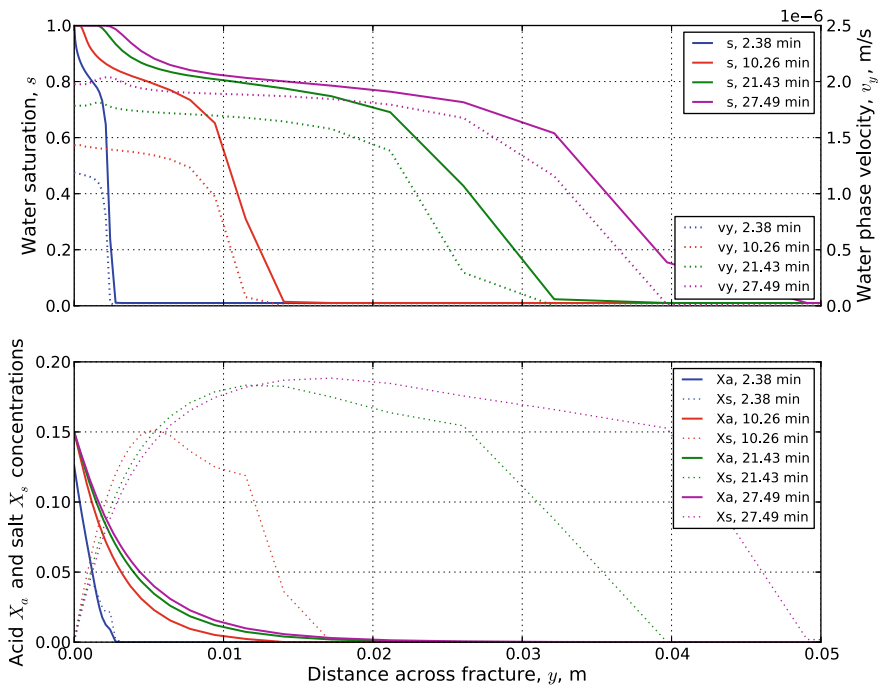


Fig. 6 Acid solution propagation into formation during injection with constant injection rate ($500 \text{ m}^3/\text{day}$). Acid concentration profile is smoothing and returns back after some period of time

performance. In this case, the time of injection determines this performance. However, if we look at the this profiles after the same time (but before any solution ends), the higher concentration will bring stronger stimulation.

3.3 Stimulated Productivity

In order to assess the efficiency of stimulation we calculate productivity. Oil production was simulated in enlarged domain with the permeability field calculated in the previous stage.

Figure 8 demonstrates the influence of acid injection rate on the stimulated productivity. Fixed volume of acid was injected into matrix under the constant wellbore pressure. All the results show that productivity goes down with acid injection rate, so that the longer stimulation provides better performance. The simulation was done for several values of the length of initial fracture and reservoir permeability. All the results for different lengths and permeabilities behave the same with changes of injection rate. They decreases almost linearly up to the injection rate of $10^4 \text{ m}^3/\text{day}$ and than they asymptotically approach to unity.

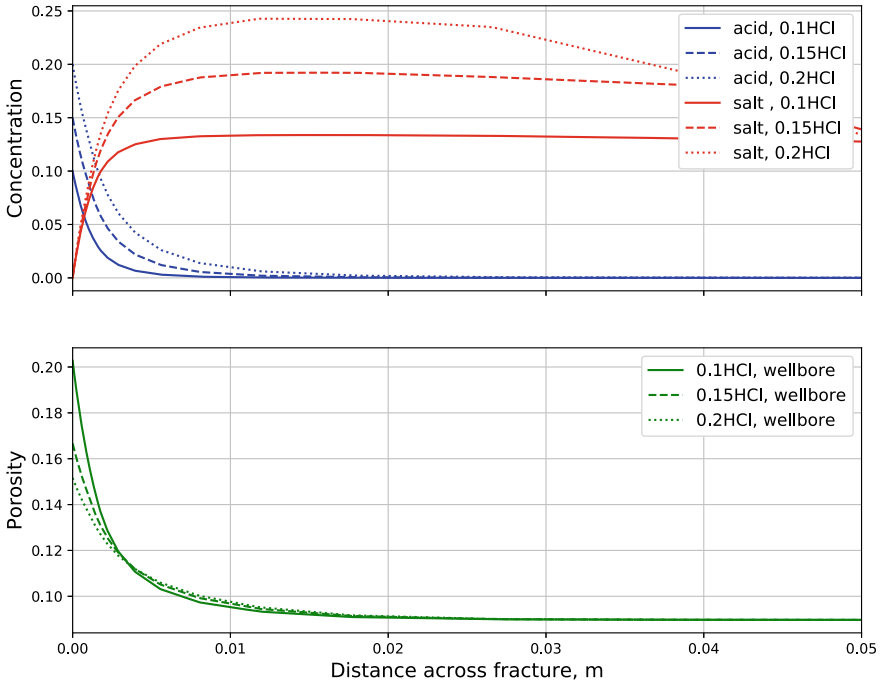


Fig. 7 Acid, salt concentrations and permeability profiles by the end of the injection of the fixed volume of HCl (7.5 m^3). Three types of solutions 10, 15 and 20% were injected with the corresponding solution volumes $75, 50, 37.5 \text{ m}^3$ over the different periods of time—60, 27, 16 minutes respectively

4 Conclusion

In this paper, we have considered the simulation of fracture acidizing in carbonate reservoir. The model of two phase multicomponent reactive Darcy flow in fracture and porous matrix was developed and used for the modelling. Convection-diffusion problem was used for the acid transport simulation in fracture. The coupled model was solved using FVM fully implicit scheme. The model assumes that all reaction products instantly dissolve in water phase. It takes into account arbitrary acid mineral interactions and dissolution kinetics. The model explicitly evaluates fluid leak-off from fracture since it consider the coupled model of fluid flow in fracture and in matrix. It allows several stages of stimulation and stimulated productivity to be calculated. Moreover, the proposed technique provides exact permeability field around fracture, allows transmissibility calculation along fracture caused by any kind of acid stimulation. This approach provides the knowledge of the exact shape of stimulated area and the value of stimulation over this area.

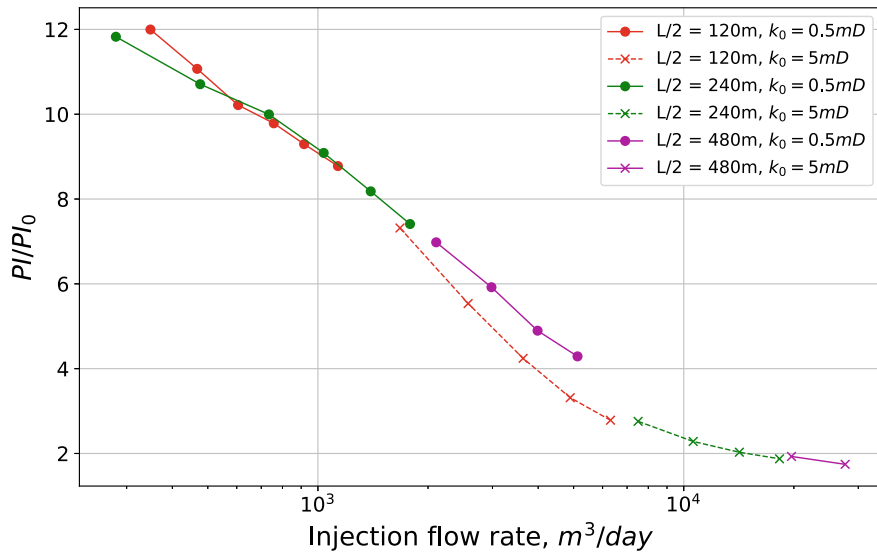


Fig. 8 Stimulated productivity divided by the initial productivity against injection rate for different values of the length of initial fracture and reservoir permeability

The considered domains cover several spatial scales and the grid convergence of performed simulation was examined. Acid propagation into matrix was investigated for different injection regimes and various concentration of acid solution. Stimulated production was calculated for a range of reservoir permeabilities and initial fracture lengths. Results show that the longer injection period provides better performance of stimulation.

References

- Berman AS (1953) Laminar flow in channels with porous walls. *J Appl Phys* 26:489
- Buijse MA, Glasbergen G (2005) A Semi-empirical model to calculate wormhole growth in carbonate acidizing. *Soc Petroleum Eng.* <https://doi.org/10.2118/96892-MS>
- Cohen CE, Ding D, Quintard M, Bazin B (2008) From pore scale to wellbore scale: impact of geometry on wormhole growth in carbonate acidization. *Chem Eng Sci* 63(12):3088–3099
- Golfier F, Zarcone C, Bazin B, Lenormand R, Lasseux D, Quintard M (2002) On the ability of a Darcy-scale model to capture wormhole formation during the dissolution of a porous medium. *J Fluid Mech* 457:213–254. <https://doi.org/10.1017/S0022112002007735>
- Golfier F, Bazin B, Lenormand B, Quintard M (2004) Core-scale description of porous media dissolution during acid injection—Part I: theoretical development. *Comp Appl Math* 23:2–3
- Golfier F, Quintard M, Bazin B, Lenormand R (2006) Core-scale description of porous media dissolution during acid injection—part II: calculation of the effective properties. *Comput Appl Math* 25(1):55–78. ISSN 2238-3603

- Lund K, Fogler HS, McCune CC (1973) Acidization I: the dissolution of dolomite in hydrochloric acid. *Chem Eng Sci* 28:691–700
- Lund K, Fogler HS, McCune CC, Ault JW (1975) Acidization II the dissolution of calcite in hydrochloric acid. *Chem Eng Sci* 30:825–835
- Mou J, Zhu D, Hill AD (2010) Acid-etched channels in heterogeneous carbonates—a newly discovered mechanism for creating acid-fracture conductivity. *Soc Petroleum Eng.* <https://doi.org/10.2118/119619-PA>
- Nierode DE, Williams BB (1971) Characteristics of acid reaction in limestone formations. *Soc Petroleum Eng.* <https://doi.org/10.2118/3101-PA>
- Oeth CV, Hill AD, Zhu D (2014) Society of petroleum engineers, acid fracture treatment design with three-dimensional simulation. <https://doi.org/10.2118/168602-MS>
- Schwalbert MP, Zhu D, Hill AD (2017) Extension of an empirical wormhole model for carbonate matrix acidizing through two-scale continuum 3D simulations. *Soc Petroleum Eng.* <https://doi.org/10.2118/185788-MS>
- Settari A, Sullivan RB, Hansen CE (1998) Society of petroleum engineers, a new two-dimensional model for acid fracturing design. <https://doi.org/10.2118/48930-MS>
- Shaik R, Tomin P, Voskov D (2018) Modeling of near-well matrix acidization. In: 43rd workshop on geothermal reservoir engineering, Stanford, February 12–14, 2018
- Soulaire C, Tehelepi HA (2016) Micro-continuum approach for pore-scale simulation of subsurface processes. *Transp Porous Med* 113:431. <https://doi.org/10.1007/s11242-016-0701-3>
- Thayer PA (2020) Relationship of porosity and permeability to petrology of the madison limestone in rock cores from three test wells in Montana and Wyoming. Geological Survey Professional Paper; 1273-C
- Tukhvatullina RR, Posvyanskii VS (2012) Mathematical modelling of acid treatment of the bottom hole zone for carbonate reservoirs. In: ECMOR XIII—13th European conference on the mathematics of oil recovery
- Volnov IA, Kanevskaya RD (2009) Seepage effects of dissolving rock by acid action on carbonate oil-bearing formations. *Fluid Dyn* 44:887. <https://doi.org/10.1134/S001546280906012X>
- Walther A, Griewank A (2012) Getting started with ADOL-C. U. Naumann und O. Schenk, *Combinatorial Scientific Computing*, Chapman-Hall CRC Computational Science, pp 181–202
- Zhuchkov SY, Kanevskaya RD (2013) Modeling the acidizing of a horizontal well opening a carbon-bearing oil reservoir. *Fluid Dyn* 48:503. <https://doi.org/10.1134/S0015462813040091>

Underground Density-Driven Convection of Saline Fluids with Constant and Variable Viscosity



E. B. Soboleva

Abstract Numerical simulation of density-driven convection in a porous medium modeling underground flows in crusts is conducted. Convective flows are initiated by an admixture source of finite length in a semi-infinite domain. An influence of the Rayleigh-Darcy number and variable viscosity on the structure and the number of convection regimes is discussed.

Keywords Density-driven convection · Porous medium · Darcy's filtration · Dissolved admixture · Variable viscosity · Numerical simulation

1 Introduction

Investigations of groundwater flows containing dissolved admixture and filling a porous medium are important for environmental management, mining, alternative energy engineering. Filtration problems are considered for carbon dioxide sequestration, underground repositories for nuclear waste, displacement of oil by water, extraction of hot fluids transporting geothermal energy.

One can specify a class of problems in which the fluid motion is driven by density inhomogeneities induced by dissolved admixture. If the system is under gravity, then natural haline convection develops. Such flows are generally called density-driven convection in the groundwater literature. Along with variable density, other factors can be essential for the hydrodynamic behavior of fluid phase, for example, temperature inhomogeneities, nonuniform solid matrix, variable physical properties of fluid.

E. B. Soboleva (✉)

Ishlinsky Institute for Problems in Mechanics RAS, Moscow, Russia

e-mail: soboleva@ipmnet.ru

URL: <http://ipmnet.ru/soboleva/>

© The Author(s), under exclusive license to Springer Nature Switzerland AG 2021

T. Chaplina (ed.), *Processes in GeoMedia—Volume II*, Springer Geology,

https://doi.org/10.1007/978-3-030-53521-6_13

In this work, the onset and development of density-driven convective flows and mass transfer in a fluid phase with constant and variable viscosity is investigated. We consider a semi-infinite porous domain bounded by the upper horizontal surface. The part of this surface is the source of admixture triggering convective flows.

2 Theoretical Background

2.1 Solution Viscosity

The viscosity of groundwater depends on the concentration and composition of dissolved salts and other matters. The temperature is considered to be constant. The data (Aleksandrov et al. 2012) for water with sodium chloride based on numerous experiments are used to estimate the viscosity change. In theoretical studies, the Frank-Kamenetskii law is often used, i.e., the viscosity of solution is fitted to an exponential function of admixture density. We have

$$\mu = \mu_0 \exp(\Gamma' \rho_c). \quad (1)$$

Here, μ and μ_0 are the viscosity of solution and pure water, ρ_c is the density of dissolved admixture, Γ' is the viscosity variation parameter. We transform Eq. (1) introducing the dimensionless density $S = \rho_c / \rho_{c(sat)}$ and dimensionless viscosity variation parameter $\Gamma = \Gamma' \rho_{c(sat)}$, i.e., replacing the product $\Gamma' \rho_c$ by the equality: $\Gamma' \rho_c = \Gamma S$. Here, $\rho_{c(sat)}$ is the density of admixture in saturated solution. Taking the logarithm of the left-hand and right-hand sides of the result equation, one can obtain the linear dependence of $\ln(\mu)$ on S : $\ln(\mu) = \ln(\mu_0) + \Gamma S$. We fit the data on μ (Aleksandrov et al. 2012) depending on S to the last linear relation and find out μ_0 and Γ . In Fig. 1, the markers coincide with data (Aleksandrov et al. 2012) corresponding to the pressure $P = 10$ MPa and the temperature $T = 423$ (a), 473 K (b). The selected thermodynamic conditions are typical for geothermal systems. The theoretical straight lines drawn for each temperature T are obtained by the method of least squares. According to our estimations, $\mu_0 = 190.7 \mu\text{Pa s}$ and $\Gamma = 1.022$ (a), $\mu_0 = 143.5 \mu\text{Pa s}$ and $\Gamma = 1.004$ (b). Note that the found viscosity of pure water is close to that in the open database NIST (National Institute of standards and Technology, USA) (NIST Chemistry WebBook 2016). We have in NIST for thermodynamic conditions indicated above: $\mu_0 = 184.9 \mu\text{Pa s}$ (a) and $\mu_0 = 136.4 \mu\text{Pa s}$ (b). Obviously, that the estimated parameter Γ does not change significantly if T varies, therefore we take $\Gamma = 1$ in numerical simulation.

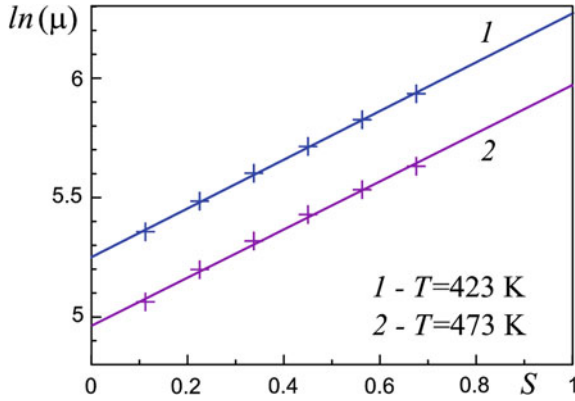


Fig. 1 Dependence of solution viscosity μ (in $\mu\text{Pa s}$) on the dimensionless density of dissolved admixture S . Markers denote the data (Aleksandrov et al. 2012), solid lines are the theoretical straight lines

2.2 Governing Equations and Numerical Method

Flows and mass transfer in a solution filling a porous medium is described by the hydrodynamic model that includes the equations of continuity, motion (in the form of the Darcy equation) and admixture transport. The model is added by the linear equation of state relating the density of solution ρ to the density of dissolved admixture ρ_c . The equations are as follows.

$$\nabla \cdot \mathbf{U} = 0 \tag{2}$$

$$\mathbf{U} = -\frac{k}{\mu}(\nabla P - \rho \mathbf{g} \cdot \mathbf{e}) \tag{3}$$

$$\phi \frac{\partial \rho_c}{\partial t} + \mathbf{U} \cdot \nabla \rho_c = \nabla(\phi D \nabla \rho_c) \tag{4}$$

$$\rho = \rho_0 + \alpha \rho_c \tag{5}$$

The values \mathbf{U} , P , ρ_0 , k , ϕ , D , g , \mathbf{e} are the filtration velocity, pressure, density of pure water, permeability, porosity, admixture diffusion coefficient, modulus of gravity acceleration and unit vector co-directional with the gravity. The constant $\alpha = 0.815$ is actual for water.

The porosity ϕ , permeability k , diffusion coefficient D and viscosity μ can be variable. The density ρ in Eq. (3) is substituted by Eq. (5) to exclude ρ from our consideration. Then, Eqs. (2)–(4) are reduced to a dimensionless form. The diffusion velocity and diffusion time are used as scales. Next, the differential equations are approximated by the finite difference equations. The last ones are solved numerically

using the numerical code designed for density-driven convective problems and effectively employed during several years (Soboleva and Tsyarkin 2014, 2016; Soboleva 2017a, b, 2018, 2019a). The code is based on the finite-difference method applied in the case of straggled nonuniform grid. The algebraic linear equations are solved by the tridiagonal matrix algorithm called also as the Thomas algorithm (Aziz and Settari 1979). At the present stage of research, the code is modified by applying a more efficient numerical scheme for the convective term (QUICK scheme instead of the central difference scheme) and extended to fluids with variable viscosity (Soboleva 2019a).

3 Numerical Simulation

3.1 Problem Under Study

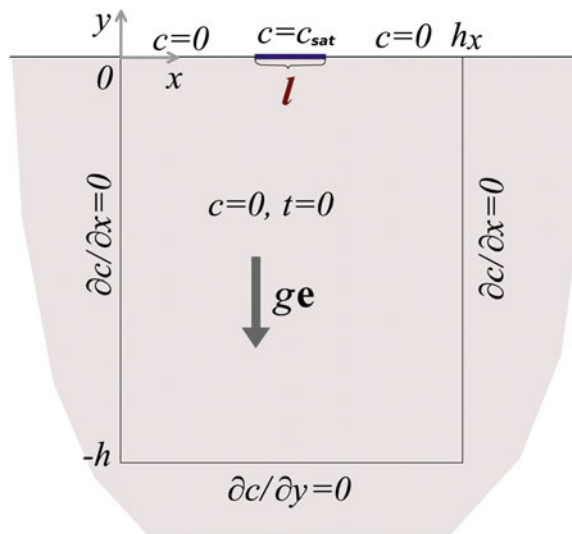
We consider a semi-infinite porous domain under the Earth’s gravity bounded by the upper horizontal surface. Initially, the domain is filled with pure water at rest. There is a source of admixture at the upper boundary with length l which is held at the constant admixture concentration c equal to one in saturation solution c_{sat} . The sketch of the problem is given in Fig. 2.

The admixture diffuses into the domain dissolving in water. Thus, a zone of concentrated solution is formed below the source. Solution is heavier than pure water and therefore tends to fall down. Gravitational density-driven convection develops.

The density of dissolved admixture ρ_c is related to c by the relation:

$$\rho_c = \rho_0 \frac{c}{1 - \alpha c} \tag{6}$$

Fig. 2 Sketch of the problem



The dimensionless system of the governing equations includes the Rayleigh-Darcy Rd number which is the criterion of similarity of convection observed. We have

$$Rd = \frac{(\rho_{sat} - \rho_0)glk_0}{\mu_0 D_0} \tag{7}$$

Here, ρ_{sat} is the density of saturated solution, subscript “0” denotes some reference values. Note, that the length scale in Eq. (7) is the source length l .

Before beginning numerical simulation, we have analyzed the Elder problem that is on thermal convection induced by a finite source in the Hele-Shaw cell (Elder 1967). Later, they started to apply this problem to haline convection as well. As shown in (Van Reeuwijk et al. 2009), the problem can have several solutions depending on the Rayleigh-Darcy Rd_h number. A single regime is induced if $Rd_h < 76$. Note, Rd_h in the Elder problem includes the cell height h being twice shorter than the source length. Recalculating the Rayleigh-Darcy number with the use of the source length, we obtain the twice bigger threshold magnitude and condition ensuring a single solution in the form: $Rd < 152$. One can believe, that the system passes through the bifurcation points in the beginning of convection when small disturbances are

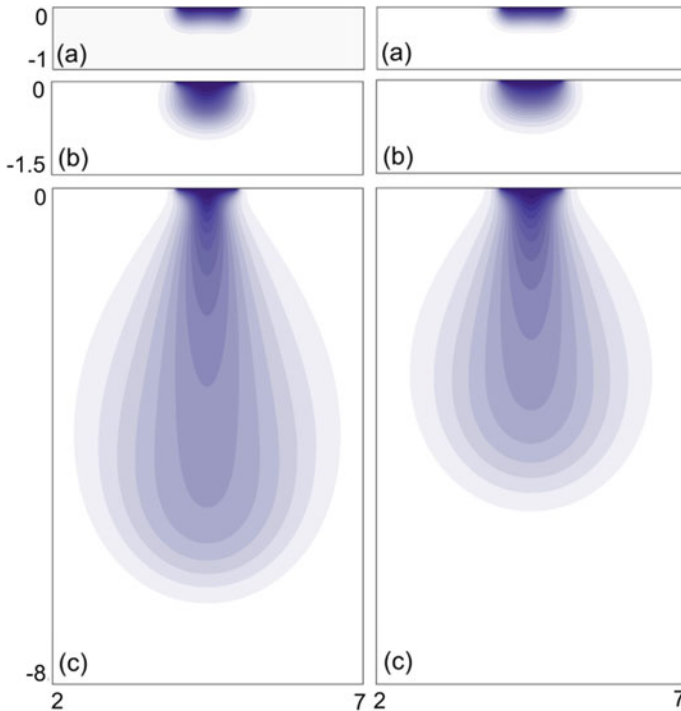


Fig. 3 Fields of admixture concentration at $Rd = 60$ and at times $t = 2.0 \times 10^{-2}$ (a), $t = 7.0 \times 10^{-2}$ (b), $t = 7.7 \times 10^{-1}$ (c). Viscosity is constant (left) and variable (right)

self-organising in the boundary layer under the source. It means, that the condition on the Rayleigh-Darcy number can be applied in the case of a semi-infinite domain and we expect to obtain several solutions if $Rd > 152$.

3.2 Results of Simulation

We conducted numerical simulation at $Rd = 60$ when regime of convection is single and analyzed the role of variable viscosity. The porous domain 9×10 is considered. The space grid is uniform and includes 900×1500 cells. The time step is $\tau = 3.3 \times 10^{-6}$. The fields of admixture concentration are shown in Fig. 3; the part of considered domain is presented. As obvious, convective structure is very simple. A single convective plum is developed. In the case of variable viscosity, the depth of penetration is shorter, as the velocity of flows near the source becomes lower. As a result, a smaller amount of admixture moves into the domain.

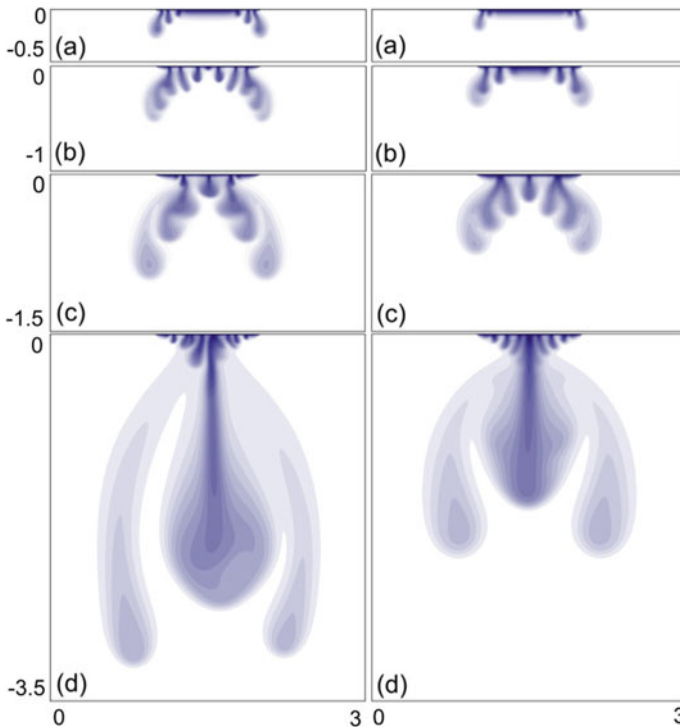


Fig. 4 Fields of admixture concentration at $Rd = 2000$ and at times $t = 1.0 \times 10^{-3}$ (a), $t = 2.0 \times 10^{-3}$ (b), $t = 3.0 \times 10^{-3}$ (c), $t = 1.3 \times 10^{-2}$ (d). Viscosity is constant (left) and variable (right)

If $Rd > 152$, we expect to obtain not a single solution. However, only one of possible regimes at $Rd = 2000$ is exhibited in Fig. 4. The porous domain is 3×5 . The space grid with steps refining near the source is 1500×2000 . The time step is $\tau = 1.25 \times 10^{-7}$. We see, that motion arises near the edges of source there the horizontal gradient of density is present. Initially, several small fingers occur. Then, motion is rearranged and a central plum is formed. Motion and mass transfer are concentrated in the central plum transporting admixture down. When variable viscosity is taken into consideration, convective structure is qualitatively similar to that observed at constant viscosity. However, convection develops slower and the depth of penetration of central plum is shorter.

4 Conclusion

We presented here some results on numerical simulation of density-driven convection triggered by an admixture source of finite length in semi-infinite porous domain. As discussed, the regime of convection strongly depends on the Rayleigh-Darcy Rd number. When $Rd > 152$ we expect to obtain several solutions. The variable viscosity taken into consideration can influence the structure and the number of convection regimes.

Acknowledgements The author would like to thank G.G. Tsyarkin for many fruitful discussions. This work has been supported by the Russian Science Foundation (grant No 16-11-10195).

References

- Aleksandrov AA, Dzshuraeva EV, Utenkov VF (2012) Viscosity of aqueous solutions of sodium chloride. *High Temp* 50(3):354–358. <https://doi.org/10.1134/S0018151X12030029>
- Aziz Kh, Settari A (1979) Petroleum reservoir simulation. Applied Science Publisher, London
- Elder JW (1967) Steady free convection in a porous medium heated from below. *J Fluid Mech* 27:29–48
- NIST Chemistry WebBook (2016) Thermophysical properties of fluid systems. <https://webbook.nist.gov/chemistry/fluid/>
- Soboleva EB (2018) Density-driven convection in an inhomogeneous geothermal reservoir. *Int J Heat and Mass Trans* 127(part C):784–798. <https://doi.org/10.1016/j.ijheatmasstransfer.2018.08.019>
- Soboleva EB (2019a) Numerical study of haline convection in a porous domain with application for geothermal systems. In: Karev V, Klimov D, Pokazeev K (eds) *Physical and mathematical modeling of earth and environment processes* (2018). Springer Proceedings in Earth and Environmental Sciences. Springer, Cham, pp 63–74. https://doi.org/10.1007/978-3-030-11533-3_7
- Soboleva E (2017a) Numerical investigations of haline-convective flows of saline groundwater. *J Phy Conf Ser* 891:012104. <https://doi.org/10.1088/1742-6596/891/1/012104>
- Soboleva E (2017b) Numerical simulation of haline convection in geothermal reservoirs. *J Phys Conf Ser* 891:012105. <https://doi.org/10.1088/1742-6596/891/1/012105>

- Soboleva EB (2019b) A method for numerical simulation of haline convective flows in porous media as applied to geology. *Comput Math Math Phys* 59(11):1893–1903
- Soboleva EB, Tsykin GG (2014) Numerical simulation of convective flows in a soil during evaporation of water containing a dissolved admixture. *Fluid Dyn* 49(5):634–644. <https://doi.org/10.1134/S001546281405010X>
- Soboleva EB, Tsykin GG (2016) Regimes of haline convection during the evaporation of groundwater containing a dissolved admixture. *Fluid Dyn* 51(3):364–371. <https://doi.org/10.1134/S001546281603008X>
- Van Reeuwijk M, Mathias SA, Simmons CT, Ward JD (2009) Insights from a pseudospectral approach to the elder problem. *Water Resour Res* 45:W04416. <https://doi.org/10.1029/2008WR007421>

Phase Spectra of a Multicomponent Wave Field



A. S. Zapevalov 

Abstract The analysis of phase relations in a complex multicomponent wave field, which is the field of sea surface waves, is carried out. A spatially uniform and stationary wave field is considered. It is shown that in such a field, the simultaneous presence of free and bound waves at the same frequency leads to a nonlinear dependence of the phase spectrum on the distance between the points for which it is defined. As a consequence, the phase velocity values calculated from the phase shift vary depending on the distance between the points for which the phase shift is determined. The distribution of wave energy in the directions leads to the same effect. The value of the phase velocity calculated for a multicomponent wave field exceeds its theoretical value, which is obtained from the dispersion equation for gravitational waves. Under the most favorable conditions, which correspond to a fully developed wind wave, at the frequency of dominant waves, the excess is 5–10%. At higher frequencies, where the angular distribution function is wider, deviations from the theoretical value of the phase velocity increase.

Keywords Phase shift · Coherence · Phase velocity · Bound components · Directional spreading function

1 Introduction

In recent years, there has been an intensive development of methods for estimating the surface current velocity from satellite optical images of the sea surface. The impetus for this was the launch of Sentinel-2 satellites, which are equipped with multi-spectral instruments. This specific instrumentation allows you to get satellite sun glitter imagery with high spatial resolution and a small time lag. The spatial resolution is 10 m, with a minimum time lag of 1 s (European Space Agency (ESA) 2012; Suetin et al. 2013).

A. S. Zapevalov (✉)
Marine Hydrophysical Institute RAS, Sevastopol, Russian Federation
e-mail: sevzepter@mail.ru

The phase spectra of the field of surface waves, which are obtained from sun glitter images, allow us to calculate the phase velocities of waves. It is assumed that the deviation of the calculated phase velocity from the theoretical value is uniquely determined by the surface current velocity (Kudryavtsev et al. 2017a, b; Yurovskaya and Kudryavtsev 2019;). The theoretical value is calculated by the dispersion relation for gravitational waves. Obviously, the accuracy of the values of the current velocity obtained by this technique depends on how much other physical mechanisms (except the current) can modify the dispersion relation.

The field of sea surface waves is a complex multicomponent field. Its main features are: the presence of components propagating at different speeds (free and bound components), the distribution of wave energy in the directions (Yuen and Lake 1982; Zapevalov 1996; Zapevalov et al. 2009; Wang and Hwang 2004). The aim of this work is to analyze the influence of these factors on the phase spectra of the wave field.

2 Description of the Wave Field

Consider a multicomponent wave field in which individual components do not interact with each other, and each component obeys its dispersion equation. The spectrum $S(\omega)$ and cross-spectrum $\chi(\omega, \vec{L})$ of such a field can be represented as (Pokazeev and Zapevalov 2019)

$$S(\omega) = \sum_{j=1}^n S_j(\omega), \quad (1)$$

$$\chi(\omega, \vec{L}) = \sum_{j=1}^n Co_j(\omega, \vec{L}) - i Q_j(\omega, \vec{L}), \quad (2)$$

where ω is the cyclic frequency; j is a number of components; n is a quantity of components; \vec{L} is a vector connecting two points for which a cross-spectrum is constructed; Co and Q are co - and quadrature spectra. If $S(\omega)$ and $\chi(\omega, \vec{L})$ are given in the form (1) and (2), it is assumed that the wave field is uniform in space and stationary. The frequency-angular spectrum $\Psi_j(\omega, \alpha)$ of each wave component is given in the traditional form

$$\Psi_j(\omega, \alpha) = S_j(\omega) \Theta_j(\omega, \alpha), \quad (3)$$

where α is the azimuthal angle; Θ is the directional spreading function. Each directional spreading function $\Theta_j(\omega, \alpha)$ satisfies the normalization condition

$$\int_{-\pi}^{\pi} \Theta_j(\omega, \alpha) d\alpha = 1. \quad (4)$$

Using Eqs. (1) and (2) we construct a phase spectrum $\varphi(\omega, \vec{L})$ and a quadratic function of coherence $R^2(\omega, \vec{L})$ for a multicomponent wave field

$$\begin{aligned} \varphi(\omega, \vec{L}) &= \text{arctg}\left(-\text{Im}\chi(\omega, \vec{L}) / \text{Re}\chi(\omega, \vec{L})\right) \\ &= \text{arctg}\left(\frac{\sum_{j=1}^n Q_j(\omega, \vec{L})}{\sum_{j=1}^n C o_j(\omega, \vec{L})}\right), \end{aligned} \quad (5)$$

$$R^2(\omega, \vec{L}) = \frac{Q^2(\omega, \vec{L}) + C o^2(\omega, \vec{L})}{S^2(\omega)} = \frac{\left(\sum_{j=1}^n Q_j(\omega, \vec{L})\right)^2 + \left(\sum_{j=1}^n C o_j(\omega, \vec{L})\right)^2}{\left(\sum_{j=1}^n S_j(\omega)\right)^2}. \quad (6)$$

The quadratic function of coherence determines the stability of phase relations. At low values $R^2(\omega, \vec{L})$ the phase spectrum is not defined.

It follows from (5) and (6) that the cross-spectrum of each component can be represented as (Jenkins and Watts 1968)

$$\chi(\omega, \vec{L}) = R(\omega, \vec{L}) S(\omega) \exp(i\varphi(\omega, \vec{L})). \quad (7)$$

3 The Effect of Bound Components

Consider a one-dimensional wave field. We assume that there are several components with a frequency ω that have different phase velocities C_j . Each component is spreading without interacting with other components. The condition $R_j^2(\omega, L) = 1$ for it is satisfied, respectively from (7) follows $\chi_j(\omega, L) = S_j(\omega) \exp(i\varphi_j(\omega, L))$. We get

$$\varphi(\omega, L) = \text{arctg}\left(\frac{\sum_{j=1}^n S_j(\omega) \sin(\varphi_j(\omega, L))}{\sum_{j=1}^n S_j(\omega) \cos(\varphi_j(\omega, L))}\right), \quad (8)$$

$$R^2(\omega, L) = \frac{\left(\sum_{j=1}^n S_j(\omega) \sin(\varphi_j(\omega, L))\right)^2 + \left(\sum_{j=1}^n S_j(\omega) \cos(\varphi_j(\omega, L))\right)^2}{\left(\sum_{j=1}^n S_j(\omega)\right)^2}. \quad (9)$$

Given that the phase velocity is related to the phase shift by the relation

$$C(\omega) = \omega L / \varphi(\omega, L), \quad (10)$$

Equations (8) and (9) can be rewritten as

$$\varphi(\omega, L) = \operatorname{arctg} \left(\frac{\sum_{j=1}^n S_j(\omega) \sin(\omega L / C_j(\omega))}{\sum_{j=1}^n S_j(\omega) \cos(\omega L / C_j(\omega))} \right), \quad (11)$$

$$R^2(\omega, L) = \frac{\left(\sum_{j=1}^n S_j(\omega) \sin(\omega L / C_j(\omega)) \right)^2 + \left(\sum_{j=1}^n S_j(\omega) \cos(\omega L / C_j(\omega)) \right)^2}{\left(\sum_{j=1}^n S_j(\omega) \right)^2}. \quad (12)$$

Consider the limiting case when the distance between the points for which the characteristics of the wave field are determined is small ("short distance" approximation). We assume that the condition $\omega L \ll C_j(\omega)$ is satisfied for all components with a frequency ω . In this case

$$\sin(\varphi_j(\omega, L)) = \varphi_j(\omega, L), \quad \cos(\varphi_j(\omega, L)) = 1 \quad (13)$$

We introduce the dimensionless parameter

$$\gamma_j = S_j(\omega) / \sum_{j=1}^n S_j(\omega). \quad (14)$$

Given (13), we obtain the equation

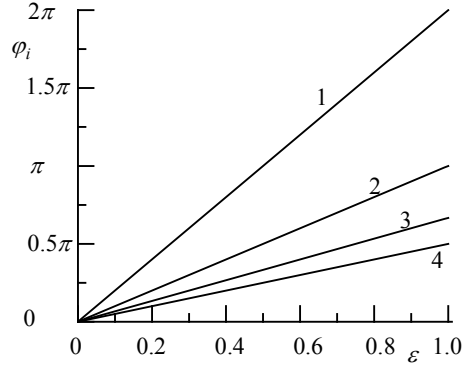
$$\varphi(\omega, L) = \operatorname{arctg} \left(\sum_{j=1}^n \gamma_j \varphi_j(\omega, L) \right). \quad (15)$$

Thus, the phase shift in a multicomponent field in the short distance approximation is equal to the average phase shift of individual components with a weight proportional to their spectral density. In this approximation, the value of the quadratic function of coherence is close to one.

For numerical analysis, we simulate the following situation. Let there be a free wave at the frequency ω obeying the dispersion equation for gravitational waves in deep water

$$\omega^2 = g \frac{2\pi}{\lambda}, \quad (16)$$

Fig. 1 Dependences on the dimensionless distance ε of phase shifts φ_i of the components of the wave field



where g is the gravitational acceleration; λ is the free wave length. Let's denote the free wave as the first component of the wave field. Also at this frequency ω there are three harmonics of lower frequency waves.

From dispersion Eq. (16) it follows that the phase velocity of the free wave $C_1 = g/\omega$, respectively, for it the phase shift at a distance L is equal $\varphi_1 = 2\pi L/\lambda$. For such a wave field, it is advisable to introduce a dimensionless distance $\varepsilon = L/\lambda$, where λ is the length of the wave component (Efimov et al. 1972). Assume that the phase velocities of the harmonics $C_2 = 2C_1$, $C_3 = 3C_1$, and $C_4 = 4C_1$, and the parameter γ_j has the following values $\gamma_1 = 0.65$, $\gamma_2 = 0.2$, $\gamma_3 = 0.1$, and $\gamma_4 = 0.05$. As the distance ε changes, the phase shift φ_i of each component changes, as shown in Fig. 1, occur linearly.

Despite the fact that all the dependences $\varphi_i = \varphi_i(\varepsilon)$ are linear, the phase shift calculated for a field including several components varies nonlinearly with distance. Moreover, the values of the quadratic coherence function rapidly decrease. Such a nature leads to the fact that the phase velocity is not a constant, but depends on the distance ε (Fig. 2). When creating Fig. 2 for clarity, the values of the phase velocities were normalized to the phase velocity of the free wave (the first component) $\tilde{C} = C/C_1$.

4 Effect of Directional Distribution

Consider another limiting case where all the components of the wave field obey the same dispersion equation, but their directional spreading function is not a Delta function. In this statement of the problem, the wave field is linear (Longuet-Higgins 1956). Then the cross-spectrum (Pokazeev and Zapevalov 2019)

$$\chi(\omega, \varepsilon, \alpha) = \int_0^{2\pi} \Psi(\omega, \alpha) \exp(i2\pi \varepsilon \cos \alpha) d\alpha. \tag{17}$$

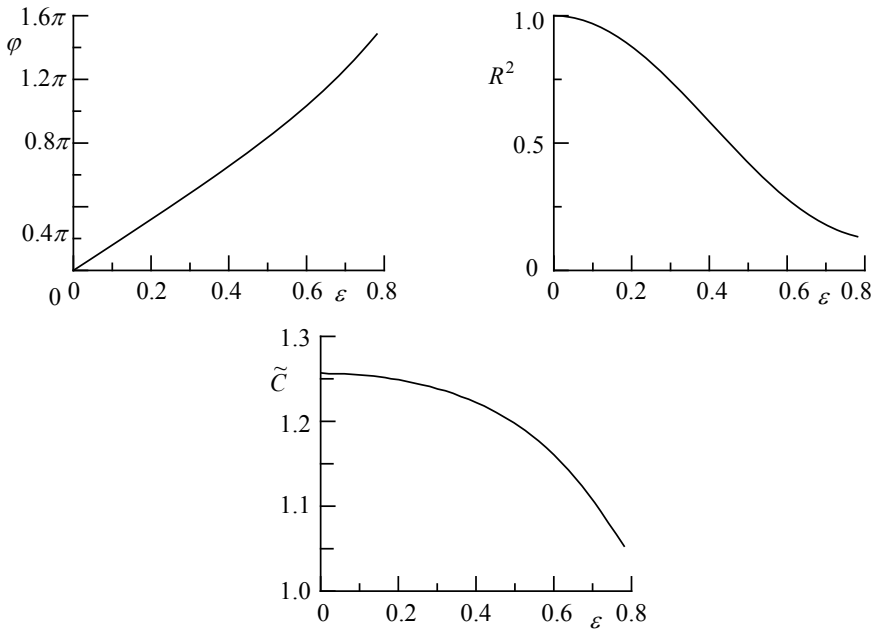


Fig. 2 Dependences of the spatial-temporal characteristics φ , R^2 and \tilde{C} of the wave field on the dimensionless distance ε

Using (3), we obtain

$$\varphi(\omega, \varepsilon, \alpha) = \operatorname{arctg} \left(\frac{\int_0^{2\pi} \Theta(\omega, \alpha) \sin(2\pi \varepsilon \cos \alpha) d\alpha}{\int_0^{2\pi} \Theta(\omega, \alpha) \cos(2\pi \varepsilon \cos \alpha) d\alpha} \right), \quad (18)$$

$$R^2(\omega, \varepsilon, \alpha) = \left(\int_0^{2\pi} \Theta(\omega, \alpha) \sin(2\pi \varepsilon \sin \alpha) d\alpha \right)^2 + \left(\int_0^{2\pi} \Theta(\omega, \alpha) \cos(2\pi \varepsilon \cos \alpha) d\alpha \right)^2. \quad (19)$$

Deviations of phase shifts and phase velocities in this case arise due to the fact that there are components of the wave field propagating at an angle to the main direction. The projections of their phase velocities to the main direction exceed the phase velocity of the waves in the main direction. Equations (18) and (19) are similar to Eqs. (8) and (9). The only difference is that the weight of the individual components is determined not by the level of their spectrum, but by the directional spreading function. The conclusions made in the previous section remain true here.

Obviously, the wider the angular distribution, the stronger the phase velocity values differ from the theoretical value obtained from the dispersion equation. The directional spreading function depends on the frequency (Babanin and Soloviev 1998). It is narrow near the frequency of dominant waves and expands when the frequency changes towards low and high values. The directional spreading function also depends on the stage of development of the wind wave field (Donelan et al. 1985). With a fully developed field of wind waves, it is narrower than with a developing one.

The numerical analysis carried out on the basis of Eq. (18) showed that the deviations of the phase velocity calculated by the cross-spectrum from the phase velocity obtained by the dispersion equation can reach 5–15%, if the field of wind waves is fully developed. In other situations, the deviations will be noticeably greater.

5 Conclusion

The effect of wind on the sea surface creates a complex nonlinear wave field. In this field, there are simultaneously components that obey different dispersion equations and propagating at different phase speeds in different directions. The paper analyzes the formation of the phase spectrum in a multicomponent field. It is shown that the effect created by the angular distribution of wave energy is similar to the effect caused by the presence at the same frequency of components propagating at different velocity.

The presence at the same frequency of waves propagating at different velocity leads to a nonlinear dependence of the phase spectrum on the distance between the points for which it is determined. As a consequence, the phase velocity values calculated from the phase shift vary depending on the distance between the points for which the phase shift is determined. The value of the phase velocity calculated for a multicomponent wave field exceeds its theoretical value, which is obtained from the dispersion equation for gravitational waves.

In a linear wave field where all components propagate at the same velocity, the excess of the calculated phase velocity over the theoretical value depends on the width of the angular distribution of the wave energy. The wider the angular distribution, the greater the excess. The minimum excess is observed at the dominant wave frequency for a fully developed wave field. It is 5–10%.

A quantitative analysis of the effect of bound components is complicated by the lack of data on their level in a real sea wave field.

This work was carried out as part of a state assignment on the topic No. 0827-2018-0003 “Fundamental studies of oceanological processes that determine the state and evolution of the marine environment under the influence of natural and anthropogenic factors, based on based methods of observation and modeling”.

References

- Babanin AV, Soloviev YP (1998) Variability of directional spectra of wind-generated waves, studied by means of wave staff arrays. *Mar Freshw Res* 49(2):89–101
- Donelan MA, Hamilton J, Hui WH (1985) Directional spectra of wind-generated waves. *Philos Trans Roy Soc A315*:509–562
- Efimov VV, Soloviev YP, Khristoforov GN (1972) Experimental determination of the phase velocity of the propagation of the spectral components of sea wind waves. *Izvestiya Academy of Sciences of the USSR. Atmos Oceanic Phys* 8(4):435–446
- European Space Agency (ESA) (2012) Sentinel-2: ESA's optical high-resolution mission for GMES operational services, Rep. ESA SP-1322/2, Eur. Space Agency, Noordwijk, Netherlands
- Jenkins G, Watts D (1968) Spectral analysis and its applications, vol 2.: Holden-Day, San Francisco
- Kudryavtsev V, Yurovskaya M, Chapron B, Collard F, Donlon C (2017a) Sun glitter imagery of ocean surface waves. Part 1: directional spectrum retrieval and validation. *J Geophys Res Oceans* 122(2):1369–1383
- Kudryavtsev V, Yurovskaya M, Chapron B, Collard F, Donlon C (2017b) Sun glitter imagery of surface waves. Part 2: waves transformation on ocean currents. *J Geophys Res: Oceans* 122(2):1384–1399
- Longuet-Higgins MS (1956) Statistical properties of a moving wave-form. *Math Proc Cambridge Philos Soc* 52(2):234–245
- Pokazeev KV, Zapevalov AS (2019) Calculation of phase velocities in the field of sea surface waves. *Mosc Univ Phys Bull* 74(4):413–418
- Suetin VS, Tolkachenko GA, Korolev SN, Kucheryavy AA (2013) Optical properties of aerosols and atmospheric correction of satellite observations of the Black sea. *Phys Oceanogr* 26(3):34–44
- Wang DW, Hwang PA (2004) The dispersion relation of short wind waves from space–time wave measurements. *J Atmos Oceanic Technol* 21(12):1936–1945
- Yuen HC, Lake BM (1982) Nonlinear dynamics of deep-water waves. *Adv Appl Mechan* 22
- Yurovskaya MV, Kudryavtsev VN (2019) Metodika otsenki skorosti poverkhnostnogo techeniya po mnogokanal'nym opticheskim izobrazheniyam so sputnika Sentinel-2. Kompleksnyye issledovaniya Mirovogo okeana. Materialy IV Vserossiyskoy nauchnoy konferentsii molodykh uchenykh. Sevastopol': MGI RAS 195. (in Russian)
- Zapevalov AS (1996) On the estimation of the angular energy distribution function of dominant sea waves. *Izvestiya—Atmos Ocean Physics* 31(6):802–808
- Zapevalov AS, Bol'shakov AN, Smolov VE (2009) Studying the sea surface slopes using an array of wave gauge sensors. *Oceanology* 49(1):31–38

Modeling the Dispersion Distribution of Sea Surface Slopes Over the Ranges of Waves Creating Them



A. S. Knyazkov  and A. S. Zapevalov 

Abstract Based on mathematical modeling the analysis of dispersion distribution of sea surface slopes on ranges of waves creating them is carried out. The functions $\chi(k)$ describing the proportion of slope dispersion of a given range from the total variance of slopes created by waves of all scales in different meteorological situations are constructed. The situations when the wave field is developing and fully developed are considered. It is shown that at the stage of developing waves the contribution of short waves to the dispersion of slopes is greater in comparison with fully developed waves. With a weak wind, the form of the function $\chi(k)$ changes greatly when the wind speed changes, with a strong wind, it acquires a universal form. The limitations of currently existing spectral models for their use in the analysis of Earth remote sensing data from space are discussed. First of all, the limitations are associated with a variety of factors that determine the thin topographic structure of the sea surface, which are difficult to take into account in mathematical modeling.

Keywords Sea surface structure · Slope dispersion · Spectral model · Wave age

1 Introduction

The interaction of radio waves with the sea surface is described in the framework of a two-scale model (Kur'yanov 1963). The boundary separating the two types of roughness depends on the length of the sensing radio wave (Danilychev et al. 2009; Zapevalov 2009). The existence of several mechanisms of radio waves scattering on a rough surface makes the problem of estimating the variance of sea surface slopes in different wave ranges relevant (Hollinger 1971).

When analyzing the formation of the field of radio waves reflected from the ocean-atmosphere boundary, one of the central problems is the lack of sufficient

A. S. Knyazkov · A. S. Zapevalov (✉)
Marine Hydrophysical Institute RAS, Sevastopol, Russian Federation
e-mail: sevzepter@mail.ru

A. S. Zapevalov
Sevastopol State University, Sevastopol, Russian Federation

data on the actual variability of sea surface slopes. The current situation is primarily explained by the technical complexity of measurements in open sea of spectral and integral characteristics of waves of gravity-capillary range (Hwang 1997; Zapevalov 2002; Zapevalov et al. 2009). Remote sensing results cannot fully replace direct measurements, since the slope variance values obtained with their help are indirect estimates (Zappa et al. 2008; Hauser et al. 2008).

In this work, to calculate the variance of the slopes of the sea surface in different wave ranges, we use mathematical models of the spectrum of elevations of the sea surface given in the ranges of gravity-capillary and gravity waves (Apel 1994; Elfouhaily et al. 1997; Kudryavtsev et al. 1999; Cheng et al. 2006). When constructing mathematical models, the lack of information about processes on the sea surface was compensated by laboratory data (Jähne and Riemer 1990; Klinke and Jähne 1992).

2 Initial Data for the Construction of Spectral Models

The elevation spectra of sea surface waves $\Psi(k)$ are fast-falling functions of the wave number k . In their graphical representation, it is convenient to build not the spectrum itself, but the spectral function $Cr(k) = k^4\Psi(k)$ corresponding to the spectrum of the second spatial derivative of the surface elevation. The first spatial derivative of the elevation of the sea surface is its local slope, the second derivative is the curvature. The spectral function $Cr(k)$ is called the curvature spectrum of the sea surface.

In (Donelan and Pierson 1987) it was made a priori assumption that the curvature spectrum must have a secondary peak, which is located in the vicinity of the wave number

$$k_{Cmin} = 2\pi / \lambda_{Cmin}, \quad (1)$$

where λ_{Cmin} is the length of the wave having the minimum phase velocity. In the gravity-capillary range, the wave frequency ω and the wavenumber k satisfy the dispersion equation

$$\omega^2 = gk + \gamma k^3, \quad (2)$$

where g is the gravitational acceleration; γ is the coefficient of surface tension. From the dispersion Eq. (2) it follows that $\lambda_{Cmin} = 0.017$ m, respectively $k_{Cmin} = 370$ rad/m.

To study the spectral properties of wind waves in the gravity-capillary and capillary ranges, a series of experiments was carried out in three wind-wave trays with different characteristics (Jähne and Riemer 1990; Klinke and Jähne 1992). In two trays, the maximum the fetch were 29 and 100 m, in the third circular tray, the fetch can be considered unlimited. The data of laboratory experiments were summarized in (Apel 1994). It was pointed out that the curvature spectra have the main following features:

- There is a secondary peak at $k_{p2} \approx 750$ rad/m;
- secondary peak grows rapidly at low wind speeds, at high approaching saturation state. Saturation occurs at wind speeds above 6–8 m/s;
- at high wave numbers $k_{dis} \approx 6283$ rad/m there is a cut due to viscous dissipation.

3 Surface Wave Spectra Models

The physical mechanisms of wave generation in the gravity and gravity-capillary ranges are different, so the model of the sea surface elevation spectrum (as well as the models of slope spectrum and curvature spectrum) represents the sum of two components $\Psi(k) = \Psi_1(k) + \Psi_2(k)$. The first component $\Psi_1(k)$ describes the spectrum of gravity waves. The known spectral models corresponding to fully developed wind waves, waves with limited fetch and developing waves are used (Pierson and Moscowitz 1964; Hasselmann et al. 1973; Donelan et al. 1985).

The second component $\Psi_2(k)$ describes the spectra of gravity-capillary and capillary waves. Different models take into account different combinations of the following main factors affecting the shape of the spectrum: energy inflow from the wind, dissipation due to molecular viscosity, dissipation due to eddy viscosity, wave breaking, generation of parasitic capillary waves, as well as wave-wave resonance interactions (Elfouhaily et al. 1997; Cheng et al. 2006).

3.1 Model of Fully Developed Wind Waves

For further analysis, we will use two models. The first model, which is here designated by the name of its first author as $\Psi_L(k)$, corresponds to a fully developed wind waves (Liu et al. 2000). For the gravity waves the model is built on the basis of Phillips spectrum in the saturation interval

$$\Psi_{L1}(k) = a_p k^{-4} \frac{1}{\left(1 + (k/k_0)^2\right)}, \quad (3)$$

where $a_p = 0.0046$; $\left(1 + (k/k_0)^2\right)^{-1}$ is low-pass filter. The parameter k_0 sets the upper limit of the wave number range for the spectrum of gravity waves. In (Liu et al. 2000) it is assumed $k_0 = 6\pi$ rad/m that corresponds to the wavelength $\lambda = 0.33$ m. Note that this value is much smaller than that obtained in (Apel 1994), where a low-pass filter was introduced, there $k_0 = 6\pi$ rad/m ($\lambda = 0.063$ m). The lower limit of the spectrum, according to (Pierson and Moscowitz 1964) is given by the expression $k_{Lp} = g / (1.2 U)^2$.

The second component of the model describes the spectrum in the range of wind induced gravity-capillary waves

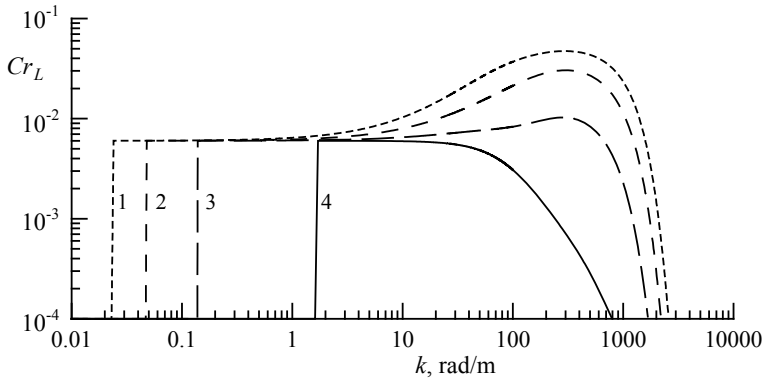


Fig. 1 The unidirectional curvature spectrum $Cr_L(k)$. Curves 1–4 correspond to wind velocity from 2 m/s to 17 m/s in increments of 5 m/s

$$\Psi_{L2}(k) = a_{L1} k^{-4} \left(\frac{u_* - u_{0*}}{C} \right)^2 \left[1 - \exp\left(-\frac{C^2}{a_{L2} W_{10}^2} \right) \right] \exp[-a_{L3} k^{2.5} (u_* - u_{0*})^{-0.75}], \quad (4)$$

where $a_{L1} = 1/320$, $a_{L2} = 0.0002$ и $a_{L3} = 0.0011$ $(\text{cm/rad})^{2.5} (\text{cm/s})^{0.75}$ are constants; u_* is the wind friction velocity, $u_{0*} = 5$ cm/s is the threshold wind friction velocity; C is the wave phase speed. The friction velocity is calculated as a function of the velocity U at a height of 10 m under the assumption of neutral stratification

$$u_* = \sqrt{c_d} U, \quad (5)$$

where c_d is the drag coefficient

$$c_d = 10^{-3} (2.717 U^{-1} + 0.142 + 0.0761 U). \quad (6)$$

Unidirectional curvature spectra calculated by the fully developed wind waves model $\Psi_L(k)$ are presented in Fig. 1.

3.2 Model of Developing Wind Waves

Модель $\Psi_E(k)$, которая учитывает стадии развития волнового поля, была построена в работе (Elfouhaily et al. 1997). As a parameter that determines the stage of development of the wave field, the ratio $\tau = U/C_p$ was used (Donelan et al. 1985). Hereinafter the index “ p ” means that this parameter is defined on the scale of dominant waves. In the range of gravity waves the spectrum has the form

$$\Psi_{E1}(k) = \frac{1}{2} \alpha_{E1} \frac{C_p}{C} k^{-3} \exp\left\{-\frac{5}{4} \left(\frac{k_p}{k}\right)^2\right\} \exp\left\{-\frac{\tau}{\sqrt{10}} \left[\sqrt{\frac{k}{k_p}} - 1\right]\right\} J(k), \quad (7)$$

where $\alpha_{E1} = 0.006 \tau^{0.55}$; $k_{Ep} = (g/U^2) \tau^2$; $J(k)$ is a function describing the spectrum changes in the peak region at different stages of development (Hasselmann et al. 1973).

In the gravity-capillary range, the model is described by the equation

$$\Psi_{E2} = \frac{1}{2} \alpha_{E2} \frac{C_{\min}}{C} \exp\left\{-\frac{1}{4} \left[\frac{k}{k_{C\min}} - 1\right]^2\right\}, \quad (8)$$

where $\alpha_{E2} = 0.014 u_* / C_{\min}$; $C_{\min} = 0.23$ m/s is the minimum phase velocity, which is achieved when the value of the wave number is equal to $k_{C\min}$.

Unidirectional curvature spectra $Cr_E(k)$ calculated by model $\Psi_E(k)$ are presented in Fig. 2. The value $\tau = 0.83$ corresponds to fully developed excitement, the value $\tau = 1.5$ corresponds to developing excitement.

Comparing the spectra of curvature of a fully developed wave calculated from two models, noticeable differences can be noted.

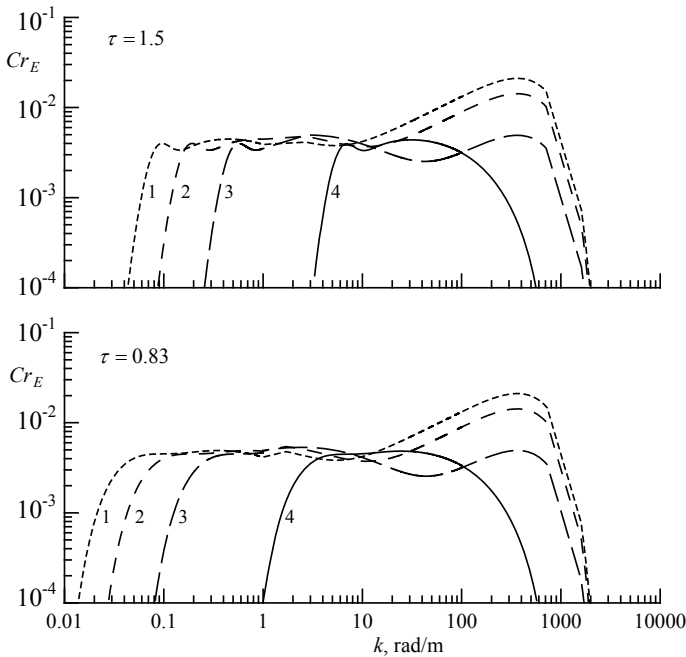


Fig. 2 The unidirectional curvature spectrum $Cr_E(k)$. Curves 1-4 correspond to wind velocity from 2 m/s to 17 m/s in increments of 5 m/s

4 Variance of Sea Surface Slopes

Dispersions of slope components oriented up σ_u^2 and across σ_c^2 the wind direction can be calculated using a spectrum of wave numbers and directions $\Phi(k, \alpha)$ (Liu et al. 2000)

$$\sigma_u^2(k) = \int_{k_1}^k k dk \int_{-\pi}^{\pi} \Phi(k, \alpha) k^2 \cos^2 \alpha d\alpha, \quad (9)$$

$$\sigma_c^2(k) = \int_{k_1}^k k dk \int_{-\pi}^{\pi} \Phi(k, \alpha) k^2 \sin^2 \alpha d\alpha, \quad (10)$$

where k_1 is the lower bound of the spectrum $\Psi(k)$; α is the azimuthal angle.

We represent the spectrum $\Phi(k, \alpha)$ in the form

$$\Phi(k, \alpha) = \Psi(k) \Theta(k, \alpha). \quad (11)$$

where $\Theta(k, \alpha)$ is the directional spreading function that satisfies the normalization condition

$$\int_{-\pi}^{\pi} \Theta(k, \alpha) dk = 1. \quad (12)$$

It follows from Eqs. (9) and (10) that the slope dispersion $\sigma^2(k) = \sigma_u^2(k) + \sigma_c^2(k)$ is described by the equation

$$\sigma^2(k) = \int_{k_1}^k k^3 \Psi(k) dk. \quad (13)$$

In (Danilychev et al. 2009; Hollinger 1971), a parameter χ was used that showed how much of the total variance of slopes $\sigma^2(k = \infty)$ is created by waves of a given range $\sigma^2(k)$. In the spectrum of sea waves, the minimum wavelength is limited by dissipation processes, i.e. $\sigma^2(k = \infty)$ can be written as $\sigma^2(k = k_{dis})$. In the notation adopted here we obtain the equations for χ

$$\chi(k) = \int_{k_1}^k k^3 \Psi(k) dk / \int_{k_1}^{k_{dis}} k^3 \Psi(k) dk. \quad (14)$$

Let us analyze the parameter χ changes within the framework of the models $\Psi_E(k)$ considered here, which describes both the developing and fully developed field of wind waves. The calculation results are comparable with the semi-empirical function obtained according to the radiometry of the sea surface (Hollinger 1971; Wilheit 1979)

$$\chi_R(f) = \begin{cases} 0.3 + 0.02f \text{ npu} & f \leq 35 \\ 1 & \text{npu } f \leq 35 \end{cases} \quad (15)$$

where f is the frequency of the radio wave, GHz. This function was obtained by minimizing discrepancies between theoretical calculations and radiometric measurements. Length Λ of the sensing radio wave is related to the frequency f by the equation $\Lambda = C/f$, where C is the speed of light. We also take into account that the contribution to specular reflection is given by surface waves satisfying the condition (shorter waves create diffuse scattering). The concept of much more in this condition is not strictly defined. Take what $\lambda = n\Lambda$, where $n = 3$ or $n = 5$.

The results of calculations $\chi_E(k)$ on the model $\Psi_E(k)$ are presented in Fig. 3.

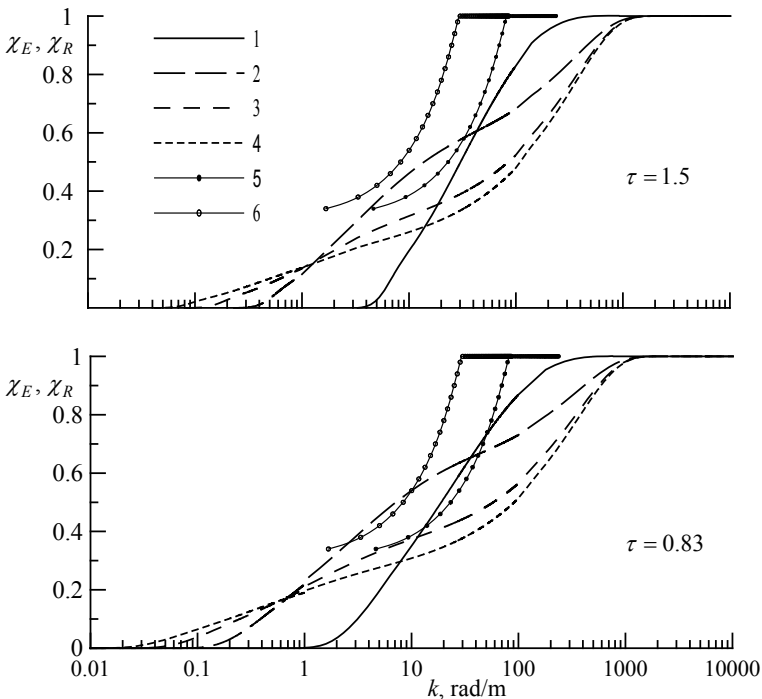


Fig. 3 Dependence of the proportion of dispersion of sea surface slopes $\chi_E(k)$ and $\chi_R(k)$ on the scale of the waves creating them. Curves 1–4 correspond $\chi_E(k)$ to wind velocity from 2 m/s to 17 m/s in increments of 5 m/s. Curves 5 and 6 correspond $\chi_R(k)$ at $n = 3$ and $n = 5$

There are also functions $\chi_R(k)$.

5 Discussion and Conclusion

Currently, a large number of mathematical models of the sea surface elevation spectrum have been constructed, however, their possibilities for use in applications related to the analysis of remote sensing data are extremely limited. This is largely due to the fact that any spectral model is built for certain conditions and within certain assumptions that can not always be controlled. The determination of such important parameters as wind speed is carried out not on the basis of models, but with the help of regression dependences constructed from quasi-synchronous measurements from meteorological buoys and remote sensing from spacecraft.

The complexity of constructing models lies in the fact that the formation of the wave field is influenced by a large number of factors different in their physical nature. Moreover, the role of these factors is different in different meteorological conditions. At the same time, spectral models allow us to better understand the physics of wave generation processes.

The obtained dependences $\chi_E = \chi_E(k)$ correspond to the position that short waves make the main contribution to the dispersion of slopes. From the analysis it follows that the dependence $\chi_E = \chi_E(k)$ varies greatly with light winds, with a strong wind it takes on a universal form. This statement is true for both developing and fully developed excitement.

A comparison of the semiempirical function $\chi_R(k)$ and the dependence $\chi_E = \chi_E(k)$ shows that they are quite close to each other.

This work was carried out as part of a state assignment on the topic No. 0827-2018-0003 “Fundamental studies of oceanological processes that determine the state and evolution of the marine environment under the influence of natural and anthropogenic factors, based on observation and modeling methods”.

References

- Apel JR (1994) An improved model of the ocean surface wave vector spectrum and its effects on radar backscatter. *J Geophys Res* 99(C8):16269–16291
- Cheng Y, Liu Y, Xu Q (2006) A new wind-wave spectrum model for deep water. *Ind J Mar Sci* 35(3):181–194
- Danilychev MV, Nikolaev AN, Kutuza BG (2009) Application of the kirchhoff method for practical calculations in microwave radiometry of wavy sea surface. *J Commun Technol Electron* 54(8):869–878
- Donelan MA, Pierson WJP (1987) Radar scattering and equilibrium ranges in wind-generated waves with application to scatterometry. *J Geophys Res* 92:4971–5029
- Donelan MA, Hamilton J, Hui WH (1985) Directional spectral of wind-generated waves. *Phil Trans R Soc A* 315:509–562

- Elfouhaily T, Chapron B, Katsaros K, Vandemark D (1997) A unified directional spectrum for long and short wind-driven waves. *J Geophys Res* 102:15781–15786
- Hasselmann K, Barnett TP, Bouws E, Carlson H, Cartwright DE, Enke K, Ewing JA, Gienapp H, Hasselmann DE, Kruseman P, Meerburg A, Müller P, Olbers DJ, Richter K, Walden H (1973) Measurements of wind-wave growth and swell decay during the joint north sea wave project (JONSWAP). *Dtsch Hydrogr Z Suppl A8(12)*:8–95
- Hauser D, Caudal G, Guimard S, Mouche AA (2008) A study of the slope probability density function of the ocean waves from radar observations. *J Geophys Res* 113(C02006)
- Hollinger JP (1971) Passive microwave measurements of sea surface roughness. *IEEE Trans Geosci Electr GE-9(3)*:165–169
- Hwang PA (1997) A study of the wavenumber spectra of short water waves in the ocean. Part II: spectral model and mean square slope. *J Atmos Oceanic Technol* 14:1174–1186
- Jähne B, Riemer KS (1990) Two-dimensional wave number spectra of small-scale water surface waves. *Geophys Res* 95:11531–11546
- Klinke J, Jähne B (1992) Two-dimensional wave number spectra of short wind waves. Results from wind wave facilities and extrapolation to the ocean. In: *Proceeding SPIE 1749, optics of the air-sea interface: theory and measurements, proceeding SPIE 1749, international society for optical engineering, San Diego*, pp 1–13
- Kudryavtsev VN, Makin VK, Chapron B (1999) Coupled sea surface-atmosphere model 2. Spectrum of short wind waves. *Geophys Res* 104(C4):7625–7639
- Kur'yanov BF (1963) The scattering of sound at a rough surface with two types of irregularity. *Sov Phys Acoust* 8(3):252–257
- Liu Y, Su M-Y, Yan X-H, Liu WT (2000) The mean-square slope of ocean surface waves and its effects on radar backscatter. *Atmos Oceanic Technol* 17:1092–1105
- Pierson WJ, Moskowitz L (1964) A proposed spectral form for fully developed wind seas based on the similarity theory of S. A. Kitaigorodskii. *J Geophys Res* 69:5181–5190
- Wilheit TT (1979) A model for the microwave emissivity of the ocean's surface as a function of wind speed. *IEEE Trans Geosci Electron GE-17(4)*
- Zapevalov AS (2002) Statistical characteristics of the moduli of slopes of the sea surface. *Phys Oceanogr* 12(1):24–31
- Zapevalov AS (2009) Bragg scattering of centimeter electromagnetic radiation from the sea surface: The effect of waves longer than Bragg components. *Izvestiya - Atmospheric Ocean Physics* 45(2):253–261
- Zapevalov AS, Bol'shakov AN, Smolov VE (2009) Studying the sea surface slopes using an array of wave gauge sensors. *Oceanology* 49(1):31–38
- Zappa CJ, Banner ML, Schultz H, Corrada-Emmanuel A, Wolff LB, Yalcin J (2008) Retrieval of short ocean wave slope using polarimetric imaging. *Meas Sci Technol* 19

Determination of Permeability–Porosity–Stresses Dependence for Loose Media Based on Inverse Problem Solution by Lab Test Data



Leonid Nazarov , Larisa Nazarova , Dominique Bruel ,
and Nikita Golikov 

Abstract The process, justified by theory and physical modeling, enables to establish dependence of poroperm properties of loose geomaterials versus fluid pressure and stresses. The laboratory unit designed and manufactured by researchers, comprises a measurement cell filled with a loose material, a hydraulic press, and a recorder of pressure, flow rate, and stress σ_m , stepwise applied to the cell. At each loading stage the permeability test was carried out at different input gas pressures p_n . The stationary measured flowrate data Q_{mn} and the back analysis were employed to establish the empirical permeability–effective stress dependence, followed with approximation by two-parameter exponential function. The measurement cell was vacuumized at fixed σ_m the cell was connected to a vessel, filled with air of a preset mass. Porosity φ_m was calculated based on the equilibrium pressure gained in “cell–vessel” system. The experiments performed with the medium-grained sand revealed that the exponent factor characterizing the relationship between permeability and effective stress is something like 0.02 bar^{-1} ; the permeability–porosity relation can be described by a power function; thereto, Kozeny–Carman equation is fulfilled with good precision as well.

Keywords Loose media · Laboratory experiment · Porosity · Permeability · Stress · Seepage · Gas · Pressure · Inverse problem

L. Nazarov (✉) · L. Nazarova
Chinakal Institute of Mining, Siberian Branch, Russian Academy of Sciences, 54 Krasny
Prospect, Novosibirsk 630091, Russia
e-mail: [mining1957@mail.ru](mailto: mining1957@mail.ru)

D. Bruel
Centre de Geosciences, MINES PariTech, 60 Boulevard Saint Michel, 75271 Paris Cedex 6,
France

N. Golikov
Trofimuk Institute of Petroleum Geology and Geophysics, Siberian Branch, Russian Academy of
Sciences, 3 Prospect Koptyuga, Novosibirsk 630090, Russia

1 Introduction

Prospecting of hydrocarbon reserves, substantiation of mining processes, well survey data interpretation, development of processes to enhance productivity of natural reservoirs and other problems dealing with oil and gas reservoir mechanics claim information on filtration-and-capacity properties of geomedia and rocks under consideration (Hsu and Robinson 2019; Ahmed 2019; Terry and Rogers 2014; Dake 2001).

Productive intervals of oil-and-gas and gas-condensate reservoirs are, as a rule, composed of weakly consolidated or loose rocks: fragmental rocks, loose sandstones (Ebinuma et al. 2005; Ryzhov 2011), which mechanical properties depend on fractional composition, porosity, packing, stresses and reservoir pressure (governing the host rock consolidation degree) along with other geological, hydrodynamic, and geomechanical factors (Istomin and Yakushev 1992; Gurova et al. 1988; Ryzhov et al. 2010; Ranaivomanana et al. 2017).

There is abundant evidence on the dependence of filtration characteristics versus stress in reservoir rocks and coals (Roi et al. 2018; Holt 1990; Nazarova and Nazarov 2016; Zhang et al. 2012), but the information on loose geomedia is scarce yet (Patino et al. 2019; Chapuis et al. 1989). Most theoretical and experimental studies focus on establishing the dependence of porosity and permeability versus granulometric composition, particle packing, and moisture (Vukovic and Soro 1992; Sezer et al. 2009; Chapuis 2004; Alyamani and Sen 1993; Sathananthan and Indraratna 2006). However, a variation in permeability near a borehole as a result of stress redistribution and formation of irreversible deformation zones appreciably influences electrohydrodynamic field parameters (Yeltsov et al. 2012; Yeltsov et al. 2014; Nazarova et al. 2013), and as a consequence, the reservoir productivity characteristics, obtained based on well logging data.

In the present paper the researchers proposed the method to establish empirical porosity–permeability–stresses dependence for granular geomedia by laboratory test data.

2 Laboratory Unit and Filtration Tests

The experimental hermetic measurement cell of parallelepiped shape is made of polyurethane (length $l = 0.09$ m, cross-section area $S = 0.0009$ m², volume $W = 81$ ml), aluminum flanged fittings at end faces are provided for connection to a compressor and a measurement instrument (Fig. 1).

Cell **5** is densely charged with pure-washed medium sand (0.18–0.25 mm fraction, $D = 0.2$ mm in average, dry density being 1550 kg/m³) and placed between plates **3** of hydraulic press **2** (maximum force being 3500 N) in pan **4**, designed to protect the cell shape under loading (Fig. 2). Vertical compression was applied under stepwise-growing stress, which magnitude σ_m was controlled in terms of pressure in hydraulic cylinder. At each loading stage m the permeability tests were carried out, viz, the

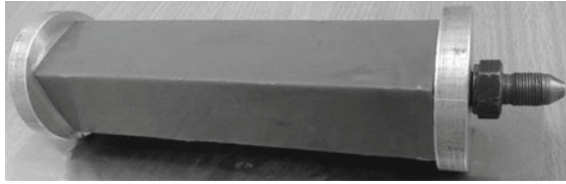


Fig. 1 Measurement cell

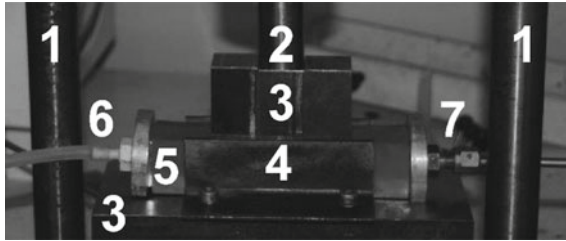


Fig. 2 Laboratory unit: 1 and 2—racks and stock of a hydraulic press; 3—plate; 4—pan; 5—measurement cell; 6 and 7—flowrate meter and compressor main lines

Table 1 Experimental data on flow rate Q_{mn} , ml/min

p_n , bar	σ_m , bar			
	0	10	20	30
1.10	78	61	49	39
1.20	163	131	103	81
1.30	257	205	161	130
1.40	356	284	226	179
1.45	408	330	261	208
1.50	468	371	293	235

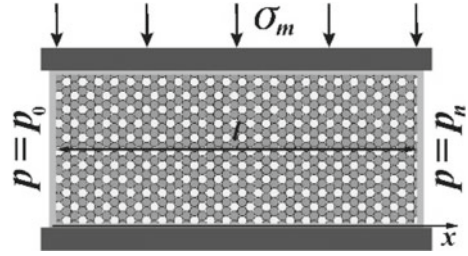
constant air pressure p_n was generated at the right end face, while the flow rate Q_{mn} was recorded at the left face in a stationary mode. The experimental results are listed in Table 1.

2.1 Experimental Model and Interpretation of Filtration Test Data

Parametrical Analysis of the Experimental Model

The mass-transfer in the measurement cell is described by the system including:

Fig. 3 Experimental design, computational domain, and boundary conditions



Continuity equation

$$\frac{\partial(\varphi\rho)}{\partial t} + \text{div}(\rho\vec{V}) = 0; \quad (1)$$

Darcy law

$$\vec{V} = -\frac{k}{\eta} \text{grad } p \quad (2)$$

and ideal gas law

$$p = \rho RT, \quad (3)$$

where φ —porosity, ρ and η —density and viscosity of gas, p —pressure, R —gas constant, T —temperature. One-dimensional fluid motion is realized in the experiment, so seepage velocity \vec{V} has a single component along axis x (Fig. 3). Permeability k depends on effective stress $s = \sigma_m - p$ (Zoback and Nur 1975)

$$k = k_0 \exp(-\alpha s), \quad (4)$$

where k_0 and α are empirical constants.

At stationary seepage mode system (1)–(4) is reduced to one equation in pressure

$$\frac{\partial}{\partial x} \left(p e^{\alpha p} \frac{\partial p}{\partial x} \right) = 0. \quad (5)$$

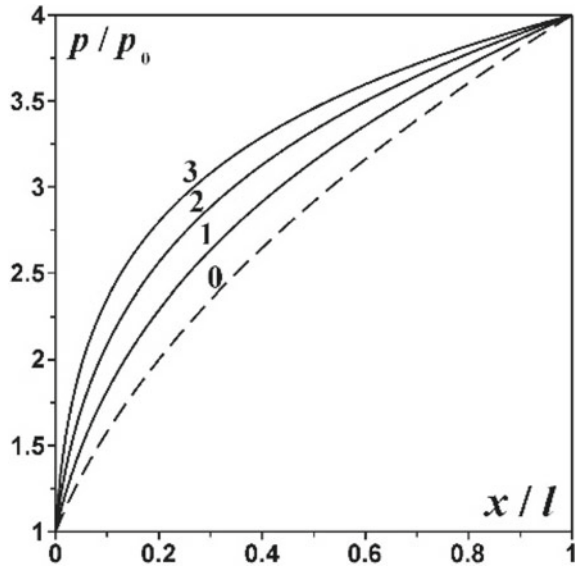
The following terms are preset at boundaries of the computational domain (Fig. 3):

$$p(0) = p_0, p(l) = p_n, \quad (6)$$

$p_0 = 1$ bar—atmospheric pressure. Solution of system (5), (6) is as follows:

$$F(p) = F(p_0) + [F(p_n) - F(p_0)]x/l, \quad (7)$$

Fig. 4 Pressure distribution in the cell at different α values



where $F(p) = (p - 1/\alpha)\exp(\alpha p)$. The known hydrostatic relation (Kochin et al. 1964; Sinaiski 2011) arises from (7) at $\alpha \rightarrow 0$:

$$p(x) = \sqrt{(p_n^2 - p_0^2)x/l + p_0^2}.$$

Figure 4 presents gas pressure distribution in the measurement cell at $p_n = 4$ bar for different α values (lines 0, 1, 2, and 3 correspond to $\alpha = 0, 0.2, 0.4$ and 0.6 bar^{-1}). As expected, the pressure and filtration rate in vicinity of the left computational domain boundary (Fig. 3) tend to grow with increasing parameter α .

Considering (2) and (4) in terms of (6), it is possible to find a flow rate at $x = 0$

$$Q = \frac{k_0 S}{\eta} \frac{F(p_n) - F(p_0)}{\alpha l p_0} e^{-\alpha \sigma_m}, \tag{8}$$

wherefrom

$$\lim_{\alpha \rightarrow 0} Q = Q_0 = \frac{k_0 S}{\eta} \frac{p_n^2 - p_0^2}{2lp_0}.$$

Figure 5 demonstrates dependence of flow rate Q on inlet pressure p_n at $\sigma_m = 2$ bar (solid lines) and $\sigma_m = 10$ bar (dashed lines) at different α values. It appeared that each α and σ_m values has corresponding p_n value, at which $Q > Q_0$.

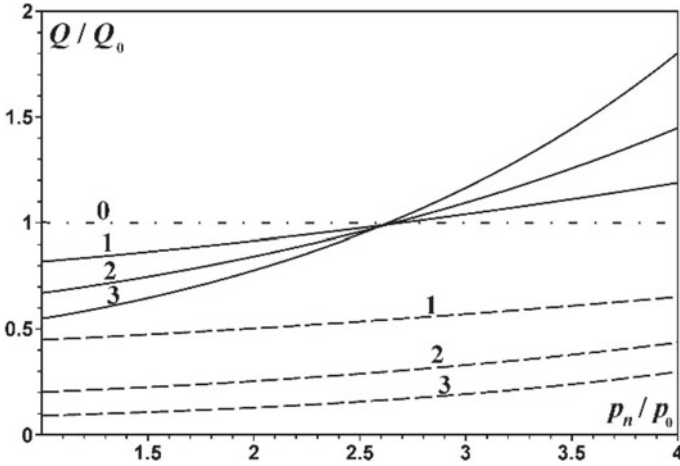


Fig. 5 Dependence $Q(p_n)$ at different α and σ_m values

Determination of Parameters of the Empirical Dependence (4)

Let formulate an inverse coefficient problem, that is to find k_0 and α by measured flow rate values Q_{mn} (Table 1). Let us introduce the cost function:

$$\Psi(k_0, \alpha) = \frac{\sqrt{20 \sum_{m=1}^4 \sum_{n=1}^5 [Q(k_0, \alpha, m, p_n) - Q_{mn}]^2}}{\sum_{m=1}^4 \sum_{n=1}^5 Q_{mn}},$$

where $Q(k_0, \alpha, m, p_n)$ is a flow rate, computed based on (8) at some argument values. Calculations were carried out at air viscosity $\eta = 18 \times 10^{-6}$ Pa · s.

Isolines of Ψ are shown in Fig. 6, where five-percent equivalence domain is toned. It is obvious, that the cost function is unimodal, its minimum, intended to provide a solution of an inverse problem, was found by the modified conjugate-gradient method (Nazarov et al. 2013; Nazarova et al. 2017). Dashed lines indicate corresponding trajectories in Fig. 6. The target parameters are estimated through intervals:

$$k_1 \leq k_0 \leq k_2, \alpha_1 \leq \alpha \leq \alpha_2,$$

where $k_1 = 0.2 D, k_2 = 0.22 D, \alpha_1 = 0.018 \text{ bar}^{-1}, \alpha_2 = 0.028 \text{ bar}^{-1}$.

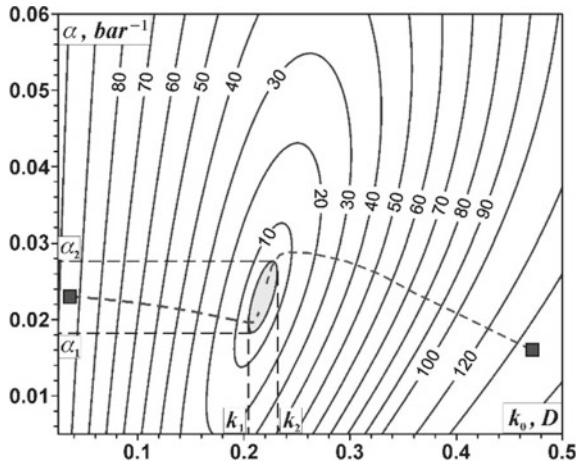


Fig. 6 Level lines of cost function Ψ , %

2.2 Evaluation of Loose Material Porosity at Different Stress Values

At every loading stage m the air was evacuated from the measurement cell **1** (Fig. 7) after the permeability tests (for various p_n) were over and vessel **2** of $V_r = 1.2$ W in volume with gas content under pressure P_r was connected to the cell. Valve **4** was opened and resultant pressure P_m in the system was recorded with high-sensitive manometer **3**. The relative variation ξ_m of cell volume was estimated by the displacement of hydraulic press stock (Fig. 2). The measurement results are cited in columns 2 and 3 (Table 2). These data can be used to evaluate porosity φ_m versus stress σ_m .

The cell pore volume $V_m = \varphi_m(1 - \xi_m)W$ then according to ideal gas law:

$$P_r V_r = [V_r + \varphi_m(1 - \xi_m)W]P_m,$$

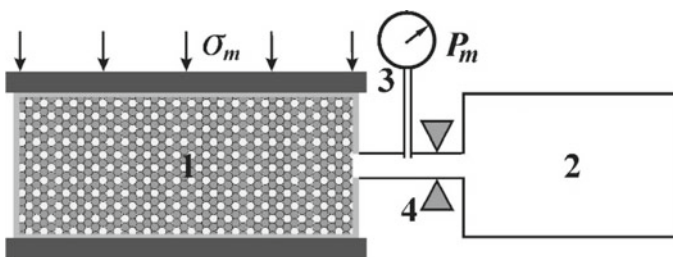


Fig. 7 The design of the experiment to determine porosity at different stress values

Table 2 Experimental data and interpretation of results

1	2	3	4	5	6	7	8	9
σ_m , bar	P_m , bar	ξ_m	φ_m	$k(\sigma_m)$, D	k , D	Δ , %	k , D	Δ , %
0	1.277	0	0.210	0.218	0.2224	2.05	0.2228	2.22
10	1.289	0.043	0.197	0.173	0.1741	0.53	0.1739	0.41
20	1.301	0.081	0.184	0.138	0.1344	2.34	0.1343	2.40
30	1.312	0.122	0.172	0.109	0.1106	1.18	0.1108	1.36

whence

$$\varphi_m = \frac{V_r(P_r/P_m - 1)}{(1 - \xi_m)W}. \quad (9)$$

The data on porosity calculation by (9) at $P_r = 1.5$ bar and are listed in column 4 (Table 2), the permeability values calculated by (4) at $k_0 = 0.5(k_1 + k_2) = 0.21D$ and $\alpha = 0.5(\alpha_1 + \alpha_2) = 0.023 \text{ bar}^{-1}$ are cited in column 5. Two functions are selected to approximate experimental data $\{k(\sigma_m), \varphi_m\}$;

$$k = A_1 D^2 \varphi^{\delta_1}; \quad (10)$$

$$k = \frac{A_2 D^2 \varphi^{\delta_2}}{(1 - \varphi)^{\delta_3}} \quad (11)$$

The least square method was used to evaluate empirical constants in (10) and (11): $A_1 = 878 \times 10^{-6}$, $\delta_1 = 3.272$, $A_2 = 289 \times 10^{-6}$, $\delta_2 = 2.832$, $\delta_3 = 1.871$. Permeability values calculated by (10) and (11), are reported in columns 6 and 8 (Table 2), respectively, while relative errors $\Delta = |1 - k/k(\sigma_m)|$ are in columns 7 and 9. It is obvious that both functions give nearly identical precision of the experimental data approximation, moreover, (11) actually coincides with the known Kozeny–Carman equation, where $\delta_2 = 3$ and $\delta_3 = 2$ (Carrier et al. 2003). Combining (4) with (10) or (11) can result in the empirical porosity–stress relationship, for example,

$$\varphi = \varphi_0 e^{-\alpha(\sigma - \sigma_0)/\delta_1},$$

where φ_0 and σ_0 are somehow reference values.

3 Conclusion

The process for quantitative evaluation of poroperm properties of loose and weakly-consolidated geomedia under variable stresses is developed and tested on a physical model. The process rests on inversion of stationary permeability tests evidence for a

loaded geomaterial specimen and enables to establish relationship between permeability and effective stress as well as to determine porosity at each loading stage by means of measuring the equilibrium pressure established in vacuumized measurement cell when a vessel containing a preset gas amount is connected to the cell. Further research is intended to analyze transient processes running in the course of the new-proposed technique implementation, in particular, evaluation of permeability in terms of the pressure variations in “measurement cell–gas vessel” system until steady state is reached.

Acknowledgements The work was partially supported by the Russian Foundation for Basic Research: Project No. 18-05-00830 and Program of Federal Scientific Investigations (Identification Number AAAA-A17-117122090002-5).

References

- Ahmed TH (2019) Reservoir engineering handbook, 5th edn. Gulf Professional Publishing, Oxford, United Kingdom
- Alyamani MS, Sen Z (1993) Determination of hydraulic conductivity from grain-size distribution curves. *Ground Water* 31:551–555
- Carrier WD, Goodbye H, Hello K-C (2003) *J Geotechn Geoenvironmental Eng* 129(11):1054–1056
- Chapuis RP (2004) Predicting the saturated hydraulic conductivity of sand and gravel using effective diameter and void ratio. *Can Geotech J* 41:787–795
- Chapuis RP, Gill DE, Baass K (1989) Laboratory permeability tests on sand: influence of the compaction method on anisotropy. *Can Geotech J* 26(4):614–622
- Dake LP (2001) *The practice of reservoir engineering*. Elsevier, Amsterdam
- Ebinuma T, Kamata Y, Minagawa H (2005) Mechanical properties of sandy sediment containing methane hydrate. In: *Proceedings of the 5th international conference on gas hydrates*, vol 2. Trondheim, pp. 907–910
- Gurova TI, Chernova LS, Potlova MM (1988) *Lithology and conditions for formation of oil and gas reservoirs of the Siberian platform*. Nedra, Moscow
- Holt RM (1990) Permeability reduction induced by a nonhydrostatic stress field. *SPE Formation Eval* 5:444–448
- Hsu CS, Robinson PR (2019) *Petroleum science and technology*. Springer, New York
- Istomin VA, Yakushev VS (1992) *Gas hydrates in natural conditions*. Nedra, Moscow
- Kochin NE, Kibel IA, Roze NV (1964) *Theoretical hydromechanics*. Wiley, Chichester
- Nazarov LA, Nazarova LA, Karchevskii AL, Panov AV (2013) Estimation of stresses and deformation properties in rock mass based on inverse problem solution using measurement data of free boundary displacement. *J Appl Ind Math* 7(2):234–240
- Nazarov LA, Nazarov LA (2016) Evolution of stresses and permeability of fractured-and-porous rock mass around a production well. *J Min Sci* 52(3):424–431
- Nazarova LA, Nazarov LA, Epov MI, Eltsov IN (2013) Evolution of geomechanical and electrohydrodynamic fields in deep well drilling in rocks. *J Min Sci* 49(5):704–714
- Nazarova LA, Nazarov LA, Shkuratnik VL, Protasov MI, Nikolenko PV (2017) An acoustic approach to the estimation of rock mass state and prediction of induced seismicity parameters: theory, laboratory experiments, and case study. In: *ISRM AfriRock—rock mechanics for Africa*. Cape Town, South Africa, pp 593–604
- Patino H, Martinez E, Gonzalez J, Soriano A (2019) Permeability of mine tailings measured in triaxial cell. *Can Geotech J* 56(4):587–599

- Ranaivomanana H, Razakamanantsoa A, Amiri O (2017) Permeability prediction of soils including degree of compaction and microstructure. *J Geomech* 17(4):1–11
- Roi R, Paredes X, Holtzman R (2018) Reactive transport under stress: permeability evolution in deformable porous media. *Earth and Planet Sci Lett* 493:198–207
- Ryzhov AY (2011) Structural features of reservoir rock voids in Botuobinskiy horizon of Chayandinskoye field. *Oil and Gas Geology* 4:49–55
- Ryzhov AY, Savchenko NV, Perunova TA, Orlov DM (2010) Influence of Chayan-dinskoye oil and gas condensate field reservoir pore space peculiarities on their filtration properties. In: *Theses of II international scientific and practical conference “world gas resources and reserves, and prospective technologies of their Development”*. Moscow, p 62
- Sathanathan I, Indraratna B (2006) Laboratory evaluation of smear zone and correlation between permeability and moisture content. *J Geotechn Geoenvironmental Eng* 132(7):942–945
- Sezer A, Goktepe AB, Altun S (2009) Estimation of the permeability of granular soils using neuro-fuzzy system. In: *Proceedings of conference on artificial intelligence applications and innovations (AIAI-2009)*. Thessaloniki, Greece, pp 333–342
- Sinaiski EG (2011) *Hydromechanics: theory and fundamentals*. Wiley, Chichester
- Terry RE, Rogers JB (2014) *Applied petroleum reservoir engineering*, 3rd edn. Prentice Hall, Upper Saddle River, USA
- Vukovic M, Soro A (1992) Determination of hydraulic conductivity of porous media from grain-size composition. *Water Res Publ*, USA
- Yeltsov IN, Nazarov LA, Nazarova LA, Nesterova GV, Epov MI (2012) Logging interpretation taking into account hydrodynamical and geomechanical processes in an invaded zone. *Dokl Earth Sci* 445(2):1021–1024
- Yeltsov IN, Nesterova GV, Sobolev AY, Epov MI, Nazarova LA, Nazarov LA (2014) Geomechanics and fluid flow effects on electric well logs: multiphysics modeling. *Russ Geol Geophys* 55(5–6):775–783
- Zhang L, Aziz N, Ren T, Nemeik J, Wang Z (2012) Permeability testing of coal under different triaxial conditions. In: *Proceedings of the 12th coal operators’ conference*, University of Wollongong and The Australasian Institute of Mining and Metallurgy, pp 277–285
- Zoback MD, Nur A (1975) Permeability and effective stress. *Bull Am Assoc Pet Geol* 59:154–158

Incompressible Viscous Steady Fluid Flows in a Plane Diffuser



S. A. Kumakshev 

Abstract The evolution of steady flows of a incompressible and viscous fluid is analyzed in a plane diffuser. For the classical formulation of the Jeffery-Hamel problem velocity profiles of flows are given. The evolution of basic single-mode flow for a fixed expansion angle into complex flows with inflow and outflow sectors (multi-mode flows) is found. The Reynolds number values corresponding to this bifurcation are calculated. It determines, in particular, that after bifurcation the single mode is impossible, while Reynolds number is growing. Also, the second bifurcation domain is explored.

Keywords Plane diffuser · Jeffery-Hamel flow

1 Statement of the Problem

Classical Jeffery-Hamel problem Jeffery (1915), Hamel (1917) for a flat diffuser flow is investigated. A fluid with dynamic viscosity ν and density ρ flows in the flat diffuser with the angle $2\beta < 2\pi$ between plane sheets. We can describe the region occupied by fluid as $r > 0$ and $|\theta| < \beta$ in the polar coordinates. At $r = 0$ flow has a singularity of a constant-power source $Q < 0$ and on the walls no-slip conditions are valid. Unfortunately, the system has two dimensionless quantities: Reynolds number $Re = Q/\nu < 0$ and angle of expansion 2β ; such values as $\{\rho, Q, \nu\}$ are dependent from each other dimensionally ($[Q] = [\nu]$). That is why we cannot make the equations of motion completely dimensionless.

S. A. Kumakshev (✉)
Ishlinsky Institute for Problems in Mechanics of the Russian Academy of Sciences,
Moscow, Russia
e-mail: kumak@ipmnet.ru

© The Author(s), under exclusive license to Springer Nature Switzerland AG 2021
T. Chaplina (ed.), *Processes in GeoMedia—Volume II*, Springer Geology,
https://doi.org/10.1007/978-3-030-53521-6_17

The velocity field is radial for a self-similar solution Jeffery (1915), Batchelor (1967)

$$v_r = -\frac{Q}{r}V(\theta), \quad v_\theta \equiv 0. \quad (1)$$

and for some function $V(\theta)$ automatically guaranteeing incompressibility condition. The components of two tensors—the stress and the strain rate—are expressed as

$$\begin{aligned} v_{rr} = -v_{\theta\theta} &= \frac{Q}{r^2}V(\theta), & v_{r\theta} &= -\frac{Q}{2r^2}V'(\theta); \\ \sigma_{rr;\theta\theta} &= -p \pm \frac{2\rho Q^2}{r^2 Re}V(\theta), & \sigma_{r\theta} &= -\frac{\rho Q^2}{r^2 Re}V'(\theta). \end{aligned} \quad (2)$$

Here the quantities (1) and (2) depends from unknown functions of the pressure p and velocity profile $V(\theta)$. The differential equation for this functions with the help of Navier-Stokes equations and expressions (2) can be derived

$$V'' + 4V - ReV^2 = C, \quad C = \text{const}; \quad (3)$$

$$p = \frac{\rho Q^2}{2r^2 Re}(C - 4V). \quad (4)$$

In this problem there are two conditions: adhesion boundary condition for the liquid and the the constant rate of outflow (integral condition):

$$V(\pm\beta) = 0, \quad \int_{-\beta}^{\beta} V(\theta)d\theta = 1. \quad (5)$$

Unknown function $V(\theta)$ so as constant $C = V''(\pm\beta)$ for some $Re < 0$ and $0 < \beta \leq \pi$ must be determined from formulas (3) and (5). Then the quantities (1), (2), (4), etc. may be calculated. Unfortunately, it is a very difficult computational problem.

Usually, in the available approaches (see Batchelor (1967), Millsaps and Pohlhausen (1953)), the nonzero velocity value on the axis of diffusor is fixed or the integral condition (5) is ignored. Thus the formulation and sense of classical Jeffery-Hamel problem are strongly distort.

An other approach is to obtain the nonlinear multidimensional boundary value problem in terms of elliptic functions by using first integral of formula (3). It leads analytically to the system of transcendental equations. Solution of this system is associated with fundamental computational difficulties.

Otherwise, with the help of special developed numerical-analytical method Akulenko et al. (2002) based on the modified Newton algorithm the nonlinear boundary value task given by formulas (3) and (5) can be efficiently solved with high accu-

racy. By introducing the normalized profile of velocity y by argument x , and two parameters g and l (which are unknown), as well as substantial known parameters a and b

$$\begin{aligned} y(x) &= 2\beta V(\theta), \quad x = \frac{1}{2} \left(\frac{\theta}{\beta} + 1 \right), \quad 0 \leq x \leq 1, \\ a &= 4\beta, \quad b = 2\beta Re, \quad \lambda = 8\beta^3 C, \quad \gamma = y'(0) \end{aligned} \quad (6)$$

original boundary-value problem is introduced as:

$$\begin{aligned} y'' + a^2 y - by^2 &= \lambda, \quad y(0) = y(1) = 0, \quad y'(0) = \gamma, \\ z' &= y - 1, \quad z(0) = z(1) = 0. \end{aligned} \quad (7)$$

Here we have the known variables a and b . The problem is to find unknown parameters γ and λ . First, we fixed the angle β in the range $0 < \beta \leq \pi/2$, i.e., a parameter a is fixed in the range $0 < a \leq 2\pi$. Then, by continuing in the Reynolds number, i.e. the parameter $b \leq 0$, we can determine γ and λ . For the initial point ($Re = 0$), a solution of problem (7) can be found in an explicit analytical form for $b = 0$. For $b = 0$, we obtain

$$\begin{aligned} y_0(x) &= \frac{a}{2D} \left[\cos(ax - \frac{a}{2}) - \cos \frac{a}{2} \right], \\ \gamma_0 &= \frac{a^2}{2D} \sin \frac{a}{2}, \quad \lambda_0 = -\frac{a^3}{2D} \cos \frac{a}{2}, \\ D &= \sin \frac{a}{2} - \frac{a}{2} \cos \frac{a}{2} \neq 0. \end{aligned} \quad (8)$$

The desired function y is obtained after the substitution of resulting parameters $\gamma(b)$ and $\lambda(b)$ and by numerically integrating Cauchy problem (7).

Now we can use solution for $b = 0$ as initial for the next Reynolds number and refine it by the special developed calculation method Akulenko et al. (2002). Thus we realize the procedure of continuation in the parameters.

2 Numerical Solution

When the angle between walls is zero we are obtain the Poiseuille flow. The presented below results is focused on analysis of flows for small angle $\beta = 10^\circ$ ($\pi/18$), because this angle can be often found in hydromechanical and engineering applications Akulenko and Kumakshev (2004). For the parameter b , depending from Reynolds number, on the interval $0 \geq b \geq -25$ the Fig. 1 shows curves $\gamma(b)$, $\lambda(b)$ obtained by above procedure using the special developed method and continuing in parameter on the basis of solution (8).

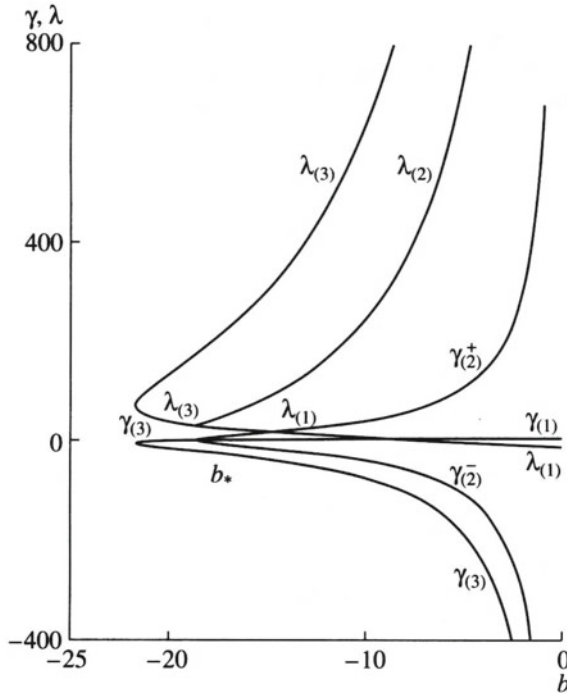


Fig. 1 Curves $\gamma(b)$, $\lambda(b)$ for $\beta = 10^\circ$ ($\pi/18$). Subscript 1 corresponding to the basic single-mode flow, subscript 2 and 3 to the double- and triple-mode flows respectively

2.1 Bifurcation of One-Mode Symmetric Flow

It is found that the single-mode flow exists only before the critical value $b_* \approx -18.8$ Akulenko and Kumakshev (2005). Here the function $\gamma = \gamma_{(1)}(b)$ is equal to zero and it means that the first derivative of fluid velocity in the vicinity of walls is zero either. With the increase of Reynolds number the inflow jets near the walls appears. So in this point the single-mode flow have a bifurcation and two double-mode and one triple-mode flows arise (see Fig. 1).

For the triple-mode flow the inflow jets near the walls are enhanced with the raise of b from bifurcation point to the turning value $b = b^* \approx -21.7$. With the increase of Reynolds number solutions of this type are disappear, because the graphs of $\gamma_{(3)}(b)$, $\lambda_{(3)}(b)$ at this value b^* have vertical tangents, as it shown on Fig. 1. The velocity profiles for the vicinity of bifurcation point is shown on Fig. 2.

As for double-mode flows it is found that they are asymmetrical. The inflow and outflow jets near walls can be replaced because both cases are equivalent. So we have two symmetric curves $\gamma_{(2)}^\pm$ (see Fig. 1).

Fig. 2 Triple-mode velocity profiles: 1 and 2 for $b = -21$ coexisting simultaneously; 3 corresponding to $b = b_*$; 4 corresponding to $b = b^*$; 5 is single-mode flow before bifurcation

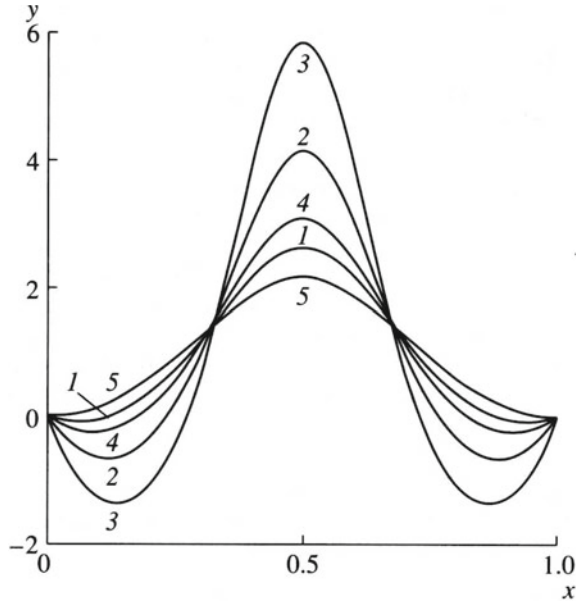
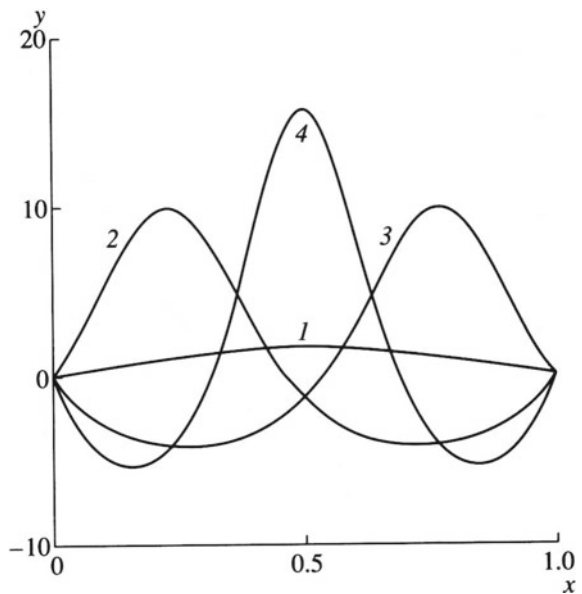


Fig. 3 Velocity profiles: 1 is single-, 2 and 3 are two double-, and 4 is triple-mode flows for $b = -10$



As we have the certain curves $\gamma(b)$, $\lambda(b)$ by substituting it for the fixed parameters a and b into the boundary value problem (7) (which is now only Cauchy problem) and by numerically integrating obtain the velocity profiles $y(x)$. The result is shown on Fig. 3.

So the full analysis of rather complicated pattern of the first bifurcation point of flows in the plane diffuser is provided.

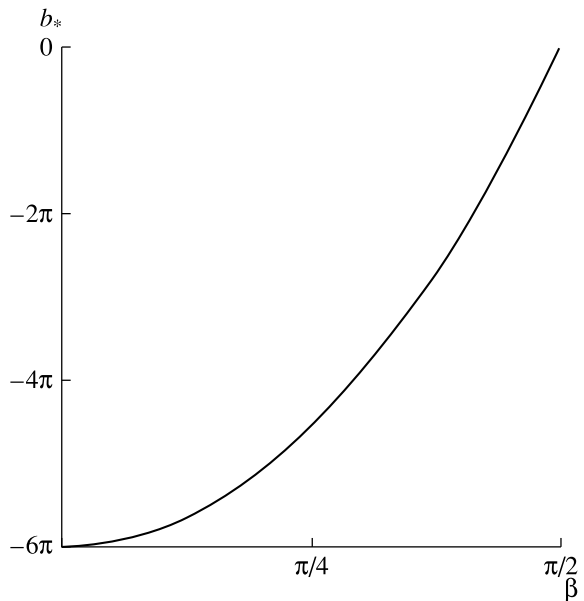
2.2 Depending of Bifurcation Point from the Diffuser Angle

We can find the function $b_*(\beta)$ for the interval for angle β from zero to $\pi/2$ that define bifurcation point dependance from diffuser angle Akulenko and Kumakshev (2004), Akulenko and Kumakshev (2005). This curve will show the boundary of the existence of the single-mode flow. By using the first integral of the first of Eqs. (7) it can be found in an implicit analytical form:

$$\begin{aligned} f(q, \xi) &= q(1 - q) [2 + \xi(1 + q)], \\ -b_* &= 6\xi L(\xi) K(\xi), \quad \beta = 2^{-1/2} K(\xi), \quad 0 \leq \xi < \infty; \\ K(\xi) &= \int_0^1 f^{-1/2}(q, \xi) dq, \quad L(\xi) = \int_0^1 f^{-1/2}(q, \xi) q dq. \end{aligned} \quad (9)$$

As we can see from Eqs. (9) for $\beta = +0$ the value b_* is equal to -6π and for $\beta = \pi/2$ equals zero. Figure 4 shows curve $b_*(\beta)$.

Fig. 4 Critical value b_* versus the half-expansion angle β of the diffuser



2.3 Second Bifurcation Point

While increasing Reynolds number from the first bifurcation point one can find the second bifurcation point as it shown on Fig. 5. For this point $b_*^{(2)} \approx -75.4$. In this domain three-, four-, and five-mode flows are possible Akulenko and Kumakshev (2004), Akulenko and Kumakshev (2008). The structure of the second bifurcation domain is qualitatively similar to the first one. But now the role of the basic flow belongs to the triple-mode flow. This flow has the different structure from the triple-flow for the first domain: it has inflow in the center of diffuser and outflows near walls.

In bifurcation point $b_*^{(2)}$ four-, and five-mode flows are arise. The mechanism of appearing one or two more inflow (outflow) jets is similar to discussed above.

Note, that for the four-mode velocity profiles the velocity value of liquid on the axis of diffuser is zero as it shown on Fig. 6. That means, that the approach for solution of this Jeffery-Hamel problem builded on proposal of nonzero liquid velocity on the center of diffuser is wrong.

Now the full analysis of the second bifurcation domain in diffuser for three-, four-, and five-mode flows is provided. The velocity profiles of these flows for $b = -60$ is presented on Fig. 6.

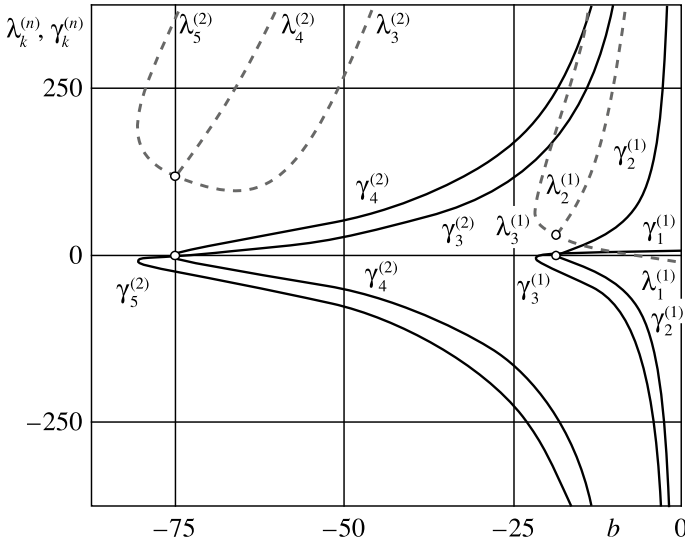
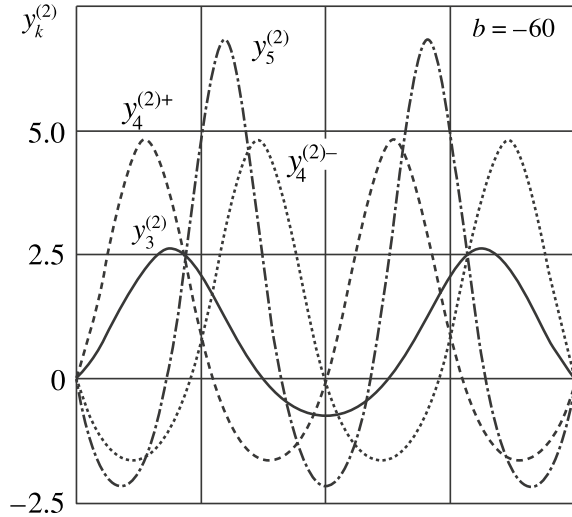


Fig. 5 The first and the second bifurcation domain

Fig. 6 Velocity profiles for the three-, four-, and five-mode flows, corresponding to the second bifurcation domain



3 Conclusion

For the first and the second bifurcation domain in diffuser the complete analysis is provided. Also, the results for the next bifurcation domains are obtained. The structure of these domains are qualitatively similar to the first and second ones. The curves $\gamma_n(b)$ and $\lambda_n(b)$ are the important result of this paper. By substituting values γ and λ into the boundary value problem (7) (which is now only Cauchy problem) and by numerically integrating we can obtain some diffuser flows features: the dependence of the velocity from the angle (1), stress and strain rate tensor components (2) as well as pressure (4). Calculation of $\gamma_n(b)$ and $\lambda_n(b)$ requires the special developed numerical-analytical method Akulenko et al. (2002) based on the modified Newton algorithm and the procedure of continuation in parameter. But after these calculations one have a full solution: the velocity profiles (and other characteristics) follows from the ordinary Cauchy problem solution.

Acknowledgements The present work was partly supported by the Government program (AAAA-A20-120011690138-6) and partially supported by RFBR (18-01-00812).

References

- Akulenko LD, Kumakshev SA (2004) Bifurcation of a flow of a viscous fluid in a plane diffuser. Doklady Phys 49(6):361–365
 Akulenko LD, Kumakshev SA (2004) Multimode bifurcation of the flow of a viscous fluid in a plane diffuser. Doklady Phys 49(12):751–755

- Akulenko LD, Kumakshev SA (2005) Bifurcation of a main steady-state viscous fluid flow in a plane divergent channel. *Fluid Dyn* 40(3):359–368
- Akulenko LD, Kumakshev SA (2008) Bifurcation of multimode flows of a viscous fluid in a plane diverging channel. *J Appl Math Mech* 72(3):296–302
- Akulenko LD, Kumakshev SA, Nesterov SV (2002) Effective numerical-analytical solution of isoperimetric variational problems of mechanics by an accelerated convergence method. *J Appl Math Mech* 66(5):693–708
- Batchelor GK (1967) *An introduction to fluid dynamics*. Cambridge University Press, Cambridge
- Hamel G (1917) Spiralformige Bewegungen zahen Flussigkeiten. *Jahresber Dtsch Math Ver* 25:34–60
- Jeffery GB (1915) The two-dimensional steady motion of a viscous fluid. *Philos Mag* 29(172):455–465
- Millsaps K, Pohlhausen K (1953) Thermal distributions in Jeffery-Hamel flows between nonparallel plane walls. *J Aeronaut Sci* 2:187–196

On Relationship Between Variations in Total Atmospheric Methane Levels and Climate Warming in the Russian Far East in Summer Months



A. V. Kholoptsev  and S. A. Podporin 

Abstract The present research focuses on rapid climate warming in the Russian Far East. The hypothesis is put forward that methane emissions from the degrading permafrost may contribute to the temperature rise in the region during the warm period of the year. The role of arctic air outbreaks in the warming process through southward transport of methane is considered. Based on the latest reanalysis data and statistical approaches, we determine correlation of interannual variations in surface air temperatures over the Far East region and the Bering Sea with the total duration of arctic air outbreaks crossing the coasts of the East-Siberian and Chukchi seas. A rather strong correlation is shown to exist in some areas of the region in question in July, August, and September. A similar correlation is established between the duration of the above mentioned outbreaks and total column methane amounts over the Far East region. A conclusion is made that atmospheric temperatures are influenced by permafrost methane emissions in August and September. The relationship is not obvious in other months.

Keywords Russian far east · Climate warming · Methane emission · Arctic air outbreak · Statistical correlation

1 Introduction

In modern era, rising levels of atmospheric greenhouse gases and subsequent climate warming are becoming a major concern for the world's population and economy (Li et al. 2018; Bush 2020a, b; Birchall 2019; Bulkeley and Tuts 2013; Hallegatte et al. 2011). However, the impact and features of the warming process vary significantly in different parts of the globe. Hence, deeper insights into the mechanisms and

A. V. Kholoptsev · S. A. Podporin (✉)
Sevastopol State University, Universitetskaya Str. 33, 299053 Sevastopol, Russia
e-mail: s.a.podporin@gmail.com

A. V. Kholoptsev
N.N. Zubov State Oceanographic Institute, Sovietskaya Str. 61, 299011 Sevastopol, Russia

consequences of regional climate changes are of key importance for physiographers, meteorologists, and climatologists.

Especially this is the case for regions exhibiting high climate warming rates, the Russian Far East (RFE) being one of them. During the last 40 years, the temperature means of summer months in some localities of the RFE have seen dramatic rise by more than 5 °C.

Since a large portion of the RFE territory lies in the permafrost zone, warming of the local climate inevitably destroys perennially frozen rocks rich in gas hydrates concentrated below the earth surface. As a result, gases (most essentially methane) escape from the permafrost into the atmosphere, which, in turn, increases fire hazards and harms fragile local ecosystems (Malkova et al. 2014).

Considering the fact that methane is a powerful greenhouse gas, we can hypothesize that increase in its total levels over the region in question due to its emission from the surface can significantly affect local temperature means of summer months.

The assumption is not straightforward as warming of the local climate is also driven by other powerful factors. One of them is the impact of blocking highs caused by arctic air outbreaks (hereinafter AAOs) into lower latitudes (Mokhov et al. 2013; Dzerdzeevskii et al. 1946).

AAOs normally manifest themselves as rapid northerly air streams formed as a result of interaction between a southern cyclone entering higher latitudes and the Arctic anticyclone. As the two vortices approach each other, the baric gradient in the cyclone's rear sector begins to rise, which in turn leads to intensification of winds along the cyclone-anticyclone boundary. Since the air transported by the AAO is cold and dry, along its entire path (which normally extends southward to the periphery of a subtropical anticyclone) the 500-hPa geopotential height tends to rise while the atmospheric temperature tends to drop. AAO-driven air streams can capture methane emitted from the underlying surface and carry it far south.

Propagation of an AAO creates a blocking high featuring clear weather and little cloudiness (Mokhov et al. 2013; Dzerdzeevskii et al. 1946). As a result, the air inside it quickly warms (especially in summer), which can also account for substantial rise in monthly means of local temperatures. The effect is the more noticeable, the longer the total duration (TD) of AAOs over the region.

The two mentioned factors (emissions of methane and AAOs) can both be responsible for substantial climate warming in the RFE region in summer months; however, the contribution of methane is to be clarified.

In our research, we aim to check the assumption about a relationship between methane emissions from the permafrost and the temperature rise in the RFE region. The following steps are followed:

1. Estimation of the total duration of AAOs that crossed Russia's arctic seacoasts during May–October of 1979–2018 period.
2. Identification of the RFE areas (including adjacent seas) where interannual variations in the total duration of AAOs crossing the coasts of the Chuckhi and East-Siberian seas exhibit significant correlation with the concurrent variations in monthly temperature means.

3. Identification of the RFE areas (including adjacent seas) where interannual variations in total column methane amount demonstrate significant correlation with the concurrent variations in the total duration of the above-mentioned AAOs.
4. Discussion of the findings.

2 Methods

In our research, we used reanalysis data as source material. The following datasets were chosen as most appropriate:

1. CAMS-reanalysis (Reanalysis 2019)—for monthly means of total column atmospheric methane (TCM);
2. ERA-Interim (ERA-interim 2019)—for daily means of meridional and zonal surface wind components, atmospheric temperature (T_a), and 500-hPa geopotential height (H_{500}).

CAMS, which stands for the Copernicus Atmosphere Monitoring Service, is a new global reanalysis dataset of atmospheric composition produced by the European Centre for Medium-Range Weather Forecasts (ECMWF). It consists of three-dimensional time-consistent atmospheric composition fields, including aerosols, chemical species and greenhouse gases (Inness et al. 2019). At the time of the research the dataset was available for the period 2003–2016. The vertical resolution of the reanalysis data included 60 model levels, with the top level at 0.1 hPa. Daily and monthly means of methane and other species at these levels are freely available from ECMWF open data service (Reanalysis 2019).

ERA-Interim reanalysis presents a variety of atmospheric parameters for 1979–2019 period. Data on wind velocities are available in spatial resolution of approximately 80 km (T255 spectral on $0.75 \times 0.75^\circ$ coordinate grid) and temporal resolution of 6 h, the number of vertical levels from the surface up to 0.1 hPa being 60. The data assimilation system used to produce ERA-Interim is based on a 2006 release of the Integrated Forecast System (Cy31r2), which includes a 4-dimensional variational analysis with a 12-h analysis window (Dee et al. 2011).

The areas with the highest atmospheric TCM, as established by use of CAMS data, were the coastal regions of the Chukchi Sea and the eastern part of the East-Siberian Sea, the whole area falling in 160° E– 160° W sector. Daily methane emissions therein reached 30 – 190 g/m². Further research was therefore carried out for the mentioned sector.

AAOs over the sector in question were identified by analyzing atmospheric patterns of H_{500} distributions. The fact of an AAO occurrence was established if the following conditions were met: (i) H_{500} values exceeded their averages for the corresponding areas, (ii) mean daily wind velocities in the identified high-pressure band had strong north components. AAO manifestations were sought for in each 2.5° -wide sector in each month of May–October period. If the fact of an AAO-occurrence was established in a certain sector, its total duration was determined. An AAO was attributed to a certain month if the period of its existence in this month was longest.

In second and third steps, we used statistical approaches. Time series of the indicators under study were formed; their linear trends were properly made up for. Correlation analysis and Student's t -test were then applied to estimate the correlation significance corresponding to 95% confidence interval and 0.34 correlation coefficient threshold level.

The results of the correlation analysis were presented on contour maps using Delaunay triangulation (Skvortsov 2002).

3 Results and Discussion

The above approach was used to identify all AAO-events in each 2.5° -wide sector of the region in question from May to October in 1979–2018 period. Their total durations were determined for each sector and each year, which enabled to build the time series. Angular coefficients of their linear trends plotted against mean longitudes of the corresponding sectors are presented in Fig. 1a. Two periods were analyzed: 1979–2018 and 1998–2018. Mean values of AAO TDs are presented on a similar plot in Fig. 1b.

As seen from Fig. 1, in 1979–2018 total durations of AAOs exhibited significant rise in all sectors of the region under study. The highest rise rates were detected in the eastern part of the East-Siberian Sea and the Bering Strait area. AAO TDs increased in eastward direction peaking in the Bering Strait sector (165° W).

In step 2 of the research, we evaluated the statistical significance of correlation between interannual variations in AAO TDs and variations in mean monthly T_a in different areas of the region in question. The strongest AAO TD— T_a correlation was established for the AAOs crossing 175 – 172.5° W sector. The latter corresponds to the Chukchi Sea coast extending from the Kolyuchin Bay to the Cape Serdtse-Kamen. The areas of significant positive AAO TD— T_a correlation in August are shown in Fig. 2.

As follows from Fig. 2, the whole area of strong AAO TD— T_a correlation for AAOs crossing 175 – 172.5° W sector lies within 50 – 69° N and 172.5° E– 167.5° W. The area is quite extensive and includes a large part of the mainland RFE, southern parts of the Chukchi Sea, as well as the central part of the Bering Sea. The strongest correlation within this area is found above the Chukchi Peninsula and off its south coast (particularly, the Anadyr Bay), as well as off the north coasts of the Aleutian Islands (particularly, the Andreanof Islands, Rat Islands, and Near Islands). The adjacent waters of the Pacific are also affected.

Distribution of mean monthly T_a change rates in August in 1979–2018 is shown in Fig. 3.

In Fig. 3, a stable increase in mean monthly T_a is seen almost over the whole area. For the last 40-year period, T_a in some parts of the area has risen by dramatic values (up to 5°C). Blocking highs can partly provide an explanation for the phenomenon. The reason for T_a increase inside a blocking high is that little or zero cloud cover leads to absorption of solar radiation by the earth surface and consequent surface

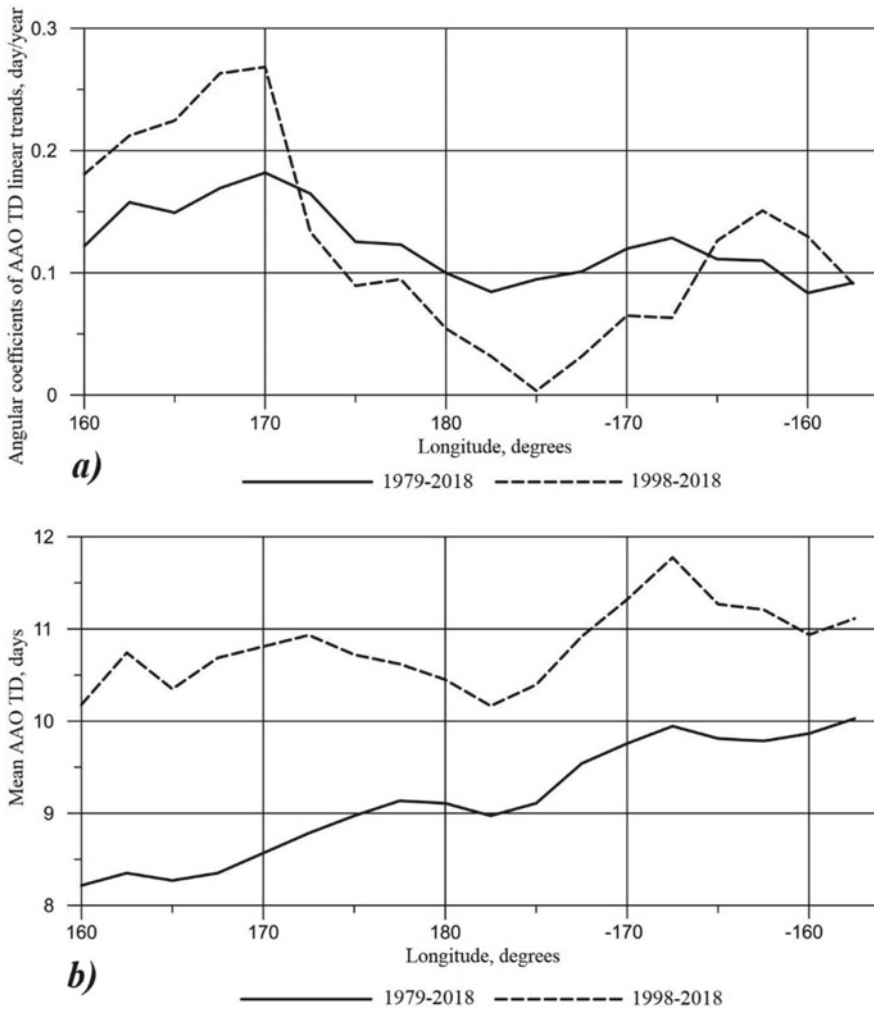


Fig. 1 Dynamics of arctic air outbreaks over the RFE region in August: **a** angular coefficients of AAO total duration linear trends; **b** mean values of the total duration of AAOs

air heating. This happens both over the land and over the sea; however, the sea is less subject to heating due to water’s much larger heat capacity. Therefore, despite the rise in the total duration of blocking highs, increase in surface temperatures of the Chukchi and the Bering seas by such dramatic values has not happened. Hence, general temperature increase in the region cannot be attributed to blocking highs only.

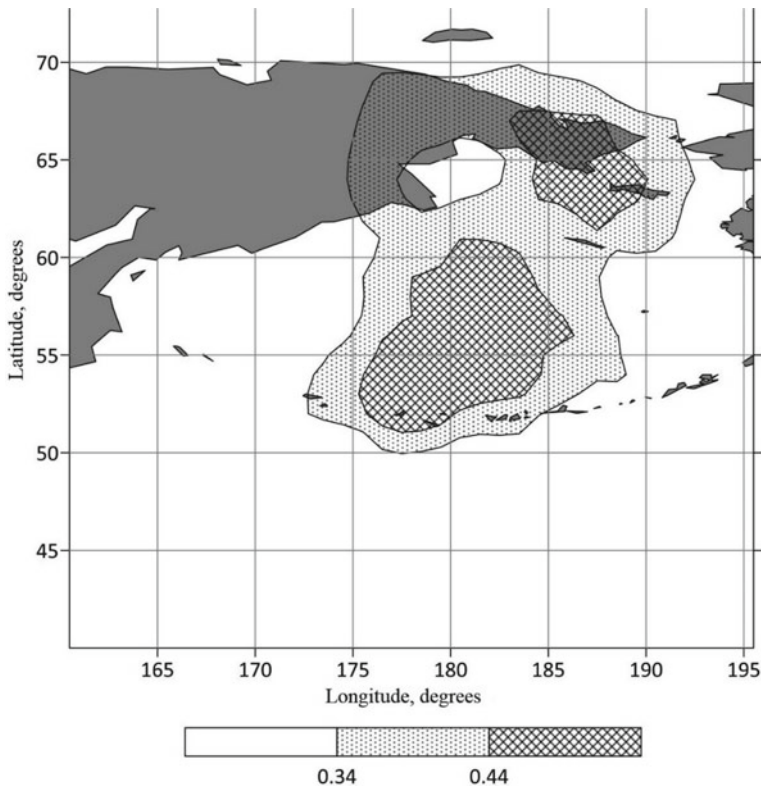


Fig. 2 Areas of significant positive correlation between the total duration of AAOs that crossed 175–172.5° W sector and mean monthly August temperatures

Similar research was performed for other months of May–October period. Significant positive AAO TD— T_a correlation has been detected over several areas of the region in question only in July–September. It has also been established that the actual temperature rise in these months cannot be explained solely by blocking highs.

In step 3, we proceeded to identify the parts of the RFE region and the adjacent seas, where interannual variations in total column methane amount demonstrated significant correlation with the concurrent variations in AAO TD monthly means.

As an example, in Fig. 4 we show the areas featuring significant positive correlation between the total duration of AAOs that happened in August in 175–172.5° W sector and monthly means of TCM over the region in question.

As follows from Fig. 4, a significant TCM—AAO TD correlation is present in near-coastal areas of the Chukchi Sea, around the Chukchi Peninsula, and in the central part of the Bering Sea. The correlation pattern is very similar to that shown in Fig. 2. This fact tells in favor of the proposed hypothesis assuming possible connection of methane emissions with the local climate warming and emphasizes the role of AOs in the southward transport of methane.

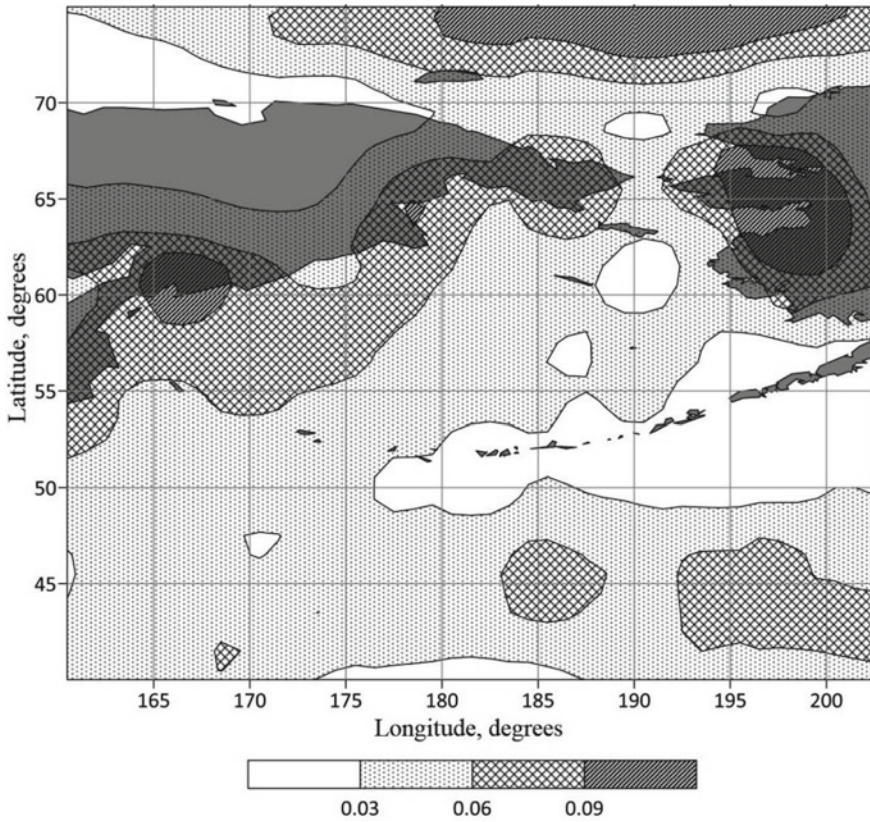


Fig. 3 Distribution of mean monthly T_a change rates in August in 1979–2018

Analogous studies carried out for other months of May–October period have revealed a similar correlation pattern in September. No similarities have been detected in other months (May, June, July, and October).

4 Conclusion

Our research has proved the existence of interconnection between rise in mean temperatures of August and September in the RFE and methane emissions from the permafrost of the East-Siberian and Chukchi seacoasts. Arctic air outbreaks have been shown to play a major role in southward transport of methane. However, similar mechanisms apparently do not work directly during other warm months, since no significant correlation between air temperatures and atmospheric methane levels has been found. Better understanding of the origins and mechanisms of the local climate warming throughout the year will require further studies.

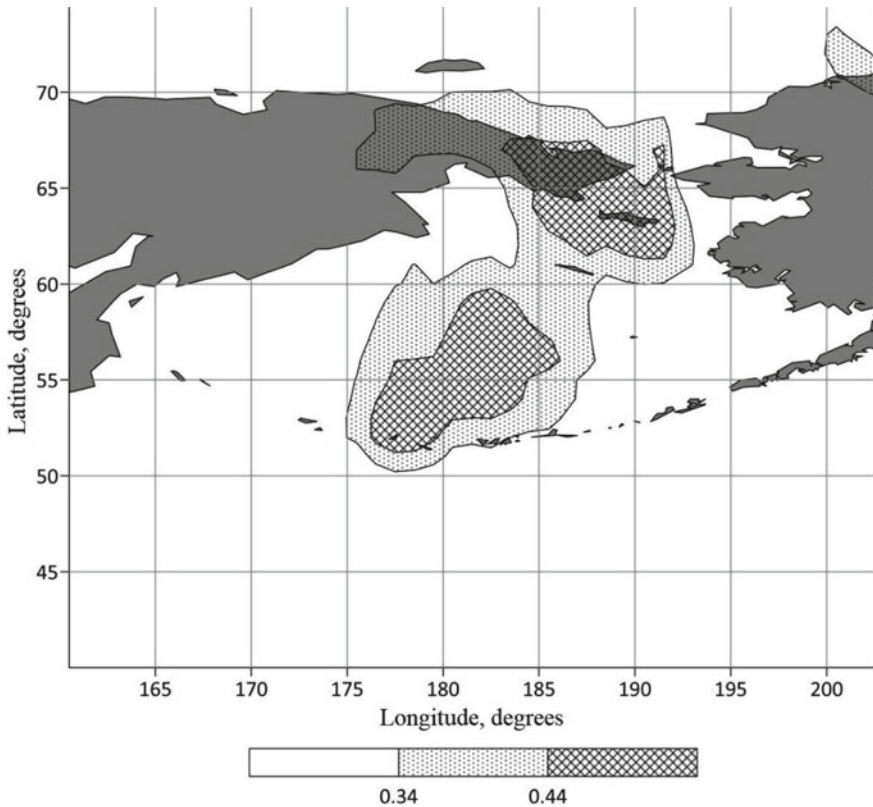


Fig. 4 Areas of significant positive correlation between the total duration of AAOs crossing 175–172.5° W sector and mean monthly values of TCM in August

Since permafrost degradation is likely to continue in the near future, methane emissions into the atmosphere will grow. The faster the growth rate, the more noticeable the methane contribution to the warming process will become.

References

- Author F, Author S (2016) Title of a proceedings paper. In: Editor F, Editor S (eds) Conference 2016, LNCS, vol 9999. Springer, Heidelberg, pp 1–13
- Birchall SJ (2019) Coastal climate adaptation planning and evolutionary governance: insights from Homer. *Marine Policy, Land and Sea Interaction, Special Issue, Alaska, IN*
- Bulkeley H, Tuts R (2013) Understanding urban vulnerability, adaptation and resilience in the context of climate change. *Local Environ* 18(6):646–662
- Bush MJ (2020a) How to end the climate crisis. In: *Climate change and renewable energy*. Palgrave Macmillan, Cham 421–475

- Bush MJ (2020b) The overheated earth. In: Climate change and renewable energy. Palgrave Macmillan, Cham, 59–108
- Dee DP et al (2011) The ERA–interim reanalysis: configuration and performance of the data assimilation system. *Q J Roy Meteorolog Soc* 137(656):553–597
- Dzrdzhevskii BL, Kurganskaya VM, Vitvickaya ZM (1946) Categorization of circulation mechanisms in the Northern Hemisphere and synoptic seasons characteristics. In: Tr. n.-i. uchrezhdenij Gl. upr. gidrometeorol. sluzhby pri Sovete Ministrov SSSR. Ser. 2. Sinopticheskaya meteorologiya, vol 21. Tsentral'nyi institut prognozov, Moscow; Gidrometizdat, Leningrad (in Russian)
- ERA-interim (2019). <https://www.ecmwf.int/en/forecasts/datasets/reanalysis-datasets/era-interim>. Last accessed 10 Sep 2019
- Hallegatte S, Ranger N, Mestre O et al (2011) Assessing climate change impacts, sea level rise and storm surge risk in port cities: a case study on Copenhagen. *Clim Change* 104(1):113–137
- Inness A et al (2019) The CAMS reanalysis of atmospheric composition. *Atmos Chem Phys* 19(6):3515–3556
- Li J, Hsu HH, Wang WC et al (2018) East Asian climate under global warming: understanding and projection. *Clim Dyn* 51:3969–3972
- Malkova GV, Gubarkov AA, Drozdov DS, Leybman MO, Khomutov AV, Sherstyukov AB (2014) The second assessment report of Roshydromet on climate change and its consequences on the territory of the Russian Federation. General summary. Federal Service for Hydrometeorology and Environmental Monitoring (Roshydromet), Moscow (in Russian)
- Mokhov II, Akperov MG, Prokofieva MA (2013) Blocking highs in the Northern Hemisphere and Euro-Atlantic region: change estimates according to reanalysis data and model computations. *Doklady akademii nauk* 449(5):1–5 (in Russian)
- CAMS Reanalysis (2019). <https://apps.ecmwf.int/data-catalogues/cams-reanalysis>. Last accessed 10 Sep 2019
- Skvortsov AV (2002) Triangulyatsiya Delone i yeye primeneniye (Delaunay triangulation and its application). Izd-vo Tomskogo gosudarstvennogo universiteta, Tomsk (in Russian)

Geology and Gold Mineralization of Lower Carboniferous Deposits of the Kommercheskoye Deposit (Kumak Ore Field)



A. V. Kolomoets, V. S. Pantelev, N. R. Kutuyeva, A. B. Mumenov, and D. F. Yakshigulov

Abstract The work considers a promising object—the Kommercheskoye deposit in the black shales of the Kumak ore field. The main ore-bearing structures are two meridional zones of the East Anikhov faults, into which quartz veins penetrate and where fracture metamorphism, metasomatism, and mineralization are intensely manifested. Significant concentrations of gold are confined to intercalation bundles of metamorphosed primary terrigenous and clay rocks, which are now transformed into a diverse composition of micaceous-quartz and quartz-micaceous chlorinated schists. The prevailing importance among them is occupied by the most favorable for mineralization carbonaceous micaceous carbonate-quartz siltstone shales, and shields for ore-bearing solutions are clays and limestones. More gold concentrations are expected at deeper horizons of the Kommercheskoye deposit, less susceptible to weathering.

Keywords Gold · Rift structures · Black shales · Anikhov graben · Carbon · Ordovic

1 Introduction

The Kumak ore field is structurally a junction of the East-Urals Rise and Tobolsk Anticlinorium, separated by the Anikhovskiy graben of the rift type. The latter is aggravated by the Kumak-Kotansun crush zone, which is one of the fragments of the Chelyabinsk deep fault that can be traced along the East Ural Rise. In the central part of the buckling zone, a number of gold ore manifestations of the Kumak ore field are stretched along its strike for tens of kilometers. The largest deposits—Kumak and Kommercheskoye—are located within the limits of the black shale thickness of the Lower Stone Age.

A. V. Kolomoets (✉) · V. S. Pantelev · N. R. Kutuyeva · A. B. Mumenov · D. F. Yakshigulov
Orenburg State University, Orenburg, Russian Federation
e-mail: kolomoyets56@mail.ru

2 Geology and Ore Content of the Kommercheskoye Deposit

The black shale strip of the Kommercheskoye deposit is a metamorphosed sedimentary formation with interlayers of effusive rocks. Primary sediments are dominated by siltstones and carbonaceous shale with carbonate interlayers. The clay shale, which is widely developed at the deposit, is macroscopically represented by black shale rocks, often with a characteristic nodularity due to the presence of otterlite porphyroblasts, with graphite greases on the slate planes. In some areas, the oil shale is cataclyzed, fledgled and penetrated by quartz veins. Hydrothermal changes are expressed by the development of sericite bands, recrystallization and isolation of quartz, and the development of carbonate, cementing and sometimes corroding quartz.

Carbonate rocks are represented by sandy limestone containing carbonaceous substance in separate interlayers, by virtue of which the rock acquires a dark grey colouring. The effusive rocks are represented by andesites, dacites, their tuffs and packs of green shale of albite-actinolitic epidote composition.

As part of the black shale strata in the area of the Kommercheskoye deposit, drilling wells discovered three submeridional packs of coal shale, which are in contact with the interlayers of serial-quartz, albite-sericite quartz and substantially sericite shale are confined to four almost vertical zones of shale formation and quartzization. During the approbation all the zones found to be gold-bearing.

The main ore-bearing structures are two meridional zones of the East-Anikhov faults, into which the quartz lodes were introduced and where the near-fault metamorphism, metasomatism and mineralization were intensively manifested.

Significant concentrations of gold are confined to the interlayers of metamorphosed primary terrigenous and clayey rocks, which are now transformed into various compositions of micaceous quartz and quartz-micaceous chlorinated shales. Among them, carbonaceous mica-carbonate-quartz alevrolite slates are the most favorable for mineralization, and clays and limestone are the screens for ore-bearing solutions. Structurally, they are confined to rock buckling and slitting blocks located at the intersection of the meridional East-Anikhov faults and their operating cracks with north-northeast and northwest ruptures. Ore bodies are clearly confined to the lower carbon shale sequence of the lower sub-thickness of the Lower Bredinic Formation (C_1 bd) of Lower Stone Age. Primary ore minerals found including sphalerite, sheelite, pyrite, arsenopyrite, chalcopyrite, bismuthine, marcasite, pyrrhotite, wolframite, native gold and silver.

According to the statistical processing of results of analyses (more than 600 spectrochemical analyses were used) it was revealed that the areas with the most significant concentrations of native microcrystalline gold are confined to quartz shale, metasomatite and vein quartz with sulfide minerals, confined to the zones of junction of differently directed tectonic ruptures (Table 1).

Table 1 Average gold content (g/t) in Middle Paleozoic deposits of Anikhov graben in Brediniac formation (C₁bd) (average content in numerator, maximum—in denominator)

Sub-formation	Sequence	Thickness, m	Rock types	Au, g/t
Upper C ₁ bd ₂	–	80–150	Conglomerates	0.002/0.07
			Tuff conglomerates	0.003/0.05
			Gravelite and topografiniai	0.020/0.03
			Arcose sandstones	0.005/0.05
			Limestones	0.002/0.02
Lower C ₁ bd ₁	Upper clayey-terrigenous	100–120	Sandstones p.-quartz	0.002/0.030
			Siltstones p.-quartz	0.003/0.040
			Clays hydrated-coalinit	0.001/0.005
	Middle terrigenous-carbonate	50–150	Arcose sandstones	0.003/0.05
			Siltstone coal. p.-quartz	0.003/0.10
			Organogenic limestones	0.002/0.01
	Lower carbon shale	200–300	Conglomerates	0.003/0.05
			Gravelites	0.002/0.03
			Silt shale mica-quartz	0.007/0.03
			Shale coal.-trunk.-carb. with pyrite and chalcopyrite	0.13/1.0
			Metasomatites ser.-quartz. with lodes of quartz with pyrite	0.15/1.0
			Quartz lodes with pyrite and arsenopyrite	0.20/1.5

3 On the Formation Conditions for Stratiform Gold Ores at the Kumak Gold Field

Within the East-Urals uplift there black shale ore-bearing gold-bearing deposits of the Middle Horde and Lower Stone Age are widely developed. Their most prominent representatives are the formation of the New Orenburg strata and the Bredinsk Formation in the north of the East-Urals uplift, which are sources of gold for gold-bearing cortices of erosion (Kirovsk, Kamensk, Belozersk, etc.) (Arifulov 2005; Pankratiev et al. 2018; Sazonov et al. 1999; Snachev et al. 2012). Carbon formations of the same age compose numerous objects of stratigraphic gold ores in the south of this tectonic division. These are the Middle Horde rocks of the Shebekta and Balaldyk strata of the East Mugodzhzar zone and the Lower Carboniferous formations of the carbonaceous-terrigenous-carbonate strata of the Kumak ore field.

The development of black shale formations began in the Ordovician period: internal deflections of the rift type were laid in the local stretch zones, in the form of shallow sedimentation basins limited by faults. There in rather warm conditions an accumulation of organic matter was performed, which created favorable reduction environment for the deposition of sulfides and precious metals. The latter were later concentrated in pyrite, arsenopyrite and organic carbon. In the process of diagenesis and early metamorphism, crystallization water was released from water-bearing minerals, which, interacting with the organism, was transformed into carbon dioxide. The carbon dioxide partially dissolved the gold and transported it to the weakened zones—numerous cracks in the rocks, especially at the intersection of numerous differently directed ruptures. This process in the North of the East-Urals uplift led to the formation of some small manifestations of noble metal with concentrations of 3–5 g/t (Loshinin and Pankrat'ev 2006; Ponomareva and Loshchinin 2013).

The Lower Carboniferous Formations inherit the history of the Middle Hordeic black shale formations of the East Ural Rise. They have a similar lithological composition of rocks and are confined to the same tectonic structures, but more pronounced grabens. The high degree of metamorphism expressed in the appearance of biotite rudiments in carbonaceous-terrigenous formations of C_1 led to a more significant concentration of syngenetic gold. Widely manifested hydrothermal-metasomatic activity associated with the introduction of acid magmas in the Upper Paleozoic time has led to both the introduction of new portions of magmatic gold and the removal of syngenetic metal fluid-hydrothermal solutions from the older sediments of the middle Ordovician and its redeployment to higher levels – black shale rocks of Lower Stone Age. This led to the formation of stratigraphic type gold occurrences (Loshinin and Pankrat'ev 2006).

4 Conclusion

Higher gold ore concentrations are expected at deeper horizons at the Kommercheskoye Deposit, which are less susceptible to weathering. This is due to the wide distribution of gold-bearing deposits in this area of the lower subfloor of the Lower Bredinic Formation (C_{1bd}), the presence of contrasting interlayers packs of clayey and terrigenous rocks in it with a significant development of carbonaceous mica-carbonate-quartz ore-bearing rocks among them, presence of sulfides and native gold in them, significant development of rock crush zones and the most favorable mineralization concentrators at the facility, timed to coincide with the multidirectional junction areas of tectonic dislocations.

Acknowledgements The work was carried out with the support of the Regional Grant in the field of scientific and technical activities in 2019 (Agreement No. 23 of 14.08.2019).

References

- Arifulov ChH (2005) Chernoslantsevye deposits of gold of various geological conditions. *Ores and metals* 2:9–19 (in Russian)
- Loshinin VP, Pankrat'ev PV (2006) Gold-bearing capacity of the lower middle paleozoic black shale formations of the Eastern Orenburg Region. *Strategy and processes of georesources development, Perm* (in Russian)
- Pankratiev PV, Kolomoets AV, Stepanov AS, Bagmanova SV, Panteleev VS, Tukhtanazarova KR (2018) Features of formation of gold manifestations in the black shale deposits of the Kumak ore field. *Processy v Geosredah* 4:1121–1125 (in Russian)
- Ponomareva GA, Loshchinin VP (2013) Golden Manifestations in the Black Shale formations of the Paleozoic of the East Orenburg Region and their genesis. *Bull Orenburg State Univ* 5(154):144–148 (in Russian)
- Sazonov VN, Ogorodnikov VN, Koroteev VA, Polenov YA (1999) Ural gold deposits. UGGGA, Yekaterinburg (in Russian)
- Snachev AV, Rykus MV, Saveliev DE, Bazhin EA, Ardislamov FR (2012) *Geology, petrogeochemistry and ore content of the carbonaceous sediments of the Southern Urals*. DesignPress, Ufa (in Russian)

Direct Numerical Simulation of Droplet Deformation in External Flow at Various Reynolds and Weber Numbers



Anna Zotova , Yulia Troitskaya , Daniil Sergeev ,
and Alexander Kandaurov 

Abstract Using the Basilisk software package, direct numerical simulation of the process of deformation of a liquid drop in a gas stream was carried out. The calculations were carried out for Reynolds numbers $Re = 50\text{--}3000$, Weber numbers $We = 2\text{--}30$. Two main modes of drop deformation were observed: bowl-shaped and dome-shaped, there is a transitional deformation mode between them. A map of deformation modes is constructed for comparison with the experimental data available in the literature. It was found that the dependence of the Weber number, corresponding to the transition from one deformation mode to another, on the Reynolds number is well described by the power law proposed in the literature.

Keywords Direct numerical simulation · Drop deformation mode

1 Introduction

The processes of deformation and secondary fragmentation of droplets play an important role in various industries: fuel, agriculture, etc. A lot of experimental work has been devoted to studying the behavior of a droplet in the flow of the external medium (Hsiang and Faeth, 1995; Krzeczkowski, 1980). Numerical experiments were also carried out to simulate the deformation and fragmentation of the droplet under the influence of a stationary external flow (Jalaal and Mehravaran, 2012; Kekesi et al., 2014; Pairetti et al., 2018). In the experiments, two types of perturbations leading to deformation and fragmentation of the droplet were investigated: a shock wave and steady disturbances. It was shown that the regime of droplet fragmentation under the influence of the shock wave depends on the ratio of the resistance forces of the medium and surface tension expressed by the Weber number $We = \rho_c d_0 u_0^2 / \sigma$, and the ratio of the viscosity forces in the drop and the forces of surface tension expressed by the Ohnesorge number $Oh = \mu_d / (\rho_d d_0 \sigma)^{1/2}$, where d_0 and u_0 are the diameter

A. Zotova (✉) · Y. Troitskaya · D. Sergeev · A. Kandaurov
Institute of Applied Physics, Nizhny Novgorod, Russia
e-mail: aniazotova@yandex.ru

© The Author(s), under exclusive license to Springer Nature Switzerland AG 2021
T. Chaplina (ed.), *Processes in GeoMedia—Volume II*, Springer Geology,
https://doi.org/10.1007/978-3-030-53521-6_20

of the droplet and its velocity relative to the medium velocity, ρ_c and ρ_d are the densities of the external medium and the droplet, respectively, μ_d is the viscosity of the droplet, and σ is the surface tension coefficient. As was shown in Hsiang and Faeth (1995), the mode of deformation and fragmentation of a droplet in a stationary flow is affected by the Weber number and Reynolds number $Re = \rho_c d_0 u_0 / \mu_c$. The authors distinguish two types of droplet deformation in the external flow: dome-shaped and bowl-shaped. In the case of the dome-shaped deformation mode, the windward side of the droplet becomes flat, the leeward side remains rounded, this shape is similar to the shape of a droplet at the initial stage of the development of a bag-breakup phenomenon. For the bowl-shaped deformation mode, on the contrary, the leeward side of the drop becomes flat, and the conditions for the formation of bowl-shaped drops are to some extent similar to the conditions of shear-breakup and, apparently, are determined by the interaction between the drag and viscous forces. A map of the dome- and bowl-shaped modes of drop deformation obtained is presented in Fig. 2 of Hsiang and Faeth (1995). Based on a comparison of the shear stress with the surface tension forces, the authors propose the following estimate of the dependence of the Weber number corresponding to the transition from one mode to another on the Reynolds number: $We = 0.5 \cdot Re^{1/2}$.

2 Drop of Liquid in a Gas Stream

When conducting experimental studies, available equipment and materials usually impose a restriction on the set of problem parameters. So it seems relevant to conduct a numerical experiment that will remove this limitation. For direct numerical simulation of droplet deformation in the external flow, the Basilisk software package was used Popinet (2020). The Navier-Stokes equations for incompressible media with variable density are solved in Basilisk:

$$\rho (\partial_t \mathbf{u} + \mathbf{u} \cdot \nabla \mathbf{u}) = -\nabla p + \nabla \cdot (2\mu \mathbf{D}) + \sigma \kappa \delta_s \mathbf{n}, \quad (1)$$

$$\partial_t \rho + \nabla \cdot (\rho \mathbf{u}) = 0, \quad (2)$$

$$\nabla \cdot \mathbf{u} = 0, \quad (3)$$

where \mathbf{u} is the medium velocity, ρ is the density of the medium, μ is the dynamic viscosity and \mathbf{D} is the deformation tensor defined as $D_{ij} \equiv (\partial_i u_j + \partial_j u_i) / 2$. The surface tension term is concentrated at the interface, this is provided by the Dirac distribution function δ_s ; σ is the surface tension coefficient, κ is the curvature, \mathbf{n} is the normal to the interface.

Fig. 1 Configuration of the problem

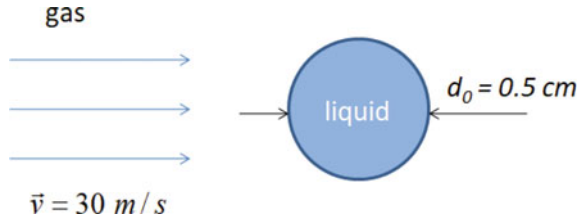


Table 1 Parameters used for modeling

d_0 , m	u_0 , m/s	ρ_d , kg/m ³	ρ_c , kg/m ³	μ_d , Pa·s	μ_c , Pa·s	σ , N/m
0.005	30	1000	1.2	1.003e-3	$\rho_c d_0 u_0 / Re$	$\rho_c d_0 u_0^2 / We$

For two-phase flows the volume fraction c of the first liquid is introduced, and the density and viscosity are determined as

$$\rho \equiv c\rho_1 + (1 - c)\rho_2, \tag{4}$$

$$\mu \equiv c\mu_1 + (1 - c)\mu_2, \tag{5}$$

where ρ_1, ρ_2 and μ_1, μ_2 are the densities and viscosities of the first and second media, respectively.

We examined the problem of the following geometry: a drop of liquid with a diameter 5 mm was placed in a gas stream at a speed of 30 m/s (see Fig. 1). The density of the liquid ρ_d and gas ρ_c correspond to the density of water and air, the viscosity of the liquid μ_d is equal to the viscosity of water. The viscosity of the gas μ_c and the surface tension at the interface between the liquid and gas σ are determined by the set values of the Reynolds and Weber numbers (see Table 1).

When considering the deformation and fragmentation of a liquid drop in a gas stream, the characteristic shear fragmentation time proposed in Ranger and Nicholls (1969) is introduced:

$$t^* = d_0 (\rho_d / \rho_c)^{1/2} / u_0 \tag{6}$$

According to measurements made by Cao et al. (2007); Dai and Faeth (2001), the initial deformation of a drop occurs in a dimensionless time approximately equal to $t/t^* = 1 - 2$ and weakly depends on the Weber number (in the range considered by the authors, see Cao et al. (2007) Fig. 7). For the parameters under consideration $t^* = 5.3$ ms, in our work we considered the deformation of the droplet at time $t = 5.5$ ms.

3 Results

In order to observe the transition from bowl-shaped to dome-shaped deformation of the droplet, a simulation was performed with parameters corresponding to Weber numbers $We = 2-30$ and Reynolds numbers $Re = 50-3000$.

The process of droplet deformation for the bowl-shaped ($Re = 50$, $We = 12$) and dome-shaped ($Re = 1000$, $We = 6$) modes is shown in the Fig. 2. It can be noted that for these parameters of the bowl-shaped mode, the shape of the drop changes significantly over time, for example, after 3 ms the drop has a narrow ledge in the direction of the wind.

Figure 3 shows an example of the obtained simulation results - a droplet shape 5.5 ms after placing a spherical droplet in a gas stream for Weber numbers $We = 8$ and $We = 12$ and various Reynolds numbers. It can be seen that for the Weber number $We = 12$, the bowl-shaped mode of deformation of the drop occurs at Reynolds numbers $Re = 50-300$, the dome-shaped mode—at $Re = 500-1000$. The transition from one mode to another occurs when the Reynolds number is about $Re = 400$. For the Weber number $We = 8$, the transition from one mode to another is shifted to the range of Reynolds numbers $Re = 200-300$.

A map of the dome- and bowl-shaped modes of drop deformation for different Weber and Reynolds numbers is shown in Fig. 4. The results corresponding to the bowl-shaped mode of deformation of the droplet are shown by black squares, and the dome-shaped mode by red circles. Transitional mode is marked by green stars.

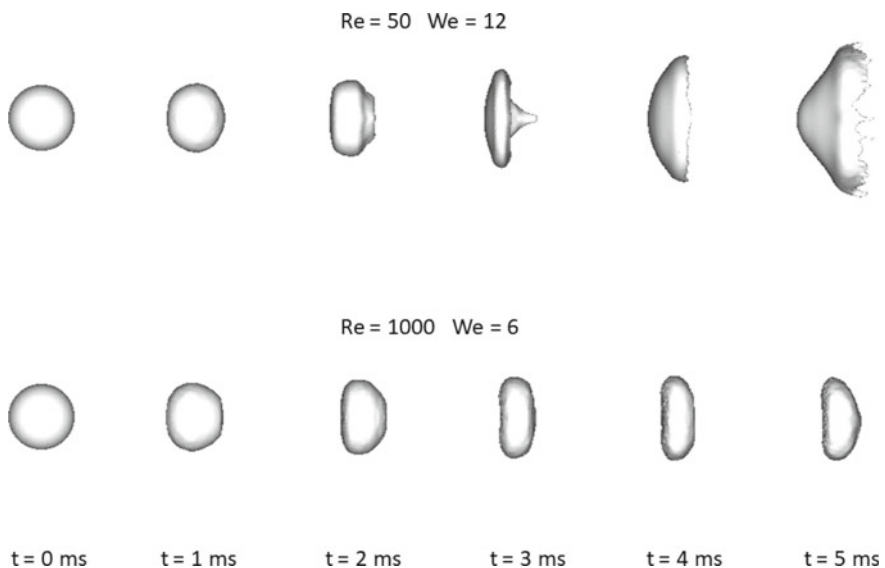


Fig. 2 Drop deformation for different points in time: bowl-shaped ($Re = 50$, $We = 12$) and dome-shaped ($Re = 1000$, $We = 6$) modes

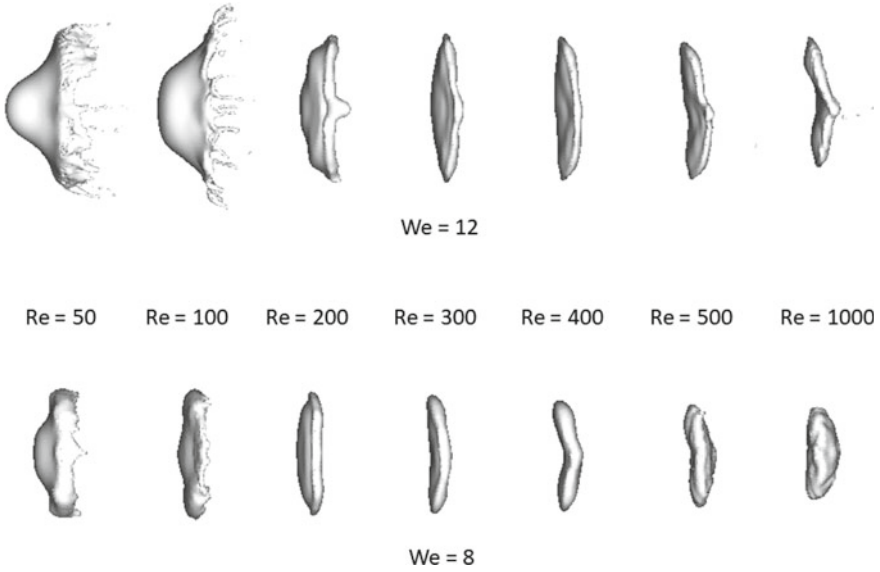


Fig. 3 The result of numerical simulation of droplet deformation in a gas stream with parameters corresponding to the Weber numbers $We = 12$ and $We = 8$ and various Reynolds numbers Re at time $t = 5.5$ ms.

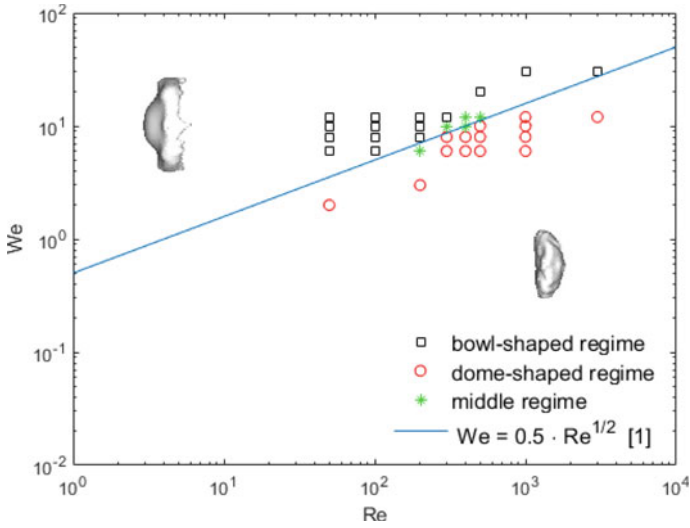


Fig. 4 Map of dome-shaped and bowl-shaped modes of drop deformation obtained as a result of numerical experiments. The line shows the dependence of the Weber number corresponding to the transition from one regime to another, on the Reynolds number obtained in Hsiang and Faeth (1995)

The blue line corresponds to the dependence of the Weber number corresponding to the transition from one regime to another on the Reynolds number proposed in Hsiang and Faeth (1995): $We = 0.5 \cdot Re^{1/2}$ (see Fig. 2 of the work Hsiang and Faeth (1995)). It can be seen that the results obtained using direct numerical simulation are in agreement both with this dependence and with the experimental data obtained in Hsiang and Faeth (1995).

Acknowledgements This work was supported by the RFBR projects 19-05-00249, 18-35-00658, 18-35-20068, 18-55-50005 (familiarization with the Basilisk software package) and the Grant of the President No. MK-3184.2019.5, work on comparison with experimental data was supported by the RSF project No. 18-77-00074, carrying out numerical experiment was supported by the RSF project No. 19-17-00209, A.N. Zotova is additionally supported by the Ministry of Education and Science of the Russian Federation (Government Task No. 0030-2019-0020). The authors are grateful to the FCEIA employee: UNR - CONICET (Rosario, Rep. Argentina) Dr. Ing. César Pairetti.

References

- Cao X-K, Sun Z-G, Li W-F, Liu H-F, Yu Z-H (2007) A new breakup regime of liquid drops identified in a continuous and uniform air jet flow. *Phys Fluids* 19:057103
- Dai Z, Faeth GM (2001) Temporal properties of secondary drop breakup in the multimode breakup regime. *Int J Multiphase Flow* 27:217–236
- Hsiang L-P, Faeth GM (1995) Drop deformation and breakup due to shock wave and steady disturbances. *Int J Multiphase Flow* 21(4):545–560
- Jalaal M, Mehravaran K (2012) Fragmentation of falling liquid droplets in bag breakup mode. *Int J Multiphase Flow* 47:115–132
- Kekesi T, Amberg G, PrahL Wittberg L (2014) Drop deformation and breakup. *Int J Multiphase Flow* 66:1–10
- Krzeczkowski SA (1980) Measurement of liquid droplet disintegration mechanism. *Int J Multiphase Flow* 6:227–239
- Pairetti C, Popinet S, Damian SM, Nigro N, Zaleski S (2018) Bag mode breakup simulations of a single liquid droplet. In: 6th European Conference on Computational Mechanics, 7th European Conference on Computational Fluid Dynamics
- Popinet S (2020) The Basilisk code. <http://basilisk.fr>
- Ranger AA, Nicholls JA (1969) The aerodynamic shattering of liquid drops. *AIAA J* 7:285

North Atlantic Oscillation and Arctic Air Outbreaks



A. V. Kholoptsev, S. A. Podporin, and T. Ya. Shulga

Abstract In this paper, we investigate the effect of outbreaks of Arctic air on changes in sea surface temperature in the areas of the North subpolar hydrological front as well as variations in mean daily values of the North Atlantic Oscillation index. We introduce a new technique for detection of Arctic air outbreaks applicable for identification of these phenomena in the areas of baric depressions such as the Icelandic Low.

Keywords North Atlantic · Arctic air outbreak · North Atlantic oscillation · Sea surface temperature · Icelandic low

1 Introduction

The North Atlantic Oscillation (NAO) plays a fundamental role in climate fluctuations in the North Atlantic. The phenomenon has significant impact on variability of the atmospheric circulation and air temperature in the Northern Hemisphere. It affects parameters of air currents and sea state in the majority of North Atlantic regions (Kurbatkin and Smirnov 2010; Mokhov and Yeliseev 2000, 2013; Hurrell et al. 2003; Johnson et al. 2008; Rodwell et al. 1999). The NAO's behavior is thus a major area of interest for geographers and meteorologists.

Fluctuations of the NAO state may arise due to a large number of factors, most substantial being variations in balances of heat and mean content of water vapor in the air over the Icelandic Low (IL) and the Azores High (AH). Such variations may be caused either by vertical heat-moisture exchange over the corresponding water areas

A. V. Kholoptsev
N.N. Zubov State Oceanographic Institute, Moscow, Russia

A. V. Kholoptsev · S. A. Podporin (✉)
Sevastopol State University, Sevastopol, Russia
e-mail: s.a.podporin@gmail.com

T. Ya. Shulga
Marine Hydrophysical Institute, Sevastopol, Russia
e-mail: shulgaty@mail.ru

or by advection of large amounts of air with different heat and water vapor content into the areas. The NAO index variability can, therefore, be affected by strong long-lasting northerly or southerly winds leading to blockings (Mokhov and Yeliseev 2000). An assumption can thus be made that the concurrence of the dates on which the positive NAO phase switches to negative while a blocking process is taking place over the North Atlantic, is not accidental. Such concurrence is described in (Nesterov 2013; Shakina and Ivanova 2010), however, its origins are not investigated.

An important type of atmospheric blocking processes are outbreaks of cold, dry, and dense Arctic air (hereinafter referred to as Arctic air outbreaks—AAO) into the mid-latitudes (Kholoptsev et al. 2018). A technique for their identification was first introduced by Boris Dzerdzhevsky in 1948 (Dzerdzhevskii et al. 1946). According to it, the fact of an AAO occurrence is established if there is an evident high-pressure band linking the Arctic anticyclone with a subtropical one. Similar baric inhomogeneities (blockings) may arise through other factors. The method, therefore, enables identification of blocking processes of any kind (Mokhov et al. 2013). However, when applied for detection of AAO-events, it can often lead to so-called ‘false alarms’ (erroneous establishment of the fact of an AAO occurrence). If, in contrast, an AAO crosses a baric depression, the event may remain undetected. Nevertheless, despite its shortcomings, the technique has been widely used by a large number of modern researchers (Kurbatkin and Smirnov 2010).

An AAO is a rapid northerly air current caused by interaction of a southern cyclone entering higher latitudes with the Arctic anticyclone situated on its way. As these two atmospheric eddies start interacting, the absolute value of the pressure gradient in their boundary area begins to rise (Mankin 2011). This, in turn, generates massive airflows capable of delivering cold Arctic air into temperate latitudes (Salby 1996).

If an AAO occurs in a sector of the North Atlantic within 60°W–0 longitude range, the consequences described above can lead to rise in atmospheric pressure in the IL area and subsequent decrease in the NAO index. The longer the AAO duration, the more noticeable such consequences may be. Therefore, it is safe to assume that variations in the NAO state can be affected by variations in the total duration (TD) of AAOs occurring in the same period.

The hypothesis we put forward will be as follows: the longer the duration of an AAO crossing the Icelandic Low area, the more frequent decreases in mean daily values of the NAO index are to be expected. Should it be confirmed, the results of AAO monitoring could be applied for NAO index prediction, as well as modelling of the related atmospheric and oceanic processes, which is of theoretical and practical interest.

This paper aims to verify the adequacy of the proposed hypothesis and investigate conditions under which outbreaks of Arctic air can lead to decrease in the NAO index.

Bearing in mind the limitations of the traditional AAO detection technique proposed by Dzerdzhevsky (hereinafter referred to as ‘traditional technique’), we have divided our research into two tasks:

1. Developing an alternative detection technique applicable for identification of AAO events in the Icelandic Low area.
2. Establishing conditions under which the proposed hypothesis is adequate.

2 Materials and Methods

In our research, we assumed that the occasions on which the NAO index would decrease while at the same time an AAO would be taking place over the IL could be quite rare. Therefore, to identify these situations, observation data for the longest available period were required. The span from 01.01.1950 to 31.12.2018 was considered. Information on mean daily variations in the NAO index was obtained from (Oscillation and (NAO)).

AAO events were identified by use of NCEP/NCAR reanalysis (NCEP/NCAR). The following characteristics (representing mean daily values) were used:

- adjusted to sea level atmospheric pressure (P_{at});
- geopotential height, corresponding to a certain pressure level (H_p);
- air temperature (T_a) at H_{1000} level.

Near-surface wind velocity (V) components inside the atmospheric inhomogeneities classified as AAOs were obtained from Arctic System Reanalysis (ASR)—a reanalysis of the Greater Arctic based on the Polar Weather Forecast Model (Arctic system reanalysis; Hines and Bromwich 2008; Bromwich et al. 2016). ASR contains data for any points of the Arctic with 3-h periodicity for 01.01.2000–31.12.2012 period in 15-km horizontal resolution. Free access is available through the official website (Arctic system reanalysis).

Data on variations in sea surface temperature (SST) distribution in the North Atlantic were obtained from NOAA reanalysis (Bromwich et al. 2016). The information is available in form of mean monthly values in $1^\circ \times 1^\circ$ coordinate resolution starting from January 1982.

The first task was addressed in three steps.

In step 1, we analyzed error sources arising from the limitations of the traditional AAO detection technique.

In step 2, we proposed a new technique for AAO detection applicable in the IL area. For this purpose, possible manifestations of AAO propagation over the North Atlantic noticeable in fields of P_{at} , H_p , T_a , and V were analyzed for the period 01.01.1948–31.10.2018.

In step 3, we tested the proposed technique's performance by comparing frequencies of successful detection of AAOs over the Crimean Peninsula using both the proposed and the traditional techniques. To establish the fact of correct AAO identification, we used data recorded at Roshydromet weather stations as reference. Local signs of AAO occurrence (atmospheric pressure rise and air temperature drop) were sought for in the stations' records on the dates when AAOs were detected by use of the above techniques.

The second task was dealt with in four steps.

In step 1, we applied the proposed technique to identify all AAO events that occurred over the North Atlantic during 01.01.2000–31.12.2018 period. Then we estimated mean values of average daily V , as well as the duration of AAO events that took place over the Denmark Strait.

In step 2, we estimated how often the periods of AAO events over the North Atlantic coincided with the periods when mean daily values of the NAO index exhibited decrease.

In step 3, we identified the areas in the North Atlantic where interannual variations of mean monthly SST in a certain month showed significant correlation with concurrent variations in TDs of AAOs over the Denmark Strait and the Faroe-Iceland passage. The correlation significance was estimated with help of correlation analysis and Student's test (Optimum Interpolation Sea Surface and Temperature 2019). The threshold correlation level was picked such that at least 90% reliability of the statistical conclusion was provided. The areas identified in such a way were plotted on a map using Delaunay triangulation (Kobzar 2006).

In step 4, we estimated the average flow rate of the current component in the Denmark Strait caused by AAOs with characteristics identified in step 1. The above indicator was evaluated with the 3D POM model described in (Skvortsov and Mirza 2006; Cherkesov et al. 1992). The Mellor-Yamada differential model was then applied to perform the parametrization of the vertical viscosity index and the turbulent diffusivity (Blumberg et al. 1987). The horizontal viscosity value was found using the subgrid viscosity model (Mellor and Yamada 1982).

To obtain tangential wind stress projections, we took wind velocities at the standard meteorological altitude. The aerodynamic drag coefficient at the sea surface was properly allowed for (Smagorinsky 1963). We assumed that no normal velocity component was present at the bottom of the strait, whereas the relation of the near-bottom tangential stresses and the wind velocity was logarithmic. The lateral boundaries were assumed to meet the adhesion conditions.

The barotropic waves stability criterion (Wannawong et al. 2011) was applied to pick the integration steps for the temporal-spatial coordinates. The model grid spatial resolution was picked 0.925 km with 21 vertical calculation levels. For the section of the strait with minimal depths (227 m), the horizontal spacing was 11 m. The integration of the equation set was performed for the area with coastline shapes and sea bottom relief identical to those in the Denmark Strait (Courant et al. 1967). All the three components of the current velocity were assumed zero in any point of the area under study at the initial moment (prior to AAO occurrence).

3 Analysis and Discussion

To detect blocking processes by use of the traditional technique, weather charts of the Northern Hemisphere compiled for 9 a.m. Moscow Time are usually used as source data. Detection of a blocking process is confirmed if on the related weather

chart a high-pressure band linking the Arctic anticyclone with a subtropical one is present. Atmospheric pressure is considered ‘high’ if it exceeds 1015 hPa.

However, to apply this technique effectively, a qualified person with sufficient experience is needed. The method is time-consuming too and subject to human errors. It is quite indicative that during 1.01.1948–31.10.2018 period, no AAOs were detected in the IL area with this technique despite quite evident occasional manifestations of such phenomena in the region. This is the case because the area in question features stable low pressure. As a result, when cold Arctic air masses travel over the IL, atmospheric pressure therein does not normally reach 1015 hPa, which prevents this technique from being used in the area.

To propose an alternative approach, we accounted for the fact that an AAO is a rapid northerly air current. This suggests that the meridional (in our case, southward) components of its near-surface velocity vector (V) exceed other V -components.

When an AAO occurs, formation of its high-pressure band usually takes no longer than one day; consequently, for any part of the affected area it is safe to conclude that

$$P_{at}(\lambda, \varphi, t) - P_{at}(\lambda, \varphi, t-1) > 0,$$

where λ represents longitude, φ —latitude, t —date.

Arctic air inside an AAO is not only dense but cold. Consequently, an outbreak originating in the Northern hemisphere creates a low-temperature band extending from the Arctic to the subtropics. The outlines of both the high-pressure and the low-temperature bands are usually similar. For any point of the low-temperature band, we can state that (General bathymetric chart of the oceans 2019).

$$T_a(\lambda, \varphi, t) - T_a(\lambda, \varphi, t-1) < 0$$

Another important fact is that an AAO is a turbulent current. Cold arctic air within the turbulent boundary layer (TBL) undergoes partial mixing with the warm air from outside. This process leads to an increase in the density of the resulting air mixture (Mankin 2011). Hence, within the TBL, H_p -values (including those corresponding to geopotential values of 700 and 300 hPa) tend to rise (Salby 1996). The areas with increased H_p normally match those with low T_a , while V -vector’s direction is southward.

Hence, for the proposed technique to be effective, it should establish the fact of an AAO occurrence on a certain date (t) if the following conditions are met:

- a baric inhomogeneity in the shape of a band linking the Arctic anticyclone with a subtropical one exists on this date;
- for all points inside the band, the following conditions are fulfilled:

$$P_{at}(\lambda, \varphi, t) - P_{at}(\lambda, \varphi, t-1) > 0;$$

$$\begin{aligned}
T_a(\lambda, \varphi, t) - T_a(\lambda, \varphi, t-1) &< 0; \\
V(\lambda, \varphi, t) &\text{ is directed southward;} \\
H_{700}(\lambda, \varphi, t) - H_{avr\ 700}(\varphi, t) &> 0; \\
H_{300}(\lambda, \varphi, t) - H_{avr\ 300}(\varphi, t) &> 0.
\end{aligned}
\tag{1}$$

$H_{avr\ 700}(\varphi, t)$ and $H_{avr\ 300}(\varphi, t)$ represent mean geopotential values of 700 hPa and 300 hPa correspondingly, averaged over all grid points of the same latitude φ on a certain date t .

To account for the fact that the high-pressure band can be of any shape, we applied the procedure of full search: all possible paths of Arctic air propagation within 60° N–75° N latitude range were considered.

The performance of the proposed technique was tested by comparing AAO detection results with real monitoring data obtained from weather stations. The testing approach was as follows. Firstly, a locality with the full set of available weather monitoring data was picked—the Crimean Peninsula. The records from the weather stations were provided by the Sevastopol branch of N.N. Zubov’s State Oceanographic Institute. Secondly, using NCEP/NCAR reanalysis as source data, we applied both the traditional and the proposed techniques to identify all AAOs that occurred in 1972–1988. For the dates when an AAO was detected over a certain weather station, we checked this station’s records for local signs of this event—atmospheric pressure rise and air temperature drop. A fact of correct AAO identification was established if records from all affected weather stations exhibited the above-mentioned signs.

In the next step, we evaluated frequencies of correct AAO identification using both techniques. The results are aggregated in Table 1.

As seen from Table 1, technique (1) yields much more consistent results thus proving its applicability and effectiveness for the purposes of AAO detection.

Addressing the second task of our research by use of the proposed technique, we have revealed multiple occasions of AAO-resembling events over the IL area. Their average characteristics in 2000–2018 period were as follows: duration—3.6 days; mean daily wind direction—5.8°; mean daily wind speed—11.7 m/s.

Situations when mean daily values of the NAO index exhibited decrease while on the same dates an AAO was present over a certain sector of the North Atlantic were

Table 1 Frequencies of correct identification of AAOs over Crimean weather stations as estimated by use of the proposed (1) and the traditional (2) techniques

Weather station	Technique		Weather station	Technique	
	1	2		1	2
Chernomorskoye	0.95	0.73	Yalta	0.92	0.75
Yevpatoriya	0.96	0.77	Alushta	0.95	0.74
Sevastopol	0.96	0.68	Feodosia	0.90	0.76
Chersonesus Lighthouse	0.95	0.69	Kerch	0.93	0.72
Mysovoye	0.94	0.72	Opasnoye	0.95	0.70

closely looked at. For each 2.5° -wide longitude sector of the area in question, we estimated frequencies (F) of these two events taking place simultaneously. Deviations of the frequency value from its mean (0.5) equal or exceeding 0.1 were regarded as significant. The estimation results are presented in Table 2.

As follows from Table 2, significant deviations (corresponding to F -values of 0.6 or more) are present in certain sectors. They are caused mostly by AAOs lasting 7 days or more. The longer the duration of an AAO, the larger number of sectors will exhibit significant deviations and the higher the frequency of such occasions will be.

In step 3 of task 2, for each month of 2000–2018 period, we estimated frequencies with which the AAOs that crossed the IL were located over the areas of the Denmark Strait and the Faroe-Iceland passage. It has been established that from November to March, AAOs' paths were situated mostly over the Faroe-Iceland passage (0.6–0.8 frequency). Frequencies of AAOs over the Denmark Strait were within 0.2–0.4. From April to September, AAOs over the Denmark Strait were, on the contrary, more frequent (0.65–0.75). In October, the distribution was more or less in balance.

The proposed technique enabled to estimate TDs of AAOs in each month of 2000–2018 period. The corresponding time series were formed. By use of correlation analysis and Student's test, we determined areas with significant correlation between interannual variations in TDs of AAOs over the Denmark Strait and concurrent SST variations. Applying the method described in (Optimum Interpolation Sea Surface and Temperature 2019), we found the 90% reliability correlation threshold for the task under study as 0.34.

Figure 1 shows North Atlantic areas exhibiting significant and stable correlation between interannual variations in TDs of AAOs over the Denmark Strait and concurrent SST variations. The situation is illustrated for September.

As seen from Fig. 1, significant negative correlation between interannual variations in the TDs of AAOs over the Denmark Strait and concurrent SST variations can be found in certain areas adjacent to it. For the period from April to August, such areas are also present, their location being quite similar to those in September. In winter months, analogous negative correlation has been established for the Faroe-Iceland passage. The areas exhibiting such correlation lie within the North subpolar hydrological front (NSHF).

As also seen from Fig. 1, AAOs affect SST distribution not only within the NSHF, but also in the areas situated much further southward. This fact is not at all surprising since AAOs are submeridional air currents that can extend as far as the subtropical anticyclone, the latter in the North Atlantic being the Azores High. The scale of this effect is quite substantial, which is evident through the presence of areas exhibiting significant positive correlation between TDs of AAOs and mean monthly SST of waters surrounding the AH. Similar correlation zones exist in other months as well, however in September their area is largest.

The above-mentioned effect can be explained by AAOs' influence on surface waters dynamics in the North Atlantic. This influence manifests itself all over AAOs' paths and is apparent not only in the Denmark Strait, but also in the North Atlantic Current (NAC) zone, which lies much further southward. AAOs cause southward expansion of this zone, which leads to penetration of warm NAC waters in the area

Table 2 Frequencies (F) with which the NAO index decreased on dates when an AAO was present over the North Atlantic as compared to the dates preceding the AAO occurrence

Longitude sector (W)	F	Longitude sector (W)	F	Longitude sector (W)	F	Longitude sector (W)	F	Longitude sector (W)	F
Minimal AAO duration threshold—7 days									
60–57.5	0.47	47.5–45	0.49	35–32.5	0.60	22.5–20	0.61	10–7.5	0.49
57.5–55	0.48	45–42.5	0.50	32.5–30	0.60	20–17.5	0.57	7.5–5	0.48
55–52.5	0.47	42.5–40	0.52	30–27.5	0.61	17.5–15	0.55	5–2.5	0.47
52.5–50	0.49	40–37.5	0.58	27.5–25	0.63	15–12.5	0.53	2.5–0	0.46
50–47.5	0.50	37.5–35	0.59	25–22.5	0.63	12.5–10	0.51		
Minimal AAO duration threshold—10 days									
60–57.5	0.48	47.5–45	0.50	35–32.5	0.60	22.5–20	0.60	10–7.5	0.48
57.5–55	0.47	45–42.5	0.50	32.5–30	0.62	20–17.5	0.57	7.5–5	0.46
55–52.5	0.48	42.5–40	0.53	30–27.5	0.62	17.5–15	0.56	5–2.5	0.46
52.5–50	0.48	40–37.5	0.60	27.5–25	0.61	15–12.5	0.53	2.5–0	0.46
50–47.5	0.49	37.5–35	0.64	25–22.5	0.63	12.5–10	0.50		

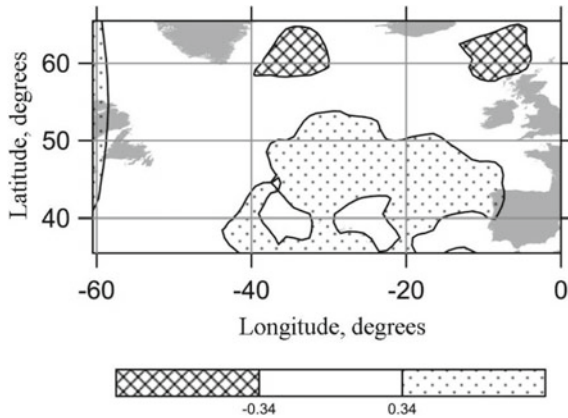


Fig. 1 Areas exhibiting significant and stable correlation between interannual variations in total durations of AAOs over the Denmark Strait and concurrent SST variations in September

of the AH. The latter results in SST rise in the northern part of the AH area, which is the more noticeable the longer the duration of the responsible AAO is. Since SST rise in the AH area leads to atmospheric pressure reduction therein, this process further intensifies the impact of variations in AAO TDs on the NAO index’s behavior.

In the final step of our research, we estimated the average flow rate of AAO-induced currents in the Denmark Strait. For this purpose, we modeled an Arctic outbreak with the following characteristics: duration—5 days, direction—0, speed—20 m/s (these values are close to maximum possible ones). The increment of the average daily flow rate, as computed by use of POM-model, was found to be 457,000 m³/s, which constitutes 12.4% of the average flow of Arctic waters entering the Atlantic through the Denmark Strait (3,694,444 m³/s). Since the AAO-induced flow increment is concentrated mostly in the near-surface layer, it is safe to conclude that AAOs’ impact on SST distribution in the affected areas of the NSHF zone is significant.

4 Conclusion

The main research results are as follows.

1. The frequency with which an outbreak of Arctic air will lead to a decrease in the NAO index depends on both the AAO duration and its location. The hypothesis presuming such correlation has been proved adequate.
2. The effect of an AAO-event on the NAO will be significant if the event lasts longer than 7 days.

3. The mechanism of this effect can be explained by AAOs' influence on flow rates of the currents delivering Arctic waters to the Icelandic Low area through the Denmark Strait and the Faroe-Iceland passage.

References

- Arctic system reanalysis. <https://climatedataguide.ucar.edu/climate-data/arctic-system-reanalysis-asr>. Accessed 01 May 2019
- Bromwich DH, Wilson AB, Bai LS, Moore GW, Bauer P (2016) A comparison of the regional Arctic system reanalysis and the global ERA–interim reanalysis for the Arctic. *Quar J R Meteorological Soc* 142:644–658
- Blumberg AF, Mellor GL (1987) A description of three dimensional coastal ocean circulation model. In: Heaps N (ed) *Three-dimensional coastal Ocean models*, vol 4. American Geophysical Union, Washington, DC, pp 1–16
- Cherkesov LV, Ivanov VA, Khartiev SM (1992) Introduction into hydrodynamics and wave theory. *Gidrometeoizdat*, St. Petersburg, p 264 ((in Russian))
- Courant R, Friedrichs KO, Lewy H (1967) On the partial difference equations of mathematical physics. *IBM J Res Dev* 11(2):215–234
- Dzrdzhevskii BL, Kurganskaya VM, Vitvickaya ZM (1946) Categorization of circulation mechanisms in the Northern Hemisphere and synoptic seasons characteristics. In: *Tr. n.-i. uchrezhdenij Gl. upr. gidrometeorol. sluzhby pri Sovete Ministrov SSSR. Ser. 2. Sinopticheskaya meteorologiya*, vol 21. Moskva: Tsentral'nyi institut prognozov; Leningrad: Gidrometizdat, p 80 (in Russian)
- Dzrdzhevskii BL (1968) Circulation mechanisms in the Northern Hemisphere atmosphere in 20th century. In: *Materialy meteorologicheskikh issledovaniy. izd. IG AN SSSR i Mezhduded. Geofiz. Komiteta pri Prezidiume AN SSSR*, p 240 (in Russian)
- General bathymetric chart of the oceans. <https://www.gebco.net>. Accessed 01 May 2019
- Hurrell JW, Kushnir Y, Ottensen G, Visbeck M (2003) An overview of the North Atlantic oscillation: climatic significance and environmental impact. *Geophys Monogr* 134:1–35
- Johnson NC, Feldstein SB, Tremblay D (2008) The continuum of Northern Hemisphere teleconnection patterns and a description of the NAO shift with the use of self-organizing maps. *J Climate* 21(23):6454–6471
- Hines KM, Bromwich DH (2008) Development and testing of Polar WRF. Part I. Greenland ice sheet meteorology. *Monthly Weather Rev* 136:1971–1989
- Kholoptsev AV, Podporin SA, Kurochkin LY (2018) Arctic air outbreaks and tendencies of weather variations in the oceanic regions of temperate climate zone. In: *World Science: Proceedings of articles the III international scientific conference. Czech Republic, Karlovy Vary–Russia*, Moscow, pp 450–460
- Kobzar AI (2006) *Applied mathematical statistics. a handbook for engineers and researchers*. Fizmatlit, Moscow, p 816 (in Russian)
- Kurbatkin GP, Smirnov VD (2010) Tropospheric temperature interannual variations associated with decadal changes in the North Atlantic Oscillation. *Izvestiya RAN Atmos Oceanic Phys* 46(4):401–413 ((in Russian))
- Mankin M (2011) *Atmospheric dynamics*. Cambridge University Press, London, p 512
- Mellor GL, Yamada T (1982) Development of a turbulence closure model for geophysical fluid problems. *Rev Geophys Space Phys* 20:851–875
- Mokhov II, Akperov MG, Prokofieva MA (2013) Blockings in the Northern Hemisphere and Euro-Atlantic region: change estimates according to reanalysis data and model computations. *Dokl Akad Nauk SSSR* 449(5):1–5 ((in Russian))

- Mokhov II, Yeliseev AV et al (2000) The North Atlantic oscillation: diagnosis and modelling of decadal variability and long-term evolution. *Izvestiya RAN Atmos Oceanic Phys* 36(5):605–616 ((in Russian))
- North Atlantic Oscillation (NAO). <https://crudata.uea.ac.uk/cru/data/nao/> Accessed 01 May 2019
- NCEP/NCAR reanalysis data. <ftp://ftp.cdc.noaa.gov/Datasets/ncep.reanalysis.dailyavgs/pressure/> Accessed 01 May 2019
- Nesterov YS (2013) North Atlantic oscillation: atmosphere and ocean, p 144. Triada, Ltd., Moscow ((in Russian))
- NOAA Optimum Interpolation Sea Surface Temperature. <https://www.esrl.noaa.gov/psd/data/gridded/data.noaa.oisst.v2.html>. Accessed 01 May 2019
- Rodwell MJ, Rowell DP, Folland CK (1999) Simulating the winter North Atlantic oscillation and European climate, 1947–1997. In: Research activities in atmospheric and oceanic modeling. Rep. №28, WMO/TD 942, pp 633–634
- Shakina NP, Ivanova AR (2010) The blocking anticyclones: the state of studies and forecasting. *Russ Meteorol Hydrol* 35(11):721–730 ((in Russian))
- Salby ML (1996) Fundamentals of atmospheric physics. Academic Press, New-York, p 560
- Skvortsov AV, Mirza NS (2006) Triangulation formation and analysis algorithms. Tomsk Univ Publ, Tomsk, p 168 ((in Russian))
- Smagorinsky J (1963) General circulation experiments with primitive equations. *Mon Weath Rev* 91:99–164
- Wannawong W, Wongwises U, Vongvisessomjai S (2011) Mathematical modeling of storm surge in three dimensional primitive equations. *Int J Math Comput Phys Electrical Comput Eng* 6:797–806

Information Resources of Marine Hydrophysical Institute, RAS: Current State and Development Prospects



T. M. Bayankina, E. A. Godin, E. V. Zhuk, A. V. Ingerov, E. A. Isaeva,
and M. P. Vetsalo

Abstract In Marine Hydrophysical Institute of Russian Academy of Sciences (MHI) the work on the development of oceanographic databases has been conducted for a long time. In recent years, a number of databases of model calculation results have been created in MHI along with databases of observed data. The article deals with some of the databases formed in MHI and some other MHI information resources, as well as with the problems of providing database access. The questions of developing a distributed information system with a single access point (MHI BOD) via local network are also under consideration in order to provide users with the access to the available information.

Keywords Databases and data banks · The Black sea · Drifters · Numerical modelling · Data access

1 Introduction

Information support is of great importance when planning and conducting oceanographic and climatic research, studying ecological state of seas and oceans, and carrying out different marine economy activities. In this regard, development and creation of oceanographic data banks and specialized databases remain a key aspect of the work in the field of up-to-date marine information systems and technologies (Intergovernmental Oceanographic Commission of UNESCO 2017). In recent years, along with observational databases, databases of model estimates have been becoming increasingly common due to the continuous improvement of mathematical modelling techniques.

In the framework of both national and international projects (<https://www.seadat.net.org>; <http://www.blackseascene.net>; <https://www.emodnet-chemistry.eu>), Marine

T. M. Bayankina (✉) · E. A. Godin · E. V. Zhuk · A. V. Ingerov · E. A. Isaeva · M. P. Vetsalo
Marine Hydrophysical Institute of RAS, Sevastopol, Russia
e-mail: bayankina_t@mail.ru

E. A. Godin
e-mail: godin_ea@mhi-ras.ru

Hydrophysical Institute (MHI) has gained an extensive experience in creating oceanographic data banks and databases and developing different information products on this basis. Let us give a brief description of several MHI information resources and databases formed in MHI.

2 The MHI Oceanographic Data Bank

The MHI Oceanographic Data Bank (BOD, <https://www.bod-mhi.ru/>) has been functioning for more than 25 years and contains oceanographic and meteorological data obtained in cruises of research vessels of MHI and other institutions in the Black, Azov, and Mediterranean seas, as well as in the Atlantic, Indian, and Pacific oceans.

A special place in the MHI BOD belongs to the Black Sea specialized database which includes oceanographic data obtained in the basin by research vessels of Russia, Ukraine, Bulgaria, Turkey, U.S.A., France, Romania, Denmark, and other countries (Fig. 1).

A part of the data entered the MHI BOD because of active involvement of the institute in the international projects and in the International Oceanographic Data and Information Exchange Programme of UNESCO Intergovernmental Oceanographic Commission.

The Black Sea database combines a number of observational arrays:

- Hydrological data (temperature and salinity at more than 165,000 oceanographic stations since 1884)
- Hydrochemical data (more than 46,000 stations since 1923; 20 chemical parameters)
- Hydrooptical data (more than 6000 Secchi disc measurements and 2,500 Forel scale observations)

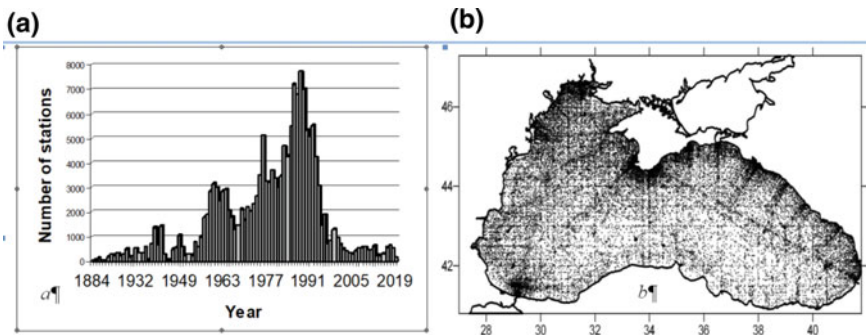


Fig. 1 Distribution of hydrological stations on years (a) and spatial distribution of oceanographic stations (b) in the Black Sea specialized database

- Meteorological data (more than 26,000 stations done by research vessels of MHI and the Black Sea Fleet Hydrographic Service).

An apparent advantage of the Black Sea database is the fact that 80% of hydrological data contained in it have passed through the quality check procedure (Eremeev et al. 2014).

According to the problems under solution, other specialized databases can be formed using the Black Sea database, e.g. for information support of coastal research, studying location of the upper boundary of anaerobic waters in the Black sea, analyzing ecological state of the Yalta bay waters, etc.

For the recent decades, drifter technologies have been widespread as a tool for the operational contact monitoring of the World Ocean. MHI considerably succeeded both in developing drifters of various types and in carrying out oceanographic research with their use. Based on the obtained drifter observations, two databases were formed to estimate the results of modelling the sea surface temperature field (SST).

The drifter database on the Black sea includes data on atmospheric pressure and seawater temperature on nominal levels with 1 h resolution which were obtained from 68 drifters of different modifications (Fig. 2a). The common duration of the drifters' work in the Black sea exceeded 150,000 h with an average drifter lifespan equal to 90 days (Motyzhev et al. 2016).

The drifter database on the Arctic region contains data from 22 temperature profiling drifters which provide measuring drift parameters, vertical profiles of temperature of ice and upper water (including under ice) layer down to 80 m, and atmospheric pressure with 1 h resolution (Fig. 2b). The duration of the drifter work is 1–3 years (Motyzhev et al. 2016).

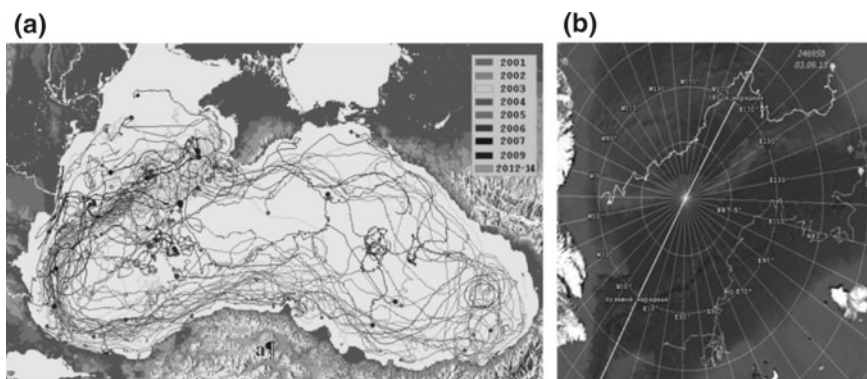


Fig. 2 Drifter trajectories in the Black sea experiments in 2001–2014 (a) and trajectories of “ice” temperature profiling drifters in the Central Arctic (b)

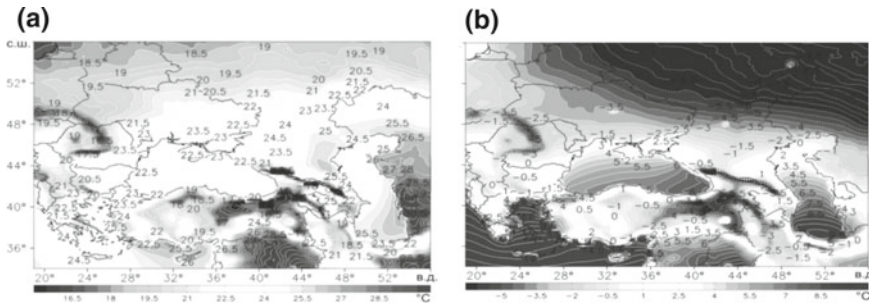


Fig. 3 Values of surface air temperature (°C) simulated using the adapted RegCM4 model data of 1979–2013 for summer (a) and for winter (b)

3 The Database on Numerical Reanalysis of the Atmospheric Circulation Characteristics for the Black Sea—Caspian Region

To form the database on numerical reanalysis of the atmospheric circulation characteristics for the Black sea—Caspian region, MHI used an up-to-date model of regional atmospheric circulation with higher spatial resolution RegCM4 developed in the International Centre for Theoretical Physics (Trieste, Italy). MHI adapted the model (25×25 km spatial resolution) with 1 min time step for the geographic peculiarities of the Black sea—Caspian region in 1979–2013 (Efimov et al. 2017). Validation of the regional model was conducted by comparing the results to the input large-scale data.

The analysis showed the model was capable to reconstruct correctly the climate in the region while maintaining the initial integral climatic characteristics. The model plausibly reconstructs the annual course and seasonal spatial distributions of the main meteorological parameters: temperature, precipitation, and wind circulation (Dee et al. 2011; Giorgi and Anyah 2012; Mearns et al. 2012). The obtained data on heat, moisture, and wind speed flows characterize the conditions of occurrence of abnormal sea surface temperature (SST) in the Black sea. Figure 3 presents an example of surface air temperature values simulated using the adapted RegCM4 model (Anisimov et al. 2015).

4 The Database of the Black Sea Hydrophysical Fields

The database of the Black sea hydrophysical fields (1993–2015) was formed in MHI using the results of reanalysis based on remote sensing data assimilation in the numerical model of the Black Sea circulation (Dorofeev et al. 2017). It includes arrays of hydrophysical parameters (seawater temperature, salinity, zonal and meridional current speed components, vertical current speed, and sea surface

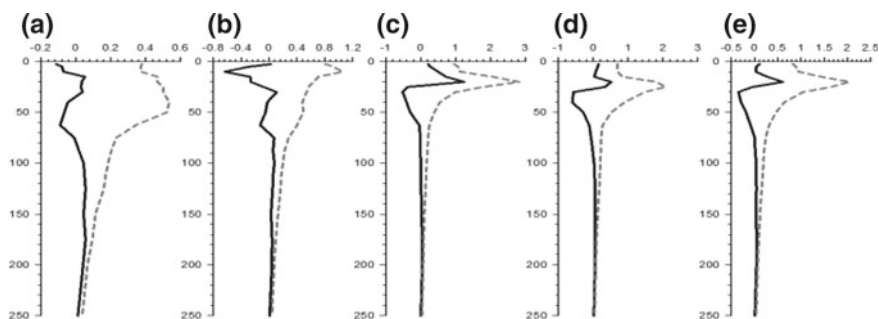


Fig. 4 Means (full lines) and standard deviations (dotted lines) of measured data from the results of the sea temperature reanalysis: **a** winter; **b** spring; **c** summer; **d** autumn; **e** statistics for the entire data array

height) calculated on a regular grid 4.8×4.8 km (238×132 knots) horizontally and at 35 uneven levels vertically with 1 day discreteness. The sea temperature data (SST), sea level anomalies, and annual-mean temperature and salinity profiles were assimilated in the circulation model of the Black sea for reanalysis. SST data were taken from the GHRSSST and NODC archives (1993–2009) and from the OSI TAC archive for the latest period (2010–2012). All the satellite altimetry data available in the NASA, AVISO, and SL TAC archives were used. To estimate the quality of reanalysis products, they were compared to hydrographic measurements using temperature and salinity profiles based on data from hydrological surveys and ARGO drifters from 1985 to 2013. At the final stage, the data were interpolated on selected levels for further calculations. Based on these data, means and standard deviations from simulations were calculated both for the entire array and for each season on design levels of the circulation model. Figure 4 shows the seawater temperature distribution on depth.

5 Satellite Database

At present, satellite techniques are of great importance in studying the ocean and atmosphere. The remote sounding allows the environmental research using qualitatively new information, which has no analogues in its spatial and temporal characteristics and is efficiently used for solving different problems of ecological monitoring. The MHI Marine portal (<https://dvs.net.ru/>) is intended to provide the access to operational satellite monitoring data for potential users. The Black sea and the sea of Azov are the main subjects of investigation. The data archive contains satellite maps and model output (Fig. 5) for the set of the sea surface parameters. All data are available with time delay 12–36 h after satellite pass. Additionally, model forecasts for sea surface temperature and surface currents are produced.

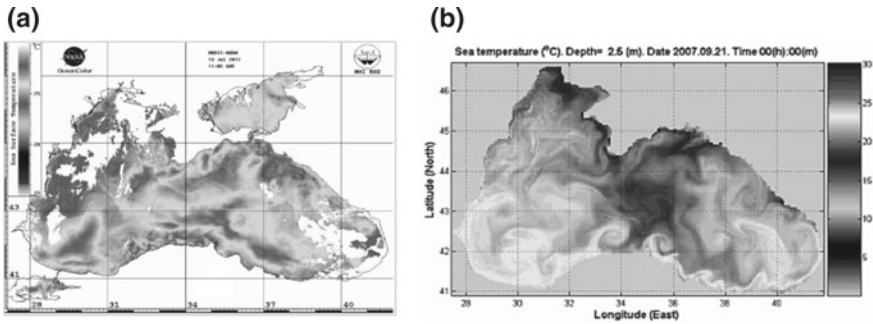


Fig. 5 The examples of data presentation at the MHI Marine portal: **a** sea surface temperature from MODIS-Aqua satellite data; **b** model output

Every day the following satellite data on the Black sea and the sea of Azov are located on the portal:

- Sea surface temperature data from AVHRR instruments onboard NOAA and MetOp satellites (from September 2004 to date; up to 10 maps per day)
- Sea surface temperature, water-leaving radiance, and chlorophyll-a concentration data from MODIS-Aqua satellite (from April 2006 to date)
- Sea surface temperature, water-leaving radiance, and chlorophyll-a concentration data from VIIRS satellite (from January 2012 to date)
- Ice situation in the Sea of Azov data from NOAA and MODIS satellites (from 2006 to date; one map per day if there is ice cover).

In addition to that, from June 2011 to date reanalysis data have been presented on the site for the following parameters:

- Geostrophic speed (one map per day, for 00.00 GMT)
- Surface current speed (4 maps per day, for 00.00, 06.00, 12.00, and 18.00 GMT)
- Wind speed (4 maps per day, for 00.00, 06.00, 12.00, and 18.00 GMT).

6 Satellite Database of Bio-optical Characteristics

Considerable satellite data arrays accumulated in MHI allowed to form the Black sea satellite database of bio-optical parameters and to create the Black sea Color information system. The database includes SeaWiFS and MODIS daily level-2 standard products (Feldman and McClain 2013). To provide a user with efficient information support, a structure for internal presentation of geographic information as maps of the Black sea bio-optical characteristics reflecting different aspects of the ecosystem state and its dynamics was developed (SeaWiFS:<http://oceancolor.gsfc.nasa.gov>).

The information system includes:

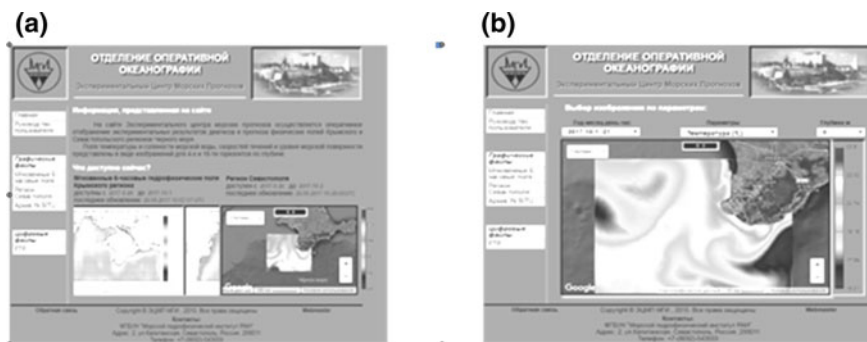


Fig. 6 The main page of ECMF website <https://www.innovation.org.ru/index.php> (a); an example of the system output (b)

- The database of processed daily satellite data on the Black sea bio-optical characteristics
- The geo-information system providing a user with the access to the database and allowing the spatial analysis of the bio-optical characteristics
- The web-based remote data access sub-system.

At present, users can access the Black sea Color information system at <https://blackseacolor.com> (Suslin et al. 2013, 2016).

7 The MHI Experimental Center of Marine Forecast

The MHI Experimental Center of Marine Forecast (ECMF) at present forecasts seawater temperature and salinity, current speed, and dynamical level of the Black sea surface up to three days before with 1 km spatial resolution. The Marine Coastal Forecasting System, improved in ECMF, is used to make the forecasts. The system prepares input data and makes prognostic calculations in automatic mode. The system outcomes are shown at <https://www.innovation.org.ru/index.php> (Fig. 6) and kept in the relevant database (Bayankina et al. 2015).

8 Data Access System: Prospects of Development

Along with formation of new databases and further development of the existing ones, providing potential users with the access to the available information is a relevant issue. At present, Internet access is enabled to the MHI BOD data (a limited array) and a number of information products, as well as to several other MHI information resources.

In order to optimize data storage and access, MHI is now developing a distributed information system with a single access point (MHI BOD) via local network (Fig. 7).

The approach will ensure data quality check and operational updating databases by relevant specialists. It will also establish necessary conditions for providing users with an opportunity to realize complex queries for selection from different databases (Fig. 8). The approach implies integration of heterogeneous data from different MHI information resources.

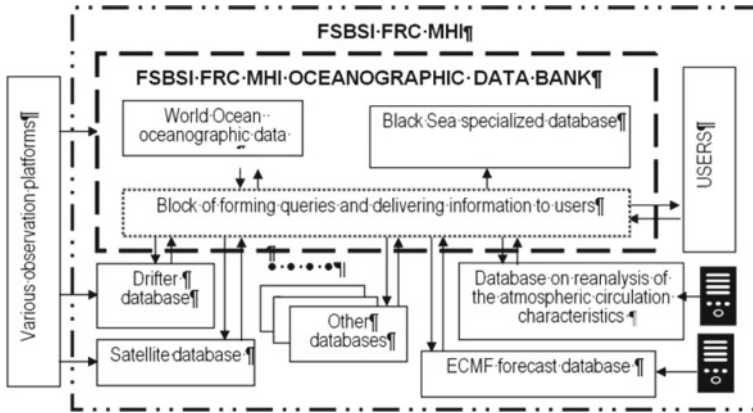


Fig. 7 Scheme of the distributed information system with a single access point via local network

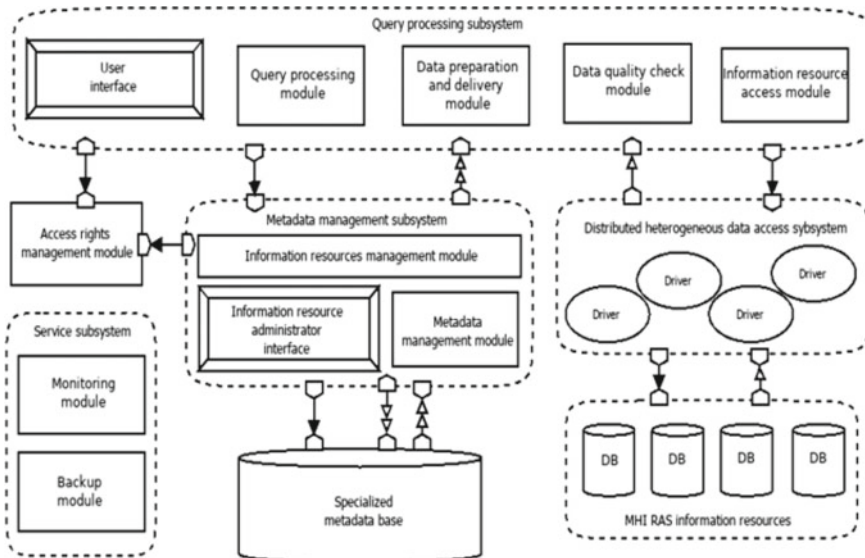


Fig. 8 Conceptual scheme of the information system providing data access and management

A specialized metadata base, containing description of basic characteristics of information resources and data stored therein, is to be designed for integrating heterogeneous data from different MHI information resources. In this case, data can be integrated based on coinciding or close characteristics such as observation time and location, a way of data obtaining, etc. The approach also allows including any additional information in metadata, particularly data authorship.

To provide metadata management it is necessary to design a subsystem including Information resources management module and Metadata management module. Information resources management module is intended for creating and editing records on information resources, which are accessible using the distributed information system mentioned above. Metadata management module will allow working with information on the data stored in a particular MHI information resource. The interaction between an operator and Metadata management subsystem is realized via Information resource administrator interface. The access to the resource can be given to an MHI specialist responsible for the relevant database. As the administrator interface within the system concept is considered to be a specific module, several different versions of the interface can be developed, including a browser one providing internet access and a local one for Windows and Linux operation systems.

To provide data access it is supposed to design Query processing subsystem realizing the whole cycle of query/response passing within the information system. The interaction between a user and the system can be ensured via a virtual System user interface, which is an instrument to form parameters of a query and provides its conversion into the internal code of the information system, its transmission for processing, and obtaining results.

User queries enter User query processing module, which produces an initial analysis of the query parameters, works out a plan of processing the query, and forms a query-processing queue. The query queue is processed by Information resources access module, which initiates addressing a relevant driver and converts data from an information resource into the internal code of the information system.

Data preparation and delivery module enables conversion of data obtained from the information resources from the internal code into a format required by a user and provides the data delivery to an end user. Therefore, the module can include a set of submodules to support conversion into some common data formats suitable for processing by specialized software, such as CSV table, oceanographic cruise data processing software "Hydrolog", NetCDF format, etc.

If it is necessary (e.g., a user sets a relevant query parameter), a special Data quality check module can be designed to provide passing of data from an information resource through an automatic quality check procedure (for the parameters where it is possible). In its turn, Data quality check module can be realized as a set of submodules to enable quality check for different kinds of data (hydrology, chemistry, biology, etc.). While working out the submodules, it is necessary to use the MHI practice and expertise in this field in full measure.

It is proposed to develop Access rights management module to differentiate the rights and levels of the data and metadata access. The module will allow configuring flexible user capabilities in the system (up to working with certain information resources) and provide keeping confidential information.

Service subsystem is intended to monitor the system operation and provide data security. Monitoring module will collect and keep technical specifications of the system operation including hardware and software (within both the subsystems in general and certain modules). The number and list of the kept parameters should give an opportunity of making informed decisions in order to prevent faults and to improve the system technical specifications. Backup module is necessary to prevent information loss (metadata and other system internal information) because of faults and to ensure version control and possibility of fast data recovery.

The further development of the MHI information capacity is related to the plans for renewal of the oceanographic platform of the Black sea hydrophysical polygon (Katsiveli) and creating a system of information collection and transmission on its basis.

The system under development is supposed to transmit real or near-real time data to relevant servers that will be involved in the distributed information system of MHI.

The activities will promote the further involvement of the MHI information resources into national (Mikhailov et al. 2014) and international oceanographic data access systems.

References

- Anisimov AE, Yarovaya DA, Barabanov VS (2015) Reanalysis of atmospheric circulation for the Black Sea-Caspian Region. *Marine Hydrophys J* 4:14–28 (in Russian)
- Bayankina TM, Ratner YB, Khaliulin AK, Godin EA, Voronina NN, Zhuk EV, Ingerov AV, Kryl' MV (2015) Interaction between MHI ECMF and BOD to provide forecasts of the state of the Black Sea Hydrophysical Fields. In: Proceedings of the International Scientific Conference “Hydrometeorological and Environmental Security of Marine Activity” (Astrakhan, Russian Federation, October 16–17, 2015. Astrakhan, pp 13–15 (in Russian)
- Dee DP, Uppala SM, Simmons AJ et al (2011) The ERA-interim reanalysis: configuration and performance of the data assimilation system. *Quart J Roy Meteorol Soc* 137(656):553–597
- Dorofeev VL Sukhikh LI, Bayankina TM, Pryakhina SF (2017) Reanalysis of hydrophysical fields on a regular grid for 1993–2015. Database State Registration Certificate No. 2017620804. Date of state registration in Register of Databases (In Russian)
- Efimov VV, Barabanov VS, Yarovaya DA, Yurovsky AV, Bayankina TM (2017) The array of numerical reanalysis of the atmospheric circulation characteristics for the Black Sea—Caspian Region for 1979–2013 Database State Registration Certificate No. 2017620805. Date of state registration in Register of Databases (in Russian)
- Eremeev VN, Khaliulin AK, Ingerov AV, Zhuk EV, Godin EA, Plastun TV (2014) Current state of the oceanographic data bank of MHI NAS of Ukraine: Software. *Marine Hydrophys J* 4:54–66 (in Russian)
- Feldman GC, McClain CR (2013) Ocean Color Web, SeaWiFS Reprocessing 2010.0, MODIS-Terra Reprocessing 2013.0, MODIS-Aqua Reprocessing 2013.1, MERIS Reprocessing 2012.0, NASA Goddard Space Flight Center. Kuring N, Bailey SW (eds). <https://oceancolor.gsfc.nasa.gov/>.

- Giorgi F, Anyah RO (2012) The road towards RegCM4. *Clim Res* 52:3–6
<https://www.seadatanet.org/>
<https://www.blackseascene.net/>
<https://www.emodnet-chemistry.eu>
- Intergovernmental Oceanographic Commission of UNESCO (2017). IOC strategic plan for oceanographic data and information management (2017–2021). Paris. (IOC Manuals and Guides, 77) 32pp. (IOC/2017/MG/77).
- Mearns LO, Arritt R, Biner S et al (2012) The North American Regional Climate change assessment program: overview of Phase I results. *Bull Am Meteorol Soc* 93:1337–1362
- Mikhailov NN, Vyazilov ED, Vorontsov AA, Ivanov VA, Khaliulin AK, Godin EA, Ereemeev VN, Tokarev YN (2014) ESIMO state and prospects with regard to formation of the Black Sea Regional Knot. *Ecological Safety of Coastal and Shelf Zones and Comprehensive Use of Shelf Resources*. Sevastopol, EKOSI-Gidrofizika Publ 28:387–402 ((in Russian))
- Motyzhev SV, Tolstosheev AP, Lunev EG, Bayankina TM, Litvinenko SR, Kryl' MV, Yurkevich NY, Mikhailova NV (2016) Database of the operational drifter observations in the Black Sea Region. Database State Registration Certificate No. 20166200404. Application No. 2016620106. Date of receipt 11.02.2016. Date of state registration in Register of Databases (in Russian)
- Motyzhev SV, Lunev EG, Tolstosheev AP (2016) The experience of barometric drifter application for investigating the World Ocean Arctic Region. *Marine Hydrophys J* 4:53–63 (In Russian).
<https://doi.org/10.22449/0233-7584-2016-4-53-63>
- Motyzhev SV, Tolstosheev AP, Lunev EG, Bayankina TM, Litvinenko SR, Kryl' MV, Yurkevich NY, Mikhailova NV (2016) Database of the operational drifter observations in the Arctic Region. Database State Registration Certificate No. 2016620889. Date of state registration in Register of Databases (in Russian)
- SeaWiFS: <https://oceancolor.gsfc.nasa.gov>
- Suslin VV, Churilova TY, Bayankina TM, Pryakhina SF (2016) The Black Sea satellite database of bio-optical parameters from SeaWiFS, MODIS, and MERIS Color Scanners. Database State Registration Certificate No. 2016621256. Date of state registration in Register of Databases 15.09.2016. Date of publication (in Russian)
- Suslin VV, Churilova TY, Suslina VN, Suslina NV (2013) Software to create website of displaying and loading bio-optical characteristics of the Black Sea, resulted from Processing Satellite Measurements, from the <https://www.blackseacolor.com> Server. Copywrite Certificate No. 48964. State Intellectual Property Service of Ukraine. Date of registration (in Russian)

Sea Bottom Sediments Pollution of the Crimean Coast (The Black and Azov Seas)



E. A. Tikhonova, E. A. Kotelyanets, and O. V. Soloveva

Abstract The aim of this research was to determine the content of trace elements and heavy metals (HM), extractable organic matter (EOM), total petroleum hydrocarbon content (TPC) in the sea bottom sediments of the Azov and Black Seas, to evaluate the ecological wellbeing of the region. The EOM amount was determined by gravimetric method, the TPC was determined by the method of infrared spectrometry. The metals and metals oxides were determined using XRF spectrometer «Max Spectroscan-G». The bottom sediments near the coast of Crimea (in 2016) were typical of the marine soils in the area. In the Black Sea, there was a trend to a progressive increase in the EOM content, but the bottom sediments were pure according to content of oil products. The content of HM varied in wide ranges. The vicinity to the pollution source did not always determine the zones of their elevated contents. In the Azov Sea, the resulting concentrations at most stations transcended those in the Black Sea. Values of Zn, V, Cr, Co exceeded their natural content in the shelf sediments throughout the expedition track. Ni content in Azov Sea demonstrated the existence of anthropogenic pollution sources.

Keywords Sea bottom sediments · Extractable organic matter · Total petroleum hydrocarbon content · Heavy metals · The Black Sea · The Azov Sea

1 Introduction

Current changes in the state of the Azov-Black Sea ecosystem are not only caused by natural factors, but also increased anthropogenic pressure (Petrenko et al. 2015). The existing problems (Petrenko et al. 2015) include pollution of rivers in the catchment area, intake of insufficiently cleaned industrial and domestic sewage, offshore gas

E. A. Tikhonova · O. V. Soloveva

A.O. Kovalevsky Institute of Biology of the Southern Seas of RAS, Russian Academy of Sciences, Sevastopol, Russia

E. A. Kotelyanets (✉)

Marine Hydrophysical Institute, Russian Academy of Sciences, Sevastopol, Russia

e-mail: plistus@mail.ru

production and use of biological resources. These days, sea transport (especially in the Kerch strait), recreation and hydraulic engineering (in particular, the Crimean bridge) provide additional pressure. Given the fact that the Azov-Black Sea basin is an inland water body with limited assimilation capacity, such level of anthropogenic load can lead to disastrous consequences for its ecosystem.

Sea bottom sediments are one of the most informative objects in the water environmental monitoring, especially near the coast. The pollutants incoming for a long time accumulate in the bottom sediments, and serve as an indicator of the ecological state of coastal ecosystems and a kind of integral indicator of the water body's pollution level. In addition, marine sediments participate in circulation of substances and energy. At the same time, they are the habitats of numerous benthic groups.

We selected coastal areas as the most representative for the environmental quality assessment, since they suffer most from anthropogenic activity, which contributes to formation of the special Black Sea ecosystems (Gurov et al. 2015). The study of physical and chemical properties of bottom sediments in the Black Sea, and observation of the processes in the "water – suspended matter – bottom sediments" system are an important part of the overall monitoring of coastal water areas (Gurov et al. 2015). The Sea of Azov is closed, shallow and suffers from increased anthropogenic load, so monitoring studies are necessary for decision making on maintaining its biological productivity.

Thus, the purpose of this research was to determine the content of trace elements and heavy metals (HM), extractable organic matter (EOM), total petroleum hydrocarbon content (TPC) in the sea bottom sediments of the Azov and Black Seas (including the north-western shelf, the Southern Coast of the Crimea (SCC), the Kerch Strait, the south-west of the Sea of Azov) to assess the ecological wellbeing of the water areas.

2 Materials

The samples were obtained in the 83rd voyage of the R/V "Professor Vodyanitsky" (winter 2016) at the stations (st.) (Fig. 1) located along the Crimea peninsula coast from the depth 24–1040 m in the Black sea and 9–18 m in the Azov sea.

Sea bottom sediments were collected with an automatic box-bottom grab ("Box corer") from an area of 25 × 25 cm. The upper 5 cm layer was used for the analysis. 11 samples were taken in the Black Sea (st. 2–15, st. 20, 21) and 4 in the Sea of Azov (st. 16–19). All the samples were packed in special containers and labeled.

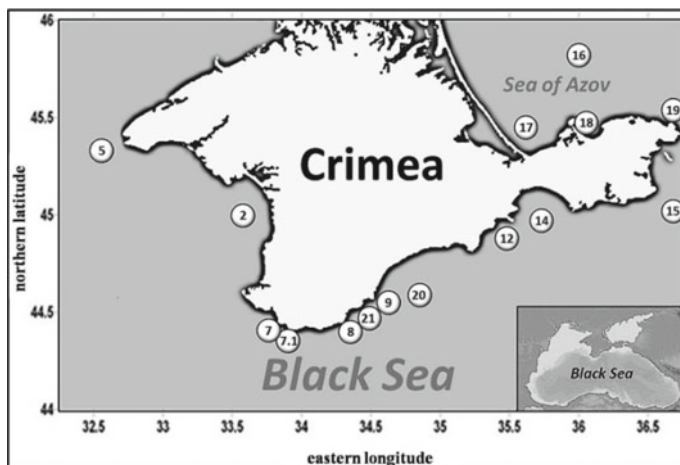


Fig. 1 Sampling stations of R/V “Professor Vodyanitsky” (83th voyage)

3 Methods

The pH and Eh values were measured in the just collected samples of bottom sediments on board using a Neutron-pH pH-meter. Under the laboratory conditions, the sediments were dried to an air-dry state and triturated in mortar. A part of each sample was sieved through sieves with a cell diameter of 0.25 mm to determine the concentrations of TPC and EOM; for HM a 0.071 mm nylon sieve was used. The total amount of EOM in the prepared samples was determined by the gravimetric method, TPC – IF-spectrometry method (SPM-1201) (Oradovskiy 1977). The total content of HM (Cr, Zn, Pb, As, Co, Sr, Ni, V) and metal oxides (MnO, TiO₂, Fe₂O₃) was measured by the method of X-ray fluorescence analysis using the spectrometer “Spectroscan Max-G” (Methods... 2002). All the results obtained for the concentrations of organic compounds were recalculated for 100 g of air-dry bottom sediments (air-dryb.s.).

The calibration characteristics for HM were plotted using certified samples of soil composition: typical black humus earth, sod-podzolic sandy-loam soil, red soil, and carbonate grey soil. The control samples (state standard samples of composition SSSC 163.1-98 and the SSSC 163.2-98) (Methods... 2002) were used to check the plot calibration correctness.

Currently, there are no national maximum permitted concentrations for the content of HM in marine sediments. Therefore, the concentrations of trace elements in bottom sediments are usually compared with either their Clarke numbers or background values for the studied marine systems (Methods... 2002; Mitropolskiy et al. 1982). Correlation analysis was made in “MS Excel 2003” and “Statistica”.

4 Results and Discussion

According to the data obtained, the content of EOM in the bottom sediments of the Black Sea was from 10 to 110 mg/100 g air-dry b. s. The concentration of TPC at most stations ranged from 1.7 to 10 mg/100 g. In the Azov Sea, the values were higher (107 to 187 mg/100 g for EOM). This corresponds to the sea bottom sediments to III-rd pollution level (Mironov et al. 1986). The TPC concentrations were in the same range as in the Black Sea (6.9–10.2 mg/100 g).

At the st. 7 in the Black Sea the highest values (Table 1) of HM (zinc, cobalt, chromium) content (44% of the samples) in the bottom sediments were noted. The amount of strontium and arsenic being close to the maximum values in the pre-strait zone (st. 15).

Table 1 Content of heavy metals in the bottom sediments of the Black and Azov Seas (Tikhonova et al. 2016)

Element	Variation limit		Average value	Content in the shelf sediments (Emelyanov et al. 2004)
	Minimum	Maximum		
Black Sea				
Zn, mg/kg	50.1	144.0	81.0	48
Ni, mg/kg	24.7	49.0	40.1	42
Co, mg/kg	35.0	164.7	71.0	14
Cr, mg/kg	84.0	178.8	124.3	45–90
V, mg/kg	58.1	324.7	162.1	90
As, mg/kg	8.6	130.4	57.4	5*
Sr, mg/kg	200.0	3085.0	666.1	300*
TiO ₂ , %	0.606	1.62	0.98	0.6–0.8
Fe ₂ O ₃ , %	3.16	10.35	6.3	5.08
MnO, %	0.028	0.06	0.04	0.38
Azov Sea				
Zn, mg/kg	84.0	195.2	117.2	48
Ni, mg/kg	45.0	54.4	48.1	42
Co, mg/kg	30.8	300.3	115.5	14
Cr, mg/kg	103.7	259.7	155.2	45–90
V, mg/kg	98.6	421.3	200.3	90
As, mg/kg	0.5	60.7	42.2	5*
Sr, mg/kg	174.6	433.0	276.2	300*
TiO ₂ , %	0.8	2.2	1.22	0.6–0.8
Fe ₂ O ₃ , %	5.3	16.1	8.61	5.08
MnO, %	0.05	0.083	0.07	0.38

*Concentrations according to B. V. Vinogradov (Dobrovolskiy 2003)

The highest amount of strontium was found at st. 15, which is most likely due to the soil texture (70% of shells), and zinc—at st. 21, near the sewage pipe of Yalta city. Lead was only found near the Karadag mountain range (st. 12). The lowest content of zinc, cobalt, chromium, vanadium and strontium was noted at st. 2 in the Kalamitsky Bay, arsenic—in the reserved water area of Karadag, nickel—in the bottom sediments of st. 15 before the entrance to the Kerch Strait.

The obtained values in the Sea of Azov at most stations exceeded those in the Black Sea, in particular, st. 16 recorded the maximum content of HM. The lowest concentration of HM was noted at st. 17 (50% of indicators), zinc and nickel at st. 19, and arsenic at st. 18.

It is known that the coastal zone is subject to hydrocarbon pollution more than other facies. The constant flux of allogenic material from various sources increases their concentration in bottom sediments. The nature of spatial distribution of pollutants, HM in particular, depends on a complex of natural and man-made factors, with sources of pollution, their power and mode being primary factors.

The sea bottom sediments studied in the framework of the 83rd expedition of the R/V “Professor Vodyanitsky” were typical of the muddy sediments mixed with shell rock and sand, which accumulate to a large extent both natural organic matter and allochthonous compounds. At some stations (st. 9, 14, 16, 18, 20) a whiff of hydrogen sulfide was noted. The bottom sediments at the Black Sea stations were consistently getting finer with depth.

The active reaction of the medium in the the Black Sea bottom sediments was slightly alkaline and the pH ranged from 7.53 to 7.82 (Fig. 2), with the exception of st. 2 near Yevpatoria, where the pH value increased to 8.42, which is most likely due to the type of sedimentation and the close recreation zone.

The redox potential directly depends on the distribution of bottom sediments particle size (Mironov et al. 1992). The reducing conditions of the environment (negative Eh) were found in the bottom sediments at two stations (st. 16—the shallow water station in the Sea of Azov (11 m) and st. 20—the deepest station in the Black Sea (1040 m)) with Eh values -165 and -174 mV, respectively (Fig. 2). The sea bottom sediments at st. 16 contained a large amount of decomposed organic matter and a strong odor of hydrogen sulfide. It was also noted at st. 20. Most of the bottom sediments of the Crimean Black Sea coast had oxidizing environmental conditions: Eh = $+82 \dots +210$ mV. The exception was st. 5 with slightly reducing medium conditions (Eh = $+3$ mV) near cape Tarkhankut, which is typical of this region according to data (Mironov et al. 1992). The bottom sediments of the Sea of Azov had slightly reducing environmental conditions (Eh = $+1 \dots +44$ mV), with the exception of st. 16. These conditions enhance accumulation of hydrocarbons, because when redox potential of the medium is low, the bitumen transformation slows down.

It is known that Eh depends on pH. To obtain comparable data in the studied bottom sediments with different pH values, we calculated the hydrogen potential index (Fig. 3) using the Clark equation ($rH_2 = Eh/29 + 2pH$) (Ganzhara 2001). This index allows to compare different sediments considering Eh and pH values simultaneously.

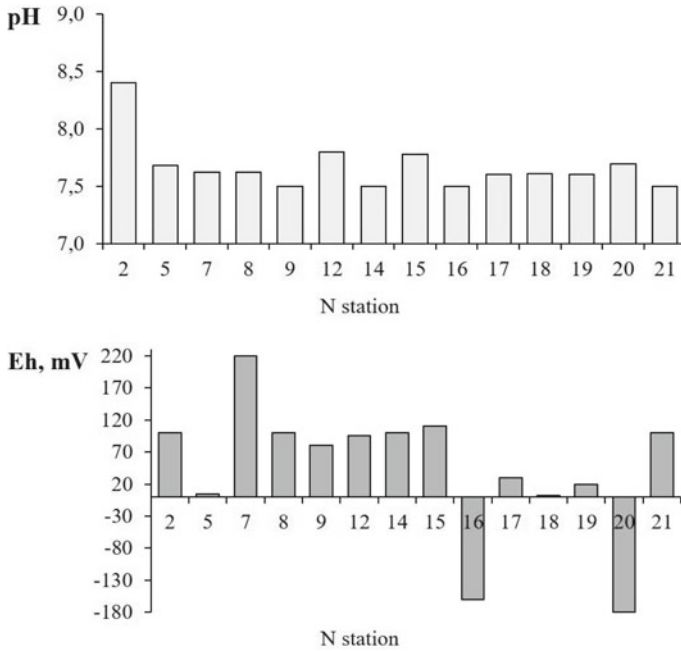


Fig. 2 Physicochemical pH and Eh parameters in the sea bottom sediments (Tikhonova et al. 2016)

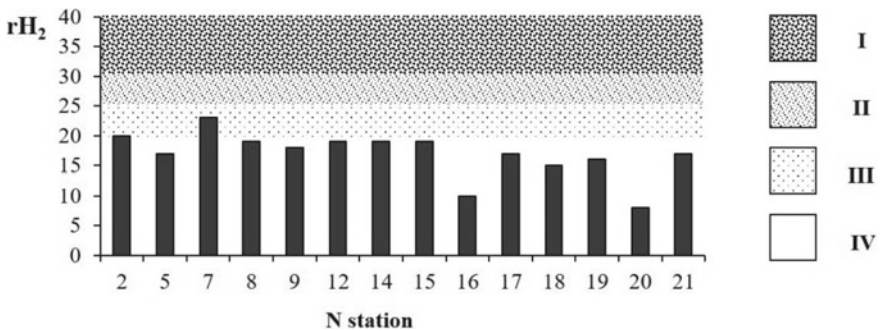


Fig. 3 Indicator rH_2 of the bottom sediment in the different parts of Crimea peninsula coast (Tikhonova et al. 2016). I—oxidation processes, II—predominantly oxidation processes, III—predominantly reduction processes, IV—reduction processes

According to scale described in (Ganzhara 2001), when rH_2 is above 27, oxidative processes prevail, when it equals 22–25 - reducing, and below 20 - intense reducing. In our case, this indicator did not exceed 27, which indicates a low level of predominating oxidative processes. Reducing reaction was characteristic of the bottom sediments at st. 7. At other stations, with $rH_2 < 20$, intensive reductive processes occurred (Fig. 3).

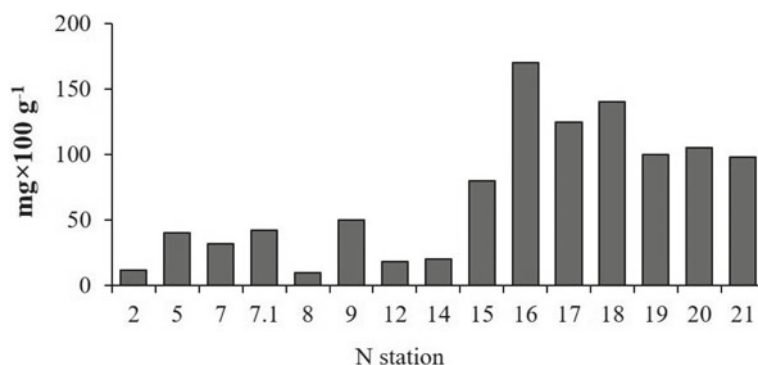


Fig. 4 EOM concentration in the different parts of Crimea peninsula coast (Tikhonova et al. 2016).

Concentration of EOM detected in the Black Sea region bottom sediments was 10–110 mg/100 g (Fig. 4). Near the cape Ai-Todor the minimum values were noted, and the maximum—at the deep-water st. 20 and near the Yalta sewage pipe (st. 21). These values were very close and amounted to 110 and 106 mg/100 g respectively. The obtained indicators (Mironov et al. 1986) referred to the III level of pollution, although they are close to its lower bound. However, this demonstrates the input of allochthonous hydrocarbons in the studied water area. At the same time, according to the department of marine sanitary hydrobiology (DMSH) of the Institute of Marine Biological Research (IMBR) data, the content of TPC at st. 20 was close to 0. It was in the open sea where wave mixing predominates and marine environment may become unrepresentative for this analysis under some weather conditions. Concerning the water area near the sewage pipe, the OH were found both in the bottom and in the surface water layers. Their concentration was lower than the MPC. Thus, we can suggest the presence of an TPC source in this area. Increased concentrations of EOM were noted in the bottom sediments of the Sea of Azov. They reached 187 mg/100 g. High values were also found at st. 15 (72 mg/100 g) at the entrance to the Kerch Strait from the Black Sea. A high level of anthropogenic load can explain these indicators.

Compare the obtained data with these of the past years. Concentrations of EOM in the bottom sediments along the coast of the Crimea were typical of the region (Mironov et al. 1992). However, at st. 12 near Karadag, it was 11 to 14 mg/100 g, while we registered 16 mg/100 g. That is, relative to 1976, levels of EOM are elevated. In general, sea bottom sediments were not contaminated with oil products.

For the bottom sediments of the Sea of Azov, the highest recorded values (187 mg/100 g) equaled to those obtained by us in 2010 (186 mg/100 g) (Yurovskiy et al. 2012). In general, the concentrations of EOM did not exceed the previously noted and inherent for the studied area (for shell rocks—20 mg/100 g, for pelitic silts - up to 230 mg/100 g) (Mironov 1996). The data obtained on the characteristics of the sea bottom sediments corresponded to the previously described results and could be called natural-pure (Krylenko and Krylenko 2013; Tikhonova and Guseva 2012).

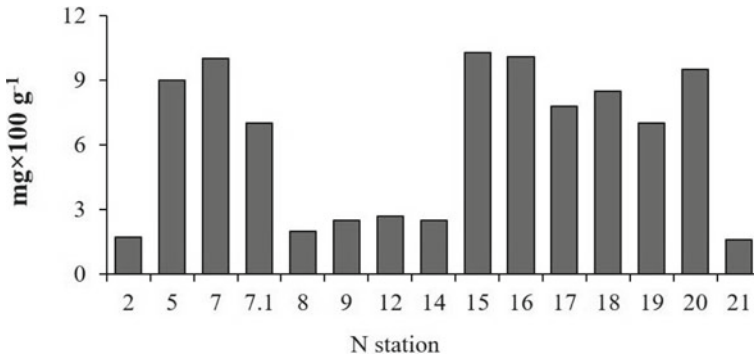


Fig. 5 The TPC concentration in the different parts of Crimea peninsula coast (Tikhonova et al. 2016).

Oil pollution was minimal in the Black and Azov Seas. At most stations, trace amounts were noted (up to 5 mg/100 g) (Fig. 5). Earlier (2010) in the bottom sediments of the Azov Sea, these figures were noted in 65% of samples (Yurovskiy et al. 2012), whereas at present we have noted concentrations higher than trace values in all samples. However, the obtained results are typical for clean and slightly polluted waters of the Black Sea.

The highest values of TPC were found at st. 15 (10.3 mg/100 g) near the entrance to the Kerch Strait and at st. 16 (10.2 mg/100 g), Azov Sea, which was natural for this shipping area. Earlier, from 2007 to 2010 (Yurovskiy et al. 2012) there was a slight decrease in the content of EOM and TPC. In 2016 we obtained higher values of these indicators. In the Black Sea part of the Kerch Strait, the content of EOM was 72 mg/100 g, whereas in 2010 only 30.2 mg/100 g; TPC—10.3 mg/100 g, and in 2010—3.4 mg/100 g. That is, the recorded concentrations of EOM and TPC were 3 times higher compared to the data of 2010. This indicates contemporary processes of oil pollution accumulation associated with constant effluence of petroleum products in the strait and pre-strait zone.

The TPC percentage (Fig. 6) of EOM ranged from 1 to 31%. The largest share

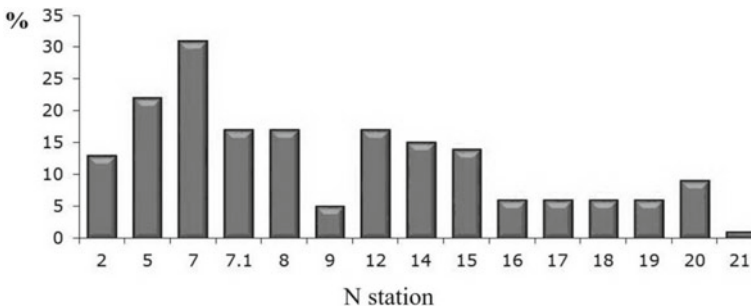


Fig. 6 The TPC percentage of EOM (Tikhonova et al. 2016)

of TPC was noted at st. 5 and st. 7, which indicates the anthropogenic origin of hydrocarbons. This was confirmed by the data on the TPC concentration in the surface layer (data of DMSH IMBI) – in the areas of nature protection the maximum permitted concentration of oil products in the water was outmatched. For example, this phenomenon was registered in the water area of cape Tarkhankut and in the area of cape Aya. In the water areas of other reserves and wildlife sanctuaries, trace values of TPC were recorded. It should be noted that in the bottom sediments of the Azov Sea region, the TPC and EOM ratio was the same at all the stations and amounted to 6%.

Correlation dependence ($r = 0.5$) between the contents of EOM and TPC in the studied region was weak. When their concentrations are high, e.g. in the sediments of ports, this dependence is stronger (Rubcova et al. 2013).

Thus, the obtained data on the content of EOM and TPC as well as physical and chemical features of the bottom sediments suggest that at present (2016) the properties of bottom sediments off the Southern Coast of the Crimea are typical of marine soils of the study region. It indicates the well-being of the study area as a whole. The bottom sediments in the Black Sea were less polluted with organic substances (level I-II) than in the Sea of Azov (level III). The exceptions in the Black Sea were at the deep-water st. 20 and st. 21 near the Yalta city sewage pipe. At the same time, the obtained values of EOM were at the lower boundary of level III. In general, there was a tendency to a gradual increase in EOM near the Black Sea coast, but the bottom sediments were not contaminated with oil products.

High concentrations of pollutants indicate the entry and existence of anthropogenic pollutants into silt bottom sediments with admixture of detritus. The maximum values of such trace elements as zinc, nickel, cobalt and chromium were found in the shallow water st. 16 in the Sea of Azov, where the sea soil was represented by silts with a large amount of EOM. The maximum content of Zn (195 mg/kg) in the bottom sediments exceeded its average value (140 mg/kg) at the shelf (Mitropolskiy et al. 1982). Earlier (Kotelyanets and Konovalov 2012), the content of this element in the area of the pre-strait zone of the Kerch Strait (st. 15) was 90 mg/kg, whereas in 2016 it was almost 2 times less (51.2 mg/kg). Zinc is a “universal pollutant”, which is a part of the technogenic streams of almost all sources (Emelyanov et al. 2004), so it was recorded throughout this anthropogenically-loaded water area (Surova and Kuznecova 2002; Sovga et al. 2008). According to the authors (Kotelyanets and Konovalov 2012), the minimum Zn content in the Kerch water area increased 1.5 times compare to 2005, although its maximum content in 2007 and 2008 did not exceed the 2005 values. That is, this element is distributed unevenly in the study area. In the Black Sea, an excess of Zn content was recorded in the bottom sediments of the shelf at st. 7 while at the other stations the average concentration was 73.97 mg/kg, which was almost 2 times smaller.

At 100% of the stations in the Sea of Azov, the Ni content exceeded (with a maximum value at st. of 16–54.41 mg/kg) the average concentrations in the sediments of the shelf (42 mg/kg) (Emelyanov et al. 2004). Nickel can accumulate in the bottom sediments, in the immediate vicinity of the main sources of input. Accumulation of Ni in bottom sediments, especially at the coastal zone, correlates with the activity

of industrial and domestic sources of pollution (Nikanorov 1989). In the Black Sea, this indicator was exceeded at 36% of the stations, with the highest values at st. 7 (46 mg/kg) and st. 21 (49 mg/kg). At the pre-strait st. 15, there was some decrease in the content of both nickel and zinc (25 mg/kg versus 37 mg/kg) (Kotelyanets and Kononov 2012). A weak dependence was noted between the concentrations of zinc and nickel in bottom sediments and EOM ($r = 0.5$).

Cobalt concentrations at all the coastal stations exceeded the average values at the shelf—14 mg/kg (Mitropolskiy et al. 1982). The content of Co in the upper layer of bottom sediments is quite high at st. 7 (165 mg/kg), and st. 8 (122 mg/kg). Its highest content (300 mg/kg) was determined at st. 16, which was 21 times higher than its average value.

Distributions of chromium and cobalt were similar. They exceeded the average shelf values (45–90 mg/kg) at all stations, except for the Black Sea st. 2, where its concentration was close to the upper limit of standard values (84 mg/kg). Usually, an increase in the Cr content is characteristic of ports and berthing areas (Emelyanov et al. 2004). The maximum chromium content (260 mg/kg) was determined at st. 16. The highest concentration of this metal exceeded the approximate maximum permitted concentration by almost 2.5 times.

Elevated concentrations of vanadium were mainly confined to the coastal areas. Almost at all stations, except for st. 2, the V content exceeded the values at the Black Sea shelf (Mitropolskiy et al. 1982). The highest concentration in the Sea of Azov was noted at st. 16 (421.3 mg/kg), and in Black Sea at st. 7 (324.7 mg/kg).

According to (Mitropolskiy et al. 1982), arsenic level in the upper layer of sediments in the Black Sea was 0–130.4 mg/kg. The data obtained correspond to these values, but the lower limit was slightly higher—8.6 mg/kg. The average values in the Black Sea were higher than in the Azov Sea—55.4 and 42.2 mg/kg, respectively. At the same time, at st. 2, 12, 18 As concentration was below the detection limit by the X-ray fluorescence method (<20 mg/kg). According to (Perelman 1989), the arsenics Clarke number is 1 mg/kg, so the samples of bottom sediments in the Crimean region can be considered rich in this element, with the exception of st. 2, 12, 18.

Concentration of strontium in the Black Sea sediments ranged from 200 (st. 2) to 647.4 (st. 8) mg/kg, with the exception of st. 15 where the highest content of 3085 mg/kg was noted. It is most likely related to sediments grain size distribution (Lukyanov et al. 2011). The values higher than the Clarke number of 510 mg/kg (Perelman 1989) were noted at 36% of stations in the Black Sea, whereas in the Azov region they did not exceed it at 100% stations.

Lead concentration in the bottom sediments was below the detection limit by the X-ray fluorescence method (Methods... 2002). However, its minimal concentrations were found in the area of the Karadag nature reserve. According to the authors (Tikhonova et al. 2015), in 2000 an excess of lead concentration was registered in water samples from the sources of Gyaur-Cheshme in the Valley of Roses (Karadag nature reserve), as well as in samples of well water at the Karadag biostation. It was more than 10 MPS (MPS = 0.1 mg/l). However, sampling in fresh and marine waters

in 2001 did not reveal it. This demonstrates that the source of Pb was non-permanent. Despite this type of pollution, at present, Karadag, was characterized by plenitude and biodiversity of bottom aquatic organisms (Kiseleva et al. 2002) in comparison with other areas of the Black Sea.

The average level of Mn in the sea bottom sediments of the Black Sea coast was 0.04%, the maximum (0.06%) was determined at the deep-water st. 20. In the Azov Sea it was 0.07% with a maximum of 0.08% at st. 18. Concentration of this element was much less than its background values in the studied region (Mitropolskiy et al. 1982).

The spatial distribution of Ti and Fe was characterized by minimal concentrations in the Kalamitsky Bay (st. 2) and elevated values in the coastal waters near cape Ayia (st. 7), the pre-strait zone of the Black Sea (st. 15) and the Azov Sea (st. 16). The average Ti content in the Black Sea was 0.98%. The maximum (1.6%, st. 7) was 39% higher than the average, which was exceeded at 36% of stations. In the Sea of Azov, the concentration of Ti at all the stations was above its content in the sediments of the shelf. The Fe content in the Sea of Azov, as well as Ti, exceeded the limit values. In the Black Sea, these figures were slightly lower. Compare titanium oxides concentrations with the Clarke number of titanium in the earth crust (0.56%) (Chertko and Chertko 2008), the content of titanium oxides in marine soils at all stations was higher. Titanium accumulates mainly with iron and the correlation between TiO_2 and Fe_2O_3 was strong ($r = 0.97$).

A number of factors define the processes of HM accumulation in sea bottom sediments; their intensity depends on their chemical composition, particle size distribution, pH, Eh etc. The ratio of redox processes is one of the major factors. However, our analysis of the dependence of HM concentration in marine sediments and the pH, did not reveal a correlation ($r < -0.4$), whereas for EOM the inverse relationship was noted ($r = -0.75$). At the same time, at stations with the highest concentrations of HM, different parameters of Eh were noted (st. 7 in the Black Sea and st. 16 in the Azov). At the deep-water st. 20 such phenomenon was not traceable.

According to data (Ramamurti 1987) one can single out compounds in which HM are related in bottom sediments. For example, the main reserves of zinc are associated with iron and manganese oxides. According to (Papina 2001), the main way of HM accumulation in sea bottom sediments is their co-sedimentation with iron and manganese hydroxides.

In general, HM values in the Sea of Azov at most stations exceeded those in the Black Sea. In the latter, the degree of soil contamination stood out at st. 7, in the Sea of Azov at st. 16. It was natural for the Sea of Azov, taking into account the level of anthropogenic load and natural conditions (shallow depth, particle size distribution, etc.), but for the water near cape Aya, a nature reserve, it was unusual. Apparently, an increase in content of heavy metals in bottom sediments was associated with technogenic pollution near Cape Aya caused by the submarine discharge of polluted ground waters (Yurovskiy et al. 2012). The approximate total flux rate of these sources is $1915 \text{ m}^3/\text{day}$ (Ivanov et al. 2008). In these water areas, geochemical barriers occur,

which contribute to accumulation of toxic substances in the “water - bottom” system. Examples of such accumulation of heavy metals in bottom sediments are known near the Long Island (United States) (Yurovskiy et al. 2012).

5 Conclusions

1. The bottom sediments of the open Crimean Black Sea coast, in relation to the content of EOM and physicochemical parameters, had properties typical of marine bottom sediments in this region. This indicated general well-being of the investigated areas. The bottom sediments in the Black Sea had levels I-II of pollution (according to concentration of EOM). The exception was the deep-water station and station near the Yalta sewage pipe, while the values obtained were at the lower boundary of level III. The Azov Sea was characterized by level III. There was a tendency to a gradual increase of EOM near the Black Sea coast, but the bottom sediments were not polluted with oil products.
2. The content of HM varied in wide ranges, and the zones with high values were not always close to the source of pollution.
3. At most stations in the Azov Sea, the HM concentrations were above those in the Black Sea, in particular, their maximum content was recorded at st. 16. Concentrations of Zn, Co and Cr, V (except for st. 2) exceed their natural content in the sediments of the shelf in all the studied areas. Ni concentration in the Azov Sea exceed Clarke number, which indicates the anthropogenic pollution sources.

The work was performed as part of the state assignment, of IBSS on the theme “Molismological and biogeochemical foundations of the marine ecosystems homeostasis” (№ AAAA-A18-118020890090-2). And MHI “Comprehensive interdisciplinary research of oceanological processes that determine the functioning and evolution of ecosystems of the coastal zones of the Black and Azov seas” (№0827-2019-0004).

References

- Chertko NK, Chertko EN (2008) Geochemistry and ecology of chemical elements: a reference manual. Publishing Center BGU, Minsk
- Dobrovolskiy VV (2003) The basics of biogeochemistry. Academia, Moscow. Emelyanov VA, Mitropolskiy AYu, Nasedkin EI (2004) The geocology of the Black Sea shelf of Ukraine. Akadempriodika, Kiev
- Ganzhara NF (2001) The soil science. Agrokonsalt, Moscow
- Gurov KI, Ovsyanyy EI, Kotelyanets EA, Kononov SK (2015) Factors of the formation and features of the physical and chemical characteristics of bottom sediments in the Balaklava Bay (the Black Sea). *Phys Oceanogr* 4:51–58
- Ivanov VA, Prusov AV, Yurovskiy YuG (2008) The submarine groundwater discharge in the cape Aya region (Crimea). *Geology and Minerals of the World Ocean* 3:65–75

- Kiseleva GA, Kulik AS, Gadzhuyeva VV (2002) The zoocenoses of *Cystoseira* of Karadag Reserve region. In: Proceeding of the 2nd scientific conference «Crimean reserves. Biodiversity in priority areas: 5 years after Gurzuf», Simferopol
- Kotelyanets EA, Konovalov SK (2012) The trace metals in the sea bottom sediments of the Kerch strait. *Phys Oceanogr* 4:50–60
- Krylenko MV, Krylenko VV (2013) The scientific support of balanced planning economic activity on the unique marine coastal landscape and suggestions on how to use on the example of the Azov-Black Sea coast. Research Report «The Sea of Azov/Southern Branch of the Institute of Oceanology of P. P. Shirshov RAS», vol 7, p 1157
- Lukyanov SA, Lebedev AA, Shvarcman YuG (2013) Granulometric composition of the ground sediments and its distribution in the estuarine zone of the Northern Dvina River. *Arctic Environ Res* 2:13–19
- Methods of measurement of the mass fraction of metals and metal oxides in dry powder soil samples by X-ray fluorescence analysis. OOO «Spektron», St. Petersburg (2002)
- Mironov OG (1996) Sanitary and biological characteristics of the Azov Sea. *Hydrobiol J* 32(1):61–67
- Mironov OG, Kiryuhina LN, Divavin IA (1992) Sanitary and biological research in the Black Sea. *Gidrometeoizdat*, St. Petersburg
- Mironov OG, Milovidova NYu, Kiryuhina LN (1986) About the maximum permissive concentrations of oil product in the sea bottom sediments of the Black Sea coastal zone. *Hydrobiol J* 22(6):76–78
- Mitropolskiy AYu, Bezborodov AA, Ovsyanyy EI (1982) *Geochemistry of the Black Sea*. Naukovadumka, Kiev
- Nikanorov AM (1989) *Hydrochemistry*.: *Gidrometizdat*, Leningrad
- Oradovskiy PG (1977) *Manual by the methods of chemical analysis of sea water*. *Gidrometeoizdat*, Leningrad
- Papina TS (2001) Transport and distribution features of heavy metals in a row: water–suspended matter–bottom sediments of river ecosystems. *Analytical Review. Ser Ecol* 62:58
- Perelman AI (1989) *Geochemistry*. Vyshayashkola, Moscow
- Petrenko OA, Zhugaylo SS, Avdeeva TM (2015) Content of petroleum products in water, ground deposits and soils in the recreation area of the Kerch and Spit Tuzla Island. *Proc YugNIRO* 53:4–18
- Ramamurti S (1987) *Heavy metals in natural waters*. Mir, Moscow
- Rubcova SI, Tikhonova EA, Burdiyan NV, Doroshenko YuV (2013) The estimation of the ecological state of Sevastopol bays by basic chemical and microbiological criteria. *Marine Ecol J* 12(2):38–50
- Sovga EE, Bashkirceva EV, Stepanyak YuD (2008) The ecological status of the water area of the Kerch Strait till the catastrophic events of November 2007. *Ecological Safety of Coastal and Shelf Zones of Sea* 17:184–193
- Surova NA, Kuznecova EYu (2002) The research of anthropogenic pollution of the Karadag natural ecosystems. In: Proceeding of the 2nd scientific conference «Crimean reserves. Biodiversity in priority areas: 5 years after Gurzuf», Simferopol
- Tikhonova EA, Burdiyan NV, Soloveva OV, Doroshenko YuV (2015) Chemical and microbiological parameters of the Kerch strait sea bottom sediments after the accident of «Volgoneft-139» ship. *Environmental Protection in Oil and Gas Complex* 4:12–16
- Tikhonova EA, Guseva EV (2012) The dynamics of oil pollution in sea bottom sediments and coastal sediments of the Kerch Strait after the emergency oil spill in November 2007. In: Proceedings of the 7th International Scientific Conference «Modern fisheries management and ecological problems of the Azov-Black Sea region», vol 1, pp 253–255
- Tikhonova EA, Kotelyanets EA, Soloveva OV (2016) Evaluation of the contamination level of sea bottom sediments on the Crimean coast of the Black and Azov Seas. *Principy Ekologii* 5:56–70
- Yurovskiy YuG, Yurovskaya TN, Prusov AV (2012) Problems of estimation of the environmental condition of sea bottom sediment and the submarine groundwater discharge. *Ecological Safety of Coastal and Shelf Zones of Sea* 26(1):58–63

Uppermost Sediments Diapirism in the Western Mediterranean



A. A. Schreider  and A. E. Sazhneva 

Abstract Upper part of sedimentary thickness in the western part of Mediterranean is consist of nontransparent and semitransparent layers with penetration of such named salt domes bodies related to halokinesis process mud and salt diapirism mainly related to the messinian salt crisis phenomena. The data of “Parasound” parametric echo-sounding survey were used for elucidate in details this part of sediment series which was represented before by ordinary seismic methods as single whole transparent layer. The detail descriptions made up for the structure of upper part of sedimentary series in western basin. The position of turbidity-terrigenous marker stratum within the series is determined. The possible age of this stratum is 10–100 thousand of years and corresponds to Vurm glacial epoch. The enormous dimensions of salt diapirs, as they were reflected on the “Parasound” displays, led to the conclusion of modern halokinetic activity on the whole western Mediterranean bottom space.

1 Introduction

The Parasound parametric echosounder (Krupp Atlas Electronic GMBH) was used by us for echo-sounding survey in the western Mediterranean in the first cruise r/v «Academican Sergei Vavilov» belonged to P.P. Shirshov Institute of Oceanology Russian Academy of Sciences. Interpretation of this data first time gives main peculiarities of diapirism processes in the uppermost tens meters of sediments in the Western Mediterranean. Analysed in present article ship track in the western Mediterranean (Fig. 1 inset) crossed the central parts of the Alboran Sea basin, south Balearin basin and Algerian basin.

A. A. Schreider (✉) · A. E. Sazhneva
Shirshov Oceanological Institute RAS, Moscow, Russia
e-mail: aschr@ocean.ru

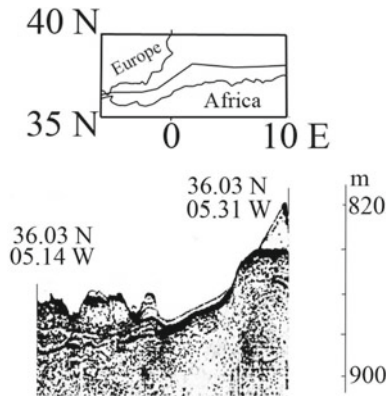


Fig. 1 Sub bottom structure of superficial sediments in the area of Gibraltar Strait. The geographical coordinates are related to the small vertical lines on the ends of profile (by Schreider 1988; Zhivago 1994 modified). The general scheme of “Academician S. Vavilov” rote in the western Mediterranean is presented in the inset

2 Geological Setting and Methods

The investigation of mud diapirism in the Alboran sea allows (Perez-Belzuz et al. 1997) to investigate the trigger mechanism of diapirism in different tectonic settings. They have recognized in mud diapirs several processes and phases of mud and salt diapirism mainly related to the messinian salt crisis phenomena (Weijermars 1985; Weijermars et al. 1993; Roveri et al. 2014; Geletti et al. 2014). Parasound is the combination of narrow beam echosounder with the small scale underbottom profiler. The using of 3.5 kHz frequency allows to obtain quite good penetration into the soft superficial sediments down to 50 m on ship velocities 7–10 knots. GPS positioning system was used for navigational purposes. The seismic velocities for superficial sediments were accepted 1600 m/s according to ODP drilling site 976 (Comas et al. 1996). Data for profiles and their geographic positions, presented on figures, were taken from (Schreider 1988; Zhivago 1994) with modifications.

In the investigations we are used the geological time scale (Gradstein et al. 2012).

3 Structural Features

The manifestation of diapirs are very clear shown on profile in the area of Gibraltar Strait (Fig. 1). The slightly folded sediment cover is represented by a set of high amplitude continuous stratified facies that grades depth to discontinuous between stratified and seismically semitransparent facies with thickness of individual layers of about first tens meters. In the easternmost part of profile the diapir take place on

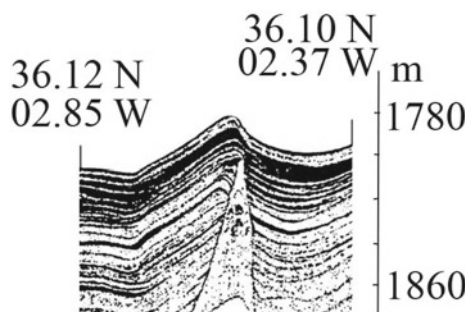


Fig. 2 Superficial sedimentary layers in the West-Alboran sea area. All other designations in this figure and in Figs. 3–8 were taken with modifications from (Schreider 1988; Zhivago 1994) and presented in subscriptions of the Fig. 1

relative steeper fold limb. It is triangle-shaped and in base part wide of 2300 m and inclination of slopes is 2.8° . Its top lies on depth 20 m under the bottom.

The wide distribution of diapirs in the Balearian and Alboran sea area was known early (Falkquist and Hersey 1969; e.a.). The detailed investigations of r/v «Academician Sergei Vavilov» cruise (Fig. 2) shows that a triangle-shaped diapir penetrates through superficial sediments. Its relative height is about 25 m and width about 1000 m. Diapiric flanks show an angle of 3.8° respect to the axial plane. The sedimentary cover is shifted vertically in the diapiric area for about 50 m.

The profile in the central part of East Alboran basin demonstrates (Fig. 3) three small hills, first tens of meters relative height. The westernmost hill is related to a triangle-shaped piercing diapir. The angles of diapiric flanks respect to the axial plane are 6° . The sedimentary cover is shifted vertically for about 3 m. The western part of the profile shows a well-stratified horizontal sedimentary layer.

The profile in the South Balearian basin demonstrates (Fig. 4) a triangle-shaped

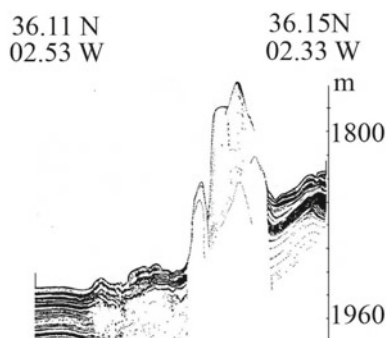
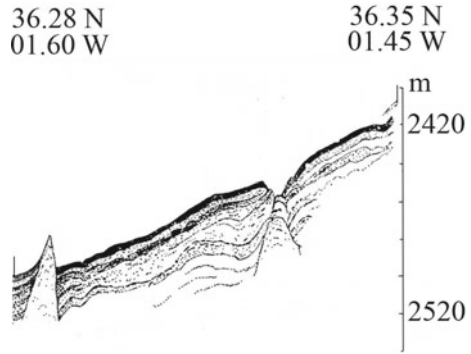


Fig. 3 Superficial sediments in the central part of East Alboran basin. All other designations in this figure were taken from [(Schreider 1988; Zhivago 1994) with modifications] and presented in subscriptions of the Fig. 1

Fig. 4 Sub bottom layers of sediments in the South Balearian basin



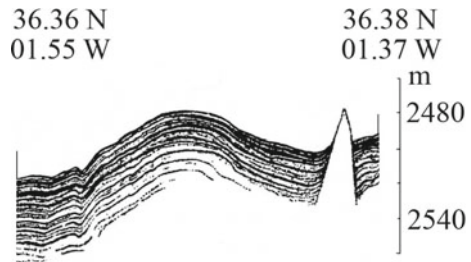
diapir penetrate superficial sediments. Its relative height about 25 m and width about 1300 m.

The diapiric flanks show an angle of 4° respect to the axial plane. Above seafloor the inclination of diapir slopes became less 3°. One more diapiric body is appeared 7 km to the east. It also penetrate superficial sediments. Its relative height is about 25 m and width about 1000 m. The diapiric flanks show an angle of 6° respect to the axial plane. The sedimentary cover is shifted vertically in the diapiric area for more 10 m. Between these two diapirs sediment layers are waveling except upper 5 m where it lays subhorizontally.

Another one profile in the South Balearian basin (Fig. 5) shows fold on depths 2500 m. In the easternmost part of profile the diapir with relative height 15 m and width 400 m can be seen. The diapiric flanks show an average angle of 6° respect to the axial plane. The sedimentary cover in west of profile is shifted vertically by fault in the diapiric area for about 3 m. The same character of bottom microrelief was pointed out for northern part of Sargena-Baleares abyssal plane in Stanley et al. (1974). Stanley described it as axample of modern basin plane deformation by salt tectonism.

Presented data allow us to classificatce the vertical and inclined shifting of sedimentary layers as faults in the sediments. The diapirs are divided on diapirs not reached the seafloor and reached it. Along profiles in last case forms on the seafloor have width not exceed 2 kmand height no more than 20 m, their slopes are very gentle

Fig. 5 Near bottom sedimentary layers in the South Balearian basin



and are about 5° . The slopes of diapirs inside sediment column are more steeper and some time reach 6° relative axial plane of diapir body. The axial plane of diapir same time has inclination up to 5° relative vertical direction.

4 Peculiarities of the Diapir Upthrusting Process

Parasound profiles demonstrates some general features of diapir upthrusting process into the uppermost quaternary sediments of western Mediterranean, which can be summarised in a some sheme. It is possible that initially upwelling process in the down space leads to form the subvertical or inclined faults in the superficial sediments (first stage). By these zones the diapir bodies intrude from the down space into the superficial sediments (second stage) and lay now on or near the seabottom (third stage).

5 Conclusions

Parasound profiles on figures in Western Mediterranean demonstrait a lot of diapirs salt or mad nature in the superficial sedimentary layer. Modell study shows that diapirs intruded along faults, related to regional or local extention. Pproceses of diapirism are not isolated and related to the general tectonic conditions in the region, coused by interaction of african and europen lithospheric plates. The numerical and mechanical models of diapirism mud and salt diapirism mainly related to the messinian salt crisis fenomena are wide known in the literature mentioned above text. But Parasound technology allowed to receive additional data for diapirism in superficial sediments and demonstrate, that upper part of sedimentary thickness in the western part of Mediterranean is consist of nontransparent and semitransparent layers with availabulance of such named salt domes bodies related to halokinesis process. It is possible that initially upwelling process in the down space leads to form the subvertical or inclined faults in the superficial sediments. By these zones the diapir bodies intrude from the down space into the superficial sediments which are lay now on or near the seabottom. New very high resolution data on diapirism is available from Parasound technology and can help to construct more contemporaneous modell of diapirism process.

Acknowledgements Some technical questions of data presentation are developed in frames of state team № 0149-2019-0005 and RFBR Project № 17-05-00075

References

- Bonifay E (1975) Lere quaternaire; definition, limites et subdivisions sur la base de la chronologie mediterraneene. *Bull Soc Geol France Ser 7*:380–393
- Camerlenghi A, Cita MB, Hieke W, Ricchiuto T (1975) 1992 Geological evidence for mud diapirism on the Mediterranean Ridge accretionary complex. *Earth Planet Sci Lett* 109:493–504
- Cita MB, Ivanov MK, Woodside JM. The Mediterranean ridge Diapiric Belt. *Mar Geol* 132(1/4):1–272
- Cita MB, Ryan WBF, Kidd RB (1978) Sedimentation rates in Neogene deep sea sediments from the Mediterranean and geodynamic implications of their changes. *Init Rep DSDP* 42(1):991–1002
- Comas MC, Zahn R, Klaus A (1996) Shipboard Scientific Party, Site 976. In: *Proceedings of ODP, Init. Rep.*, vol 161, pp 179–297
- Davison I, Insley M, Harper M, Weston P, Blandell D, McClay K, Qualington A, Falquist DA, Hersey JB (1969) Seismic refraction measurements in the western Mediterranean Sea. *Bull Inst Oceanogr Monaco* 67(1386):173
- Geletti R, Zgur F, Del Ben A et al (2014) The Messinian Salinity Crisis: new seismic evidence in the West-Sardinian Margin and Eastern Sardo-Provençal basin (West Mediterranean Sea). *Mar Geol* V 351:76–90
- Gradstein F, Ogg J, Schmitz M, Ogg G (2012) *The Geologic Timescale*. Elsevier, Amsterdam, p 1139p
- Initial Reports of the Deep Sea Drilling Project. Wash (D.C.) V.42, pt 1., 1249 p. (1978)
- Kuptsov VM (1991) *Methods of Quaternary sediments chronology in oceans and seas*. M., Nauka, 271p (in Russian)
- Nalpas T, Brun JK (1993) Salt flow and diapirism related to extension at crustal scale. *Tectonophysics* 228:349–362
- Olivet J-L, Pautot G, Auzende J-M (1973) Alboran Sea. *Init Rep DSDP* 13(1):1417–1430
- Perez-Belzuz F, Alonso B, Ercilla G (1997) History of mud diapirism and tigger mechanisms in the Western Alboran Sea. *Tectonophysic* 282:399–422
- Podladchicov Y, Talbot C, Poliakov ANB (1993) Numerical models of complex diapirs. *Tectonophysics* 228:189–198
- Robertson A (1996) Ocean Drilling Program Leg 160 Scientific Party. Mud volcanism on Mediterranean ridge: Initial Results of Ocean Drilling Program Leg 160. *Geology* 24(3):239–242
- Roveri M, Flecker R, Krijgsman W et al (2014) The Messinian Salinity Crisis: past and future of a great challenge for marine sciences. *Mar Geol* V 352:25–58
- Schreider AA (1988) Technical Report of the R.V. Academican Sergei Vavilov cruise 1 geoacustical investigations. P. P. Shirshov Institute of Oceanology RAS anal., 25p (in Russian)
- Schultz-Elba DD, Jackson MPA, Vendeville BC (1993) Mechanics of active salt dipirism. *Tectonophysics* V 228:275–312
- Stanley DJ, McCoy FW, Diester-Haass L (1974) Balearic abissal plane: an example of modern basin plane deformation by salt tectonism. *Mar Geol* V 17(3):183–200
- Vendeville BC, Jackson MPA (1992) The rise of diapirs during thin-skinned extension. *Mar Petrol Geol* 9:331–353
- Weijermars R (1985) Uplift and subsidence history of the Alboran Basin and profile of the Alboran diapir (West Mediterranean.). *Geol Mijnbouw* 64:349–356
- Weijermars R, Jackson MPA, Vendeville B (1993) Rheological and tectonic modeling of salt provinces. *Tectonophysics* 217:143–174
- Zhivago AV (1994) Manifestations on salt tectonics within the upper series of bottom sediments in the Mediterranean. M: Nauka., 62p (in Russian)

Method for Detection of the Vessel Trace Anomalies in the Sea Surface Images Based on Analysis of Color Gradient Correlations



M. K. Klementiev , V. N. Nosov , V. I. Timonin ,
and L. M. Budovskaya 

Abstract The paper presents the statistical method for detecting the ship trace manifestations in the sea surface images. The method is based on comparison of correlation parameters of image color gradients in different directions. The set of correlations for different parts of image is clustered, followed by checking the clusters obtained of the vessel trace lateral components for the compliance. The method efficiency is illustrated by example.

Keywords Vessel trace (ship trace) · Model of trace · Anomaly · Correlation pattern of image · Statistical features · Spectral clustering · Angle between the anomalies

1 Introduction

Multispectral imaging forming several images of the same area of sea surface (SS) in different intervals of electromagnetic radiation spectrum simultaneously is the main data source for the problems on Earth remote sensing (ERS) by artificial satellites (*WorldView-2,3*; *DMC-3*; *Resource-P1,2,3*; *Kompsat-3,3A*, etc.). Color photography is a special case of this method when three spectral intervals of visible light corresponding to human perception are chosen.

One of the problems related to ERS is identifying the trace of passed vessel formed by two lateral components (right and left sides), as well as the area between them including turbulent trace, in SS images. The main method for solving this problem is to split the image into separate non-crossing areas (clusters, or segments) according to some criterion of difference between these areas. Any criterion is implemented

V. N. Nosov

Vernadsky Institute of Geochemistry and Analytical Chemistry RAS, Moscow, Russia

e-mail: victor_nosov@mail.ru

M. K. Klementiev · V. I. Timonin (✉) · L. M. Budovskaya

Bauman Moscow State Technical University, Moscow, Russia

e-mail: timoninmgtu52@mail.ru

by some algorithm using certain parameters of multispectral image data (statistical, spectral or texture). All such algorithms are termed as *data clustering algorithms*.

2 The Basis of the Method

Up to date, a large number of different algorithms for clustering multidimensional data have been developed (Ayvazyan et al. 1989; Ahmed 2015; Aggarwal and Reddy 2014; Kashkin and Sukhinin 2008). The efficiency of applying one or another algorithm mainly depends on specific problem to be solved, and even more so, on set of parameters representing the basic features discerning clusters from each other.

In (Timonin et al. 2016, 2018) the method for detecting the ship trace in sea surface (SS) images based on comparing statistical features of color intensities (R , G , B) in separate areas Δ_{ij} , $i = \overline{1, n}$; $j = \overline{1, m}$, splitting the image (each area of size $N = ks$ pixels) to their values throughout the image $\Delta = \bigcup_j \Delta_{ij}$ (or throughout background area image) was proposed and founded. Correlation coefficients $r(\text{grad}X(\alpha_1), \text{grad}X(\alpha_2)) = r(\alpha_1, \alpha_2)$ of indicator gradients X (rates of X change) in directions at angles α_1, α_2 to the fixed axis (for example, to horizontal axis of the image) were proposed to be used as statistical features. The parameter X may represent the intensity of any color, the main component of intensities, or another feature. The rate $\text{grad}X(\omega, \alpha)$ for specific pixel ω in direction α was calculated using standard differential operators (Shovengerdt 2010). Correlation coefficients for the area Δ_{ij} , $i = \overline{1, n}$; $j = \overline{1, m}$, were estimated by set of vectors $(\text{grad}X(\omega_{rt}, \alpha_1), \text{grad}X(\omega_{rt}, \alpha_2))$, $\omega_{rt} \in \Delta_{ij}$, $r = \overline{1, k}$; $t = \overline{1, s}$. As functional for comparing correlation coefficients $r_{ij}(\alpha_u, \alpha_v)$ and $\bar{r}(\alpha_u, \alpha_v)$ in the area Δ_{ij} and image Δ in directions α_u, α_v , respectively, statistics is used

$$Z_{ij} = \frac{\text{Arth}(\bar{r}(\alpha_u, \alpha_v)) - \text{Arth}(r_{ij}(\alpha_u, \alpha_v))}{1/\sqrt{N-3}}, \quad (1)$$

where $\text{Arth}(x) = \frac{1}{2} \ln \frac{1+x}{1-x}$ is the hyperbolic arctangent x .

The paper (Timonin et al. 2018) shows that one can obtain either significant differences between coefficients $r_{ij}(\alpha_1, \alpha_2)$ and $\bar{r}(\alpha_1, \alpha_2)$ for the areas Δ_{ij} located at one or two side components of the trace, or the absence of significant differences for all Δ_{ij} , depending on the choice of α_1 and α_2 .

To explain the mentioned above, Fig. 1 shows the results of processing image 1b given in (Timonin et al. 2018). Figure 1a shows the directions used for calculating the gradients $\text{grad}B(\alpha)$ of blue color intensity B ; Fig. 1c, d show infograms of trace areas for different pairs α_1, α_2 . The term infogram denotes the image divided into sections of partition Δ_{ij} , each of which is colored correspondingly to the numerical value of functional Z_{ij} according to the color scale shown in Fig. 2.

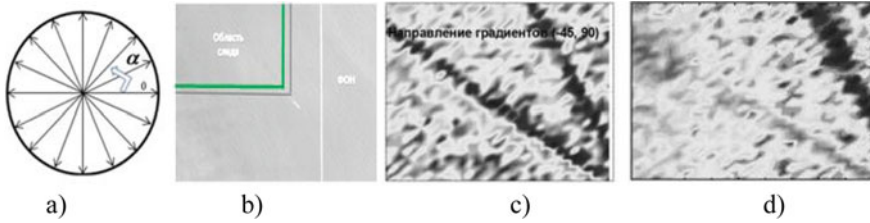


Fig. 1 **a** The field of gradient directions; **b** SS image with outlined areas for analysis and background section; **c** Infogram for the larger area at $\alpha_1 = -45^\circ$, $\alpha_2 = 90^\circ$; **d** Infogram for the smaller area at $\alpha_1 = 0^\circ$, $\alpha_2 = -45^\circ$

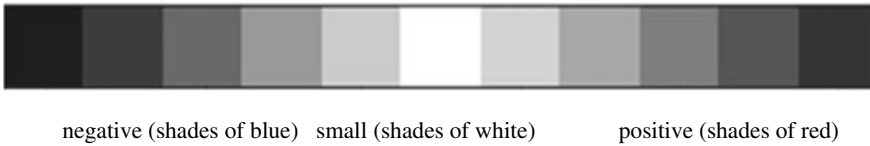


Fig. 2 Scale of statistical values Z_{ij} and corresponding colors

Comment. Hereinafter, we'll assign the numbers to the areas of sections of partition corresponding to different values Z_{ij} (and colored differently), but indistinguishable in black-and-white infogram image, for their differentiation.

3 Algorithm Description and Results

In this paper we propose the method allowing us to extend the analysis of correlation parameters $r(gradX(\alpha_1), gradX(\alpha_2))$ of scalar indicator X to the set of several indicators $r^{X,Y}(\alpha_1, \alpha_2) = r(gradX(\alpha_1), gradY(\alpha_2))$, $X, Y \in \{R, G, B\}$. In addition, a set of programs based on this method has been developed to allow us select automatically the indicative structures for the vessel trace in SS image, from the resulting correlation pattern (set of correlation relationships).

We propose to compare each sector Δ_{ij} to background for all possible pairs of directions (α_u, α_v) based on functional:

$$F_{ij}(\alpha_u, \alpha_v) = \max_{X,Y} (Z_{ij}^{X,Y}(\alpha_u, \alpha_v)); X, Y \in \{R, G, B\}. \tag{2}$$

For example, in the case of 16 directions (Fig. 1a) the set of functional values $F_{ij}(\alpha_u, \alpha_v)$ (correlation pattern of image or sector) will contain 720 values.

To compare obtained results to the data given in (Timonin et al. 2018) and shown in Fig. 1 we have analyzed SS image presented in Fig. 1b.

Variational series of functional values $F_{ij}(\alpha_u, \alpha_v)$ for all sectors Δ_{ij} was compiled and percentiles of 5% and 95% levels were found, for each pair of directions α_u, α_v .

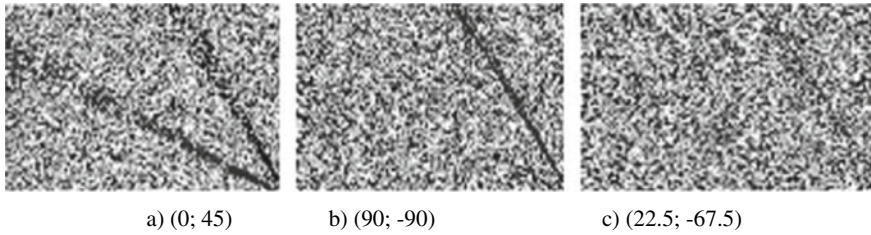


Fig. 3 Infograms of image 1b for different pairs of directions, based on functional values $F_{ij}(\alpha_u, \alpha_v)$

Then set of functional values was censored below and above, respectively to the percentile levels, in order to remove extreme values. To compile infogram of image the scale similar to that shown in Fig. 2 was used.

Figure 3 shows infograms of image 1b based on statistical values $F_{ij}(\alpha_u, \alpha_v)$, for different pairs of directions. Depending on the angles and their difference, we get significant differences either on one side, or on both sides of the trace, or significant differences are absent.

The infograms obtained (Fig. 3) were averaged by sliding window including $4K^2$ sectors. For sector Δ_{ij} sectors from $\Delta_{i-K, j-K}$ to $\Delta_{i+K-1, j+K-1}$ fell into the window. The averaged infograms for the pairs of directions shown in Fig. 3 are represented in Fig. 4.

Note that elsewhere below the number 1 corresponds to the blue, and the number 2 corresponds to the red for selected anomalous sections of the infograms.

To be precise, in averaging we used *RGB-to-HSV* conversion, and then the inverse transformation. The reason is the fact that in *HSV* color model only one parameter (*S*) may be used for averaging colors in selected scale (Fig. 2), while in *RGB* model blue-to-red transition changes firstly one pair of parameters (*R, G*), and then another pair (*G, B*). [To learn more detailed about *RGB* and *HSV* systems as well as about relationship between these two color models, see (Shovengerdt 2010)].

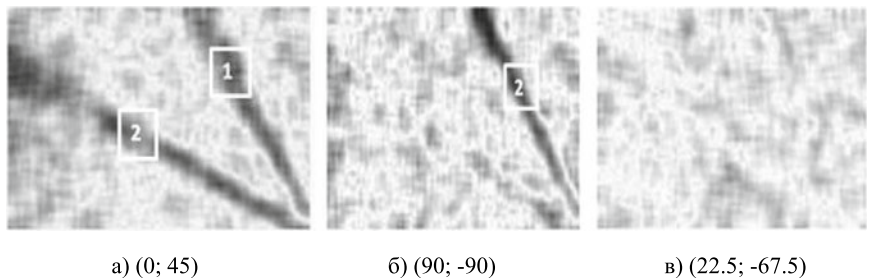


Fig. 4 Infograms of image 1b for different pairs of directions, based on averaged functional values $F_{ij}(\alpha_u, \alpha_v)$

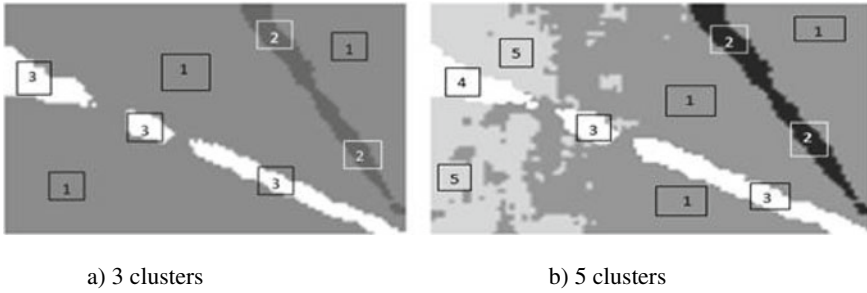
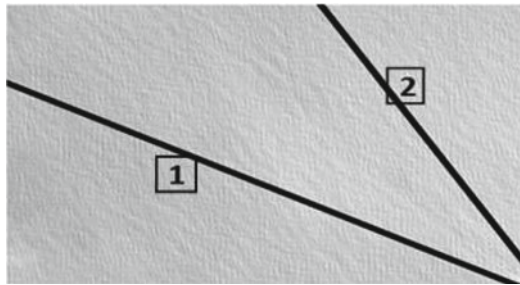


Fig. 5 Selected clusters in *SS* image

Fig. 6 Outlined anomalies in *SS* image



Furthermore, all image sectors were clustered using the spectral clustering method (regarding algorithm of the method, see (Aggarwal and Reddy 2014)). The colors of each sector in the averaged infograms for all pairs of directions (120 values) were used as its features. Examples of clustering results for different number of clusters are shown in Fig. 5. The following color coding is used:

In Fig. 5a: 1—red, 2—blue, 3—green;

In Fig. 5b: 1—red, 2—blue, 3—yellow, 4—green, 5—lilac.

Thereafter, for each obtained cluster, the hypothesis of linear arrangement of its elements in the image was checked and, when performed, the corresponding regression line was drawn at *SS* image. The results are shown in Fig. 6.

To be precise, the graphical representations of calculation results are shown only to illustrate the methods in use. In applying the method in specific case, the calculation results in the regression lines (if detected) in *SS* images.

4 Conclusion

Comparison of correlation characteristics of color intensity gradients in different directions leads to the splitting of the sea surface image into areas of different structure. The application of cluster analysis methods to the division of the sea surface

image sections by the criterion of similarity of correlation characteristics allows to distinguish the structures characteristic for the trace of a moving vessel.

References

- Ayvazyan SA, Bukhshtaber VM, Enyukov IS et al (1989) Applied statistics. Classification and reduction of dimension. M.: Finansy I statistika, 607p (in Russian)
- Ahmed N (2015) Recent review on image clustering. *Image Processing, IET* 9(11):1020–1032
- Aggarwal CC, Reddy CK (2014) Data clustering: algorithms and applications. CRC Press, 626p
- Kashkin VB, Sukhinin AI (2008) Earth remote sensing from the Space. *Image digital processing. M.: Logos*, 264p (in Russian)
- Timonin VI, Kurbatov RA, Nosov VN (2016) One statistical method of anomaly detection in the sea surface images. *Processes in Geological Media* 4:363–370 ((in Russian))
- Timonin VI, Tyannikova ND, Nosov VN, Ivanov SG, Klementiev MK (2018) Application of multi-dimensional correlation procedures for detection of trace structures in space sea surface images. *Processes in Geological Media* 4:1221–1225 ((in Russian))
- Shovengerdt (2010) Remote sensing. *Image processing: models and methods. M.: Tekhnosfera*, 560p (in Russian)

Current Water and Salt Regime of the Sivash Bay



E. E. Sovga, E. S. Eremina, L. V. Kharitonova, and T. V. Khmara

Abstract To assess the water and salt regime of the Sivash Bay after the overlapping of the North-Crimean Canal in 2014 the integrated approach was used, it includes the expeditionary studies of salinity changes in the Eastern Sivash, mathematical modeling of its hydrodynamic regime and usage of satellite images to keep track of changes in the coastal zone of the bay. Spatial heterogeneity of salinity growth over the entire Eastern Sivash with a gradual increase from north to south is shown. In the Southern Sivash the maximum growth of salinity were noted, it reached 93‰ in November 2018, which was twice than the salinity in 2014. The salinity growth is confirmed by the mathematical modeling of hydrodynamic regime of the bay (currents and level of the bay). According to satellite data, we assessed the changes in the coastline of flooded and drained areas of the Sivash Bay after the North-Crimean Canal overlapping in 2014.

Keywords Sivash bay · North-crimean canal overlapping · Water and salt regime · Hydrodynamic regime · Morphometric parameters

1 Introduction

The Sivash Bay of the Sea of Azov is a unique natural recoverable mineral salt deposit. The water and salt regime of the Bay is dynamically changing under the climatic and anthropogenic influence.

The Sea of Azov water exchange, atmospheric precipitation, evaporation, river runoff, possible filtration of the Sea of Azov water through the Arabat Spit is the natural and climatic factors affecting the water and salt regime of the bay. Anthropogenic factors affecting the water and salt regime of the bay include dams that regulate water exchange in the Western and Central Sivash, the functioning and overlapping of real irrigation systems (the North-Crimean Canal and the Kakhovkaya irrigation system).

E. E. Sovga (✉) · E. S. Eremina · L. V. Kharitonova · T. V. Khmara
Marine Hydrophysical Institute RAS, Sevastopol, Russia
e-mail: shchurova88@gmail.com

The Sivash Bay is a vast (area $\sim 2540 \text{ km}^2$) shallow (depths to 0.5–3 m) saline bay of the Sea of Azov (Gidrometeorologicheskii spravochnik Azovskogo morya 1962; Ponizovsky 1965; Dyakov et al. 2013). In the west, the bay border is the Perekop Isthmus, and in the east there is the Arabat Spit. The bay comprises a number of shallow salt water areas, which is significantly differed in hydrological and chemical regimes; they are separated by a large number of islands, droughts, dams. The Sivash Bay is usually accepted to divide into two large regions, namely, the Western Sivash and Eastern Sivash with area of 1110 and 1433 km^2 respectively (Ponizovsky 1965). The area of water level is 581 km^2 for the Western Sivash and about 1300 km^2 for the Eastern Sivash, the islands and droughts take up a rest of area.

The Kutaran blank earth dam, constructed in 1959 in connection with the reconstruction the Krasno-Perekopsky bromine plant, had divided the Western Sivash into two isolated reservoirs, the Western one (the Kutaran Bay) with an area of 202 km^2 and the Middle water area (area 353 km^2) (Fig. 1). At present the Western reservoir is a practically isolated evaporating basin, where a water level is fully regulated by the Kutaran dam and maintained to the extent necessary for the bromine plant functioning.

The hydrological and chemical regime of the Middle (Central) reservoir is also regulated by the construction of dams with locks (the Biyuk-Naimanskaya, the Chongarskaya, etc.). Currently the existing dam system allows maintaining the high concentration saline for the chemical industry demands (Kostyushina and Fesenko 2007). The Central and Eastern Sivash interflows at present. The water exchange



Fig. 1 The chart of stations fulfilled during expeditions in the Eastern Sivash Bay for 2014–2018

through the Chongar Strait (1–1.2 km length, 200–300 m width and 0.5–1.5 m depth) is limited (Ponizovsky 1965; Dyakov and Belogudov 2015)

The water exchange of the Sivash Bay with the Sea of Azov is carried out through the Genichesk (Tonkiy) Strait (Ponizovsky 1965; Dyakov and Belogudov 2015). The strait has length of 4 km, the average width of 100 m, the maximum depth of 4.7–5 m (Dyakov and Belogudov 2015).

The Eastern Sivash is bounded by the Arabat Spit in the east, the Biyuk-Naimanskaya dam in the west, the Shakalinsky narrowing in the south; it is connected with the Sea of Azov through the Genichesk Strait in the north. The Eastern Sivash is conditionally divided into several water areas, which differ mainly in thermohaline conditions (Stashchuk et al. 1964) (Fig. 1).

In accordance with previous study (Kostyushina and Fesenko 2007; Kostyushin and Gorodiskaya 2000), the Eastern Sivash, the largest section of the bay with area over 60% of the Sivash Bay total area and the most deep-water, had undergone a most change from freshwater discharges of irrigation system. An increase in fresh water entering the bay had led to salinity decrease and Sivash level increase and, as a result, the volume of water from the Sea of Azov had decreased. According to (Kostyushina and Fesenko 2007), in the Eastern Sivash the average salinity diminished from 141‰ in 1955 to 22.60‰ in 1989, and in 1997 reached the minimum value of 17‰.

Currently, after the termination of the Dnieper water supply through the North-Crimean Canal in 2014, the Sivash Bay state is extremely dynamic changing. To predict the development and variability of the water area of the bay as a promising salt deposit and wetland of international importance, a regular monitoring of water and salt regime using in situ and remote methods takes on special significance.

The purpose of the study is a comprehensive assessment of changes in the water and salt regime of the Sivash Bay under the overlapping the North-Crimean Canal, taking into account natural and climatic variability.

A comprehensive assessment of changes in the water and salt regime of the Sivash Bay includes in situ researches, numerical modeling of the hydrodynamic regime (currents under different wind conditions, level changes), as well as the study of morphometric changes using satellite data.

The relevance of research conducted in the water area of the bay is due to the global transformation of its ecosystem in the new conditions, and is associated with need to develop and implement a modern monitoring system for the water and salt regime of the bay for scientifically based recommendations for rational nature management.

2 Materials and Methods

We analyzed all available information on expeditionary study of the water and salt regime of the Sivash Bay, obtained during the functioning of the North-Crimean Canal. After the North-Crimean Canal overlapping the study of the water and salt regime of the Sivash Bay was carried out on the basis of field observations obtained during 20 land expeditions of the Marine Hydrophysical Institute, jointly the

Sevastopol Department of State Oceanographic Institute to the Eastern and Southern Sivash since June, 2014 to May, 2019, in whole 78 stations were made. Figure 1 demonstrates the chart of stations fulfilled during expeditions in the Eastern Sivash for 2014–2018.

Salinity was determined by various methods. In (Sovga et al. 2014), it was shown that the pycnometric method is the most accurate method of analysis, and the refractometric method for determining salinity is promising technique for field research.

3 Main Results

3.1 Field Research

In 2014, 2015 and 2016 the expeditionary researches were carried out in the Rogachinsky, Knyazhevicha, Balganovsky bays, as well as north of the Shakalinsky narrowing, and in 2016, the area of Southern Sivash adjacent to the Arabat Spit was also covered. The results of these expeditionary studies are presented in (Shchurova et al. 2016), where the water and salt regime of the Eastern Sivash and the Southern Sivash is analyzed.

According to (Shchurova et al. 2016), the anthropogenic impact revealed itself unequally in various parts of the Eastern Sivash. The variability of water and salt regime to north of the Shakalinsky narrowing (Fig. 1) is sufficiently dependent on natural and climatic factors: intense summer evaporation and decrease of atmospheric precipitation. At the same time, spatial heterogeneity of salinity growth was observed at all stations. If in spring, 2014 in the Eastern Sivash the salinity was varied from 27‰ to 34‰ from north to south, then in October, 2014 it was also changed from 26‰ to 46‰. Near the Shakalinsky narrowing the seasonal variability of salinity was well-marked; the interannual growth of salinity was observed, from 2014 to 2018 salinity was increased from 46‰ to 55‰ during fall study.

The overlap of the North-Crimean Canal and the artificial decrease of the Salgir River runoff led to an increase in salinity of the Southern Sivash that was found in field research.

In the Southern Sivash, the current dynamics of salinity is analyzed and compared with (Sovga et al. 2014). In June, 2013 salinity varied from 47 to 55‰, and in June 2016 salinity increased to 67 and 75‰, respectively, at the same stations. According to the results of expeditionary study of the Marine Hydrophysical Institute in May and November, 2018, salinity in the Southern Sivash continues increasing; at the same points salinity ranged from 75‰ to 82‰ in May and from 89‰ to 92‰ in November. Thus, for four years after the North-Crimean Canal overlapping salinity doubled in the Southern Sivash.

It should be noted that the resource potential of the Southern Sivash was highly appreciated in the middle of XXth century, when during large-scale chemical surveys

(Kostyushina and Fesenko 2007), salinity was practically constant (115–135‰). It was favorable conditions for creating a powerful raw material base for halurgy. If salinity increases further, it will lead to rise in the resource salt potential of the Southern Sivash. So the concept of environmental management in this water area should be revised, including a balanced economic development of the region while minimizing environmental damage.

In 2018 the expeditionary study was carried out according to the chart of stations proposed by the Marine Hydrophysical Institute and the Sevastopol Department of State Oceanographic Institute for monitoring of the water and salt regime of the Sivash Bay (Sovga et al. 2018), taking into account the current boundaries of wetland according to (Prikaz Ministerstva ekologii i prirodnykh resursov respubliky Krym ot 18 dekabrya 2017).

The North-Crimean Canal overlapping has affected not only the water and salt regime, but also the input and output items of its water balance (Sovga et al. 2018).

The expeditionary research carried out by the Marine Hydrophysical Institute in the Eastern Sivash revealed the problems that need to be solved to effectively monitor the state of the bay in the new conditions.

The Crimean Department of Hydrometeorological Stations should restore regular observations at the Chongarsky Bridge, interrupted in 2014. Observations at this post have been conducted for almost 80 years; their restoration will allow us to estimate of changes in the meteorological and hydrological conditions of this part of the bay at various scales (from synoptic to interannual).

It is necessary to control salinity in the Sivash Bay additionally in points close to the Arabat Spit. In (Shchurova et al. 2016), based on the satellite images it was found that in the Southern Sivash along the Arabat Spit a peculiarity of spatial distribution of water temperature and its optical properties exist in some cases. Moreover, temperature anomalies, as a rule, arise as a local areas (offshore jets), and in the optical range an areas with reduced dissipation (turbidity) are observed here. The analyze of NOMADS NOAA data (https://dvs.net.ru/mp/data/main_ru.shtml) revealed that water infiltration through the Arabat Spit is possible due to preceding wind conditions, which were defined by strong east and north-east winds more than 10 m/s velocity. Such winds lead to a water level increasing from the Azov side of sandbar and accordingly a level decreasing from the Sivash side and contribute to increased filtration (intrusion) of water through the sandbar. Intrusions of the Azov waters can make a significant contribution to the water and salt regime of the Sivash Bay, so near the Arabat Spit salinity is necessary to monitor.

4 The Hydrodynamic Regime of Sivash Bay Using Mathematical Modeling

The water and salt regime of the Sivash Bay is largely determined by its constantly changing and insufficiently explored hydrodynamic regime.

In the Sivash Bay there are two kinds of currents: drift (wind) and runoff (compensation), arising due to the level differences in a various reservoirs. These differences arise due to unequal evaporation rates or winds (Mikhaylov 2006).

When north and north-east winds with average speeds (6–8 m/s) dominate over the Sivash Bay, strong wind-driven currents are observed along the northern and eastern shores; this occurs often in winter. Correspondingly, the southern and western coasts in winter develop under powerful surges, when significant low-land coasts are flooded.

The shallow water area, high air temperature and low humidity in summer and autumn, as well as the hydrodynamic regime contribute to large evaporation from the Sivash Bay surface and lead to a decrease in water level in relation to the Sea of Azov surface. According to the seasonal level (Gidrometeorologicheskkiye usloviya morey Ukrainy 2012) in April, the water level is actually high over the entire Eastern Sivash, in the summer it decreases slightly due to evaporation, and from August to October it rises to the spring level due to precipitation. The general tendency of water level decrease in the spring is also associated with the long-term, steady western winds over the Eastern Sivash.

To study the structure of current patterns in the Eastern Sivash, a numerical non-stationary hydrodynamic model is used (Ivanov and Tuchkovenko 2006), which allows one to calculate wind (drift and compensation) currents in estuaries, bays, and on a shallow continental shelf.

For real unsteady winds, the circulation pattern constantly changes depending on the wind speed and direction, and a steady state is rarely attained in complex systems such as Sivash Bay. Therefore modeling was carried out for constant winds of various directions. Figure 2 demonstrates modeled patterns of surface currents and level fluctuations in the Eastern Sivash Bay.

It was impossible to isolate runoff flows due to low currents. They were noticeable in narrow straits, for example, in the Shakalinsky narrowing, connecting the Southern Sivash with the Sivash Bay.

Drift currents are extremely short-term; occurring immediately after the wind intensifies and also quickly decays after its termination. Shallow depths do not permit the development of large speeds and preserve currents after the wind termination. Despite this, both in the Eastern Sivash and in some areas of the Western Sivash it is possible to distinguish the stream and its direction.

In the Eastern Sivash, the stream extends from the Genichesk Strait along the western shore to a narrow channel. Once in the middle subarea, the stream is again off the west coast, turns to the southeast. Then the current passes along the western coast and, having reached the southern basin, bifurcates and decreases its speed. In very shallow areas, such as, for example, the Western Sivash, and with strong winds, the currents are invisible.

Usage of numerical model made it possible to evaluate influence the coastal orography and bay morphometry on the water dynamics in the Eastern Sivash and to confirm the influence of the hydrodynamic regime on the salinity distribution throughout the Eastern Sivash. The water is spreading from north to south and

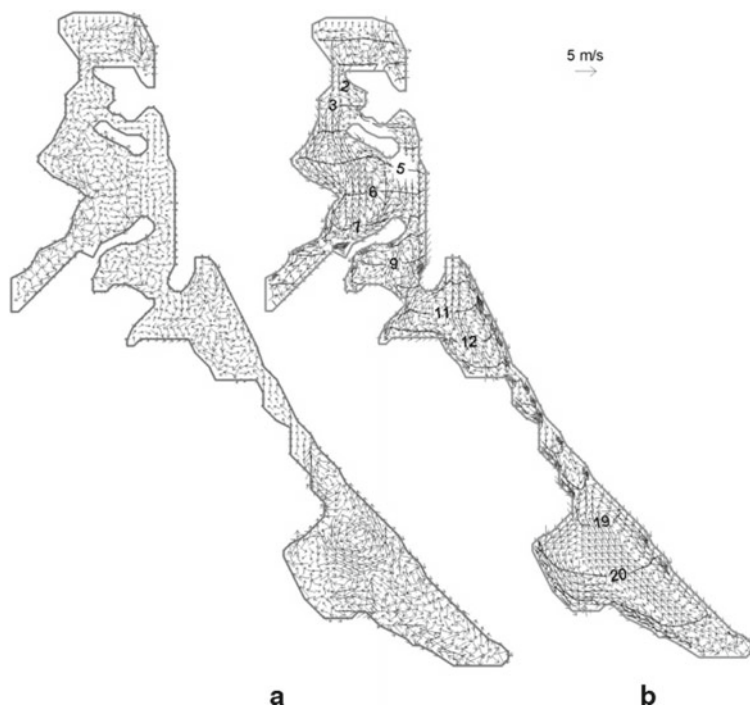


Fig. 2 Patterns of surface currents and level fluctuations (cm) in the Eastern Sivash Bay no wind (a) and at north wind of 5 m/s (b)

provides a gradual increase in salinity in the same direction, with a maximum in the Southern Sivash as a result of its isolation.

5 The Variations of the Morphometric Parameters of the Sivash Bay

The function of the North-Crimean Canal and irrigation systems and their overlapping contributed not only to a change in the water and salt regime of the bay, but affected some morphometric parameters to a certain extent.

The change in the water and salt regime as a result of the North-Crimean Canal function led firstly to a significant development of reed vegetation due to drainage waters enriched with biogenic elements. It weakened the wind-driven circulation, which is the main hydrodynamic process in the Sivash, accumulated sludge sediments on shallow water, changed low shore configuration (Mikhaylov and Kalinchuk 2017).

In (Mikhaylov and Kalinchuk 2017) an analysis of the satellite images revealed that the total area of reed vegetation is a little more than 15 km², while the largest

area of vegetation occupies more than 8 km² in the Rogachinsky Bay, 5 km² in the Balaganovsky Bay, and about 1 km² in the Knyazhevichi Bay.

To 2018 the reed vegetation is significantly decreased according to the expeditionary studies of the Marine Hydrophysical Institute.

To trace the changes in the coastline of flooded and drained territories after the North-Crimean Canal overlapping in 2014, the water surface of the Eastern Sivash was calculated. The results of a study of the seasonal and long-term dynamics of the Sivash Bay coastline are given in (Eremina et al. 2018). Based on the digitization of Landsat satellite images, the morphometric parameters of water surface in the Eastern Sivash, coastal water areas and rice fields were calculated. A detailed technique for the images selection and processing is given in (Eremina et al. 2018).

The obtained morphometric parameters of the Eastern and Southern Sivash in August, 2013 and August, 2016 were compared (Eremina et al. 2018). The total area of lagoon lakes, rice fields and reservoirs of drainage system in the low-water period (July–August) decreased by 79.24 km² (5.6%), while 2.45 km² are related to fresh and saline reservoirs, 76.79 km² are to rice fields (Eremina et al. 2018).

6 Conclusions

Thus, comprehensive studies of the Sivash Bay, composed of expeditionary studies, satellite data on changes in the morphometric parameters of the bay coasts, as well as numerical modeling of the bay dynamics, can become the basis for an actual system to monitor the water and salt regime in the bay.

The expeditionary studies carried out in the Eastern Sivash confirmed a constant change in the water and salt regime by water salinity increasing as a result of the North-Crimean Canal overlapping. Salinity grows unevenly, gradually increasing from north to south, with a maximum increase 93‰ in the Southern Sivash in November, 2018.

After the North-Crimean Canal overlapping in 2014, a transitional period began. In addition to natural and climatic factors, it contributes to gradual salinization of the bay, decrease in freshwater component and transition to a conditionally natural state.

The availability of remote sensing methods to study the factors affecting the water and salt regime of the bay and the morphometric parameters (variations of the coastal zone, drainage and flooding areas) is confirmed.

The numerical hydrothermodynamic model is able to evaluate a number of necessary parameters of the bay (wind-driven regime and water level), what are not always possible to obtain in situ, but they significantly affect the water and salt regime.

The considered study showed the possibility to predict the trend of changing in the shallow water areas. It allows to take into account the expected consequences of economic program and to search for a scientifically based environmental protection measures, thus being a link between environmental theory, research and management.

Acknowledgements This work was supported by Russian Federation State Task № 0827-2019-0004.

References

- Dyakov NN, Belogudov AA, Timoshenko TYu (2013) Otsenka Sostavlyayuschikh Vodnogo Balansa Zaliva Sivash (Assessment of Water Balance Components of the Sivash Bay). In: MHI, Ekologicheskaya Bezopasnost' Pribrezhnoj i Shel' fovoj Zon i Kompleksnoe Ispol'zovanie Resursov Shel' fa (Ecological Safety of Coastal and Shelf Zones and Comprehensive Use of Shelf Resources). MHI, Sevastopol. Iss. 27, pp 439–445 (in Russian)
- Dyakov NN, Belogudov AA (2015) Vodoobmen Zaliva Sivash s Azovskim Morem cherez Proliv Genicheskij (Tonkiy) (Water Exchange of the Gulf Sivash with the Sea of Azov through the Strait Genichesk (Tonkiy)). SOI Proceedings. Moscow: SOI. Issue 216:240–253 ((in Russian))
- Eremina ES, Kharitonova LV, Stanichniy SV (2018) Otsenki vliyaniya perekrytiya Severo-Krymskogo kanala na izmenchivost' morfometricheskikh kharakteristik zaliva Sivash po sputnikovym dannym (Estimates of the effect of the North-Crimean Canal overlapping on the variability of the morphometric parameters of the Sivash Bay from satellite data). Sovremennyye Problemy Distantionnogo Zondirovaniya Zemli Iz Kosmosa (Modern Problems of Remote Sensing of the Earth from Space) 15(7):175–183 ((in Russian))
- Gidrometeorologicheskij spravochnik Azovskogo morya. (Hydrometeorological handbook of the Sea of Azov). Hydrometeoizdat, Leningrad. 853p (1962) (in Russian)
- Gidrometeorologicheskiye usloviya morey Ukrainy, vol 2. Chernoye more (Hydrometeorological conditions of the seas of Ukraine. vol. 2. The Black Sea). In: EKOSI-Gidrofizika, Sevastopol, 421p (in Russian)
- Ivanov VA, Tuchkovenko YuS (2006) Prikladnoe Matematicheskoe: Modelirovanie Kachestva Vod Shel' fovykh Morskikh Ekosistem (Applied Mathematical Modeling of Water Quality of the Shelf Marine Ecosystems). EKOSI-Gidrofizika, Sevastopol, 368p (in Russian)
- Kostyushin VA, Gorodiskaya GA (eds) (2000) The current status of Sivash: collection of scientific papers. Wetlands International-AEME, Kiev, 104p (in Russian)
- Kostyushina VA, Fesenko GV (eds) (2007) Sivash Region: a brief socio-economic overview. Wetlands International Black Sea Progr. Kiev, 178p (in Russian)
- Mikhaylov VA (2006) Geograficheskaya evolyutsiya Sivashskoy laguny (Geographical evolution of the Sivash lagoon). In: Kul'tura narodov Prichernomor'ya (Culture of the Black Sea peoples), № 82, pp 11–14 (in Russian)
- Mikhaylov VA, Kalinchuk IV (2017) Morfologiya i dinamika beregov prirodnogo parka «Kalinovskiy» (Morphology and dynamics of the shores of the Kalinovsky Natural Park). In: 2017. In: Proceeding of conference «Nauchnyye issledovaniya na zapovednykh territoriyakh» (Scientific Researches in the Wildlife Areas), dedicated to the 160th founder of the Karadag Scientific Station T. Vyazemsky and the year of ecology in Russia, 9–14 Oct Kurortnoye, Feodosiya, p 68 (in Russian)
- Ponizovsky AM (1965) Solyanye Resursy Kryma (The Salt Resources of the Crimea). Simferopol: Krym, 163p (in Russian)
- Prikaz Ministerstva ekologii i prirodnykh resursov respubliki Krym ot 18 dekabrya 2017 goda № 2919 “O utverzhdenii Polozheniya o vodno-bolotnom ugod'ye «Vostochnyy Sivash» (The order of the Ministry of Ecology and Natural Resources of the Crimea Republic dated December 18, No. 2919 “On approval of the Regulation on the wetland “the Eastern Sivash”) (2017) (in Russian)
- Schurova ES, Sovga EE, Khmara TV, Lomakin PD (2016) Izmeneniya Resursnogo Potenciala Zaliva Sivash (Azovskoe More) posle Perekrytiya Severo-Krymskogo Kanala v 2014 Godu (Changes in the Resource Potential of the Sivash Bay (the Sea of Azov) after the North-Crimean

- Canal Overlap in 2014). In: SFU, Ekologija. Ekonomika. Informatika. Azovskoe More, Kerchenskij Proliv i Predprolivnye Zony v Chernom More: Problemy Upravlenija Pribrezhnyimi Territorijami dlja Obespechenija Jekologicheskoj Bezopasnosti i Racional'nogo Pririodopol'zovanija: sbornik materialov III Vserossijskoj konferencii (Ecology. Economy. Informatics. The Sea of Azov, the Kerch Strait and Near-Strait Zones in The Black Sea: The Problems of Management of Coastal Territories to Ensure Ecological Safety and Sustainable Nature Exploitation: proceedings of the 3d all-Russian conference). SFU Publ, Rostov-on-Don, pp 296–307 (in Russian)
- Shchurova ES, Stanichnaya RR, Stanichnij SV (2016) Ispol'zovaniye sputnikovykh dannykh dlya issledovaniya sovremennogo sostoyaniya zaliva Sivash (Using satellite data to study the current state of the Sivash Bay). In: MHI, Ekologicheskaya Bezopasnost' Pribrezhnoj i Shel'fovoj Zon Morya (Ecological Safety of Coastal and Shelf Zones of Sea). MHI, Sevastopol, issue 3, pp 61–64 (in Russian)
- Sovga EE, Lomakin PD, Shchurova ES, Ovsyaniy EI (2014) Ekspeditsionnyye issledovaniya MGI v Vostochnom Sivashe letom i osen'yu 2014 goda (Expeditionary studies of MHI in the Eastern Sivash in summer and autumn of 2014). In: MHI, Ekologicheskaya Bezopasnost' Pribrezhnoj i Shel'fovoj Zon i Kompleksnoe Ispol'zovanie Resursov Shel'fa (Ecological Safety of Coastal and Shelf Zones and Comprehensive Use of Shelf Resources). MHI, Sevastopol, issue 28, pp 138–145 (in Russian)
- Sovga EE, Eremina ES, D'yakov NN (2018) Sistema ekologicheskogo monitoringa zaliva Sivash v sovremennykh usloviyakh (The system of ecological monitoring of the Sivash Bay in current conditions). In: MHI, Ekologicheskaya Bezopasnost' Pribrezhnoj i Shel'fovoj Zon Morya (Ecological Safety of Coastal and Shelf Zones of Sea). MHI, Sevastopol, issue 2, pp 22–38 (in Russian)
- Sovga EE, Eremina ES, Khmara TV (2018) Water balance in the Sivash Bay as a result of variability of the natural-climatic and anthropogenic factors. *Phys Oceanogr* 25(1):67–76
- Stashchuk MF, Suprychev VL, Khitraya MS (1964) Mineralogiya, geokhimiya i usloviya formirovaniya donnykh otlozheniy Sivasha (Mineralogy, geochemistry and conditions for the formation of Sivash bottom sediments). *Naukova dumka*, Kiev, 174p (in Russian)

Continuum Model of Layered Medium for Reservoir of Bazhenov Formation



V. I. Golubev, A. V. Ekimenko, I. S. Nikitin, and Yu. A. Golubeva

Abstract The paper investigates the process of seismic waves propagation in a heterogeneous geological medium. The linear elastic isotropic model was used. The geological model of the Bazhenov formation was constructed. To describe the dynamic behavior of the mudstone layer the continuous model of a layered medium taking into account interlayer slippage and delamination was used. Also, it takes into account the presence of a static rock pressure in the geological massif. Wave patterns and synthetic seismograms on the day surface were examined.

Keywords Oil and gas fields · Seismic exploration · Mathematical modeling · Numerical methods · Parallel algorithms · Continuum models

1 Introduction

The number of discoveries of large deposits with a relatively simple geological structure (pore reservoir type, large thicknesses) is decreasing, and hard-to-recover reserves (TRIZ) are of increasing interest. Thanks to new mining technologies, the development of such reserves is becoming cost-effective. In the case of Western Siberia, the main oil-producing region, the study of the Bazhenov formation and its analogues is of the greatest interest. The area of the distribution of rocks of this type is more than 1 million km² with an average thickness of 30 m. Rocks occur at depths of 2–3 km. According to some estimates, the oil resources contained in it can be up to 500 billion tons. The Bazhenov formation is formed by rocks of deep-water genesis: mudstones with interbeds of carbonate (limestone and dolomite) and siliceous (flask) rocks (Alexeev 2009; Braduchan et al. 1986). Collectors of the Bazhenov formation

V. I. Golubev (✉) · Yu. A. Golubeva
Moscow Institute of Physics and Technology, Dolgoprudny, Russia
e-mail: w.golubev@mail.ru

A. V. Ekimenko
Gazprom Neft Science and Technology Centre, Saint Petersburg, Russia

I. S. Nikitin
Institute of Computer Aided Design, Russian Academy of Sciences, Moscow, Russia

can be confined to micro-layered, sheet-like mudstones with interlayer voids with a high content of organic matter. The hollow space of the reservoirs is formed mainly as a result of autofluidic fracturing of rocks according to the stratification that occurs under the action of the conversion of organic matter from solid to liquid. This type of inhomogeneous medium can be effectively described by the continuum model of a layered medium with allowance for interlayer slippage and delamination (Nikitin 2008).

In this paper, we investigated the possibility of using the continuum model of a layered medium to describe the dynamic behavior of the Bazhenov formation reservoir.

2 Geological Model

As part of this work, a seismic geological model was constructed that describes the section of Western Siberia (Kontorovich et al. 1975). A typical section of wells in this region is the intercalation of sandstones of continental and shallow-water genesis and clayey rocks of a deeper water origin.

The geological section is thin-layered and generates a very complex wave field, the analysis of which is difficult, therefore the structure was generalized for current calculations. The terrigenous stratum of the Lower Cretaceous rocks is underlain by a regional mature layer of mudstones of the Bazhenov formation. A relatively high-speed terrigenous sequence begins again under the Bazhen layer. Such an approach makes it possible to single out only those features of the wave field that are caused by the presence of micro-layering (micro-fracturing).

The lithological composition of the Bazhenov formation determines the relatively low propagation velocity of seismic waves (less than 3000 m/s) and makes this stratum the most confident regional reference point.

The morphology of the reflecting boundaries is set based on the interpretation of the results of field seismic surveys. It is worth noting structural features: relatively small angles of inclination of the boundaries of the layers (do not exceed 5°), there are local uplifts and layers of variable thickness.

The geometry and elastic properties of each of the layers are shown at Fig. 1.

The main feature of the model is a fundamentally new approach to the description of the layer of Bazhenov mudstones of interest. As a rule, all layers of the model are considered as absolutely elastic; in this case, it is proposed to describe the Bazhenov formation as a medium with micro-layering, whose properties can vary depending on the stress state. The lithological composition (clay mudstone) and the properties (leafiness) of the formation make this approach justified and applicable.

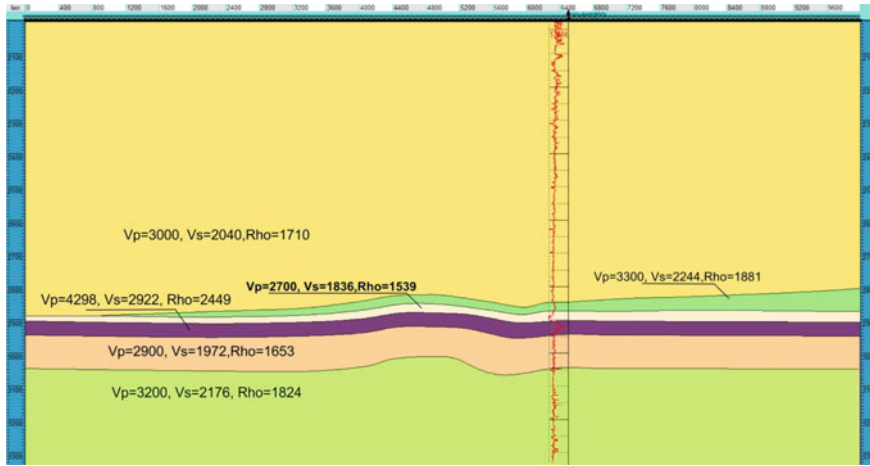


Fig. 1 Seismo-geological model

3 Mathematical Model of Geological Medium

For the description of the dynamic behavior of the geological medium the linear slip model was used

$$\rho \dot{v}_i = \nabla_j \sigma_{ij},$$

$$\dot{\sigma}_{ij} = q_{ijkl} e_{kl},$$

$$e_{ij} = (\nabla_j v_i + \nabla_i v_j)/2,$$

where ρ —the density, v_i —the velocity vector, σ_{ij} and e_{ij} —stress and strain tensors, ∇_j —the spatial derivative along j -th coordinate and q_{ijkl} —the rheology tensor. For isotropic medium it can be written as

$$q_{ijkl} = \lambda \delta_{ij} \delta_{kl} + \mu (\delta_{ik} \delta_{jl} + \delta_{il} \delta_{jk}).$$

where λ and μ —Lame constants and δ_{ij} —the Kronecker delta. For numerical simulation we used the rectangular grids each node of which contained material constants.

4 Bazhenov Formation Reservoir Model

In the mudstone layer models proposed in this work, the layers themselves are deformed linearly elastically. The equations of motion and rheological relations between tensors of tension and strain rate are used. Thus, the governing system of equations is a first-order partial-differential hyperbolic system.

Two additional variables are also introduced—the slippage velocity along the boundaries of the layer $\boldsymbol{\gamma}$ and the delamination velocity $\boldsymbol{\omega}$, perpendicular to it. If the normal stress at the interlayer contact boundary $\sigma_n < 0$, then the friction sliding mode is realized

$$\boldsymbol{\gamma} = \frac{\boldsymbol{\tau}}{\eta|\boldsymbol{\tau}|} \left\langle \frac{|\boldsymbol{\tau}|}{q|\sigma_n|} - 1 \right\rangle \text{ and } \boldsymbol{\omega} = 0 \quad (1)$$

where $\boldsymbol{\tau}$ —the tangential stress on the contact boundary, q —the dry friction coefficient, η —the contact viscosity, $\langle F \rangle = FH(F)$, $H(x)$ —the Heaviside function. In the other case, the delamination mode is realized, when $\Omega > 0$, $\boldsymbol{\tau} = \sigma_n = 0$, where Ω —displacement jump (delamination) along the normal to the boundaries of the layers, $\dot{\Omega} = \boldsymbol{\omega}$.

In order to proceed to a continuum model of the medium containing a system of such slip-delamination planes, $\boldsymbol{\gamma}$ and $\boldsymbol{\omega}$ are considered as continuous functions of coordinates and time. Relations of the theory of the slippage are applied, which was used by many authors to construct models of inelastic media with a continuous distribution of slip planes. These relations make it possible to take into account the contribution of slip rates $\boldsymbol{\gamma}$ and delamination $\boldsymbol{\omega}$ to inelastic strain rate tensors \mathbf{e}^γ and \mathbf{e}^ω , accordingly (Nikitin 2008):

$$\mathbf{e}^\gamma = (\mathbf{n} \otimes \boldsymbol{\gamma} + \boldsymbol{\gamma} \otimes \mathbf{n})/2, \boldsymbol{\gamma} \cdot \mathbf{n} = 0$$

$$\mathbf{e}^\omega = (\mathbf{n} \otimes \boldsymbol{\omega} + \boldsymbol{\omega} \otimes \mathbf{n})/2 = \boldsymbol{\omega} \mathbf{n} \otimes \mathbf{n}, \boldsymbol{\omega} = \boldsymbol{\omega} \mathbf{n}$$

Full strain rate tensor \mathbf{e} is the sum of elastic and inelastic parts:

$$\mathbf{e} = \mathbf{e}^e + \mathbf{e}^\gamma + \mathbf{e}^\omega, \mathbf{e} = (\nabla \mathbf{v} + \nabla \mathbf{v}^T)/2.$$

Here \mathbf{v} —“macroscopic” velocity of medium particles, \mathbf{e}^e —the elastic part of the strain tensor, that is related to Hooke’s law.

Everything written above is true for the case of a pre-unloaded medium. However, at a depth of 2–3 km, the static rock pressure is already so huge that it should be taken into account in the model. Consider the elastic half-space. Then at depth y (the OY axis is directed upwards) the steady state is determined as

$$\sigma_{yy} = \rho g y < 0, \sigma_{xx} = \sigma_{zz} = \frac{\lambda}{(\lambda + 2\mu)} \rho g y$$

Let's consider the plane with the normal $\mathbf{n}(n_x, n_y, n_z)$. The normal stress can be calculated as

$$\sigma_n^0 = \mathbf{n} \cdot \boldsymbol{\sigma} \cdot \mathbf{n} = \sigma_{ij} n_i n_j = \sigma_{xx} n_x^2 + \sigma_{yy} n_y^2 + \sigma_{zz} n_z^2$$

Consequently,

$$\sigma_n^0 = \rho g y \left(\frac{\lambda}{(\lambda + 2\mu)} n_x^2 + n_y^2 + \frac{\lambda}{(\lambda + 2\mu)} n_z^2 \right) < 0 \quad y < 0$$

And in 2D case

$$n_z = 0, \sigma_n^0 = \rho g y \left(\frac{\lambda}{(\lambda + 2\mu)} n_x^2 + n_y^2 \right)$$

The tangential stress at the plane with the normal \mathbf{n}

$$\boldsymbol{\tau}_n^0 = \boldsymbol{\sigma} \cdot \mathbf{n} - (\mathbf{n} \cdot \boldsymbol{\sigma} \cdot \mathbf{n}) \mathbf{n}$$

$$\tau_x^0 = \sigma_{xx} n_x - (\sigma_{xx} n_x^2 + \sigma_{yy} n_y^2 + \sigma_{zz} n_z^2) n_x$$

$$\tau_y^0 = \sigma_{yy} n_y - (\sigma_{xx} n_x^2 + \sigma_{yy} n_y^2 + \sigma_{zz} n_z^2) n_y$$

$$\tau_z^0 = \sigma_{zz} n_z - (\sigma_{xx} n_x^2 + \sigma_{yy} n_y^2 + \sigma_{zz} n_z^2) n_z$$

And when $\sigma_{xx} = \sigma_{zz} = \frac{\lambda}{\lambda + 2\mu} \rho g y$, $\sigma_{yy} = \rho g y$

$$\tau_x^0 = -\frac{2\mu}{\lambda + 2\mu} \rho g y \cdot n_y^2 n_x,$$

$$\tau_y^0 = \frac{2\mu}{\lambda + 2\mu} \rho g y \cdot (n_x^2 + n_z^2) n_y,$$

$$\tau_z^0 = -\frac{2\mu}{\lambda + 2\mu} \rho g y \cdot n_y^2 n_z$$

In 2D case, when $n_z = 0$, $n_x^2 + n_y^2 = 1$, $\tau_z^0 = 0$

$$\tau_y^0 = -\frac{2\mu}{\lambda + 2\mu} \rho g y \cdot n_x^2 n_y, \tau_x^0 = -\frac{2\mu}{\lambda + 2\mu} \rho g y \cdot n_y^2 n_x,$$

$$|\boldsymbol{\tau}_n^0| = \sqrt{(\tau_x^0)^2 + (\tau_y^0)^2} = \frac{2\mu}{\lambda + 2\mu} \rho g |y| |n_x| |n_y|$$

We can simplify these relations. Define α —the angle between the plane and the OX axis. Then

$$\tau_n^0 = \frac{\mu}{\lambda + 2\mu} \rho g y \cdot \sin 2\alpha,$$

$$\sigma_n^0 = \rho g y \left(\frac{\lambda}{\lambda + \mu} \cdot \sin^2 \alpha + \cos^2 \alpha \right),$$

and the contact condition (1) taking into account the preliminary stress state associated with rock pressure, subject to the tightened boundary $\sigma_{nn} + \sigma_n^0 < 0$, should be modified as follows

$$\gamma = (\sigma_{n\tau} + \tau_n^0) \left\langle \frac{|\sigma_{n\tau} + \tau_n^0|}{q|\sigma_{nn} + \sigma_n^0|} - 1 \right\rangle \frac{1}{\eta|\sigma_{n\tau} + \tau_n^0|}.$$

The corresponding differential equation for the component of the tangential stress $\sigma_{n\tau}$ on the considered site, oriented by the normal \mathbf{n} , taking into account possible slippage, is as follows:

$$\dot{\sigma}_{n\tau} = \mu(v_{n,\tau} + v_{\tau,n}) - \mu \frac{\sigma_{n\tau} + \tau_n^0}{\eta|\sigma_{n\tau} + \tau_n^0|} \left\langle \frac{|\sigma_{n\tau} + \tau_n^0|}{q|\sigma_{nn} + \sigma_n^0|} - 1 \right\rangle$$

When $\sigma_{nn}^{n+1e} + \sigma_n^0 < 0$, $|\sigma_{n\tau}^{n+1e} + \tau_n^0| > q|\sigma_{nn}^{n+1e} + \sigma_n^0|$ the correction formula resulting from the implicit approximation of this equation has the form

$$\sigma_{n\tau}^{n+1} = \text{sign}(\sigma_{n\tau}^{n+1e} + \tau_n^0) q |\sigma_{nn}^{n+1e} + \sigma_n^0| \frac{(1 + \delta|\sigma_{n\tau}^{n+1e} + \tau_n^0|)}{(1 + \delta q |\sigma_{nn}^{n+1e} + \sigma_n^0|)} - \tau_n^0$$

where $\sigma_{n\tau}^{n+1e} = \sigma_{n\tau}^n + \mu(v_{n,\tau}^{n+1} + v_{\tau,n}^{n+1})\Delta t$ —values of the stress components in the new time layer after calculating the “elastic” step, Δt —is the time step in the used difference scheme for the numerical solution of the system of equations, $\delta = \eta/(\mu\Delta t)$.

In the case of horizontal layers considered in the work, the correction formula for the tangential stress after the “elastic” calculation step has the form:

$$\sigma_{xy}^{n+1} = \text{sign}(\sigma_{xy}^{n+1e}) q |\sigma_{yy}^{n+1e} + \rho g y| \frac{(1 + \delta|\sigma_{xy}^{n+1e}|)}{(1 + \delta q |\sigma_{yy}^{n+1e} + \rho g y|)}.$$

5 Numerical Method

Various numerical approaches are used to describe dynamic processes in geological media (Dumbser et al. 2007; Etgen and O'Brien 2007; Hestholm 2009; Hobro et al. 2014). Sufficiently comprehensive reviews of various methods are presented in Virieux et al. (2011; Carcione et al. 2002). Between latest papers, we can distinguish (Lisitsa et al. 2016), devoted to the construction of a hybrid numerical method, and (Golubev 2019), that generalizes the grid-characteristic method to inverse migration problems.

Let us consider in more details the numerical method used to solve the elastic part of the problem. In the three-dimensional case, the vector of unknowns contains nine components

$$\mathbf{u} = \{v_1, v_2, v_3, \sigma_{11}, \sigma_{12}, \sigma_{13}, \sigma_{22}, \sigma_{23}, \sigma_{33}\}^T.$$

Initial system of equations can be rewritten in the canonical form

$$\frac{\partial \mathbf{u}}{\partial t} = \sum_{j=1}^3 \mathbf{A}_j \frac{\partial \mathbf{u}}{\partial x_j},$$

where \mathbf{A}_j — 9×9 matrices and (x_1, x_2, x_3) —the Cartesian system. After the splitting procedure we obtain three system of equations.

$$\frac{\partial \mathbf{u}}{\partial t} = \mathbf{A}_j \frac{\partial \mathbf{u}}{\partial x_j}, \quad j = 1, 2, 3$$

Each of systems is hyperbolic and appropriate eigenproblem can be solved analytically

$$\frac{\partial \mathbf{u}}{\partial t} = \mathbf{\Omega}_j^{-1} \mathbf{\Lambda}_j \mathbf{\Omega}_j \frac{\partial \mathbf{u}}{\partial \xi_j}$$

where $\mathbf{\Omega}_j$ contains eigenvectors and $\mathbf{\Lambda}_j$ —the diagonal matrix with eigenvalues

$$\mathbf{\Lambda}_j = \text{diag}(c_1, -c_1, c_2, -c_2, c_2, -c_2, 0, 0, 0)$$

where $c_1 = \sqrt{(\lambda + 2\mu)/\rho}$, $c_2 = \sqrt{\mu/\rho}$.

Taking into account Riemann invariants $\mathbf{v}_j = \mathbf{\Omega}_j \mathbf{u}$, we obtain a set of independent linear transport equations

$$\frac{\partial \mathbf{v}_j}{\partial t} + \mathbf{\Lambda}_j \frac{\partial \mathbf{v}_j}{\partial \xi_j} = 0.$$

Using the interpolation procedure with chosen approximation order we solve these equations. And then apply inverse transformation for calculated invariants.

Note that, to calculate the dynamic behavior of the mudstone layer, it is enough to simply apply the correcting relations given above after each elastic time step.

6 Numerical Results

In this work, a computer simulation of seismic waves propagation in the Bazhenov formation model was carried out. A 2D statement of the problem was considered. The calculation parameters were selected to obtain results that are most similar to those used in geological exploration.

The computational domain was a rectangle with sizes 10 km \times 1.5 km, covered with a square computational grid with a spatial step of 1 m. The total number of nodes in the grid was 15 million. In each node of the model, the P-wave velocity, the S-wave velocity and density were stored. To describe the dynamic behavior of a thin-layered mudstone layer, a continuum model was used. The time step was chosen from the Courant condition and was 0.3 ms. A total of 3000 timesteps were completed. As a source of perturbation, a longitudinal wave was used, initially buried by 400 m, to reduce the calculation time. The time dependence of the source signal was set in the form of a Ricker pulse with a main frequency of 30 Hz. In a numerical experiment, a vertical velocity component was recorded on the surface every 100 m. Figure 2

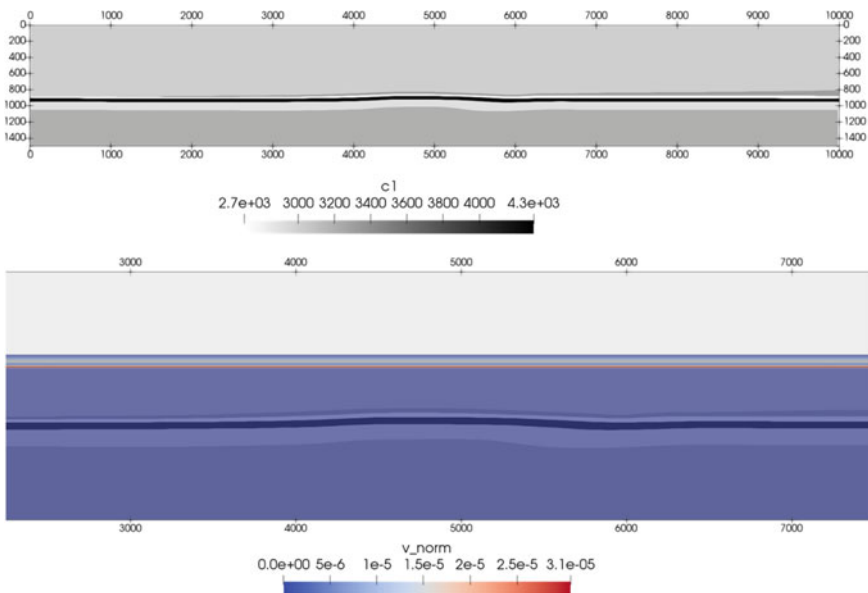


Fig. 2 Spatial distribution of P-wave velocity in the model (above) and the wave field (below)

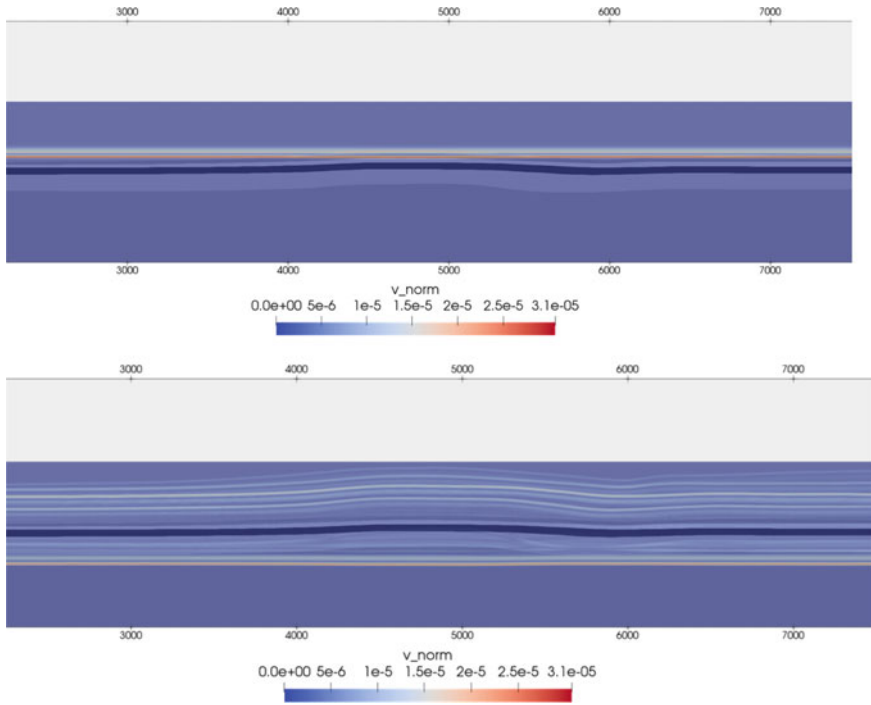


Fig. 3 The wave field in the consecutive time moments

shows the model loaded into the program, as well as the distribution of the wave field at the moment when the initial wave passed the mark of 500 m. Wave patterns at successive times are shown at Fig. 3.

The calculated wave fields show complete agreement with the elastic solution for the case when microcracks are closed (see Fig. 4a, b). On the other hand, with a change in the stiffness parameters of micro-layering (micro-fracturing), a change in the shape of the reflected wave is observed. The blue rectangle marks the portion of the target interval where the changes are most clearly visible. In the case of open microlayers, reflection becomes more intense. The presented results show the principal applicability of the continuous model for studying the influence of rocks having a thin-layered, shale structure. Mathematical modeling can be used to assess the degree of influence of the openness of micro-layers (microcracks) on the wave field recorded on the day surface.

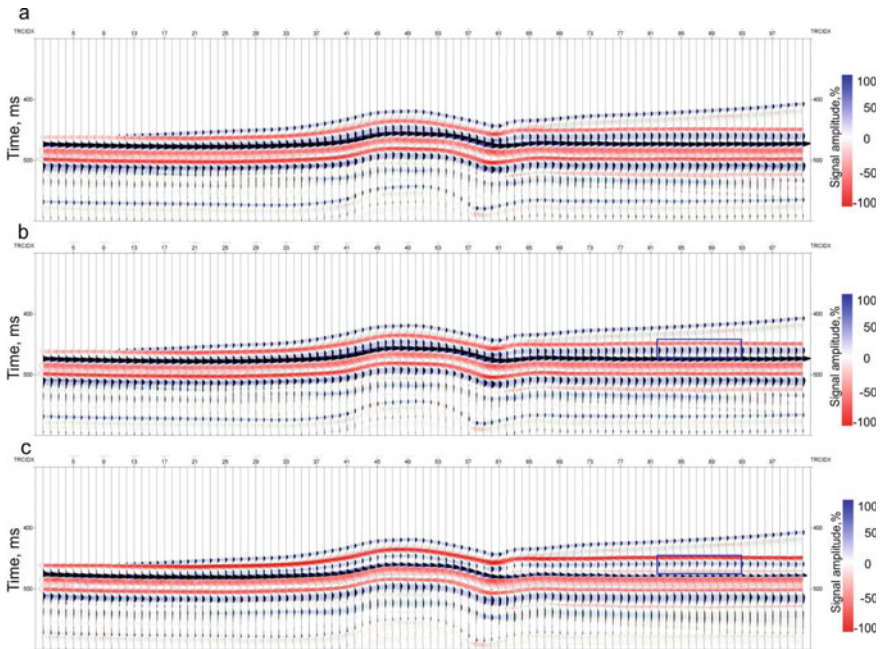


Fig. 4 Seismograms for investigated geological model. Variants: **a** elastic medium (continuous model is not applied), **b** continuous model is used, and cracks are closed, **c** continuous model is used, and cracks are opened

It is worth noting that in this article only modeling and analysis of the results simulating ground-based seismic surveys is considered. At the same time, calculations performed for modifications of borehole seismic surveys: vertical seismic profiling (VSP) and acoustic logging (AK) are also of interest. Such calculations may be a continuation of the current work.

Acknowledgements This work was carried out with the financial support of the Russian Science Foundation, project no. 19-71-10060.

References

- Alexeev AD (2009) Natural oil reservoirs in sediments of the Bazhenov formation in the west of the latitudinal Ob. Ph.D. thesis, Moscow (in Russian)
- Braduchan YV, Gurari FG, Zakharov VA et al (1986) Bazhenov horizon of Western Siberia, Novosibirsk. "Science" Siberian Department, 217 p (1986) (in Russian)
- Carcione JM, Herman GC, Kroode PE (2002) Y2K review article: seismic modeling. *Rev Lit Arts Am* 67(4):1304–1325
- Dumbser M, Käser M, De La Puente J (2007) Arbitrary high-order finite volume schemes for seismic wave propagation on unstructured meshes in 2D and 3D. *Geophys J Int* 171:665–694

- Etgen JT, O'Brien MJ (2007) Computational methods for large-scale 3D acoustic finite-difference modeling: a tutorial. *Geophysics* 72:SM223-SM230
- Golubev VI (2019) The usage of grid-characteristic method in seismic migration problems. *Smart Innov Syst Technol* 133:143–155
- Hestholm S (2009) Acoustic VTI modeling using high-order finite differences. *Geophysics* 74:T67–T73
- Hobro JWD, Chapman CH, Robertsson JOA (2014) A method for correcting acoustic finite-difference amplitudes for elastic effects. *Geophysics* 79:T243–T255
- Kontorovich AE, Nesterov II, Salmanov FK et al (1975) The geology of oil and gas in Western Siberia. Nedra, Moscow, 680 p (in Russian)
- Lisitsa V, Tcheverda V, Botter C (2016) Combination of the discontinuous Galerkin method with finite differences for simulation of seismic wave propagation. *J Comput Phys* 311:142–157
- Nikitin IS (2008) Dynamic models of layered and block media with slip, friction, and separation. *Mech Solids* 43(4):652–661
- Virieux J, Calandra H, Plessix RE (2011) A review of the spectral, pseudo-spectral, finite-difference and finite-element modelling techniques for geophysical imaging. *Geophys Prospect* 59(5):794–813

Intensifying Mixing During Vortex Motion in a T-Shaped Micromixer



A. Yu. Kravtsova , Yu. E. Meshalkin, M. V. Kashkarova, A. V. Bilsky, and I. V. Naumov 

Abstract The efficiency of mixing in the T-microchannel under external periodic perturbation of the flow by the LIF method for various flow regimes realized in the mixing channel has been studied. The transition to a non-stationary flow regime at a frequency of 500 Hz has been registered. A significant change in the mixing efficiency up to 35% at the determined frequencies of external influence is shown.

Keywords Micromixer · Flow visualization · T-junction · Vortex flow · LIF technique

1 Introduction

The development of high-precision technology and medicine puts forward new requirements for the miniaturization of devices. Effective and resource-saving systems based on microelectromechanical (MEM) technologies are becoming increasingly important. For example, micromixers are used for chemical reactions and medical tests, in the production of drugs and in the biological industry. Their advantages are the small volume of necessary reagents and the possibility of continuous, controlled and safe reactions with the release of heat or toxic substances. Since microchannel mixers operate, as a rule, in laminar flow regimes, the task of increasing the mixing efficiency (productivity) is urgent.

The flow pattern structure and mixing processes in a T-shaped micromixer were investigated by various authors. Thus, in the work of Engler et al. (2004) it was shown that the motion of two parallel flows in a microchannel leads to the formation of stationary symmetric Dean vortices. When the Reynolds number increases to 150, the Dean vortices lose their symmetry. The authors of work (Gobert et al. 2006) studied stationary non-symmetric ($Re = 186$) and non-stationary periodic ($Re = 240$) regimes by the methods of mathematical modeling of flow hydrodynamics and using an experimental method of velocity measurement by Particle Tracking

A. Yu. Kravtsova · Yu. E. Meshalkin · M. V. Kashkarova · A. V. Bilsky · I. V. Naumov (✉)
Kutateladze Institute of Thermophysics, Siberian Branch of the Russian Academy of Sciences,
Novosibirsk, Russia
e-mail: naumov@itp.nsc.ru

Velocimetry—PTV. As a result, a detailed picture of the concentration distribution in the mixing process was obtained. Wong et al. (2004) investigated the mixing efficiency of two liquids in the Reynolds number range from 50 to 1400 and showed that the most effective mixing occurs when unsteady flow regimes appear. This was also confirmed in the work of Dreher et al. (2009). Hoffman et al. (2003) experimentally studied the motion of liquids in mixing channels of different sizes by laser-induced fluorescence and particle image velocimetry. On the basis of the obtained data, the efficiency of mixing flows was calculated. It was shown that with an increase in the Reynolds number, the flow in the output channel changes its configuration, a transfer of reagents occurs in the transverse direction relative to the main flow and, as a consequence, the mixing efficiency increases. It was noted that the occurrence of a pair of intense longitudinal vortices in the output channel is associated with the Kelvin–Helmholtz instability arising from the interaction of counter-flows flowing into the output channel. A deeper study of the flow structure in the T-microchannel for Reynolds numbers from 5 to 600 was carried out in the work of Minakov et al. (2013). The authors presented three-dimensional vortex structures, realized in the output channel, and showed that at Reynolds numbers over 240, the flow has a periodic flow regime, and at Re over 400 the regime is quasi-periodic. The frequency of velocity pulsations for these regimes was calculated. It was shown that for some flow regimes, a selected pulsation frequency with the highest amplitude was observed.

The study of the possibility to control the flow and efficiency of liquid mixing by applying a pulse flow to the inputs of the T-microchannel was conducted in Glasgow et al. (2004), Goulet et al. (2005), Ma et al. (2008), Mao and Xu (2009). Thus, in the work of Glasgow et al. (2004) it was shown that an increase in the frequency of external flow pulsations enhances mixing. Goulet et al. (2005) demonstrated the effect of phase shift pulsations on the mixing efficiency in the T-microchannel. Then, Ma et al. (2008) found that there are optimal flow pulsation frequencies for increasing mixing in the case of low Reynolds numbers ($Re < 0.24$). Mao and Xu (2009) showed that mixing at low Reynolds numbers ($Re < 10$) may be amplified by a pulse flow with large amplitude. Erko et al. (2016) numerically demonstrated the effect of in-phase pulsations of the liquid flow rate at phase shift on the dynamics and structure of the flow and the mixing efficiency in the T-microchannel at $Re = 300$.

Basically, to increase the efficiency of the flow mixing in the output channel of the T-type mixer, the researchers used a periodic flow rate of liquid at the inlet of the micromixer. At that, the amplitude of the flow rate pulsations was commensurate or exceeded the average value of the flow rate. The idea of this work is to apply low-amplitude perturbations to influence the flow instability for intensification of large-scale vortices, just as, for example, low-amplitude external influence leads to the intensification of vortices in jet flows (Alekseenko et al. 2001, 2003, 2004). The paper presents an experimental study of the mixing efficiency in a T-shaped microchannel at moderate Reynolds numbers under conditions of external low-amplitude periodic flow disturbance.

2 Experimental Setup and Measurement Technique

To obtain the flow characteristics, the method of laser induced fluorescence with micron resolution (μ LIF) inverted into a microscope (Carl Zeiss Axio Observer.Z1) is used. A T-shaped microchannel made of optically transparent SU-8 material is mounted on the microscope stage. The constant liquid flow rate in the channel is set by a KD Scientific syringe pump with two outputs. Its maximum nominal flow rate is 106.6 ml/h. Distilled water is supplied to one input of the microchannel, and the other input is fed with distilled water with Rhodamine 6gG dye, dissolving at the molecular level. The solution concentration is 15 mg of dye per liter of water. The flow in a microchannel is illuminated by the mercury lamp. Using a filter, a wavelength of 532 nm is selected from its spectrum to correspond to the maximum absorption spectrum of the dye. The light emitted by the dye in the red wavelength range is reflected by a dichroic mirror on a 2048×2048 pixels CCD camera. The resulting images are processed on a personal computer using the software package "ActualFlow".

To create external disturbances, a unique system of flow excitation on a piezoelectric actuator, creating a flow rate with pulsations of a given frequency and amplitude was developed and assembled. The free run of the piezoactuator at a minimal preload of 1 kN and a maximum voltage of 150 V (U_+) is 150 μ m. Under the action of an alternating voltage with a given frequency and amplitude, the piezoceramic actuator, deforming, transmits disturbances to the flow through the rod, displacing the volume of the working fluid equal to the cross section of the rod multiplied by the actuator run. The flow rate of the supplied liquid for half of the period is 3.14×10^{-5} m³/s at the frequency of external pulsations $f = 1000$ Hz. The scheme of the experimental site is shown in Fig. 1.

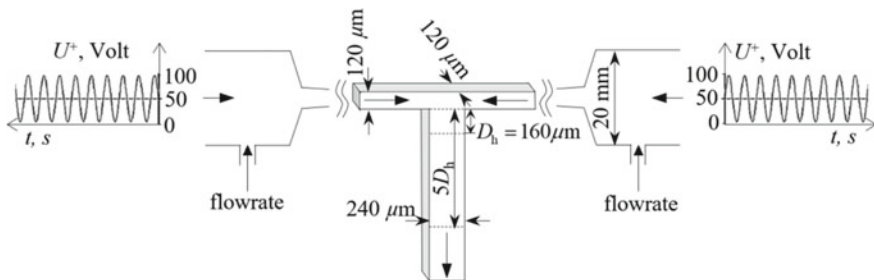


Fig. 1 Sketch of experimental channel

3 The Experimental Conditions

Studies were conducted in a T-shaped microchannel with dimensions of $120 \times 120 \times 240$ microns (height, width of the input channel and width of the output channel, respectively). The amplitude of the external periodic perturbations of the flow was fixed and equaled $100 \mu\text{m}$. The pulsation frequency f varied between 0 and 1100 Hz with a step of 100 Hz. In the region of the greatest change in the mixing efficiency (from 400 to 1000 Hz), the frequency step of external pulsations was 25 Hz. Pulsations were created in the same phase at both inputs of the T-microchannel. The study of the flow structure and measurement of its mixing efficiency were carried out for three different regimes, implemented in the mixing channel: stationary vortex $\text{Re} = 120$, non-stationary vortex $\text{Re} = 186$ and quasi-periodic non-stationary $\text{Re} > 400$ (Minakov et al. 2013). The Reynolds number $\text{Re} = U_0 D_h / \nu$ was calculated from the mean flow velocity in the mixing channel U_0 , the hydraulic diameter of the rectangular output channel $D_h = 160 \mu\text{m}$ and the kinematic viscosity ν , the value of which was taken with account for the room temperature. The Dankwerts segregation intensity was used to calculate the mixing efficiency in the T-microchannel (Dankwerts 1952): $I_M = 1 - \sigma / \sigma_0$, where $\sigma^2 = \frac{1}{N} \sum_{i=1}^N (c_i - \bar{c})^2$, \bar{c} was the average value of the dye concentration in the flow, $\sigma_0^2 = \bar{c}(c_{\max} - \bar{c})$ corresponded to the maximum standard deviation of the liquid mixing with concentrations 0 and c_{\max} . I_{M0} was the mixing efficiency in case of undisturbed flow. The mixing efficiency was calculated from the time-averaged concentration fields obtained by the μLIF method at a distance of D_h and $5D_h$ from the entrance to the mixing channel for each flow regime with and without superimposed pulsations. Normalized profiles of undisturbed flow concentration for $\text{Re} = 186$ are shown in Fig. 2.

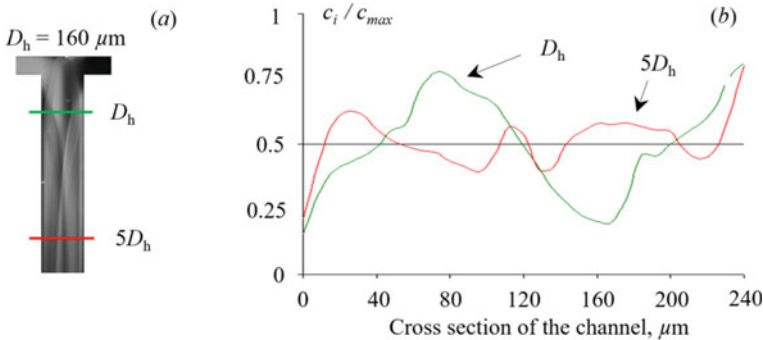


Fig. 2 The time-average concentration field for undisturbed flow at $\text{Re} = 186$ (a). The normalized concentration profiles on distance D_h and $5D_h$ from inside mixing channel (b)

4 Results

For each flow regime under study, the figures below References (a) show the three-dimensional structure of the flow realized in the mixing channel in the case of an undisturbed flow. The results of mathematical modeling are provided from the work of Minakov et al. (2013). The time-averaged concentration fields obtained by the μ LIF method are shown in Figs. 3, 4 and 5b–e in the flow without disturbance and in the case of the greatest change in the flow structure at frequencies $f = 500, 700, 800, 1000$ Hz.

4.1 Vortex Stationary Flow Regime

The first series of experiments is presented for the stationary vortex flow regime $Re = 120$ (Fig. 3), which is characterized by the presence of symmetric vortices, called Dean vortices (Fig. 3a).

The time-averaged concentration field for the undisturbed stationary flow regime is shown in Fig. 3b. When the frequency of external influences increases to 500 Hz, a slight broadening of the interface between liquids is observed (Fig. 3c), however, at a frequency of 700 Hz, it narrows (Fig. 3d). Further, as the frequency of external disturbances increases, the interface expands (Fig. 3e), and at a frequency of 1000 Hz

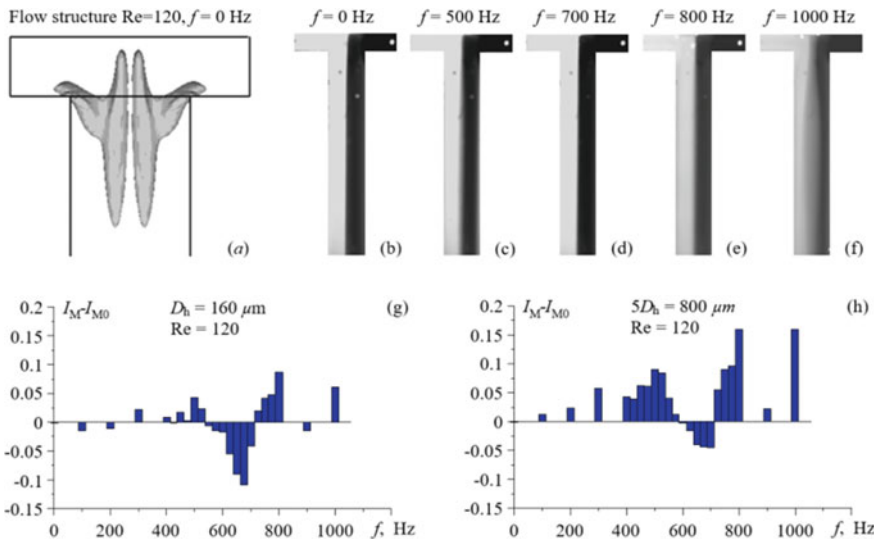


Fig. 3 $Re = 120$. The three-dimensional flow structure—Dina vortex (Minakov et al. 2013) (a), concentration field for external perturbation frequency **b** $f = 0$ Hz, **c** $f = 500$ Hz, **d** $f = 700$ Hz, **e** $f = 800$ Hz, **f** $f = 1000$ Hz, the plot of fluid effective mixing for different frequencies for distance **g** D_h **h** $5D_h$

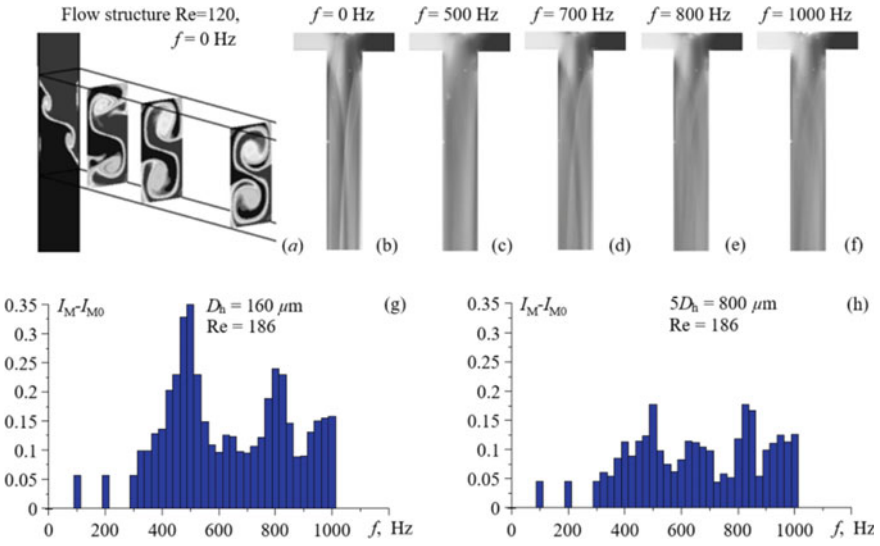


Fig. 4 $Re = 186$. The three-dimensional S-vortex structure (Minakov et al. 2013) (a), concentration field for external perturbation frequency **b** $f = 0$ Hz, **c** $f = 500$ Hz, **d** $f = 700$ Hz, **e** $f = 800$ Hz, **f** $f = 1000$ Hz, the plot of fluid effective mixing for different frequencies for distance **g** D_h и **h** $5D_h$

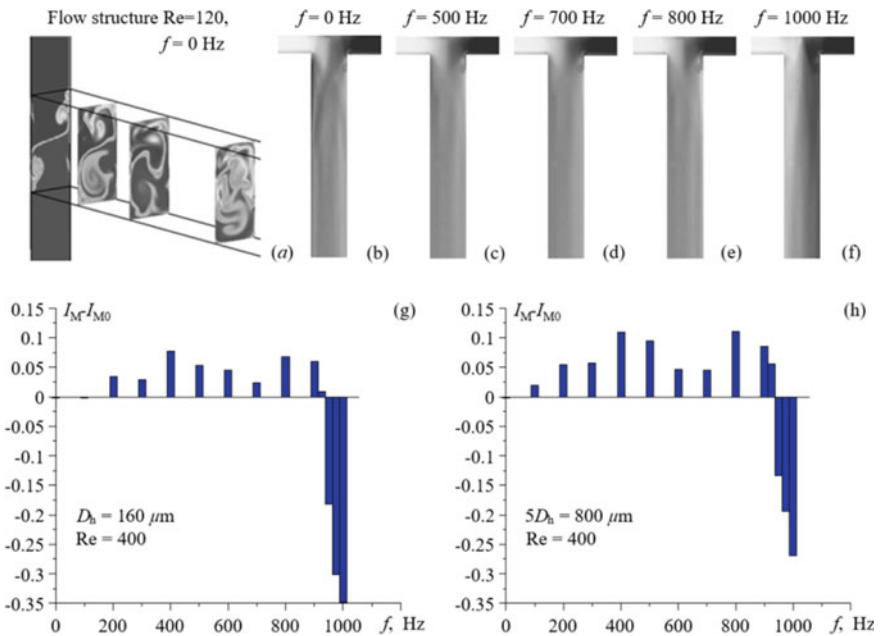


Fig. 5 $Re = 400$. The quasi periodic three-dimensional vortex structure (Minakov et al. 2013) (a), concentration field for external perturbation frequency **b** $f = 0$ Hz, **c** $f = 500$ Hz, **d** $f = 700$ Hz, **e** $f = 800$ Hz, **f** $f = 1000$ Hz, the plot of fluid effective mixing for different frequencies for distance **g** D_h and **h** $5D_h$

its maximum width is about a third of the width of the mixing channel (Fig. 3f). Assumingly, with an increase in the frequency of external disturbances, Dean vortices still exist in the microchannel, however, they shift closer to the walls of the output channel, and their length decreases. The results of estimation of mixing efficiency are presented in Fig. 3g, h. The zero value corresponds to the value of the mixing efficiency in the case of an unperturbed flow. Positive values of $I_M - I_{M0}$ value correspond to an increase in the mixing efficiency in relative units, and negative values correspond to a decrease. It can be seen that when the frequency increases from 0 to 500 Hz at a distance D_h from the entrance to the mixing channel, the mixing efficiency increases by 4.3%, but already at a distance $5D_h$, the influence of external pulsations becomes stronger by 9%. With a further increase in the frequency of external action to 650 Hz, the mixing efficiency is significantly reduced relative to the undisturbed flow—by 11% at a distance D_h and by 4% at $5D_h$. Further increase in frequency leads to increased mixing efficiency. At a frequency of 800 Hz, the increase in mixing efficiency reaches its maximum: at a distance D_h , it increases by 9%, and at a distance $5D_h$ —by 16% relative to the undisturbed flow. Thus, the mixing efficiency can be significantly changed at external periodic perturbations of the flow.

4.2 Stationary Asymmetrical Regime

For the stationary asymmetric vortex mode $Re = 186$ (Fig. 4a, b) the mixing efficiency at the distance D_h from the entrance to the mixing channel with an increase in frequency from 0 to 500 Hz increases by 35% (Fig. 4g). As it is seen in Fig. 4c, at the frequency of external disturbances $f = 500$ Hz, the flow undergoes significant changes: it becomes homogeneously mixed and, as can be assumed, there is a transition to a non-stationary flow regime due to the occurrence of the Kelvin–Helmholtz instability at the boundaries of the vortex structure. A further increase in the frequency of external disturbances up to 700 Hz (Fig. 4d) leads to flow structuring and contraction, and the mixing efficiency is reduced by 26% at a distance D_h . However, relative to the undisturbed flow, the mixing efficiency for the flow regime with the frequency of 700 Hz increases by 9%. The efficiency up to 800 Hz results in a 24% increase in mixing efficiency at D_h distance and a 12% increase at $5D_h$. The concentration field becomes more uniform (Fig. 4e).

In the frequency range from 800 to 900 Hz, the mixing efficiency decreases to the level of the regime with a frequency of 650 Hz, and in the range from 900 to 1000 Hz, it again increases. Relatively to the undisturbed regime, the mixing efficiency for the 1000 Hz mode increases by 16% at a distance D_h (Fig. 4g), and at a distance $5D_h$ it rises by 13% (Fig. 4h).

4.3 Quasi-Periodic Nonstationary Flow Regime

The measurement results for the quasi-periodic nonstationary flow regime $Re > 400$ are presented in Fig. 5. This mode is characterized by the formation of an S-shaped structure at the entrance to the mixing channel and its rather rapid destruction downstream (Fig. 5a, b). With an increase in the frequency of periodic external flow disturbances (up to $f = 800$ Hz), the concentration fields in the output channel become more uniform (Fig. 5c–e) compared to the undisturbed flow. The maximum mixing efficiency at a distance D_h is achieved at a frequency $f = 400$ Hz and is 8%. At a distance $5D_h$ the maximum mixing efficiency is achieved at frequencies of 400 and 800 Hz—11%. However, as it is seen in Fig. 5 g, h, at a frequency of 1000 Hz, a decrease in mixing efficiency was found to be 27% at a distance $5D_h$ and 35% at a distance D_h from the entrance of the mixing channel. At the same time, the structure of the flow varies greatly (Fig. 5f).

5 Conclusion

In this paper, the concentration fields have been measured for different flow regimes implemented in the T-shaped microchannel: stationary vortex, stationary asymmetric, quasi-periodic non-stationary-with the presence of external periodic perturbations of the flow of different frequencies by the method of μ LIF. A significant change in the flow structure, as well as the transition from stationary to non-stationary flow regimes at selected frequencies has been observed.

On the basis of the time-average concentration fields obtained by the Dankwerts segregation method (Dankwerts 1952), the mixing efficiency has been calculated for each investigated flow regime with and without external influence on the flow. A significant change in the mixing efficiency has been found for all studied flow regimes in the case of an external perturbation of the flow. The mixing efficiency can be increased almost two times by applying external excitation with different frequencies: for a stationary symmetric vortex regime ($Re = 120$) $f = 800$ Hz, and for a stationary asymmetric regime ($Re = 186$) $f = 500$ Hz, $f = 800$ Hz. The suppression of mixing of two liquids has been also registered in the work: for a stationary symmetric vortex regime ($Re = 120$) $f = 700$ Hz and a quasi-periodic unsteady regime ($Re = 400$) $f = 1000$ Hz.

Acknowledgements This work was supported by Russian Science Foundation (grant № 19-79-10217).

References

- Alekseenko SV, Bilsky AV, Heinz O, Ilyushin BB, Markovich DM, Vasechkin VN (2001) Statistical description of turbulent axisymmetric impinging jet with excited coherent structures. TSFP digital library online. Begel House Inc., New York
- Alekseenko S, Bilsky A, Heinz O, Ilyushin B, Markovich D (2003) Turbulent structure of excited axisymmetric impinging jet. In: Sedimentation and sediment transport. Springer, Netherlands, pp 93–100
- Alekseenko SV, Bilsky AV, Markovich DM (2004) Application of the method of particle image velocimetry for analyzing turbulent flows with a periodic component. *Instrum Exp Tech* 47(5):703–710
- Dankwerts PV (1952) The definition and measurements of some characteristics of mixtures. *Appl Sci Res* 3:279–296
- Dreher S, Kockmann N, Woias P (2009) Characterization of laminar transient flow regimes and mixing in T-shaped micromixers. *Heat Transf Eng* 30(1):91–100
- Engler M, Kockmann N, Kiefer T, Woias P (2004) Numerical and experimental investigations on liquid mixing in static micromixers. *Chem Eng J* 101:315–322
- Erko E, Fonte CP, Dias MM, Lopes JC, Santos RJ (2016) Numerical study of active mixing over a dynamic flow field in a T-jets mixer—induction of resonance. *Chem Eng Res Des* 106:74–91
- Glasgow I, Lieber S, Aubry N (2004) Parameters influencing pulsed flow mixing in microchannels. *Anal Chem* 76(16):4825–4832
- Gobert C, Schwert F, Manhart M (2006) Lagrangian scalar tracking for laminar micromixing at high Schmidt numbers. In: Proceedings of ASME joint U.S.-European fluids engineering summer meeting, Miami, No. FEDSM2006-98035, pp 1053–1062
- Goulet A, Glasgow I, Aubry N (2005) Dynamics of microfluidic mixing using time pulsing. *Discrete Continuous Dyn Syst* 2005(4):327–336
- Hoffmann M, Rabiger N, Schluter M, Blazy S, Bothe D, Stemich C, Warnecke H-J (2003) Experimental and numerical investigations of T-shaped micromixers. In: 11th European conference on mixing, Bamberg, Germany, pp 269–276
- Ma Y, Sun CP, Fields M, Li Y, Haake DA, Churchil BM, Ho CM (2008) An unsteady microfluidic T-form mixer perturbed by hydrodynamic pressure. *J Micromech Microeng* 18(4):45015
- Mao WB, Xu JL (2009) Micromixing enhanced by pulsating flows. *Int J Heat Mass Transf* 52(21):5258–5261
- Minakov A, Yagodnitsyna A, Lobasov A, Rudyak V, Bilsky A (2013) Study of fluid flow in micromixer with symmetrical and asymmetrical inlet conditions. *Houille Blanche*, no 5, pp 12–21
- Wong SH, Ward MCL, Wharton CW (2004) Micro T-mixer as a rapid mixing micromixer. *Sens Actuators B* 100:359–379

Manifestation of the Quintet of the Fundamental Spheroidal Mode ${}_0S_2$ of Earth's Free Oscillations in Electromagnetic Variations at the Mikhnevo Observatory



S. A. Riabova, A. A. Spivak, and V. A. Kharlamov

Abstract In this work, we study the splitting of the lowest frequency ${}_0S_2$ of the Earth's free oscillations in the Earth's electromagnetic field during large earthquakes. The work analyzes the results of electromagnetic monitoring at the Mikhnevo geophysical observatory of Sadovsky Institute of Geosphere Dynamics of Russian Academy of Sciences (54.96° N, 37.77° E), carried out using a LEMI-008 magnetometer (magnetic field components) and INEP fluxometer (vertical component of electric field). The estimates of the ${}_0S_2$ singlet frequencies, obtained from experimental data on the detection of magnetic and electric fields, are determined with sufficiently high accuracy and have values rather close to theoretical ones. The theoretical frequencies are calculated by the Earth model 1066A.

Keywords Geomagnetic variations · Variations of atmospheric electricity · Earth's free oscillations · Singlet · Multiplet

1 Introduction

Since the globe is a limited elastic body, under the influence of various factors, including strong earthquakes, the Earth can resonate at certain frequencies the Earth's free oscillations are excited. These are families of oscillations of two types: spheroidal ${}_nS_l$ and torsional (toroidal) ${}_nT_l$, where the indices n and l denote the number of nodal surfaces inside the globe and the number of sectors bounded by such surfaces on its surface, respectively (Ness et al. 1961).

For the first time, a variation with a period of 57 min (the lowest-frequency spheroidal mode) in seismic vibrations, probably due to the Earth's free oscillations, was detected according to the registration data during the Kamchatka earthquake in 1952 (Becel et al. 2011). According to the registration data of the Chilean earthquake on May 22, 1960, the periods of dozens of spheroidal and toroidal free oscillations of the Earth were determined (Adushkin et al. 2018; Milyukov et al. 2018). The

S. A. Riabova (✉) · A. A. Spivak · V. A. Kharlamov
Sadovsky Institute of Geosphere Dynamics, Russian Academy of Sciences, Moscow, Russian Federation
e-mail: ryabovasa@mail.ru

period of spheroidal oscillations of ${}_0S_2$ from these observations was estimated to be approximately 54 min, which is in good agreement with the early theoretical estimates obtained by Bromwich (Benioff 1958) and Love (Gilbert and Dziewonski 1975). The oscillations in the ${}_0S_2$ main mode resemble the deformation of an elastic ball. Two nodal lines on the surface of the sphere coincide with the parallels of the Northern and Southern hemispheres. Subsequently, the Earth's free oscillations were observed by many researchers, and to date, the number of detected modes amounts to hundreds (Alsop et al. 1961; Masters and Widmer 1995; Rosat et al. 2005). In addition, it was found that in the spectra of other geophysical fields during some earthquakes, harmonics are observed that are close to the modes of the Earth's free oscillations, in particular, in the Earth's geomagnetic field (European Space Agency 2012). Studies have shown that due to the rotation and non-sphericity of the real Earth, each observed spheroidal ${}_nS_l$ (or toroidal ${}_nT_l$) mode is a multiplet and splits into $2l + 1$ singlets: ${}_nS_l^m$ (or ${}_nT_l^m$), where m is the azimuthal number (Love 1911).

The frequencies of the Earth's free oscillations are determined by changes in the density and elastic moduli in the deep regions of the planet, which allows them to be used to study the internal structure of the planet and build models of its bowels. Thanks to the use of geophysical data (in particular, geomagnetic monitoring), not only seismic monitoring, it became possible to significantly refine the results of experimental studies of the fine structure and periods of Earth's free oscillations.

The subject of this study is the Earth's lowest frequency free oscillation ${}_0S_2$, which, due to the rotation of the Earth, splits into 5 components with frequencies 300.0, 304.6, 309.2, 313.8 and 318.4 μHz (Nishida 2013). The study is carried out with the use of electromagnetic monitoring data during large earthquakes. The parameters of the considered events are listed in Table 1.

Table 1 Parameters of the considered in work earthquakes

No	Date	Time (UTC)	Latitude	Longitude	Mw	Depth, km	Region
1	April 16, 2013	10:44:20	28.033° N	61.996° E	7.7	80.0	83 km west of Khash, Iran
2	June 2, 2013	01:12:25	10.799° S	165.114° E	8.0	24.0	76 km west of Lata, Solomon Islands
3	April 3, 2014	02:43:13	20.571° S	70.493° W	7.7	22.4	53 km southeast of Iquique, Chile
4	April 25, 2015	06:11:25	28.231° N	84.731° E	7.8	8.2	36 km west of Hoody, Nepal
5	September 16, 2015	22:54:32	31.573° S	71.674° W	8.3	22.4	48 km east of Illapel, Chile

2 Initial Data and Data Processing

The initial data are the results of electromagnetic monitoring at the Mikhnevo Geophysical Observatory of Sadosky Institute of Geosphere Dynamics of Russian Academy of Sciences (54.96° N, 37.77° E). The monitoring is performed using a LEMI-008 magnetometer (magnetic field components) and an INEP fluxometer (vertical component of the electric field).

For analysis, recording sections of 15 days in length during the earthquakes were selected (the parameters of the considered earthquakes are given in Table 1) with a sampling step of 1 min. Then, filtering of the selected data sections was performed using a 7th-order Butterworth bandpass filter in the period interval 53–54 min. In order to increase the level of discrimination of spectral components of a multiplet close in periods, in addition to parametric spectral analysis, narrow-band adaptive notch filtering was used in this work. The results of spectral estimation are reflected in the form of spectra and STAN-diagrams.

The frequencies of the main mode ${}_0S_2$ estimated by this algorithm were compared with the frequencies calculated by the Earth model 1066A (Dahlen and Sailor 1979). Frequencies according to the Earth model 1066A were calculated using the perturbation method to calculate the splitting of an isolated degenerate eigenfrequency (Bromwich 1898).

3 Results and Its Discussion

As an example, we consider the splitting of the main spheroidal mode ${}_0S_2$ based on the analysis of electromagnetic variations during the 2015 Illapel earthquake, which occurred 46 km from Illapel (Chile) at a depth of 25 km on September 16, 2015 at 22:54:33 UT with moment magnitude 8.3 (according to the U.S. Geological Survey).

The results of the estimates of the spectra of variations in the electric and magnetic fields during the 2015 Illapel earthquake are shown in Fig. 1. The field of Fig. 1 shows the theoretical values of the frequencies of the ${}_0S_2$ quintet in the form of vertical lines. Figure 1 demonstrates that the values of the frequencies estimated from the data of variations in the electric and magnetic fields during this earthquake are close to the frequencies calculated by the model.

More detailed information on the identification of the spectral harmonics of the ${}_0S_2$ quintet is provided by STAN-diagrams. As an example, Figs. 2 and 3 show STAN-diagrams of variations in the geomagnetic and electric fields during the Chile (Illapel) earthquake on September 16, 2015, respectively. Analysis of the STAN-diagrams showed that all harmonics of the ${}_0S_2$ quintet are well resolved both for the geomagnetic field and for the electric field.

Of interest is the fact that the ${}_0S_2$ mode singlets were able to identify not only in the period close to the main shock, but also for several days after it, with the intensity and frequency of the singlets changing.

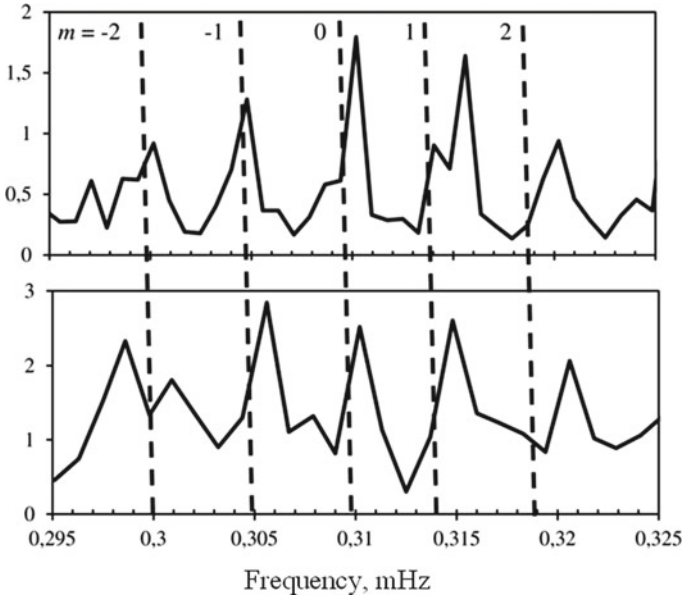


Fig. 1 Spectra of variations in the geomagnetic (upper panel) and electric fields (low panel) during the earthquake in Chile on September 16, 2015, showing the quintet of the spheroidal mode of Earth's free oscillations ${}_0S_2$

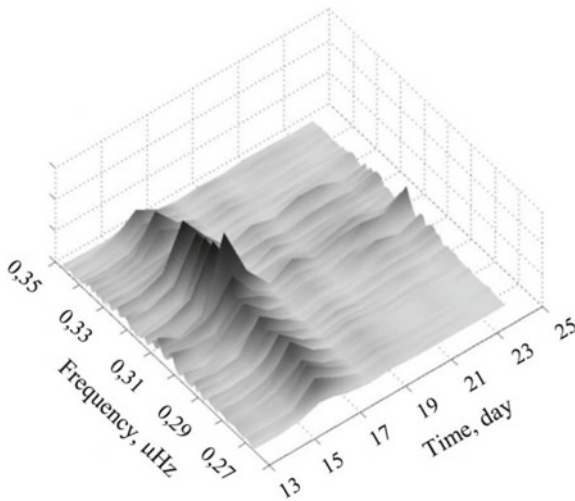


Fig. 2 STAN-diagram of geomagnetic field variations during the earthquake in Chile on September 16, 2015, showing the quintet of the mode of Earth's free oscillations ${}_0S_2$ and its dynamics

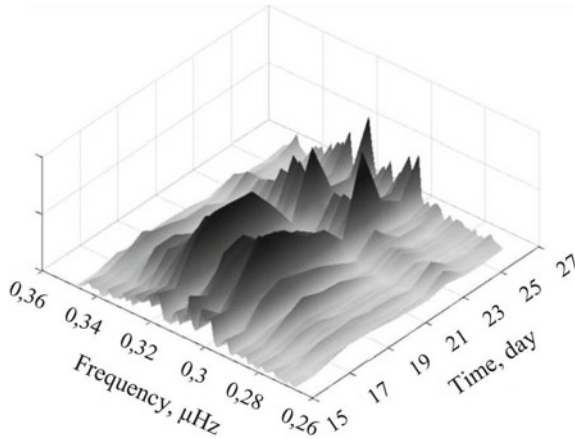


Fig. 3 STAN-diagram of electric field variations during the earthquake in Chile on September 16, 2015, showing the quintet of the mode of Earth’s free oscillations ${}_0S_2$ and its dynamics

The results of the estimation of the frequencies of the ${}_0S_2$ quintet for the Chile (Illapel) earthquake on September 16, 2015 are presented in Table 2. Table 2 also shows the theoretical frequencies calculated using the Earth model of 1066A. Based on the data in Table 2, we can conclude that the frequency estimates obtained according to experimental data, they are determined with sufficiently high accuracy and have values that are quite close to theoretical (i.e., the difference between the observed and theoretical values does not exceed 0.7% for both geophysical fields recorded at the Mikhnevo observatory).

Table 2 Frequencies of singlets of the ${}_0S_2$ mode of free oscillations, determined according to the monitoring of geomagnetic and electric fields during the earthquake in Chile on September 16, 2015, in comparison with those calculated using the model 1066A

Parameter	Azimuth Number				
	$m = -2$	$m = -1$	$m = 0$	$m = 1$	$m = 2$
Frequency values calculated by the model					
Frequency	0.2999	0.3048	0.3095	0.3140	0.3184
Frequency values calculated from magnetic field registration data					
Frequency	0.3002	0.3048	0.3101	0.3155	0.3202
Discrepancy relative to the theoretical value, %	0.100	0	0.193	0.475	0.562
Frequency values calculated from electric field registration data					
Frequency	0.2986	0.3056	0.3102	0.3148	0.3206
Discrepancy relative to the theoretical value? %	-0.435	0.262	0.226	0.254	0.686

Processing and analysis data of instrumental observations of variations in the components of the geomagnetic field and the vertical component of the electric field in the near-surface layer of the Earth's atmosphere during all considered events showed that in spectra of electromagnetic variations there are harmonics of the quintet of the fundamental spheroidal mode of the Earth's free oscillation ${}_0S_2$, close to theoretical ones. The intensity and frequency of singlets vary over time.

4 Conclusions

The study conducted in this work showed that according to the data of electromagnetic monitoring after large earthquakes (with a moment magnitude is more 7.5) it is possible to distinguish a quintet of the Earth's fundamental spheroidal mode ${}_0S_2$. Moreover, the frequency of singlets will coincide with the values calculated according to the 1066A model. It is necessary to continue research in this direction with the use of electromagnetic monitoring data for other earthquakes including weaker ones, while attention should be paid to the dynamics of the development of the quintet in time.

Acknowledgements The research was carried out within the state assignment (registration number AAAA-A19-119021890067-0, registration code 0146-2019-0009).

References

- Adushkin VV, Spivak AA, Kharlamov VA (2018) Manifestation of the lunar–solar tide and free oscillations of the Earth in the variations of the magnetic field. *Izv Phys Solid Earth* 54(6):859–871
- Alsop LE, Sutton GH, Ewing M (1961) Free oscillations of the Earth observed on strain and pendulum seismographs. *J Geophys Res* 66:631–641
- Becel A, Laigle M, Diaz J, Montagner JP, Hirn A (2011) Earth's free oscillations recorded by freefall OBS ocean-bottom seismometers at the Lesser Antilles subduction zone. *Geophys Res Lett* 38:L24305
- Benioff H (1958) Long waves observed in the Kamchatka earthquake of November 4, 1952. *J Geophys Res* 63:589–593
- Bromwich TJ (1898) On the influence of gravity on elastic waves, and, in particular, on the vibrations of an elastic globe. *Proc Lond Math Soc* 30:98–120
- Dahlen FA, Sailor RV (1979) Rotational and elliptical splitting of the free oscillations of the Earth. *Geophys J Roy Astron Soc* 58:609–623
- European Space Agency (ESA) (2012) Sentinel-2: ESA's optical high-resolution mission for GMES operational services. Rep. ESA SP-1322/2, European Space Agency, Noordwijk, Netherlands
- Gilbert F, Dziewonski AM (1975) An application of normal mode theory to the retrieval of structural parameters and source mechanism from seismic spectra. *Philos Trans Roy Soc A* 278:187–269
- Love AEH (1911) *Some problems of geodynamics*. Cambridge University Press, Cambridge
- Masters G, Widmer R (1995) Free oscillation: frequencies and attenuations. In: *Global earth physics. A handbook of physical constants*. American Geophysical Union, Washington, pp 104–125

- Milyukov VK, Vinogradov MP, Mironov AP, Myasnikov AV (2018) Earth's free oscillations excited by the 2013 Okhotsk Sea earthquake. *Izv Atmos Oceanic Phys* 54:1595–1603
- Ness NF, Harrison JC, Slichter LB (1961) Observations of free oscillations of the Earth. *J Geophys Res* 66:621–629
- Nishida K (2013) Earth's background free oscillations. *Annu Rev Earth Planet Sci* 41:719–740
- Rosat S, Sato T, Imanishi Y, Hinderer J, Tamura Y, McQueen H, Ohashi M (2005) High resolution analysis of the gravest seismic normal modes after the 2004 Mw = 9 Sumatra earthquake using superconducting gravimeter data. *Geophys Res Lett* 32:L13304
- Woodhouse JH, Deuss A (2015) Theory and observations—Earth's free oscillations. In: *Treatise on geophysics*, 2nd edn. Elsevier, Oxford, pp 79–115

Structure Factors of Gold Mineralization Formation on the Example of Kumak Gold Deposit (Eastern-Urals Uplift)



A. V. Kolomoets, P. V. Pankratev, M. Yu. Nesterenko, R. S. Kisil,
and V. S. Pantelev

Abstract Ore-controlling faults and magmatism manifestations are considered in the paper, which reflect the features of the conditions for the formation of gold mineralization in rift structures. It is noted that the mesh of mineralized cracks of the Kumak deposit was formed as a result of many tectonic impulses manifested at different orientation of the deformation plane. With the divergent tectonics structures and formation of the diagonal shifts-spreads on the cleavage background favorable conditions for the penetration of hydrothermal solutions and deposition of gold mineralization in area of Kumak deposit were created.

Keywords Gold · Rift structures · Faults · Cracks · Kumak deposit · Anikhov graben · Old-Karabutak graben · East-urals uplift

1 Introduction

The Kumak gold deposit is confined regionally to a large tectonic seam of the Chelyabinsk Fault at rift-type sites. Its feature is that it consists of several wings, coming in behind each other with a slight shift to the North. Each wing represents a major discontinuous disruption and has its own name: Balandinskiy Fault, Western Chelyabinsk graben limit, Tarutinsko-Nasledninskiy fault.

During geodynamic mapping of the Southern Urals, it was established that the early coal collision of the mature Devonian island arc with its continental margin manifested itself within its Eastern slope in the form of a deep echelonized system of rearward shear-rotation, which is syncollision passive rifting under the convergent

A. V. Kolomoets (✉) · P. V. Pankratev · V. S. Pantelev
Orenburg State University, Orenburg, Russian Federation
e-mail: kolomoyets56@mail.ru

M. Yu. Nesterenko
Orenburg Federal Research Center, Federal State Budgetary Institution of Science,
Ural Branch of the Russian Academy of Sciences, Yekaterinburg, Russian Federation

R. S. Kisil
Primorskaya Mining and Geological Company LLC, Dalnegorsk, Russian Federation

regime conditions accompanied by decompression mantle magmatism (Bochkarev and Yazeva 2001).

Purpose of work is the identification of the role of structural factors in the localization of gold mineralization.

Research methodology is analysis of ore control structures of the Kumak gold deposit based on the generalization of stock material and field studies. The tectonic map is created in ArcGis (version 10.0).

2 Geological Position of the Field in Regional Structures

Fragments of the Chelyabinsk fault are represented by Anikhov and Old-Karabutak grabens (Fig. 1). They are composed of Lower and Middle Paleozoic volcanogenic-sedimentary formations and are represented by three structure floors separated by regional stratigraphic unconformities.

The lower structure floor is represented by the Shebekta (O₂sb) and Balataldyk (O₂bt) deposits of the middle Ordovician strata, which are presented in the East Mugodzhzar zone on the Old-Karabutak Graben square. The Shebekta strata is composed of two subtopics: lower—volcanosedimentary (quartz sandstones, quartz-mica, quartz-chlorite and basic-type composition effusives) 400–600 m and upper—carbonaceous-terrigenous-shale (intermittent quartz sandstones, carbonaceous clay, sericite quartz and quartz-sericite shales) 300–600 m. The lower limit of the thickness has not been opened. It is overlapping with a break in the carbon-terrigenous-carbonate thickness of the upper structure floor (Pankratiev et al. 2018; Pankratiev and Loshinin 2005).

Formations of the Balaldyk graben in the east of the Old-Karabutak graben are developed in the form of tectonic blocks (conglomerates, quartz sandstones, carbonaceous phyllite shales) with a total capacity of 600 m.

The middle structure floor is marked only within the limits of Anikhov graben. It is composed of Middle-Upper Devonian volcanogenic-sedimentary rocks. Its lower boundary is not exposed, and it is overlapped with the erosion of carbonaceous-carbonate-terrigenous thickness of the lower carbon. A full section of its constituent sediments is exposed on the right bank of the Kumak River, and some exits are found in the areas of the West and East Anikhov faults. The base of the middle structure floor (200–300 m) is predominantly shale, and in the middle and upper parts there are tuffs of acidic composition, tuffaceous, tuffa-alavrolites, tuffoconglomerates with interlayers of siltstones and carbonaceous clay shales (500–600 m).

The upper structure floor is fixed both in Anikhov and Old-Karabutak grabens. This floor is presented by carbonaceous-terrigenous-carbonate C₁ thickness, which consists of two subfloors: the lower one—carbonaceous-carbonate-shale (midtourney-Visaeon) 350–650 m and the upper one—olcanogenic-sedimentary (upper-Visaeo-Serpukhovian) 80–150 m. The lower subsoil consists

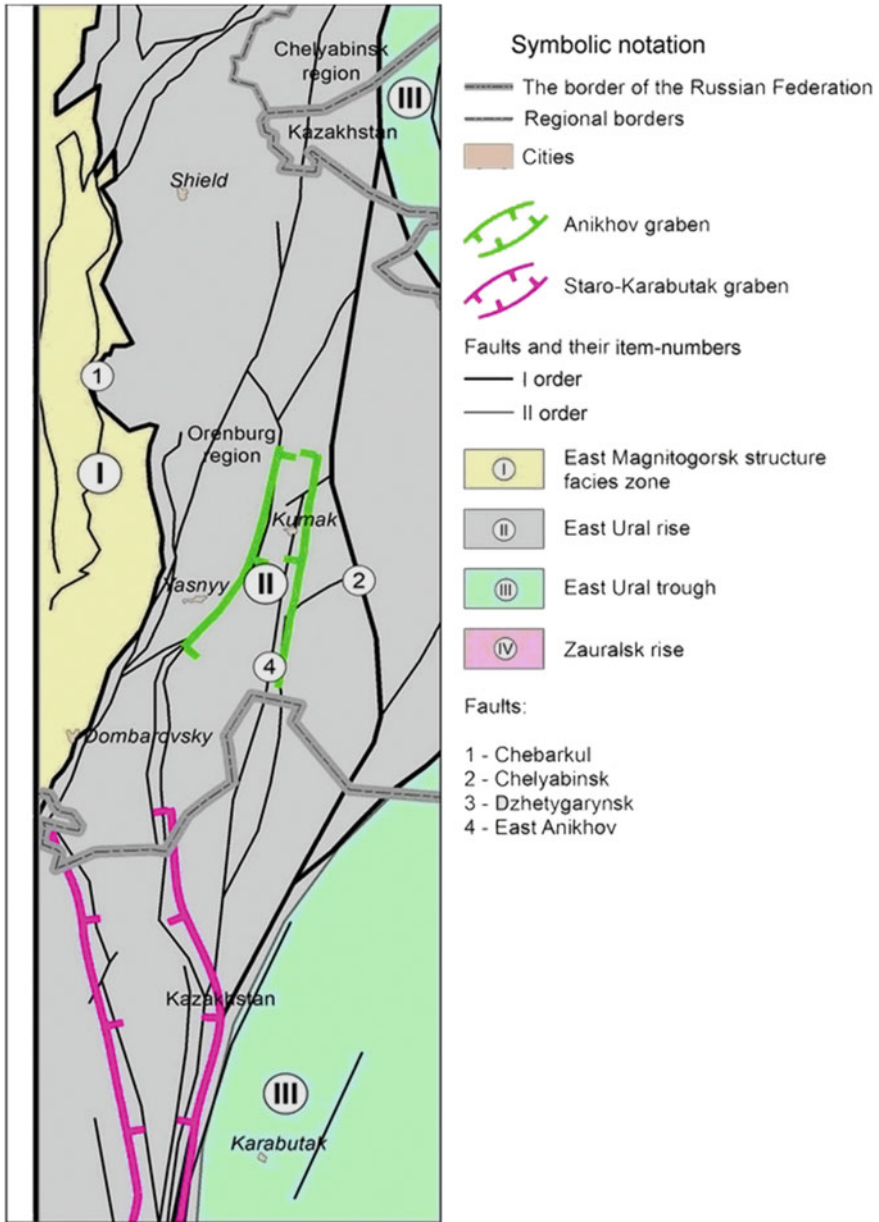


Fig. 1 Structure and tectonic map of Anikhov and Old-Karabutak grabens

of carbonaceous-mica-quartz shales (prevailing), conglomerates, gravelites, sandstones, siltstones, limestones; the upper subsoil consists of conglomerates, tuffoconglomerates, tuffa-alavrolites, sandstones and limestones.

Lower coal deposits of the Kumak deposit are united in the Bredinskaya Formation (C₁bd) (Sazonov et al. 1999; Snachev et al. 2012; Tevelev et al. 1999), traced from the South-West to the North-East (total strike of the strip CB 15–20°). The geological section is dominated by black shale carbonaceous terrigenous-sedimentary formations: siltstones, carbonaceous clay shales and sandstones. Dacite and andesite porphyrite effusives and their tuffs, which are mainly at the base of the section, are secondary importance. The black shale layer contains organic matter (1–9%), large volume of carbonate rocks (10–50%), sulfides (pyrite, arsenopyrite), the amount of which in the ore zones reaches 2–5%. Carbon shale is represented by dense, coarsely separated rocks with a significant amount of carbon dioxide in the finely sprayed state and in the form of graphitized concretions.

The Anikhov graben divides the Eastern-Urals uplift into the Western part—the Adamov-Mugodzhzar anticlinorium and the Eastern part—Tekeldytau anticlinorium. The latter is divided by the Trans-Ural fault zone into the Dzhabygasai and Taldysai anticlinoria, which are the structures of the 3rd order. Small fracture intrusions of ultramafic basites are observed in the fault zone. The structure of the Taldysai anticlinorium is dominated by pre-Cambrian formations, which are represented by a huge thickness of deeply metamorphosed rocks divided into gneiss and shale complexes. In the central part of the anticlinorium, the pre-Cambrian strata is broken through by Zheltinsk and Anikhov granitoid intrusions in the North.

Anikhov and Old-Karabutak grabbens of rift type play the main ore controlling role in the distribution of gold ore mineralization. Their formation is connected with the revelation of a shear-splitting character, similar to the shift-spread type transtensive structures (Tevelev et al. 1999). In the course of the development of a large regional shift structure, the formation of tonalite-plagiogranitic intrusions also occurred. Volcanites of different compositions were released within the shallow shelf zone and terrigenous-carbonate sedimentation.

3 Specific Features of Local Structures that Accompanied by Shift-Spread Strains of Gold Ore Structures

Feature of the internal structure of grabens is the presence of bursting disturbances of several directions and different nature. The disturbances of submeridional and North-Western strike are most clearly manifested. In addition, the sublatitudinal and Northeastern ruptures have developed. The submeridional breaks include the limiting from the east, the East-Anikhov and at the Southern extension—East-Mugodzhzar fractures and the fractures limiting from the West the Southern parts of grabens, and the group of parallel fractures in grabens inner parts.

Transverse faults in the North-Western direction are mainly developed in the Northern parts of both grabens. The fractures of submeridional and North-Western strike determine the form of grabens—have narrow elongated form in the Southern parts, where they are bounded on both sides by submeridional faults, and expand sharply to the North-West in the North-closure due to the development of North-Western strike fractures here. Northern restrictions of grabens have significant differences: Anikhov graben from the North is limited by faults of North-North-eastern strike, and Old-Karabutak forms a sharp branch to the North-West of its wing.

On the maps of magnetic and gravitational fields on the closure and displacement of anomalies the sublatitudinal directions are traced in both grabens, which bind to fractures in the foundation. The axes of small and medium folds are oriented parallel to the breaking structures that limit the blocks, i.e. they are fractured. In all grabens formations, rock fracture is quite intense. Rock mass that performed graben, experienced compression and tension, which was confirmed by the reconstruction of the paleo-stress fields.

The mineralization develops both in the fault zones themselves and in the associated lateral cracks. Quartz lodes are localized mainly in the systems of fracture and chipping cracks that operate the removal and slitting zones, less often within the zones themselves. The quartz lode belts are controlled by second- and third-order fault zones, and the lode systems and curves forming the belts are directly related to smaller tectonic disturbances, i.e. the crush and slanting zones of lower orders.

Wings of quartz lodes are localized “feathering” way near the zones of crumpling cracks rupture or chipping. These wings are developed mostly in rocks directly adjacent to the zone, or in areas between two wing-like zones, or at the junction of zones of different strikes intersection. Location and orientation of quartz veins within the limits of such wings is clearly consistent with the orientation of the violations that control them and is determined by the location of the systems of “feathering” cracks of rupture or chipping, in the vast majority of cases.

Very favorable condition for the localization of gold mineralization of the Kumak-type should also be considered an intensive chalking and the resulting high permeability of shale rocks of the Anikhov graben for ore-bearing solutions, which increases even more in the areas of development of submeridional zones of crush, superimposed on the dragfolded rocks. Diagonal (North-eastern and North-western) disturbances are insignificant in comparison with the meridional disturbances and are not an important factor in the localization of gold mineralization within the Anikhov graben, as their role in increasing the permeability of ore-bearing strata is relatively small compared to the role of shale and other meridional dislocations.

4 Magmatic Factor of Gold Ore Deposits Connection with Riftogenesis

Magmatites are indicators of geodynamic conditions in collision, suture and stress zones. The beveled compression mode on the borders of the non-conductible bark blocks is specific. This leads to the formation of a system of subvertical shear-slitting dislocations that can penetrate to the asthenospheric layer of the mantle. The melts formed in these conditions will have a “dry” basaltoid composition, low viscosity and high mobility. Magmatites in these conditions are represented by K-Na tholeiite and K-Na-subalkaline (hawaiiite-mujierite) series or lime-alkaline magmatites. These associations are noted in the paleoriftogenic structures of the active margins of the Siberian Craton and Northern Mongolia, which are associated with oblique collision of the island arc with the continental margin. Volcanites are also found in continental rifts (Bochkarev and Yazeva 2001).

Thus, early coal-bearing basaltoids can serve as an indicator of the magmatic collision conditions of rift structures and associated gold deposits of the black shale formation.

5 Conclusion

Ore control faults and magmatism reflect the features of gold mineralization formation in rift structures. The mesh of mineralized cracks was formed as a result of many tectonic impulses that appeared at different orientation of the deformation plane.

The formation of the Kumak field took place at the collision stage of geodynamic development of the territory and is closely related to the “active” riftogenesis, when some parts of the regional rift structures underwent shear-rolling dislocations.

In connection with the differently directed tectonics of structures and the formation of diagonal shifts-rotations on the background of shale formation, favorable conditions were created for the penetration of hydrothermal solutions and the deposition of gold mineralization. It follows that the formation of shift-spread zones on a regional scale is favorable for the formation of a gold deposit of the black shale formation.

Acknowledgements The work was carried out with the support of the Regional Grant in the field of scientific and technical activities in 2019 (Agreement No. 23 of 14.08.2019).

References

- Bochkarev VV, Yazeva RG (2001) Collision of island arc and continent-indicator magmatic formations of Ural variscide. *Geotectonics* 1:73 (in Russian)
- Pankratiev PV, Loshinin VP (2005) Golden mineralization of the riftogenic basins of the Orenburg region. Strategy and processes of georesources development, Perm (in Russian)
- Pankratiev PV, Kolomoets AV, Stepanov AS, Bagmanova SV, Panteleev VS, Tukhtanazarova KR (2018) Features of formation of gold manifestations in the black shale deposits of the Kumak ore field. *Processy Geosredah* 4:1121–1125 (in Russian)
- Sazonov VN, Ogorodnikov VN, Koroteev VA, Polenov YA (1999) Ural gold deposits. UGGGA, Yekaterinburg (in Russian)
- Snachev AV, Rykus MV, Saveliev DE, Bazhin EA, Ardislamov FR (2012) Geology, petrogeochemistry and ore content of the carbonaceous sediments of the Southern Urals. DesignPress, Ufa (in Russian)
- Tevelev AV, Tikhomirov PL, Degtyarev KE, Kosheleva IA, Moseichuk VM, Pravikova NV, Surin TN (1999) Geodynamic conditions of formation of coal-fired volcanic complexes of the Southern Urals and Trans-Urals. In: col. of essays on regional tectonics “The Southern Urals”, vol 1. GIN RAS, Moscow, pp 213–247 (in Russian)

About the Modern System of Three Energy-Carrying Intensive Vortices in the Earth's Mantle



S. Y. Kasyanov and V. A. Samsonov

Abstract The paper represents investigation of the consequences of a large temporary satellite being immersed in the Earth's mantle, resulting in the formation of gliding body traces and vortex half-rings under the Pacific Ocean. Tides in the mantle during prolonged satellite movement caused melting of asthenosphere substance and formation of seismic boundary at the depth of 220 km. After the satellite was buried in the Earth's mantle, an area with intensive vortex motion of the heated substance of the mantle in a two-phase saturated state, in which a vortex ring (eddy torus) was formed. The collapse of the vortex ring has led to the formation of a modern system of vortices based on three intensive energy-carrying vortices in the Earth's mantle, which have a significant influence on the history and climate of the Earth. The structure, dynamics and parameters of this vortex system are considered in the paper.

Keywords Tangential fall of the Earth's temporary satellite · Gliding · Tides in the mantle · Formation of asthenosphere and seismic boundary of 220 km · Intensive high-temperature vortices in the Earth's mantle · Two-phase saturated state of the mantle substance · Magnetic dynamo of the Earth · Global magnetic anomalies · Warming in the arctic

1 Introduction

Usually the collision of bodies with the Earth at a high angle is considered (Schulte et al. 2010; Alvarez et al. 1980). However, ancient sources allow to assume the tangential fall of a temporary Earth satellite in the 3rd millennium B.C., which took place about 9 revolutions a day around the Earth. According to the Chinese

S. Y. Kasyanov (✉)

N.N. Zubov State Oceanographic Institute, 119034 Moscow, Russia

e-mail: skas53@yandex.ru

V. A. Samsonov

Institute of Mechanics, M.V. Lomonosov Moscow State University, Moscow, Russia

e-mail: samson@imec.msu.ru

© The Author(s), under exclusive license to Springer Nature Switzerland AG 2021

T. Chaplina (ed.), *Processes in GeoMedia—Volume II*, Springer Geology,

https://doi.org/10.1007/978-3-030-53521-6_31

tractate “Huainanzi”, in the time of emperor Yao **10 suns** came out at once and “**9 infants**” appeared, in other words, 9 demons of fire and water (Philosophers from Huaynani 2004), what means 9 high waves of mantle and water tides. The body was in contact with the atmosphere and was burning. Therefore, it is possible to accept typical composition of iron meteorites content of 40% (Fe + Mn) and to estimate the period, mass and body radius which is equal to approximately 930 km (Kasyanov 2012).

The gliding of the body along the Earth’s surface and its gradual deepening into the perigee orbits lasted for about 7 years (Kasyanov 2012), until the period of its circulation was longer than the period of long gravitational waves in the layer between the Earth’s surface and the boundary of the solid core (Kasyanov and Samsonov 2017a). The tides in the mantle caused by the pull of the body led to the melting of the mantle layer, on the place of which a modern asthenosphere layer was formed later, and it also led to the formation of a seismic boundary at the depth of 220–230 km (Kasyanov and Samsonov 2017b). After the gliding had stopped, the body was completely immersed in the mantle. It occurred when the period of its circulation became less than the period of long gravitational waves around the Earth in the layer between the surface of the Earth and the boundary of the solid core (Kasyanov and Samsonov 2017a, b). The velocity of horizontal body projection movement at the end of gliding coincides with the velocity of P-waves at the seismic boundary at the depth of 220 km (Kasyanov and Samsonov 2017b), which confirms the correctness of the selected parameters of the body (Kasyanov 2012) on the basis of Chinese data (Philosophers from Huaynani 2004).

It appears that traces of body gliding have been saved in the Pacific Ocean lithosphere relief in the form of a system of zonal transform fractures (Clipperton, Clarion, Molokai, Murray, and Mendocino) in the ferromanganese sediments Clipperton-Clarion field (Andreev et al. 2006). The final deepening of the body occurred on trajectory between Hawaiian and Philippine Islands (Kasyanov 2018). Traces of body burial have been saved in the relief of the lithosphere and in the fields of anomalies of gravity and magnetic field (Kasyanov 2018).

Gliding and deepening of the body in the Earth’s mantle could lead to the formation of intensive vortices system in it (Kasyanov 2018). During the satellite gliding along the mantle surface and partial immersion into the mantle, vortex half-rings (Kasyanov 2018) were formed, the outputs of which are visible in the relief and gravity anomalies field, in particular, in the Banda Sea and the Bismark Sea.

In the present paper the hypothesis that full immersion of the satellite in the Earth’s mantle forms an intensive hot vortex ring, covering almost the entire depth of the mantle. Subsequently, as a result of the decay of the vortex ring and the evolution of its parts, a system of intense hot vortices was formed and evolved in the Earth’s mantle. By the present time the system of intensive hot vortices has come to the quasi-stationary state in which the total vector of the kinetic moment of all vortices is almost collinear to the angular velocity of the Earth rotation. The structure and parameters of this vortex system are discussed in this part.

2 Structure of the Modern System of Three Energy-Carrying Vortices in the Earth’s Mantle

Now three of the major energy-carrying vortices in the mantle have been identified. These are the **Himalayas + Tien Shan-Kolyma (HTSh-K)** vortices (1), (2) **Kolyma-Yellowstone (K-Y)**, and (3) **Yellowstone Hudson Bay-Eastern Mediterranean Sea (Greece) (Y-HB-MS)** (Fig. 1). Let’s consider the approximate primary estimation of the spatial arrangement and parameters of vortices of this system, which can be specified further.

Vortex 1 (Himalayas + Tien Shan-Kolyma) (Fig. 2) is in contact with the liquid core of the Earth, which is manifested on the day surface in the form of the Baikal rift and the relief of the lithosphere around Lake Baikal, which could be formed by isostatic compensation of stationary hydrodynamic perturbation arising from the vortex interaction with the liquid core and mantle. The movement of the medium in the vortex is two-phase, clockwise when viewed from the South. The center of the HTSh-K vortex South output lies near the point (39.768° N, 88.720° E) at a depth of about 1200 km, the vortex output radius is about 1300 km in the mantle or about 1600 km on the surface. The vortex substance moves in an inclined plane with large depth and hydrostatic pressure differences. Wavy line—manifestation of the stationary front of condensation-evaporation of matter at its motion in the vortex on the day surface. Vortex 1 (HTSh-K) is clearly manifested in the field of gravitational anomalies according to WGM2012 data (Bonvalot et al. 2012) (Fig. 3).



Fig. 1 Structure of three related intense vortices system in the Earth’s mantle

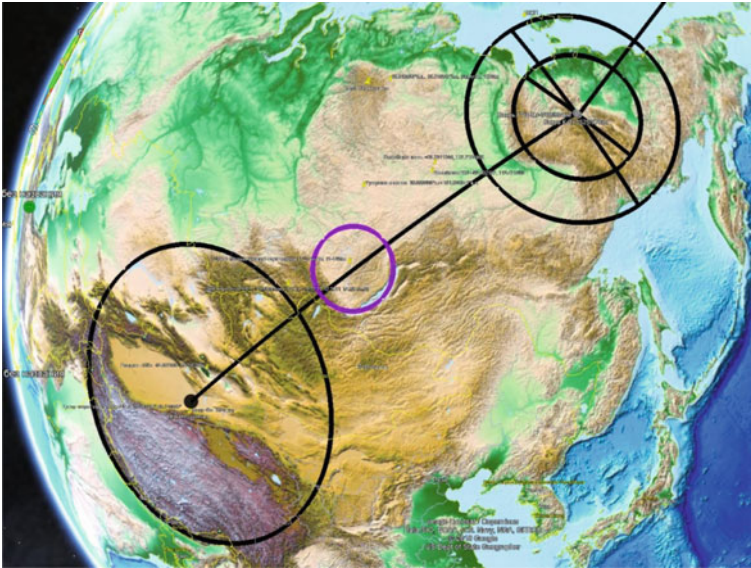


Fig. 2 Schematic representation of the Vortex 1 (Himalayas + Tien Shan-Kolyma)

In the Bouguet anomalies, a decompaction in the hot area of the vortex that is most clearly manifested at the vortex ends.

In the Kolyma node (Fig. 4), Vortex 1 (HTSh-K) comes into contact with the overlying Vortex 2 (Kolyma-Yellowstone). The Northern output of Vortex 1 (HTSh-K) with a radius of about 954 km on the surface (700 km in the mantle), with the center at 67.194° N 140.339° E at a depth of about 1700 km, is in contact with the output of the outlying Vortex 2 (K-Y), which has a radius of about 570 km on the surface (525 km in the mantle), and the center at 67.006° N 140.694° E at a depth of about 500 km. The end of Vortex 1 is deepened to the NorthEast and the output of Vortex 2 is deepened to the South West. The vortex outputs in the figures are schematically represented in circles. In fact, the axes of vortices 1 and 2 in the Kolyma node are tilted to the vertical at angles of 71.8° and 65.6° , and the axes of the vortices outlets can be tilted to the vertical at lower angles due to the influence of gyroscopic forces. Due to the influence of gyroscopic forces on the differently rotating vortices, the area above the boundary of the lower vortex, along the valley of the Lena River, is lowered, and above the boundary of the upper vortex, along the Verkhoyansk ridge—raised.

Vortex 2 (Kolyma-Yellowstone) is conical and passes significantly above the liquid core surface. Seismic tomography (<https://vimeo.com/125650792>; Obrebski et al. 2010) shows the presence of three connected vortices under Yellowstone (Fig. 5).

The system of three vortices has the outburst under the Mediterranean Sea. In Fig. 6 the most recent and the largest of the several vortex traces that can be identified in the relief of the Mediterranean lithosphere is depicted.

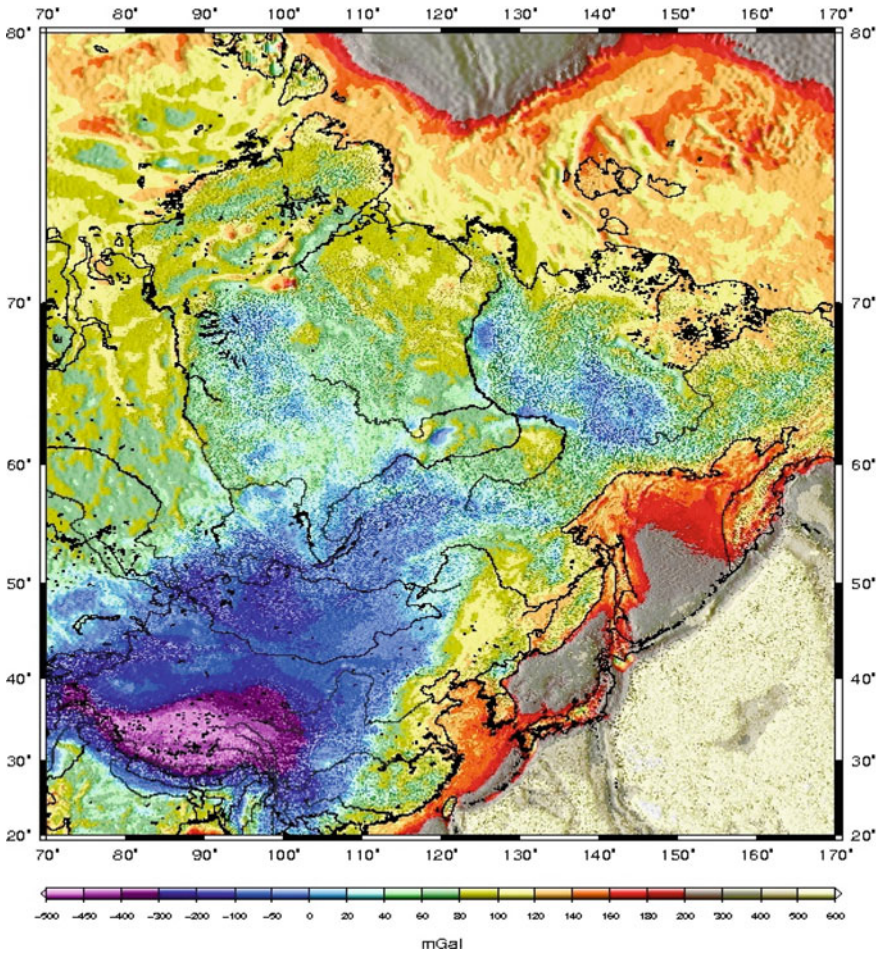


Fig. 3 Vortex 1 (Himalayas + Tien Shan-Kolyma)—complete spherical Bouquet anomalies (mGal) according to WGM2012 (Bonvalot et al. 2012). In the Bouquet anomalies, one can see a decomposition in the hot area of the vortex that is most clearly manifested at the vortex outputs can be observed

3 The Dynamics of the Three-Vortex System

At a gravitational resonance in the Solar System the solid core of the Earth according to Barkin (2014) shifts, and at the same time the equipotential surfaces and also the external boundary of the liquid core are displaced, as a result the liquid core substance enters the region of Vortex 1 under Baikal and displaces the substance from Vortex 1 to Vortex 2. The substance from Vortex 2 is being displaced into Vortex 3. The exchange of mass momentum and kinetic momentum exists between the three vortices within the system and between them and the mantle, heat release due to deceleration on

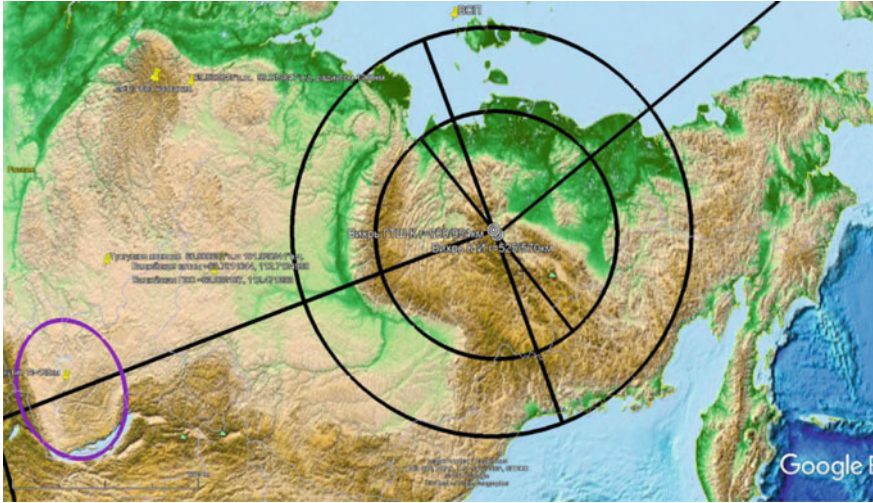


Fig. 4 Schematic representation of the Kolyma node

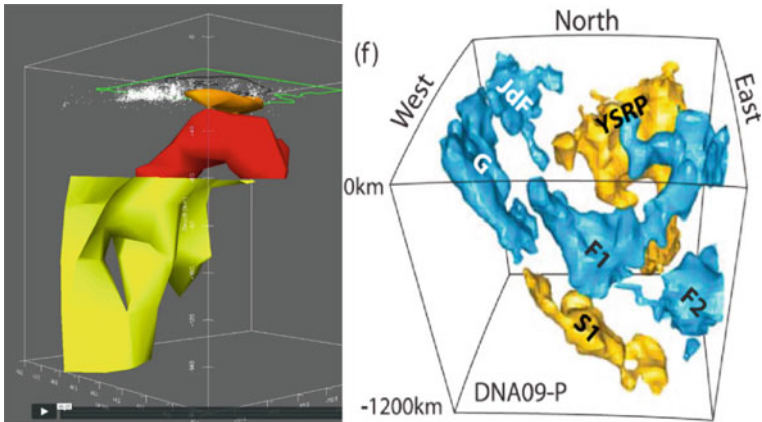


Fig. 5 Seismic tomography of the area near Yellowstone. Under Yellowstone, there are three linked vortex rings. On the left (<https://vimeo.com/125650792>)—the small upper yellow hot ring in the mantle near Yellowstone with the center at a depth of about 100 km, a quasi-horizontal axis and a radius of 30–50 km. This ring is in contact with the hot ring below (yellow on the right) (Obrebski et al. 2010), with which the cold ring (blue in the Fig. on the right) is linked as chain. The small upper ring is a part of the Vortex 2 of Kolyma-Yellowstone, the large hot ring with a diameter of about 700 km is the tip of the Vortex 3 of Yellowstone-Greece (Mediterranean Sea). Upper and lower hot vortices are contacting, decelerating, heating and “illuminating” each other in the form of hot rings. The cold blue ring is the tip of the slowing down vortex (Chukchi Rise-Yellowstone), which may have been a continuation of Vortex 1 (Himalayas + Tien Shan-Kolyma). Vortex 2 (Kolyma-Yellowstone) was formed over this vortex as secondary to it and rotating in the opposite direction. Area on the right: from 37° N to 49° N and from –107° E to –124° E, (1332 km along meridian and 1380 km along parallel 43° N)



Fig. 6 The outburst of the vortex under the Mediterranean Sea

interaction of differently directed flows and thermal expansion occurs. As a result, high potential heat is released and the position of the center of mass, the kinetic momentum and the volume of the Earth's mantle change in a jumpy manner, and hence the Ocean level.

4 Energy Release in the Vortex Nodes Due to the Deceleration and Matter Transport from One Vortex to Another

When a substance flows from one vortex to another, it is assumed that the mass of the substance flowing into the vortex is small compared to the total mass of the vortex and the substance flowing into the vortex fully perceives the velocity of the substance in the vortex. Since the velocities in the vortices differ, the kinetic energy of the substance mass that has passed from one vortex to another and taken its velocity changes with the overflow. As a result, heat is released in the nodes and the Mediterranean outburst of the system of three vortices. The amount of the heat energy is estimated equal to the sum of the kinetic energy of the relative motion of the substance of Vortex 1 flowing in the Kolyma node into Vortex 2, and the kinetic energy of the substance that has passed into the tip of the Mediterranean vortex and slowed down there. At the Yellowstone node, heat energy released under the mainland lithosphere, which slows and limits its transmission to the Ocean. Due to this reason and also because, according to the estimates, the heat energy release at dissipation in the Yellowstone node is almost by an order of magnitude less than the energy released under the Ocean, in this work its indirect influence on the heating of the World Ocean through the Atmosphere is not taken into account.

5 Evaluation of the Parameters of the Three-Vortex System

While Barkin (2014) considers the movement of the solid core of the Earth as the only and immediate cause of the jump in geophysical parameters of 1997–1998, here we consider the displacement of the core only as a trigger mechanism that have started the redistribution of rotating masses through the system of vortices and attribute the measured movement of the center of masses of the Earth mainly due to the redistribution of masses between the liquid core and the system of vortices.

The available data (Barkin 2014) on changes in the Ocean surface level and temperature (Fig. 7), the location of the Earth's center of mass (Fig. 8), the duration of the day (Fig. 9), and the position of the pole (Figs. 10 and 11) for the jump in geophysical parameters of 1997–1998 make it possible to obtain an assessment of the seven values—three velocities and three densities of matter at the periphery of vortices, as well as the volume of matter of the liquid core that entered the vortex near Baikal. Thus section of Vortex 1 under Baikal is considered as terminal, so it is considered that at an input of substance of a liquid core in the Vortex 1, there are no essential changes in this vortex at Himalayan-Tyan-Shan, and weight of substance under Himalayan-Tyan-Shan mountain ridge does not vary. Since the liquid core substance goes out into Vortex 1 symmetrically relative to Baikal, it is considered that the substance goes out in the vortex section under Baikal, which is formally taken as the Southern end of Vortex 1 during the modeling.

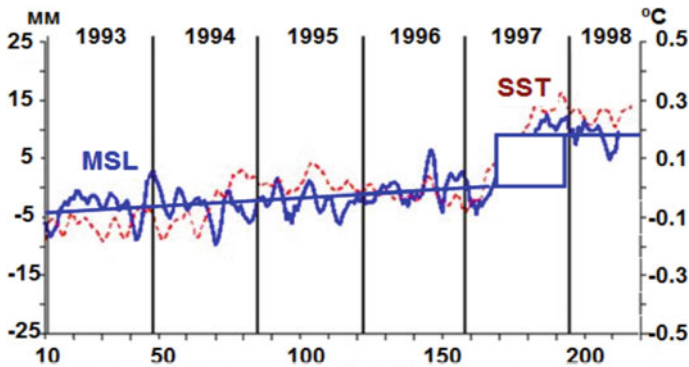


Fig. 7 Global ocean level (MSL) leap 1997 (Barkin 2014) by 8–9 mm from satellite altimetry data and of mean ocean surface temperature (SST) by 0.16 °C. The abscissa axis shows the TOPEX-Poseidon cycles (years on the upper axis). The ordinate axis shows the level of the world ocean in mm and the temperature according to global warming science (www.appinsys.com/GlobalWarming)

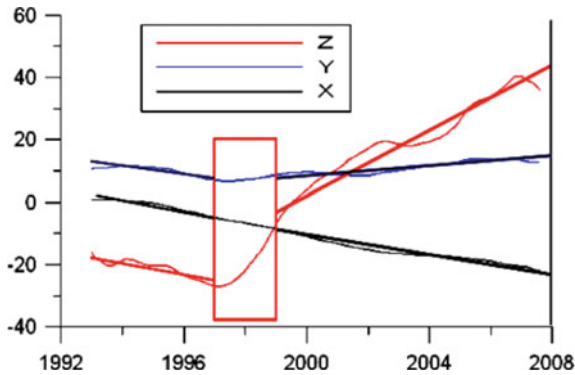


Fig. 8 Change in the position of the Earth's center of mass in mm relative to the geometric center of the Earth. The trend components of the Earth mass center coordinates in the period 1993–2007 and the jump in the values of its Cartesian Greenwich geocentric coordinates in the period 1997–1998 (from Barkin 2014 with changes)

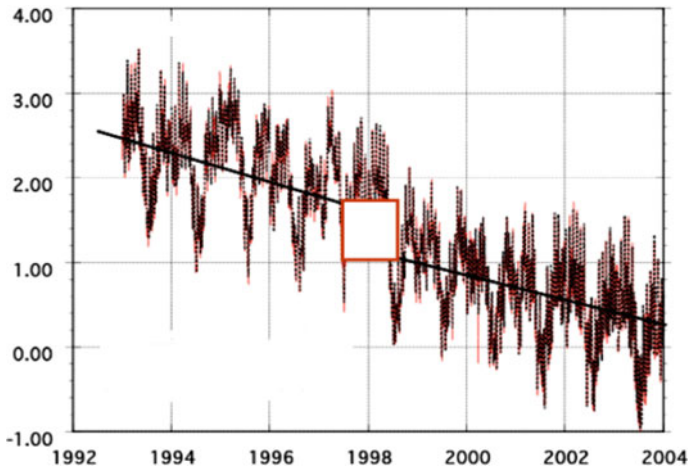


Fig. 9 The jump in the duration of the day in 1997–1998 in ms (from Barkin 2014 with changes)

6 Estimation of Velocities and Densities in Three Vortices

Based on the preservation of the kinetic momentum and the position of the system's centre of mass, and also assuming that changes in sea level follow changes in the Earth's radius and volume, seven indeterminate variables can be identified from the seven baseline data described above. Therefore, the maximum linear velocities and densities at the periphery of each of the three vortices were assumed to be constant along the vortex axis. The seventh indeterminate is the volume of liquid

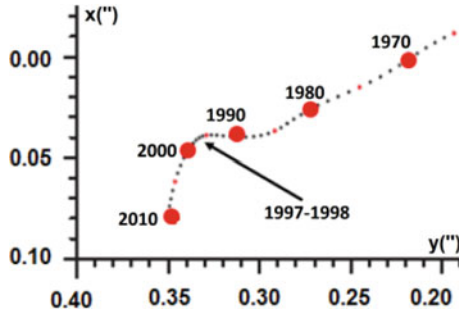


Fig. 10 Earth rotation pole trajectory from 1965 to 2010 (from Barkin 2014), according to Scalera (2011). In 1997–1998, the direction of movement of the Earth’s rotation pole and the direction of movement of the center of mass of the Earth changed

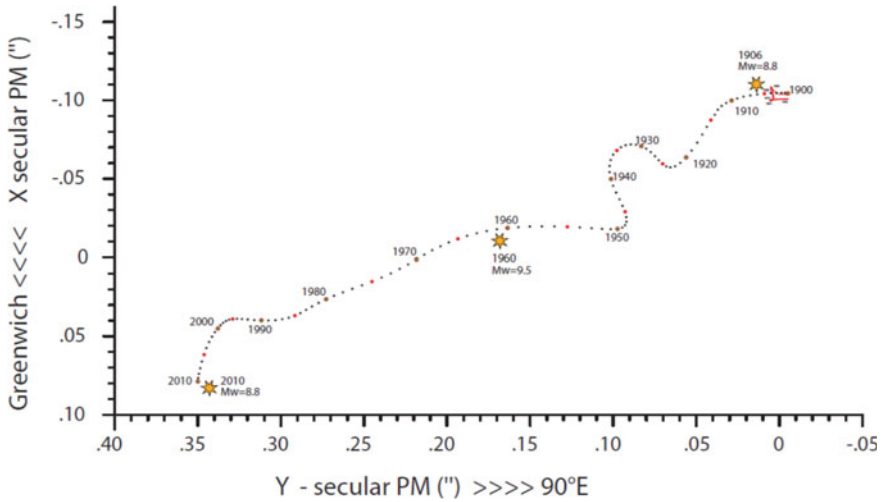


Fig. 11 Trajectory of Earth rotation pole movement from 1900 to 2010 (Scalera 2011)

core substance released into the Vortex 1. Then a nonlinear system of seven algebraic equations with seven unknowns emerges from the condition of satisfying the observation data. The system is solved numerically.

For the jump of geophysical parameters of 1997–1998, in accordance with the data described above (Barkin 2014), the following values are used (in the geocentric Greenwich coordinate system): the jump in the position of the Earth’s rotation pole by (0.00140845, 0.00234375) angular seconds, jump in the duration of the day by 0.0009 s, jump in the position of the center of masses of the Earth (0.00357962 m, 0.0009214 m, 0.015203 m), jump in the ocean level by 0.008 m. The ocean surface temperature jump in 1997–1998 was 0.16 °C.

At the value of the coefficient of thermal expansion of the vortex substance equal to 2.32×10^{-5} [which is close to the value of 2×10^{-5} for the substance of the upper mantle (Dobretsov et al. 2001)], for which the estimate of the World Ocean temperature jump is equal to the value of 0.16°C observed in 1997–1998. At this value of the thermal expansion coefficient from the estimation model of three vortices the maximum linear velocities estimations are 4130.76 m/s, -1244.69 m/s, 2940.59 m/s, respectively. The minus sign in this case shows that the angular velocity of Vortex 2 is directed from Yellowstone to Kolyma. The obtained estimate of the Vortex 1 velocity agrees with the estimation of 4370 m/s for the velocity of the vortex for the period of Biblical Exodus (about 1200 B.C.), obtained on the basis of the condition of equality of the specific kinetic energy of the vortex jet with the specific heat of vaporization of liquid SiO_2 —component of basalt and mantle substance with the lowest boiling temperature, at the hypothetical complete deceleration of the liquid SiO_2 jet in the vortex. Density at the periphery of vortices is respectively $11,800 \text{ kg/m}^3$, 4600 kg/m^3 , and 4180 kg/m^3 .

The magnetic numbers of Reynolds in the vortices are accordingly equal: 6073.3, -985.4 and 1906.7. Critical values for magnetic dynamo with similar geometry of rotating rotors arrangement obtained in Lowes and Wilkinson laboratory experiments (Lowes and Wilkinson 1968) are in the range from 200 to 1000.

Thus, the magnetic Reynolds numbers in Vortices 1 and 3 estimated to exceed the critical ones. This means that the motion of vortices 1 and 3 in the system of three vortices starts the magnetic dynamo of the Earth and explains the origin of the Canadian and Siberian global magnetic anomalies.

7 The Mechanism of Energy Transfer from the Vortex to the Ocean

If the substance in the vortices is in a saturated state, the increase of its energy leads to the evaporation of the most easily boiling fraction of the mantle, that is, SiO_2 . Evaporation occurs when the external hydrostatic pressure decreases during the lifting of the substance in the upper part of the ascending branch of the trajectory of the moving substance in the vortex. In Vortex 1, the ascending part of the trajectory (in the projection on the day surface) covers the Novosibirsk islands from the North, and in Vortex 2—the Laptev Sea coast. In these areas, the SiO_2 vapour escaping upwards is retained in a gaseous state for a long time due to the pressure drop as it rises. SiO_2 vapours can condense in the lithosphere near the ocean floor or in water. If SiO_2 vapours condense directly in contact with water, fine sediment is formed and mud volcanoes can be formed in such places. Thus, intensive local heat sources at the Ocean floor associated with volcanoes and faults appear. Thermal energy released in the Kolyma node and Vortex 3 is invested in the volume of the World Ocean and is used to calculate the estimation of changes in ocean temperature. Thus, as a result

of modeling the system of three vortices, the temperature jump in the World Ocean in 1997–1998 is estimated.

8 Independent Proof of the Correctness of the Three Vortices Model

The model reproduces the observed magnitude of the ocean temperature leap in 1997–1998. During the analysis of the obtained results the dependence of vortex parameters derived from the system on the value of the substance thermal expansion coefficient in the model was revealed. A common value of the thermal expansion coefficient for all three vortices was used in the simulation. The observed temperature leap of the World Ocean in 1997–1998 with the value of 0.16 °C can be obtained at the value of the thermal expansion coefficient for the vortex substance 0.0000232, close to the thermal expansion coefficient of the substance 0.00002 for the upper mantle (Dobretsov et al. 2001).

The color temperature of the light flashes in the “Old Servant” steam geyser in Yellowstone (4000–5000 K) corresponds to the deceleration temperature of the jets at the contact of Vortices 2 and 3.

9 Impact of Mantle Vortices on Climate and Ecology. Formation of Ice-Free Areas in the East Arctic Seas as a Result of Intensive Heat Fluxes from the Ocean Floor Through the Fractures Above the Borders of Mantle Vortices

The heat fluxes generated at the boundary of intensive mantle vortices adjoining the Kolyma node are transmitted through underwater volcanoes and faults to the Ocean and lead to the melting of Arctic ice.

Space images (see Fig. 12) show that vast areas of the Ocean in the Eastern Arctic remain either completely ice-free or have very low ice thickness at air temperatures significantly below zero.

The reasons for this important phenomenon for Northern Sea Route navigation remain unclear. An intensive source of heat from the Ocean floor, different from an insignificant heat flux from the Ocean floor due to thermal conductivity, is required for the long-term existence of the aforementioned regions.

Such a source are (in our opinion) existing for a long time intensive high-temperature vortices of the Earth’s mantle substance moving in the two-phase (liquid and gaseous) saturated state described above . The greatest energy losses in the

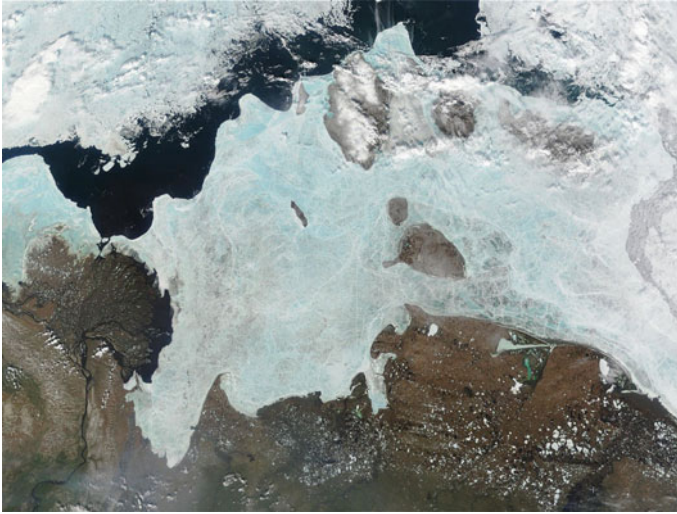


Fig. 12 Polynya of the edge of shore ice in the Laptev Sea North of the Novosibirsk Islands (<https://s3.nat-geo.ru/images/2019/4/10/f223b12de1c6437389e3ce9e6a6083ae.max-2000x1000.jpg>)

moving vortex occur due to friction at the boundaries, where, accordingly, the greatest release of heat energy occurs. Polynya of the edge of shore ice in the Laptev Sea North of the Novosibirsk islands (Fig. 12), as well as polynya of the edge of shore ice in the East Siberian Sea, are located above the border of the counter-clockwise rotating deep Vortex 1, directly above the zone of the substance lifting in the Northern tip of the vortex, where due to a decrease in the external hydrostatic pressure in the mantle during the lifting of the vortex substance evaporation of the superheated substance occurs.

The velocity of the substance in Vortex 1 is significantly higher than in Vortex 2. Therefore, when Vortex 1 and Vortex 2 are mixed, Vortex 1 is decelerated and heat is released, resulting in additional evaporation of a part of the moving substance. It evaporates the most easily boiling component of the mantle substance, namely SiO_2 . Hot vapors of SiO_2 are picked up by the flows of Vortex 1 and 2 being light, tend to rise through the mantle upwards and approach to the bottom of the Ocean in the fault zones and underwater volcanoes, where they completely condense. Thus, local intensive heat sources at the ocean floor leading to ice melting are formed above the boundaries of vortices.

10 Formation in the East Arctic Seas of the Areas of Intensive Methane Outflow from Gas Hydrates on the Shelf as a Result of Intensive Heat Fluxes from the Ocean Floor Through the Faults Above the Boundaries of Mantle Vortices

Along with the formation of the Great Siberian polynya (open water patch), the tip of the deep Vortex 1 delivers the heat fluxes necessary for gasification of methane-hydrates in the Novosibirsk Islands, in particular, in Bennett Island (Masurenkov et al. 2013), from which noticeable gas plume departs in the Atmosphere.

Intensive methane outflows from gas hydrates were detected (Shakhova et al. 2010) in the Laptev Sea and in the East Siberian Sea (Fig. 13).

It can be seen that the most intensive methane emission observed in the near-bottom layer takes place at the 165th meridian, just where the boundary of the deep vortex in Fig. 4, at the beginning of his ascent zone. The second area of intensive methane yield is in the area of Tiksi settlement, under which the upper vortex boundary lies (lays) (see Fig. 4). The upper vortex rotates clockwise, and thus the area of intense methane output is the area where the vortex substance rises, where the superheated substance boils.

Thus, the presence of mantle vortices well explains the origin of methane outflow zones on the shelf of Eastern Siberia and the formation of the Great Siberian Polynya.

The presence of intensive mantle vortices can cause intensive heat outbursts in the Arctic and Siberia, and thus may represent a regional cause of global warming.

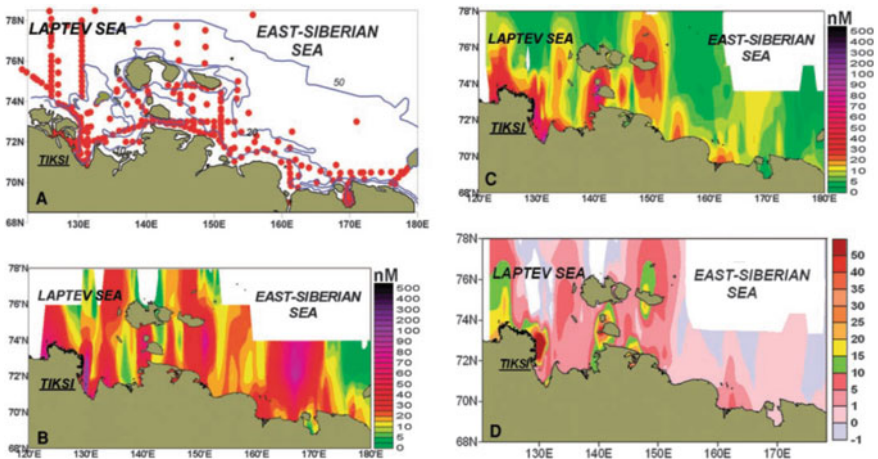


Fig. 13 Summer observations of dissolved methane (Shakhova et al. 2010): location of the oceanographic stations (a) in the Eastern Laptev Sea and in the East Siberian Sea, dissolved methane (b) in bottom water, dissolved methane (c) in the surface water layer, methane flux (d) to atmosphere by ESAS

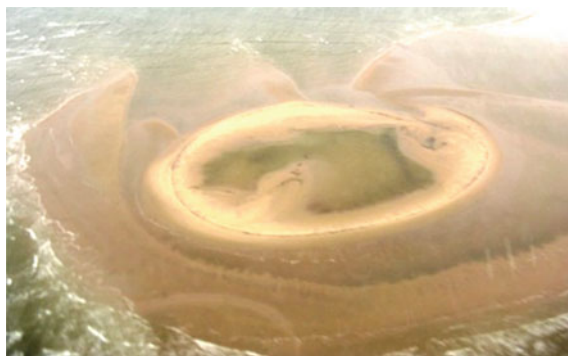


Fig. 14 Yaya Island (<http://arcticuniverse.com/set/000417.jpg>), which formed near the extinct Vasilievsky Island

11 Formation of Yaya Island and Change of the Bottom Relief in the Laptev Sea and East Siberian Sea

A gentle underwater cone, presumably of volcanic origin, was found above the ascending Northern part of the vortex, on its border, near Bennett Island. In this area, plumes of intensive methane outflows to the atmosphere are observed. Above the rising North-Western part of the vortex, on its border, in the Laptev Sea, by 1936, disappeared Vasilievsky Island, and by 2013, new Yaya Island (73.990333° N, 133.091139° E) had been formed near this place (Fig. 14).

It seems that the sandy Yaya Island could have been formed due to the release of SiO_2 and possibly Al_2O_3 vapors into the Ocean from the vortex, boiling due to the pressure lowering at the ascending branch of the vortex. Submerged mud volcanoes can be formed in the same way. Apparently, the decrease of pressure in the vortex at evaporation of its substance after 1902 led to the lowering of the lithosphere in the vicinity of the Vasilievsky Island. It appears that by 2013, possibly due to the 1997–1998 event caused by gravity resonance in the solar system, near the disappeared Vasilievsky Island the upstream of SiO_2 jet rising to the Ocean bottom was formed, leading to the formation of Yaya Island.

12 The Great Siberian Vortex and Related Hazards

Figure 15 shows the red circle of the Great Siberian Vortex (GSV), in the center of which is the Siberian global magnetic anomaly. The center of the GSV lies near the point with coordinates 66.957468° N 102.355739° E, its radius in projection on the bottom surface is about 693 km.



Fig. 15 Part of the vortex system in the mantle near Eastern Siberia. Red shows the Great Siberian vortex with a radius of about 693 km (on the day surface)

The character of the relief of the day surface indicates that the GSV is inclined Northward. In the North, you can see the projection of the phase transition structure in the lower part of the vortex on the day surface, which has a characteristic form of “masquerade mask” (Fig. 16). The picture of the “masquerade mask” is similar to that observed in the vortex outlet in the Himalayas-Tien Shan (Fig. 2).

The Southern and South-Eastern parts of the GSV vortex are raised and close to the surface. Here, along the edge of the vortex, we can see the outputs to the surface of the vortex tubes that begin in the vortex veil of the vortex tubes, which appeared as diamondiferous kimberlite tubes in Mirny, and the well-known Tunguska

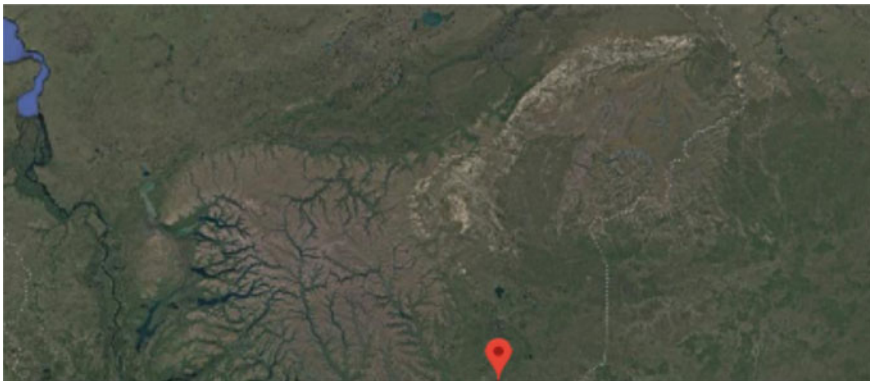


Fig. 16 The characteristic structure of the “masquerade mask” of the phase transition in the lower part of the Great Siberian Vortex (GSV), manifested in the relief of Eastern Siberia. In the corners of the “mask” one can see circular traces in the relief—sinking in the NorthEast corner of the “mask” and rising in the Southwest corner. The center of the vortex is marked

phenomenon of 1908. The vortex border also passes under the Viliui HPP reservoir and under the valleys of the Viliui and Olguidakh rivers. Above the Northwest border of the vortex, near Norilsk, contains metal ores.

Close to the center of the Great Siberian Vortex is located the Siberian global magnetic anomaly, which can be explained by the presence of a vortex, the motion of the conducting substance in which should create a maximum magnetic field in the center of the vortex. The vortex of the GSV, apparently (see Fig. 15), rotates clockwise, comes into contact with Vortex 1 and receives from its periphery substance, in particular, heavy metals. Apparently, the speed in the GSV is related to the speed in Vortex 1 and can be determined by it. The genesis of the GSV is not fully understood. This important natural phenomenon represents a great danger to the people and infrastructure of Siberia due to the continued formation of vortex cords emanating from the vortex veil on the edge of the vortex, so it needs to be comprehensively studied in the near future.

13 A Phenomenological Mechanism of the Great Siberian Vortex Formation

The Great Siberian Vortex appears to occur in the contact area of the vortex outputs 1 and 2. At contact of energy-carrying Vortex 1, on which periphery there is a heavy metal (with density on depth of occurrence of a vortex in a mantle, equal $11,800 \text{ kg/m}^3$) with a stream of a Vortex 2 substance of a vortex heats up above boiling point of metal as a result of what there is an evaporation both metal, and the fused substance of a mantle in vortices. The contact of vortices 1 and 2 takes place on the ascending branch, near the upper point of Vortex 1 output and the lower point of Vortex 2 output. Additionally heated light liquid substance of the mantle and its vapors rise up and form a Vortex 2 with a density at the depth of the vortex in the mantle, equal to 4600 kg/m^3 . The substance of vortices and metal on the periphery of vortices at the contact of jets of vortices are heated up inhomogeneously.

Part of the vortex substance 1, which had time to heat up to a lesser extent, being denser, with a slightly heated part of the metal at the periphery of the vortex, continues to move in Vortex 1 and falls down. At the same time, the part of the metal from the periphery of Vortex 1 has time to heat up to high temperatures, perhaps even the boiling point of the metal, and together with the vapors of this metal form a jet, the density of which is higher than the density of matter at the periphery of Vortex 2, but lower than the density of matter at the periphery of Vortex 1. Due to its density, this jet outputs the point of contact of vortices 1 and 2 below the jet of Vortex 2, but above the jet of Vortex 1. This jet, rising at a slight angle to the horizontal, forms the vortex ring of the Great Siberian Vortex. With this mechanism of formation, the Greater Siberian Vortex should rotate clockwise. Due to the presence of the vertical component of the initial velocity of the GSV vortex jet approaches the day surface in the Southern part of the Great Siberian Vortex. The pressure in the vortex jet drops

when it rises, and the share of steam in the two-phase flow increases. Metal vapors and mantle substances (SiO_2 , Al_2O_3), rising to the surface, form vortex cords. In particular, by condensing on the lower surface of the permafrost layer containing organics, rotating metal pairs can form axially symmetrical formations from carbon alloys.

14 Conclusions

By the present time, a system of quasi-stationary vortices has been formed in the Earth's mantle, in which intensive motion of the hot substance in the saturated state occurs. The rapid evaporation of the superheated substance in the areas of intense vortices in the Earth's mantle, the vapors of which rise up and condense near the Ocean floor, is the cause of intense heat outbursts in the Eastern Arctic and a possible cause of climate warming. Built on the jump of geophysical parameters in 1997–1998 the assessment of the corresponding temperature jump (without direct use of temperature data) is close to the observed value of the World Ocean temperature change for 1997–1998.

The system of three quasi-stationary vortices in the mantle produces magnetic dynamo, responsible for the Earth's magnetic field formation and determines its structure. The system of three vortices excites secondary vortices. The secondary Great Siberian vortex is especially dangerous: on the periphery of it outlets of vortex cords are currently manifested as diamondiferous kimberlite pipes near the town of Mirny, known Tunguska phenomenon of 1908, currently formed cylindrically symmetrical "pits" in the permafrost on the Yamal Peninsula with symmetrical round shafts of the thrown-out rock, the lowest layers of which were the furthest from the center of the pit (which is possible only in the presence of significant azimuthal velocity of substance in the vortex), and a number of other dangerous phenomena.

References

- Alvarez LW, Alvarez W, Asaro F, Michel HV (1980) Extraterrestrial cause for the cretaceous-tertiary extinction. *Science (New Series)* 208:1095–1108
- Andreev SI, Goleva RV, Yubko VM (2006) Economic and geopolitical problems of development of mineral resources of the world ocean. *Econ Manag* 3:72–78 (in Russian)
- Barkin YV (2014) Geophysical consequences of relative displacements and oscillations of the Earth's nucleus and mantle. IFZ, UMTS, Moscow. https://www.ifz.ru/fileadmin/user_upload/subdivisions/506/OMTS/2014/16.09/Barkin_16_09_14.pdf
- Bonalot S, Balmino G, Briais A, Kuhn M, Peyrefitte A, Vales N, Biancale R, Gabalda G, Reinquin F, Sarrailh M (2012) World gravity map. Commission for the Geological Map of the World. BGI-CGMW-CNES-IRD, Paris
- Dobretsov NL, Kirdyashkin AG, Kirdyashkin AA (2001) Deep geodynamics. Novosibirsk (in Russian) <https://arcticuniverse.com/set/000417.jpg>

<https://www.appinsys.com/GlobalWarming>

<https://s3.nat-geo.ru/images/2019/4/10/f223b12de1c6437389e3ce9e6a6083ae.max-2000x1000.jpg>

<https://vimeo.com/125650792>

Kasyanov SY (2012) Modeling of the orbital motion of a large asteroid at decrease with deepening into the lithosphere and mantle of the Earth. *Phys Probl Ecol (Ecol Phys)* 18:151–164 (in Russian)

Kasyanov SY (2018) Excitation of the system of intensive vortices in the mantle at the burial of a large temporary Earth satellite. In: *Physical and mathematical modeling of processes in geospheres*. IPMech RAS, Moscow, pp 165–166 (in Russian)

Kasyanov SY, Samsonov VA (2017a) Estimation of tidal wave heights during gliding of a large satellite on the surface of a liquid attraction spherical layer with a solid core. *Proc MIPT* 9(3):14–20 (in Russian)

Kasyanov SY, Samsonov VA (2017b) Influence of a tidal wave of a large gliding satellite as the reason of formation of seismic boundary of 220 km and division of the mantle into blocks. In: *Physical and mathematical modeling of processes in geospheres*. IPMech RAS, Moscow, pp 119–122 (in Russian)

Lowes FJ, Wilkinson I (1968) Geomagnetic dynamo: an improved laboratory model. *Nature* 219:717–718

Masurenkov YP, Slezin YB, Sobisevich AL (2013) Gas plumes near the island of Bennetta. *Izv RAS Ser Geogr* 3:86–95 (in Russian)

Obrebski M, Allen RM, Xue M, Hung S-H (2010) Slab-plume interaction beneath the Pacific Northwest. *Geophys Res Lett* 37:L14305. <https://doi.org/10.1029/2010GL043489>

Philosophers from Huaynani (2004) (trans: Pomerantseva LE). *Mysl'*, Moscow (in Russian)

Scalera G (2011) South American volcanoes and great earthquakes. Volcano-seismic correlation vs. secular PM. In: *37th interdisciplinary workshop of the international school of geophysics, Erice, Sicily*, pp 125–129

Schulte P et al (2010) The chicxulub asteroid impact and mass extinction at the cretaceous-paleogene boundary. *Science* 327(5970):1214–1218

Shakhova N, Semiletov I, Salyuk A, Yusupov V, Kosmach D, Gustafsson Ö (2010) Extensive methane venting to the atmosphere from sediments of the east Siberian arctic shelf. *Science* 327(5970):1246–1250. <https://doi.org/10.1126/science.1182221>

Multidecadal Variability of the Hydrothermodynamic Characteristics of the North Atlantic Subpolar Gyre



N. A. Diansky  and P. A. Sukhonos 

Abstract Variability of the hydrothermodynamic characteristics of the North Atlantic subpolar gyre on multidecadal scale is analyzed using ORA-S3 ocean re-analysis data for the period 1959–2011 and the COREv2 data for the period 1949–2006. It was shown that an increase in the outflow of heat from the ocean to the atmosphere since late 1990s in the Subtropical Atlantic was accompanied by a corresponding decrease in heat loss from the ocean surface in the Subpolar Atlantic. This is consistent with the Gulf Stream meridional displacement to the south in the warm phase of the Atlantic multidecadal oscillation (AMO). In the positive AMO phase, the depth of convective mixing at the Labrador Sea decreases, the sea surface height increases and cyclonicity in the subpolar gyre weakens from January to March. During these months, the response of the subpolar gyre circulation to long-term changes in the intensity of convective mixing at the Labrador Sea occurs with a 5–10 years delay.

Keywords Atlantic multidecadal oscillation · Subpolar gyre · North Atlantic

1 Introduction

Pronounced long-period variations in the upper ocean temperature in the North Atlantic (NA) are called the Atlantic multidecadal oscillation (AMO) (Kerr 2000). It is a natural mode of multidecadal variability in the ocean–atmosphere system with a typical period of about 65–70 years (Schlesinger and Ramankutty 1994; Kushnir 1994). To measure the AMO, an index which is determined by the field of sea surface

N. A. Diansky

Lomonosov Moscow State University, GSP-1, Leninskie Gory, Moscow 119991, Russia
e-mail: nikolay.diansky@gmail.com

Institute of Numerical Mathematics of the RAS, Gubkina st., 8, Moscow 119333, Russia

N.N. Zubov State Oceanographic Institute, Kropotkinsky lane, 6, Moscow 119034, Russia

P. A. Sukhonos (✉)

Institute of Natural and Technical Systems, Lenina st., 28, Sevastopol 299011, Russia
e-mail: pasukhonis@mail.ru

temperature (SST) in the NA averaged within 0–70° N is used (Enfield et al. 2001). The spatial structure of the AMO is a large-scale warming/cooling of the upper NA layer at a multidecadal scale with larger amplitude in the subpolar gyre and smaller amplitude in the tropics and subtropics.

The influence of the AMO on hydrophysical characteristics in the Northern Hemisphere is described in a large number of works. It underlines the important role of this climate signal in the study of the climate change. In addition, recent papers are dedicated to the effect of the AMO on other climate signals: the North Atlantic Oscillation (Delworth et al. 2017), El Niño–Southern Oscillation (Levine et al. 2017) and Tropical Atlantic Variability Modes (Martín-Rey et al. 2018).

The mechanisms that form multidecadal variability in the NA are being revised now. It was generally thought that the multidecadal variations in the NA heat content were caused by long-term changes in the thermohaline circulation (Latif et al. 2004; Knight et al. 2005). However, some authors note that volcanic activity can also lead to the long-term changes in radiative forcing, which, in turn, modulates the AMO phase (Otterå et al. 2010). Other authors argue that radiative forcing of aerosols is the major contributor to multidecadal variability in the NA (Booth et al. 2012). Further discussion of this point is given in article (Zhang et al. 2013). An idea that anthropogenic and natural factors together form long-term variability in the NA has been recently expressed (Tandon and Kushner 2015). As regards the natural causes of multidecadal variability, some authors report that variability in the ocean–atmosphere system at the AMO scale can arise due to the atmospheric heat fluxes at the ocean surface independently from the processes in the ocean (Clement et al. 2015). Other authors note that the main mechanism that forms the low-frequency variability of the SST in the NA is the quasiperiodic oscillations of oceanic meridional heat transport (MHT), although in this case, there are disagreements among the published points of view. Some authors believe that quasiperiodic oscillations of the MHT in the NA arise due to a phase shift between the haline and thermal modes (Frankcombe and Dijkstra 2011; Volodin 2013). Other authors prove only thermal origin of the AMO (Voskresenskaya and Polonskii 2004). Thus, the discussion regarding the causes of generation of multidecadal variability in the NA continues.

The largest AMO amplitude is observed in the NA subpolar gyre. Therefore, this article refines the multidecadal variability of the NA subpolar gyre using homogeneous and long-term data.

2 Data and Methods

The monthly data on the mixed layer depth (MLD), zonal and meridional components of the ocean current velocity vector and sea surface height (SSH) from ORA-S3 ocean re-analysis for 1959–2011 (Balmaseda et al. 2008) were used. A scheme based on the semi-empirical theory of turbulence was used to calculate the MLD in the ORA-S3 re-analysis. The key idea of the scheme is to calculate the Richardson number as in

(Pacanowski and Philander 1981). The MLD is assumed to be equal to the depth at which the Richardson number reaches a critical value $Ri_{crit} = 0.3$.

The monthly data on the latent and sensible heat fluxes, balances of shortwave and longwave radiation on the ocean surface were taken from the Coordinated Ocean Research Experiments version 2 (COREv2) for 1949–2006 (Large and Yeager 2009). According to this dataset, the net surface heat fluxes for each month were calculated.

The vorticity of current velocity for each month was calculated as: $rot_z \mathbf{u} = \partial V_y / \partial x - \partial V_x / \partial y$ (s^{-1}), where V_x , V_y are the zonal and meridional components of the current vector at the horizons of 415 and 535 m.

The vertical axis is directed up. In the analysis of the vorticity values, anticyclonic (cyclonic) vorticity refers to negative (positive) values. In the analysis of the net heat fluxes, positive (negative) values mean the outflow (influx) of heat from (to) the ocean surface. Negative (positive) SSH anomalies correspond to the intensification (weakening) of the subpolar gyre. The linear trend was removed from the time series.

3 Results

Notable multidecadal changes in the current velocity field in the 0–300 m layer in January formed by the AMO are not detected in the whole NA (Fig. 1a). In the Gulf Stream—North Atlantic current system, an increase in the amplitude of fluctuations of all hydrophysical characteristics is observed. In the Gulf Stream, after it separates from the continental slope, and in the North Atlantic Current a

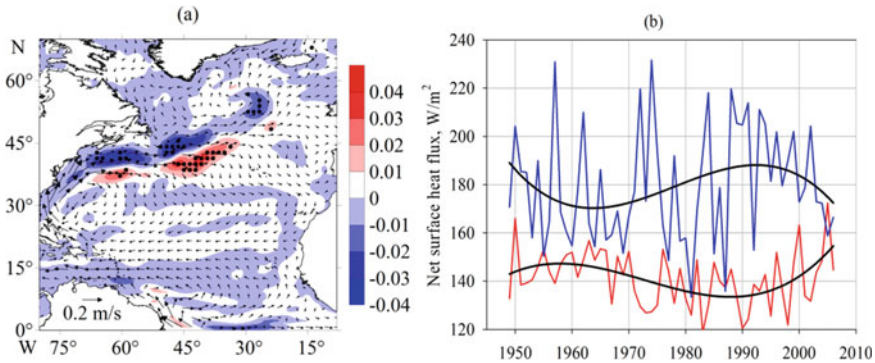


Fig. 1 **a** The difference between the detrended anomalies of the current velocity modulus in the 0–300 m layer in January (m/s) in the positive and negative AMO phases. A twelve-year period from 2000 to 2011 is the positive AMO phase and a twelve-year period from 1969 to 1980 is the negative one. The black dots indicate the nodes of the spatial grid, in which the difference is significant at 95% confidence level. Vectors represent the average current velocity for the period 1959–2011. **b** Time evolution of the net surface heat flux (W/m^2) in January over the latitudinal bands 15–40° N (red) and 41–65° N (blue) from COREv2 data. Smoothed black line is an approximate polynomial of the third degree

considerable decrease in the current velocities during the positive AMO phase (2000–2011) is noted. The obtained result indicates a shift of the Gulf Stream southward in the warm AMO phase. This means that on a multidecadal scale the subtropical gyre decreases (increases) its meridional dimensions during warming (cooling) of the NA upper ocean layer. Analysis of observational data showed that during the radial compression of the subtropical gyre, it intensifies (Iselin 1940).

Temporal variability of the net heat fluxes on the ocean surface in January in the middle (15–40° N) and high (41–65° N) latitudes of the NA is represented by intense interannual fluctuations (Fig. 1b). The amplitude of interannual fluctuations of the net heat fluxes on the ocean surface over the subpolar gyre is greater than over the subtropical gyre. The variance of the interannual fluctuations of the net heat fluxes on the surface of the subpolar gyre exceeds that of the subtropical gyre by a factor of 4. Despite this, in the second half of the twentieth century, the field of net heat fluxes on the NA ocean surface in January shows intense multidecadal variability. Long-term variations in the net heat fluxes on the ocean surface in January are in antiphase between the middle and high latitudes of the NA. In the mid-1960s, in the subtropical latitudes, intense heat release from the ocean to the atmosphere was noted, and in the subpolar latitudes, on the contrary, heat loss by the ocean was minimal. An increase in the outflow of heat from the ocean to the atmosphere since late 1990s in the subtropical latitudes was accompanied by a corresponding decrease in heat loss from the ocean surface in the subpolar latitudes. The result obtained is consistent with the meridional displacement of the Gulf Stream southward in the warm AMO phase (Fig. 1a). Thus, the low-frequency variations of heat flux from the ocean surface in winter are controlled by large-scale changes in the circulation of the upper ocean layer.

Unlike heat fluxes on the ocean surface (where interannual fluctuations are important), interannual variations of the SSH, the MLD and the vorticity of current velocity at the horizons of 415 and 535 m in the subpolar gyre describe a significant proportion of low-frequency variability.

Deep convection in the Labrador Sea covers the period from January to March (Zelenko and Resnyansky 2007). For these months, time series of the MLD were obtained for the part of the Labrador Sea (53–59° N 40–50° W) where the greatest depths of convective mixing are observed (Fig. 2a). Thus, intense interannual-interdecadal variations in the MLD occurred in the second half of the twentieth century. Moreover, in some years that are quite close in time, the MLD in the Labrador Sea can vary by 1–1.5 km, which was previously obtained from the observational data (Lab Sea Group 1998). The variance of interannual fluctuations (frequency band less than 10 years) of the MLD is comparable with that of interdecadal fluctuations (frequency band more than 10 years) of the MLD. This suggests a significant effect of low-frequency processes in the ocean–atmosphere system on the intensity of deep convection at the NA high latitudes. On the interdecadal scale, the MLD undergoes a significant increase in the 1970s, 1980s and 1990s. In early 2000s, there is a decrease in the MLD, which means a weakening of the convective processes at high latitudes. The obtained result indicates that the interdecadal variations in the intensity of convective mixing in the NA were caused by the AMO. Moreover, the

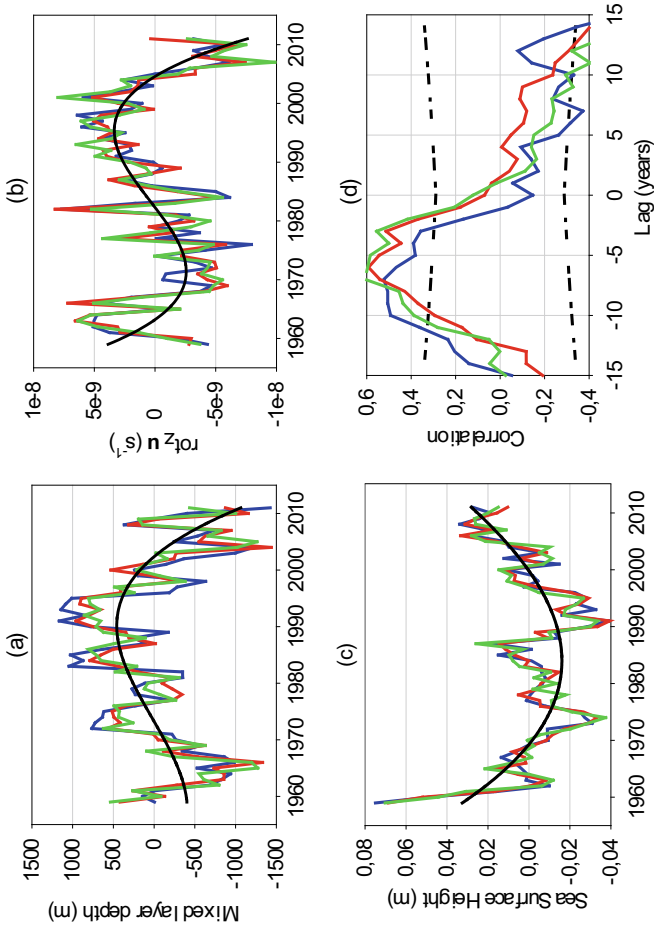


Fig. 2 Time series of the detrended mixed layer depth, *m*, **a** in a part of the Labrador Sea (53–59° N 40–50° W), vorticity of currents on 415 m, *s*⁻¹, **b** and sea surface height, *m*, **c** in the latitudinal band 41–65° N. The blue/red/green lines indicate the values in January/February/March. Smoothed black line is an approximate polynomial of the third degree. Lagged correlations between the values in figures **(a)** and **(b)** are shown in **(d)**. Dotted black lines denote 95% confidence level. Negative lags mean that the mixed layer depth leads

negative AMO phase demonstrates an intensification of convective processes in the NA subpolar latitudes.

Development of deep convection in the ocean requires three conditions: favorable atmospheric forcing, weakened water stratification below the seasonal thermocline and the presence of cyclonic circulation (Marshall and Schott 1999). Such circulation leads to the rise of weakly stratified water from the deep layers closer to the ocean surface. The long-period intensification of cyclonic circulation in the subpolar gyre took place from the beginning of the 1970s to the end of the 1990s (Fig. 2b). This provided favorable conditions for the penetration of convective mixing to great depths. In the early 2000s, the cyclonicity of circulation in the NA subpolar gyre began to weaken which also affected the MLD. Note that temporal changes in the vorticity of current velocity at 415 and 535 m in the latitude band 41–65° N have a similar behavior. The described changes in the intensity of circulation of the subpolar gyre are consistent with low-frequency variations in the current velocity in a layer of 0–300 m (Fig. 1a).

The SSH in the subpolar gyre experiences significant interdecadal fluctuations due to the AMO (Fig. 2c). These variations manifest themselves in a large-scale rise of the SSH in the positive phase of the climate signal. Moreover, time evolution in the SSH similarly show a weakening of the NA subpolar gyre after the 2000s.

Thus, the positive AMO phase shows a decrease in the depth of convective mixing at high latitudes, an increase in the SSH, and a weakening of cyclonicity in the subpolar gyre. Indirect confirmation of these results is given in (Hakkinen and Rhines 2009).

Between the time series of the MLD and the vorticity of current velocity at the horizon of 415 m (similar results were obtained for the values of the vorticity of current velocity at the horizon of 535 m) in January, February, and March for the period 1959–2011 lead-lag correlation coefficients were calculated (Fig. 2d). Significant correlation coefficients of more than 0.5 are observed between these time series when the MLD is 5–10 years leading. Thus, the response of the circulation of the subpolar gyre to changes in the intensity of convective mixing at high latitudes occurs with a 5 to 10 years delay.

4 Conclusions

The results obtained in this paper and the results of previously published works (including the results by the authors (Diansky and Sukhonos 2018)) made it possible to formulate the following regularities.

The negative AMO phase (1971–1980): intense convection at high latitudes, the northern position of the Gulf Stream, increase in the heat transfer to the Arctic from the NA, weak (intense) subtropical (subpolar) gyre, negative (positive) SSH anomaly in the area of the subtropical (subpolar) gyre.

Intermediate state: intense ice melting in Greenland and the Arctic. After some delay, a freshwater lens spreads in the Subpolar Atlantic and locks the deep convection in the Labrador Sea. With some delay, the circulation of the subpolar gyre begins to weaken.

Positive AMO phase (2001–2010): weaker convection at high latitudes, the southern position of the Gulf Stream, weaker heat transport to the Arctic from the NA, the NA upper ocean layer (0–300 m) warms up, intense (weak) subtropical (subpolar) gyre, rising SSH in the central and eastern parts of the NA.

Acknowledgements This study was supported by the Russian Scientific Foundation (grant 17-17-01295) and by the Russian Foundation for Basic Research (grant 18-05-01107).

References

- Balmaseda MA, Vidard A, Anderson DLT (2008) The ECMWF ocean analysis system: ORA-S3. *Mon Wea Rev* 136(8):3018–3034. <https://doi.org/10.1175/2008MWR2433.1>
- Booth BBB, Dunstone NJ, Halloran PR et al (2012) Aerosols implicated as a prime driver of twentieth-century North Atlantic climate variability. *Nature* 484(7393):228–232. <https://doi.org/10.1038/nature10946>
- Clement A, Bellomo K, Murphy LN et al (2015) The Atlantic Multidecadal Oscillation without a role for ocean circulation. *Science* 350(6258):320–324. <https://doi.org/10.1126/science.aab3980>
- Delworth TL, Zeng F, Zhang R et al (2017) The central role of ocean dynamics in connecting the North Atlantic Oscillation to the extratropical component of the Atlantic Multidecadal Oscillation. *J Clim* 30(10):3789–3805
- Diansky NA, Sukhonos PA (2018) Multidecadal variability of hydro-thermodynamic characteristics and heat fluxes in North Atlantic. *Phys Math Model Earth Environ Process*. Springer, Cham, pp 125–137. https://doi.org/10.1007/978-3-319-77788-7_14
- Enfield DB, Mestas-Nunez AM, Trimble PJ (2001) The Atlantic multidecadal oscillation and its relation to rainfall and river flows in the continental U.S. *Geophys Res Lett* 28(10):2077–2080
- Frankcombe LM, Dijkstra HA (2011) The role of Atlantic—Arctic exchange in North Atlantic multidecadal climate variability. *Geophys Res Lett* 38(16):L16603. <https://doi.org/10.1029/2011GL048158>
- Hakkinen S, Rhines PB (2009) Shifting surface currents in the northern North Atlantic Ocean. *J Geophys Res* 114(C4):C04005. <https://doi.org/10.1029/2008JC004883>
- Iselin COD (1940) Preliminary report on long-period variations in the transport of the Gulf Stream System. *Pap Phys Oceanogr Meteorol* 8(1):1–40
- Kerr RA (2000) A North Atlantic climate pacemaker for the centuries. *Science* 288(5473):1984–1985
- Knight JR, Allan RJ, Folland CK et al (2005) A signature of persistent natural thermohaline circulation cycles in observed climate. *Geophys Res Lett* 32(20):L20708. <https://doi.org/10.1029/2005GL024233>
- Kushnir Y (1994) Interdecadal variations in North Atlantic Sea surface temperature and associated atmospheric conditions. *J Clim* 7(1):141–157
- Lab Sea Group (1998) The Labrador Sea Deep Convection Experiment. *Bull Amer Meteorol Soc* 79(10):2033–2058
- Large WG, Yeager SG (2009) The global climatology of an interannually varying air–sea flux data set. *Clim Dyn* 33(2–3):341–364

- Latif M, Roeckner E, Botzet M et al (2004) Reconstructing, monitoring, and predicting multidecadal-scale changes in the North Atlantic thermohaline circulation with sea surface temperature. *J Clim* 17(7):1605–1614
- Levine AFZ, McPhaden MJ, Frierson DMW (2017) The impact of the AMO on multidecadal ENSO variability. *Geophys Res Lett* 44(8):3877–3886
- Marshall J, Schott F (1999) Open-ocean convection: observations, theory, and models. *Rev Geophys* 37(1):1–64
- Martín-Rey M, Polo I, Rodríguez-Fonseca B et al (2018) Is there evidence of changes in tropical Atlantic variability modes under AMO phases in the observational record? *J Clim* 31(2):515–536
- Otterå OH, Bentsen M, Drange H et al (2010) External forcing as a metronome for Atlantic Multidecadal variability. *Nat Geosci* 3(10):688–694. <https://doi.org/10.1038/ngeo955>
- Pacanowski RC, Philander SGH (1981) Parameterization of vertical mixing in numerical models of tropical oceans. *J Phys Oceanogr* 11(11):1443–1451
- Schlesinger ME, Ramankutty N (1994) An oscillation in the global climate system of period 65–70 years. *Nature* 367(6465):723–726
- Tandon NF, Kushner PJ (2015) Does external forcing interfere with the AMOC's influence on North Atlantic sea surface temperature? *J Clim* 28(16):6309–6323. <https://doi.org/10.1175/JCLI-D-14-00664.1>
- Volodin EM (2013) The mechanism of multidecadal variability in the Arctic and North Atlantic in climate model INMCM4. *Env Res Lett* 8(3):035038. <https://doi.org/10.1088/1748-9326/8/3/035038>
- Voskresenskaya EN, Polonskii AB (2004) Low-frequency variability of hydrometeorological fields and heat fluxes over the North Atlantic. *Phys Oceanogr* 14(4):203–220. <https://doi.org/10.1007/s11110-005-0015-4>
- Zelenko AA, Resnyansky YD (2007) Deep convection in the ocean general circulation model: Variability on the diurnal, seasonal, and interannual time scales. *Oceanology* 47(2):191–204. <https://doi.org/10.1134/S0001437007020063>
- Zhang R, Delworth TL, Sutton R et al (2013) Have aerosols caused the observed Atlantic Multidecadal Variability? *J Atmos Sci* 70(4):1135–1144. <https://doi.org/10.1175/JAS-D-12-0331.1>

On the Factors Affecting Mixed Layer Depth in the Inland Water Objects



D. Gladskikh , V. Stepanenko , and E. Mortikov 

Abstract The problem of numerical modeling of inland water objects (lakes and reservoirs) and, in particular, mixing processes in this basins are considered in the paper. The basic instrument applied is the one-dimensional LAKE model based on the averaging of three-dimensional RANS equations over the horizontal cross-section of a water object. This model also uses pressure gradient parametrization, which allows to take into account gravitational vibrations (seiches). In addition to LAKE, the three-dimensional hydrostatic model developed at the M.V. Lomonosov Moscow State University Research and Development Center is applied. Verification of models on the basis of numerical realization of the classical laboratory experiment of Kato-Phillips is carried out. Hypotheses of the influence of such characteristics as horizontal dimensions of the reservoir, initial temperature gradient and momentum flux on mixing are considered. The effect is confirmed, along with the necessity of taking into account seiches during modeling of lakes and reservoirs with horizontal dimensions much less than the Rossby internal deformation radius.

Keywords Numerical modeling · Inland waters · Turbulence · Seiches

1 Introduction

Inland water objects, by which lakes and reservoirs are recognized, occupy approximately 1.3–1.8% of the total area of continents (Downing et al. 2006; Messenger et al. 2016), play a huge role in various spheres of life of the human population and are of

D. Gladskikh (✉)

Division of Geophysical Research, Institute of Applied Physics, Russian Academy of Sciences, Nizhny Novgorod, Russian Federation
e-mail: daria.gladskikh@gmail.com

D. Gladskikh · V. Stepanenko · E. Mortikov

M.V. Lomonosov Moscow State University, Research Computing Center, Moscow, Russian Federation

E. Mortikov

Institute of Numerical Mathematics, Russian Academy of Sciences, Moscow, Russian Federation

interest for a number of studies in limnology, hydrology, ecology, meteorology and climatology. The thermo-hydrodynamic characteristics of lakes and reservoirs have a strong influence on a number of general circulation processes in the Atmosphere, Ocean and inland waters. In addition, changes of temperature in lakes and reservoirs can provoke processes of eutrophication (Gorbunov 2011; Kozitskaya 1989; Kreiman et al. 1992)—increasing the biological productivity of water objects, in particular, resulting in growth of diatoms and harmful blue-green algae biomass, which can lead to pestilence of fish and deterioration of water quality.

It is also necessary to note the role of inland water objects in climate change and the reaction of water objects to these changes (Adamenko 1985; Tranvik 2009). In regions with a large number of lakes and reservoirs, marked climate warming (Stepanenko 2007) is registered, which leads to an earlier of ice opening period and a shorter duration of freeze-up. In order to take into account the two-way interaction of inland water objects and the atmosphere, it is necessary to include the calculation of thermo-hydrodynamic and biological characteristics of land waters into climate models. Correct consideration of lakes thermo-hydrodynamics of is crucial in mesoscale models, where spatial resolution reaches several kilometers.

An important aspect of modeling the thermohydrodynamics of inland water objects is the correct description of mixing processes, including those associated with gravitational oscillations (seiches). Seiches arise from mass redistribution and pressure gradient effects and are not taken into account in most existing one-dimensional models. However, when modeling lakes and reservoirs with horizontal dimensions much less than the Rossby internal deformation radius L_R , Coriolis force becomes negligible in comparison with the force of the horizontal pressure gradient (Stepanenko 2018b), and the models that do not take into account the seiches do not allow to obtain correct description of the processes in such reservoirs and, in particular, the dynamics of the mixed layer thickness (the overestimation of this value, especially during the summer stratification of lakes and reservoirs takes place). For temperate latitudes, the value L_R is approximately 2–3 km, and it is expected that the seiches will have significant influence on the mixing processes in the relatively small lakes that make up major share of inland water objects.

2 Methods and Approaches to Description of Processes of Thermo-Hydrodynamics of Inland Water Objects

Now there are mathematical models of different spatial dimensions that allow to calculate the distribution of thermo-hydrodynamic parameters of inland water objects. The most detailed description is given by complete three-dimensional models (see (Abbasi et al. 2016; Kelley et al. 1998)), the basis of which, in most cases, is the Navier–Stokes equation system averaged over Reynolds, in hydrostatics and Boussinesque approximations (Monin 1965). Such models often require a lot of computational resources and, therefore, lots of machine time. At the same time, use of these

models makes sense only in the presence of detailed information about the water object under study: spatial and temporal pattern of flows, data on the meteorological situation in the area of the reservoir with spatial resolution, taking into account the features of its bathymetry and topography of the surrounding territory.

Two-dimensional modelling is hardly used for practical weather forecasting purposes. Application of such models makes sense only in specific cases: for example, mathematical modeling of a thermobar (Zilitinkevich and Kreiman 1990; Tsydenov and Starchenko 2013).

The basic types of one-dimensional models are: horizontal-averaged models and boundary layer models. In the first case, the averaging of three-dimensional RANS-equations over the horizontal section of a reservoir is applied, in the second case, the equations of the atmospheric or oceanic boundary layer obtained from the RANS system are also used, supplemented by a turbulent closure. For the second type of models, it is assumed that the fields of all physical values are homogeneous in horizontal direction, which can only be fulfilled for sufficiently large water objects and far from the shore. One-dimensional models are usually applied for shallow water objects, as in the deep lakes and reservoirs there are specific effects that play an important role, which cannot be reproduced in a one-dimensional approximation. However, for most real cases, one-dimensional models demonstrate high accuracy in reproducing physical and hydrological characteristics.

As the basic model for thermo-hydrodynamic processes description in inland waters, the one-dimensional LAKE model was chosen (see (Stepanenko 2018b) for a details), developed at M.V. Lomonosov Moscow State University. Currently, this model is used in the latest version of the climate model of the Institute of Computational Mathematics of the Russian Academy of Sciences (Volodin 2013).

The model is based on horizontally averaged equations for temperature and momentum:

$$\begin{aligned}
 c_w \rho_w \frac{\partial \bar{T}}{\partial t} &= -c_w \rho_w A_T + \frac{1}{A} \frac{\partial}{\partial z} \left(A(\lambda_m + c_w \rho_w K_h) \frac{\partial \bar{T}}{\partial z} \right) - \frac{1}{A} \frac{\partial A \bar{R}_s}{\partial z} \\
 \frac{\partial \bar{u}}{\partial t} &= -A_u - \overline{\left(\frac{1}{\rho_w} \frac{\partial p}{\partial x} \right)} + \frac{1}{A} \frac{\partial}{\partial z} \left(A(K_m + \nu_m) \frac{\partial \bar{u}}{\partial z} \right) + \frac{1}{A} \frac{\partial A}{\partial z} F_{u,b}(z) \\
 \frac{\partial \bar{v}}{\partial t} &= -A_v - \overline{\left(\frac{1}{\rho_w} \frac{\partial p}{\partial y} \right)} + \frac{1}{A} \frac{\partial}{\partial z} \left(A(K_m + \nu_m) \frac{\partial \bar{v}}{\partial z} \right) + \frac{1}{A} \frac{\partial A}{\partial z} F_{v,b}(z)
 \end{aligned}$$

where c_w —specific heat capacity of water, ρ_w —its density, T —temperature, with indices marked the components responsible for the inflows, sources and ground-water feeding of the reservoir, $A(z)$ —horizontal section of the reservoir, λ_m —molecular heat conductivity coefficient, K_h —coefficient of turbulent thermal conductivity, R_s —short-wave radiation flux (with index b —horizontally homogeneous), $F_{T,b}(z)$ —heat flux to bottom sediments, u and v —velocity components, p —pressure, K_m —turbulent viscosity coefficient, ν_m —molecular viscosity coefficient, $F_{u,b}(z)$,

$F_{v,b}(z)$ —vertical fluxes at the bottom, f —Coriolis parameter, horizontal line means averaging.

The main parameter at the description of vertical turbulent heat exchange in reservoirs is the coefficient of turbulent heat conductivity K_h ; its parameterization depending on meteorological conditions is one of the main problems in the construction of one-dimensional models. A variant with k - ε parameterization (Lykosov 1992; Mellor and Yamada 1974) based on the equations for the kinetic energy of turbulence (k) and its dissipation rate (ε). This closure includes the following equations:

$$\begin{aligned}\frac{\partial k}{\partial t} &= \frac{1}{A} \frac{\partial}{\partial z} A (K_m + \nu_m) \frac{\partial k}{\partial z} + P + B - \varepsilon \\ \frac{\partial \varepsilon}{\partial t} &= \frac{1}{A} \frac{\partial}{\partial z} A \left(\frac{K_m}{\delta_s} + \nu_m \right) \frac{\partial \varepsilon}{\partial z} + \frac{\varepsilon}{k} (C_{1\varepsilon} \cdot P + C_{3\varepsilon} \cdot B - C_{2\varepsilon} \cdot \varepsilon) \\ P &= K_m \left[\left(\frac{\partial u}{\partial z} \right)^2 + \left(\frac{\partial v}{\partial z} \right)^2 \right] \\ B &= -\frac{g}{\rho_w} K_h \left(\alpha_T \frac{\partial T}{\partial z} + \alpha_s \frac{\partial s}{\partial z} \right) \\ K_m &= C_s \frac{E_K^2}{\varepsilon} \\ K_m &= C_{s,T} \frac{E_K^2}{\varepsilon} = \frac{C_{s,T}}{C_s} K_m\end{aligned}$$

Here the summand corresponds to the generation of turbulence energy due to the velocity shear, and B describes the generation or consumption of energy due to the action of buoyancy forces, while α_T —the coefficient of thermal expansion, and α_s —the coefficient of expansion relative to the salinity s , ν_m —the coefficient of molecular viscosity δ_k , δ_ε —turbulent Schmidt numbers. $C_{1\varepsilon}$, $C_{2\varepsilon}$, $C_{3\varepsilon}$ —empirical constants, and $C_{3\varepsilon} = 1.14$ at $B > 0$, and -0.4 at $B < 0$ (Burchard 2002), C_s and $C_{s,T}$ stability functions for momentum and scalars respectively.

In order to take into account seiches, the necessity of which was discussed in the introduction, the LAKE model uses a method based on the explicit reproduction of the first horizontal mode (Stepanenko 2018a). The multi-layer liquid consisting of N layers of constant density ρ_i increasing with depth is considered $\rho_{i+1} > \rho_i$. In this case, the thickness of each layer experiences small disturbances near the average values. In each layer, the horizontal pressure gradient is calculated using the values of the velocity components from one-dimensional model, averaged vertically within the corresponding layer.

In addition to the LAKE model, for the description of the thermohydrodynamics of inland water objects, the present study uses a three-dimensional hydrostatic model developed at the Research and Development Centre of Moscow State University on

the basis of a unified hydrodynamic code that combines DNS/LES/RANS approaches to calculate geophysical turbulent flows at high spatial and temporal resolution (see, for example, (Mortikov 2016; Mortikov et al. 2019)). This model describes the system of equations of hydrodynamics in the hydrostatic and Boussinesque approximations in the Cartesian coordinate frame:

$$\frac{\partial u}{\partial t} = -A(u) + D_H(u, \chi_m) + D_z(u, K_m) - g \frac{\partial \eta}{\partial x} - \frac{g}{\rho_0} \frac{\partial}{\partial x} \int_z^{B(x,y)} \rho dz + f v,$$

$$\frac{\partial v}{\partial t} = -A(v) + D_H(v, \chi_m) + D_z(v, K_m) - g \frac{\partial \eta}{\partial y} - \frac{g}{\rho_0} \frac{\partial}{\partial y} \int_z^{B(x,y)} \rho dz + f u,$$

$$\nabla \cdot \mathbf{u} = \frac{\partial u}{\partial x} + \frac{\partial v}{\partial y} + \frac{\partial w}{\partial z} = 0,$$

$$\frac{\partial T}{\partial t} = -A(T) + D_H(v, \chi_h) + D_z(T, K_h),$$

$$\rho = \rho(T),$$

where u, v, w —velocity vector components, η —free surface deviation from the equilibrium state, $B(x, y)$ —bottom relief, f —Coriolis parameter. Also here $A(q)$ is the advection operator, and $D_H(q, \chi)$ and $D_z(q, K)$ are the horizontal and vertical diffusion operators with coefficients χ and K respectively.

As in the LAKE model, the standard k - ε scheme is used to describe the vertical mixing processes.

As for the numerical methods used in the calculations, the semi-implicit method is used to integrate the time equation system, and the advective transport and horizontal diffusion are described by explicit schemes, which defines time step limits.

3 Model Verification

With help of one-dimensional LAKE model and three-dimensional hydrostatic model the numerical realization of classic Kato-Phillips laboratory experiment (Kato and Phillips 1969) which serves as the basic material for calibration of turbulent closure has been carried out. The obtained results were compared with the calculations of the mixed layer depth change in idealized reservoirs with different horizontal dimensions, where it is necessary to take into account the new effects associated with the seismic vibrations.

In the Cato-Phillips experiment, a homogeneous stratified liquid of sufficiently large depth is considered, and vertical boundaries are absent. The initial temperature profile is linear and the only source of turbulence is the wind with a constant speed.

In the classical statement described in the article (Kato and Phillips 1969), the ring tank was considered, the surface of which was influenced by friction stress in the direction of the circle. The inner and outer diameters were 106.7 and 152.4 cm, respectively, so that the channel width was 22.8 cm. The depth of the tank was 28 m.

The following parameters were used for the numerical implementation of the experiment:

- depth of the reservoir 10 m,
- calculation time 7 days,
- initial temperature gradient $\partial T/\partial z = 1.5^\circ\text{C/m}$,
- surface impulse flux $\tau = 10^{-2} \text{ N/m}^2$,
- Brunt-Vaisala (buoyancy) frequency: $N = 4 \times 10^{-2} \text{ s}^{-1}$,
- the Coriolis effects are not taken into account.

For this experiment, there is a theoretical relation (Price 1979), where the mixed layer depth is a function of time:

$$MLD(t) = \frac{1.05u_* \sqrt{t}}{\sqrt{N(t=0)}}$$

where MLD is the mixed layer depth, u_* —friction—velocity ($u_* = \sqrt{\tau/\rho_0}$).

Both of these models were successfully verified in the classical Catho-Phillips experiment and showed good agreement with the analytical solution (see Fig. 1).

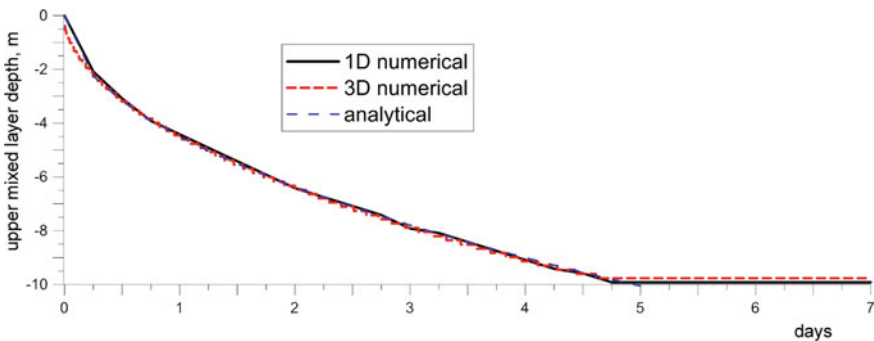


Fig. 1 Changes in the mixed layer depth with time for the numerical implementation of the classic Kato-Phillips experiment and comparison with the analytical formula

4 Numerical Experiments

4.1 Influence of Horizontal Dimensions on Mixing Processes

Two idealized reservoirs with rectangular cross-section and horizontal dimensions of 1000 and 10 m were considered. The other parameters were chosen in the same way as in the numerical formulation of the Cato-Phillips experiment. A water object with horizontal dimensions of 1000 m is a typical case, while 10 m is an extreme case, and the hydrostatic approximation used in a three-dimensional model may not be quite correct to reproduce the processes taking place in such an object.

First, the dynamics of the mixed layer depth for 7 days was analyzed (Fig. 2). It is demonstrated that with the increase in the size of the reservoir the mixing rate also increases, and the more the reservoir is, the closer the result will be to the result of the classical Cato-Phillips experiment, where vertical walls are absent.

The characteristics related to the turbulent mixing processes in lakes and reservoirs were also compared. The vertical distribution of temperature and flow velocity module for the 7th day of calculation were considered (see Fig. 3a, b).

A good agreement in the temperature profiles between the models is demonstrated. Time scale of several days, just when correct temperature reproduction is crucial, for example, for forecasting purposes. As for the flow velocity profiles, there are certain differences in the results, which can be related to the features of the models: the one-dimensional model is built on the averaging of three-dimensional equations. Nevertheless, the attention should be paid to the fact that in both models the molecular viscosity affects the reduction of vibration velocity below the thermocline.

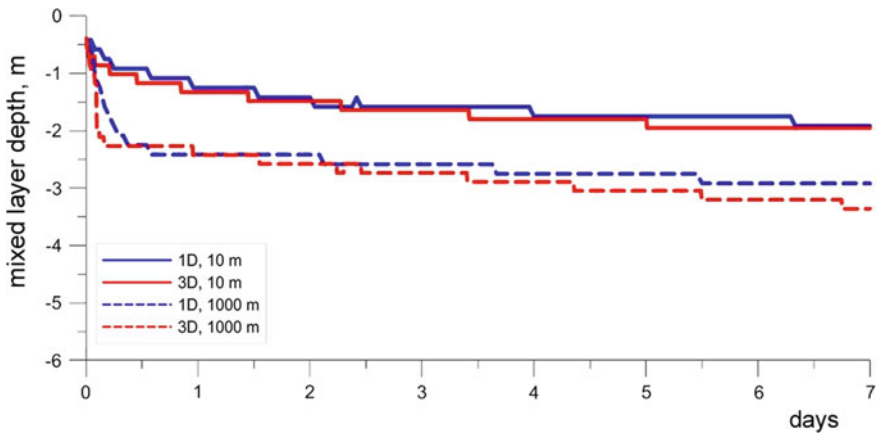


Fig. 2 Change in the mixed layer depth with the time for reservoirs with horizontal dimensions of 1000 and 10 m

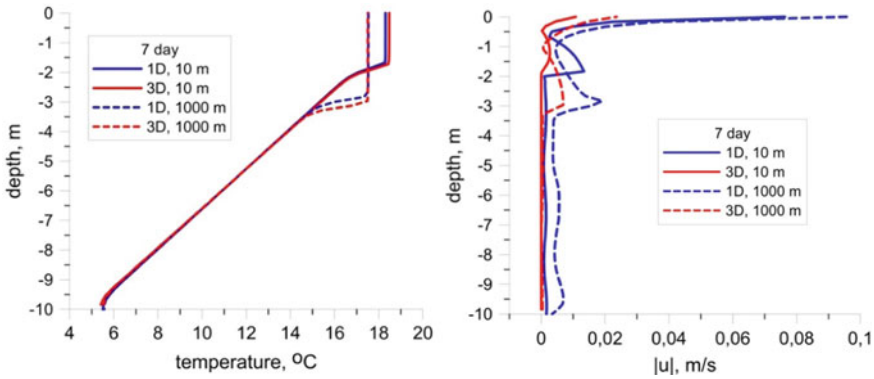


Fig. 3 Vertical distribution of temperature (a) and flow velocity (b) for the 7th day of calculation

4.2 Influence of Initial Temperature Gradient and Pulse Flow

In addition to the horizontal dimensions of the reservoir, such parameters affecting the mixed layer depth as the initial temperature gradient and momentum flux are considered. An idealized tank with a horizontal size of 1000 m is considered, because, as mentioned earlier, this size is typical of real water objects, and then registered dynamics of the mixed layer depth for 7 days, using two models (see Fig. 4).

In weak winds, when the value of the momentum flux is small, changes in the initial temperature gradient do not have a significant effect on the mixing, while in strong winds, the mixing velocity depends significantly on the initial gradient. It should be noted that with a small momentum flux and a small temperature gradient,

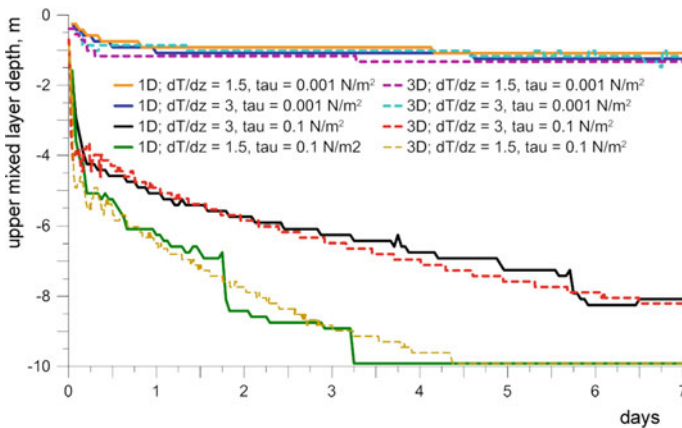


Fig. 4 Changes of the mixed layer depth at different values of the initial temperature gradient and momentum flux for 7 days

one-dimensional model showed some inaccuracy in determining the thickness of the mixed layer, but in average values the agreement between the models is good enough.

5 Conclusions

Within the presented study, the influence of various factors on the change in the mixed layer depth in internal reservoirs (lakes and reservoirs) was studied. The horizontal dimensions of the reservoir, as well as the initial temperature gradient and momentum flux on the surface were considered as such factors. As the basic instrument for carrying out calculations the one-dimensional LAKE model was used. This model includes parametrization of the pressure gradient, and the three-dimensional hydrostatic model. To describe the vertical exchange processes in both models, $k-\varepsilon$ was applied as closure.

Verification of models was carried out on the basis of numerical realization of classical laboratory experiment of Kato-Phillips for homogeneous liquid with depth of 10 m. Calculations have shown good agreement with the theoretical formula describing the time dependent thermocline deepening in the Kato-Phillips experiment.

Also idealized reservoirs with horizontal dimensions of 10 and 1000 m and rectangular cross-section were considered, and calculations of mixed layer depth change by one-dimensional and three-dimensional models were made. The experiment has shown that the larger the horizontal dimensions of the reservoir, the faster the mixing process takes place, and the closer the result to the result of the Kato-Phillips experiment, where there were no vertical walls. It should be noted that this experiment has confirmed the need to take into account the seiches to correctly describe the dynamics of mixing in water objects with horizontal dimensions much smaller than the Rossby deformation radius.

A series of experiments related to the study of such parameters as the initial temperature gradient and momentum flux have shown that the role of the influence of the initial temperature gradient on the mixing depends on the momentum flux: in a weak wind the sensitivity to the temperature gradient is weak, and in a strong wind the mixing rate is significantly dependent on the initial gradient.

As a conclusion, authors note that the performed studies confirm the impact, first of all, of the horizontal dimensions of the reservoir on the mixing processes in lakes and reservoirs, and second of all the need to take into account the seiches in the description of such processes in real water objects. Thus, the LAKE model, which includes pressure gradient parametrization, can be successfully applied to most real lakes and reservoirs.

Acknowledgements The work was financially supported by the Russian Foundation for Basic Research (projects № 17-05-41117, 18-05-00292, 18-35-00602). Calculations with the use of three-dimensional model were made in the framework of the project of the Russian Scientific Foundation № 17-17-01210.

References

- Abbasi A, Annor FO, Giesen NV (2016) Investigation of temperature dynamics in small and shallow reservoirs, case study: Lake Binaba, Upper East Region of Ghana. *Water* 8(3):84
- Adamenko VN (1985) Climate and lakes (to assess the present, past and future). *Gidrometeoizdat, Leningrad* S. 264.
- Burchard H (2002) Energy-conserving discretisation of turbulent shear and buoyancy production. *Ocean Model* 4(3):347–361
- Downing JA, Prairie YT, Cole JJ, Duarte CM, Tranvik LJ, Striegl RG, McDowell WH, Kortelainen P, Caraco NF, Melack JM (2006) The global abundance and size distribution of lakes, ponds, and impoundments. *Limnol Oceanogr* 51(5):2388–2397
- Gorbunov MY (2011) Vertical distribution of bacteriochlorophylls in the humic lakes of the Volga-Kama Reserve (Republic of Tatarstan)/M.Yu. Hunchbacks. *Volga Ecol J* 3:280–293
- Kato H, Phillips OM (1969) On the penetration of a turbulent layer into stratified fluid. *J Fluid Mech* 37(4):643
- Kelley JGW, Hobgood JSK, Bedford W, Schwab DJ (1998) Generation of three-dimensional lake model forecasts for lake Erie. *Wea Forecast* 13:659–687
- Kozitskaya VN (1989) The influence of environmental factors (lighting, temperature) on the growth of algae. *Hydrobiol J* 6:55–70
- Kreiman KD et al (1992) Effect of turbulent mixing on phytoplankton. *Water Resour* 3:92–97
- Lykosov VN (1992) About the problem of closing the turbulent boundary layer models with the help of the equations for the turbulence kinetic energy and its dissipation rate (in Russian). *Izvestia, USSR Academy of Sciences, V.N. Lykosov. Atmos Oceanophys* 28:696–704
- Mellor CL, Yamada T (1974) A hierarchy of turbulence closure models for planetary boundary layers. *J Atmos Sci* 31:1791–1806
- Messenger ML, Lehner B, Grill G, Nedeva I, Schmitt O, Schmiel HM, Bastviken D, Tranvik LJ, Downing JA et al (2016) Estimating the volume and age of water stored in global lakes using a geo-statistical approach. *Nat Commun* 7:13603
- Monin AS (1965) *Statistical hydromechanics. Part 1.* Golitsyna GS, Monin AS, Yaglom AM (eds) Science, Moscow, p 640
- Mortikov EV (2016) Numerical simulation of the motion of an ice keel in stratified flow. *Izv Atmos Ocean Phys* 52:108–115
- Mortikov EV, Glazunov AV, Lykosov VN (2019) Numerical study of plane Couette flow: turbulence statistics and the structure of pressure-strain correlations. *Russ J Numer Anal Math Model* 34(2):1–14
- Price JF (1979) On the scaling of stress-driven entrainment experiments. *J Fluid Mech* 90(4):50
- Stepanenko VM (2007) Numerical modeling of the interaction of the atmosphere with land bodies of water. *Lomonosov Moscow State University*. 159p
- Stepanenko VM (2018a) Parametrization of seiches for a one-dimensional model of a reservoir/V.M. Stepanenko. *Works of MIPT* 10(1):97–111
- Stepanenko VM (2018b) Mathematical modeling of the thermal regime and the dynamics of greenhouse gases in water bodies of land. *Lomonosov Moscow State University* 361p
- Tranvik LJ (2009) Lakes and reservoirs as regulators of carbon cycling and climate/Tranvik LJ, Downing JA, Cotner JB, Loiselle SA, Striegl RG, Ballatore TJ, Dillon P, Knoll LB, Kutser T et al *Limnol Oceanogr* 54:2298–2314
- Tsydenov BO, Starchenko AV (2013) Numerical model of the river-lake interaction using the example of a spring thermal bar in Kamloops Lake. *Bulletin of Tomsk State University. Math Mech* 5:102–115
- Volodin EM (2013) Earth system model INMCM4: reproduction and forecast of climatic changes in the 19–21 centuries using the model of the Earth climate system of the INM RAS/E.M. Volodin, N.A. Diansky, A.V. Gusev. *Proc RAS. Physics Atmos Ocean* 49(4):379–390
- Zilitinkevich SS, Kreiman KD (1990) Theoretical and laboratory research of a thermal bar. *Oceanology* 30(5):750–755

The Forecasting and Searching Gemstone Deposits. Criteria for Forecasting



V. G. Gadiyatov, V. V. Bagdasarova, P. I. Kalugin, O. V. Sibirskikh,
and A. I. Demidenko

Abstract The article describes the geotectonical, structural, magmatic, lithologic and stratigraphic, mineralogical and geochemical and genetic criteria for predictive assessment and prospecting for gemstone deposits. As magmatic and lithologic and stratigraphic criteria, we considered igneous, volcanogenic-sedimentary and exogenous formations, reflecting the genetic or paragenetic connections of gemstones with host rocks.

Keywords Gemstones · Ore-bearing criterion · Platforms · Shields · Tectonic-magmatic activation · Geology province · Magmatic formation · Facies · Mineral paragenesis · Geochemistry · Genesis

1 Introduction

In recent years, there has been an intensive development of methods for estimating the surface current velocity from satellite optical images of the sea surface. The impetus for this was the launch of Sentinel-2 satellites, which are equipped with multi-spectral instruments. This specific instrumentation allows you to get satellite sun glitter imagery with high spatial resolution and a small time lag. The spatial resolution is 10 m, with a minimum time lag of 1 s (Kazhdan 1984; Gadiyatov 2013).

The criteria for potential ore-bearing include the prerequisites and signs of ore-bearing (Kazhdan 1984). Prerequisites are a set of geological factors that determine the distribution of minerals in the earth's crust. Signs of ore potential are minerals or a high content of a useful component in the studied samples. The predicting estimate of territory for gemstones is based on a set of favorable geological prerequisites and signs of ore-bearing (hereinafter, criteria). We considered geotectonic, structural, igneous, lithologic-stratigraphic, mineralogical-geochemical, and genetic criteria for the prediction of gemstone deposits.

V. G. Gadiyatov (✉) · V. V. Bagdasarova · P. I. Kalugin · O. V. Sibirskikh · A. I. Demidenko
Voronezh State Technical University, Voronezh, Russian Federation
e-mail: gadiatovvg@mail.ru

2 Geotectonic Criteria

The geodynamic deposits of gemstones are located on platforms, in geosynclines, foldmountains, middle massifs and other structures of the earth's crust. Each type of structure is characterized by certain deposits. Therefore, the tectonic position of the structures is one of the main regional factors for distinguishing geotectonic criteria.

Marble onyx, hematite bloodstone, amber are developed on platforms in terrigenous-carbonate and terrigenous rocks. Displays of basalt, ultramafic, kimberlite magmatism associated with deposits of diamond, chrysolite, demantoid, pyrope, chrysoprase, nephrite and other minerals are confined to the zones of tectono-magmatic activation of the platform areas.

On ancient shields, one can find deposits of ruby, sapphire, spinel, beryl, emerald, topaz, tourmaline, alexandrite and other precious and semi-precious stones, which are contained in the metamorphic, ultrametamorphic formations, protohorogenic metamorphosed and magmatic complexes. On the territory of the Russian Federation, the Karelia-Kola, Aldan-Stanovoy and Oleneksk-Anabar sub-provinces of gemstones are located on the shields; they are described in the works on mineragenic zoning of the Russian Federation and the spatial distribution of deposits of gemstones, along with other structures (Gadiyatov 2013; Gadiyatov 2013).

Rock crystal, moonstone, obsidians, topaz, beryl, common in Timan-Ural, South Siberian, Mongol-Okhotsk, Far Eastern and Kamchatka-Sakhalin gemstone provinces are associated with the salic formations of the orogenic zones of the fold regions.

A whole series of gem deposits of Russia, Brazil, South Africa, and Southeast Asia are located among the middle massifs, anticlinoria, deep fault zones, and ophiolite belts.

3 Structural Criteria

Structural criteria, like geotectonic ones, are based on regularities in the location of gemstone deposits, but, unlike them, lower order structures are used as criteria (flaws, various folds, thrusts, faults, etc.). The brachyanticline uplifts with an asymmetrical structure complicated by faults and fine folding on the wings are confined to crystal-rich mineralization, which is contained in the anticlinoria cores or at the boundaries of their articulation with the mobile zones. The Perekatnoerock crystal deposit in the South Yakut crystal province, localized in the core of the Perekatninskaya anticline can be an example (Gadiyatov 2005). Quartz mineralization is controlled by a large contact fracture, separating the ore-displaced quartzite stratum from the gneiss stratum. The most productive deposits of rock crystal are usually located between intensely and weakly fractured blocks of rock. Crystal-bearing veins are localized in areas of increased tectonic activity, manifested by milonitization and brecciation of host Precambrian formations.

Gemstones can be found in large ring structures that are igneous complexes, anticlinal folds; they are also controlled by zones of intersection or conjugation of tectonic disturbances. On the Aldan shield, ring structures are represented by arrays of alkaline-ultrabasic rocks of the central type Kondyor, Chad, Arbarasta, Inagli. The chromian-diopside deposit of the same name is associated with the latter (Gadiyatov 2000).

The most important source of jewelry stones are areas of tectonic-magmatic activation, which appeared at different times and in rocks of different ages. The Paleozoic magmatic activation of the Baltic Shield led to the formation of numerous ring alkaline massifs, including Khibiny and Lovozero with rare eudialyte, tinguaitite, luyauvrit, and zircon, nepheline, sodalite, etc.

During the Paleozoic tectonic-magmatic activation of the Sayanay protrusion of the basement of the Siberian platform, syenite-pegmatites with sapphire-like corundum were formed. In the Transbaikalia and in the Eastern Sayan, topaz, tourmaline, aquamarine, amethyst, phenakite are genetically associated with with mesozoic activation and miarolitic pegmatites and fault metasomatites.

In the areas of development of the Middle and Late Mesozoic tectonic-magmatic activation of the Aldan-Stanovoy subprovince rocks, mineragenic zones with corundum, spinel, garnet, beryl, amethyst, charoite, chromian-diopside and others are located. As a result of the Middle Proterozoic activation of this region, monomineralic quartz veins were formed in the deposits of the South Yakut crystal-bearing province.

In Precambrian greenstone belts of different cratons of the world, there are deposits of emerald, beryl, and corundum. These include the group of Sandavan emerald deposits in Zimbabwe (Zeus, Eros, Juno, Eris, Orpheus, etc.), which are located along the northern branch of the Precambrian greenstone belt Mweza. In Afghanistan, emerald deposits are located in the Panjarian junction, in Pakistan—in the zone of the Indian junction—on the border of the Indo-Pakistani subcontinent and Asia, in Russia (Emerald mines of the Urals)—at the junction of the European and Asian plates. Deposits of nephrite, jadeite and chrysolite are associated with ophiolite belts. On the territory of Siberia, more than twenty major belts are known, including those with rodingite mineralization.

4 Magmatic and Lithological-Stratigraphic Criteria

The basis of the igneous and lithologic and stratigraphic criteria for searching gemstones deposits is the logical connection of gems with the host rocks or with their complexes, combined into appropriate geological formations. Geological formations are divided into sedimentary, igneous, volcanogenic, volcanogenic-sedimentary, exogenous, metamorphic, metasomatic and ore. Among them, the importance belongs to widespread magmatic formations (Gadiyatov and Bagdasarova 2013). As prospecting criteria, we identified magmatic, volcanic-sedimentary and exogenous formations.

1. Magmatic formations

Just like other minerals, gemstones are connected to certain rock associations. A significant amount of them accounts for magmatic formations (Table 1). The basis of their selection is the similarity of petrographic, petrochemical and geochemical characteristics of rocks; development within a single large geodynamic structure; connection with a single stage of the tectono-magmatic evolution of the structure (Kuznetsov 1989; Bogatikov et al. 1987). By their material composition, magmatic formations are subdivided into ultramafic, mafic, mafic-salic, and salic, and they, in turn, are divided by facies into intrusive (plutonic), volcanic-intrusive, and volcanic (Mosaitis and Moskaleva 1979).

Many gems are associated with ultramafic formations developed in different regions. Among them, there are emerald, ruby, demantoid, chrysolite, jadeite, chrysoprase, etc.

The explanation of this “phenomenon” is quite simple: in gemstones of bright green and red colors, chromium from ultrabasites is the chromophore element. Ultramafic formations include formations with normal alkalinity of rocks (dunite-harzburgite, dunite-clinopyroxenite-gabbro, pyroxenite-peridotite) and alkaline-ultramafic (alkaline-ultramafic with carbonatites, kimberlite).

The group of ultramafic formations with normal alkalinity of rocks is confined to subduction zones, ophiolite complexes and rifts. They are controlled by deep regional faults. Ultrabasites are distinguished by increased magnesia (MgO —40–48%), undersaturation of silica, alkalis and aluminum. In jadeite, elevated levels of F, Cl, Be, Cr and V are noted; in nephrite-containing rocks—Ba, Sr, Zn, Cr and Ni.

The complex of rocks of the dunite-clinopyroxenite-gabbro formation is represented by dunites, gabbros, wehrlites, etc. The deposits of emerald, chrysolite ruby, and demantoid are associated with the formation. An example is the above-mentioned group of Sandavan emerald deposits, in which emeralds are found in the zone of contact between pegmatites and ultrabasic rocks, and they are concentrated in pockets, where pegmatites are heavily crushed. The most favorable factor for emerald mineralization is the presence of actinolite schist zones in pegmatite and pegmatite veinlets in adjacent actinolite schists (Zwaan 1997).

The rocks of the pyroxenite-peridotite formation (Iherzolites, websterites, olivinities) contain demantoid and chrysoprase. The main minerals are olivine, pyroxene, hornblende. The formation is characterized by low magnesium concentrations (up to 20–30%) in ultrabasites and high silica, iron, and calcium contents. Formations include the Bobrowka, Poldnevskoye (Middle Ural subprovince), the Chechatvayam and Tamvatneydemantoid deposits (Koryak-Kamchatka subprovince), and the chrysoprase deposit—Sarykulboldy (Kazakhstan).

The group of alkaline-ultramafic formations is distributed on shields, in the marginal parts of ancient platforms, in the zones of their activation and in the continental rift zones. A distinctive feature of the alkaline-ultramafic formation with carbonatites is a high content of alkalis, Al, Ti, Ca, P, Fe, along with a high content of Cr, Mg in olivinities and pyroxenites. Accessory minerals are represented by sphene,

Table 1 Magmatic formations containing gemstones

Magmatic formations	Tectonic position	Region	Rock complex	Mineralparagenesis	Chemical composition of rocks	Main gemstones	Deposit, province/country
1	2	3	4	5	6	7	8
Dunite-harzburgite	Subduction zones, ophiolitic belts, rift zones	Ural, Altai-Sayan region, Verkhoyansk-Kolyma fold system, Kamchatka	Dunites, harzburgites, lherzolites, rarely gabbro	Olivine (F ₈₅₋₁₀), orthopyroxene (F ₈₁₀₋₁₂), chrome-spinellid, serpentine	SiO ₂ 40–38%, Al ₂ O ₃ 1.5–6%, MgO 40–48%, Cr ₂ O ₃ 0.3–0.5%, Na ₂ O+K ₂ O 0.1–0.3%	Nephritis, jade, chrysolite, chrysoptase, listvenite, serpentine	Borus, Ulanhodinskoe (S. Sibirsk.), Puserskoe (Timan-Ural), Selyuyakh, Mumlikan (Northeast)
Dunite-clinopyroxenite-gabbro	Deep fracture zone	The Urals, Koryak Highlands, Alaska	Dunites, verfite, clinopyroxenite, gabbro, diorite	Diopside, olivine (F ₈₁₀₋₂₀), homblende, plagioclase, ilmenite, chromite	SiO ₂ 40–45%, Al ₂ O ₃ 0.40–4.5%, MgO 40–20%, Na ₂ O+K ₂ O 0.3–1.0%	Emerald, chrysolite, demantoid, ruby	Bor-Uryakh (East Siberian), Sandavana (Zimbabwe),
Pyroxenite-peridotite	Folded structures	Altai-Sayan region, Urals, Kamchatka, Kazakhstan	Lherzolites, websterites, olivine	Olivine, pyroxene, homblende	SiO ₂ 45–50%, MgO 20–30%, Al ₂ O ₃ 1–2%	Demantoid, chrysoptase	Bobrovskoe, Poldnevskoe (Timan-Ural), Chechatvayam, Tamvatney (Kamchatka-Sakhalinsk), Sarykulboday (Kazakhstan)
Alkalineultramaficwithcarbonatites	Platform activation zones, continental rift zones	Karelia-Kola region, Aldan shield, Ural	Olivinites, peridotites, pyroxenites, urtites, yolites, alkalinepicrites, skarns, carbonatites	Olivine diopside, aegirine, nepheline, phlogopite, alkaline amphibole, nepheline	SiO ₂ 30–52%, MgO 35–40%, Al ₂ O ₃ 2.5–18%, Na ₂ O 0.8–9.0%, K ₂ O 0.2–2.5%	Chrysolite, chrome diopside, zircon, fluorite	Inagli (East-Siberian), Kugda, Bor-Uryakh (EastSiberian)

(continued)

Table 1 (continued)

Magmatic formations	Tectonic position	Region	Rock complex	Mineralparagenesis	Chemical composition of rocks	Main gemstones	Deposit, province/country
1	2	3	4	5	6	7	8
Kimberlite	Platfomaactivationzones	Siberian and East European platforms	Olivine kimberlites, mica, melilitite, tuff breccia, picroitcophyrites	Olivine, enstatite, phlogopite, calcite, serpentinite, pyrope, chromite	SiO ₂ 34–35%, TiO ₂ 1.2–1.6, MgO 30–35%, Na ₂ O 30–35%, K ₂ O 1.0–1.4%	Diamond, chrysolite, pyrope	Udachnaya, Mir(EastSiberian)
Andesite-basalt	Orogenic zones of fold structures	Altai - Sayan region, Kamchatka, Caucasus, Ural	Basalts, andesi-basalts, andesites, dacite	Augit, hypersten, amphibole, plagioclase	SiO ₂ 50–58%, TiO ₂ 0.6–0.8%, Al ₂ O ₃ 15–16%, MgO 5–7%, Na ₂ O 2.5–4%, K ₂ O 0.9–1.5%	Agate, cornelian, Icelandspar	Burunda, Norskoe (Mongolo-Okhotsk)
Basalt-dolerite	Platfomaactivationzones (syncline)	Siberian, East European platform, India, Africa	Toleic basalts (traps) gabbro-dolerites, dolerite, tuffs	Augit, pigeonite, diopside, olivine, plagioclase, magnetite, titanomagnetite	SiO ₂ 43–50%, TiO ₂ 1.0–3.0%, Al ₂ O ₃ 12–15%, MgO 5–7.0%, Na ₂ O 2–2.5%, K ₂ O 0.5–1.2%	Agate, cornelian, amethyst, Iceland spar	Ievskoe, Chaichye (Timan-Ural), Vilyuiskagatonousregio (East Siberian)
Trachybasal	Deflection zones of the marginal parts of the platforms	Western slope of the Urals, Eastern Sayan Mountains, Altai-Sayan Region, Tian-Shan	Trachybasalts, tefrites, basalts	Titan-augit, plagioclase, augite, orthoclase, zircon, sanidine, ayalit, alkalinelaamphibole, zircon	SiO ₂ 46–48%, TiO ₂ 2–3%, Al ₂ O ₃ 14–17.0%, MgO 6.5–8.5%, Na ₂ O 2.8–4.0%, K ₂ O 0.7–3.0%	Feruginous olivine (gortonolith, fayalite), zircon, sapphirite	S. Sibirsk (Timan-Ural)
Alkaline basalt and alkaline gabbroids	Epirogenicriftogenesis, zones of deep faults	Karelo-Kola region, Kuznetsk Alatau, Aldan-Stanovoy shield.	Teralit, tefrit, orthoclase gabbro, eseksites	Diopside, titan-augite, anortite, bitovnite, orthoclase, microcline, nepheline, aegirine	SiO ₂ 51–53%, TiO ₂ 3–5%, Al ₂ O ₃ 12–21%, MgO 3–11.0%, Na ₂ O 1.0–7.0%, K ₂ O 0.5–5.0%	Chrysolite, chromiumdiopside, sapphirite, zircon	Tok, (EastSiberian)

(continued)

Table 1 (continued)

Magmatic formations	Tectonic position	Region	Rock complex	Mineralparagenesis	Chemical composition of rocks	Main gemstones	Deposit, province/country
1	2	3	4	5	6	7	8
Gabbro-anorthosite	Precambrianplatforms	Karelia, Ukrainian shield, Primorye, Aldan-Stanovoy shield	Anorthosites, labradorites, gabbros, pyroxenites, gabbro-anorthosites	Anortite, olivine, bitovnite, labrador, magnetite, diopside, hypersthene	SiO ₂ 48–53%, TiO ₂ 0.3–0.7%, Al ₂ O ₃ 24–26%, MgO 1.0–9.0%, Na ₂ O 3–4%, K ₂ O 0.4–1.0%	Iridescent labrador.	Saibalakh, Geran (East-Siberian)
Dacite-liparite	Foldareas	Okhotsk-Chukotka belt, East Sikhote-Alin volcanic belt, Caucasus	Andesi-dacite, dacites, liparites, granodiorite porphyry, quartz porphyry.	Quartz, sanidine, anorthoclase, oligoclase	SiO ₂ 70–78%, Al ₂ O ₃ 13–14.0%, Na ₂ O 3.0–3.5%, K ₂ O 3.0–4.0%	Moonstone, agate, camelian, rose quartz	Mustahskoye (North-Eastern)
Liparite	Fold areas, orogenic stage of tectonic-magmatic activation	East Sikhote-Alin, Chukot-Okhotsk belt, Verkhoyansk-Kolyma fold system, Caucasus	Liparites, ignimbrites, perlitites, porphyry granite, quartzporphyry	Quartz, sanidine, anorthoclase, albite, oligoclase, obsidian	SiO ₂ 70–74%, Al ₂ O ₃ 13–14%, CaO 0.5–1.5%, Na ₂ O 3.0–3.5%, K ₂ O 4.0–4.5%	Obsidian, perlite, moonstone, agate, camelian, amethyst	Payalpan, Nosichan (Kamch.-Sakhalin), Kedon (Northeast)
Granite	Deep faults in fold areas	(Kalbinsky massif), Transbaikalia, Yakutia, Caucasus, Ural, Kazakhstan	Normal two-feldspar granites, granodiorites, aplites, pegmatites, greisens, skarns	Quartz, oligoclase, microcline, orthoclase, biotite, muscovite	SiO ₂ 71–72%, Al ₂ O ₃ 14–14.9%, CaO 1.4–2.0%, Na ₂ O 3.6–3.8%, K ₂ O 3.7–4.7%	Topaz, beryl, tourmaline, rock crystal, morion, amethyst; epidote, garnet, vesuvian (in skarns)	Murzinskoe, Vaitha, Khasavarka, Shaitanskoye (Timan-Ural), Adun-Chelonskoe (Mongolia-Okhotsk)
Granites-rapakivi	Precambrianplatforms, Protonestage	Karelia (Vyborg, Salminkymassifs), Transbaikalia, Ukrainian shield	Porphyritic granites-rapakivi, fine-grained granites, granite-porphyry, aplites, syenites, greisens	Microcline, orthoclase, quartz, oligoclase, biotite, homblende	SiO ₂ 70.3–71%, Al ₂ O ₃ 14.1–15%, Na ₂ O 3.8–3.3%, K ₂ O 3.9–4.5%, CaO 1.3–1.8%	Fluorite, rock crystal, morion, amethyst, topaz, beryl	Vozrozhdeniye, Mustavaara (EastEuropean)

(continued)

Table 1 (continued)

Magmatic formations	Tectonic position	Region	Rock complex	Mineralparagenesis	Chemical composition of rocks	Main gemstones	Deposit, province/country
1	2	3	4	5	6	7	8
Leucogranite	Orogenic regime of fold areas. In the composition of volcano-plutonic associations	Altai-Sayan fold area, East-Asian volcanogenic belt, Transbaikalia, Ural	Porphyritic granites, aplites, pegmatites, greisens.	Albit, oligoclase, potassium feldspars, quartz, biotite, zircon, monazite, xenotime, fluorite, cassiterite, lepidolite, clevelandite	SiO ₂ 75-71%, Al ₂ O ₃ 12.6-14%, Na ₂ O 2.4-3.7%, K ₂ O 4.1-4.6%, CaO 0.5-1.4%	Tourmaline, topaz. Fluorite, rock crystal	Malkhansko, Mokhovaya vein and others (Mongolia-Okhotsk)
Alaskit	Orogenic regime of fold areas. Volcano-plutonic associations	Gorny Altai, Okhotsk-Chukotka belt, Central Kazakhstan	Alaskites, leucocratic porphyry granites, pegmatites, alkaline granites, greisens.	Quartz, orthoclase, albite, xenotime, pyrochloride, pyrite, cassiterite, wolframite, tourmaline	SiO ₂ 73-75%, Al ₂ O ₃ 13-15%, Na ₂ O 3.5-4.0, K ₂ O 4.7-6.0%, CaO 0.4-1.2%	Rock crystal, topaz, beryl, tourmaline	S. Sibirsk, Kamchatka-Sakhalinsk
Alkalinegranite	Zones of activation of hard archaic blocks	Karelia-Kola region, Aldan, Anabar shields, Eastern Transbaikalia, Sayan	Alkaline, granites, aplites, alkalinepegmatites	Albit, microcline, orthoclase, alkaline amphibole, aegirine	SiO ₂ 73-75%, Al ₂ O ₃ 11.0-13.5%, Na ₂ O 4.5-4.7%, K ₂ O 4.3-4.5%, TiO ₂ 0.38-0.16%	Zircon, fluorite, spinel	EastEuropean, East Siberian, Mongolia-Okhotsk
Phonolites, alkaline trachytes, nepheline syenites.	Zones of activation of Precambrian platforms and shields, rift structures	Karelia-Kola region, Aldan-Anabarsky shields, Ilmen mountains	Urtites, yollites, melteigites, luyavrites, khibinites, foyaity	Nepheline, microcline, orthoclase, aegirine, ribekit, phlogopite, leucite, cancrinite, alkalineamphiboles	SiO ₂ 50-55%, Al ₂ O ₃ 21-15%, TiO ₂ 0.8-1.5%, Na ₂ O 8-10%, K ₂ O 3-5%	Zircon, sodalite, cancrinite, evdialyte	EastEuropean, East Siberian

(continued)

Table 1 (continued)

Magmatic formations	Tectonic position	Region	Rock complex	Mineralparagenesis	Chemical composition of rocks	Main gemstones	Deposit, province/country
1	2	3	4	5	6	7	8
Leucitofir, nepheline, pseudoleucite, andalkalinesyenite	Post-orogenic rift structures, zones of tectonic-magmatic activation of rigid blocks	Aldan-Stanovoy shield (Murunmassif), Balkal-Vitim highlands, Caucasus.	Epileucite porphyry, tachyptonolite, leucitofire, alkaline and pseudo leucite syenites.	Nepheline, microcline, albite, leucite, pseudoleucite, phlogopite, alkaline amphibole, diopside	SiO ₂ 50-58%, Al ₂ O ₃ 20-22%, Na ₂ O 1.0-4.5%, K ₂ O 1.0-1.4%, NiO ₂ 0.3-0.7%	Charoite, zircon, amethyst	Lilac stone, Obman (East Siberian)

zircon, apatite, eudialyte. An example is the Inagli deposit of chromian-diopside, the Kugda and Bor-Uryakh deposits of chrysolite.

The kimberlite formation is confined to the areas of activation of the platform areas and to the zones of long-lived faults common in the Yakut diamondiferous province. Diamondiferous rocks of the formation are kimberlites, tuff breccias, picritic porphyrites; in the Argyll deposit—lamproites. The rock-forming minerals are olivine, serpentine, phlogopite, enstatite, pyrope, chromite, magnetite, ilmenite, apatite, calcite, etc. They are characterized by high magnesia, undersaturation of silica, elevated potassium, chromium, titanium, phosphorus, CO_2 , H_2O . Lamproites consist of forsterite, diopside, phlogopite, leucite, orthoclase. Accessory minerals are chromic spinel, ilmenite, zircon, perovskite.

In addition to diamonds, kimberlites contain pyrope and chrysolite. The industrial contents of the latter are in the diamondiferous mines Mir, Udachnaya-Zapadnaya (pyrope), Udachnaya-Vostochnaya (chrysolite).

The mafic formations include andesite-basalt, basalt-dolerite, trachybasalt formations, as well as alkaline basaltoid and alkaline gabbroid formations. Agates, carnelian, Iceland spar are associated with the andesite-basaltic formation. Distributed in the orogenic zones of folded structures. As an example, Burunda and Norskoie agate and carnelian deposits, included in the Selemdzhinskiy group of fields.

The basalt-dolerite formation occupies significant areas on the Siberian platform and is also common on the East European platform. It is confined to negative structures of the platforms activation zones. Like the previous formation, it contains agate, carnelian, Iceland spar and amethyst. The complex of rocks is represented by tholeiitic basalts (trapps), dolerites, gabbros, and tuffs. They are characterized by sodium and potassium types of alkalinity; the silica content does not exceed 55%. The main deposits are Ivskoye and Chaichye (Timangemstoneregion), Vilyuiskagatonous region (Oleneksk-Anabarsubprovince).

The deflection zones of the marginal parts of the platforms are occupied by formations of the trachybasalt formation, which are known on the western slope of the Urals, in the Eastern Sayan Mountains, etc. The rocks are trachybasalts, tefrites, and basalts; lie in the form of flows in the fault zones. They are moderately undersaturated with silica (SiO_2 46–48%), enriched with Ti and alkalis ($\text{Na} > \text{K}$). The main gemstones of the formation are ferruginous olivine, zircon, sapphire, but they do not form large clusters. The formation of alkaline basaltoids and alkaline gabbroids is characteristic of regions with epigenetic rifting and for zones of deep faults (Karelia-Kola region, Kuznetsk Alatau, Aldan-Stanovoy shield). The main gemstones are chrysolite, chrome diopside, sapphire, zircon.

The mafic-salic formations include a group of andesitic and granodiorite formations that include basalts, andesites, gabbrodiorites, etc. The formations are located on Precambrian platforms, making up folded areas and shields and are poorly productive for gemstones.

The gabbro-anorthosite formation is located on the Aldan-Stanovoy shield, in Karelia, Primorye, etc. It contains an iridescent labrador. It is represented by anorthosites, labradorites, gabbros, pyroxenites, gabbro-anorthosites. In the Charo-Olekminskaya and Uchur-Maimakanskaya subprovinces of the East-Siberian

province, there are, respectively, the Saibolokh deposit of iridescent anorthosite and the Gerandeposit of labradorite.

Salic formations (dacite-liparite, liparite, granite, rapakivi granites, leucogranitic, alaskitic, alkaline-granite) include acid effusive and intrusive rocks that are supersaturated with silica.

The dacite-liparite formation is developed in fold areas. It is associated with the manifestations of moonstone, agate, carnelian, rose quartz. It is represented by a complex of rocks containing andesi-dacite, dacite, liparite, granodiorite-porphry, quartz porphyry. All rocks are supersaturated with silica (SiO_2 —70–78%). The formation is spread in the Okhotsk-Chukotka and East-Sikhote-Alin volcanic zones, in the Caucasus, etc. The Mustahskoyediposit of carnelian, located in the Kolyma-Indigirskysubprovince, can be an example.

No less productive is the liparite formation, which, in addition to the fold regions, also develops into the orogenic stage of tectonic-magmatic activation. Among the gemstones, the leading place is occupied by obsidian, perlite, moonstone, carnelian, amethyst. The complex of rocks is represented by liparites, ignimbrites, perlitites, granite-porphyrines, quartz porphyries, also supersaturated with silica.

The formation is widespread in the Eastern Sikhote-Alin, the Chukotka-Okhotsk belt, the Verkhoysansk-Kolyma fold system, in the Caucasus. The Kedon amethyst deposit is located in the mineralized rhyolites of the Kolyma-Indigirka subprovince, and the Payalpan and Nosichanobsidians deposits are located in the Koryak-Kamchatka subprovince.

The granite formation is developed in zones of deep faults and in fold areas. It includes normal two-feldspar granites, granodiorites, aplites, pegmatites, greisens, skarns. Postmagmatic gemstone deposits, including beryl, topaz, rock crystal, amethyst, epidote, garnet, vesuvian, are genetically associated with the formation. In the rocks of this formation, there are the Murzinskoye beryl deposit, the Vatikh amethyst deposit (Middle Ural subprovince), the Adun-Chelonskoe topaz deposit, Sherlovogorsky beryl deposit (Mongolia-Okhotsk subprovince), etc.

The rapakivi granite formation is characteristic of the protogornic stage of the Precambrian platforms. Miarolitic pegmatites with rock crystal, amethyst, topaz, beryl are associated with rapakivi granites. The complex of the rocks is represented by porphyreous rapakivi granites, fine-grained granites, granite-porphyrines, aplites, syenites, and greisens. The formation is common in Karelia and Transbaikalia. An example is the Karelia-Kola subprovince, which occupies the territory of the Baltic shield. In the area of the towns of Vyborg and Pitkyaranta, there are the Vyborg massif of rapakivi granites (the Vozrozhdenie, Ilinskoe, Ala-Noskou deposits) and the Salminsky massif (the Mustovara deposit).

Tourmaline, topaz, fluorite, rock crystal are localized in the rocks of the leucogranite formation. An example is the Malkhanskoe deposit of tourmaline, Veins Mokhovaya, Savvateevskaya and Gremyachinskaya Mine, represented by miarolitic pegmatites, but slightly replaced by lepidolite and cleavelandite.

The Alaskan formation combines the association of ultra-acidic and acidic rocks associated with the vulcanites of the liparite composition. This association completes the granitoid magmatism of the orogenic stage, with the characteristic association

of bodies of alaskites and volcanics to ring structures. Topaz, beryl, and tourmaline are associated with the rocks of this formation. Petrographic composition of rocks is represented by alaskites, leucocratic porphyric granites, subalkaline granites. The development of greisens and pegmatites is characteristic. Alaskite granites are distributed within the Okhotsk-Chukotka volcanic belt, the Gorno-Altai region, the junction zone of the caledonides of the Dzungaro-Balkhash and Chingiz-Tarbagatay fold systems.

The alkaline-granite formation is known within the fold areas and ancient platforms (Transbaikalia, Kola Peninsula). The main gemstones are zircon, spinel, fluorite. Alkaline granites are composed of potassium feldspar, albite; dark minerals are represented by aegirine, ribekite, lepidomelane. Zircon-sphen-magnetite-apatite-fluorite accessory mineralization is characteristic for the rocks of the formation; spinel, garnet, epidote, rutile, astrophyllite, uraninite, uranotorite may be present.

Zircon, sodalite, cancrinite, eudialyte, astrophilite are associated with the formation of phonoliths, alkaline trachytes, nepheline (agpaitic) syenites. The complex of rocks is represented by urtites, yolites, melteigites, luyavrites, khibinites, and foyaites. An example of this formation is the Khibinsky and Lovozero massifs on the Kola Peninsula, Tomtor and Dogdo massifs in the marginal part of the Aldan shield, alkaline volcanic-intrusive complexes of the East African rift.

The main gemstones of the leucitofir, nepheline, pseudoleucite and alkaline syenite formation are charoite, amethyst, zircon. The main minerals are nepheline, microcline, albite, pseudoleucite, aegirine-augite, arfvedsonite, gastsingsit, lepidomelan; accessory and minor minerals—apatite, sphene, zircon, baddeleyite, fluorite, analcime, cancrinite, zeolites, scapolite, tourmaline, fluorite. In the western and central parts of the Aldan-Stanovoy shield, there are deposits of the Lilac Stone charoite and the Obman amethyst, which are associated with alkaline Mesozoic formation complexes (Gadiyatov and Sibirskikh 2015).

2. Volcanogenic-sedimentary and exogenous formations

Many gemstones are genetically associated with volcanogenic-sedimentary and exogenous rocks, combined in a formation given in Table 2. Among volcanogenic-sedimentary rocks, the main importance belongs to effusive-siliceous and shale-siliceous formations, which are widespread in the middle massifs and fold structures.

An effusive-siliceous formation is characteristic of the middle massifs of the fold zones. It combines the association of basic and acidic effusive, siliceous shales, tuffs and jaspers. The main gemstones are rhodonite and jasper. In the Urals, rhodonite deposits formed in the Devonian in tectonically active areas. They are confined to the wings of negative structures, on which manganese precipitated in the sea basin. The bodies of jasper are associated with stratification of interbedded acidic and basic effusive, volcanic tuffs, and sedimentary deep-water siliceous rocks. In the formation of deposits, the leading role belongs to regional metamorphism.

Shale-siliceous formation is common in the fold zones. Rocks are represented by siliceous shales, but sometimes tuffs are included. Primary importance belongs to rhodochrosite and rhodonitis.

Table 2 Volcanogenic-sedimentary and exogenous formations with gemstones. According to V.P. Drozdov (Drozdov et al. 1986)

Family of formations	Group of formations	Formations	Rock complex	Typomorphic minerals	Tectonic position	Gem stones
Volcanogenic-sedimentary	Siliceous	Effusivesiliceous	Basic and acid effusions, siliceous slates, jasper, tuffs	Rhodonite, bustamite	Medianmassifs, foldstructures	Rhodonite, jasper
		Shale-siliceous	Siliceousslates, rarelytuffs	Rhodochrosite, rhodonite	Foldzones	Rhodochrosite, rhodonite
Exogenous	Sedimentary	Chemogenic-carbonate	Shalesandcarbonaterocks	Onyx, amber, jet	Folds, shields	Marbleonyx, amber, jet
	Weatheringcrust	Linearfissurecrusts	Crust of weathering of igneous and volcanic-sedimentary rocks	Turquoise, malachite, chrysoprase, cacholong	Platformsandfold areas	Turquoise, malachite, chrysoprase, opal, cacholong
Placers	Placers	Continentalplacer	Sandy-claysediments	Gemstones	Platforms and fold areas	Precious and semiprecious stones
		Coastalplacer	Sandy-clay and detrital sediments	Amber, agate, chalcedony	Platformcover	Amber, agate, chalcedony

Exogenous formations that are genetically associated with weathering crusts and placers are common in folds of structures and on shields. They include chemogenic-carbonate, linear-fractured weathering crusts, continental and coastal alluvial deposits. A chemogenic-carbonate formation contains deposits of marble onyx, amber, and jet. The enclosing rocks are carbonate formations and various shales. The rocks of the linear-fractured crust formation contain deposits of turquoise, malachite, chrysoprase, opal, and cacholong. It is confined to weathering crusts of igneous and volcanic-sedimentary rocks. Placer formations are developed on platforms, folded areas, on a platform cover. It contains rhinestone and various precious and semiprecious stones.

5 Mineralogical and Geochemical Criteria

As mineralogical and geochemical criteria, we distinguish a set of criteria with stable links between gemstones, minerals and their chemical properties. The presence of certain minerals or elevated concentrations of chemical elements in ore-bearing rocks is the object of study.

When searching for gemstones, one of the leading places is assigned to the typomorphic features of the minerals, thanks to which ore bodies and mineragenic zones that are promising for gemstones can be distinguished. Thus, the criterion of ruby mineralization in marbles is pyrite and pseudomorphs on it, forming octahedra and pentadodecahedra.

Reliable criteria for prospecting and searching are accessory minerals and their associations. Thus, ruby accessories are red spinel, phlogopite, chrome margarite, green tourmaline, rutile, sphene, fluorite, pyrite, margarite, diasporas. Crystal-bearing veins in quartzites are accompanied by pyrite, apatite, sphene, monazite, tourmaline, calcite, fluorite, barite, etc. The presence of fluorite is one of the prospecting criteria for finding beryl in miarolitic pegmatites or greisens (Yurgenson 2001). Fluorite from druse contains high amounts of Y, Sn, Bi, Yb, La.

In pegmatites with gemstones, the role of F, Cl, Hg increases, the total content of Fe decreases and the ratio Si/Al, K/Rb, Rb/Cs decreases; Rb, Cs, Tl, Li contents increase in micas and potassium field spars (Drozdov et al. 1986). According to the content of rare alkaline elements in microcline, muscovite and beryl, micaceous and rare metal pegmatite can be distinguished. In these minerals of rare-metal pegmatites, concentrations of Li and Rb are significantly increased compared with micaceous pegmatites. In addition, the ratio of K/Rb and K/Cs in muscovite and microcline is several times higher than in mica-bearing pegmatites. The rock-forming minerals of rare-metal pegmatites are characterized by elevated levels of Li, Rb, Cs, Be, Tl, F and low ones of Ba, Pb. High concentrations of Rb, Cs, K, as well as a low Rb/Cs ratio, are noted in miarolitic pegmatites (Solodov et al. 1980). Pegmatite vein minerals with beryllium mineralization contain high concentrations of Be.

Serpentinized dunites enriched in magnetite and halos of Cr, F, Ni, Hg, Ba, Sr serve as criteria for identifying zones of metasomatites with chrome diopside in the Inaglideposit (Gadiyatov 2002).

6 Genetic Criteria

Genetic criteria are an integral part of the scientifically based prospecting of gemstone raw materials; they are based on the spatial and genetic relationship of gemstones with rocks of a certain genesis. According to the conditions of formation, gemstone deposits are divided into endogenous, exogenous and metamorphogenic. Most of the deposits are of endogenous origin and are igneous, pegmatite, hydrothermal-metasomatic, hydrothermal, etc. The composition of igneous rocks is determined by the concentrations of chemical elements and, accordingly, their specialization in gemstones.

The main industrial minerals of magmatic deposits are diamond, pyrope, chryso-lite, sapphire, zircon, etc. Pegmatite deposits contain quartz, aquamarine, topaz, beryl, emerald, tourmaline, amazonite, kunzite, etc. Emerald deposits are genetically associated with ultrabasic massifs but localized in exocontact of granitoid complexes with leucocratic, alaskite, subalkaline, and fluorine-lithium granites of rare metal specialization.

The exogenous deposits of turquoise, chrysoprase, opal, cacholong, malachite, marble onyx, bloodstone hematite, amber, gagata are localized in weathering crusts, placers and in sedimentary rocks.

Metamorphogenic deposits of rhodonite, jasper, petrified wood, almandine, rhodolite, spessartine, rock crystal, corundum, sapphire, and spinel are found in metamorphic and metamorphic formations. The metamorphism of the amphibolite facies is a favorable sign of corundum mineralization in the rocks of the dunite-harzburgite formation (Tatarinov 2002). In this metamorphic facies, gabbroids turn into amphibolites, orthopyroxenites undergo gabbroization, and plagioclase develops in them; corundum-phlogopite-oligoclase, corundum-phlogopite-vermiculite metasomatites, ruby-spinel-containing magnesian skarns are formed. The metamorphism of the amphibolite facies is manifested in Precambrian ultramafites and in a number of other rocks of the Aldan-Stanovoy subprovince.

Phlogopite deposits of the same subprovince containing spinel are confined to areas of granulitic facies of metamorphism of low pressures. The formation of diopside-spinel rocks occurs at the initial stage of the formation of magnesian skarns. Spinel develops on alkaline and aluminous rocks, and diopside—on rocks enriched with quartz. In areas with lower metamorphism of dolomite marbles, lapis lazuli is formed, crystallization of which occurs when the alkalinity of the mineral-forming medium that occurs during skarn formation is high.

The formation of rock crystal, garnet, jadeite, jade and other gemstones occurs at the regressive stage of regional metamorphism. Regional metamorphism of dolomite

marbles also contributes to the formation of ruby. In this case, the rocks should be metamorphosed not lower than the epidote-amphibolite facies.

During the formation of deposits of gemstone raw materials, a significant contribution was made by regional-metamorphic, metasomatic, hydrothermal and contact-metasomatic processes, which should be taken into account when prospecting.

7 Conclusions

1. Geotectonic, structural, igneous, lithologic-stratigraphic, mineralogical-geochemical, and genetic criteria are used in prospecting and searching for gemstone deposits. Geotectonic and structural criteria can be considered as a regional prospecting carried out at the initial stage.
2. The main value belongs to the magmatic, volcanogenic-sedimentary and exogenous formations, which are given as prospecting criteria. They are based on the regular connections of gemstones with host rocks or their complexes. The magmatic formations are characterized by confinement to certain types of tectonic structures and have petrogeochemical features inherent only in them.
3. The main proper magmatic minerals are diamond, pyrope, chrysolite, sapphire, zircon, agate, carnelian, and others. Pegmatites contain quartz, aquamarine, topaz, beryl, emerald, tourmaline, and others. Emerald deposits are genetically associated with ultrabasic rocks but localize in exocontacts with complexes of leucocratic sublattice, fluorine-lithium granites with rare metal specialization.
4. Exogenous deposits of turquoise, chrysoprase, opal, kahalong, malachite, marble onyx, bloodstone hematite, amber, jet are found in the weathering crusts of sedimentary rocks and in placers.
5. Deposits of rhodonite, jasper, silicified tree, almandine, rhodolite, spessartine, rock crystal, corundum, sapphire, spinel are confined to metamorphic and metamorphosed rocks. The metamorphism of the amphibolite facies is a favorable sign of corundum mineralization in the rocks of the dunite-harzburgite formation.
6. If there are accessory minerals or elevated concentrations of chemical elements and their associations in various ore-bearing rocks, mineralogical and geochemical criteria are used.
7. The belonging of gemstone deposit to a certain genetic group is the basis for prospecting using the corresponding genetic criteria. However, at the same time, it is necessary to take into account the secondary processes that have affected the host rocks.

References

- Bogatikov OA, Kovalenko VI, Tsvetkov AA, Yarmolyuk VV, Borsuk AM, Bubnov SN (1987) Magmatic associations, formations, series. Magmatic rocks. The evolution of magmatism in the history of the Earth, Chap 1. Nauka, Moscow, pp 7–18
- Drozdov VP, Komov IL, Vorob'ev EI (1986) Searching and estimation of deposits of Piezo-optic and gemstone raw materials, 224 p. Nedra, Moscow
- Gadiyatov VG (2000) Gemstones of Yakutia and their deposits, 328 p. Cultural Information Bank, Ekaterinburg
- Gadiyatov VG (2002) Minerageny of gemstone materials of the Eastern part of the Siberian platform and Verkhoyansk-Chukotka fold area: dissertation for the degree of Doctor of Geological and Mineralogical Sciences, Chita, 360 p
- Gadiyatov VG (2005) Gemstone formations of Northeast Asia, 272 p. Voronezh State University, Voronezh
- Gadiyatov VG (2013) Mineragenic zoning of the territory of the Russian Federation for gemstones. In: New ideas in earth sciences: report of 11th international conference, Moscow, vol 1, pp 234–235
- Gadiyatov VG (2013) Spatial distribution of gemstones deposits in the territory of the Russian Federation. In: Gemology: materials of VI scientific conference, pp 28–36
- Gadiyatov VG, Bagdasarova VV (2013) Typification and distribution of magmatic formations with gemstones. *Sci Educ* 2:26–30
- Gadiyatov VG, Sibirskikh OV (2015) East-Siberian semiprecious stone province: zoning and minerageny. *Sci Educ* (2):16–22
- Kazhdan AB (1984) Prospecting of mineral deposits. The scientific foundations of prospecting, 285 p. Nedra, Moscow
- Kuznetsov YuA (1989) Selected works. Nauka, Novosibirsk
- Mosaitis VL, Moskaleva VN et al (eds.) (1979) Magmatic formations of the USSR. Leningrad, Nedra, vol 318, vol II, 279 p
- Solodov NA, Balashov PS, Kremenetsky AA (1980) Geochemistry of lithium, rubidium, cesium, 226 p. Nedra, Moscow
- Tatarinov AV (2002) Geological prerequisites for prospecting gemstones deposits in the Dunite-Harzburgite formation. *Explor Protect Min Res* 10:8–11
- Yurgenson GA (2001) Precious and semiprecious stones of Transbaikalia, 390 p, Novosibirsk, Nauka
- Zwaan JC (1997) Update on emeralds from the sandawana mines. Zimbabwe. *Gems Gemol. Sum* 33(N2):80

Weddell-Scotia Continental Bridge Destruction



A. A. Schreider and A. E. Sazhneva

Abstract The paleogeodynamical poles and rotation angles, describing the process of the Weddell–Scotia America Continental Bridge destruction for the first time are calculated. On this basis the first paleogeodynamical reconstruction of fragmentation at the areas of south Scotia-Weddell area is restored.

Keywords Weddell · Scotia · Continental bridge · Paleogeodynamics

The presence of a continental bridge between the South American and Antarctic continents in the geological past is not in doubt (Hain 2001). At the same time, the initial configuration and stages of its destruction in time and space are interpreted contradictory in the world literary sources. In the published studies there is no single approach to c (figuration and mutual position of individual elements of the bridge determination at the initial stage of its development (Brown et al. 2006; Wit 1977; Verand et al. 2012). The dating of the continental bridge split beginning also varies in different studies. So in (Livermote et al. 2005) it dates back to the age of 34 million years and in (Verand et al. 2012; Eagles et al. 2006) it dates back to the age of 27 million years. In (Barker et al. 2013) the split process is limited to a time frame of 25.2–45.2 million years. There is no quantitative basis for reconstructing the stages of bottom evolution, including Euler poles and angles of turns in the published studies. This reflects (for example, (Eagles and Vaughan 2009)) the scarcity of available geological and geophysical materials, which does not allow to confidently restore the evolution of the bridge elements.

In recent years, a certain amount of geological and geophysical data has been obtained in the South-East of the Scotia Sea, primarily in the expeditions of the Spanish research vessel “Hesperidas”. The complex analysis of these data allows to find out questions of evolution of elements of the bridge among which the important role is given to underwater elevations of the continental nature shoals Herd man,

A. A. Schreider · A. E. Sazhneva (✉)
Shirshov Institute of Oceanology, Russian Academy of Sciences, Moscow, Russia
e-mail: alexe@ocean.ru

A. A. Schreider
e-mail: aschr@ocean.ru

Disco very, Bruce, Peary, Terror with the separating basins Scan, Dow, Protector, Presented work is devoted to studying of a bottom of these basins.

The computer technique for the best combination of isobaths limiting slopes of continents on edges of Atlantic Ocean was offered in (Buillard et al. 1965), The combination was carried out by trial and error, by minimizing the angular disagreement measured along Eulerian latitudes. The technique illustrated the principle that the best alignment can be made for Mb contours that are established or assumed to have once formed a single contour, № implementing the principle of better alignment, it is possible to achieve reunification and restoration of the primary continuity of all contours, including isochrones, isobaths, isohypses, etc., According to the electronic Soal on bottom bathymetry (www.topex.ucsd.edu/html/mar_topo.html) the slopes profiles of the basins Scan, Dow, Protector in the direction perpendicular to the strike are built with inter-profile intervals of 10 miles. The analysis of the slopes profiles obtained testifies that practically all of it consist of three parts. The upper and lower parts of the slopes are characterized by varying steepness along the profile. The upper part of the slope lies shallower than 2 km for the Scan basin, shallower than 2.3 km for the Dow basin and 2.1 km for the Protector basin. The lower part of the slope lies below 3.1 km for (the Scan basin, deeper 3.3 km for the Dow basin and 3.1 km for the Protector basin. The Central part of the slopes, enclosed in the depth range of 12.3–3.0 km (Scan and Protector basins), 2.5–3.2 km (Dow basin), is the steepest and has a relatively constant slope along each individual profile. The distance between the slope isobaths 2.3 and 3.0 km projections to the day surface (Scan basin), 2.5–3.2 (Dow basin), 2.3–3.0 (Protector basin) is considered as a working base for the individual slope angle (steepness) calculation along each of the profiles.

Sedimentation in various areas of the depressions (basins) led to filling them with sedimentary rocks, accompanied by flattening in time (routing of slope angle) due to the slopes smoothing with sediments. The smoothing is uneven in time and space. This unevenness is associated with both the distribution and redistribution of areas of demolition, and with the sliding of the accumulated sediments down the slope due to stability breakdown. Instability of sediments occurs due to the accumulation of critical mass, leading to the excess of the sliding force over the friction force (along the interface inside the sediments or along the basement surface), which keeps the sediments from sliding at a given slope steepness. The movement of specific portions of the sediments occurs gradually or is of a pulsed nature. An important contribution to the mobility of the sedimentary mass on the continental slope is also made by the steepness of the moving mass basement surface. At low angles of inclination and other conditions being equal, the movement of sedimentary mass on the slope will take place with very low velocities. Estimates show that in order to overcome the adhesion force between sediment layers (in the Scan, Dow, Protector, Powell basins there are silts, clays, sandstones) and avalanche-like disruption of them down the slope and quicken to a significant (up to many tens of km h) sliding velocities, other conditions being equal, the sliding surface slope have to exceed 3° (Zhmur et al. 2002; Schreider 2005). Among the triggering causes of sediments sliding down the slope, an important place is occupied by the impact of exogenous (for example,

regular currents) and endogenous (for example, earthquakes) factors on the sediment mass.

Based on the above, in this paper, Bullard's method is first used for the case of imbibing the isobaths of the Scan, Dow, Protector, Powell basins slopes. Numerous tests of the correctivity of different sections of different and homonymous isobaths have shown that the most suitable for the paleogeodynamic analysis are sections of isobaths in the intervals 3.3–2.9, 2.5–3.0, 2.5–2.9 km, respectively. The slopes in this range of depth are the steepest (the average slope angle of the slope surface exceeds 5th) and, according to the above information about the causes of the sedimentary layer slip, having the least power of sediments layer (or even completely stripped).

Calculations of Euler poles and rotation angles were carried out according in the original programs developed in the Laboratory of Geophysics and Tectonics of the World Ocean Floor of Shirshov Institute of Oceanology, Russian Academy of Sciences, incorporated into the software environment Global Mapper (Schreider 2011; Zonenshain et al. 1990) and the calculation principles for which are set out in (Zonenshain et al. 1990; Schreider et al. 2016).

The most profound part of the analyzed basins Scan, Dow, Protector has width of about a hundred or more kilometers and is characterized by depths up to 4 km. Formation of this basins could go in accordance with known Wernicke scheme NB, Due to discrepancy (sliding) of the continental crust block of Bruce elevation Eastern part and Western periphery of the continental block Discovery shoal (Scan basin), shoals Piri Eastern part and Western periphery of the Bruce shoal continental block (Dow basin), Terror shoal Eastern part and Western periphery of the Piri shoal continental block (Protector basin).

Numerous tests of the connectivity of different sections of different and eponymous isobaths slopes of basins showed the following results. At the position of the Euler pole of finite rotation at the point with coordinates 58.42° S, 33.43° W it is possible to obtain a very good combination of the isobath 2.6 km of the Western slope of Herdman Shoal with such an isobath on the Eastern slope of the Discovery Shoal on the South of 60° S for 60 km. The angle of rotation was $2.9^\circ \pm 0.7^\circ$, The standard deviation in the calculated alignment points was 12 km (7 alignment points). According to calculations, at the position of the Euler pole of finite rotation at a point with coordinates 57.28° S 38.13° W it is possible to obtain a very good combination of the isobaths 2.6 km in the Western slope of the Discovery Shoal with such an isobaths on the Eastern slope of the Bruce Rise on the South of 61° S for 80 km. The angle of rotation was $6 \pm 0.9^\circ$, The standard deviation in the calculated alignment points was 8 km (6 alignment points) Fig. 1.

At the position of the Euler pole of finite rotation at a point with coordinates 56.2 I^h S 42.09' W it is possible to obtain very good combination of the isobath 2.6 km of the Western slope of the Bruce Shoal with that of the isobaths on the Eastern slope of the Pirie Shoal on the South of 59.5° S for 110 km. The angle of rotation was $8.7^U \pm 1.2^\circ$. The standard deviation in the calculated alignment points was 12 km (9 alignment points).

According to calculations, at the position of the Euler pole of finite rotation at a point with coordinates 57.32° S 49.3 Γ W it is possible to obtain a very good

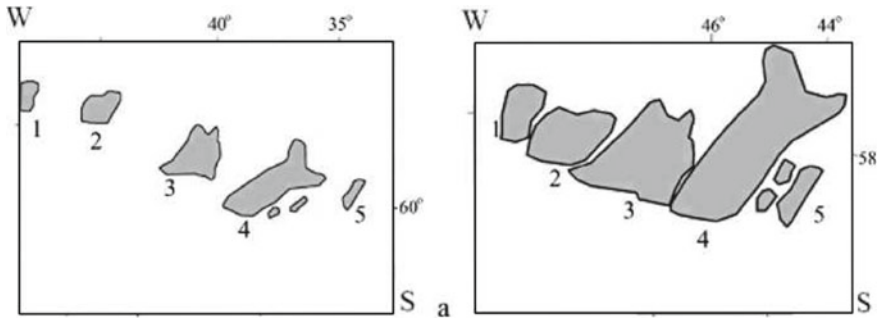


Fig. 1 The current (a) position of the basins in the Scotia sea: Teror (1), Piri (2), Bruce (3), Discovery (4), Herdman (5) at an isobaths of 2.6 km and restored (b) configuration of the American-Antarctic continental bridge Herdman Discovery Bruce Piri Teror as a result of paleogeodynamic reconstructions. The values of latitude and longitude in the area of the restored continental bridge are given to those Teror the present position of the Teror Shoal (according to [16] with modification)

combination of the isobaths 2.6 km of the Western slope of the Piri Shoal with that of the isobath on the Eastern slope of the Teror Shoal on the South of 60.3° S for 90 km. The angle of rotation was $2.9^\circ \pm 0.5^\circ$, the standard deviation in the calculated alignment points was 8 km (10 alignment points).

The reconstruction of the single continental uplift Herdman Discovery Bruce Piri Teror original configuration is produced as a result of the performed paleogeodynamic calculations. It had a length of up to seven hundred kilometers with a width of one and a half hundred kilometers (Fig. 1). The above estimates of the time of splitting and divergence of continental fragments do not contradict the assumption (Barker et al. 2013) that this process took place in the interval 45–25 million years ago.

Thus, the first paleogeodynamic reconstructions of the destruction (fragmentation) of the American-Antarctic continental bridge, which merged numerous underwater shoals in the Scotia sea, the most important of which are Teror, Pirie, Bruce, Discovery, Herdman, separated by tectonic disturbances and Protector, Dow, Scan basins, were carried out in the basis of Eulerian poles and angles of rotation calculation,

Acknowledgements Part of the study related to the improvement of the methods of kinematic calculations performed in the framework of a State programme project No 0149-2019-0005, part of the study related to paleogeodynamic reconstruction of the American-Antarctic continental bridge, was performed with the financial support of the Russian Foundation for Basic Research, project № 20-05-00089,

References

- Barker P, Lawver L, Larier R (2013) Heat-flow determinations of basement age in small oceanic basins of the southern central Scotia Sea. *Geol Soc London Spec Pub.* <https://doi.org/10.1144/SP381.3>
- Brown B, Gaina C, Muller D (2006) Circum Antarctic paleobathymetry: illustrated example from Cenozoic to recent times. *Paleogeogr. Paleoclim Paleocool* 231:158–168
- Buillard E, Everett J, Smith A (1965) The fit of continent ground Atlantic, Symposium on continental drift. *Philos Trans R Soc Lond* 258A:41–51
- Eagles G, Vaughan A (2009) Gondwana breakup and plate kinematics: business as usual. *Geophys Res Lett* 36(LI0302)
- Eagles G, Livermore R, Morris P (2006) Small basins in the Scotia Sea: the Eocene Drake Passage gateway. *Earth Planet Sci Lett* 242(3–4):343–353
- Hain VE (2001) Tectonics of continents and oceans. Nauchny Mir, Moscow ((in Russian))
- Livermore R, Nankivell A, Eagles G, Morris P (2005) Paleogene opening of Drake Passage. *Earth Planet Sci Lett* 236(1–2):459–470
- Schreider ALA (2005) Disclosure of the deep-water basin of the Black sea. *Oceanol* 45(4):592–604 (in Russian)
- Schreider ALA (2011) Formation of the deep-water basin of the Black sea. Nauchny Mir, Moscow ((in Russian))
- Schreider AA, Schreider ALA, Klyuev MS, Sazhneva AE (2016) Destruction of the American-Antarctic continental bridge. *Procesy V Geosredah* 4:378–382 ((in Russian))
- Verand C, Floies K, Stampfli G (2012) Geodynamic reconstructions of the South America-Antarctic paleo system. *J Geodynamic* 53:43–60
- Wit DM (1977) The evolution of the Scotia arc as a key to the reconstruction of southern Gondwanaland. *Tectonophysics* 37:53–81
www.topex.ucsd.edu/html/mar_topo.html
- Zhmur VV, Sapov DA, Nechaev ID et al (2002) Intensive gravitational currents in the bottom layer of the ocean. *Izv. AN. Ser Phys* 66(12):1721–1726. (in Russian)
- Zonenshain DD, Lomize MG, Ryabukhin AG (1990) Manual for practical classes in geotectonic. Publishing house, Moscow, MSU ((in Russian))

Influence of Large-Scale Atmospheric Circulation Modes on the Danube Runoff Anomalies During the Flood Period



V. L. Pososhkov

Abstract The statistical model for the anomalies of mean monthly runoff of the Danube River forecast in the spring season is proposed. An artificial neural network is used as a model. The predictors are the mean monthly values of the atmospheric circulation indices in wintertime. The time interval between 1950 and 2910 is considered. The model is tested using two criteria: correlation coefficient and Willmott's "agreement index". Their values in the most successful forecasts are 0.59 and 0.75 respectively. It is shown that the greatest impact on the Danube River runoff is caused by the Eurasian with a lead time of up to three months.

Keywords Danube runoff · Atmospheric circulation indices · Artificial neural networks

1 Introduction

Despite the fact that the dynamics of the Danube's flow has been studied well enough, the interest in this issue is still not weakening. This is related both to flood safety in the Danube basin countries and to problems affecting the environment and the development of hydropower, fisheries and agriculture.

As far as the Black Sea region is concerned, the predictability of the Danube's runoff is important in terms of its impact on the desalination of the North-Western Black Sea (NWBS) waters. It is well known that (Bolshakov 1970; Ivanov and Belokopytov 2011) the NWBS differs in many features from other areas of the sea. At a relatively shallow average depth of 27.7 m and a volume of water of about 1910 (Berenbeim 1963), the discharge of Black Sea rivers such as the Danube, Dnieper and other rivers in the volume of about 265–267 km³ per year (Ivanov and Belokopytov 2011; Berenbeim 1963) has a significant impact on the hydrological and biochemical characteristics of waters in the area.

V. L. Pososhkov (✉)
Marine Hydrophysical Institute of
Russian Academy of Sciences, Sevastopol, Russian Federation
e-mail: vla_po@mail.ru

Statistical models of the Danube runoff forecast are attempted using long-distance links between riverbed water discharge and large-scale processes in the Atlantic-European Ocean-Atmosphere system. Thus, the relations between the variability of the Danube runoff anomalies and the North Atlantic Oscillation Index (NAO) and the El Niño–South Oscillation (ENSO) is studied in (Rimbu et al. 2004). The authors have shown that both NAO and ENSO have a significant influence on the variability of the Danube river runoff.

The statistical scheme of seasonal forecasting of Danube runoff anomalies using surface temperature (SST) anomalies in several key Atlantic regions as predictors is described in (Rimbu et al. 2005).

The scheme of statistical forecasting of the Danube runoff anomalies on the basis of atmospheric circulation in the Atlantic-European sector is constructed in (Polonsky et al. 2010). The forecast scheme is based on artificial neural networks (ANN). The first and second order autoregressive models are used.

In this paper, we pose the problem of the role of teleconnection atmospheric indices (as a function of influence) in the fluctuations of the Danube runoff not in a particular month, but entirely during the spring flood, when the Danube runoff anomalies are maximum. During this flood period (March–May) the average runoff is about 34% of the annual flow rate (Berenbeim 1963).

In the prognostic problem, the time lag between the atmospheric predictors and the Danube runoff anomalies is of great importance. It depends on a variety of processes and conditions above the catchment area and takes into account the duration of the channel water recharge process throughout the river.

The purpose of this work is to assess the degree of predictability (with appropriate lead time) of the anomalies of mean monthly Danube flow rate during the flood period using the atmospheric circulation indices.

2 Materials Used and Research Methods

To solve the posed problem, long-term series of mean monthly Danube runoff and standardized indices of atmospheric circulation for the period 1950–2010, are used. The circulation indices from January 1950 are taken at the website of the prognostic climatic center of the USA (ftp://ftp.cpc.ncep.noaa.gov/wd52dg/data/indices/tele_index.nh). Despite the fact that the time series of the Danube flow is recorded at the Orsova station (44.40° N, 22.22° E), starting from 1840, in this work we have to limit ourselves to a shortened time period along the Danube runoff due to the lack of data on the atmospheric indices in the period up to 1950. As a result, the total time interval for all series provided by the data was 1950–2010.

Artificial neural networks (ANN) are used to construct a statistical forecast scheme. Danube runoff anomalies are an integral indicator of atmospheric conditions over the catchment. They only indirectly depend on atmospheric conditions through a lot of intermediate interactions. All this is difficult to take into account in

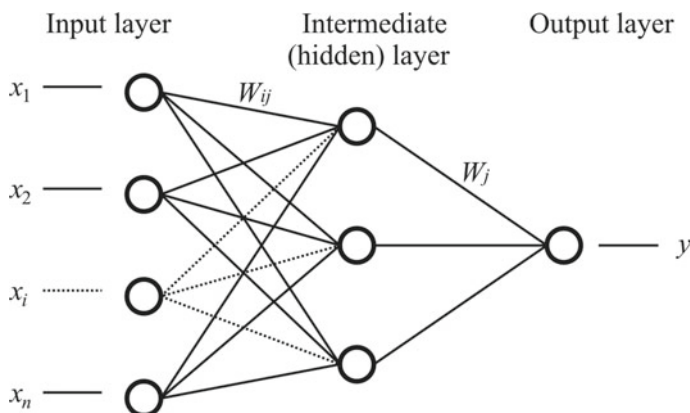


Fig. 1 Schematic representation of the neural network architecture

linear models, so in this paper, instead of a linear multi-regression approach, preference is given to non-linear statistical model of the ANN. The advantages of the ANN method over the multiple regression method are mentioned, in particular, in (Efimov and Pososhkov 2003).

Thus, the model used a three-layer straight propagation ANN. Schematically, the neural network architecture is shown in Fig. 1. The network consists of an input layer (predictors), an intermediate or hidden layer, and an output layer. The essence of the direct propagation network is that the input signals $x_i = (x_1 \dots x_n)$ pass through the neural layers in one direction in succession, without feedback. The outlet layer (predictants) is represented as a single time series, i.e. the average monthly runoff anomalies of the Danube during the flood period.

W_{ij} , W_j in the figure denote the weight parameters to be determined. The sigmoid function has been used as an activation function in this paper:

$$f(x) = \frac{1}{1 + e^{-x}}$$

Optimal weights and offsets are achieved by minimizing the target function, which is based on RMS error functional. Calculation procedure, including minimization of target function according to the scheme presented in Fig. 1, is close to that described in (Efimov and Pososhkov 2003). As predictors, the standardized atmospheric circulation indices are used.

Of the nine indices explaining on average about 60% of the dispersion of the geopotential field anomalies at the level of 500 hPa, five modes are analyzed, which have the main influence on the European region of the Northern hemisphere. These are the North Atlantic Oscillation (NAO), East Atlantic Oscillation (EA), Polar-Asian (POL), Eurasian (EA/WR) and Scandinavian (SCAND) modes (ftp://ftp.cpc.ncep.noaa.gov/wd52dg/data/indices/tele_index.nh).

3 Results of the Analysis

The mean monthly values of the atmospheric circulation indices are applied as predictors to the ANN input. Each index is considered as a separate predictor. When selecting the significant predictors, the corresponding correlation coefficients between the runoff anomalies and indices for the three winter months and the first month of the flood period are preliminary calculated, which are given in Table 1.

It can be seen from the table, first of all, that the East-Atlantic oscillation EA is of little significance not only in the months with a large time lag, but even in the first month of the flood (March). Therefore, in further calculations, this index is excluded from the number of predictors and only 4 atmospheric modes are used in the following results.

The largest lag (December) relative to the flood period is noted at the Eurasian and Scandinavian indices, and the smallest (February) at the Polar-Eurasian mode. The month of March on the basis of the table above is the most significant month for the North Atlantic oscillation and Polar-Eurasian mode. It is more interesting in the autoregressive model; the months preceding the flood period are more interesting in our forecast scheme. In addition, by excluding indices for March from the list of predictors and leaving only the winter ones for December – February, it is possible to increase the prior time of the statistical forecast up to 3 months

Predictors for the entire cold period of the year were used in the trial calculations, but in the final version the choice is made on the 7th winter modes, highlighted in Table 1 in bold font. The solid line in Fig. 2 refers to the observed anomalies of the Danube flow rate, the dotted line marks the model curve from the ANN output.

The process of minimizing the rms error functional is called neural network training. At the same time, the study period 1950–2010 is divided into two half-periods (two samples—calibration and validation). One of the samples is used to train the network. The rest of the data (not the tinted area in Fig. 2) is used for validation and forecasting.

The calibration period is arbitrary. Due to the lack of data, the possibility of varying the lengths of the calibration and testing samples is limited. In order to absorb as

Table 1 Correlation coefficients between monthly average values of circulation indices and anomalies of the Danube discharge during the flood period

Index	December	January	February	March
NAO	– 0.02	–0.31	–0.26	–0.34
EA	0.06	– 0.17	– 0.16	– 0.16
POL	0.04	0.08	–0.21	–0.33
EA/WR	–0.32	–0.28	–0.33	– 0.06
SCAND	0.24	0.12	– 0.05	0.09

Values that are statistically significant according to Fisher's test are in bold type in the table

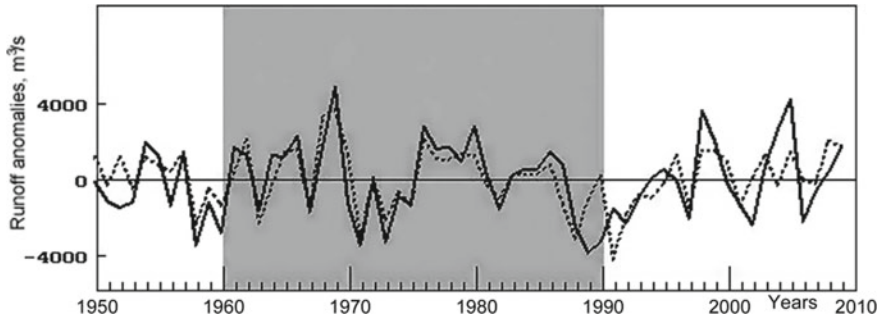


Fig. 2 Mean monthly runoff anomalies of the Danube River over the flood period (March–May) according to observations (solid line) and model calculations (dotted line). The tinted area of the figure refers to the training data sample

many properties of the observed data set as possible, the training period is chosen to be close to the climatic one, i.e. about 30 years.

Visually, the model good enough replicates observation data both in the future (forecast) and in the past (“retrospective forecast”) regarding to the period of network training. Let’s turn to the quantitative estimates. We will use two numerical criteria. The first is the estimation using the usual correlation coefficient (r). The second criterion is the so-called “consent index” (Wilmott d-measure (Willmott 1992)), which is widely used in Western literature:

$$d = 1 - \frac{\sum_{i=1}^N (P_i - O_i)^2}{\sum_{i=1}^N (|P'_i| + |O'_i|)^2}$$

where N is the total number of values in the data sample, P_i is the model value, O_i is the observed value, \bar{O} the average value of the observed value, $P'_i = P_i - \bar{O}$, $O'_i = O_i - \bar{O}$ —deviations from the average value.

Table 2 shows these numerical criteria r and d related to Figs. 2 and 3 and the numerical estimates are quite significant. The mixed scheme of the statistical forecast of the ANN (Polonsky et al. 2010) using the atmospheric structures together with the autoregressive model gives more convincing results, but does not allow us to identify the influence of atmospheric modes in “pure” form. Here, even if in a limited form, the main purpose of the forecast is to predict the output signal based on predictors with a high level of advance up to three months.

Table 2 The validation criteria corresponding to Figs. 2 and 3 (left column—calibration, right—testing)

	r	r	d	d
Figure 2	0.84	0.59	0.95	0.75
Figure 3	0.84	0.54	0.92	0.71

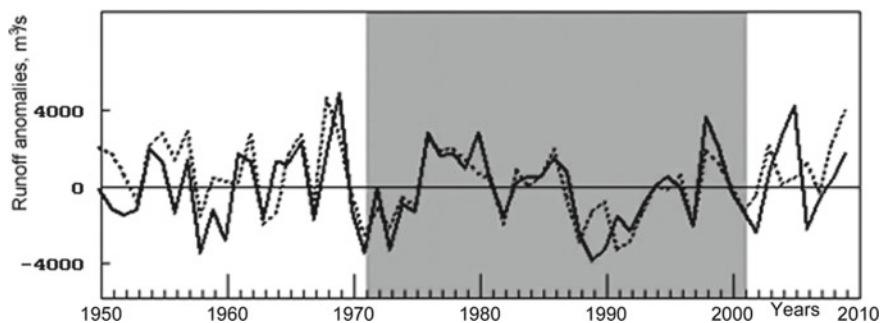


Fig. 3 The result of modeling with the same parameters as in Fig. 2, but with a different training sample. The notation is the same as in Fig. 2

Let us focus on the issue of sustainability of the forecast results during the period under review. As an example, Fig. 3 shows a variant of the forecast obtained from another training sample shifted in time relatively to Fig. 2 by 11 years.

Only the training sample has been changed. All other parameters of calculations exactly correspond to Fig. 2. Numerical indicators for this case are also given in Table 2.

As can be seen from the table, the numerical estimates are close to the ones obtained during the network training in another sample. The presented examples show the most successful forecasts made. This results are obtained by carefully adjusting the neural network parameters. Additional analysis of the stability of correlation coefficients at different time intervals of the period under consideration is required. Such a task is difficult at this stage because of the limited length of time series. In the long run, as new data are accumulated, it will be possible to increase the reliability of the presented forecast scheme.

4 Conclusion

The scheme of statistical forecast of the Danube runoff anomalies with the use of atmospheric circulation indices as predictors is constructed in this work. The used indices actually reflect the spatio-temporal structure of the large-scale atmospheric circulation in the Atlantic-Eurasian region.

As a result of calculations based on the proposed prognostic model with the use of ANN, the optimal combination of the average monthly winter indices of atmospheric circulation, which have a significant impact on the runoff anomalies of the Danube River in the spring flood period.

Calculations have shown that the Eurasian mode is more significant in terms of time lags. Its influence on the runoff anomalies during the flood period begins in December of the previous year and does not weaken until March.

It can be assumed that this large-scale mode due to its large spatial extent has a significant impact on weather anomalies in all parts of the Danube catchment area. Thus, due to the vast catchment area the response of the runoff over time will be different relative to different parts of the catchment area.

The results are validated using numerical criteria such as the correlation coefficient and Willmott's consent index, which are equal to one when ideally predicted. Despite relatively low correlation coefficients between individual predictors and predicted runoff, ANN model achieves an approach to observations of 59% correlation coefficient and of 75% agreement index.

These values are far from perfect, since large-scale atmospheric processes are not the only source of river flow disturbances. But here it is important to emphasize that: firstly, numerical estimates are significant enough to confirm the existence of long links to predict flow anomalies during the flood period, and secondly, the time lag of the predictors involved in the model can reach three months.

Of course, the work presents the best results from the number of performed calculations which was obtained by careful adjustment of the neural network. The stability of the result when changing the network parameters may not be sufficient, but the fact that at this stage relatively short time series are used should be taken into account.

References

- Berenbeim DY (1963) River runoff and salinity of the North-Western part of the Black Sea. Proc AzChernIRO 19:10–18 (in Russian)
- Bolshakov VS (1970) Transformation of river waters in the Black Sea. Naukova Dumka, Kiev (in Russian)
- Efimov VV, Pososhkov VL (2003) Statistical estimation of the daily sums of winter precipitation using the neural network method. Izvestiya RAS Atm Ocean phys 39(1):14–25 (in Russian)
- Ivanov VA, Belokopytov VN (2011) Black Sea oceanography. Marine Hydrophysical Institute, Sevastopol (in Russian)
- Polonsky AB, Voskresenskaya EN, Pososhkov VL (2010) Statistical forecast of the average monthly flow of the Black Sea rivers on the basis of the circulating atmospheric processes. Dopovidi Nat Acad Sci Ukraine 11:95–101 (in Russian)
- Rimbu N, Dima M, Lohmann G, Stefan S (2004) Impacts on the North Atlantic Oscillation and the El Niño-Southern Oscillation on Danube river flow variability. Geophys Res Let 31:L23203. <https://doi.org/10.1029/2004gl020559>
- Rimbu N, Dima M, Lohmann G, Musat I (2005) Seasonal prediction of Danube flow variability based on stable teleconnection with sea surface temperature. Geophys Res Let 32:L21704
- Willmott C (1992) Some comments on the evaluation of model performance. Amer Meteorol Soc 63:1309–1313
- ftp://ftp.cpc.ncep.noaa.gov/wd52dg/data/indices/tele_index.nh

Experimental Study of the Effect of Filtration for Low-Mineralized Water with High Temperature on Changes in Elastic and Strength Properties of Reservoir Rocks



S. N. Popov and A. S. Kusaiko

Abstract The paper presents the results of experimental study of the effect of filtration of low-mineralized water with high temperature through terrigenous core samples on the elastic-strength and capacitive properties of reservoir rocks. The technique of laboratory experiments is adduced. The rules of changes in the modulus of elasticity, Poisson's ratio and strength properties of samples depending on porosity and after exposure to water filtration are described. A significant decrease in physical and mechanical properties of rocks after filtration of low-mineralized high temperature water is shown. The change of compression curves after water injection is revealed. The results of changes in the elastic-strength properties of reservoir rocks should be necessarily taken into account during deposits modeling.

Keywords Elastic modulus · Poisson's ratio · Tensile strengths · Porosity · Permeability · Core samples · Low saline water

Injection of reservoir or service water is most often implemented to support stratum pressure (Mikhailov 2008) in oil fields development. Due to the fact that water is a chemically active agent, especially if chemical composition differs significantly from reservoir water, in the injection process, mechanical and chemical effects may occur, resulting into changes in both the filtration-capacitance and physical-mechanical properties of reservoir rocks (Hickman 2004; De Gennaro et al. 2009; Karmansky 2010; Popov 2015; Mikhailov and Popov 2015; Popov 2013). If the temperature of the injected water is much higher than the reservoir temperature, then such effects will be even more intense.

In connection with the above, in this paper, experimental study of changes in elastic and strength properties of reservoir rocks without and with filtration of low-mineralized fresh water are depicted. The studies were carried out on the example

S. N. Popov (✉)

Institute of Oil and Gas Problems, Russian Academy of Sciences, Moscow, Russia

e-mail: popov@ipng.ru

A. S. Kusaiko

LLC "NPP Geoprofi", Volgograd, Russian Federation

e-mail: a.s.kusaiko@mail.ru



Fig. 1 Prepared for the research terrigenous core samples

of core samples taken from the terrigenous productive object of one of the Komi Republic deposits. In the studied deposit-field, oil has very high viscosity, and therefore, steam injection is used to intensify the outflow.

Due to certain technical difficulties in simulating steam injection in a filtration facility, it was decided to use in experiments distilled water with temperature close to the boiling point of water (about 95 °C) as a pumped agent. Such an assumption can take place if mechanical properties of rocks during steam or water injection are mainly influenced by the Rebinder effect (reduction of strength due to adsorption of fresh water) (Rebinder et al. 1944), and not by the effects of dissolution of the rock. Since the experiments used samples of terrigenous rocks, which are very weakly soluble in water, this assumption is quite applicable in laboratory modeling.

First of all, core samples were made for research. Samples were drilled from the original core material so that in each group of six samples (4 standard size samples with a diameter and height of 30 mm, and 2 samples with a diameter of 30 mm and a height of 60 mm) were located as close as possible to each other to preserve, if possible, close filtration-capacitance and physical-mechanical properties. 30 samples were thus drilled: 20 of standard size (diameter and height 30 mm) and 10 with a size ratio of 2:1 (diameter 30 mm and height 60 mm). After drilling, all samples were extracted and dried. Figure 1 illustrates some of the samples obtained.

The characteristics of open porosity, absolute gas permeability and volume density were then determined for the samples (Fig. 2). The sample collection was quite representative and covers a wide range of changes in porosity and permeability, characteristic of this productive object. Also, based on the analysis of these graphs, it can be concluded that the high correlation coefficients between the porosity, permeability and density of samples indicate their sufficiently homogeneous structure, and therefore it is possible to compare their other properties (in particular elastic and strength) before and after filtration of hot distilled water.

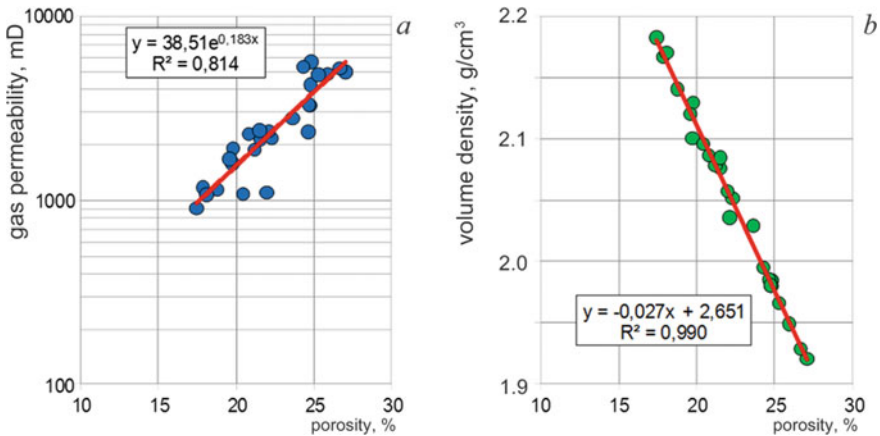


Fig. 2 Relation of absolute gas permeability (a) and volume density (b) of core samples on porosity

After preliminary studies, the samples were saturated with a reservoir water model for which mineralization was created by dissolving the NaCl at a concentration of 30 g/dm³. Then the elastic-strength and compression properties were studied without distilled water filtration for the half of samples (15 pieces):

1. Five definitions of strength limit, according to standard (GOST (state standard) 2115)
2. Five definitions of elastic properties (modulus of elasticity and Poisson’s ratio) and compressive strength under reservoir conditions;
3. Five definitions of relation of the porosity change with different values of effective stresses.

In determining the elastic properties and compressive strength under reservoir conditions, typical “stress-strain” diagrams were obtained, which displayed the change in axial and longitudinal deformations depending on the applied axial load. Figure 3 illustrates two such diagrams for two of tested samples.

The elastic modulus and Poisson’s ratio were determined on the basis of the obtained stress-strain diagrams (Fig. 3). The maximum value of stresses on these graphs corresponds to the compressive strength and characterizes the destruction of the sample.

Further experiments were made with the second half of the samples (15 pieces). Ten pore volumes of distilled water were filtered through all experimental samples at a temperature of 95° C to simulate steam injection into the productive formation. As for the first half of the samples, 5 definitions of tensile strength, 5 determination of modulus of elasticity, Poisson’s ratio and compressive strength were made, and 5 compression studies were also carried out.

In Fig. 4, the final results of determining the elastic and strength properties of core samples without and with distilled high temperature water filtration are presented in graphic form. Due to the fact that in addition to the mechanical and chemical effect

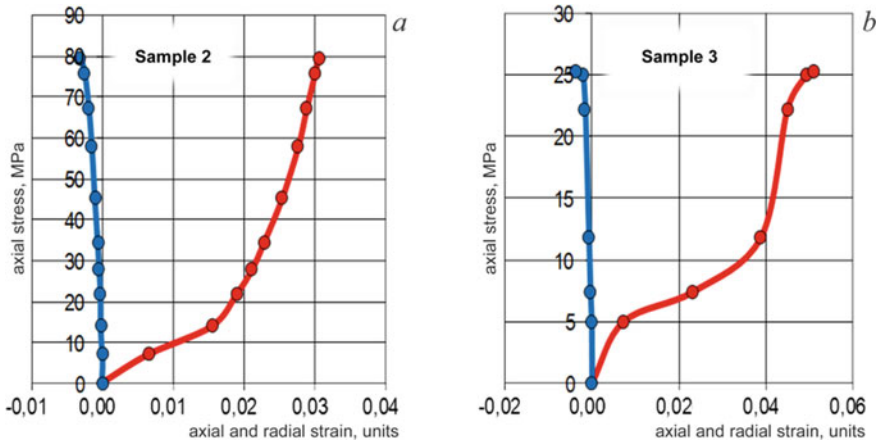


Fig. 3 Change of axial (red) and transverse (blue) deformations of core samples depending on axial load

of the influence of water filtration on the elastic-strength properties, the porosity parameter also is affected, the graphs are plot as the dependency on the value. There is a clear pattern of changes in strength characteristics and modulus of elasticity from porosity (Fig. 4), the exception is the Poisson's ratio. At the same time, the lines of dependency of these properties on the capacitive characteristic after water filtration are significantly lower than without filtration.

Thus, after water filtration, the strength limit of the samples decreased, on average, by 23.6%, the compressive strength by 31.2%, the elasticity modulus by 26.1%, the Poisson's ratio by 28.5%. This fact indicates a very significant effect of filtration of low-mineralized water with high temperature on the elastic and strength properties of the reservoir rock and the mechanical and chemical effects manifestation in this case, including the Rebinder effect. And these facts have to be taken into account when modeling geomechanical processes in the developing deposits.

Finally, the dependences of the porosity parameter change on the logarithm of the effective stress change for some samples without and with high temperature distilled water filtration are presented (Fig. 5). Table 1 shows the compression testing program.

Figure 5 compares the results of compression studies for samples with close porosity value. While porosity value, for convenience, is compared with maximum initial value. As can be seen from the figures, water filtration also has significant impact on the porosity changes patterns with effective stresses increase. In this case, the limit of porosity reduction increases by several percent, which should indicate an even more intense decrease in permeability after exposure to distilled water at high temperature.

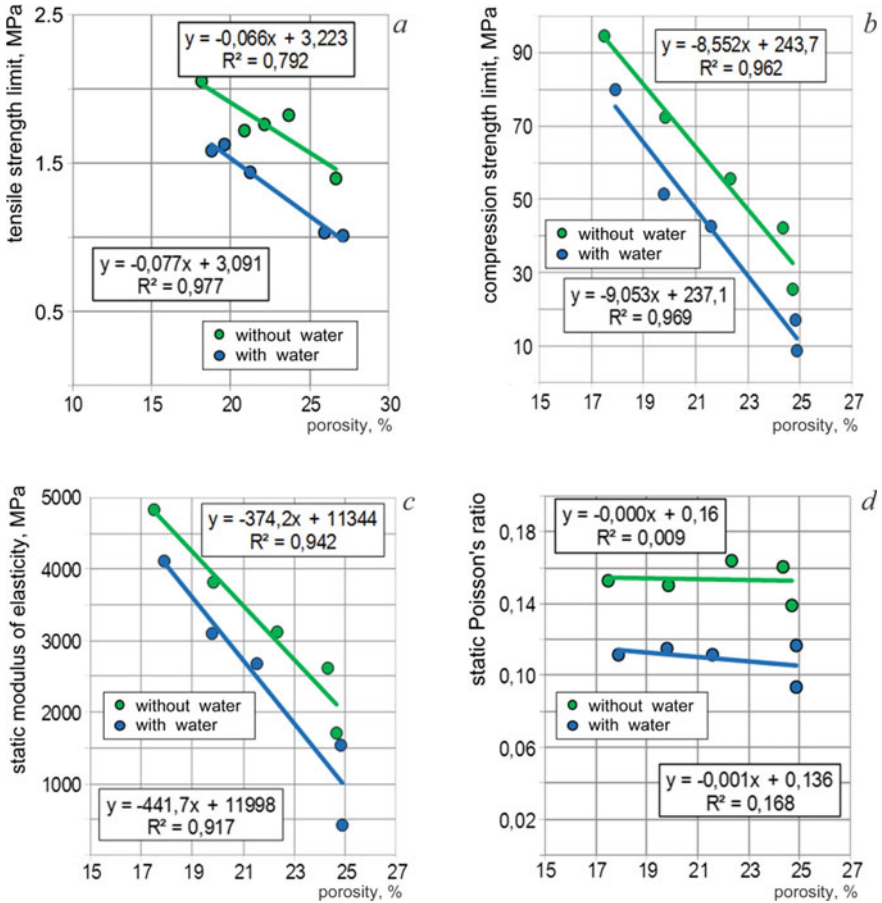


Fig. 4 Change of strength limit (a), compressive strength (b), modulus of elasticity (c) and Poisson's ratio (d) of core samples depending on porosity without and with effect of high temperature distilled water filtration

The following conclusions can be drawn from all the above:

1. As part of the work, compression studies and studies of the physical and mechanical properties of core samples taken from a terrigenous productive object, without and taking into account the filtration of low-mineralized water at high temperature, are carried out.
2. The results of studies of elastic-strength properties showed very high decrease in elastic (up to 28.5%) and strength (31.2%) properties of the reservoir after water filtration, which indicates the manifestation of mechanical and chemical effects, in particular the Rebinder effect.

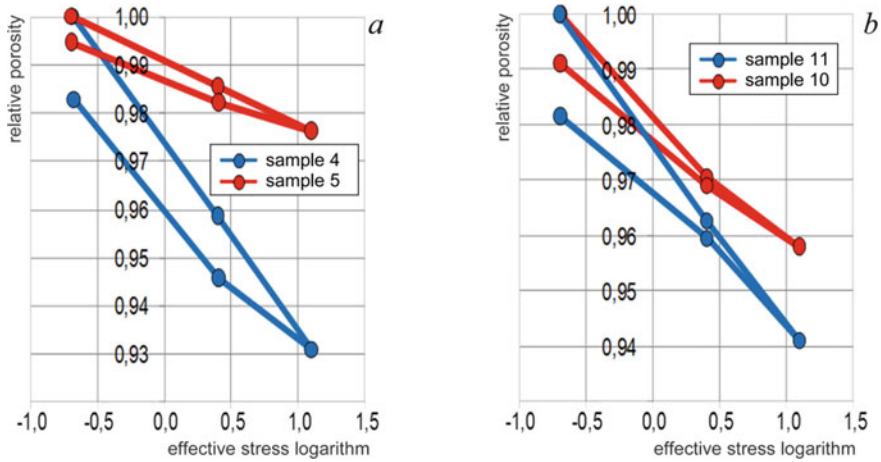


Fig. 5 Results of compression studies of some core samples (red—without water filtration, blue—after water filtration)

Table 1 Core sample compression testing program

No. of step	P _{por} , MPa	P _{pres} , MPa	P _{eff} , MPa	Exposition, min
1	1.4	1.9	0.5	20
2	1.4	2.9	1.5	20
3	1.4	4.4	3.0	20
4	1.4	2.9	1.5	20
5	1.4	1.9	0.5	20

3. Compression studies have shown that the ultimate change in porosity increases by several percent after filtration of distilled high temperature water, which should indicate an even more intense decrease in permeability after such exposure.
4. The obtained experimental results indicate the necessity to take into account the effects of the elastic-strength properties reduction for reservoir rocks in the process of water injection in geomechanical modeling of the studied deposit-field.

References

De Gennaro V, Pereira JM, Gutierrez M, Hickman RJ (2009) Viscoplastic modeling of fluids filled porous chalks. *Rivista Italiana Di Geotechnica* 1:44–64

GOST (state standard) 21153. 3–85. Rocks. Methods for determination of ultimate strength in uniaxial tension. Method of destruction of cylindrical samples by compression on generatrices. (in Russian)

- Hickman RJ (2004) Formulation and implementation of a constitutive model for soft rock. Dis. for the degree of Doctor of Philosophy, Blacksburg, Virginia, USA
- Karmansky AT (2010) Experimental substantiation of strength and destruction of saturated sedimentary rocks. Dis. for the degree of academic step. doctor. tech. sci, Saint-Petersburg, Russia (in Russian)
- Mikhailov NN (2008) Physics of oil and gas formation. MAX Press, Moscow (in Russian)
- Mikhailov NN, Popov SN (2015) Experimental and theoretical studies of the influence of mechanochemical effects on the filtration-capacitive, elastic and strength properties of reservoir rocks. Act Probl of Oil Gas 1(11). http://oilgasjournal.ru/vol_11/popov.html (in Russian)
- Popov SN (2013) Geochemical interaction between the reservoir and injected waters with crack-watami carbonate reservoirs. Oil Ind 5:76–79 (in Russian)
- Popov SN (2015) Influence of mechanic-chemical effects on filtration-capacitive and physical-mechanical properties of reservoir rocks. Geol Geophys Dev Oil Gas Fields 8:49–61. (in Russian)
- Rebinder PA, Schreiner LA, Zhigach KF (1944) Hardness reducers in drilling. Physico-chemical method to facilitate mechanical destruction of solid rocks during drilling. Publ. house of the USSR, Moscow. (in Russian)

Study of the Sea Foam Impact on the Wind-Wave Interaction Within the Laboratory Modeling



G. A. Baydakov , M. I. Vdovin , A. A. Kandaurov , D. A. Sergeev ,
and Yu. I. Troitskaya 

Abstract The results of laboratory modeling of the foam effect on the short-wave part of the surface wave spectrum and on the pulse exchange in the boundary layer of the atmosphere are presented. It is shown that the height and root-mean-square slope of the waves decrease with an increase in area of the surface covered with foam. At the same time, a significant increase in the coefficient of drag due to an increase in the overall surface roughness, not associated with waves, is demonstrated.

Keywords Sea foam · Wind-wave interaction · Wave spectrum · Laboratory modeling

1 Introduction

The interaction of wind flow with surface waves is one of the central problems of research and parameterization of exchange processes in the boundary layers of the Atmosphere and Ocean. Much attention is paid to the problem of explaining the effect of the sea surface coefficient of drag saturation at wind velocities exceeding 30 m/s (see for example (Letchford and Zachry 2009)). The idea of saturation (and even decrease) of the coefficient of drag of the sea surface at hurricane wind velocity was first proposed on the basis of theoretical analysis (Emanuel 1986) of the sensitivity of the maximum wind velocity in a hurricane to the ratio of the enthalpy and momentum exchange coefficients, and then was confirmed by a number of field and laboratory experiments, which showed that the drag coefficient of the sea surface is much smaller compared to the predicted parameterizations obtained for moderate and strong winds.

Theoretical explanations for the reduction of sea surface drag coefficient are based on the use of either the characteristics of the air flow over the collapsing waves (Kudryavtsev and Makin 2007), or the influence of sea spray on the exchange

G. A. Baydakov (✉) · M. I. Vdovin · A. A. Kandaurov · D. A. Sergeev · Yu. I. Troitskaya
Institute of Applied Physics, Russian Academy of Sciences, Nizhny Novgorod, Russia
e-mail: baydakov@ipfran.ru

G. A. Baydakov · M. I. Vdovin
Lobachevsky State University of Nizhny Novgorod, Nizhniy Novgorod, Russia

of momentum between the wind and the waves (Kudryavtsev and Makin 2011). Recently, an alternative hypothesis is proposed in (Golbraikh and Shtemler 2016), where one of the reasons for the decrease in surface drag is the effect of the sea foam on surface aerodynamic roughness.

2 Experimental Facility

In a laboratory experiment, the influence of foam on the water surface roughness is studied. The experiments are carried out on the high-Velocity wind-wave tank of the Institute of Applied Physics of the Russian Academy of Sciences. The channel has a cross section of 0.4×0.4 m above the water surface and a length of 10 m, the air flow velocity range on the axis of the channel is 3–25 m/s, the air temperature can take values between 20 and 30 °C. The pool is filled with fresh water with temperature of 15 to 20 °C, that is, there is a weak temperature stratification in the air flow. The value of the surface tension coefficient σ is $(7.0 \pm 0.15) 10^{-2}$ N/m.

Based on the shape of the wind velocity profile in the turbulent boundary layer described by the logarithmic curve

$$U(z) = \frac{u_*}{\kappa} \ln \frac{z}{z_0} \quad (1)$$

where u_* is the dynamic wind velocity and $\kappa = 0.4$ Karman parameter, the roughness parameter z_0 is uniquely related to the drag coefficient C_D :

$$C_D = \left(\frac{u_*}{U(z = 10 \text{ m})} \right)^2 = \left(\frac{\kappa}{\ln(z/z_0)} \right)^2 \quad (2)$$

The dependence of the drag coefficient on the dynamic wind velocity and the characteristics of the underlying surface in presence and absence of foam is studied in the experiments. The scheme of the experimental facility is shown in Fig. 1a.

To create stable foam with a fixed density on the water surface, a specially designed device (foam generator) is used (Fig. 1b). The generator consists of two tubes with diameter of 1 cm with side holes with diameter of 2 mm with spatial increment of 7 mm), with side surfaces connected with each other, wrapped in foam rubber. The device is located horizontally, perpendicular to the channel, with the embedment of upper part for 2.5 cm. The distance from the beginning of the channel (air flow inlet) 1.2 m. Through one of the diffusers under height level pressure of 1.5 m solution is fed with foam-forming agent (main component is sodium lauryl sulfate), compressed air (1.5 atm) is supplied through the second diffuser for pushing the solution of foam-forming agent through the foam rubber layer. As a result, a thin layer of foam is formed on the surface of the water and maintained constant during the experiment by controlling the pressure and level of the foam solution. A special

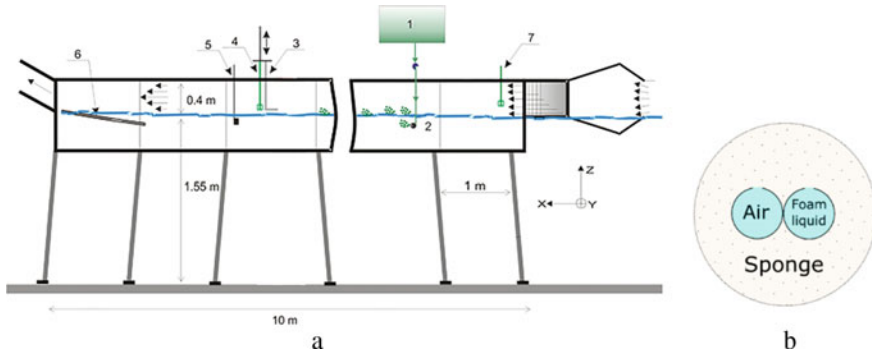


Fig. 1 Scheme of the pilot facility (a): 1—tank with foaming solution, 2—foam generator, 3 and 4—Pitot tube and anemometer mounted on the scanning device, 5—string 3-channel wave recorder, 6—wave absorber, 7—anemometer, cross-section (b) of the foam generator

series of measurements aimed at assessing the effect of the foam generator on the surface wave in the case when only compressed air is supplied to the system showed that the changes in the parameters of the surface wave compared to a completely disconnected foam generation system are insignificant (see the results of experiments below).

Measurements are carried out for three conditions: (1) clean water; (2) clean water with compressed air supply to the foam generator, but without the supply of foaming agent; (3) with a fully functioning foam generation system. The measurements are performed at 6 values of the air flow rate in the channel, which are determined by the fan velocity. Before and after each series of measurements, the pool water parameters are monitored to assess the effect of the foaming agent on the water properties. The surface tension coefficient is measured by the drip method, as well as the viscosity of the liquid. In all cases, the differences from the initial values of these parameters are within the accuracy of measurements. Thus, the change in the properties of the water in th, and, consequently, possible influence on the wind-wave interaction, is excluded.

Each set of experimental conditions is determined by the parameters of the air flow (dynamic velocity, wind velocity at standard height, and drag coefficient), the characteristics of the surface waves (frequency and wave number spectra and the significant waves height and surface slope dispersion) and the parameters of foam (area covered by foam and the bubble sizes distribution).

3 Methods and Results of Experiments

The measurement of the air flow parameters is carried out by profiling. For this purpose, in the working section (at a distance of 7 m from the entrance to the tank), velocity profiles are measured by use of Pitot tube. The self-similarity of the velocity

profile is used to determine the parameters of the air boundary layer, the algorithm is described in (Troitskaya et al. 2012).

For Fig. 2 shows the dependence of the drag coefficient on wind velocity and dynamic velocity. It can be seen that at wind velocities below 25 m/s (dynamic velocity about 0.9 m/s) the presence of foam leads to an increase in the drag coefficient, and at large values of dynamic velocity, a statistically significant dependence of the drag coefficient on the foam is not revealed.

The waveform characteristics in the tank are measured by the antenna of their three resistive waveguides located in the corners of a triangle of equal side with a side of 2.5 cm, the sampling rate of the data is 100 Hz. Space-time spectra are obtained using the algorithm (Troitskaya et al. 2012), similar to the Wavelet Directional Method, but using Fourier transform. This data processing makes it possible to obtain three-dimensional spectra of surface waves $S(\omega, k, \theta)$ dependence on the wave frequency ω , wave number k and angle relative to the wind direction θ . Integration of the obtained spectra by wave number or frequency, gives temporal $S(\omega, \theta)$ or spatial angular spectra $S(k, \theta)$, respectively. Integration by θ gives isotropic spectra in frequency and wave number. The upper limit of the wavenumber spectrum is given by the distance between the waveforms in the wave antenna d , $k_{\max} = \pi/d$ in the configuration used $k_{\max} = 1.25 \text{ cm}^{-1}$.

Analysis of the results showed that the foam changes the spectra of surface waves. In particular, the effect of decreasing the peak frequency ω_p and wave number k_p decreases with increasing velocity. This effect is clearly seen in Fig. 3, where the dependences ω_p and k_p on the wind velocity for different modes are presented.

Analysis of the spectra of wind waves showed that the foam causes a noticeable decrease in the energy of surface waves. This effect of increasing the dissipation of

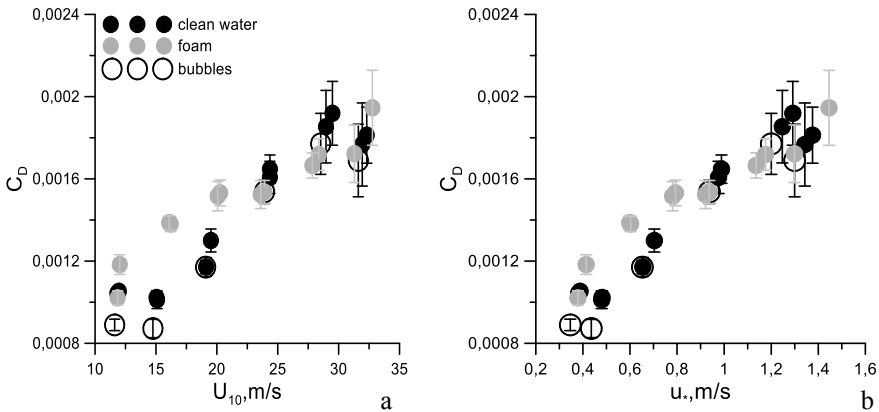


Fig. 2 The dependence of the drag coefficient on the wind velocity at an altitude of 10 m (a) and the friction velocity (b). Black symbols—pure water, gray symbols—when working with sodium lauryl sulfate foam generator, open circles—when working with pure water foam generator

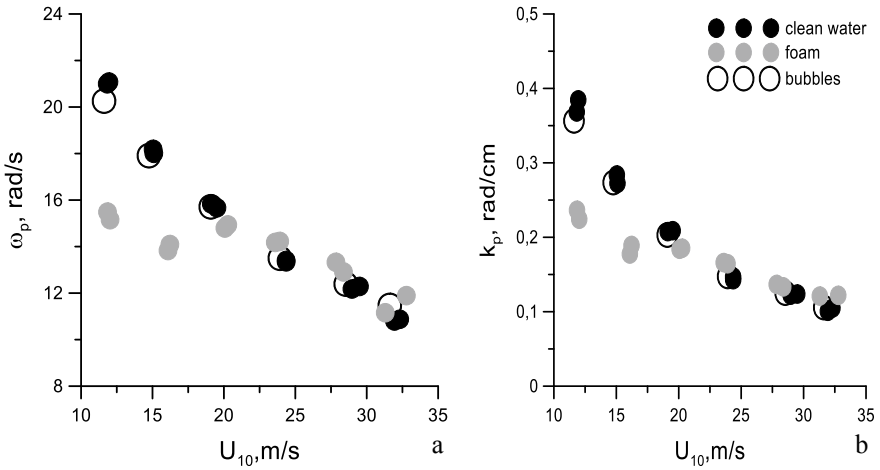


Fig. 3 The macro button chooses the correct format Dependency of ω_p and k_p on wind friction velocity for different modes

surface waves in the foam is confirmed by the dependence of the significant wave height on the wind friction velocity (Fig. 4a).

In combination with a decrease in the peak wave number, this leads to a strong decrease in the RMS slope (Fig. 4b). Therefore, the foam on the water surface should lead to a decrease in the nonlinear effects of wind waves and a decrease in the waveform resistance.

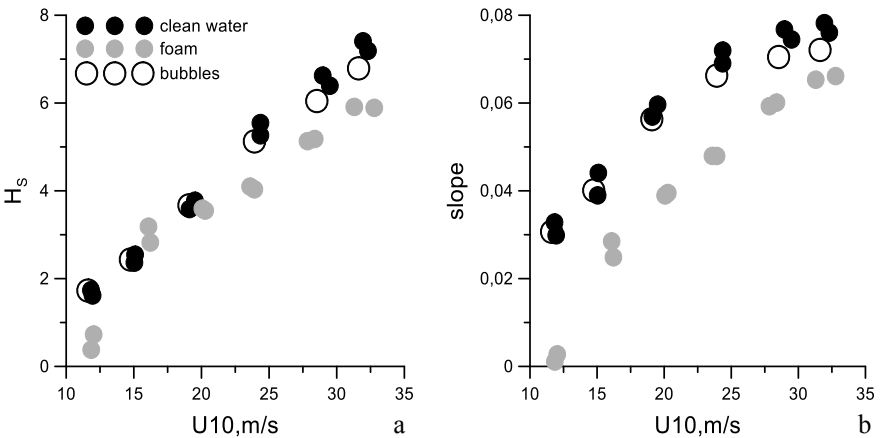


Fig. 4 Dependences of significant wave height on wind friction velocity and mean square surface slopes for different modes

However, the comparison with Fig. 2 shows that despite the decrease in the wave-form resistance, C_D increases with the foam on the water, since the foam causes roughness not associated with waves.

4 Conclusion

In the course of laboratory modeling of the impact of sea foam on the wind-wave interaction, it is found that with an increase in the surface coverage area, the high-frequency waves sharply decrease, which leads to a significant decrease in the mean square surface slopes of the waves, as well as reduces height of waves. An increase in the aerodynamic drag coefficient in moderate winds, which is caused by an increase in the overall non-waves roughness of the surface, is demonstrated.





Acknowledgements The study is conducted under support of RFBR grant 18-35-20068 and grants of President of Russian Federation MK-144.2019.5 and MK-3184.2019.5.

References

- Emanuel KA (1986) An air-sea interaction theory for tropical cyclones. Part I: steady-state maintenance. *J Atmos Sci* 43:585–605
- Golbraikh E, Shtemler YM (2016) Foam input into the drag coefficient in Hurricane conditions. *Dyn Atmos Oceans* 73:1–9
- Kudryavtsev V, Makin V (2007) Aerodynamic roughness of the sea surface at high winds. *Boundary-Layer Meteorol* 125:289–303
- Kudryavtsev V, Makin V (2011) Impact of ocean spray on the dynamics of the marine atmospheric boundary layer. *Boundary Layer Meteorol* 140:383–410
- Letchford CW, Zachry BC (2009) On wind, waves, and surface drag. In: EACWE-5, Florence, Italy, pp 32–42
- Troitskaya YuI, Sergeev DA, Kandaurov AA, Baidakov GA, Vdovin MA, Kazakov VI (2012) Laboratory and theoretical modeling of air-sea momentum transfer under severe wind conditions. *JGR* 117:C00J21

On the Influence of Stratification and Shear on the Turbulent Mixing in Inland Waters



D. Gladskikh , I. Soustova , Yu. Troitskaya , and E. Mortikov 

Abstract The article is devoted to the connection between such characteristics as the gradient Richardson number and the turbulent Prandtl number, and the authors propose a parameterization taking this connection into account. The parameterization was obtained on the basis of a modified model of turbulent closure, developed by L. A. Ostrovsky and Yu. I. Troitskaya back in 1987. In the model, the kinetic approach was used to determine the turbulent fluxes of momentum, kinetic and potential turbulence energies in the stratified medium. Proposed parameterization was used by the authors in the calculation of the thermo-hydrodynamic regime of inland water objects with the use of three-dimensional hydrostatic model with the modified k - ε scheme, which allows to take into account the temperature stratification and its influence on the processes of turbulent mixing. The numerical experiment directed on research of influence of turbulent number of Prandtl on the description of processes of thermo-hydrodynamics of lakes and reservoirs on an example of the idealized water object has been carried out.

Keywords Turbulence · Numerical modeling · Inland water object · Stable stratification · Turbulent Prandtl number · Gradient Richardson number

D. Gladskikh (✉) · I. Soustova · Yu. Troitskaya
Division of Geophysical Research, Institute of Applied Physics, Russian Academy of Sciences,
Nizhny Novgorod, Russian Federation
e-mail: daria.gladskikh@gmail.com

D. Gladskikh · E. Mortikov
M.V. Lomonosov Moscow State University, Research Computing Center, Moscow, Russian
Federation

E. Mortikov
Institute of Numerical Mathematics, Russian Academy of Sciences, Moscow, Russian Federation

1 Introduction

Inland water objects play a significant role in the processes of interaction between the Atmosphere and the Hydrosphere, and in this regard, a reliable description of the thermodynamics of water objects in large-scale weather and climate prediction models is required (Adamenko 1985; Tranvik 2009; Mironov 2006, 1991; Long 2007; Ljungemyr 1996). In order to study the physical and hydrological characteristics of inland water objects on seasonal, annual and climatic scales, one-dimensional models are of most interest today, due to their computational simplicity. However, in order to study the circulation in particular water object, it is possible to use three-dimensional models, which, as a rule, imply the approximation of hydrostatics. In description of the vertical turbulent mixing processes, most numerical models use local closure with the use of gradient hypotheses (Monin 1965) to express momentum of the higher order characterizing the turbulent flows of a particular value through the moments of a lower order.

The most popular are schemes involving such prognostic equations as the turbulent kinetic energy (k , TKE) equation and the TKE dissipation rate equation. In the standard k - ε model the turbulent Prandtl number $\text{Pr}_T = K_m/K_h = \kappa_\rho^{-1}$ linking $\text{Pr}_T = K_m/K_h = \kappa_\rho^{-1}$ the coefficients of turbulent viscosity K_m and thermal conductivity K_h is constant and does not depend on the type of stratification and shear flow. However, as shown by laboratory and field experiments (Monin 1965), $\kappa_\rho = \text{Pr}_T^{-1}$ is a decreasing function of the gradient Richardson number $\text{Ri} = N^2/V_{0z}^2$, (where N —the Brunt-Vaisala frequency, and V_{0z} —velocity shift), which characterizes the balance between the shear and stratification. The question of relation type $\kappa_\rho(\text{Ri})$ is extremely important to clarify the possibility of maintaining turbulence by weak shear in stratified liquids characteristic of the ocean and stratified inland water objects.

For this reason, numerous empirical relations have been proposed $\text{Pr}_T(\text{Ri})$ (see, for example, (Baas et al. 2008; Schumann and Gerz 1995)). In the presented paper, the parameterization of the Prandtl number on the basis of the modified theory of turbulent closure in stratified shear flows developed by one of the authors back in 1987 (Ostrovsky and Troitskaya 1987) is proposed. The obtained relation for the Prandtl number is used in calculations of the thermo-hydrodynamic regime of inland water objects within the model of different spatial resolution in the three-dimensional hydrostatic model (Mortikov 2016, 2019) with the modification of k - ε scheme.

2 Key Provisions of the Turbulent Transport Model in a Stratified Shear Stream

For a detailed description of the Ostrovsky and Troitskaya model, see (Ostrovsky and Troitskaya 1987). In this model the kinetic approach is used, and turbulent characteristics (momentum fluxes, kinetic and potential energies) in a stratified medium were defined using this approach. In particular, it was shown that the consideration

of bilateral transformation of energy pulsations allows explaining the maintenance of turbulence by small velocity shifts, including those generated by internal waves. The procedure for obtaining the appropriate equations for the averaged values to that used in the kinetic theory of gases and includes the equations of balance for the moments of the second order (kinetic and potential energy of turbulence and vertical fluxes of impulse and buoyancy) in a stable stratified liquid. Some important but usually neglected effects are taken into account, such as the dependence of vertical anisotropy on stratification and a non-gradient correction to the traditional expression of the turbulent mass flux. The proposed model allows the existence of turbulence at any value of gradient Richardson number.

The model includes equations for speed $\langle \vec{u} \rangle$, density $\langle \rho \rangle$ and kinetic energy of turbulence $b = 3(u^2 + v^2 + w^2)/2$ and density fluctuations $\langle \rho^2 \rangle$. The model allows to take into account the bilateral exchange between the kinetic and potential components of the total turbulence energy, the value of which determines the potential energy density field

$$\begin{aligned} \frac{\partial \langle u_i \rangle}{\partial t} + \langle u_i \rangle \frac{\partial \langle u_i \rangle}{\partial x_j} + \frac{1}{r_0} \frac{\partial \langle \rho \rangle}{\partial x_i} + g_1 \frac{\langle \rho \rangle - \rho_0}{\rho_0} \\ = \frac{\partial}{\partial x_j} \left(L \sqrt{b} \left(\frac{\partial \langle u_i \rangle}{\partial x_j} + \frac{\partial \langle u_j \rangle}{\partial x_i} \right) \right), \end{aligned} \quad (1)$$

$$\frac{\partial \langle \rho \rangle}{\partial t} + \langle u_i \rangle \frac{\partial \langle \rho \rangle}{\partial x_i} = \frac{\partial}{\partial x_i} L \sqrt{b} \left(\frac{\partial \langle \rho \rangle}{\partial x_i} + \frac{3}{2b\rho_0} (g_i \langle \rho^2 \rangle + g\beta_i) \right) \quad (2)$$

$$\begin{aligned} \frac{\partial b}{\partial t} + \langle u_i \rangle \frac{\partial b}{\partial x_i} - L \sqrt{b} \left(\frac{\partial \langle u_i \rangle}{\partial x_j} + \frac{\partial \langle u_j \rangle}{\partial x_i} \right)^2 - \frac{g}{\rho_0} L \sqrt{b} \left(\frac{\partial \langle \rho \rangle}{\partial z} + \frac{3g}{2b\rho_0} (\langle \rho^2 \rangle + \beta_z) \right) \\ + \frac{Cb^{3/2}}{L} = \frac{5}{3} \frac{\partial}{\partial x_i} \left(L \sqrt{b} \frac{\partial b}{\partial x_i} \right) \end{aligned} \quad (3)$$

$$\frac{\partial \langle \rho^2 \rangle}{\partial t} + \langle u_i \rangle \frac{\partial \langle \rho^2 \rangle}{\partial x_i} + 2 \frac{\partial \langle \rho \rangle}{\partial x_i} L \sqrt{b} \left(\frac{\partial \langle \rho \rangle}{\partial x_i} + \frac{3}{2b\rho_0} (g_i \langle \rho^2 \rangle + g\beta_i) \right) \quad (4)$$

Note that in Eqs. (3) and (4) Kolmogorov approximations are taken to describe dissipative processes: $\varepsilon = Cb^{3/2}/L$ and $\varepsilon_D = Db^{1/2}\langle \rho^2 \rangle/L$, where.

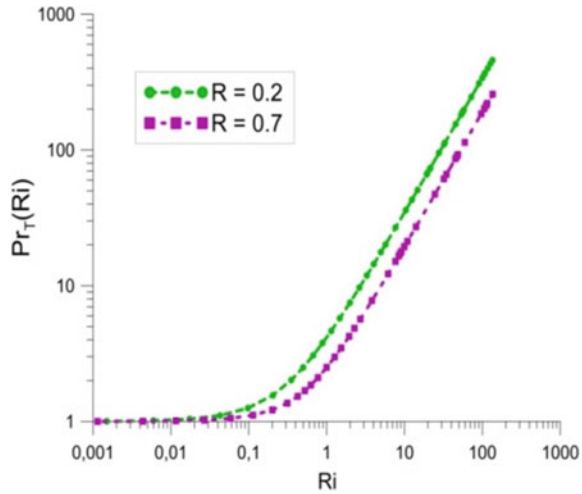
$D \sim C = 0.09$ the empirical constant (Fig. 1).

Under the specific approach it was possible to obtain the relation of Pr_T to Ri :

$$\text{Pr}_T(\text{Ri}) = 0.5 \left((4 - 3R)\text{Ri} + 1 + \left(((4 - 3R)\text{Ri} + 1)^2 - 4\text{Ri} \right)^{1/2} \right) \quad (5)$$

where R is the constant, which is a function of the ratio of vertical L_z and horizontal L_r scales of the field of density field fluctuations.

Fig. 1 The function $f = Pr_T(Ri)$ at R equal to 0.2 and 0.7



In the next section the results are demonstrated of the obtained parameterization of Pr_T (5) in the calculations of the thermo-hydrodynamics of an idealized inland water object.

3 Calculation of Thermodynamic Regime of Idealized Inland Water Object with Regard to the Acquired Parameterization

In order to assess the impact of the parameterization of the Prandtl turbulent number on the mixing processes in inland waters, the present study uses a three-dimensional hydrostatic model developed at the Research and Development Centre of the M. V. Lomonosov Moscow State University on the basis of a unified hydrodynamic code that combines DNS/LES/RANS approaches to calculate geophysical turbulent flows at high spatial and temporal resolution (see (Mortikov 2016, 2019)).

The numerical model includes the equations of hydrodynamics in the stratified turbulent rotating liquid layer in the shallow water approximation, as well as the equations for heat transfer taking into account the horizontal and vertical diffusion:

$$\frac{\partial u}{\partial t} = -A(u) + D_H(u, \chi_m) + D_z(u, K_m) - g \frac{\partial \eta}{\partial x} - \frac{g}{\rho_0} \frac{\partial}{\partial x} \int_z^{B(x,y)} \rho dz + fv,$$

$$\frac{\partial v}{\partial t} = -A(v) + D_H(v, \chi_m) + D_z(v, K_m) - g \frac{\partial \eta}{\partial y} - \frac{g}{\rho_0} \frac{\partial}{\partial y} \int_z^{B(x,y)} \rho dz + fu,$$

$$\nabla \cdot \mathbf{u} = \frac{\partial u}{\partial x} + \frac{\partial v}{\partial y} + \frac{\partial w}{\partial z} = 0,$$

$$\frac{\partial T}{\partial t} = -A(T) + D_H(v, \chi_h) + D_z(T, K_h),$$

$$\rho = \rho(T),$$

where u, v, w —velocity vector components, η —free surface deviation from the equilibrium state, ρ —density, K_h —vertical turbulent thermal conductivity coefficient, λ_h —horizontal turbulent thermal conductivity coefficient, K_m —vertical turbulent viscosity coefficient, λ_m —horizontal turbulent viscosity coefficient, ν, χ' —molecular diffusion adjustments, T —temperature, f —Coriolis parameter, $B(x, y)$ —bottom relief, z —depth. Also here $A(q)$ $A(q)$ is the advection operator, $D(q, \chi)$ and $D_H(q, \chi)$ and $D_z(q, K)$ are the horizontal and vertical diffusion operators with coefficients χ and K respectively.

To describe the processes of vertical turbulent mixing, the k - ε model (Lykosov 1992; Mellor 1974) is used. For convenience and uniformity, the turbulent kinetic energy is denoted as b .

$$\frac{\partial}{\partial t} = \frac{\partial}{\partial z} \left(\frac{K_m}{\delta_k} + \nu \right) \frac{\partial k}{\partial z} + P + B - \varepsilon,$$

$$\frac{\partial \varepsilon}{\partial t} = \frac{\partial}{\partial z} \left(\frac{K_m}{\delta_s} + \nu \right) \frac{\partial \varepsilon}{\partial z} + \frac{\varepsilon}{k} (C_{1\varepsilon} \cdot P - C_{2\varepsilon} \cdot \varepsilon + C_{3\varepsilon} \cdot B)$$

$$K_m = C_s \frac{b^2}{\varepsilon}$$

$$K_h = C_{s,T} \frac{b^2}{\varepsilon} = \frac{C_{s,T}}{C_s} K_m$$

Here the term P corresponds to the generation of energy of turbulence due to the velocity shift, and B describes the generation or consumption of energy due to the action of buoyancy forces, δ_k, δ_s —turbulent Schmidt numbers, $C_{1\varepsilon}, C_{2\varepsilon}, C_{3\varepsilon}$ —empirical constants, C_s and $C_{s,T}$ stability functions for momentum and scalars respectively, assumed to be constant.

To estimate the influence of the Prandtl turbulent number and, in particular, its parameterization on the description of the processes of turbulent mixing a numerical experiment is carried out.

During the experiment, the calculations within the modernized k - ε scheme were compared with the standard ones, in which the Prandtl number Pr_{T0} was supposed to be equal to one, as in the parameterization above with $Ri \rightarrow 0$ to the value of the Prandtl number $Pr \sim 1$.

The model modification consisted in the fact that the coefficient of turbulent thermal conductivity was expressed as:

$$K_h = \frac{K_m}{Pr_T(Ri)}$$

where relation $Pr_T(Ri)$ is determined by formula (5).

The idealized reservoir of rectangular cross-section and depth of 10 m at a constant flow of momentum on the surface was considered. At the time origin, a linear temperature profile was set. Such statement is a modification of the numerical Kato-Phillips experiment (Kato and Phillips 1969), which considers the depth of the mixed layer at a constant wind in a horizontally homogeneous region.

Parameters of the experiments were:

- water object with a rectangular cross-section and horizontal dimensions of 500 m by 500 m,
- depth of 10 m,
- calculation time—one day,
- surface temperature 20 °C,
- initial temperature gradient $\partial T/\partial z = 1.5 \text{ }^\circ\text{C/m}$,
- surface impulse flux $\tau = 10^{-1} \text{ N/m}^2$,
- two-dimensional wind forcing,
- Coriolis force is taken into account (latitude 60°),
- $R = 0.2, R = 0.7$,
- Brunt-Vaisala (buoyancy) frequency: $N = 4 \times 10^{-2} \text{ s}^{-1}$.

The results are shown in Figs. 2a, b and 3a, b.

The obtained results show that in this case the use of parameterization has little effect on the mixed layer depth. However, there is a significant decrease in the

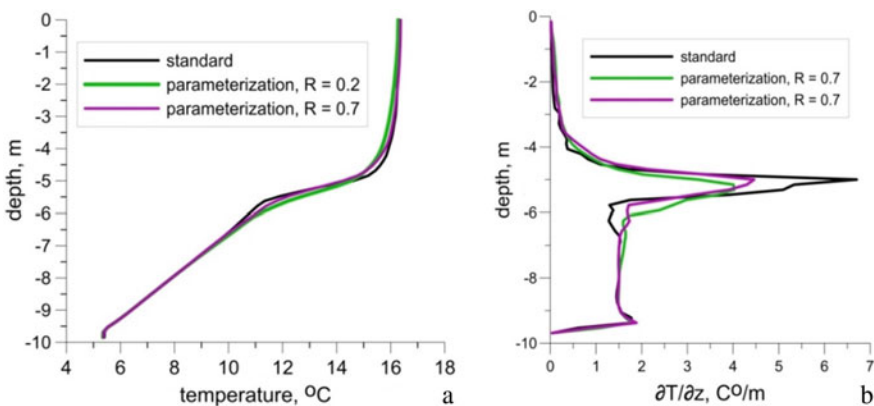


Fig. 2 Comparison of vertical **a** temperature **b** temperature gradient distribution calculated using the standard $k-\varepsilon$ scheme and parameterization from the model (Ostrovsky and Troitskaya 1987)

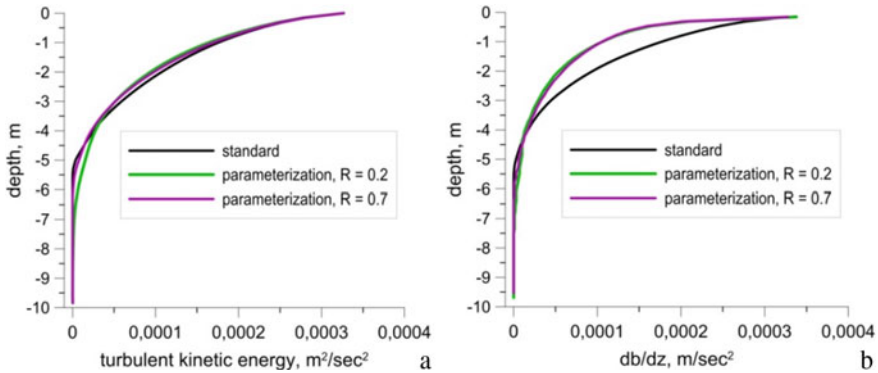


Fig. 3 Comparison of vertical **a** turbulent kinetic energy **b** turbulent kinetic energy gradient distribution calculated using the standard k - ε scheme and parameterization from the model (Ostrovsky and Troitskaya 1987)

maximum temperature gradient in the thermocline. Thus, the characteristic parameters of the thermocline are very sensitive to the used parameterization $Pr_T(Ri)$, which is important, in particular, to reconstitute the biochemical substances concentration field (Karpowicz and Ejsmont-Karabin 2017).

4 Conclusion

The parameterization scheme for Pr_T obtained using the model (Ostrovsky and Troitskaya 1987) considering the mutual interaction of energies of turbulent pulsations is proposed and implemented. In order to test the assumption of the influence of the parameterization of Pr_T on the processes of turbulent mixing in internal reservoirs and, in particular, to verify correct consideration of stratification and shear in the calculation of the thermo-hydrodynamic regime, a numerical experiment was carried out using a three-dimensional hydrostatic model for the idealized geometry of the reservoir.

The results of the calculations allow to conclude that the description of vertical mixing in inland waters, even in an idealized formulation, is sensitive to the parameterization of Pr_T . The values of temperature gradient and turbulence kinetic energy are determined by the character of $Pr_T(Ri)$ relation at transition from weak to strong stability. Such result testifies to the necessity to implement the turbulent Prandtl number justified parameterization in numerical models of inland water objects, especially when calculating seasonal and interannual dynamics.

Acknowledgements The work was financially supported by the Russian Foundation for Basic Research (projects № 17-05-41117, 18-05-00292, 18-35-00602, 18-05-60126, 18-05-60184). Calculations with the use of three-dimensional model were made in the framework of the project of the Russian Scientific Foundation № 17-17-01210.

References

- Adamenko VN (1985) Climate and lakes (to the assessment of present, past and future). Hydrometeoizdat, Leningrad, p 264
- Baas P, de Roode S, Lenderink G (2008) The scaling behavior of a turbulent kinetic energy closure model for stably stratified conditions. *Bound-Layer Meteorol* 127:17–36
- Kato H, Phillips OM (1969) On the penetration of a turbulent layer into stratified fluid. *J Fluid Mech* 37(4):643
- Karpowicz M, Ejsmont–Karabin J (2017) Effect of metalimnetic gradient on phytoplankton and zooplankton (Rotifera, Crustacea) communities in different trophic conditions. *Environ Monit Assess* 189(8):367
- Ljungemyr P (1996) Parameterization of lake thermodynamics in a high-resolution weather forecasting model/P. Ljungemyr, N. Gustafsson, A. Omstedt. *Tellus A* 48:608–621
- Long Z (2007) Northern Lake impacts on local seasonal climate/Z. Long, W. Perrie, J. Gyakum, D. Caya, R. Laprise. *J Hydrometeorol* 8(4):881–896
- Lykosov VN (1992) About the problem of closing the turbulent boundary layer models with the help of the equations for the turbulence kinetic energy and its dissipation rate (in Russian). *Izvestia, USSR Academy of Sciences, V. N. Lykosov. Atmos Ocean Phys* 28:696–704
- Mellor CL (1974) A hierarchy of turbulence closure models for planetary boundary layers/C.L. Mellor, T. Yamada. *J Atmos Sci* 31:1791–1806
- Mironov DV (1991) Seasonal changes of temperature and mixing conditions in a lake/Mironov DV, Golosov SD, Zilitinkevich SS, Kreiman KD, Terzhevik AY Modelling air–lake interaction. Physical background. Zilitinkevich SS (ed) Springer, Berlin, pp 74–90
- Mironov DV (2006) Parameterization of lakes in numerical weather prediction: description of a lake model, single-column tests, and implementation into the limited-area NWP model. Mironov DV, Terzhevik A, Beyrich F, Golosov S, Haise E, Kirillin G, Kourzeneva E, Ritter B, Schneider N *Bound. Lay. Meteor.* 2006. Spec. issue. 56p
- Monin AS (1965) Statistical Hydromechanics. Part 1. Under the editorship of G.S. Golitsyn./A.S. Monin, A.M. Yaglom. Moscow: Science, p 640
- Mortikov EV (2016) Numerical simulation of the motion of an ice keel in stratified flow. *Izv Atmos Ocean Phys* 52:108–115
- Mortikov EV (2019) Numerical study of plane Couette flow: turbulence statistics and the structure of pressure–strain correlations/Mortikov EV, Glazunov AV, Lykosov VN *Russ J Num Anal Math Model* 34(2):1–14
- Ostrovsky LA, Troitskaya YI (1987) The model of turbulent transport and the dynamics of turbulence in a stratified shear flow/Izvestiya. *Atmos Ocean Phys* 3:1031–1040
- Schumann U, Gerz T (1995) Turbulent mixing in stably stratified shear flows. *J Appl Meteorol* 34:33–48
- Tranvik LJ (2009) Lakes and reservoirs as regulators of carbon cycling and climate/Tranvik LJ, Downing JA, Cotner JB, Loiselle SA, Striegl RG, Ballatore TJ, Dillon P, Knoll LB, Kutser T et al *Limnology and oceanography* 54, p 2298–2314

Experimental Studies of the Earth Rotation Impact on Tides in the Curvilinear Bays



V. N. Zyryanov  and M. K. Chebanova 

Abstract The paper discusses the Earth rotation impact on the asymmetry of tidal wave evolution in the curvilinear convergent bays with the right bend (against the earth rotation direction) and with the left bend (in the direction of the earth rotation). The laboratory modeling on the rotating setup shows that the effect of the curvature of convergent bays can have an influence on the asymmetry of the right and left bays and the amplitude of the tide in the right bays maybe approximately 1.5 times higher than in the left bays. The asymmetry of the tidal amplitude in the curvilinear convergent bays is explained based on the potential vorticity conservation law, resulting in additional friction and dissipation of the energy of the tidal wave in the left bays in comparison to the right bays.

Keywords Laboratory modeling · Tidal wave · Estuary · Lateral shear stress · Seishes · Curvilinear convergent bays

1 Introduction

In the coastal continental zone, the amplitudes of the tides usually do not exceed 2 m, amplitudes of more than 6 m are observed only in various types of narrow channels: the tops of bays, mouths of rivers, in straits. The largest tidal range on Earth is observed in the Bay of Fundy, located between the Nova Scotia Peninsula and the mainland. The tide amplitude increases from 6 m at the entrance to the bay, reaching a maximum of 18 m in one of the bays at the top of it (Shokal'skii 1959; Greenberg 1983; Tatsusaburo and Spaulding 1984). Significant tides are also observed off the coast of Patagonia in the bays of San Matias and San Jorge (up to 9–12 m), at the mouth of the river Gallegos amplitudes reach 14 m (Shokal'skii 1959). On the east coast of the Atlantic Ocean along the French coast of the English Channel in the

V. N. Zyryanov (✉) · M. K. Chebanova
Institute of Water Problems RAS, Moscow, Russia
e-mail: v.n.zyryanov@yandex.ru

M. K. Chebanova
e-mail: ejek@inbox.ru

Gulf of Saint-Malo tidal amplitudes reach 11–12 m. The amplitude of the maximum syzygy tide in the estuary of r. Severn (Bristol Bay) is 14.6 m. In the seas of Russia, the maximum tides are observed in the Mezen Bay, White Sea, and in the Penzhina Bay of the Sea of Okhotsk. In the Mezen bay the height of the tide is on average 5–7 m (Babkov 1998), the maximum is up to 9 m, in the Penzhina Bay it is up to 14 m (Shokal'skii 1959).

As one can see, most of the bays with record tides are characterized by a funnel-shaped coastline and a decrease in depth towards the top of the bays (see Fig. 1). As shown in Zyryanov and Chebanova (2016), the evolution of a tidal wave in an estuary is influenced by two competing factors—the effect of convergent channel (confusor effect), which amplifies the tide amplitude, and the effect of turbulent friction, which leads to energy dissipation and a decrease in the wave amplitude.

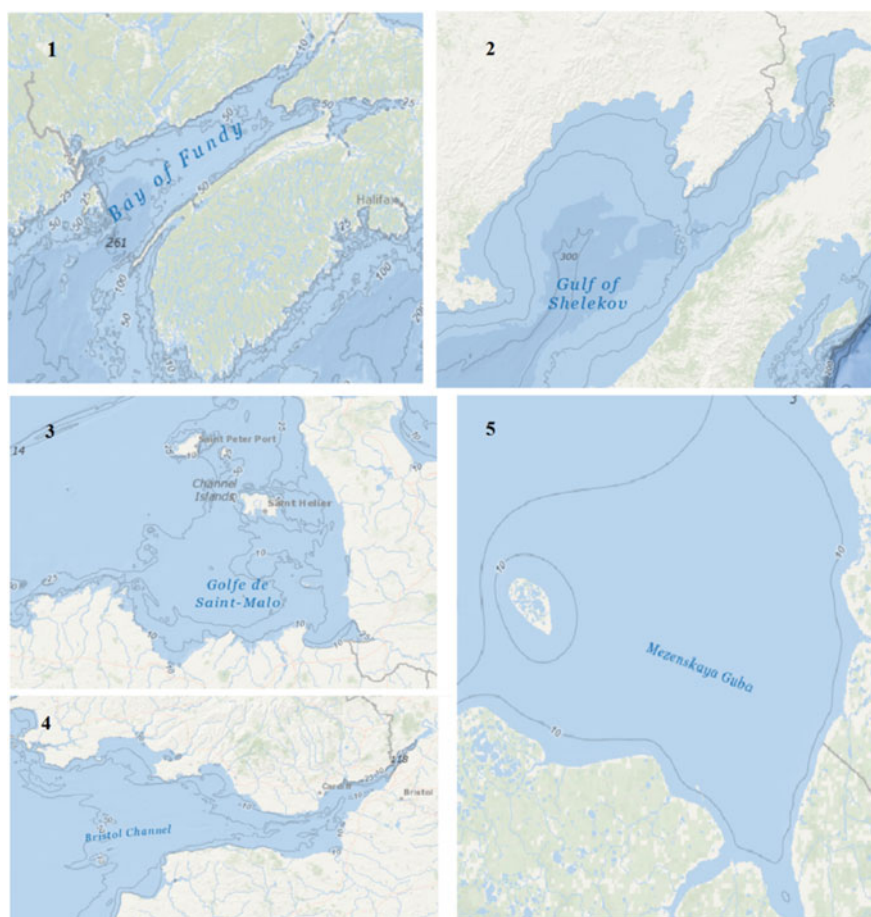


Fig. 1 Gulfs: 1—Fundy [5], 2—Penzhina Bay [5], 3—Gulf of Saint-Malo [5], 4—Bristol Bay [5], 5—Mezen Bay [5]

Most of the bays mentioned above narrow towards the top of the bay, bending at the top to the left (in the direction of the Earth's rotation) or to the right (against the Earth's rotation direction) (see Fig. 1). The Bay of Fundy at its top divides into 2 bays, one of which—Noel Bay—has record tides (Shokal'skii 1959; Greenberg 1983; Tatsusaburo and Spaulding 1984). As seen from the map (Fundy Bay scheme, Fig. 1), Noel Bay refers to the bays with the right bend.

Penzhina Bay, the Mezen and the Bristol Bays also have the right bends, as shown in Fig. 1. Note that the Gulf of Saint-Malo off the coast of France belongs to the left-bend bay.

In Zyryanov and Chebanova (2016) the Earth's rotation is not taken into account. And in this case, the conditions in bays with the left or right bend will be symmetrical. However, a review of the bays with significant tides shows that the majority of the bays with substantial tides have the right bend, i.e. against the rotation of the Earth.

The objective of below studies is to investigate the influence of the Earth's rotation impact on the asymmetry of tidal wave evolution in curvilinear convergent bays with the right bend (against the direction of the Earth's rotation) or with the left bend (in the direction of the Earth's rotation). It is rather difficult to find an analytical solution to this problem; therefore, laboratory experiments are conducted to investigate this effect.

2 Description of the Laboratory Setup

The laboratory setup consists of a cylindrical glass reservoir 1 with a height of 38 cm and a diameter of 30 cm, which is fixed on a rotating platform 2 (Fig. 2). The rotation is carried out by a pulse-driven electromotor 3. On the side of the reservoir a halogen light source 6 is set. The light source illuminates a water column 11. A webcam is attached to the top cover of the reservoir to transfer the image of the fluid motion picture to the computer in real time. On the other side of the rotating platform there is a Sony HDR-PJ580E digital video camera, which is set slightly at an angle to the direction of light. It records level fluctuations. The whole system rotates counterclockwise at a speed of 52 rpm. The rotational speed of the setup is controlled through a computer via the "Arduino" electronic unit 4, which is connected via a USB cable 12. The video image from the webcam is transmitted to the second computer via another USB cable and recorded. Thus, the continuous registration of processes in a rotating water column is carried out in real time both from the top and from the side.

An aluminum semicircle 8 is used to simulate the conditions of the left and right bays. The curvature of the semicircle is slightly greater than the curvature of the side wall of the reservoir. The semicircle is adjacent to the reservoir wall, creating a left bay on the left and a right one on the right (for the top view of the reservoir please see Fig. 3).

A cylindrical wave maker (plunger) 7 is set up to generate waves. It moves up and down with definite frequency under the action of a small electric motor 9. The

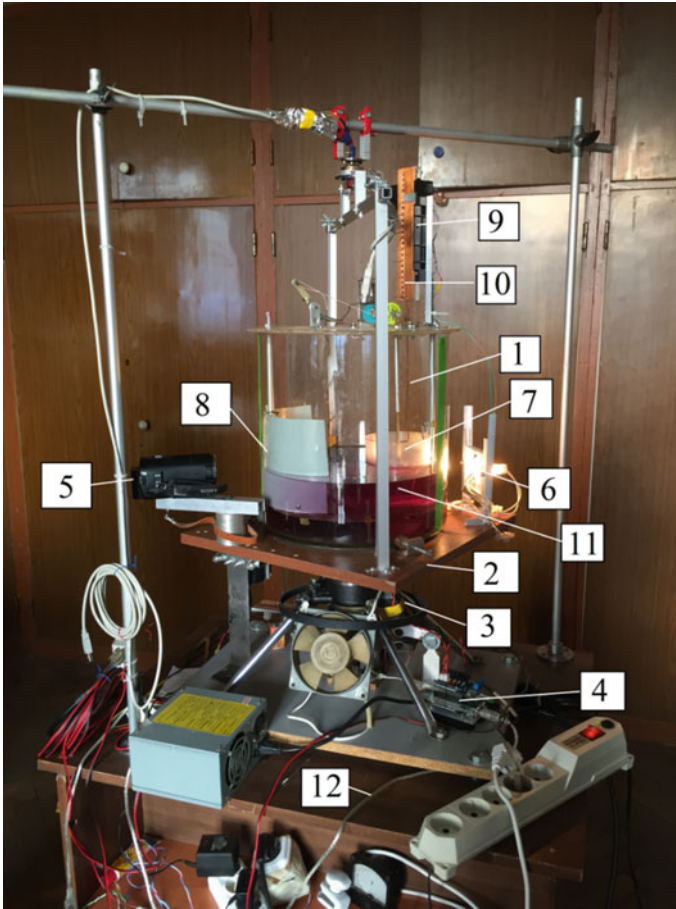


Fig. 2 Photos of the laboratory setup

vertical movement of the plunger is adjusted using contact rail 10, with wire braces soldered at regular intervals. The amplitude and frequency of movement of the wave maker are adjusted by bending the antennae.

1. Glass reservoir;
2. Rotating platform;
3. Electric motor;
4. Arduino electronic unit;
5. Sony camcorder;
6. Halogen lamp;
7. Cylindrical plunger (wave maker);
8. Aluminum semicircle for creating left and right confusers;
9. Motor of the wave maker;

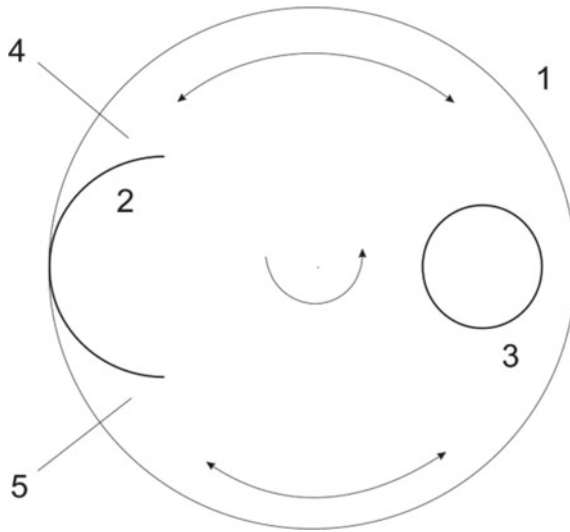


Fig. 3 Scheme of the experimental setup (top view): 1—glass reservoir; 2—aluminum semicircle; 3—cylindrical plunger (wave maker); 4—left confusor; 5—right confusor

- 10. Contact rail for changing the amplitude and frequency of the wave maker;
- 11. Water;
- 12. USB cable to computer

3 Calculation of the Mode of Water Movement in the Experiment

In order to simulate a real situation in nature with diurnal and semi-diurnal tidal waves entering the bay it was necessary to coordinate the periods of rotation of the laboratory setup and the movement of the plunger in the experiment. The period of movement of the plunger is set equal to 0.87 s to match the rotation period of the set up. Thus, the diurnal tidal wave is simulated. The water layer is poured in the reservoir in order to produce the first mode of seiche, which should coincide with the period of rotation of the reservoir. It is necessary to create symmetric conditions for the waves in the left and right bays. Using the Merian formula for the case of a non-rotating fluid, we obtain the value for the water layer:

$$h = \frac{1}{g} \left(\frac{2L}{T} \right)^2, \tag{1}$$

where g is the acceleration of gravity, $L = 29$ cm is the diameter of the can, $T = 0.87$ s is the period of rotation of the reservoir. As a result, we obtain the value of $h = 4.5$ cm for the water layer height.

In fact, this calculation has to be corrected, because the free surface of the water when rotating takes the form of a paraboloid. It is necessary to use the average level of the liquid during rotation in the calculations of the seiche period (1). The free surface curve is expressed by the formula:

$$\zeta(r) = \frac{\omega^2 r^2}{2g}, \quad (2)$$

then, the volume of water above the lower point of the paraboloid will be equal to

$$V = \frac{2\pi\omega^2}{2g} \int_0^{L/2} r^3 dr = \frac{\pi\omega^2}{4g} \left(\frac{L}{2}\right)^4. \quad (3)$$

Dividing the volume (3) by the bottom area of the reservoir, we obtain the expression for the average water level in a paraboloid:

$$h_{av} = \frac{\omega^2}{4g} \left(\frac{L}{2}\right)^2. \quad (4)$$

With a rotation speed of 52 rpm we get $h_{av} = 1.6$ cm.

The photos in Fig. 4 show the fluctuations of the water level in the left and right confusors in the experiment.

Based on the analysis of the Fig. 4, we can conclude that the increase in the amplitude of the tidal wave in the right confusor is substantially larger than in the left one. The range of the level oscillations for the right bay is 2.2 cm (the range of oscillations on the photoshots is 49.4–51.6), for the left one—1.3 cm (49.6–50.9).

4 Discussions

Experiments have shown that the rotation of the Earth contributes to the emergence of the asymmetry of left and right bays in the tidal wave propagation. This asymmetry can be explained based on the potential vorticity conservation law for a rotating fluid.

As known, a potential vortex for a selected vertical volume is preserved when moving in a rotating homogeneous fluid (Zyryanov 1995):

$$\frac{\zeta + f}{H} = \text{const}, \quad (5)$$

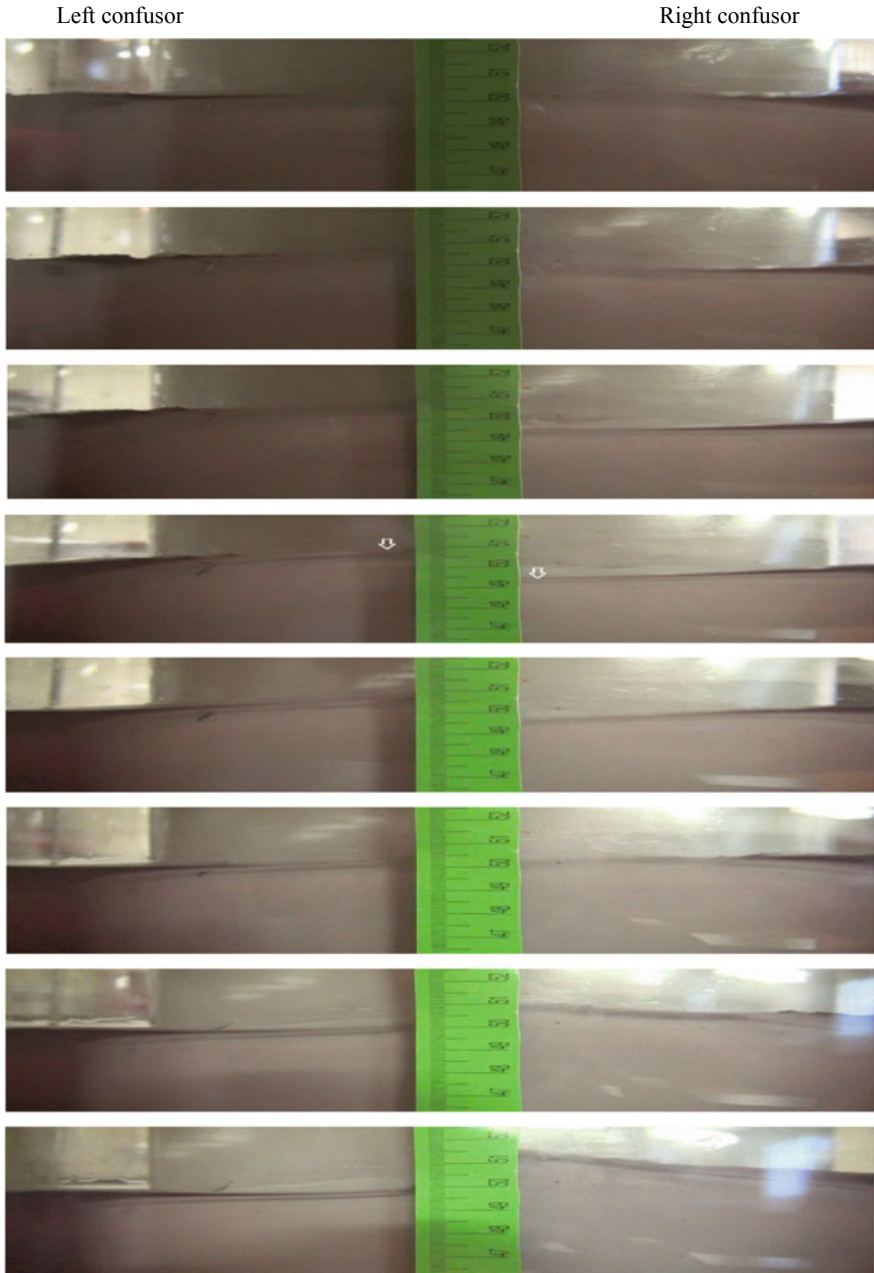


Fig. 4 Photo shots from a video camera; water level positions in the left and right confusors

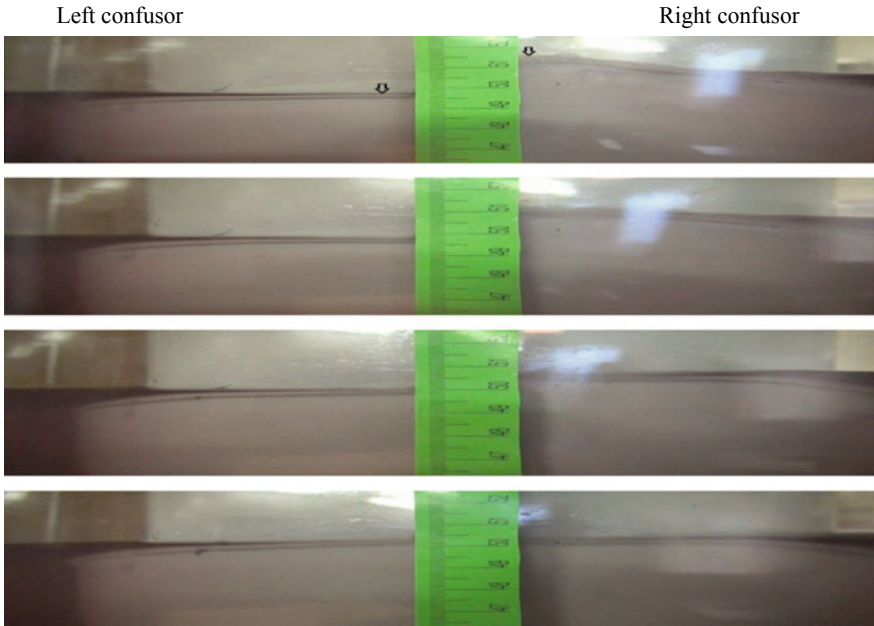


Fig. 4 (continued)

Where ζ is the volume vorticity; $f = 2\Omega \sin \phi$ is the Coriolis parameter; H is the thickness of the water layer.

Let us define a certain water column A in the bay (Fig. 5). When a wave enters the bay, the volume A takes the position B , its height increases by ΔH and acquires the vorticity ζ_2 . Then, from (5) we have

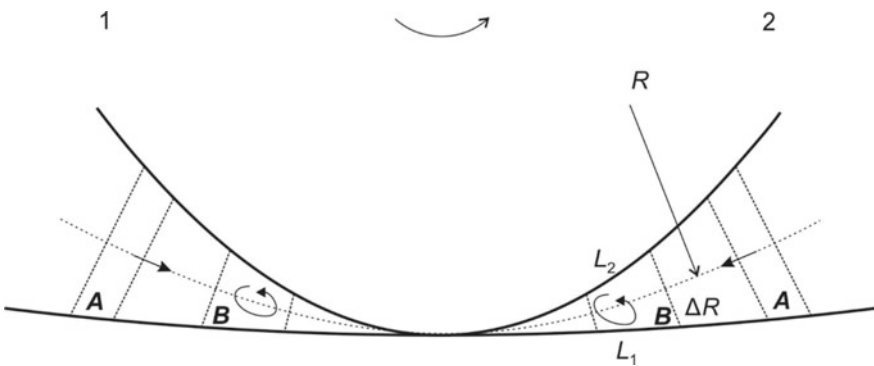


Fig. 5 Emergence of a vortex of a water column in the left (1) and right (2) confusors

$$\frac{\zeta_1 + f}{H} = \frac{\zeta_2 + f}{H + \Delta H}. \tag{6}$$

From (6) it follows

$$\zeta_2 - \zeta_1 = \frac{\zeta_1 + f}{H} \Delta H. \tag{7}$$

Suppose that the initial vorticity of volume A was zero, i.e. $\zeta_1 = 0$. Then, we get from (7) that

$$\zeta_2 = f \frac{\Delta H}{H}. \tag{8}$$

Thus, when the volume of water moves from position A to position B under the action of the tide, the volume acquires a positive vorticity, i.e. counterclockwise in the northern hemisphere and clockwise in the southern.

As a result, when volume A enters the right bay (volume A seems to “roll in” into the bay) the water velocity on the outer shore of the bay will be less than when volume A enters the left bay (Fig. 5). In the left bay, due to the rotation of volume A , the flow velocity on the outer shore of the bay will be greater than in the right one. This causes additional friction and dissipation of the energy of the tidal wave.

Let us make a quantitative assessment. Consider the right bay. Let us draw an axial line and let R be the radius of the axial line curvature in the section from A to B . Then, for the flow velocity along the axial line we can write $U = \omega R$ (Fig. 5), where ω is the angular velocity of the volume B along the axial line. As a result, the flow velocities during the movement of the volume at the boundaries L_1 and L_2 are

$$U_{L_1} = \omega(R + \Delta R), \quad U_{L_2} = \omega(R - \Delta R). \tag{9}$$

The angular velocity Ω of the local rotation of volume B is related to the vorticity $\Delta \xi$ by the Stokes theorem

$$\Omega = \frac{\Delta \xi}{2}. \tag{10}$$

The flow velocity at the boundaries L_1 and L_2 in the volume B rotating with the angular velocity Ω is equal to

$$V = \Omega \cdot \Delta R. \tag{11}$$

As a result, for shear rates at the boundaries L_1 and L_2 we get from (9) and (11)

$$\begin{aligned} \Delta U_{L_1} &= \omega(R + \Delta R) - \Omega \Delta R, \\ \Delta U_{L_2} &= \omega(R - \Delta R) + \Omega \Delta R. \end{aligned} \tag{12}$$

With the use of the quadratic law of friction, we can write for the friction force F_r of volume B in the right bay:

$$F_r = k[(\Delta U_{L_1})^2 L_1 + (\Delta U_{L_2})^2 L_2], \quad (13)$$

where k is the coefficient of friction. Similarly, we obtain for the left bay

$$F_l = k\{[\omega(R + \Delta R) + \Omega \Delta R]^2 L_1 + [\omega(R - \Delta R) - \Omega \Delta R]^2 L_2\}. \quad (14)$$

Subtracting (14) from (13) in view of (12) yields

$$F_r - F_l = -2k\omega\Omega \Delta R [R(L_1 - L_2) + \Delta R(L_1 + L_2)] < 0. \quad (15)$$

The ratio of friction forces is equal to

$$\frac{F_r}{F_l} = \frac{[\omega R + (\omega - \Omega)\Delta R]^2 L_1 + [\omega R - (\omega - \Omega)\Delta R]^2 L_2}{[\omega R + (\omega + \Omega)\Delta R]^2 L_1 + [\omega R - (\omega + \Omega)\Delta R]^2 L_2} < 1. \quad (16)$$

It follows from (15) and (16) that the friction force acting on the volume B in the right bay is less than in the left one.

Substitute the numerical values in (16). To determine ω , let us use the fact that fluid movements in a reservoir occur under the action of the first mode of seiche oscillations, i.e. single node seiche

$$\zeta = \zeta_0 \sin(kr) \sin(\tilde{\omega} t), \quad (17)$$

where $k = \pi/(2R)$, R is the reservoir radius, $\tilde{\omega} = 2\pi/0.87 \text{ sec}^{-1}$ is the frequency of the reservoir rotation and seiche. Differentiating (17) with respect to r and integrating with respect to t , we obtain the expression for the flow velocity

$$U(r) = \frac{g}{\tilde{\omega}} \zeta_0 k \cos(kr) \cos(\tilde{\omega} t), \quad (18)$$

where g is the acceleration of gravity. Substituting into (18) the average amplitude of the level fluctuations at the top of the confusor $\zeta_0 = 0.8 \text{ cm}$ (from the experiment) and $r = 7 \text{ cm}$ (distance from the seiches nodal line to the entrances to confusor), we obtain the value for the velocity $U = 8.5 \text{ cm/s}$. As a result, we have $\omega = 0.77 \text{ s}^{-1}$. It follows from (8), that, with $H = 4.5 \text{ cm}$ and $\Delta H \approx 1 \text{ cm}$, $\Delta \xi = 3.52 \text{ s}^{-1}$. Now we can get $\Omega = 1.76 \text{ s}^{-1}$. Based on the sizes of confusors, we can accept $L_1/L_2 \approx 1.42$, $\Delta R \approx 1.5 \text{ cm}$, $R = 11 \text{ cm}$. Substituting it into (16), we get $F_r/F_l \approx 0.74$, i.e., according to theoretical estimates, friction in the left confusor should be 1.4 times more than in the right. In the experiment, the amplitude of oscillation in the right confusor was 1.5 times greater than the amplitude in the left confusor, i.e. the numbers are quite close and, therefore, it can be assumed that it is friction that causes the asymmetry of left and right bays in tidal wave propagation in nature.

5 Conclusion

Based on the results of laboratory modeling on a rotating setup, it can be concluded that the rotation of the Earth can lead to the asymmetry of left and right bays in the dynamics of tidal waves. Due to the conservation of the potential vorticity, a water column gets the cyclonic vorticity when entering a convergent bay. As a consequence, water column height increases. This results in the lateral shear stress growth in the left bays and its decrease in the right bays. That is why, the dissipation of a tidal energy in the right bays is lower and the amplitude of a tide is higher approximately 1.5 times than that in the left bays.

References

- Babkov AI (1998) Hydrology of White Sea. SPb (in Russian)
- Greenberg D (1983) Modeling the mean barotropic circulation in the Bay of Fundy and Gulf of Maine. *J PhysOceanogr* 13:886–890
- Maps and Geospatial Products. <https://maps.ngdc.noaa.gov>
- Shokal'skii YM (1959) Oceanography. Gidrometeoizdat, Leningrad (in Russian)
- Tatusaburo I, Spaulding ML (1984) A model of the tidally induced residual circulation in the Gulf of Maine and Georges Bank. *J PhysOceanogr* 14:1119–1126
- Zyryanov VN (1995) Topographic eddies in sea current dynamics. Moscow. (in Russian)
- Zyryanov VN, Chebanova MK (2016) Hydrodynamic effects at the entry of tidal waves into estuaries. *Water Res* 43:621–628

Mathematical Modeling of the Dynamics of a Rotating Layer of an Electrically Conducting Fluid with Magnetic Field Diffusion Effects



S. I. Peregudin, E. S. Peregudina, and S. E. Kholodova

Abstract The present paper is concerned with dynamical processes in an electrically conducting rotating incompressible liquid with consideration of the inhomogeneity of density and the magnetic field diffusion effect. By introducing auxiliary functions, the given system of partial differential equations can be reduced to one scalar equation. This in turn suggests the analytic nature of the magnetohydrodynamic characteristics under consideration. In this study, the dissipative effects (the magnetic field diffusion) are taken into account.

Keywords Magnetic hydrodynamics · Hydrodynamics · Wave theory · Electrically conducting liquid · Incompressible liquid · Magnetic field diffusion · Dissipation effects

1 Introduction

The interest in the study of the Earth core continues unabated, because the core has a substantial effect on various Earth geophysical phenomena and global processes that can also be manifested on the Earth surface. Moreover, in a number of cases the existence of the core and its dynamics are known control to a great extent the evolutions of the planet.

Electromagnetic processes occurring in the Earth core are related to various processes in its mantle, and therefore, according to (Braginskii 1967a), the study of the magnetic field is a relevant problem in geophysical studies of the evolution and internal structure of Earth.

S. I. Peregudin (✉)

Saint Petersburg State University, Saint Petersburg, Russia

e-mail: s.peregudin@spbu.ru

E. S. Peregudina

Saint Petersburg Mining University, Saint Petersburg, Russia

S. E. Kholodova

Saint Petersburg ITMO University, Saint Petersburg, Russia

Since the equations describing the magnetohydrodynamic processes in the Earth core are quite involved, a considerable amount of research has been primarily focused on searching solutions to the Maxwell equations for given velocity field distributions. The models in which the motion velocity of a liquid is specified and the magnetic field is the only unknown magnitude are called *kinematic models* for the Earth dynamo. This approach has been extensively studied.

The development of computers has facilitated the search of direct numerical solutions of kinematic dynamo problems for model flows in various geometrics—for example, on a sphere (Busse 2000; Cattaneo and Hughes 1996; Glatzmaier and Roberts 1996a, 1997a; Jones 2000; Leighton 1969; Matthews 1999; Plunian and Radler 2002; Soward 1974; Zheligovsky et al. 2001), in a planar and spherical layer (Serebryanaya and Kropachev 1985; Solov'yov 1985a; Julien et al. 1998; Soward 1988), between two rotating coaxial cylinders (Graeva and Solov'yov 1989; Ruzmaikin et al. 1989; Solov'yov 1985b, c, 1987a, b; 1989; Arnol'd and Korkina 1983; Gibson and Roberts 1967, 1969), and in the space-periodic setting. The best known works in this field are due to (Glatzmaier et al. 1999; Glatzmaier and Roberts 1995a, b, 1996a, b; 1997b, c). The main issue in this approach is that modern supercomputers are capable of calculating 3D kinematic dynamo problems only when the magnetic Reynolds numbers are much smaller than those required in practical astrophysics, in which large magnetic Reynolds numbers are typical. Besides, for the outer Earth core the Ekman number E is of order $10^{-10} - 10^{-15}$, whereas the available computers can deal only with E of order 10^{-4} . For small E , boundary layers appear near the boundaries of the outer layer, whose dynamics cannot be numerically described with sufficient accuracy. Therefore, this suggests the necessity of analytic methods in the mathematical analysis of the problem. Moreover, in the problems under consideration, the Rossby number and the Ekman number are small, and in numerical studies the Rossby number was assumed to be zero and the Ekman number was taken to be small, notwithstanding the fact that the later number is smaller by several orders than the former one. If the Ekman number tends to zero, the models under consideration become numerically unstable.

Among the variety of such kinematic models, of special value is S. I. Braginskii's dynamo [see (Braginskii 1964, 1967b)], because it was constructed for extremely large Reynolds numbers. In dynamo (Braginskii 1964, 1967b) it was shown that the system of iteration equations, which are obtained by expanding in powers of the reciprocal of the square root of the magnetic Reynolds number, has a solution. Later Braginskii (1978) in his dynamo model had interpreted the fluctuating part of the velocity field as Alfvén waves moved by buoyancy force.

In the present study, as distinct from the presently available researches, we consider boundary-value problems of involved topography. We also use the complete system of magnetohydrodynamic equations with due consideration of the inertia forces in motion equations and in which the dissipative effects are taken into account.

2 Statement of the Problem

The aim of the present paper is to reduce the nonlinear system of partial differential equations that simulates perturbations in an ideal electrically conducting rotating liquid with due account of the inertia forces, the gravity forces, the Coriolis and Lorentz forces, and with proper consideration of the available density inhomogeneities.

The results obtained can be used in geophysics and astrophysics, and in particular, in the study of processes occurring in the Earth liquid core and in stellar interiors.

The interest in the Earth core stems from the fact that it has a substantial effect on many geophysical phenomena and processes which did happen or are happening inside Earth and which can be also manifested on its surface. In addition, S. I. Braginskii’s ideas (1987) on the available density stratification of the Earth liquid core, which is responsible in a number of cases for its principal dynamics (which is a relevant factor of the planetary evolution), are of special interest for further analytic research.

So, let us consider the motion of a perfect ideal electrically conducting incompressible stratified rotating liquid. The oscillations of the liquid under consideration are described by the following system of equations [see (Alfvén and Fälthammar 1963; Aleshkov 2001; Gun’ko et al. 2003; Landau and Lifshitz 1984; Shercliff 1967)]:

$$\begin{aligned} \frac{\partial \mathbf{v}}{\partial t} + \langle \mathbf{v}, \nabla \rangle \mathbf{v} &= -\frac{\nabla p}{\rho} - 2[\boldsymbol{\omega}, \mathbf{v}] - g\mathbf{z} + \frac{1}{\mu\rho} [\text{rot } \mathbf{B}, \mathbf{B}], \text{div } \mathbf{v} = 0, \\ \frac{d\rho}{dt} = 0, \frac{\partial \mathbf{B}}{\partial t} &= \text{rot} [\mathbf{v}, \mathbf{B}] + \lambda\Delta\mathbf{B}, \text{div } \mathbf{B} = 0. \end{aligned} \tag{1}$$

Let us investigate the propagation of small perturbations in a conducting medium placed in a homogeneous constant magnetic field \mathbf{b}_0 . We assume that the total magnetic field $\mathbf{B} = \mathbf{b}_0 + \mathbf{b}$ is a superposition of the unperturbed field \mathbf{b}_0 and the field \mathbf{b} induced by the wave motion. We assume that the liquid is stratified along the vertical axis and its density in the unperturbed state depends only on z , i.e., $\rho_0 = \rho_0(z)$ and $\rho(x, y, z, t) = \rho_0(z) + \rho_1(x, y, z, t)$, where $\rho_1(x, y, z, t)$ is the dynamical correction describing the variation of the density due to liquid motions.

Equations (1) for small perturbations \mathbf{b} , ρ , p and \mathbf{v} assume the form

$$\begin{aligned} \frac{\partial \mathbf{v}}{\partial t} + [\boldsymbol{\alpha}, \mathbf{v}] + \frac{\nabla p}{\rho_0} + \frac{g\rho_1}{\rho_0} \mathbf{z} + \frac{1}{\mu\rho_0} [\mathbf{b}_0, \text{rot } \mathbf{b}] &= 0, \text{div } \mathbf{v} = 0, \\ \frac{\partial \rho_1}{\partial t} + \rho'_0(z)\langle \mathbf{v}, \mathbf{z} \rangle = 0, \frac{\partial \mathbf{b}}{\partial z} &= \text{rot} [\mathbf{v}, \mathbf{b}_0] + \lambda\Delta\mathbf{b}, \text{div } \mathbf{b} = 0, \end{aligned} \tag{2}$$

where $\boldsymbol{\alpha} = 2\boldsymbol{\omega}$.

In the first equation of system (2), we transform the last term using the well-known vector identity

$$[\mathbf{b}_0, \text{rot } \mathbf{b}] = [\mathbf{b}_0, [\nabla, \mathbf{b}]] = \nabla \langle \mathbf{b}_0, \mathbf{b} \rangle - \mathbf{b} \langle \mathbf{b}_0, \nabla \rangle = \nabla \langle \mathbf{b}_0, \mathbf{b} \rangle - \langle \mathbf{b}_0, \nabla \rangle \mathbf{b}. \quad (3)$$

A similar transform is applied to the right-hand side of the next-to-last equation in (2):

$$\text{rot}[\mathbf{v}, \mathbf{b}_0] = [\text{rot}, [\mathbf{v}, \mathbf{b}_0]] = \mathbf{v} \langle \nabla, \mathbf{b}_0 \rangle - \mathbf{b}_0 \langle \nabla, \mathbf{v} \rangle = \langle \mathbf{b}_0, \nabla \rangle \mathbf{v}. \quad (4)$$

With the use of transformations (3) and (4), the system of Eqs. (2) is reduced to the system of partial differential equations:

$$\begin{aligned} \frac{\partial \mathbf{v}}{\partial t} + [\boldsymbol{\alpha}, \mathbf{v}] + \frac{1}{\rho_0} \left(\nabla p + \frac{\langle \mathbf{b}_0, \mathbf{b} \rangle}{\mu} \right) + \frac{g \rho_1}{\rho_0} \mathbf{z} - \frac{1}{\mu \rho_0} \langle \mathbf{b}_0, \nabla \rangle \mathbf{b} &= 0, \\ \text{div } \mathbf{v} = 0, \frac{\partial \rho_1}{\partial t} + \rho_0'(z) \langle \mathbf{v}, \mathbf{z} \rangle = 0, \frac{\partial \mathbf{b}}{\partial z} = \langle \mathbf{b}_0, \nabla \rangle \mathbf{v} + \lambda \Delta \mathbf{b}, \text{div } \mathbf{b} &= 0. \end{aligned} \quad (5)$$

Excluding the function $\rho_1(x, y, z, t)$ from the result of time differentiation of the corresponding equations in system (5), we can write the system in the form

$$\begin{aligned} \rho_0 \left(\frac{\partial v_x}{\partial t} - \alpha v_y \right) + \frac{\partial \eta}{\partial x} - \frac{1}{\mu} D b_x = 0, \quad \rho_0 \left(\frac{\partial v_y}{\partial t} - \alpha v_x \right) + \frac{\partial \eta}{\partial y} - \frac{1}{\mu} D b_y = 0, \\ \rho_0 \left(\frac{\partial^2 v_z}{\partial t^2} + \omega_0^2 v_z \right) + \frac{\partial^2 \eta}{\partial t \partial z} - \frac{1}{\mu} D \frac{\partial b_z}{\partial t} = 0, \quad \text{div } \mathbf{b} = 0, \frac{\partial \mathbf{b}}{\partial t} = D \mathbf{v} + \lambda \Delta \mathbf{b}. \end{aligned} \quad (6)$$

In these equations, ω_0^2 is the squared Väisälä–Brunt frequency, $\omega_0^2 = -\frac{g \rho_0'(z)}{\rho_0(z)}$, $\eta = p + \frac{\langle \mathbf{b}_0, \mathbf{b} \rangle}{\mu}$ is the hydromagnetic pressure, is the differential operator.

Let us consider the functions $\tilde{\eta}(x, y, z, t)$, $\tilde{\mathbf{b}}(x, y, z, t)$ defined by

$$\begin{aligned} \eta(x, y, z, t) &= -\rho_0 (D_t^2 + \alpha^2) (D_t^2 + \omega_0^2) \tilde{\eta}(x, y, z, t), \\ \mathbf{b}(x, y, z, t) &= \mu \rho_0 (D_t^2 + \alpha^2) (D_t^2 + \omega_0^2) \tilde{\mathbf{b}}(x, y, z, t), \end{aligned} \quad (7)$$

where $D_t = \partial/\partial t$. It can be shown that the above functions $\tilde{\eta}$ and $\tilde{\mathbf{b}}$ are defined by (7) not uniquely: if the function $\eta_0(x, y, z, t)$ satisfies the first relation in (7), then this relation is also satisfied by the function of the form

$$\begin{aligned} \eta(x, y, z, t) &= \eta_0(x, y, z, t) + \eta_1(x, y, z) \cos \alpha t + \eta_2(x, y, z) \sin \alpha t \\ &+ \eta_3(x, y, z) \cos \omega_0 t + \eta_4(x, y, z) \sin \omega_0 t, \end{aligned} \quad (8)$$

where $\eta_j(x, y, z)$, $j = \overline{1, 4}$, are arbitrary functions. Similarly, the second equality in (7) defines the family of functions $\tilde{\mathbf{b}}(x, y, z, t)$ of the form

$$\begin{aligned} \tilde{\mathbf{b}}(x, y, z, t) &= \tilde{\mathbf{b}}^{(0)}(x, y, z, t) + \tilde{\mathbf{b}}^{(1)}(x, y, z) \cos \alpha t + \tilde{\mathbf{b}}^{(2)}(x, y, z) \sin \alpha t \\ &+ \tilde{\mathbf{b}}^{(3)}(x, y, z) \cos \omega_0 t + \tilde{\mathbf{b}}^{(4)}(x, y, z) \sin \omega_0 t, \end{aligned} \quad (9)$$

where $\mathbf{b}^{(j)}(x, y, z)$, $j = \overline{1, 4}$, are arbitrary functions of their arguments in the domain under consideration.

We further assume that the function $\rho_0(z)$ is exponential, i.e., $\rho_0(z) = A \exp(-\beta z)$, where A and β are positive constants. In this case, $\omega_0^2 = \text{const}$.

Substituting the functions η and \mathbf{b} from (7) into the first and second of (6), we get the equation in matrix form

$$\begin{pmatrix} D_t - \alpha \\ \alpha \quad D_t \end{pmatrix} \begin{pmatrix} v_x \\ v_y \end{pmatrix} = (D_t^2 + \alpha^2) (D_t^2 + \omega_0^2) \begin{pmatrix} \tilde{\eta}_x \\ \tilde{\eta}_y \end{pmatrix} + \left(D + \frac{\rho'_0}{\rho_0} b_{0z} \right) \begin{pmatrix} \tilde{b}_x \\ \tilde{b}_y \end{pmatrix}. \tag{10}$$

Integrating (10), we find that

$$\begin{aligned} \begin{pmatrix} v_x \\ v_y \end{pmatrix} &= (D_t^2 + \omega_0^2) \begin{pmatrix} D_t - \alpha \\ \alpha \quad D_t \end{pmatrix} \begin{pmatrix} \tilde{\eta}_x \\ \tilde{\eta}_y \end{pmatrix} + \left(D + \frac{\rho'_0}{\rho_0} b_{0z} \right) \begin{pmatrix} \tilde{b}_x \\ \tilde{b}_y \end{pmatrix} \\ &+ C_1(x, y, z) \begin{pmatrix} \cos \alpha t \\ \sin \alpha t \end{pmatrix} + C_2(x, y, z) \begin{pmatrix} \sin \alpha t \\ \cos \alpha t \end{pmatrix}, \end{aligned} \tag{11}$$

where $C_1(x, y, z)$ and $C_2(x, y, z)$ are arbitrary functions. Substituting the functions $\tilde{\eta}$ and \tilde{b}_x from (7) and (8) into (11), we get

$$\begin{aligned} \begin{pmatrix} v_x \\ v_y \end{pmatrix} &= (D_t^2 + \omega_0^2) \begin{pmatrix} D_t - \alpha \\ \alpha \quad D_t \end{pmatrix} \left[\begin{pmatrix} \tilde{\eta}_{0x} \\ \tilde{\eta}_{0y} \end{pmatrix} + \left(D + \frac{\rho'_0}{\rho_0} b_{0z} \right) \begin{pmatrix} \tilde{b}_x^{(0)} \\ \tilde{b}_y^{(0)} \end{pmatrix} \right] \\ &+ \left[C_1(x, y, z) + \alpha(\omega_0^2 - \alpha^2) \begin{pmatrix} \frac{\partial \eta_1}{\partial y} + \frac{\partial \eta_2}{\partial x} \end{pmatrix} + \alpha(\omega_0^2 - \alpha^2) \left(D + \frac{\rho'_0}{\rho_0} b_{0z} \right) \right. \\ &\times (b_y^{(1)} + b_x^{(2)}) \left. \begin{pmatrix} \cos \alpha t \\ -\sin \alpha t \end{pmatrix} + [C_2(x, y, z) + \alpha(\omega_0^2 - \alpha^2) \begin{pmatrix} \frac{\partial \eta_2}{\partial y} - \frac{\partial \eta_1}{\partial x} \end{pmatrix} \right. \\ &\left. + \alpha(\omega_0^2 - \alpha^2) \left(D + \frac{\rho'_0}{\rho_0} b_{0z} \right) (b_y^{(2)} - b_x^{(1)}) \right] \begin{pmatrix} \sin \alpha t \\ \cos \alpha t \end{pmatrix}. \end{aligned} \tag{12}$$

Consider a vector $\mathbf{C}(x, y, z) = (C_2(x, y, z), -C_1(x, y, z), 0) \in H_2(\Omega)$, $C_j(x, y, z) \in L_2(\Omega)$, $j = 1, 2$, where $H_2(\Omega)$ is the subspace of the Hilbert space $L_2(\Omega)$ of bounded square integrable vector functions $\mathbf{v} = (v_1, v_2, v_3)$ defined on a bounded domain $\Omega \in R^3$ with piecewise smooth boundaries and having components v_k , $k = \overline{1, 3}$, lying in the Hilbert space of real functions $L_2: H_2(\Omega) = \{ \mathbf{v} \in L_2 : \mathbf{v} = (v_1, v_2, 0) \}$, i.e., $H_2(\Omega)$ is the set of all vector functions $\mathbf{v} \in L_2$ with zero third component.

The following result on representation of vector functions from the subspace $H_2(\Omega)$ is useful in the further analysis.

Theorem (Maurin 1965). *For any $\mathbf{C}(x, y, z) \in H_2(\Omega)$, there exists a pair of functions $\varphi(x, y, z)$, $\psi(x, y, z) \in L_2(\Omega)$ such that $\mathbf{C}(x, y, z) =$*

$(\varphi_x + \psi_y, \varphi_y + \psi_x, 0)$, where $\varphi_x, \varphi_y, \psi_x, \psi_y$ are the partial derivatives of the functions $\varphi(x, y, z)$ and $\psi(x, y, z)$.

Using this theorem and putting

$$\eta_2 = -\frac{\psi(x, y, z)}{\alpha(\omega_0^2 - \alpha^2)}, \quad b_y^{(1)} = -b_x^{(2)}, \quad \eta_1 = \frac{\phi(x, y, z)}{\alpha(\omega_0^2 - \alpha^2)}, \quad b_x^{(1)} = b_y^{(2)}$$

in (12), we find that

$$\begin{pmatrix} v_x \\ v_y \end{pmatrix} = (D_t^2 + \omega_0^2) \begin{pmatrix} D_t & -\alpha \\ \alpha & D_t \end{pmatrix} \begin{bmatrix} \tilde{\eta}_x \\ \tilde{\eta}_y \end{bmatrix} + \left(D + \frac{\rho'_0}{\rho_0} b_{0z} \right) \begin{pmatrix} \tilde{b}_x \\ \tilde{b}_y \end{pmatrix}. \tag{13}$$

Substituting (8) and (9) into the third equation of system (6), this gives

$$(D_t^2 + \omega_0^2)v_z = D_t(D_t^2 + \alpha^2)(D_t^2 + \omega_0^2) \left[\frac{\rho'_0}{\rho_0} \tilde{\eta} + \tilde{\eta}_z + D\tilde{b}_z + \frac{b_{0z}\rho'_0}{\rho_0} b_z \right], \tag{14}$$

Integrating relation (14) with respect to time, we get

$$\begin{aligned} v_z &= D_t(D_t^2 + \alpha^2) \left[\frac{\rho'_0}{\rho_0} \tilde{\eta} + \tilde{\eta}_z + D\tilde{b}_z + \frac{b_{0z}\rho'_0}{\rho_0} b_z \right] \\ &\quad + d_1(x, y, z) \sin \omega_0 t + d_2(x, y, z) \cos \omega_0 t, \end{aligned} \tag{15}$$

where $d_j(x, y, z)$, $j = 1, 2$, are arbitrary functions. Using representations (8) and (9) we can write (15) in the form

$$\begin{aligned} v_z &= D_t(D_t^2 + \alpha^2) \left[\frac{\rho'_0}{\rho_0} \eta_0 + \eta_{0z} + D b_z^{(0)} + \frac{b_{0z}\rho'_0}{\rho_0} b_z^{(0)} \right] + [d_1(x, y, z) + \\ &\quad + \omega_0(\omega_0^2 - \alpha^2) \left(\frac{\rho'_0}{\rho_0} \eta_3 + \eta_{3z} + \left(D + \frac{b_{0z}\rho'_0}{\rho_0} \right) b_z^{(3)} \right)] \sin \omega_0 t + \\ &\quad + [d_2(x, y, z) - \omega_0(\omega_0^2 - \alpha^2) \left(\frac{\rho'_0}{\rho_0} \eta_4 + \eta_{4z} + \left(D + \frac{b_{0z}\rho'_0}{\rho_0} \right) b_z^{(4)} \right)] \cos \omega_0 t. \end{aligned} \tag{16}$$

We choose arbitrary function $\eta_j(x, y, z)$, $b_z^{(j)}$, $j = 3, 4$, so that the expression in the square brackets in (16) would vanish. This can be done by Hörmander’s theorem integration of partial differential equations with constant coefficients in $L_2(\Omega)$ (Maurin 1965; Gabov and Sveshnikov 1990). According to this result, there exist functions $\eta_j(x, y, z)$, $b_z^{(j)} \in L_2(\Omega)$, $j = 3, 4$, which are differentiable with respect to x, y and z and such that

$$\omega_0(\omega_0^2 - \alpha^2) \left(\frac{1}{\rho_0} \frac{\partial}{\partial z} (\rho_0 \eta_j + b_{0z} \rho_0 b_z^{(j)}) + b_{0x} \frac{\partial b_z^{(j)}}{\partial x} + b_{0y} \frac{\partial b_z^{(j)}}{\partial y} \right)$$

$$= (-1)^j d_j(x, y, z), \quad j = 3, 4.$$

With this choice of the functions $\tilde{\eta}$ and \tilde{b}_z , Eq. (16) assumes the form

$$v_z = D_t(D_t^2 + \alpha^2) \left[\frac{\rho'_0}{\rho_0} \tilde{\eta} + \tilde{\eta}_z + D\tilde{b}_z + \frac{b_{0z}\rho'_0}{\rho_0} \tilde{b}_z \right]. \tag{17}$$

Combining (13) and (17), we get in the vector form

$$\begin{aligned} \mathbf{v} = & (D_t^2 + \omega_0^2) \left[D_t \frac{\nabla \rho_0 \tilde{\eta}}{\rho_0} - [\boldsymbol{\alpha}, \nabla \tilde{\eta}] + \left(D + \frac{\rho'_0}{\rho_0} b_{0z} \right) (D_t \tilde{\mathbf{b}} - [\boldsymbol{\alpha}, \tilde{\mathbf{b}}]) \right] \\ & + (\alpha^2 - \omega_0^2) D_t \left[\frac{\rho'_0}{\rho_0} \tilde{\eta} + \tilde{\eta}_t + \left(D + \frac{\rho'_0}{\rho_0} b_{0z} \right) \tilde{b}_z \right] \mathbf{z}. \end{aligned} \tag{18}$$

In view of (18), the equation

$$\frac{\partial \mathbf{b}}{\partial t} = D\mathbf{v} + \lambda \Delta \mathbf{b}$$

assumes the form

$$\begin{pmatrix} \tilde{F} & \alpha Df \\ -\alpha Df & \tilde{F} \end{pmatrix} \begin{pmatrix} \tilde{b}_x \\ \tilde{b}_y \end{pmatrix} = D \begin{pmatrix} D_t & \alpha \\ -\alpha & D_t \end{pmatrix} \begin{pmatrix} \tilde{\eta}_x \\ \tilde{\eta}_y \end{pmatrix}, \tag{19}$$

$$(D_t^2 + \alpha^2) F \tilde{b}_z = D D_t (D_t^2 + \alpha^2) \left[\frac{\rho'_0}{\rho_0} \tilde{\eta} + \tilde{\eta}_z \right], \tag{20}$$

where

$$\tilde{F} = (D_t - \lambda \Delta) \mu \rho_0 (D_t^2 + \alpha^2) - Df D_t,$$

$$F = (D_t - \lambda \Delta) \mu \rho_0 (D_t^2 + \omega_0^2) - D_t \left(D^2 + \frac{\rho'_0}{\rho_0} b_{0z} \right)$$

are differentiation operators.

Introducing in place of the function $\tilde{\eta}$ the function ξ by the formula

$$\begin{aligned} \tilde{\eta} = & (D_t^2 + \alpha^2) \left\{ (D_t - \lambda \Delta) \mu \rho_0 (D_t^2 + \omega_0^2) - D_t \left(D^2 + \frac{\rho'_0}{\rho_0} b_{0z} \right) \right\} \\ & \times \left\{ [(D_t - \lambda \Delta) \mu \rho_0 (D_t^2 + \omega_0^2) - Df D_t]^2 + \alpha^2 D^2 f^2 \right\} \xi, \end{aligned}$$

and integrating Eqs. (19) and (20), we get the following expressions for the magnetic field components:

$$\begin{pmatrix} \tilde{b}_x \\ \tilde{b}_y \end{pmatrix} = \begin{pmatrix} (D_t - \lambda\Delta)\mu\rho_0(D_t^2 + \omega_0^2) - Df D_t & \alpha Df \\ -\alpha Df & (D_t - \lambda\Delta)\mu\rho_0(D_t^2 + \omega_0^2) - Df D_t \end{pmatrix} \\ \times (D_t^2 + \alpha^2)\{(D_t - \lambda\Delta)\mu\rho_0(D_t^2 + \omega_0^2) \\ - D_t(D^2 + \frac{\rho'_0}{\rho_0}b_{0z})\} D \begin{pmatrix} D_t & \alpha \\ -\alpha & D_t \end{pmatrix} \begin{pmatrix} \xi_x \\ \xi_y \end{pmatrix}, \\ \tilde{b}_z = D D_t(D_t^2 + \alpha^2) \{[(D_t - \lambda\Delta)\mu\rho_0(D_t^2 + \omega_0^2) - Df D_t]^2 \\ + (\alpha Df)^2\} \left(\frac{\rho'_0}{\rho_0}\xi + \xi_z\right).$$

Arbitrary functions in the result of integration can be excluded by the above method.

The vector $\tilde{\mathbf{b}}$ is a solution of the system

$$\rho_0 \left(\frac{\partial v_x}{\partial t} - \alpha v_y \right) + \frac{\partial \eta}{\partial x} - \frac{1}{\mu} D b_x = 0, \quad \rho_0 \left(\frac{\partial v_y}{\partial t} + \alpha v_x \right) + \frac{\partial \eta}{\partial y} - \frac{1}{\mu} D b_y = 0, \\ \rho_0 \left(\frac{\partial^2 v_z}{\partial t^2} + \omega_0^2 v_z \right) + \frac{\partial^2 \eta}{\partial t \partial z} - \frac{1}{\mu} D \frac{\partial b_z}{\partial t} = 0, \quad \text{div } \mathbf{b} = 0, \quad \frac{\partial \mathbf{b}}{\partial t} = D \mathbf{v},$$

and hence the solenoidity condition of the magnetic field gives the equation for the function $\tilde{\xi}(x, y, z, t)$:

$$F(\tilde{F} D_t - \alpha^2 Df) \Delta_2 \tilde{\xi} + D_t(\tilde{F}^2 - \alpha^2 D^2 f^2) \left(\frac{\rho'_0}{\rho_0} \tilde{\xi}_z + \tilde{\xi}_{zz} \right) \\ - D_t(D_t^2 + \alpha^2) \mu \lambda \rho_0'' \left(\frac{\rho'_0}{\rho_0} \tilde{\xi} + \tilde{\xi}_z \right) = 0, \quad \xi = D(D_t^2 + \alpha^2) \tilde{\xi}, \quad (21)$$

here $\Delta_2 = \frac{\partial^2}{\partial x^2} + \frac{\partial^2}{\partial y^2}$ is the Laplace operator.

3 Analysis of the Results

The following theorem summarizes the results obtained above.

Theorem Any solution $\mathbf{v}(x, y, z)$, $\mathbf{b}(x, y, z)$, $\eta(x, y, z)$ of the spatial problem on small perturbations of wave motions in the exponentially-stratified electrically conducting rotating liquid with due regard of the diffusion of a sufficiently smooth magnetic field can be written as

$$\eta(x, y, z) = \rho_0 (D_t^2 + \alpha^2) (D_t^2 + \omega_0^2) \tilde{\eta}(x, y, z), \\ \mathbf{b}(x, y, z) = \mu \rho_0 (D_t^2 + \alpha^2) (D_t^2 + \omega_0^2) \mathbf{b}(x, y, z),$$

$$\mathbf{v}(x, y, z, t) = (D_t^2 + \omega_0^2) \left[D_t \frac{\nabla \rho_0 \tilde{\eta}}{\rho_0} - [\boldsymbol{\alpha}, \nabla \tilde{\eta}] + \left(D + \frac{\rho'_0}{\rho_0} b_{0z} \right) (D_t \tilde{\mathbf{b}} - [\boldsymbol{\alpha}, \tilde{\mathbf{b}}]) \right] + (\alpha^2 - \omega_0^2) D_t \left[\frac{\rho'_0}{\rho_0} \tilde{\eta} + \tilde{\eta}_t + \left(D + \frac{\rho'_0}{\rho_0} b_{0z} \right) \tilde{b}_z \right] \mathbf{z},$$

$$\begin{pmatrix} \tilde{b}_x \\ \tilde{b}_y \end{pmatrix} = \begin{pmatrix} (\tilde{F} D_t - \alpha^2 D f) F & \alpha F (\tilde{F} + D f D_t) \\ -\alpha F (\tilde{F} + D f D_t) & (\tilde{F} D_t - \alpha^2 D f) F \end{pmatrix} \begin{pmatrix} \tilde{\xi}_x \\ \tilde{\xi}_y \end{pmatrix},$$

$$\tilde{b}_z = D_t (\tilde{F}^2 + \alpha^2 D^2 f^2) \left(\frac{\rho'_0}{\rho_0} \tilde{\xi} + \tilde{\xi}_z \right), \quad \xi = (D_t^2 + \alpha^2) \tilde{\xi},$$

$$\tilde{\eta}(x, y, z) = (D_t^2 + \alpha^2) F \left\{ [(D_t - \lambda \Delta) \mu \rho_0 (D_t^2 + \alpha^2) - D f D_t]^2 + (\alpha D f)^2 \right\} \xi,$$

$$D_t = \frac{\partial}{\partial t}, \quad D = (\mathbf{b}_0, \nabla), \quad f = D + \frac{\rho'_0}{\rho_0} b_{0z},$$

where the function $\tilde{\xi}$ is the solution of Eq. (21). The density correction is given by the equation

$$\frac{\partial \mathbf{v}}{\partial t} + [\boldsymbol{\alpha}, \mathbf{v}] + \frac{1}{\rho_0} \nabla \left(p + \frac{\langle \mathbf{b}, \mathbf{b}_0 \rangle}{\mu} \right) + \frac{g \rho_1}{\rho_0} \mathbf{z} - \frac{1}{\mu \rho_0} \langle \mathbf{b}_0, \nabla \rangle \mathbf{b} = 0.$$

It can be noted that the reduction for the case of wave motions of nonelectrically conducting incompressible liquid due to oscillations of a planar wall was considered in the paper (Peregudin and Kholodova 2010), and a similar problem for wave motions in a stratified electrically conducting rotating liquid was considered in the paper (Kholodova 2009).

4 Conclusions

In the present study, we investigate processes in a rotating electrically conducting incompressible liquid with due regard of density inhomogeneity and dissipative effects (namely, the magnetic field diffusion effect).

For the corresponding mathematical realization of the dynamical process under study, we reduce the equations of dynamics of spatial wave perturbations in inhomogeneous electrically conducting rotating liquid with magnetic field diffusion effects.

By introduction of auxiliary functions, the above system of partial differential equations can be reduced to a single equation. This in turn suggests the analytic nature of the magnetohydrodynamic characteristics.

The vector system of 3D differential equations of dynamics of incompressible electrically conducting rotating liquid with density inhomogeneity and diffusion

effects in the magnetic field is reduced by appropriate transformations to a scalar equation, whose analysis shows the solvability of all the appearing initial boundary-value problems in the theory of waves in stratified rotating liquids in the magnetic field and which have arbitrary values of electrical conductivity.

References

- Aleshkov YZ (2001) Mathematical modeling of physical processes. St. Petersburg Gos Univ, St. Petersburg (in Russian)
- Alfvén H, Fälthammar C-G (1963) Cosmical electrodynamics. Oxford, Clarendon
- Arnol'd VI, Korkina EI (1983) The growth of a magnetic field in a three-dimensional steady incompressible flow. *Moscow Univ Math Bull* 38(3):50–54
- Braginskii SI (1964) On the self-excitation of a magnetic field by a well conducting moving liquid. *Zh Exp Teor Fiz* 47:1084–1098
- Braginskii SI (1967a) Foundations of the theory of the Earth's hydromagnetic dynamo. *Geomagn. Aeronom.* 7:401–416
- Braginskii SI (1967b) Magnetic waves in the Earth's core. *Geomagn Aeron* 7(6):1051–1060
- Braginskii SI (1978) A nearly axisymmetric model of hydromagnetic dynamo of the Earth. *Geomagn Aeron* 18(2):340–351
- Braginskii SI (1987) Waves in a stably stratified layer on the surface of Earth's core. *Geomagn Aeronomika* 3:476–482
- Busse FH (2000) Homogeneous dynamos in planetary cores and in the laboratory. *Ann Rev Fluid Mech* 32:383–408
- Cattaneo F, Hughes DW (1996) Nonlinear saturation of the turbulent α -effect. *Phys Rev E* 54:R4532–R4535
- Gabov SA, Sveshnikov AG (1990) Linear problems in the theory of time-dependent interior waves. Nauka, Moscow (in Russian)
- Gibson RD, Roberts PH (1967) Some comments on the theory of homogeneous dynamos. In: Hindmarsh WR, Lowes FG, Roberts PH, Runcorn SK (eds) *Magnetism and the cosmos*. Oliver & Boy, Edinburgh, pp 108–120
- Gibson RD, Roberts PH (1969) The bullard gellman dynamo. In: *Application of modern physics to the Earth and planetary interiors*. In: Runcorn SK (ed) Wiley, Interscience, pp 577–601
- Glatzmaier GA, Roberts PH (1995a) A three-dimensional convective dynamo solution with rotating and finitely conducting inner core and mantle. *Phys Earth Planet Inter* 91:63–75
- Glatzmaier GA, Roberts PH (1995b) A three-dimensional self-consistent computer simulation of a geomagnetic field reversal. *Nature* 377:203–209
- Glatzmaier GA, Roberts PH (1996a) Rotations and magnetism of Earth's inner core. *Science* 274:1887–1891
- Glatzmaier GA, Roberts PH (1996b) An anelastic geodynamo simulation driven by compositional and thermal convection. *Physica D* 97:81–94
- Glatzmaier GA, Roberts PH (1997a) Simulating the geodynamo. *Contemp Phys* 38:269–288
- Glatzmaier GA, Roberts PH (1997b) Simulating the geodynamo. *Contemp Phys* 38:269–288
- Glatzmaier GA, Roberts PH (1997c) Computer simulations of the Earth's magnetic field. *Geowissenschaften* 15:95–99
- Glatzmaier GA, Coe RS, Hongre L, Roberts PH (1999) The role of the Earth's mantle in controlling the frequency of geomagnetic reversals. *Nature* 401:885–890
- Graeva EM, Solov'yov AA (1989) Asymptotics of the process of excitation of a magnetic field by Couette-Poiseuille flow in a conductive liquid. In: *Field theory and interpretation algorithms of geophysical data*. Computational seismology, vol 22. Nauka, Moscow, pp 84–92

- Gun'ko YuF, Norin AV, Filippov VB (2003) Electromagnetic Gas Dynamics of Plasma. S.-Peterb. Gos. Univ, St. Petersburg (in Russian)
- Jones CA (2000) Convection-driven geodynamo models. *Phil Trans Roy Soc A* 358:873–898
- Julien K, Knobloch E, Weme J (1998) A new class of equations for rotation-ally constrained flows. *Theor Comput Fluid Dynamics* 11:251–261
- Kholodova SE (2009) Wave motions in a stratified electrically conducting rotating fluid. *Comput Math Math Phys* 49(5):881–886
- Landau LD, Lifshitz EM (1984) *Theoretical physics, Vol. VIII: electrodynamics of continuous Media*. Nauka, Moscow, 1992; Pergamon, New York
- Leighton RB (1969) A magnetic-kinematic model of the Solar cycle. *Astrophys J* 136:1–26
- Matthews PC (1999) Asymptotic solutions for nonlinear magneto convection. *J Fluid Mech* 387:397–409
- Maurin K (1965) *Metody przestrzeni Hilberta*. Paunstwowe Wyd. Naukowe, Warszawa, 1959; Mir, Moscow, 1965
- Peregudin SI, Kholodova SE (2010) The wave motions caused by the oscillations of a flat wall. *Zapiski Gornogo Inst* 187:113–116
- Plunian F, Radler K-H (2002) Harmonic and subharmonic solutions of the Roberts dynamo problem. *Appl Karlsruhe Exp Magnetohydrodynamics* 38:95–106
- Ruzmaikin AA, Sokolov DD, Shukurov AM (1989) *Magnetic fields of galaxies*. Nauka, Moscow (in Russian)
- Serebryanaya PM, Kropachev EP (1985) Kinematic dynamo model in a sphere with partial stratification. *Geomagn, I Aeronomiya* 25(2):289–296
- Shercliff JA (1967) *A textbook of magnetohydrodynamics* (Pergamon, Oxford, 1965. Mir, Moscow
- Solov'yov AA (1985a) Magnetic field excitation by an axisymmetric motion of a conducting liquid. *Izv AN SSSR Fizika Zemli* 4:101–103
- Solov'yov AA (1985b) Description of the parameter range a spiral Couette-Poiseuille flow of conductive liquid for which magnetic field excitation is possible. *Izv AN SSSR Fizika Zemli* 2:40–47
- Solov'yov AA (1985c) Existence of magnetic dynamo for dynamically possible flow of conductive liquid. *DAN SSSR* 282(1):44–48
- Solov'yov AA (1987a) Magnetic field excitation by spiral motion of a conductive liquid. *IFZ AN SSSR, Moscow* (in Russian)
- Solov'yov AA (1987b) Magnetic field excitation by motion of a conductive liquid with large values of the magnetic Reynolds number. *Izv AN SSSR Fizika Zemli* 5:77–80
- Solov'yov AA (1989) Threshold values of the magnetic Reynolds number for excitation of magnetic field. In: *Field theory and interpretation algorithms of geophysical data. computational seismology. vol 22*. Nauka, Moscow, pp 80–83
- Soward AM (1974) A convection driven dynamo I. The weak field case. *Phil Trans Roy Soc Lond A* 275:611–651
- Soward AM (1988) Non-linear marginal convection in a rotating magnetic system. *Geophys Astrophys Fluid Dyn* 44:91–116
- Zheligovsky VA, Podvigina OM, Frisch U (2001) Dynamo effect in parity-invariant flow with large and moderate separation of scales. *Geophys Astrophys Fluid Dyn* 95:227–268

Geomagnetic Diurnal Variation at Mikhnevo Geophysical Observatory



Riabova Svetlana

Abstract In the course of this study, we used the results of geomagnetic field monitoring at the Mikhnevo Geophysical Observatory of Sadovsky Institute of Geosphere Dynamics of Russian Academy of Sciences, Russian Federation, Moscow region, Mikhnevo village (its geographic coordinates are 54.96° N, 37.77° E). It has been established that for all three components the diurnal geomagnetic variations show a similar tendency, that is, two hours before the climax of the Sun, a minimum is observed, and approximately three and a half hours after noon, a maximum is observed. In addition, the time of the beginning of the quiet interval approximately coincides with the time of sunset, and the time of the end of the quiet interval is close to the time of sunrise. The latest beginning of the quiet interval is observed in summer, and the earliest in winter, this result is to some extent predictable, because the start of a quiet interval approximately corresponds to the time of sunset. Spectral analysis of time series of geomagnetic field monitoring demonstrates the presence of variations with periods of 6, 8, 12, and 24 h.

Keywords Diurnal regular variation of geomagnetic field · Sun's position · Day-to-day variability · Periodicity · Ionospheric dynamo currents

1 Introduction

Information about quiet diurnal geomagnetic variations is in demand when we research electrodynamic processes in the high layer of Earth's atmosphere, precursors of volcano and seismic activities, climate change, etc.

Geomagnetic diurnal variations are regular: they are repeated every day in similar way. This phenomenon was first described by Graham (1724), although it is probably known before. In 1722, using compass needle together with microscope, Graham established that during the day the needle changes its position. Moreover, in addition to these slow variations, he found a more rapid irregular change in geomagnetic field.

R. Svetlana (✉)
Sadovsky Institute of Geosphere Dynamics of Russian Academy of Sciences (IDG RAS),
Moscow, Russian Federation
e-mail: ryabovasa@mail.ru

Summing up the results of Graham, he was the first to separate quiet and perturbed diurnal magnetic variations. Now it is well known that quiet magnetic variations are observed in the absence of geoeffective disturbances on the Sun, are strictly periodic in time and are caused by the Earth's daily rotation (solar tides), its orbital motion, the Moon's position relative to the horizon (lunar tides).

The process of air ionization in the upper atmosphere (thermosphere) under the influence of the Sun wave radiation creates a charged layer of the atmosphere (ionosphere) and simultaneously heats the thermosphere, which result in the forming regular large-scale wind systems at solar ion heights (Campbell 1989). These winds cause the conductive medium (ionosphere) to move in the geomagnetic field, which leads to the generation of electric currents at altitudes of 90–150 km (Campbell and Jacobs 1989; Yamazaki et al. 2014). These currents create solar-quiet (Sq -) diurnal variations (Chapman 1919). Under the influence of thermal-tidal and thermospheric winds, electrically charged ions move in the geomagnetic field, as a result of which current vortices form over the northern and southern hemispheres (Riabova 2018). The amplitude of these variations reaches ~50 nT at mid-latitudes, during day at the magnetic equator the amplitude of Sq -variations can increase to 200 nT (equatorial electrojet) (Butcher and Brown 1981).

Researches of solar quiet diurnal geomagnetic variations show that Sq -variation for the current day may differ from ones for the following days not only in amplitude and phase, but also in latitude of Sq -current system focus (Palumbo 1981; Kirchhoff and Carpenter 1976; Hibberd 1981). This variability from day to day is largely due to changes in currents in the field of the dynamo of the ionosphere, which are determined by ionospheric conductivity and tidal winds, which vary depending on solar radiation and ionospheric conditions (Torta 1997; Yamazaki et al. 2011). Solar-diurnal variations differ in that at points with the same latitude they are the same, if the field changes are attributed to local time. During the day, intensity of solar-diurnal variations is greater than at night. Moreover, their amplitude is more in summer period than in winter period.

Today it is cleanly established that in addition to the Sq -variations, the geomagnetic variations which are monitoring at near-surface layer of the Earth's atmosphere also contain lunar spectral components. However Sq -variation is commonly much bigger than such lunar (L) variations (Palumbo 1981). Atmospheric lunar tides affect the current systems of the ionosphere, which lead to L -variations at the Earth's surface (Maeda and Fujiwara 1967; Riabova 2017). Atmospheric lunar tides are caused by the gravitational moon effect on the lower atmosphere, ocean and solid earth (Tarpley 1970; Hollingsworth 1971). The distortions of the Sq -form are caused by the action of secondary currents from coastal ocean currents, heterogeneities of ionospheric conductivity or other regional, high-latitude sources.

The paper presents the results of the analysis of diurnal and seasonal changes in the shape of geomagnetic variations at Mikhnevo Geophysical Observatory of Sadvovskiy Institute of Geosphere Dynamics of the Russian Academy of Sciences. In course of this research, only during quiet solar days the results of geomagnetic monitoring by fluxgate magnetometer LEMI-018 made from 2008 to 2017 are used.

2 Data and Method of Analysis

In this work, as initial data we used the results of geomagnetic monitoring made from 2008 to 2017 at Mikhnevo Geophysical Observatory of Sadovsky Institute of Geosphere Dynamics of Russian Academy of Sciences. The observatory location (its geographic coordinates are 54.96° N; 37.77° E) is south of Moscow region, center of the East European Platform, away from electromagnetic interference (Adushkin et al. 2005; Riabova and Spivak 2019).

The registration of three geomagnetic field components B_x , B_y , and B_z was carried out in a stationary pavilion. The fluxgate LEMI-018 magnetometer which is located in pavilion write geomagnetic variations with discretization of 1 s in geographic coordinate system (X -axis is directed to geographic north, Y -axis is directed to the geographic east, and the Z -axis is directed along the gravity vector). It should be noted that the LEMI-018 is a highly sensitive magnetometer and the results obtained on it are little envied by temperature drift. All data with LEMI-018 magnetometer are passed to the computer by RS-232 interface. Then they enter to the server of Sadovsky Institute of Geosphere Dynamics of the Russian Academy of Sciences. The results of geomagnetic element monitoring are presented in graphical form at website of Sadovsky Institute of Geosphere Dynamics of the Russian Academy of Sciences (Website of Institute of Geosphere Dynamics of Russian Academy of Sciences 2018).

In the study of the daily course of three components of geomagnetic field we used the local time (LT). The discrepancy between the local time (LT) in which the magnetic field is recorded and the global time (UT) is 3 h. We select only magnetically quiet days according to the three-hour geomagnetic K index. For such day one calculated the baseline (average from midnight plus minute values for an hour before and after midnight), Sq amplitude (the difference between values of measured geomagnetic components and the baseline values) of the components. Then we corrected for noncyclic variation (due to the difference values at 12:00 p.m. (LT) from the values at 11:00 p.m. (LT) (Vestine 1947).

Because the magnetic records contained outliers and omissions, the data have been prepared before analyzing. We identified (Pustylnik 1968; Popukaylo 2016) and eliminated of spikes and the filled of omissions by linear interpolation and the double Fourier transform (Kassandrova and Lebedev 1970). When performing such actions we get minute equidistant data for each components of geomagnetic variation.

Thought analysis of daily regular variation, we calculated median, first quartile and third quartile (Sizova 2005). Briefly give their definitions. The median (second quartile) is a value in which exactly half of the elements from the investigated digital series are larger than it, and the other half are smaller. The first quartile is the average value between the smallest value and the median of the investigated digital series and the third quartile is the average value between the median and the largest value of investigated digital series.

In this paper, the spectral characteristics of diurnal geomagnetic variations are studied. One of the methods for spectral analyses a time series is based on the supposition that it is formed by sinusoids and cosine waves of different frequencies (time required to complete a full cycle) and amplitudes (maximum/minimum value during a cycle) (Vasiliev and Shevaldin 2014). Graphically, the results of identification the dominant periods of diurnal geomagnetic field variations are shown as periodograms.

3 Results and Discussion

3.1 Diurnal Variation

As we can see in Fig. 1, the diurnal variation of each element of geomagnetic field has a similar tendency throughout the day for all researched days. Figure 1 shows the overlap of the regular diurnal variation of the geomagnetic field during magnetically quiet days for ten years (from 2008 to 2017). The analysis shows that the

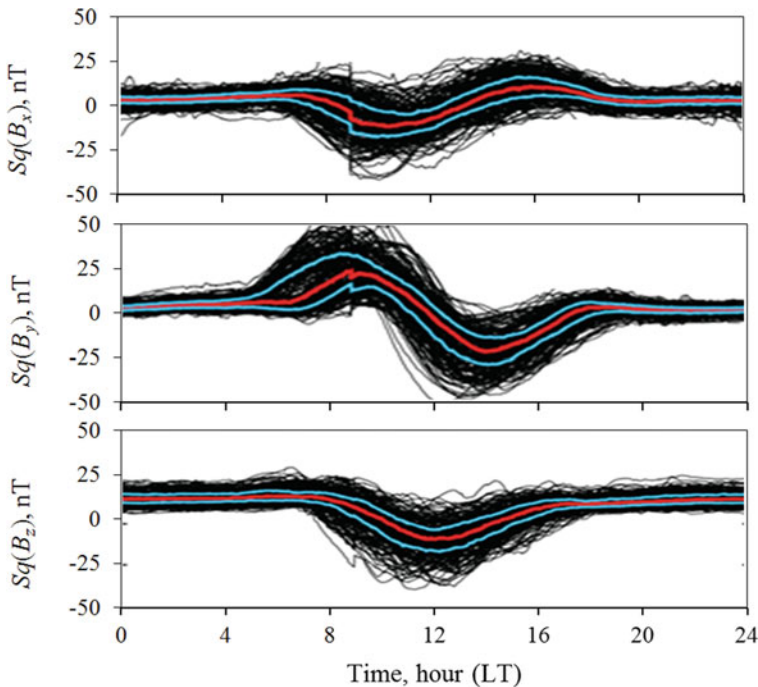


Fig. 1 Diurnal variations of geomagnetic field components at Mikhnevo observatory for magnetically quiet days: B_x (top panel), B_y (middle panel), B_z (bottom panel). The red line is the median (second quartile), the lower blue line is the first quartile, the upper blue line is the third quartile

regular diurnal change in the geomagnetic field at the Mikhnevo Observatory is approximately few tens of nanoteslas.

The minimum value for the northern component B_x of the geomagnetic field is recorded around at 10:00 a.m., and the maximum is recorded at 3:30 p.m., the beginning of the quiet interval is noted at 6:40 p.m., and its end is noted at 07:00 a.m.

If we compare the diurnal variations of the northern component with the change in the Sun's position throughout the day, the minimum will be observed approximately 2 h before the climax of the Sun, and a maximum approximately 3 h after the climax of the sun. In this case, the time-interval between sunset and sunrise is equal to the time interval between the beginning (~6:40 p.m.) and the end of the geomagnetic quiet interval (~7:00 a.m.).

The diurnal regular variation for the eastern component B_y of the geomagnetic field with a minimum at 2:00 p.m. and a maximum at 9:00 a.m. is opposite to the daily variation for the northern component. The start time is 5:00 p.m. and the end of 6:30 a.m. is a quiet interval for the eastern component is approximately the same as for the northern component.

When analyzing the change in the values of the vertical component during the day we obtained that the minimum is observed during the culmination of the Sun around 12:00 a.m., is clearly distinguished, but the maximum could not be identified, the beginning of the quiet interval is at 4:00 p.m., and the end is at 08:00 a.m.

Thus, analysis of the diurnal variation for the three components allow establish that the values of the geomagnetic elements vary with the position of the Sun. However, it should be noted that the time of characteristic points of a regular change of the magnetic field does not fully coincide with the time of changing the position of the Sun during the day (sunrise-culmination-sunset). Basically, the Sq -variation pattern observed according to geomagnetic recording data is approximately similar to the pattern of daily variations of an ideal Sq -current system (Mayaud 1965; Pham Thi Thu et al. 2011).

3.2 Seasonal Variation

In the study of changes in diurnal geomagnetic variations, according to the season during 2008–2017, only for magnetic-quiet days were considered. According to the results of the analysis, their amplitude is bigger in the summer period for all three components of the geomagnetic field. Moreover, in winter period it is significantly less.

Seasonal fluctuations of the geomagnetic field during 2008–2017 are also shown by Table 1, which contains the time of four characteristic points of the diurnal variation, i.e. the time of the minimum, maximum, beginning and end of the quiet interval depending on the season for all three components (B_x , B_y , and B_z). The earliest minimum of the daily variation for the northern component of the geomagnetic field is observed at 09:50 in the summer, the latest minimum is observed at 11:25 a.m.

Table 1 Seasonal variations of characteristic points for three components of the geomagnetic field (from 2008 to 2017)

	Minimum			Maximum			Beginning of the quiet interval			End of the quiet interval		
	B_x	B_y	B_z	B_x	B_y	B_z	B_x	B_y	B_z	B_x	B_y	B_z
Spring	10.6	14.2	11.9	15.5	9	7.4	18.5	17.9	16.6	7.2	6.8	8.2
Summer	9.8	13.7	10.8	15.6	8.4	6.1	18.6	18.7	18.5	6.3	5.2	6.6
Autumn	10.7	13.8	12.4	15.8	9	7.6	18.5	17.7	16.7	7.6	7.7	8.2
Winter	11.4	14.0	12.2	15.8	10.2	7.7	18.0	16.9	15.4	8.8	7.6	8.3

in the winter. Since the magnetic field varies slightly until 3:00 p.m. (it fluctuates around the average annual value), it was not possible to determine the maximum in the winter period.

In all four seasons of the year, the start of the quiet interval is observed at 6:30 p.m., and the earliest end of the quiet interval is observed in the summer at 6:20 a.m., the latest in the winter at 9:00 a.m. For the eastern component, the start of the quiet interval is observed at 5:00 p.m. in the fall and winter (the earliest) and at 6:40 p.m. in the summer (the latest). In the study of the diurnal variation for the vertical component, it was obtained that it is similar to the diurnal variation for the eastern component. At the same time, the start and the end of the quiet interval begin at about the same time in autumn and winter, and they are observed at 4:40 p.m. and 8:10 a.m., respectively. The quiet interval begins at the latest time (6:30 p.m.) and ends first of all (6:40 a.m.) in the summer.

To sum up, for all three geomagnetic components (B_x , B_y , and B_z) quiet interval is shorter in summer and longer in winter. Seasonally changes in the Earth's ionospheric current systems cause changes in the position of the maximum and minimum in seasonal variations of geomagnetic field, in which seasonal variations of maximum and minimum connection exhibit a similar trend with variations of the current system position (Stening 2008).

3.3 Periodicities of Diurnal Variation

The study of diurnal recordings of geomagnetic monitoring at the Mikhnevo observatory shows that the diurnal variation is formed under the influence of a variety of irregular changes. The diurnal variation is a superposition of spectral harmonics which amplitudes increase with decreasing frequency. The main reason for the appearance of harmonics in the spectrum of geomagnetic variations can presumably be the change in current systems which form and develop in magnetosphere and upper atmosphere.

As an example, Fig. 2 demonstrates the spectral composition of the magnetic registration data at the Mikhnevo observatory for 2014 year. In general, for magnetically quiet days, magnetic records smoothly change with the dominant spectral harmonics of 24, 12, 8, and 6 h, the presence of which is due to the Earth's rotation (Lilley 1975; Campbell 1976), however, spectra can also be present harmonics with both shorter and longer periods in the spectrum. It is worth noting briefly that besides solar components in spectra we observed components of lunar origin. It requires further research on the analysis of the lunar solar tidal influence on the geomagnetic field.

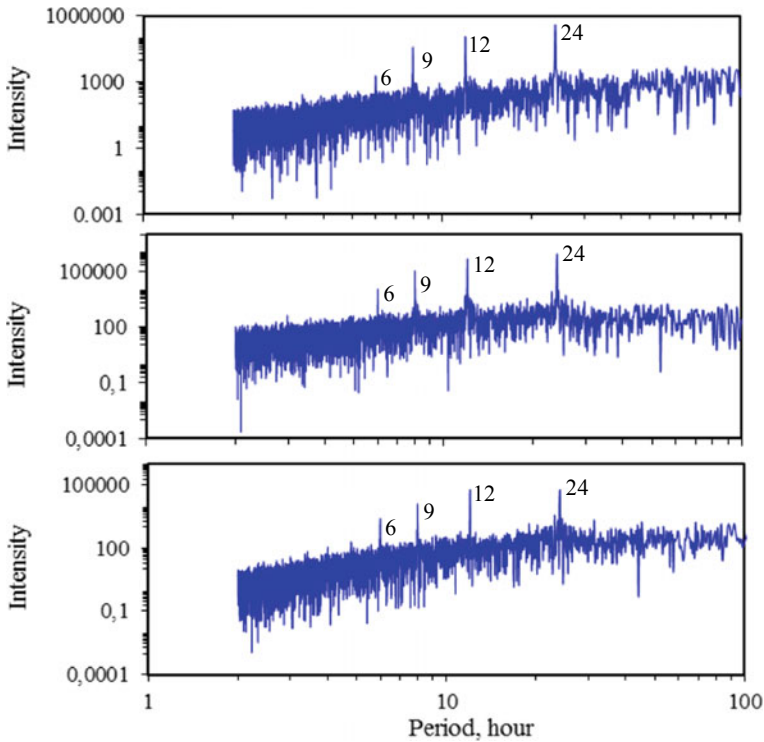


Fig. 2 Periodograms of the average hourly values of the components of geomagnetic field: B_x (top panel), B_y (middle panel), B_z (bottom panel) for 2014 year

4 Conclusion

In this work, diurnal and seasonal variations of results of the geomagnetic monitoring at Mikhnevo observatory which located in mid-latitudes were analyzed.

When we research dynamics of diurnal geomagnetic changes without taking into account the effect of solar activity, only for magnetically quiet days geomagnetic monitoring data was used.

In the course of this study, results were obtained that did not contradict the results of previous studies for middle latitudes (Campbell 1989; Pham Thi Thu et al. 2011). When considering the diurnal variation for all three components of the geomagnetic field, we found that the maximum and minimum of diurnal variation are observed approximately two–three hours before and after the Sun’s climax, and the quiet interval starts after sunset and ends at sunrise.

With regard to seasonal changes, in summer period the amplitude of geomagnetic variation increases, while the quiet interval duration is reduced. Otherwise speaking, the quiet interval ends earlier in the summer that we can explain earlier sunrise. In addition quiet interval lasts longer in winter due to late sunrise. So, the diurnal

variations are due to the movement of current systems above the observation point, which forms mainly from the side of the Earth illuminated by the Sun. It is obvious that changes in the geomagnetic field at middle latitudes, if irregular disturbances in the geomagnetic record are excluded, are mainly associated with changes in the current system.

In the calculated Fourier spectra of all data sets at the Mikhnevo Observatory we can clearly identify the periodicities of geomagnetic regular diurnal variation as separate peaks at 24, 12, 8, and 6 h, corresponding to the Sq -variations and its first three harmonics.

References

- Adushkin VV, Zetser YuI, Gavrilov BG, Sanina IA, Spivak AA (2005) The Mikhnevo observatory measuring system of geophysical fields and processes of the interaction of geospheres, in *Dinamicheskie protsessy v sisteme vnutrennikh i vneshnikh vzaimodeistviyushchikh geosfer* (Dynamical Processes in the System of Inner and Outer Interactions of Geospheres). GEOS, Moscow, 13–18
- Butcher EC, Brown GM (1981) The variability of $Sq(H)$ on normal quiet days. *The Geophys J R Astronomical Soc* 64(2):527–537
- Campbell WH (1976) An analysis of the spectra of geomagnetic variations having periods from 5 min to 4 hours. *J Geophys Res* 81(7):1369–1390
- Campbell WH (1989a) The regular geomagnetic-field variations during quiet solar conditions. In: Jacobs J (ed) *Geomagnetism*, vol 3. Academic Press, San Diego, Calif, USA, pp 386–460
- Campbell WH (1989b) An introduction to quiet daily geomagnetic fields. *Pure Appl Geophys* 131:315–331
- Chapman S (1919) The solar and lunar diurnal variation of the earth magnetism. *Philos Trans R Soc A* 218:1–118
- Graham G (1724) An account of observations made of the variation of horizontal needles at London, in the latter part of the year 1722 and beginning 1723. *Philosophical Transactions of the Royal Society of London A* 33:96–107
- Hibberd FH (1981) Day-to-day variability of the Sq geomagnetic field variation. *Aust J Phys* 34(1):81–90
- Hollingsworth A (1971) The effect of ocean and Earth tides on the semi-diurnal lunar air tide. *J Atmos Sci* 28:1021–1044
- Kassandrova ON, Lebedev VV (1970) Processing the results of observations. Nauka, Moscow
- Kirchhoff VWJH, Carpenter LA (1976) The day-to-day variability in ionospheric fields and currents. *J Geophys Res* 81:2737–2742
- Lilley FEM (1975) The analysis of daily variations recorded by magnetometer arrays. *Geophys J R Astronomical Soc* 43(1):1–16
- Maeda H, Fujiwara M (1967) Lunar ionospheric winds deduced from the dynamo theory of geomagnetic variations. *J Atmos Terr Phys* 29:917–936
- Mayaud PN (1965) Analyse morphologique de la variabilité jour-à-jour de la variation journalière régulière SR du champ magnétique terrestre, II – Le système de courants CM (Régions non-polaires). *Ann Geophys* 21:514–544
- Palumbo A (1981) Lunar and solar daily variations of the geomagnetic field at Italian stations. *J Atmos Terr Phys* 43(7):633–642
- Pham Thi Thu H, Amory-Mazaudier C, Le Huy M (2011) Sq field characteristics at Phu Thuy, Vietnam, during solar cycle 23: comparisons with Sq field in other longitude sectors. *Ann Geophys* 29:1–17

- Popukaylo VS (2016) Detection of abnormal measurements when processing small data. *Technol Des Electron Equipment* 4–5:42–46
- Pustyl'nik EI (1968) *Statistical methods of analysis and processing of observations*. Nauka, Moscow
- Riabova SA (2017) Tidal effects in variations of the geomagnetic field at the Mikhnevo (IDG RAS). In: XXIV international conference of students, graduate students and young scientists in basic sciences “Lomonosov-2017”. Section “Physics”. Physics Department of Moscow State University, Moscow, pp 152–153 (2017).
- Riabova SA (2018) Daily variations of the Earth's magnetic field at the Mikhnevo observatory. XIX Ural Youth Scientific School of Geophysics. IGF UB RAS, Yekaterinburg, pp 146–148
- Riabova SA, Spivak AA (2019) *Geomagnitnye effecty v prizemnom sloe Zemli (Geomagnetic effects in the surface layer of the Earth)*. Grafiteks, Moscow
- Sizova TM (2005) *Statistics: textbook.*: SPb GUITMO, Saint Petersburg
- Stening RJ (2008) The shape of the Sq current system. *Ann Geophys* 26:1767–1775. <https://doi.org/10.5194/angeo-26-1767-2008>
- Tarpley JD (1970) The ionospheric wind dynamo—I: Lunar tide. *Planet Space Sci* 18:1075–1090
- Torta JM (1997) Behavior of the quiet day ionospheric current system in the European region. *J Geophys Res* 102(2):2483–2494
- Vasiliev SN, Shevaldin VT (2014) *Harmonic analysis. M-in education and science Ros. Federations, Urals, Federa. un-t, Yekaterinburg*, Publishing House Ural University
- Vestine E (1947) *The geomagnetic field, its description and analysis*. Carnegie Institute, Washington, DC, USA
- Website of Institute of Geosphere Dynamics of Russian Academy of Sciences, <https://idg.chph.ras.ru/mikhnevo.php>, last accessed 2018/10/21.
- Yamazaki Y, Yumoto K, Cardinal MG, Fraser BJ, Hattori P, Kakinami Y, Liu JY, Lynn KJW, Marshall R, McNamara D, Nagatsuma T, Nikiforov VM, Otadoy RE, Ruhimat M, Shevtsov BM, Shiokawa K, Abe S, Uozumi T, Yoshikawa A (2011) An empirical model of the quiet daily geomagnetic field variation. *J Geophys Res* 116:A10312. <https://doi.org/10.1029/2011JA016487>
- Yamazaki Y, Richmond AD, Maute A, Wu Q, Ortland DA, Yoshikawa A, Adimula IA, Rabiou B, Kunitake M, Tsugawa T (2014) Ground magnetic effects of the equatorial electrojet simulated by the TIE-GCM driven by TIMED satellite data. *J Geophys Res* 119:3150–3161

Modeling of the Extreme Wind Waves in the Gorky Reservoir



E. V. Stolyarova, S. A. Myslenkov, G. A. Baydakov, and A. M. Kuznetsova

Abstract This paper is devoted to the modeling of extreme wind wave parameters in the Gorky Reservoir. The third generation model SWAN version 41.10 is used. The parameters of wind waves calculated on a special unstructured triangulation grid with spatial resolution from 100 m near the coast and up to 700 m in the central part. The constant wind data for several directions with the speed of 15 m/s and duration of 23 h were used in wave modeling. As a result of modeling, significant wave height fields, the average period and the mean wavelength for each of the wind directions were obtained. The parameters of the waves were analyzed under the influence of the wind for 12 and 23 h.

Keywords Gorky Reservoir · Wind waves · Wave simulation · SWAN · Unstructured grid · Wave height

1 Introduction

Many works currently are devoted to the study of wind waves in the seas and oceans using spectral wave models (Myslenkov et al. 2015; Myslenkov and Stolyarova 2016; Van Vledder and Akpinar 2015). However, the problem of hindcast and forecast of waves for small areas is also relevant. Simplified empirical dependencies of waves on wind are usually used to estimate wave heights for small lakes and reservoirs (Stroyizdat 1977). However, due to the intricate topography of the bottom and coastline, such estimates may not be accurate. Previously, the authors have already applied the wave model WAVEWATCH III for the water area of the Gorky Reservoir. Numerical calculations using parameterization of WAM 3, Tolman and Chalikov, and WAM 4

E. V. Stolyarova · S. A. Myslenkov (✉)
Department of Oceanology, Faculty of Geography, Lomonosov Moscow State University,
Moscow, Russia
e-mail: stasocean@gmail.com

G. A. Baydakov · A. M. Kuznetsova
Institute of Applied Physics of the Russian Academy of Sciences, Nizhny Novgorod, Russia

showed an overestimation of the values of wave heights compared with measurements. Based on the results of a field experiment to study the features of wind-wave interaction at fetch-limited cases, the source function was modified for the WAM 3 and Tolman and Chalikov parameterizations, which significantly reduced the difference between the calculated and experimental data. The results of the study and the description of the experiment are described in more detail in (Kuznetsova et al. 2016; Kuznetsova 2016).

In this paper, the wave parameters in the Gorky Reservoir under extreme winds were estimated using the SWAN model on the unstructured grid.

2 Data and Methods

The spectral wave model of the third generation SWAN version 41.10 was chosen to get wave parameters in the Gorky Reservoir. This model was created specifically for calculating wind waves parameters in the coastal zone using the specified fields of wind and currents, bottom topography (Booij et al. 1999). SWAN is developed and distributed by the Delft University of Technology. A comparison of the results of numerical calculations, using this model, with the results of calculations, using other models (WAM and WAVEWATCH III), shows, that the SWAN model has a similar quality of calculations in the deep sea (Abuzarov and Lukin 2013). This model has already been used to simulate waves in several Russian seas and showed good quality of wave modeling results (Myslenkov et al. 2015; Myslenkov and Stolyarova 2016; Myslenkov and Chernyshova 2016; Medvedeva et al. 2015). For the Black Sea, good results were obtained when compared with observations in deep water, the correlation coefficient was 0.85, and the standard deviation was 0.3 m (Myslenkov and Chernyshova 2016).

The SWAN model implements the following processes related to wave propagation: wave propagation in space, refraction and diffraction of waves, wind generation, dissipation due to whitecapping, dissipation due to depth-induced wave breaking; dissipation under friction on the bottom, non-linear interaction of waves with each other both in the deep sea (quadruplets) and in the shallow water (triads) (Booij et al. 1999).

In this work, the parameters of wind waves are calculated on a special unstructured triangulation grid with spatial resolution from 100 m near the coast and up to 700 m in the central part (Fig. 1). The number of nodes in the grid was 14,057 pcs. The grid was created in the program Surface Water Modeling System (SMS Aquaveo). To create a computational grid, 2200 depth points were digitized. Earlier, similar unstructured grids were successfully used to simulate waves in the Black, Baltic and Barents Seas (Myslenkov et al. 2015; Myslenkov and Stolyarova 2016; Myslenkov and Chernyshova 2016; Medvedeva et al. 2015).

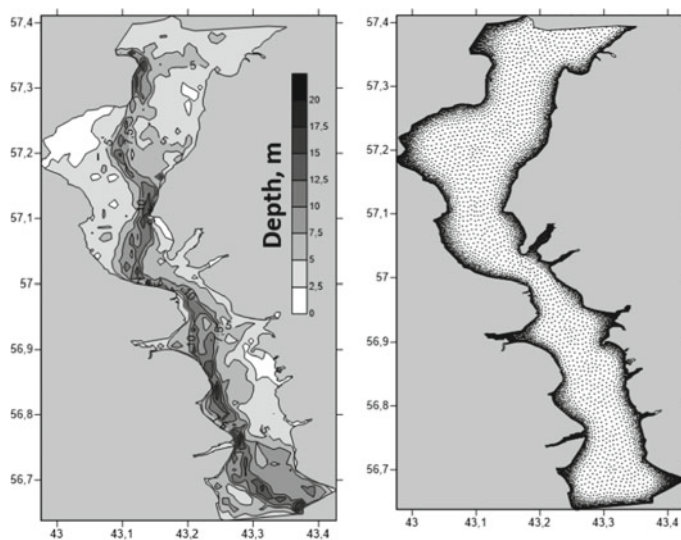


Fig. 1 Special unstructured triangulation grid for the Gorky Reservoir

The constant wind data from all directions (with a step 45°), with a speed of 15 m/s and duration of 23 h were used in wave model. The configuration and parameterization for the SWAN model were used the same as in (Kuznetsova et al. 2016; Kuznetsova 2016).

3 Results

As a result of modeling, significant wave height fields (corresponding to value of the heights of one third of all highest waves), the average period and the mean wavelength for each of the wind directions were obtained. The parameters of the waves were analyzed under the influence of the wind for 12 and 23 h. The results for north wind of 23 h presented in Fig. 2. The maximum significant wave height of 1.2 m is observed in the southern part of the reservoir. The maximum period (3.2 s) and wavelength (15 m) are also observed there. Also, high values are observed in a wide part in the north of the reservoir. It is seen that in a case of short fetch significantly limits the waves growing in the reservoir. It is clear that under the influence of the east or west wind the wave height will be significantly less.

Under the south wind effect (Fig. 3), the maximum wave height (1.1 m) is observed both in the southern and in the northern part of the reservoir. Wind with speeds of 15 m/s during the day is a very extreme event for this region. Therefore, the calculated parameters of the waves can be considered as extreme. It is known that the maximum height of waves can be 1.6 times higher than the significant wave

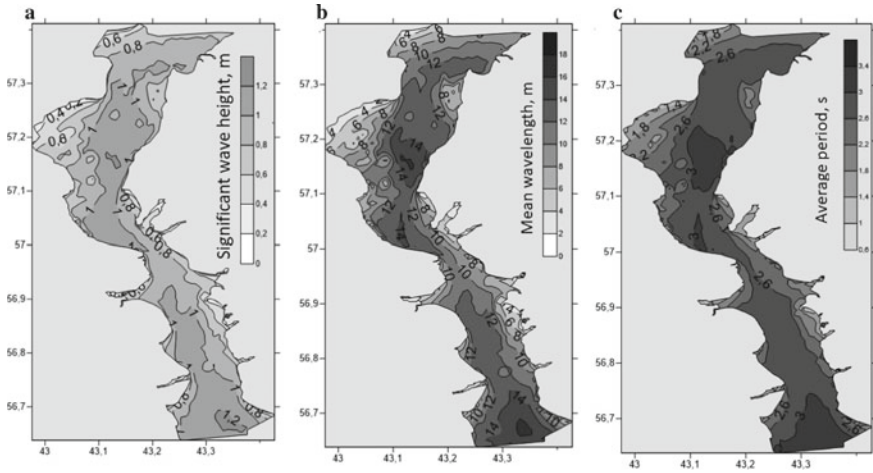


Fig. 2 Significant wave height (a), the mean wavelength (b) and the average period (c) for the north wind (duration 23 h)

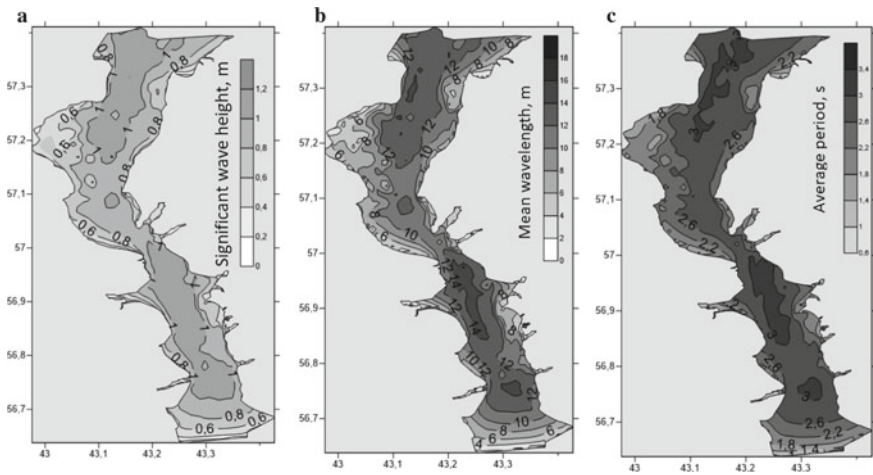


Fig. 3 Significant wave height (a), the mean wavelength (b) and the average period (c) for the south wind (duration 23 h)

height. Consequently, it can be assumed that the maximum height of the waves in the Gorky Reservoir with a constant wind of 15 m/s can reach 2 m. However, this conclusion needs to be checked using wind according to observations or reanalysis.

The significant wave heights were also analyzed under the influence of the wind from the different directions for duration 12 h (Fig. 4). When the wind effect decreases to 12 h, the wave height reaches a maximum of 0.8–0.9 m. With the west and the east wind forcing, areas where the wave height exceeds 0.8 m are very small. The

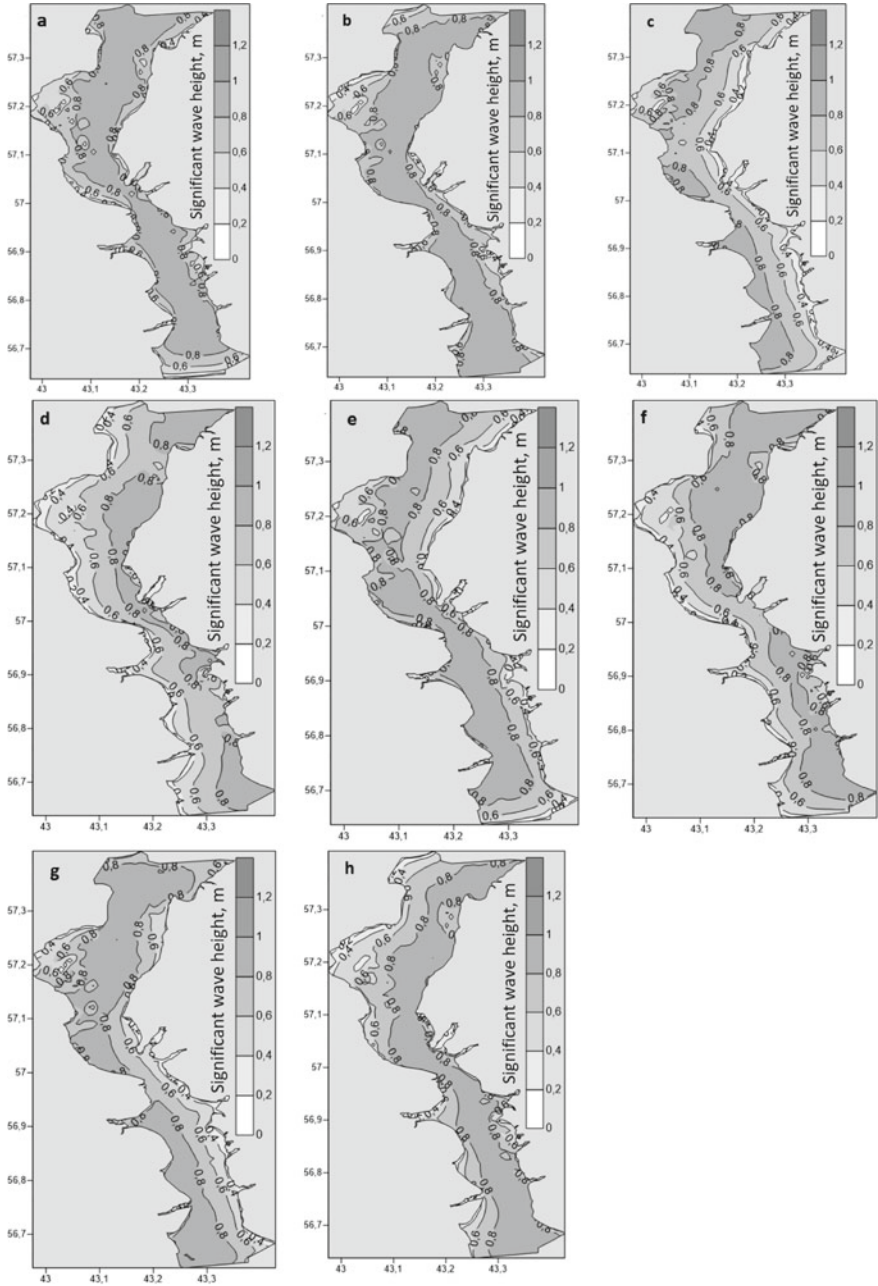


Fig. 4 Significant wave height for the north (a), the south (b), the west (c), the east (d), the north-west (e), the north-east (f), the south-west (g), the south-east (h) winds (duration 12 h)

maps show that both fetch limit and orientation and the intricate configuration of the basin significantly affect the wave propagation. Such maps can be used to estimate wave parameters for different wind directions.

4 Conclusion

Based on the SWAN wave model and an unstructured computational grid, data on extreme wind waves in the Gorky Reservoir were obtained. During the simulation, a constant wind field was used with a speed of 15 m/s for duration up to 23 h.

With a north wind influence for 23 h, the maximum wave height 1.2 m is observed in the southern part of the reservoir, the maximum period is 3.2 s, and the wavelength is 15 m. Under the influence of the south wind, the maximum wave height is 1.1 m and it is observed both in the southern and northern parts of the reservoir.

The wave height reaches a maximum of 0.8–0.9 m when the wind influence from different directions has duration of 12 h. With the west and the east wind, areas where the wave height exceeds 0.8 m are very small.

The maximum wave height in the Gorky Reservoir with a constant wind of 15 m/s can reach 2 m.

The maps show that both fetch limit and orientation and the intricate configuration of the basin significantly affect the wave propagation.

Acknowledgements The work of Baydakov G. A. was supported by RFBR grant 17-05-41117. The work of Kuznetsova A.M. was supported by RFBR grant 18-05-00292.

References

- Abuzarov ZK, Lukin AA, Nesterov ES (2013) Wind wave regime, diagnosis and forecasting oceans and seas: scientific and procedural guide. In: Nesterov ES (ed) *Gidrometeorol. Nauch.-Issled.* Tsentr RF, Moscow (in Russian)
- Booij N, Ris RC, Holthuijsen LH (1999) A third-generation wave model for coastal regions: 1. Model description and validation. *J Geophys Res: Oceans* 104(C4):7649–7666
- Kuznetsova A et al (2016) Adjusting of wind input source term in WAVEWATCH III model for the middle-sized water body on the basis of the field experiment. *Adv Meteorol* 2016:13p. P. Article ID 8539127
- Kuznetsova AM et al (2016) Field and numerical study of the wind-wave regime on the Gorky Reservoir. *Geogr Environ Sustain* 9(2):19–37
- Medvedeva A, Arkhipkin V, Myslenkov S, Zilitinkevich S (2015) Wave climate of the Baltic Sea following the results of the SWAN spectral model application. *Moscow University Bulletin. Series 5. Geography* 1:12–22 ((in Russian with English summary))
- Myslenkov S, Chernyshova A (2016) Comparing wave heights simulated in the Black Sea by the SWAN model with satellite data and direct wave measurements. *Russ J Earth Sci* 16(5):1–12

- Myslenkov SA, Stolyarova EV (2016) Wave forecast for the Black Sea using wind forecasts of different space resolution. In: Proceedings of the Hydrometeorological Scientific Research Center of the Russian Federation 2016. No. 362. S. 55–65. (In Russian with English summary)
- Myslenkov S, Platonov V, Toropov P, Shestakova A (2015) Simulation of storm waves in the Barents Sea. Moscow University Bulletin. Series 5. Geography 6:65–75 ((in Russian with English summary))
- Sroyizdat L (1977) Guidelines for determining the loads and impacts on hydraulic structures (wave, ice and from ships) (In Russian)
- Van Vledder GPh, Akpinar A (2015) Wave model predictions in the Black Sea: sensitivity to wind fields. Appl Ocean Res 53:161–178